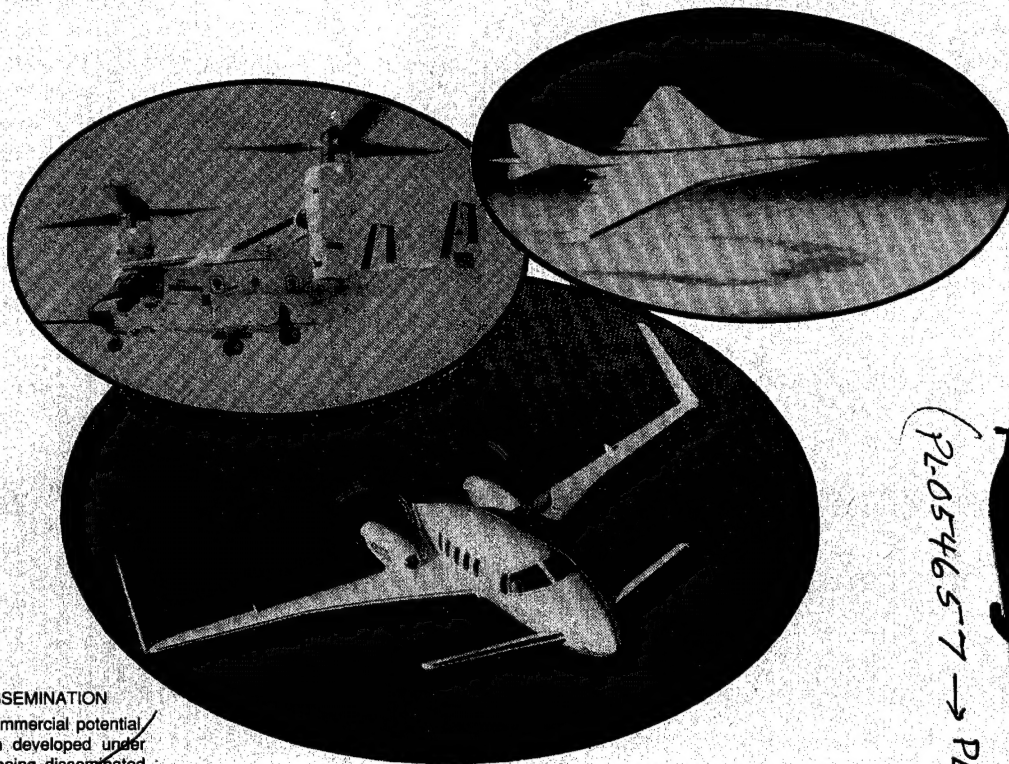


orig ADD 44 3608

(ADD 443609 → ADD 443615) NASA Conference Publication 3087  
Part 1

# Eighth DoD/NASA/FAA Conference on Fibrous Composites in Structural Design

19960628 121



## NOTICE

### FOR EARLY DOMESTIC DISSEMINATION

Because of its significant early commercial potential this information, which has been developed under a U.S. Government program, is being disseminated within the United States in advance of general publication. This information may be duplicated and used by the recipient with the express limitation that it not be published. Release of this information to other domestic parties by the recipient shall be made subject to these limitations.

Foreign release may be made only with prior NASA approval and appropriate export licenses. This legend shall be marked on any reproduction of this information in whole or in part.

Review for general release September 30, 1992

## DISTRIBUTION STATEMENT A

Approved for public release  
Distribution Unlimited

Proceedings of a conference held in  
Norfolk, Virginia  
November 28-30, 1989

DEPARTMENT OF DEFENSE  
PLASTICS TECHNICAL EVALUATION CENTER  
ARDEC PICATINNY ARSENAL, N.J. 07806

5

NASA

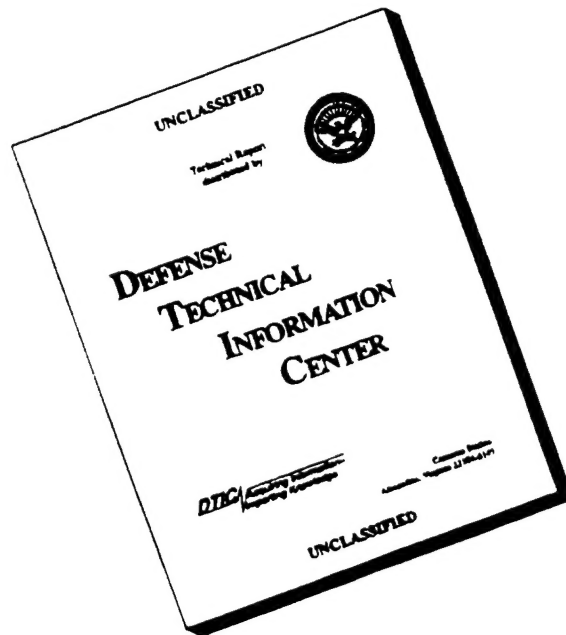
DTIC QUALITY INSPECTED 1

PLASTIC 054656

054656

PL-054656

# DISCLAIMER NOTICE



**THIS DOCUMENT IS BEST QUALITY AVAILABLE. THE COPY FURNISHED TO DTIC CONTAINED A SIGNIFICANT NUMBER OF PAGES WHICH DO NOT REPRODUCE LEGIBLY.**



ADD 44360 8

NASA Conference Publication 3087  
Part 1

# **Eighth DoD/NASA/FAA Conference on Fibrous Composites in Structural Design**

*Compiled by*  
James H. Starnes, Jr.  
*NASA Langley Research Center*  
*Hampton, Virginia*

Herman L. Bohon  
*Lockheed Engineering & Sciences Company*  
*Hampton, Virginia*

Sherry B. Garzon  
*NASA Langley Research Center*  
*Hampton, Virginia*

Proceedings of a conference sponsored by the  
Department of Defense, Washington, D.C., the  
National Aeronautics and Space Administration,  
Washington, D.C., and the Federal Aviation  
Administration, Washington, D.C., and held in  
Norfolk, Virginia  
November 28-30, 1989

**NASA**

National Aeronautics and  
Space Administration

Office of Management

Scientific and Technical  
Information Division

1990

PL-054656

## PREFACE

The Eighth DoD/NASA/FAA Conference on Fibrous Composites in Structural Design is one of a series of conferences jointly sponsored by the National Aeronautics and Space Administration, the U.S. Air Force, the U.S. Army, the U.S. Navy (Department of Defense), and the Federal Aviation Administration. The purpose of this series of conferences is to convene periodically key government and industry research and design engineers to present and discuss the status, problems, and requirements in the technical disciplines related to the design of composite structures. This series of conferences provides a forum for the scientific community to exchange composite structures design information and an opportunity to observe recent progress in composite structures design and technology.

The Eighth DoD/NASA/FAA Conference on Fibrous Composites in Structural Design was held in Norfolk, Virginia during November 28–30, 1989. The conference consisted of 42 presentations by senior managers and experts in the field of composite structures. The conference was organized into six sessions that emphasized perspectives in composites (one session), applications in design (one session), concepts in design (one session), methodology in design (two sessions), and reliability in design (one session). This publication contains the papers presented in the applications in design, methodology in design, and reliability in design sessions of the conference.

*Certain materials are identified in this publication in order to specify adequately which materials were used in the structural design or research efforts. In no case does such identification imply recommendation or endorsement of a product by NASA, DoD, or FAA, nor does it imply that the materials are necessarily the only ones or the best ones available for the purpose. In many cases equivalent materials are available and would probably produce equivalent results.*

The Conference Organizing Committee would like to take this opportunity to thank all the authors and presenters for their outstanding contributions to the conference technical program as well as the conference attendees, whose contributions to the conference discussions helped to make the conference a successful technology exchange forum for current composite structural design issues.

**James H. Starnes, Jr.**  
**Herman L. Bohon**  
**Sherry B. Garzon**

**James H. Starnes, Jr.**  
General Chairman  
NASA Langley Research Center  
Hampton, Virginia

**Herman L. Bohon**  
Technical Chairman  
Lockheed Engineering  
& Sciences Company  
Hampton, Virginia

**Sherry B. Garzon**  
Administrative Assistant  
NASA Langley Research Center  
Hampton, Virginia

### Conference Organizing Committee

James H. Starnes, Jr.  
Thomas E. Hess  
Don W. Oplinger  
J. David Oetting  
Danny E. Good  
Joseph R. Soderquist

NASA Langley Research Center  
Naval Air Development Center  
Army Materials Technology Laboratory  
Wright Research and Development Center  
Army Aviation Applied Technology Directorate  
Federal Aviation Committee

<u>V</u>	9	}	19 in Part 1
<u>VI</u>	10		
<u>VII</u>	11	}	15 in Part 2
<u>VIII</u>	4		



# CONTENTS

PREFACE . . . . .	iii
CONFERENCE ORGANIZING COMMITTEE . . . . .	iv

## Part 1

### **Applications in Design**

Chairman: Dan Good  
Aviation Applied Technology Directorate  
USAARTA (AVSCOM)

<b>Design, Evaluation, and Experimental Effort Toward Development of a High Strain Composite Wing for Navy Aircraft . . . . .</b>	<b>PL-054657</b>	<b>(3)</b>	<b>(01)</b>
Joseph Bruno and Mark Libeskind			
<b>Composite Structural Armor for Combat Vehicle Applications . . . . .</b>	<b>PL-054658</b>	<b>(29)</b>	<b>(02)</b>
Wm. E. Haskell III, A. L. Alesi, and G. R. Parsons			
<b>Applications of Composites to Armaments . . . . .</b>	<b>PL-054659</b>	<b>(49)</b>	<b>(03)</b>
D. W. Oplinger			
<b>The Weight Optimization of an Armored Crashworthy Crewseat Through the Use of Advanced Composites and Design . . . . .</b>	<b>PL-054660</b>	<b>(103)</b>	<b>(04)</b>
Howard A. Lindsay, Stephen M. Motoyama, and Kent F. Smith			
<b>Design, Analysis, and Testing of a Reusable Wingbox for Ballistic Evaluation of Composite Structures . . . . .</b>			<b>119</b>
W. G. Baron and J. D. Oetting			
<b>Development of Composite Wing Carrythrough Bulkheads for Fighter Aircraft . . . . .</b>			<b>131</b>
J. C. Goering, R. S. Behrens, and M. Libeskind			

### **Concepts in Design**

Chairman: Dave Oetting  
Wright Research and Development Center

<b>Braided Composite Bore Evacuator Chambers for Tank Cannons . . . . .</b>	<b>PL-054661</b>	<b>(151)</b>	<b>(05)</b>
Philip C. Wheeler			
<b>The Use of Curvilinear Fiber Format to Improve Buckling Resistance of Plates With Central Circular Holes . . . . .</b>			<b>167</b>
H. H. Lee and M. W. Hyer			
<b>Development of Thermoplastic Components for Structural Validation . . . . .</b>			<b>179</b>
John G. Avery and Gary G. Cassatt			

**A Protection And Detection Surface (PADS) For Damage Tolerance . . . . . 199**  
M. J. Stuart, C. B. Prasad, and S. B. Biggers

**Investigation Into the Fabrication of a Composite Top Attack Recoilless Rifle . . . . . 221**  
Kevin R. Miner

**Structural Assessment of Ultralightweight Composites . . . . . 227 (06)**  
D. M. Kane, M. A. Jankowski, and R. S. Whitehead

**Methodology in Design (A)**  
Chairman: Don Oplinger  
Army Materials Technology Laboratory

**A Curved Beam Test Specimen for Determining the Interlaminar Tensile Strength  
of a Laminated Composite . . . . . 247 (07)**  
Clement C. Hiel, Mark Sumich, and David P. Chappell

**Out of Plane Analysis for Composite Structures . . . . . 263**  
P. C. Paul, C. R. Saff, K. B. Sanger, M. A. Mahler, H. P. Kan, and  
E. F. Kautz

**Global/Local Methods Research Using the CSM Testbed . . . . . 281**  
Norman F. Knight, Jr., Jonathan B. Ransom, O. Hayden Griffin, Jr., and  
Danniella M. Thompson

**Efficient Finite Element Modeling of Laminated Composite Plates Based on  
Higher-Order Theory . . . . . 311**  
Alexander Tessler and Erik Saether

**A New Approximate Fracture Mechanics Analysis Methodology for Composites With a  
Crack or Hole . . . . . 325**  
H. C. Tsai and A. Arocho

**Computational Simulation of Structural Fracture in Fiber Composites . . . . . 355**  
C. C. Chamis and P. L. N. Murthy

**Scaling of Fiber Composite Structures . . . . . 373**  
Todd M. Wieland and John Morton

## **Part 2\***

### **Reliability in Design**

Chairman: Joe Soderquist  
Federal Aviation Administration

<b>Evaluation of Composite Components on the Bell 206L and Sikorsky S-76 Helicopters . . .</b>	<b>393</b>
Donald J. Baker	
<b>Supportability Evaluation of Thermoplastic and Thermoset Composites . . . . .</b>	<b>429</b>
G. R. Chanani, D. Boldi, S. G. Cramer, and M. W. Heimerdinger	
<b>Residual Strength of Repaired Graphite/Epoxy Laminates After Five Years of Outdoor Exposure . . . . .</b>	<b>439</b>
Jerry W. Deaton	
<b>Survivability Characteristics of Composite Compression Structure . . . . .</b>	<b>455</b>
J. Avery, M. R. Allen, D. Sawdy, and S. Avery	
<b>Damage Tolerance Certification Methodology for Composite Structures . . . . .</b>	<b>479</b>
Han Pin Kan, Robin S. Whitehead, and Edward Kautz	
<b>Certification of Damage Tolerant Composite Structure . . . . .</b>	<b>499</b>
Andrew J. Rapoff, Harold D. Dill, Kenneth B. Sanger, and Edward F. Kautz	
<b>Statistically Based Material Properties: a Military Handbook-17 Perspective . . . . .</b>	<b>515</b>
Donald M. Neal and Mark G. Vangel	

### **Methodology in Design (B)**

Chairman: Thomas Hess  
Naval Air Development Center

<b>Compression Behavior of Graphite-Epoxy and Graphite-Thermoplastic Panels With Circular Holes or Impact Damage . . . . .</b>	<b>537</b>
Dawn C. Jegley	
<b>Impact Response of Graphite/Epoxy Fabric Structures . . . . .</b>	<b>559</b>
Paul A. Lagace and Michael J. Kraft	
<b>Postbuckling Behavior of Curved Panels Under Combined Compression and Shear Loads . . . . .</b>	<b>573</b>
Ravi B. Deo, Han Pin Kan, and Narain M. Bhatia	
<b>Postbuckling of Stiffened Composite Plates Under Combined Loading . . . . .</b>	<b>591</b>
Richard K. Kunz	

---

\*Part 2 is presented under separate cover



<b>Initial Postbuckling Response of an Unsymmetrically Laminated Rectangular Plate . . . .</b>	<b>609</b>
Raphael T. Haftka and Eric R. Johnson	
<b>Buckling and Postbuckling Behavior of Square Compression-Loaded Graphite-Epoxy Plates With Circular Cutouts . . . . .</b>	<b>625</b>
Michael P. Nemeth	
<b>A New Approach to Fibrous Composite Laminate Strength Prediction . . . . .</b>	<b>663</b>
L. J. Hart-Smith	
<b>Shear Buckling of Specially Orthotropic Plates With Centrally Located Cutouts . . . . .</b>	<b>695</b>
Vicki L. Owen and Eric C. Klang	

# **PART 1**

## **Applications in Design**

Chairman: Dan Good  
Aviation Applied Technology Directorate  
USAARTA (AVSCOM)

DESIGN, EVALUATION AND EXPERIMENTAL EFFORT TOWARD  
DEVELOPMENT OF A HIGH STRAIN COMPOSITE WING  
FOR NAVY AIRCRAFT

Joseph Bruno  
Grumman Aerospace Corporation  
Bethpage, NY

Mark Libeskind  
Naval Air Development Center  
Warminster, PA

SUMMARY

This design development effort, sponsored by the Naval Air Development Center, addressed significant technical issues concerning the use and benefits of high strain composite wing structures ( $\epsilon_{ult} = 6000$  micro-in/in) for future Navy aircraft.

These issues were concerned primarily with the structural integrity and durability of the novel/innovative design concepts and manufacturing techniques which permitted a 50 percent increase in design ultimate strain level (while maintaining the same fiber/resin system) as well as damage tolerance and survivability requirements. An extensive test effort consisting of a progressive series of coupon and major element tests was an integral part of this development effort, and culminated in the design, fabrication and test of a major full-scale wing box component. The successful completion of the tests demonstrated the structural integrity, durability and benefits of the design. Low energy impact testing followed by fatigue cycling verified the damage tolerance concepts incorporated within the structure. Finally, live fire ballistic testing confirmed the survivability of the design.

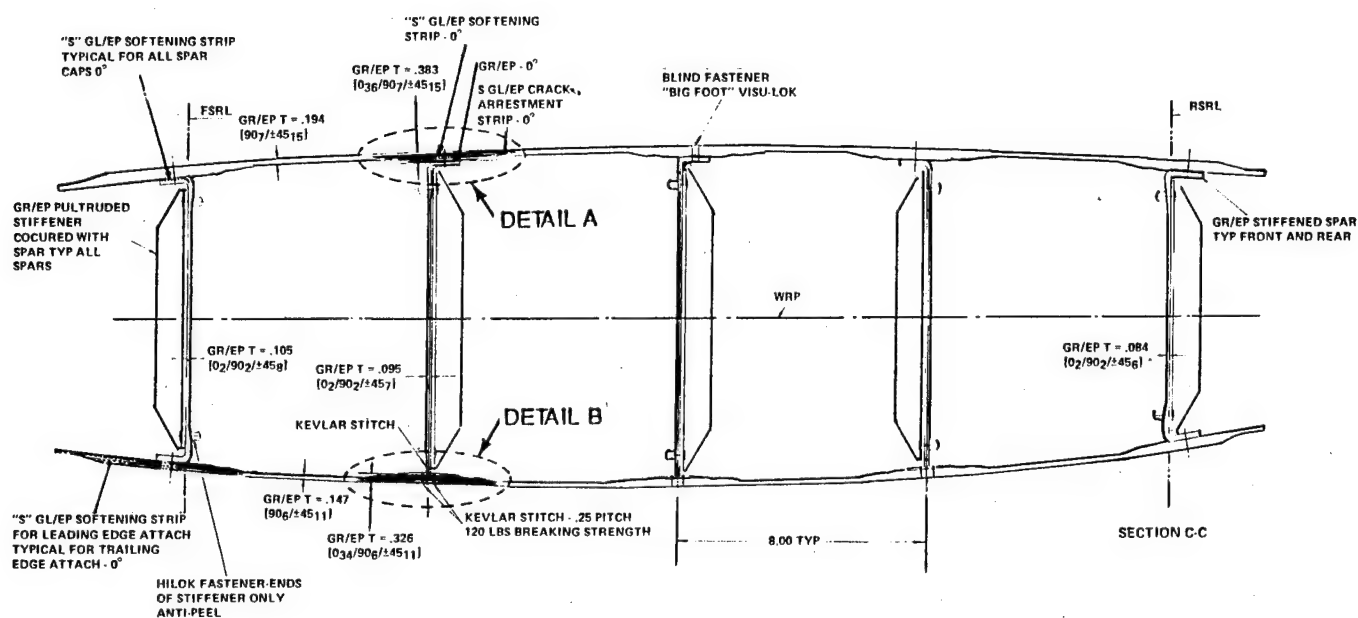
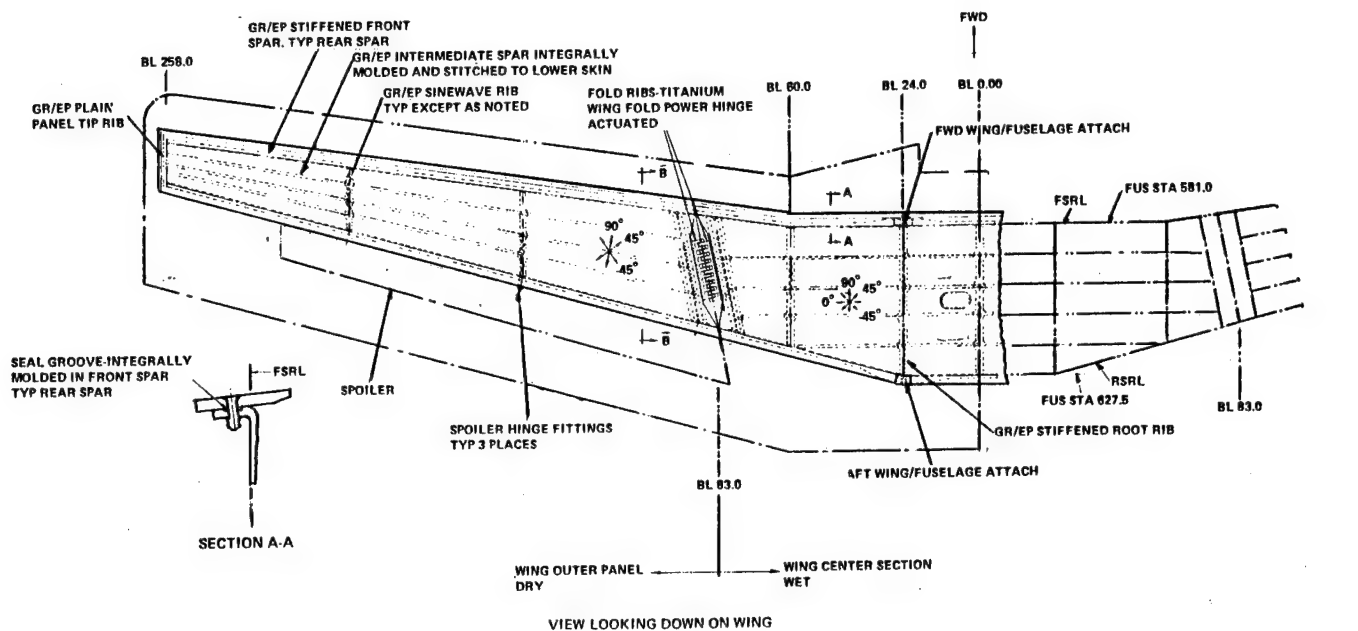
The potential benefits of combining newer/emerging composite materials and new or previously developed high strain wing design to maximize structural efficiency and reduce fabrication costs, was the subject of subsequent preliminary design and experimental evaluation effort.

INTRODUCTION

Polymer matrix composite (PMC) materials have found increasing application in the aerospace industry because of their high strength and stiffness-to-weight ratios and potentially lower unit costs. While weight savings on the order of 15-30 percent have been realized (on a component basis) in first generation applications, PMC structures have not yet met their full potential in terms of weight savings. This has been due in part to conservatism in design as a result of which strain levels have been suppressed to account for reduced performance under hot/wet conditions and the presence of notches and/or damage.

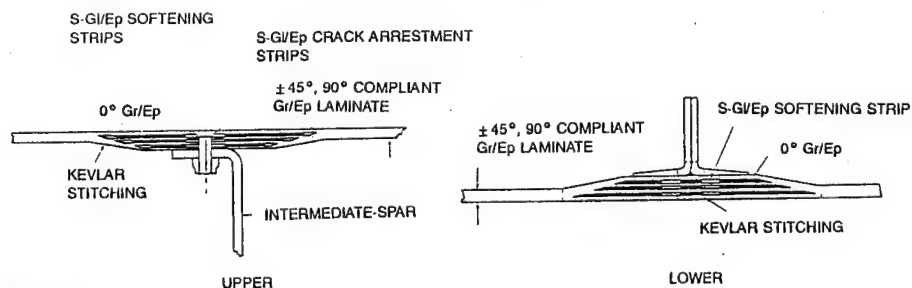
This paper reviews the technology that can lead to improved composite wing structures and associated structural efficiency by increasing design ultimate strain levels beyond their current limit of 3500-4000 micro-in/in to 6000 micro-in/in, through the development of novel and innovative design concepts and manufacturing techniques, while maintaining the same fiber/resin system and without sacrificing structural integrity, durability, damage tolerance, survivability, or repairability. A subsonic patrol multi-mission aircraft was selected as the baseline for this study.





• DETAIL A

• DETAIL B



R89-0547-068

Fig. 1 High Strain Wing Planform & Structural Arrangement

Recently, a number of new PMC material systems with improved fibers and toughened resin systems have been introduced by material suppliers. Compared to existing composite material systems used on operational aircraft, the emerging new/improved composite fibers offer increased strength, stiffness, and higher strain-to-failure in the presence of a notch, while new emerging resin systems (both toughened thermosets and engineered thermoplastics) have increased toughness and improved elevated temperature/wet retention of properties. This paper also covers the potential benefits that can be realized through the combination of newer/emerging fiber composite materials with tougher resin systems and a new and/or previously developed high strain wing design in terms of maximized composite wing structural efficiency and reduced production costs.

The subject design evaluation and experimental effort provided the design data base and "know-how" needed to achieve significant improvement in structural efficiency for weight-critical structures, through exploitation of the maximum capability of existing composite materials and the introduction and use of new and improved composite materials.

#### HIGH STRAIN WING DESIGN DEVELOPMENT

The planform and basic geometry for a Navy subsonic multi-mission type aircraft wing baselined for this effort are shown in Fig. 1. The wing has a span of approximately 44 ft and a fold span of 16 ft, and is sized to allow installation of a conformal radar in the leading and trailing edges. The thickness-to-chord ratio (T/C) is 14 percent at the root and 12 percent at the tip with a maximum depth of 14.4 in. at the centerline. Fuel is carried in the wing box center section from fold-joint to fold-joint. Roll control in conventional flight is provided by spoilers mounted off the rear beam. The vehicle performance goals indicated a need for significant structural weight reductions over the state-of-the-art (SOA) level of composite structural design technology. A 50 percent increase in design ultimate strain level ( $\epsilon_{ult} = 6000$  micro-in/in) to achieve a 20 percent weight reduction goal over a SOA composite wing was needed in part to achieve the vehicle performance goals.

Design criteria established for this effort are presented in Fig. 2. The environmental conditions were established based upon aircraft operating temperatures, mission profiles and typical deployment areas. Damage tolerance requirements are similar to current design requirements, i.e., ultimate load

WEIGHT:	20% WEIGHT REDUCTION FROM CURRENT SOA COMPOSITE DESIGN
STRAIN LEVEL:	6000 MICRO-IN/IN. DESIGN ULTIMATE STRAIN FOR TENSION AND COMPRESSION COVERS
ENVIRONMENTAL CONDITIONS:	160 DEG F AND 1.3% MOISTURE
DAMAGE TOLERANCE:	SUSTAIN DUL AFTER LOW ENERGY IMPACT
SURVIVABILITY:	EXPERIENCE SINGLE HIT BY 23MM HEI PROJECTILE AND RETAIN CAPABILITY TO CARRY DESIGN LIMIT LOAD
MAINTENANCE:	ONE COVER REMOVABLE FOR INSPECTION & REPAIR
FUEL CONTAINMENT:	DESIGNED TO WITHSTAND MAX FUEL PRESSURES; HYDRODYNAMIC RAM EFFECTS CONSIDERED

R89-0547-069

Fig. 2 High Strain Wing Design Criteria

capability with the presence of low energy impact damage (LEID). Survivability considerations required the structure to carry limit load following a single hit from a ballistic projectile and to tolerate hydrodynamic ram effects due to high energy impact. Supportability requirements dictated that one cover be removable for maintenance and repair. This requirement eliminated the use of blind or interference type fasteners from the design. In addition, removable access panels for maintenance of internal wing systems were included in the design. Finally, the wing box is an integral fuel containing structure and was therefore designed to withstand maximum fuel pressures encountered during refueling or flight conditions.

During the initial phase of the program, numerous design concepts and structural configurations with the capability to operate at significantly higher strain levels were generated to identify the maximum weight savings. Design studies were performed on two levels: structural arrangement and structural component geometry. Typical variations in structural arrangement (the quality and location of structural members) included both multi-spar and multi-rib designs as shown in Fig. 3. Certain structural geometries (the physical shapes and proportions of structural system elements) are more efficient than others for a particular type of loading. The various structural geometric configurations investigated for the cover and substructure components are illustrated in Fig. 4 and 5. The optimum cross-sectional area (i.e., least weight, height/width/thickness combination) for each structural configuration was determined so that the various geometric shapes could be compared on a common basis.

The major thrust of the design and trade study effort, however, was the definition of notch strain concentration reduction techniques in the highly strained 0-deg. Gr/Ep plies. Since fastener holes are the most common form of notches in the composite wing design (and therefore one of the major limitations in achieving increased design allowable strains) several design approaches were studied to eliminate the notch sensitivity effects of the fastener holes in the 0-deg Gr/Ep. These techniques, also shown in Fig. 4 and 5, include the utilization of compliant high strain-to-failure laminates with concentrated and unnotched 0-deg plies; use of S-Gl/Ep softening strips to locally replace highly strained 0-deg Gr/Ep plies in those areas affected by a bolt hole; use of Kevlar/epoxy (K/Ep) stitches for cover-to-substructure attachment to reduce significantly the notch concentration effect over that of a standard attachment bolt; integral construction techniques whereby cover and stiffener/substructure elements are integrally cured in a single autoclave operation eliminating bolt holes and their associated notch concentration effects entirely; and cover-to-substructure attachment at reduced box chordal height where strains are lower.

The configuration selected for detail development was a multi-spar wing consisting of five spars outboard of the wingfold, six inboard, and 15 ribs. The basic upper and lower covers are compliant high strain-to-failure Gr/Ep (AS1/3501-5A) laminates consisting of 90 and  $\pm 45$ -deg plies only. The required axial load carrying 0-deg plies are concentrated and banded in discrete caps over the spar supports. The upper cover is attached to the substructure with mechanical fasteners through nut-plates, which satisfies the requirement for cover removal for maintenance and repair. O-rings are used under the heads of the fasteners in the fuel tank area. An S-glass/epoxy (S-Gl/Ep) softening strip locally replaces the 0-deg Gr/Ep plies in the vicinity of the discrete cap affected by the fastener holes, thereby eliminating the resulting strain concentration in the 0-deg Gr/Ep. The lower cover is integrally co-cured and stitched to the intermediate spars, which eliminates mechanical fasteners and associated strain concentrations caused by the holes to accommodate fastener installation. The high tensile strength K/Ep stitches



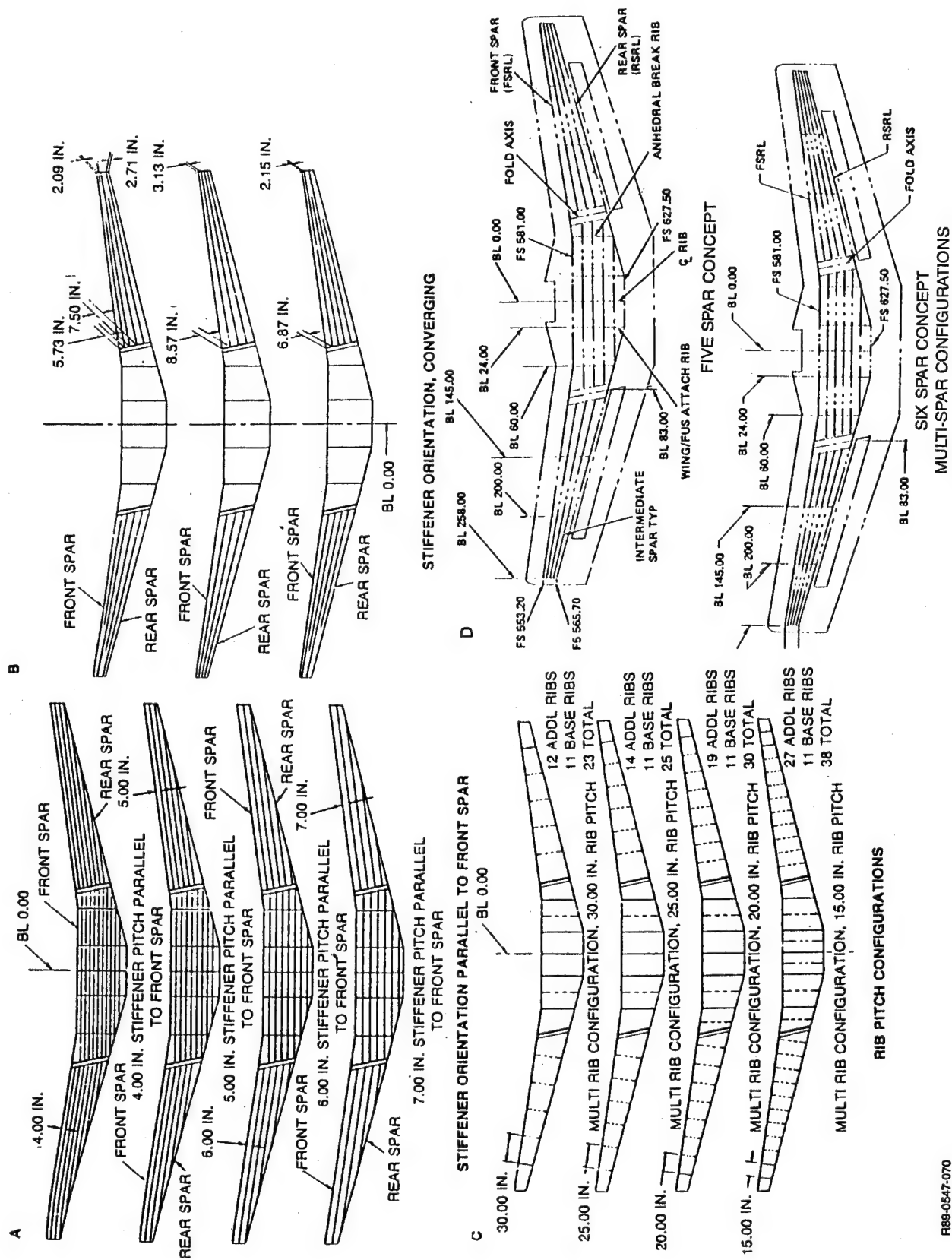
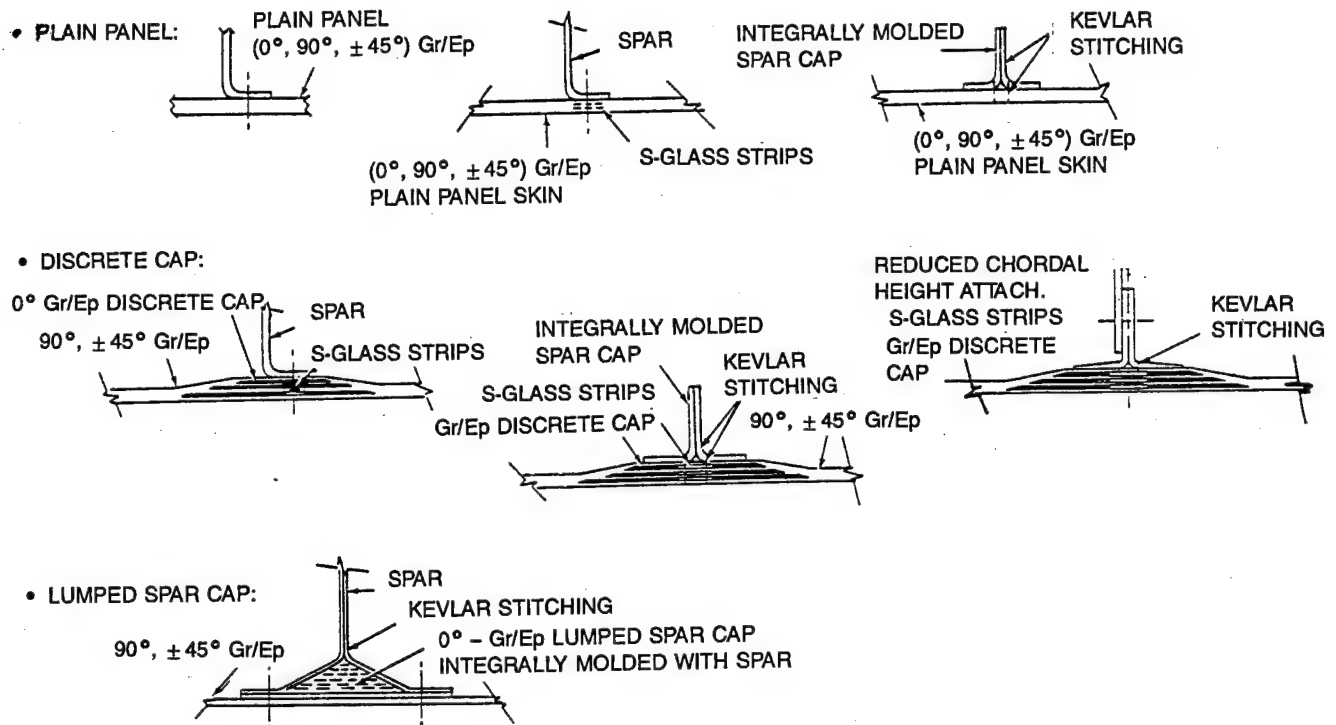


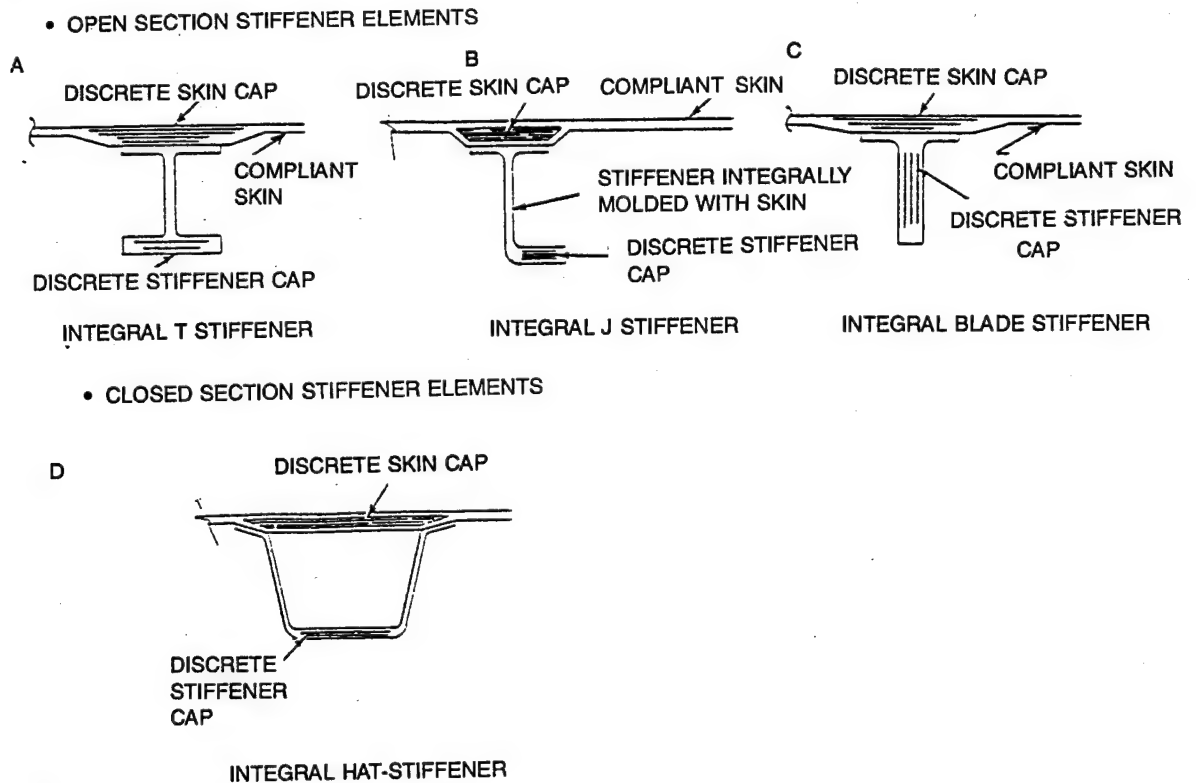
Fig. 3 Typical Structural Arrangement Trades

R89-0547-070

## Multi-Spar Cover Concepts



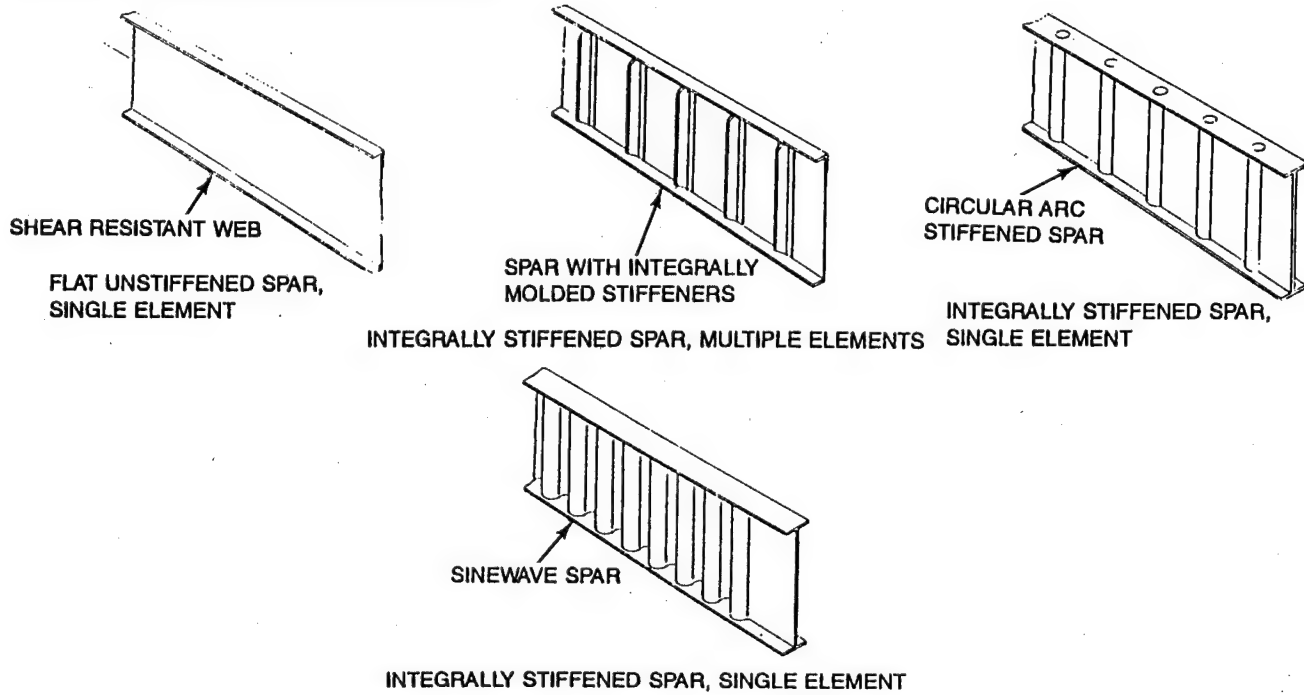
## Multi-Rib Stiffened Cover Concepts



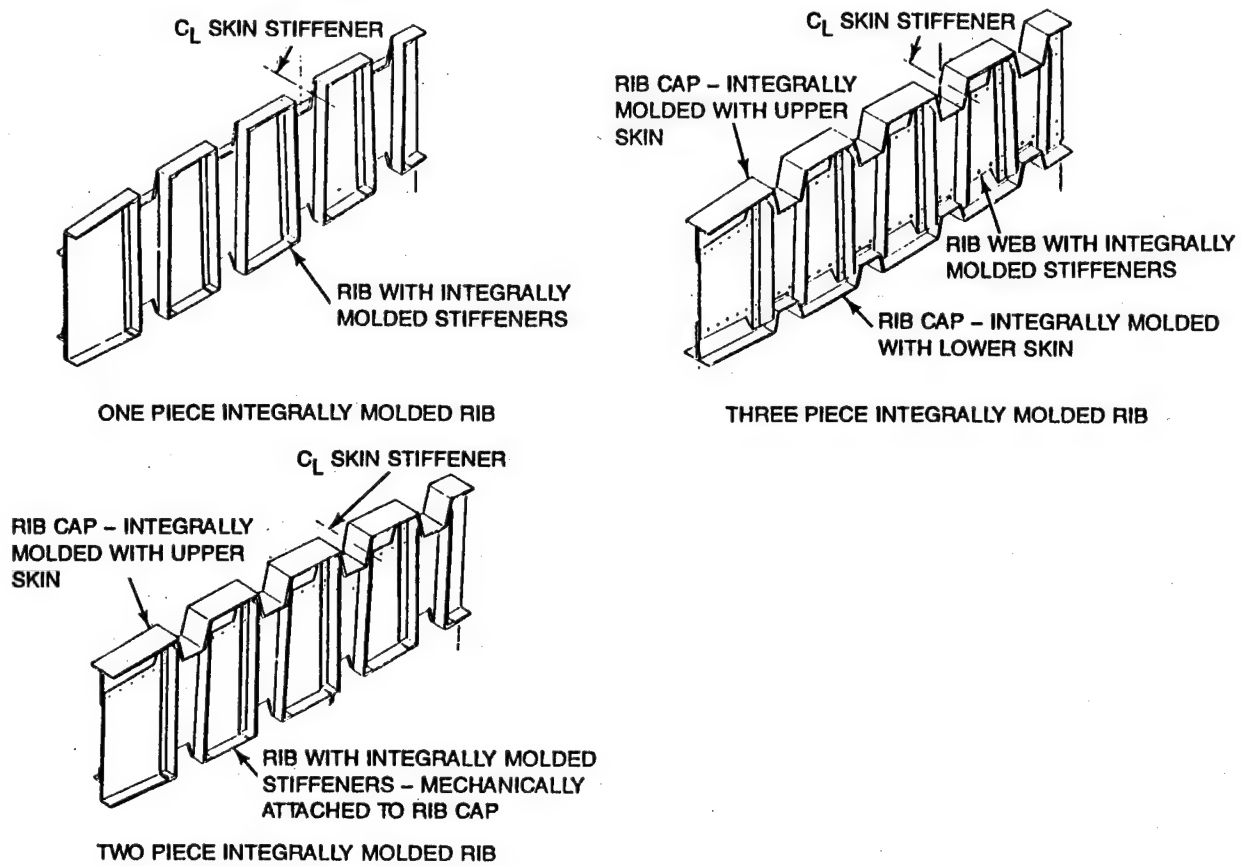
R89-0547-071

Fig. 4 Typical Cover & Notch Strain Reduction Concept Trades

### Spar Concepts (Multi-Spar & Multi-Rib Designs)



### Rib Concepts (Stiffened Cover Types)



R89-0547-072

Fig. 5 Typical Substructure Configuration Trades

incorporated through the thickness prior to cure provide reinforcement for out-of-plane loads. To reduce the strain concentration effect caused by the stitching operation in the cover and spar caps the 0-deg Gr/Ep plies are locally replaced by S-GI/Ep softening strips.

Damage tolerance is achieved through the inherent survivability features of the high strain wing multi-spar design which provides multiple load paths around damage, and the incorporation of crack-arrestment strips (to each side of the discrete caps) made of a compliant material to contain damage and prevent the damage from growing to catastrophic failure under design loads. S-GI/Ep strips were selected as the crack-arrestment medium because of their high strain-to-failure. In addition K/Ep stitches were incorporated through the crack-arrestment strips to provide translaminar reinforcement to arrest delamination growth and to provide a controlled tear path in the basic lightly loaded region of the cover for hydrodynamic ram survivability requirements.

An extensive design development and verification test effort has been an integral part of this development program. Design development testing consisted of over 140 coupons and 32 major elements prior to final design of a full-scale wing box subcomponent. The development test objectives were to

- Derive material allowables for notched high strain laminates with S-GI/Ep softening strips
- Correlate and confirm the adequacy of the analytical procedures used to define and analyze the design concept
- Demonstrate the structural integrity of critical design areas
- Demonstrate the ability of the high strain wing to sustain cyclic loading consistent with the aircraft's design life
- Demonstrate the effectiveness of the stitched S-GI/Ep crack-arrestment strips for LEID and battle damage
- Establish the confidence to proceed to the fabrication and test of the full-scale representative subcomponent aimed at
  - Verification of the high strain wing design under combined loading and fuel pressure
  - Demonstration of the manufacturing approach.

The coupon and element tests successfully met their objectives by establishing and confirming the design criteria utilized in satisfying the structural requirements high strain structural integrity, durability, damage tolerance and survivability. More details of the development test data relative to these areas are presented in the following section.

#### SUBCOMPONENT SELECTION AND DEFINITION

To demonstrate the features and structural adequacy of the design on a larger scale, a section of the wing was selected to be represented by a large component test article. The basic criteria used to identify and select this design verification component were that it be of a generic nature and contain a broad range of structural features. In addition, it should be subjected to a complex state of loading and should address the critical design areas so that analytic techniques may be verified and extended. Finally, the selected component must be capable of demonstrating the fabrication techniques applicable to full scale high strain wing production.

Using these criteria, the wing center section was selected as the demonstration article because this portion of the wing contains the highest load intensities and strain levels, as well as the greatest weight savings. It also contains all the major design areas of concern generic to wings for a future Navy multi-mission aircraft. The component, shown in Fig. 6, is a 95-in. long, 38-in. wide and 13-in. deep three-cell box structure consisting of two intermediate spars integrally molded and stitched to the lower cover; and mechanically attached to the discrete cap upper cover. The front and rear spars are mechanically attached to both the upper and lower covers. A typical access door, located in the center bay, is incorporated into the component's upper cover.

Fabrication of the subcomponent consisted of 12 major composite details and numerous metal details. All metal details and machine parts were fabricated at Grumman's Bethpage, NY facility. Composite details, which include the front spar, rear spar, six intermediate spar segments, upper cover, lower cover and two BL12.0 ribs were layed-up and cured at Grumman's Milledgeville, GA composite fabrication facility. Upon completion of NDI the composite details, and the integrally co-cured/stitched lower cover and intermediate spars sub-assembly were shipped to Bethpage for final assembly and instrumentation. Fuel sealing around the tank periphery was accomplished by injecting a fluorsilicone compound into a wide channel incorporated in the flanges of the substructure, through which the box assembly hardware passes. O-rings were used under the heads of the box assembly hardware at the intermediate spar and BL±12 rib location.

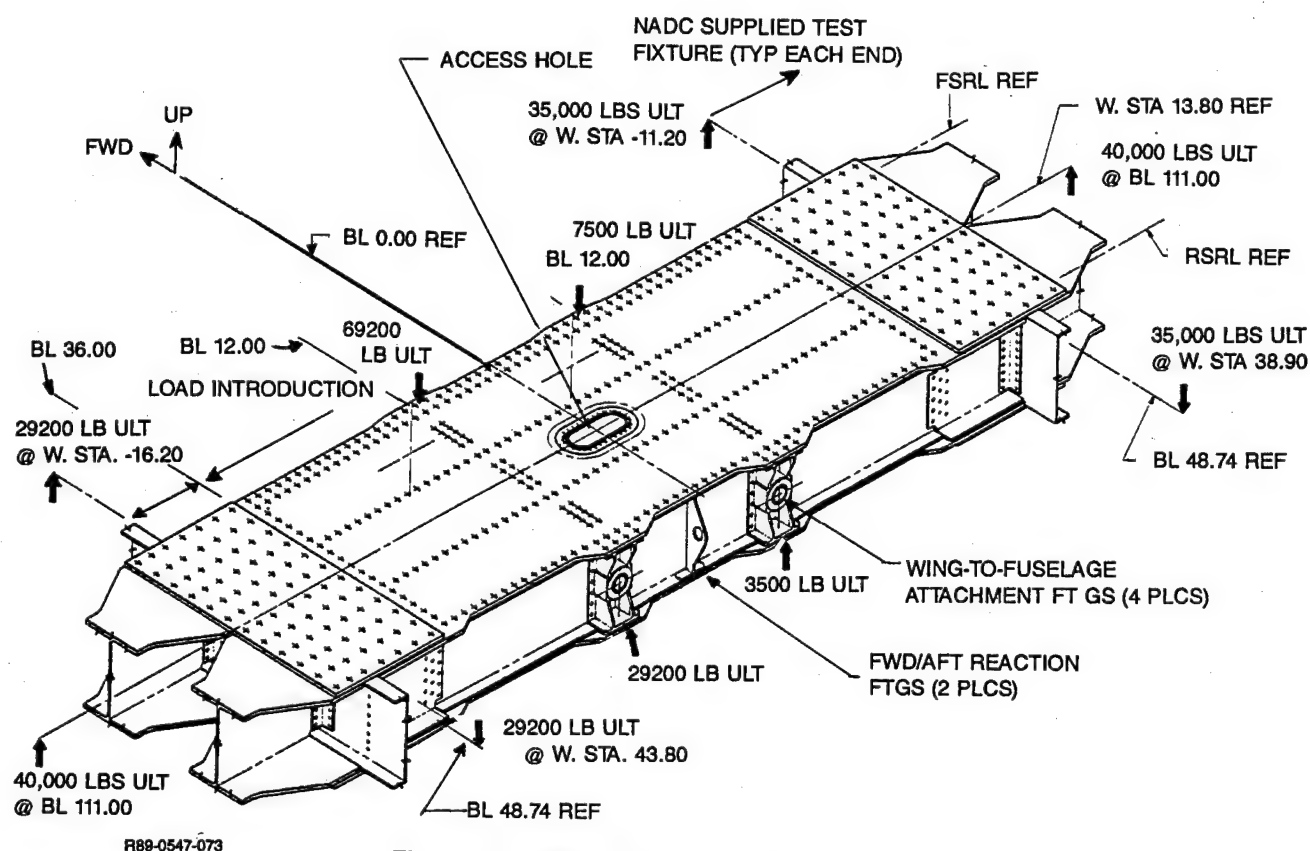


Fig. 6 High Strain Wing Subcomponent

## INSTRUMENTATION

Prior to final attachment of the upper cover during manufacturing, strain gages were applied to internal surfaces of the box. Wiring from internal instrumentation was routed to the outside of the box through a bulkhead fitting installed through the rear spar. Following completion of the box assembly, external gages were applied to the specimen. A total of 42 axial, 10 shear and 30 rosette gages were installed. In addition to the strain gages, the subcomponent was monitored with 14 deflection transducers. These strain and deflection measurements permitted the confirmation of stress analysis predictions and were used as a means of monitoring the specimen during test.

Applied mechanical loads were measured by calibrated load cells installed in line with the load applying hydraulic cylinders. Pressure measurements were monitored via a pressure gage attached to the subcomponent at one of the two pressure bulkhead fittings.

## TEST SET-UP

The subcomponent was tested as a through box indicative of the actual aircraft. Load introduction simulating actual flight conditions was accomplished through non-test structure attached to both ends of the box at BL±49. The moment connection was accomplished by a set of steel plates which spliced two reinforced steel "I" beams extending from BL49 to BL111. Both the plate and beams were attached to the subcomponent with multiple rows of fasteners into the steel transition plates on the Gr/Ep covers, and steel angles attached to the spars. Torsion loads were applied to a 1.5 in. thick steel plate extending forward and aft and attached at BL49. The subcomponent was attached to steel fixture frames for test, with four wing-to-fuselage titanium attachment fittings to the test frames. Reactions at the four wing-to-fuselage attachment points were shear only, with the bending moment carried across the subcomponent. Figure 7 is a photograph of the subcomponent set-up for test. All loads were applied through self-aligning bearings to eliminate out-of-plane loading due to specimen deflections and fixed actuator locations.

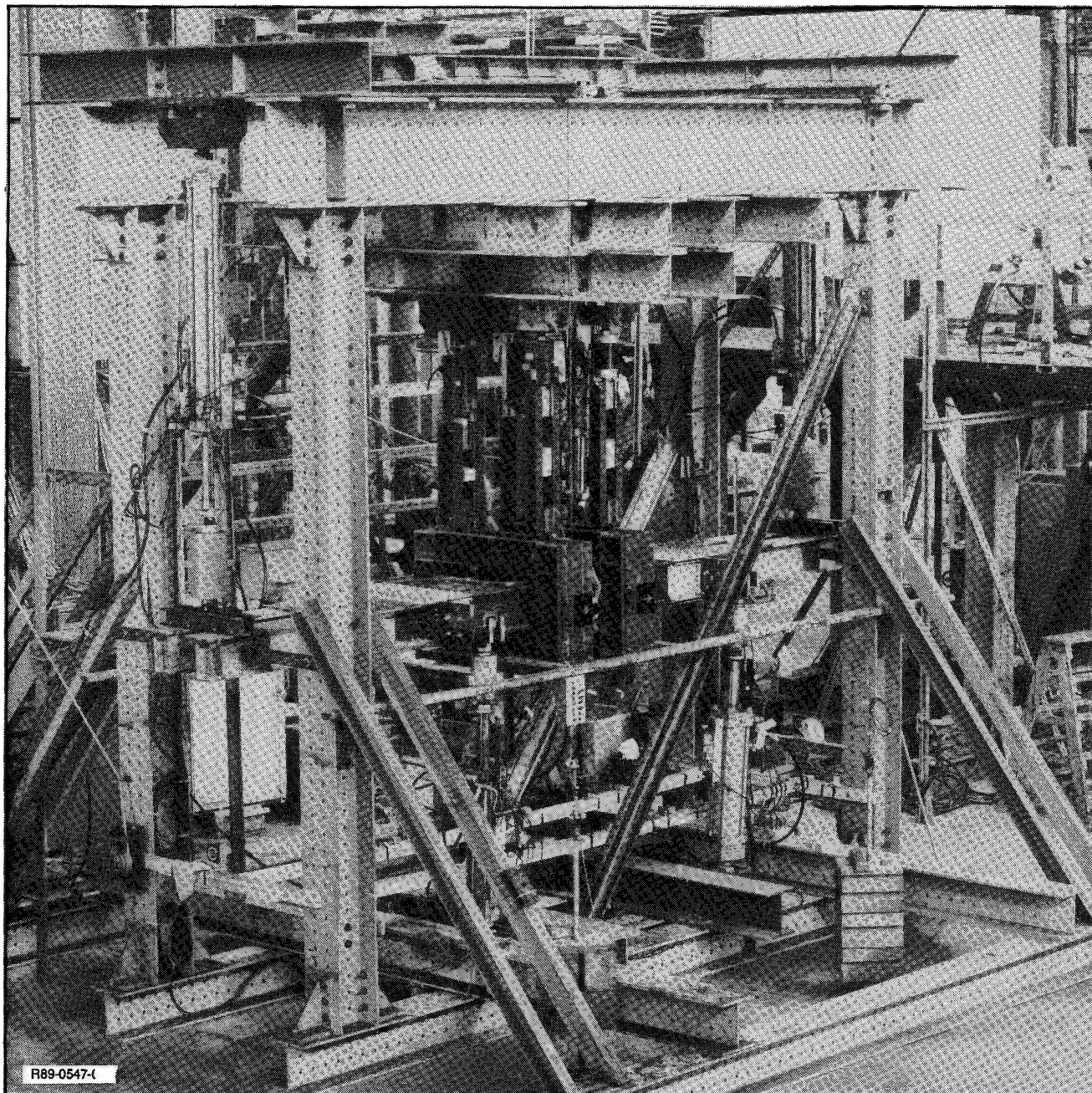
## TEST PROCEDURE

The sequence of structural tests performed to demonstrate the capability of the design is presented in Fig. 8. Test numbers 1 through 4 were functional runs to check out the test specimen, test fixturing, test control equipment and instrumentation. Test number 5 demonstrated the ability of the subcomponent to withstand static application of the critical loads to 114% DLL. Test 8 subjected the specimen to two lifetimes of combined mechanical and internal pressure fatigue loading. During the fatigue test the internal pressure of the subcomponent was maintained at a constant 5.3 psig which is equivalent to design limit pressure. Test 7 demonstrated the design ultimate strength capability of the component by loading the specimen to 150% design limit load. Tests 8 through 10 were damage tolerance tests which demonstrated the capability of the design to sustain low energy impact damage and continue to carry the required design loads.

## DESIGN ULTIMATE TEST

Following the preliminary pressurization and system checkout tests, the test box was incrementally loaded to design ultimate load. Strain gage and deflection transducer readings were recorded at each load increment and critical readings were compared with predictions to ensure proper loading and test specimen response. Nondestructive inspection performed following the ultimate load test did not disclose any anomalies.





**Fig. 7 High Strain Wing Subcomponent Set-up for Test at NADC**



TEST NUMBER	DESCRIPTION OF TESTS
1	MECHANICAL LOADS SURVEY TO 50% DLL
2	MECHANICAL LOADS SURVEY TO -25% DLL
3	DESIGN LIMIT PRESSURE
4	COMBINED MECHANICAL LOADS TO 50% DLL WITH INTERNAL LIMIT PRESSURE
5	COMBINED MECHANICAL LOAD AND PRESSURE TEST TO 114% DLL
6	TWO LIFETIME SPECTRUM FATIGUE TEST WITH INTERNAL LIMIT PRESSURE
7	COMBINED MECHANICAL LOAD AND PRESSURE TEST TO 150% DLL
8	COMBINED MECHANICAL LOAD AND PRESSURE TEST TO 114% DLL
9	ONE LIFETIME SPECTRUM FATIGUE TEST
10	MECHANICAL LOAD TEST TO 114% DLL

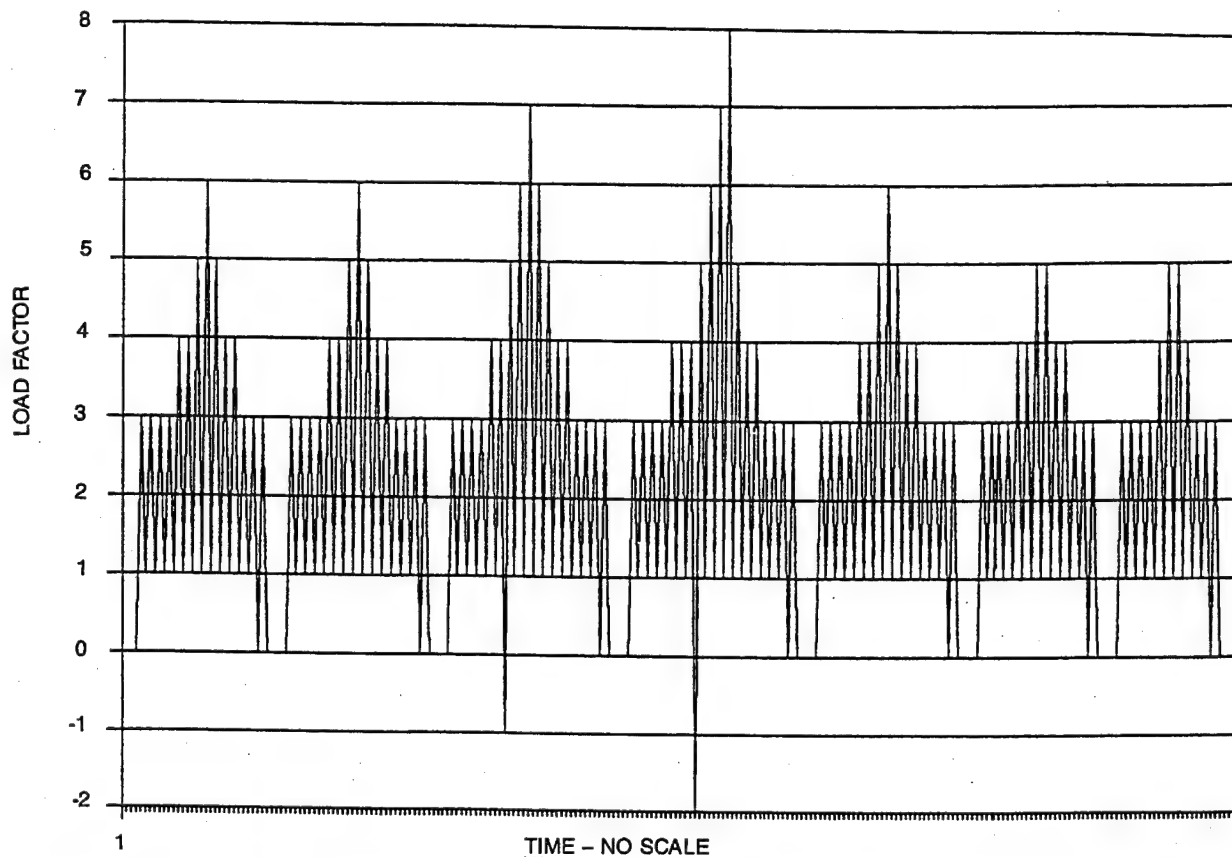
R89-0547-075

**Fig. 8 High Strain Wing Subcomponent Sequence of Tests**

#### DURABILITY AND DAMAGE TOLERANCE TESTS

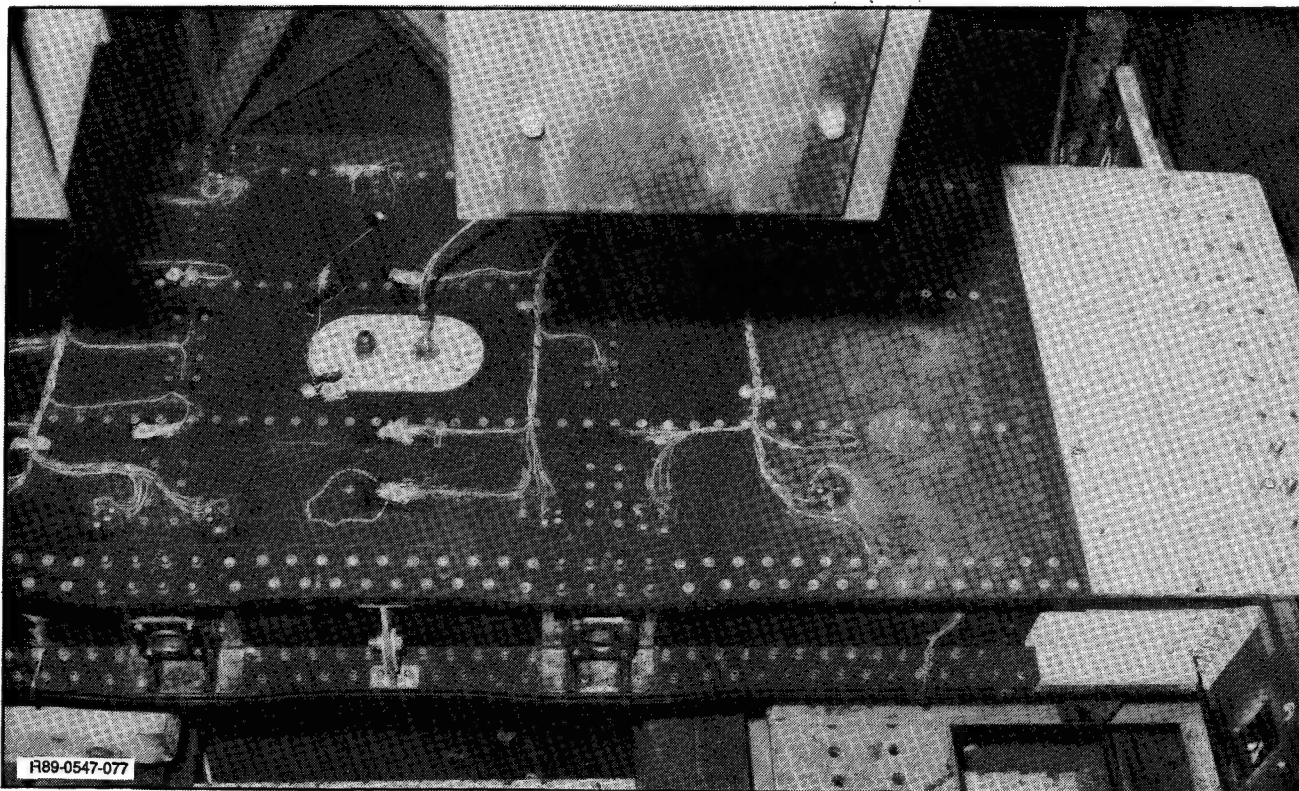
The subcomponent was tested to the equivalent of 12,000 flight hours of fatigue testing. The spectrum used for this testing was an AV-8B flight by flight spectrum which consists of seven flights encompassing a total of six flight hours. This seven flight sequence was repeated 2000 times to obtain the required two lifetimes of testing. As can be seen from the plot of the load peaks of this spectrum (Fig. 9) applied loads ranged from a maximum of 114% DLL to a minimum of -25% DLL. Strain surveys at the maximum spectrum load were performed every 1/4 lifetime, and nondestructive inspections were performed every 1/2 lifetime. No anomalies were detected upon evaluation of the strain data nor from the results of the inspections.

Upon completion of the fatigue testing, damage tolerance testing was performed to demonstrate the capability of the incorporated design features to arrest delamination growth under combined loading. Specifically, the intent of this testing was to show that the Kevlar stitching provided a positive boundary at which the delamination would be arrested. An instrumented drop tower was positioned over the specimen and used to impart visible low energy impact damage at two selected locations on the component upper cover. These locations were mid-bay (between spars) and thus centered between the rows of Kevlar stitching. Based upon previous survey results, 40 ft-lb was the energy level selected for use in producing the desired level of damage. Figure 10 shows the delaminated area following the two drops as determined by ultrasonic inspection. As shown in the photograph, the first delamination was circular and did not reach the stitch lines, while the second delamination extended to and was partially arrested by the stitch line. The component was then fatigue tested for one additional spectrum life in an attempt to determine whether the delaminations would propagate and be arrested by the stitch lines. Following this cycling, however, ultrasonic inspection did not reveal any growth in the original delaminated area.



R89-0547-076

**Fig. 9 Fatigue Spectrum**



**Fig. 10 Subcomponent Impact Locations Damage**

### SURVIVABILITY TEST

Upon completion of the structural testing, the component was removed from the test fixture and shipped to the Naval Weapons Center (NWC) for ballistic testing. The intent of this testing was to demonstrate the survivability of the design to the impact of 30 mm high explosive incendiary (HEI) rounds and the accompanying hydraulic ram loading. Three concepts were incorporated into the design to contain ballistic damage. These concepts, controlled tear paths in the basic cover panels formed through the use of Kevlar stitching, fiberglass crack arrestment strips and a discrete cap configuration, were to be evaluated through this testing.

Although the wing box was originally designed to be tested in four-point bending, testing facilities and fabrication restrictions at NWC required that the box be tested as a cantilevered beam. The box was mounted in a test fixture, clamped at one end and loaded at the other end with load applying air bags. Pressure in the air bags was increased until 55% DLL was obtained at the fixed end of the specimen. The 30 mm gun mount was placed on the ground beneath the test pad at a distance of 25 feet from the box. Fluid level in the box was set at 75% full and ullage pressurization was set at the design limit level of 5.3 psig. Figure 11 is a photograph of the test set-up.

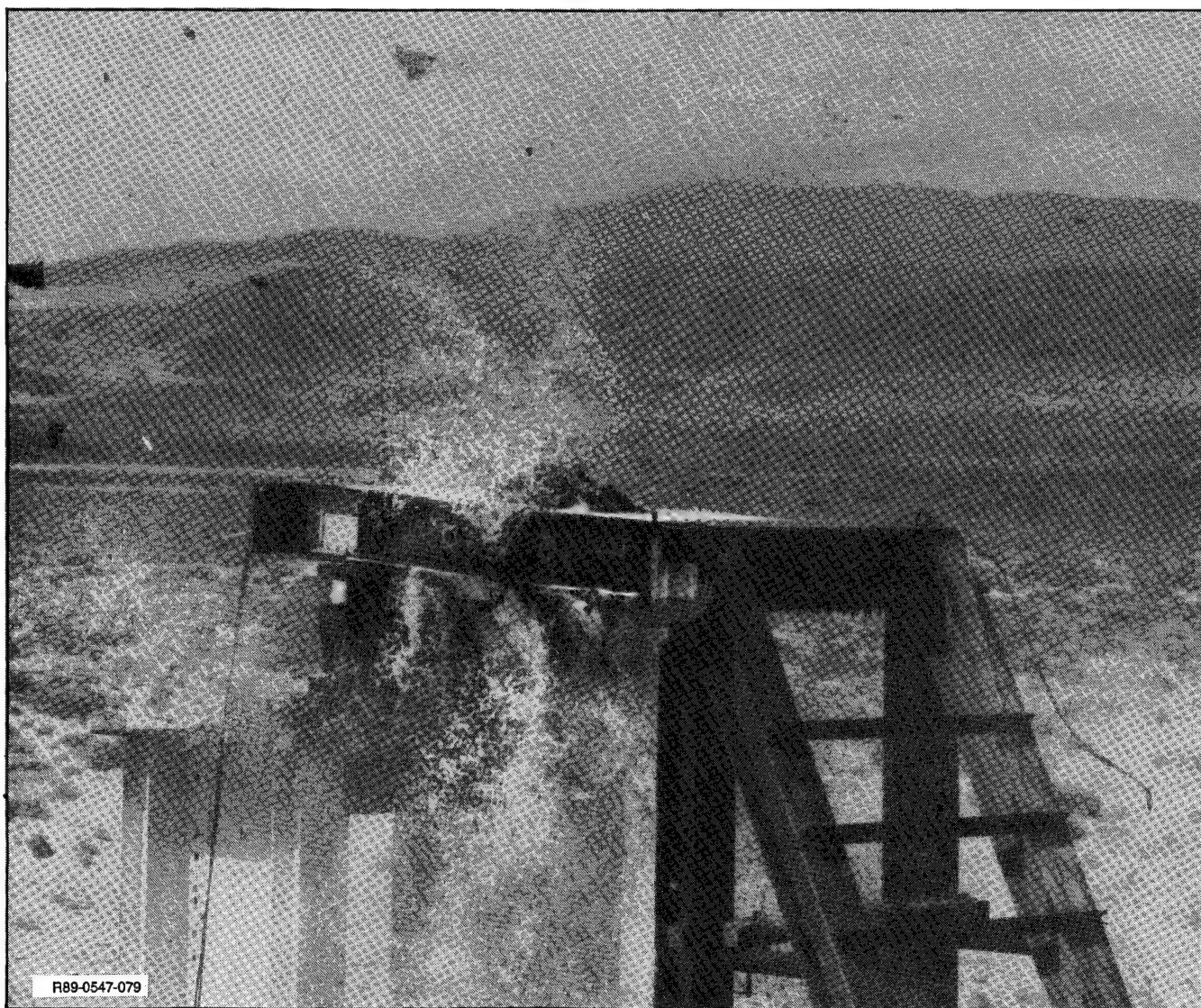


Fig. 11 Subcomponent Survivability Test Set-up at Naval Weapons Center

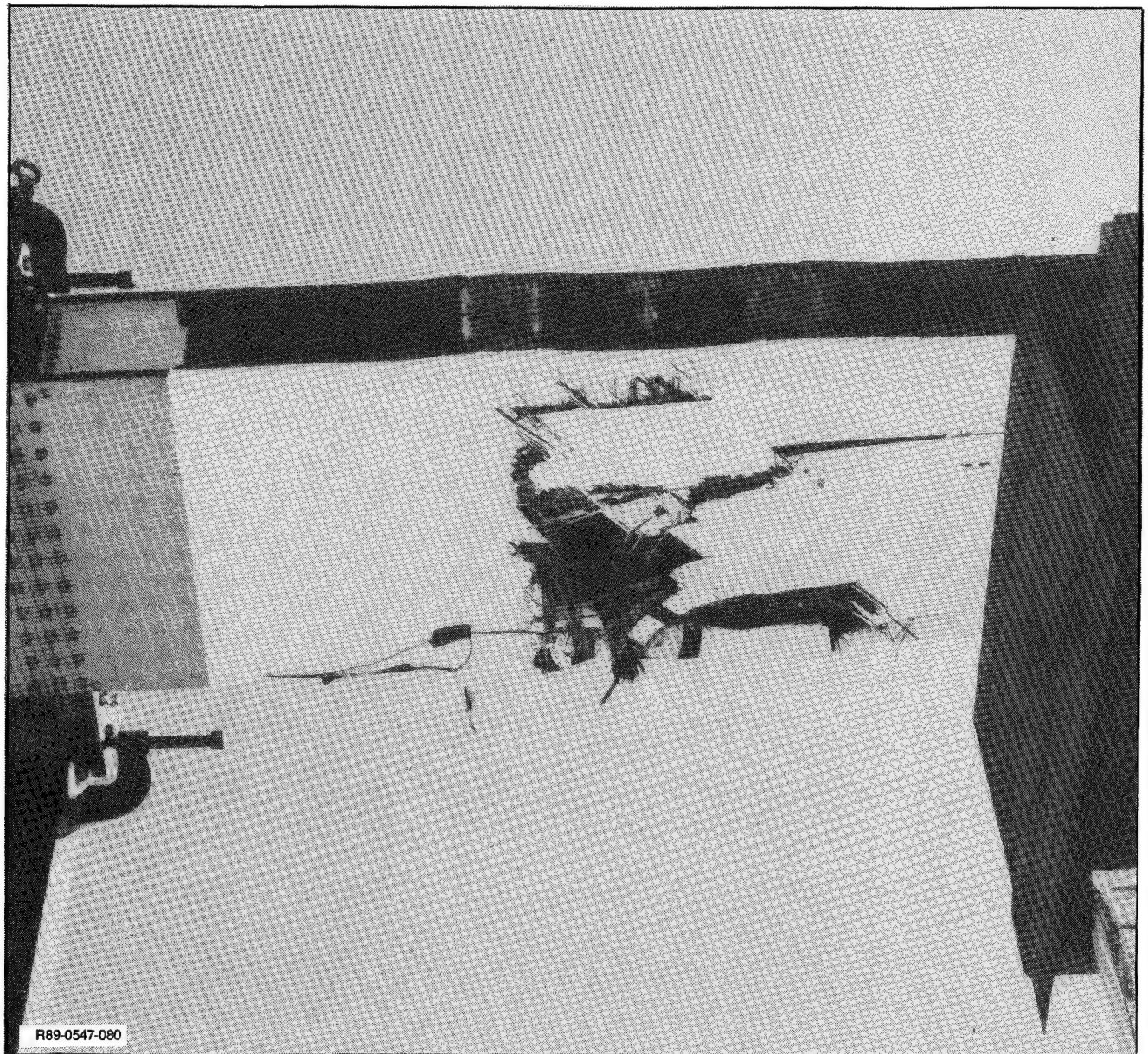


Upon firing, the round entered the cover at the lower aft bay and 1.25 inches to the left of the box centerline. The round detonated inside the box, probably while passing through the aft intermediate spar. Figure 12 is a photograph of the component taken approximately 3 milliseconds after impact of the round.

Post-test examination of the lower cover (Fig. 13) revealed ripping along the stitch lines crossing into the right bay. The aft center portion of the lower cover failed along the chordwise stitching as planned, but some damage did extend forward of the aft bay. As seen in the photograph of the upper cover, Fig. 14, almost all of the visible damage is confined to the middle and aft central bays with failures along both the stitch lines and the fastener rows. Damage to the spars and ribs ranged from no visible damage to the front and rear spars to destruction of the intermediate spars. Damage to the right rib was not apparent and damage to the left rib was localized to the lower cap.



**Fig. 12 30-mm HEI 3 Milliseconds After Impact**



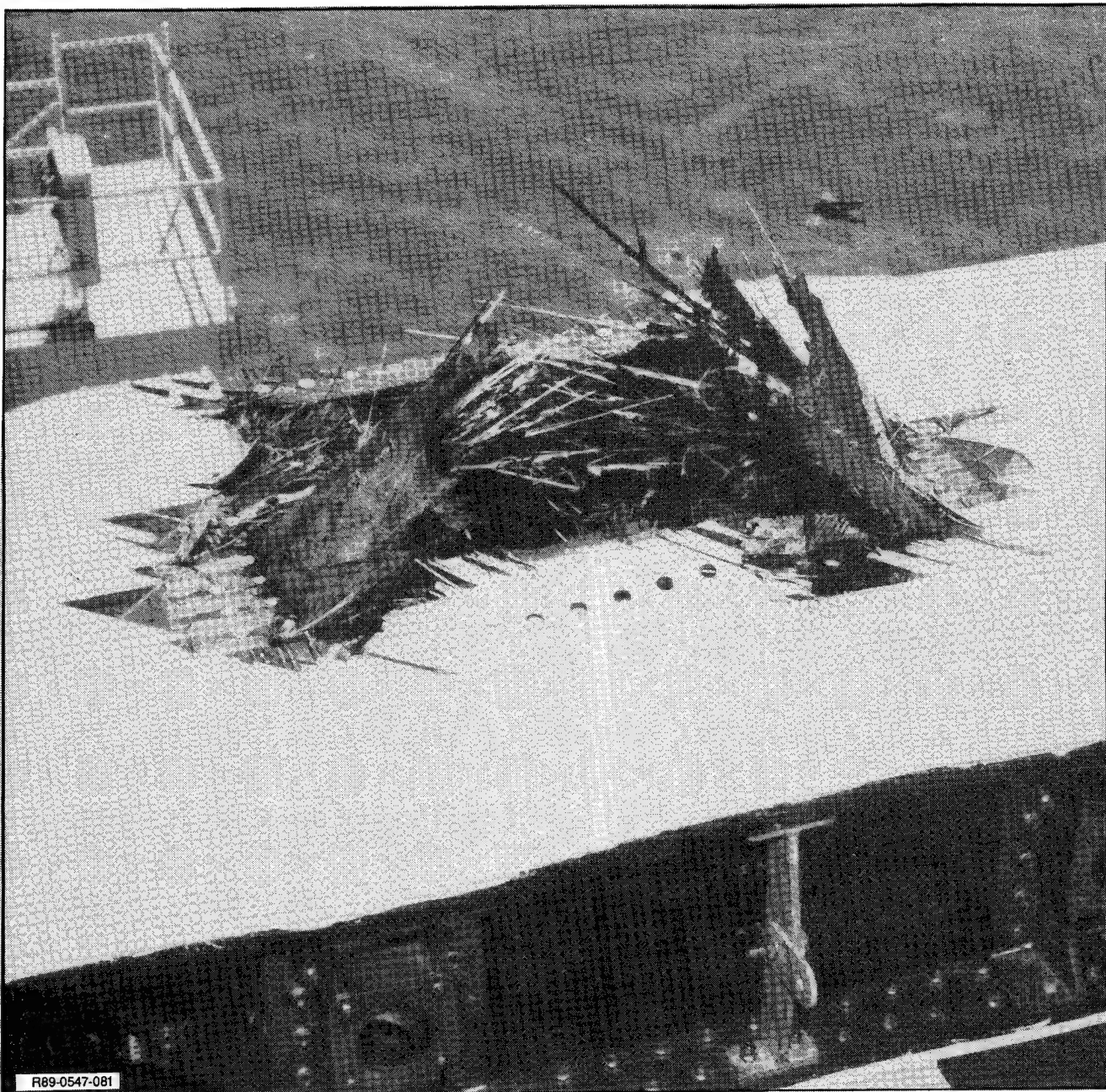
**Fig. 13 Damaged Lower Cover**

In summary, although extensive skin and substructure damage was incurred, the structure was capable of supporting the applied loading both during and after the test. The lines of Kevlar stitching, although inconsistent, did provide tear paths which appeared to control and limit the damage area. Finally, fiberglass softening and crack arrestment strips increased the overall bolted joint strength enough to permit bolt failure in tension, rather than bolt pull-through.

#### TECHNICAL ISSUES

The program has addressed significant technical issues affecting the use of high strain advanced composite wing structures. These issues concerned primarily





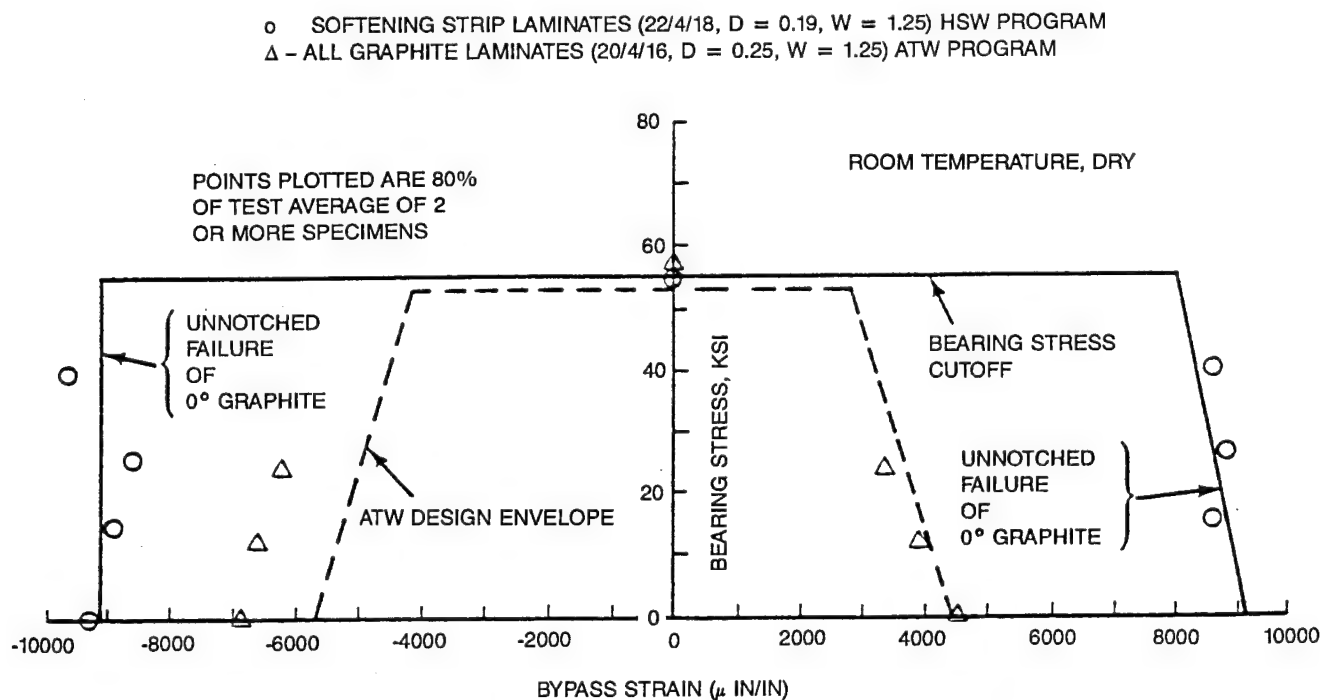
**Fig. 14 Damaged Upper Cover**

structural integrity and durability of a high strain Gr/Ep wing and ability of this type of structure to satisfy vehicle damage tolerance and ballistic survivability requirements. The feasibility of satisfying these requirements while achieving a 21.5 percent weight savings over a standard strain wing has been demonstrated.

Coupon test results were used to provide basic materials data on the unique hybrid configuration and to provide a better analysis basis for the design. Coupon type specimens included simple tension and compression specimens with loaded holes

to develop bearing/bypass load interaction curves, like that illustrated in Fig. 15, for the softened laminate. The effectiveness of the softening strip concept is vividly depicted in Fig. 15. This figure illustrates that the softening strip approach permitted attainment of the full unnotched strength of the Gr/Ep, and that this strain level can be sustained at design bearing stress levels in excess of 55 ksi. In contrast, the all-Gr/Ep laminates were capable of sustaining slightly more than half that value with no bolt load, and displayed a pronounced sensitivity to increased bearing stress. Coupon tests also included bolt-pull through and integral cover-to-substructure flatwise tension specimens. Various element type specimens representative of critical areas of the design were tested to ensure the structural integrity of the design concept and subcomponent. Element tests performed included combined longitudinal tension and flatwise tension beams of the wing integral lower cover and spar attachment; spar termination elements demonstrated the ability of the spar/rib intersection to sustain high tension and compression longitudinal strains, access hole elements verified the ability of the upper cover to sustain high compressive strains in the presence of a large access hole, and shear elements demonstrated the shear/buckling strength of the covers and spars. The durability of the design was demonstrated by fatigue testing of coupons and elements in excess of two lifetimes, followed by a residual static strength test to failure above 6000 micro-in/in.

To demonstrate that the high strain wing design concept/features can provide the degree of damage tolerance and survivability previously mentioned, a series of elements representative of the high strain wing covers was tested to verify that



R89-0547-082

Fig. 15 Comparison of Softening Strip Laminates & All-Graphite Laminates

LEID, which has grown to a significantly larger size due to the high operating strain level, is arrested by the stitched S-GI/Ep crack-arrestment strips, while damage from high energy impact is also arrested at the crack-arrestment strips. Three distinct locations of the wing covers were of particular interest: the basic cover between spars, the discrete cap cover spars, and near the edge but not on the discrete cap/spar. Tests indicated that the stitches were effective in stopping initial delamination growth caused by impact. Spectrum fatigue and static testing to design ultimate levels of elements containing LEID and penetrations (representative of small ballistic threats) produced no significant propagation. The static testing of a major element representing a three cap/spar segment of the lower cover, with an 8-in. dia. hole incorporated through the center cap simulating a 23 mm hit, demonstrated the effectiveness of the stitched crack-arrestment strips in arresting the propagation of a combined crack/delamination which had started from the edge of the hole at a strain level of 4200 micro-in/in and permitting the panel to sustain the higher load in the fatigue spectrum (Pxx - 4700 micro-in/in) without subsequent growth or catastrophic failure. A single cell test box filled with JP-4 fuel, pressurized to 5.3 psi and ballistically impacted with a 5/8-in dia. steel ball at 4500 ft/sec demonstrated the feasibility of the lines of stitches through the crack-arrestment strips to provide a "controlled tear path," thereby isolating/containing the damage resulting from the hydrodynamic ram effects on one basic cover bay.

Finally, the subcomponent provided a full scale demonstration of the structural integrity and durability of the most critical portion of the wing under combined loading and fuel pressure, as well as satisfaction of the damage tolerance and survivability requirements of the baselined vehicle.

#### ADVANCED WING DESIGN DEVELOPMENT

Coincident with this development effort, the trend toward increased structural efficiency and damage tolerant structures has emphasized the need for and vigorous development of newer/emerging composite materials consisting of improved graphite fibers in combination with toughened resin systems. Compared with composite material systems used on operational aircraft these newer/emerging graphite fibers offer increased strength, stiffness and strain-to-failure in the presence of a notch. New/emerging resin systems, both toughened thermoset and engineered thermoplastic, have increased toughness and improved elevated temperature/wet retention of properties. The potential benefits that can be realized through the combination of these newer/emerging fibers and tougher resin systems with new and/or previously developed high strain wing designs (to maximize structural efficiency and reduce fabrication costs while maintaining to the greatest extent possible the weight savings, durability, damage tolerance and survivability, demonstrated by the high strain wing) was assessed in a subsequent design and experimental evaluation effort also sponsored by NADC.

Two categories of new and/or improved graphite fibers - high strain (1.8 percent or greater elongation) and higher modulus (40 MSI or greater with at least 1.5 percent elongation) - were considered in conjunction with two categories of resin



systems: toughened thermosets and "engineered" thermoplastics. A total of 28 toughened thermoset and nine thermoplastic material systems, summarized in matrix format in Fig. 16 and 17, have been evaluated for screening purposes. Grumman's extensive data base and material supplier data were used, in part, to perform the screening. In addition, industry standardized coupon tests were performed to obtain sufficient data where lacking, and to characterize the candidate material systems to allow comparison on a common basis. Standardized coupon tests consisted of unidirectional tension, compression, horizontal shear, and double cantilever beam (DCB). DCB tests measured critical Mode I interlaminar fracture toughness ( $G_{Ic}$ ) which provided a timely experimental indication of the relative damage tolerance of the numerous material systems. Coupons consisting of a 6/2/8 laminate (number of plies in the 0/90/ $\pm$ 45-deg orientations) were tested in compression to correlate 0-deg compressive layer strength with the unidirectional test results. Five replicates of each specimen type were tested to determine a coefficient of variation and evaluate material properties variability, thereby providing a better indication of average material properties. Four toughened thermoset (IM8/8551-7A, G40-800/F584, HITEK 46/E7T1-2 and T800/F3900) and two thermoplastic material systems (IM7/APC-II and T650-42/RADEL-X) exhibited an overall balanced improvement in mechanical properties and were selected for characterization testing and further consideration for the preliminary design and trade study effort. In addition, the IM8/8551-7A material system had the highest compression after impact (CAI) strength, G40-800/F584 exhibited excellent handling characteristics and was considered one of the best systems for adaptability to automated processing techniques deemed essential to achieving high strain wing structures with lower production, and both the HITEK-46/E7T1-2 and T800/F3900 exhibited high compression strength/stiffness with good CAI strength.

Material characterization testing consisted of a series of simple tension and compression unnotched specimens and notched specimens with filled and loaded holes to determine the notch sensitivity of the material, develop allowable bearing/passing load interaction envelope curves, and establish a data base of design values for use during the advanced wing preliminary design and trade study effort. Based on the comparative coupon test results it was concluded generally that these newer/emerging composite materials provided advantages that could increase structural performance of future Navy aircraft wing primary structures. Specifically, compression after impact strength was increased by approximately 100 percent, notched tensile strength was improved approximately 50 percent, and notched design ultimate strain levels in excess of 6000 micro-in/in for tension-dominated structures were developed without the use of S-GI/Ep softening strips. Notched compression failure strains, however, were comparable to non-toughened Gr/Ep materials (without S-GI/Ep softening strips) used on current operational aircraft.

Preliminary design and trade studies performed were aimed at identifying the optimum balance between maximum structural efficiency and low fabrication cost by combining the most promising candidate material systems with design concepts that permit maximum translation of their unique properties to achieving the 50 percent increase in design ultimate strain level without the use of S-GI/Ep softening strips and crack-arrestment strips, while maintaining to the greatest extent possible the weight savings, durability, damage tolerance and survivability of the original high strain wing design.

Two categories of design concepts emphasizing both material and configuration orientation concepts were generated. The first category, materials oriented concepts, relied ostensibly on improved material properties to achieve program

Fiber Manufacturer	Fiber Type	Fiber Tensile Strength (KSI)	Fiber Tensile Modules (MSI)	R6376/CIBA	CYCOM1827/CYAN	XU71787/DOW	F584/HEXCEL	8551/HERCULES	HG9105-2/HYSOL	5745C/NARMCO	E7K8/US POLY	974/FIBERITE	ERLIX 1928/AMOCO	E1T1-2/US POLY	T3900/HEXCEL	Availability
BASF/CELION	G-40 -600	600	43.5	✓			✓			✓	✓					Developmental
BASF/CELION	G-40 -700	690	49				-									Developmental
BASF/CELION	G-40 -800	820	43.5				✓									Developmental
BASF/CELION	CELION-ST	580	35	✓												Full Production
HERCULES	IM6	635	40		✓		✓	✓		✓						Full Production
HERCULES	IM7	680	41			✓		✓								Full Production
HERCULES	IM8	750	45					✓								Full Production
HERCULES	AS6	650	35					✓								Full Production
HITCO	HITEX-42	600	42							✓	✓					Full Production
HITCO	HITEX-46	900	46								✓		✓			Full Production
AMOCO	T-650	650	42										✓			Full Production
AMOCO	T-40X	820	41	✓			✓				✓	✓				Full Production
HYSOL	IM-S	820	43						✓							Limited Production Quant
HYSOL	APPOLLO-M	820	53				✓	✓								Limited Production Quant
HEXCEL	T800	850	42												✓	Limited Production Quant

R89-0547-083

Fig. 16 Toughened Thermoset Prepregs

Fiber Manufacturer	Fiber Type	Fiber Tensile Strength (KSI)	Fiber Tensile Modules (MSI)	APC-2(PEEK)/ICI	PPS(RYTON)/PHILLIPS	KII(AVIMID)/DUPONT	PAI(TORLON)/AMOCO	KIII(AVIMID)/DUPONT	RADEL-X/AMOCO	Availability
BASF/CELION	G-40 -600	600	43.5		✓					Developmental
HERCULES	IM6	635	40		✓	✓	✓		✓	Full Production
HERCULES	AS6	650	35				✓		✓	Full Production
HYSOL R89-0547-084	APPOLLO-M	820	53		✓					Limited Production Quant

Fig. 17 Engineered thermoplastic Prepregs

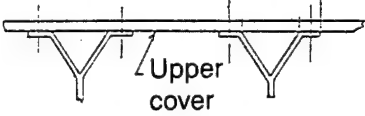
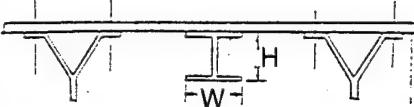
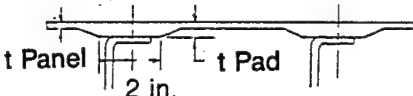
objectives. Using a metals-like approach the application of the optimum material system to a specific component was based on matching the superior/unique material properties with critical design requirements/parameters of that component in order to satisfy them in an optimum manner. For example, a material system with high tensile strength/stiffness, strain-to-failure in the presence of a notch, and high through-the-thickness toughness was considered for application to the tension cover, while a material system with high compression strength/stiffness, strain-to-failure in the presence of a notch, and high fracture toughness against delamination was more desirable for application to the compression cover. This category of concepts permitted maximum design flexibility at minimum fabrication cost by permitting mechanical attachments through regions of the covers containing high concentrations of 0-deg Gr/Ep plies without the need for S-GI/Ep softening strips or other strain concentration reduction techniques (in the 0-deg Gr/Ep). Concepts investigated under the second category, configuration oriented concepts, did not rely as heavily on improved material properties to achieve their goal. Concepts in this category emphasized compliant high strain-to-failure laminates and other softening techniques at substructure attachment areas, thereby minimizing strain concentration effects due to notches and isolating high concentrations of unnotched 0-deg. plies. Here again, the use of S-GI/Ep softening strips and crack-arrestment strips was eliminated to simplify the design and reduce fabrication costs. The material and configuration oriented concepts investigated are illustrated in Fig. 18 and 19, respectively.

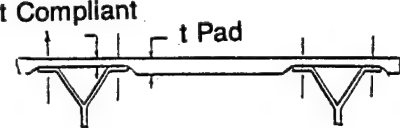
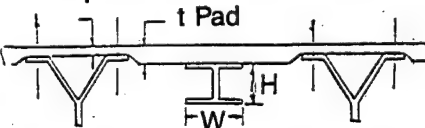
#### MATERIAL/DESIGN TEST EVALUATION

Material/design validation testing, an integral part of this design and experimental effort, also addressed technical issues concerning structural integrity, durability, damage tolerance and survivability of the selected material system/design concept combination. The capability of the material/design concept to achieve the degree of durability, damage tolerance and survivability exhibited by the original high strain wing, was experimentally evaluated through a series of point design oriented major element representative of the compression critical upper cover.

The durability/damage tolerance element is a three cap cover segment, made of sufficient size to permit the independent experimental evaluation of LEID in three separate and distinct areas of the cover element in one test: directly over the discrete cap/spar support, the basic cover between spar supports, adjacent to but not over the discrete cap/spar support. The specimens were subjected both to static and cyclic loading to demonstrate the capability of the combined material toughness/design concept to prevent the delamination damage from growing to catastrophic proportions under the high working strain level.

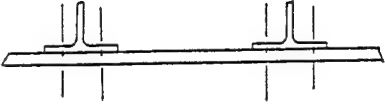
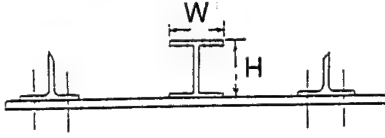
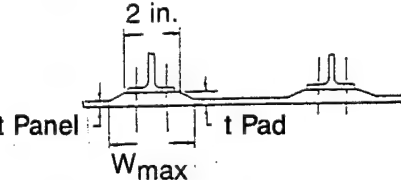
The survivability specimens being set up for test at the time of writing are identical to the durability/damage tolerance specimens tested under the previous high strain wing program. They will be ballistically impacted in the center cap with a 23 mm HEI round while the specimen is loaded in tension to approximately 55% of DLL (2500 micro-in/in). A series of smaller single bay cover specimens ballistically impacted with a 23 mm HEI round while mounted to a tank test fixture filled with water demonstrated the ability of toughened material/design concepts to isolate/contain the damage from the hydrodynamic ram effects to one basic cover panel leaving the discrete cover and spar cap with their axial load carrying material intact.

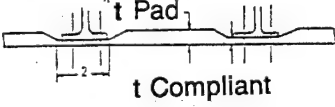

Materials Oriented Concepts	Advantages	Disadvantages
Spread zero upper cover (with "Y" intermediate spars) 	<ul style="list-style-type: none"> <li>• Least cover fab cost</li> <li>• Very efficient comp cover when combined with Y spar</li> <li>• Easily repaired</li> <li>• Good battle damage tolerance due to multiple load paths</li> </ul>	<ul style="list-style-type: none"> <li>• Max rows of fasteners – assy cost impact</li> <li>• High strain concentration – fasteners through laminate with high % of 0-deg plies</li> <li>• Damage tolerance totally material dependent</li> <li>• Excessive S/S shear carrying material</li> </ul>
Spread zero upper cover with integral "I" stiffener 	<ul style="list-style-type: none"> <li>• Minimizes number of spars</li> <li>• Reduced assembly costs</li> <li>• Good battle damage tolerance due to multiple load paths</li> </ul>	<ul style="list-style-type: none"> <li>• High strain concentrations – fasteners through laminate with high % of 0-deg plies</li> <li>• Damage tolerance totally material dependent</li> <li>• Difficult to repair</li> </ul>
Discrete cap upper cover 	<ul style="list-style-type: none"> <li>• Most efficient comp cover design for multi-spar configuration</li> <li>• Min number of substructure attachments</li> <li>• Excellent damage tolerance due to multiple load paths &amp; compliant laminates</li> </ul>	<ul style="list-style-type: none"> <li>• Increased laminate tailoring</li> <li>• High strain concentration factor – fasteners through laminate with high % 0-deg plies</li> <li>• Difficult to repair</li> </ul>

Configuration Oriented Concepts	Advantages	Disadvantages
Isolated spread zero 	<ul style="list-style-type: none"> <li>• Efficient comp cover when combined with Y spar</li> <li>• Min strain-concentration factor-fasteners through compliant laminate</li> <li>• Good battle damage tolerance-multiple load paths</li> </ul>	<ul style="list-style-type: none"> <li>• Increased cover laminate tailoring-manuf cost impact</li> <li>• Max number of substructure attachment fasteners – assy cost impact</li> <li>• Excessive substructure shear carrying material</li> </ul>
Isolated spread zero w/integral "I" stiffener 	<ul style="list-style-type: none"> <li>• Minimizes number of spars</li> <li>• Good overall damage tolerance due to multiple load paths &amp; compliant laminates</li> <li>• Min strain concentration factor-fasteners through compliant laminate</li> </ul>	<ul style="list-style-type: none"> <li>• Not most efficient comp cover</li> <li>• Difficult to repair</li> <li>• High cover complexity due to laminate tailoring &amp; integrally molded stiffener</li> </ul>

R89-0547-085

Fig. 18 Upper Cover Structural Configurations

Materials Oriented Concepts	Advantages	Disadvantages
Spread zero lower cover – Tee & angle spar support 	<ul style="list-style-type: none"> <li>• Least cover fab cost</li> <li>• Very efficient comp cover when combined with Y spar</li> <li>• Easily repaired</li> <li>• Good battle damage tolerance to multiple load paths</li> </ul>	<ul style="list-style-type: none"> <li>• Max rows of fasteners – assy cost impact</li> <li>• High strain concentration – fasteners through laminate with high % of 0-deg plies</li> <li>• Damage tolerance totally material dependent</li> <li>• Excessive S/S shear carrying material</li> </ul>
Lower cover with integral “I” stiffener 	<ul style="list-style-type: none"> <li>• Minimizes number of spars</li> <li>• Reduced assembly costs</li> <li>• Good battle damage tolerance due to multiple load paths</li> </ul>	<ul style="list-style-type: none"> <li>• High strain concentrations – fasteners through laminate with high percent of 0-deg plies</li> <li>• Damage tolerance totally material dependent</li> <li>• Difficult to repair</li> </ul>
Discrete cap lower cover 	<ul style="list-style-type: none"> <li>• Most efficient comp cover design for multi-spar configuration</li> <li>• Min number of substructure attachments</li> <li>• Excellent damage tolerance due to multiple load paths &amp; compliant laminates</li> </ul>	<ul style="list-style-type: none"> <li>• Increased laminate tailoring</li> <li>• High strain concentration factor-fasteners through laminate with high % 0-deg plies</li> <li>• Difficult to repair</li> </ul>

Configuration Oriented Concepts	Advantages	Disadvantages
Discrete cap lower cover (un-notched zeros) 	<ul style="list-style-type: none"> <li>• Efficient comp cover when combined with Y spar</li> <li>• Min strain-concentration factor-fasteners through compliant laminate</li> <li>• Good battle damage tolerance – multiple load paths</li> </ul>	<ul style="list-style-type: none"> <li>• Increased cover laminate tailoring – manuf cost impact</li> <li>• Max number of substructure attachment fasteners – assy cost impact</li> <li>• Excessive substructure shear carrying material</li> </ul>
Discrete cap lower cover w/integral “I” stiffener (un-notched zeros) 	<ul style="list-style-type: none"> <li>• Minimizes number of spars</li> <li>• Good overall damage tolerance due to multiple load paths &amp; compliant laminates</li> <li>• Min strain concentration factor-fasteners through compliant laminate</li> </ul>	<ul style="list-style-type: none"> <li>• Not most efficient comp cover</li> <li>• Difficult to repair</li> <li>• High cover complexity due to laminate tailoring &amp; integrally molded stiffener</li> </ul>

R89-0547-086

Fig. 19 Lower Cover Structural Configurations

## CONCLUSIONS

Conclusions reached as a result of the described efforts have been encouraging and have met overall project objectives.

Specifically, the incorporation of composite design improvements to achieve high strains at design ultimate load resulted in a wing structure that is

- Lighter than composite baseline
  - Multi-spar design: 22%
  - Multi-rib design: 30%
- Lower in cost than composite baseline
  - 10% via: Reduced laminate ply count, reduced part count (integral construction), with fewer fasteners, holes and less assembly time
- Durable/damage tolerant
  - K-Ep stitches through S-Gl/Ep crack-arrestment strips were effective in stopping initial delamination growth resulting from impact
  - Major wing cover elements and wing box subcomponent sustained cyclic loading consistent with twice the airframe design life and ultimate load with impact damage
- Survivable
  - Incorporation of S-Gl/Ep crack-arrestment strips within the Gr/Ep laminate can blunt the growth of a through crack
  - High strain design concepts and features can sustain a 30-mm HEI ballistic penetration while carrying design limit load
  - K/Ep stitches through the crack-arrestment strips were effective in isolating and containing damage resulting from hydrodynamic ram effects.

Newer/emerging composite materials appear to provide improvements that can be utilized on high strain wing structures for future Navy aircraft in order to reduce fabrication cost and increase structural efficiency and supportability

- Toughened thermoset and thermoplastic material systems provided almost 100 percent increase in compression after impact strength
- Notched static tensile strengths were improved by approximately 50 percent
- Developed design ultimate strain levels in excess of 6000 micro-in/in for notched tension dominated structures without use of S-Gl/Ep softening strips
- Developed design ultimate strain levels notched for compression dominated structures (without softening strips) were comparable to current non-toughened Gr/Ep materials. However, the increased stiffness of the newer intermediate modulus fibers provides increased load carrying capability which also can be translated into increased structural efficiency and weight savings, without increase in design ultimate strain level.

## COMPOSITE STRUCTURAL ARMOR FOR COMBAT VEHICLE APPLICATIONS

Wm. E. Haskell III, A. L. Alesi, and G. R. Parsons  
Composites Development Branch  
Army Materials Technology Laboratory  
Watertown, MA

### INTRODUCTION

MTL has worked on several projects that have demonstrated the advantages of using thick composite armor technology for structural applications in armored combat vehicles. The first involved composite cargo doors for the Marine Corps LVTP-7 amphibious landing vehicle (1). Another was a demonstration composite turret that offered a weight reduction of 15.5% (2). The advantages of this composite armor compared to metallic armors used for combat vehicle hull and turret applications are

- \* Reduced weight at equal ballistic protection
- \* Reduced back armor spall
- \* Excellent corrosion resistance
- \* Reduced production costs by parts consolidation
- \* Inherent thermal and acoustic insulative properties

Based on the encouraging results of these past programs, MTL started the Demonstration Composite Hull Program in September 1986 (3). To demonstrate this composite armor technology, MTL selected the Army's newest infantry fighting vehicle, the Bradley Fighting Vehicle (BFV), as a model. A composite infantry fighting vehicle, designated the CIFV for this program, has been designed and fabricated and is currently undergoing a 6000 mile field endurance test. The CIFV demonstration vehicle uses the BFV engine, transmission, suspension, track and other equipment. This MTL program involves a major contract with FMC Corporation, Advanced Systems Center, Santa Clara, CA. The FMC Corporate Technology Center (CTC), Santa Clara, CA was responsible for the fabrication of the composite hull sections and bottom plate.

### SELECTED HULL DESIGN

During the design development work, five proposed hull concepts were developed by the contractor and presented to MTL for review. The hull structures had to meet the structural and ballistic performance requirements of the BFV M2A1 plus the additional dynamic loads associated with an advanced threat armor package. This armor package would add from 30 to 75 psf additional weight to various areas of the vehicle. The thick compos-



ite armor does offer significant weight advantages when compared to aluminum but does have an elastic modulus which is approximately one third that of aluminum. Because of this fact, the composite hull utilizes a unique design to achieve adequate rigidity.

Figure 1. shows the concept selected for fabrication in the second phase of the contract and includes the armor package configuration designed to resist the required M2A1 ballistic threats. This concept with attached ceramic and expanded metal armor offers a weight reduction of 25% compared to the M2A1 aluminum hull structure with steel armor. Figure 2. shows an exploded view of the hull. The hull is composed of a composite left and right hull sections, a composite bottom plate, an aluminum structural turret shroud, and an aluminum chassis. The aluminum components could conceivably be made from composite materials, for example, hybrid reinforcements of carbon, aramid and glass fibers in an epoxy resin. That accomplishment would not be essential to this demonstration and would incur additional time and cost to the program. The structural turret shroud performs two important functions. First, it adds considerable torsional rigidity to the hull and compensates for the composite lower elastic modulus. Second, it takes the weight of the turret off the hull roof and transmits the static and dynamic loads down into the hull chassis. The chassis provides metallic attachment points for the engine, transmission, and suspension and also contributes to hull torsional rigidity. Figure 3 shows the ply count in the different areas of the hull sidewalls.

#### MATERIALS CHARACTERIZATION

Experience gained on the MTL Composite Turret Program showed that laying up the wet S-2 glass/polyester system was difficult. It was found more desirable to use a dry preimpregnated S-2 woven roving fabric (prepreg). By keeping tight controls on the percentage of resin applied to the fabric, more consistent and predictable laminate quality can be attained. Four prepreg suppliers competed in a screening process in which their prepreg systems were molded into a complex shape. Based on criteria such as ballistic performance (20mm FSP), flammability characteristics, processability, physical properties and cost, the American Cyanamid CYCOM 4102/S-2 glass prepreg system was selected.

Mechanical and physical property characterization of four ply laminates having 0/90 orientation is conducted as a quality control method for screening the incoming prepreg (4). Property requirements are listed in Table 1. The properties for laminates subjected to simulated climactic conditioning are listed in Table 2. The climactic condition having the most adverse effect on the properties of a composite vehicle would be a hot/wet environment. The specimens were totally immersed in 110 degree F water until



their weight gain approached equilibrium. Equilibrium was reached after 15 days for most of the specimens. Figure 4 plots specimen weight gain versus immersion time. The ply orientation of all of the specimens, except the through-thickness specimens, was 0/90/+45/-45/-45/+45/90/0. The through-thickness specimens were machined from 44 ply ballistic panels which had a balanced 0/90/+45/-45 ply orientation.

Rough terrain operation of armored combat vehicles imposes severe long-term dynamic loading conditions. The fatigue behavior of the composite, primarily in bending, had to be characterized in order to design a safe and durable composite hull structure. The contractor designed and fabricated a flexural fatigue testing machine that evaluated the composite under displacement control conditions. The equipment could monitor the load required to induce the desired deflection for a three point loading test configuration. This test fixture was designed to fit into an environmental chamber and the tests were run at 110 degrees F and 100% relative humidity. The flexural fatigue test fixture is shown in Figure 5. Each test involved cycling the specimens through a maximum and minimum deflection which induced strain amplitudes from approximately 26 to 80% of the ultimate flexural strain. For each strain amplitude the number of cycles was determined when the resisting load dropped to 70% of the initial load. The results of this testing in graphical form are displayed in Figure 6.

#### COMPOSITE HULL PROCESS DEVELOPMENT

The first full size hull molding try was conducted in August 1988 and was successful. This left side hull section, being lifted from the tool, is shown in Figure 7. The quality of the section was excellent as indicated by the smooth surface and had no apparent wrinkling of the fabric in corners. After machining, the cut edges indicated a sound laminate. The right side section was molded using the same process procedures and is shown in Figure 8. The success of the moldings can be attributed to the information gained from process development work early in the program. Nine process development lay-up trials were conducted on two different tools prior to the lay-up on the full size hull tools.

The first tool used for process development was the 3 foot materials screening tool which is pictured in Figure 9. This tool was later modified by adding a 36 inch vertical extension which simulated the hull roof section. The primary finding during work with this tool was that the prepreg on the vertical surface would slowly slide downward during lay-up causing severe wrinkling in the corners. A method was developed that held the prepreg to the tool wall.

The second tool molded an 11 foot process development

specimen pictured in Figure 10. The most important process development information gained during the use of this tool was in identifying the optimum bagging technique which would yield the best part quality. The selected bagging sequence is shown in Figure 11. The proper vacuum bagging of heat cured laminates is important in removing excess resin and volatiles. The S-2 glass prepreg is produced with extra resin to permit flow and consequent reduction of voids; 2 to 4% of resin must be removed during cure to yield a final resin content of approximately 32% by weight. Two important changes made were replacing the 10 oz fiberglass cloth bleeder previously used with high elongation bleeder felt and the use of high elongation barrier release films. These changes allowed better consolidation of the prepreg into the tight radii of the mold.

The curing of polyester resin involves cross-linking through a condensation reaction. The cure cycle is started by bringing the curing oven, tool and lay-up to a temperature of 150 degrees F, then raising the oven temperature to 170 degrees F. Once the cure reaction begins, the heat of reaction generation rate must be carefully controlled when curing large thick laminates. If the exotherm is not controlled, very high internal laminate temperatures can be generated. This may result in blisters and unbonded areas. Due to varying structural and ballistic requirements, the hull segments have regions varying from 22 to 69 plies. The exothermic temperature reached at the mid-point of the 69 ply region will be higher than at the thinner regions. Because of this, the cure cycle developed for the hull sections is based on the exotherm of the 69 ply regions. The cure cycle used for the hull sections is shown graphically in Figure 12. Notice that the oven temperature is held at 170 degrees F until the peak exotherm reaches its maximum of 230 degrees F and then starts to subside. At that point the oven temperature is increased to 250 degrees F for the final post cure.

#### QUALITY ASSURANCE

A preliminary quality assurance plan has been developed by the contractor based on molding experience gained on the smaller tools (5). Quality assurance includes inspection of the glass reinforcement, the resin system, and of the prepreg. These requirements have been incorporated into a government specification MIL-L-46197(MR). The plan includes storage requirements for the prepreg to assure that its physical property characteristics are maintained during its prescribed shelf life.

The fabrication method of these structures must follow prescribed processing procedures to assure that mechanical and ballistic property requirements are met. Lay-up records must be kept to assure that ply number and orientation are correct. Vacuum bagging and cure procedures are described in detail. The

manufacturing process procedures used to make the full size sections have been documented and will be updated during this program (6).

The quality assurance plan further requires that the cured composite sections be subjected to a variety of inspection techniques including mechanical testing of tag end specimens and non-destructive evaluation (NDE). Radiography and ultrasonic testing methods are currently being explored and the methods that prove most reliable, as well as economical, will be incorporated into future quality assurance plans for this application. A one-sided pulse/echo ultrasonic technique appears promising. Automatic scanning by low frequency (0.5 MHz) transducer with a water squirter coupling of the left hull section indicated only random porosity (7). The feasibility of a radiographic technique has been demonstrated by an MTL Phase I SBIR contract (8). The glass fraction of the composite can be determined from gamma radiation backscatter. A hand held testing unit that requires access to only one side is being built during Phase II.

#### COMPOSITE HULL ASSEMBLY

The left and right sections were machined using a conventional portable air-driven saw, router, and drill. Diamond coated blades and bits were used due to the abrasive nature of the high glass content laminates. The composite hull assembly with ceramic and expanded metal armor was estimated to offer a 27% weight reduction over the BFV M2A1. The aluminum hull with steel armor and spall liner would weigh 12,310 pounds while the CIFV with ceramic and expanded metal armor is estimated to weigh 8900 pounds. Throughout the fabrication of the composite and metallic components, items have been weighed for comparison to predicted results. The machined left-hand hull section was predicted to weigh 1884 lbs and had an actual weight of 1897 lbs. The two composite aft plates were predicted to weigh 84 lbs; actual weight is 80 lbs. The aluminum chassis was predicted to weigh 1846 lbs and has an actual weight of 1920 lbs. These differences in actual weights of fabricated components translates to a 25% weight savings over the BFV M2A1 aluminum hull assembly with steel armor. Figure 13 shows the high quality of straight and curved machined edges of the laminate achieved with these hand held air driven tools. The fitup of the left and right hull sections to the aluminum chassis was excellent. The roof lines came within about 1/16th of an inch to each other. The clamped assembly is shown in Figure 14. This close fitup can be attributed to the process development work completed prior to fabricating the full size tools. Part distortion caused during the cooldown of the complex composite sections was accurately predicted from the two smaller tools. This distortion was accounted for in the design of the large tools. The flatness of the molded hull sections is evident by sighting down the compos-

ite hull sidewall in the direction as viewed in Figure 15.

As shown previously in Figure 2, the CIFV is fitted with a composite bottom plate. The composite laminate offers superior blast resistance compared to equal areal density aluminum (9). This composite bottom plate was laid up and cured on a simple flat aluminum tool. The composite bottom plate, ready for attachment to the aluminum chassis, is shown in Figure 16. A special ceramic filled epoxy coating will be applied to the underside of the bottom plate and the horizontal and vertical sponsons and evaluated for abrasion resistance during the field test.

#### OUTFITTING AND FIELD TESTING

Figure 17 shows the assembled CIFV hull ready for outfitting with components made available by the BFVS-PMO. After installation of the powertrain and suspension system, a metal M2A1 turret was installed on the vehicle. Initial shakedown of the CIFV was conducted at the FMC test facility at San Jose, CA. Figure 18 shows the left side of the vehicle on which ceramic armor tile is bonded to meet the required ballistic threat requirements. Figure 19 shows the right side of the vehicle from which the tile was left off to allow attachment of field test instrumentation. Prior to starting the field test, 21,000 pounds of ballast were added to the vehicle to bring the total weight up to 60,000 pounds. The purpose of this ballast is to simulate the weight and loadings that an uparmoring package would place on the hull structure. The vehicle has completed approximately 1000 miles of field testing without problems related to the composite hull structure. The total 6000 mile test is planned to be completed by March 1990 followed by distribution of the Phase II technical report.

#### PHASE III - HEAVY COMPOSITE HULL

The final phase of the contract will involve the design, fabrication and structural evaluation of a composite hull for a heavy armored combat vehicle in the 55 ton weight range. The design and application of composites to a heavy armored vehicle hull will probably be structurally driven, unlike the CIFV design which was ballistically driven. The majority of ballistic protection could be provided by modular armor. This final phase will start early in 1990 with a period of performance of twenty-four (24) months.

## REFERENCES

1. MTL TR84-41, "Lightweight Combat Vehicles Doors", Final Report, Contract No. DAAG46-83-C-0077, October 1984.
2. MTL TR84-39, "Reinforced Plastic Turret For M2/M3", Final Report, Contract DAAG46-83-C-0041, August 1987.
3. Phase I Technical Report, CDRL SEQ No. A010, MTL Contract DAAL04-86-C-0079.
4. MIL-L-46197(MR), "LAMINATE: S-2 GLASS, FABRIC-REINFORCED, POLYESTER RESIN PREIMPREGNATED", 23 December 1987.
5. Phase II Preliminary Quality Assurance Program Plan, CDRL SEQ No. A008, MTL Contract DAAL04-86-C-0079.
6. Phase II Manufacturing Process Procedures, CDRL SEQ No. A007, MTL Contract DAAL04-86-C-0079.
7. Y. Zhang and B. Smith, "On-Site UT Inspection Of CIFV Hull Section", AMDATA Inc., August 1988.
8. SBIR Phase I Final Report, "Rapid, Non destructive Determination of Resin/Fiber Content in Composites", MTL Contract DAAL46-85-C-0047.
9. C. White, "Preliminary Report on Explosive Shock Testing of Composite Materials (Phase IV), Internal Technical Report, FMC Corporation, San Jose, CA, 7 June 1987.

TABLE 1.

\*

LAMINATE PHYSICAL AND MECHANICAL PROPERTIES

Resin Content (ASTM D2584)	32 + 3 % by wt
Density (ASTM D792)	1.84 - 1.98 g/cc
Tensile Strength (ASTM D638)	72.0 ksi
Tensile Modulus (ASTM D638)	2.7 msi
Flexural Strength (ASTM D790)	40.0 ksi
Flexural Modulus (ASTM D790)	3.0 msi
Compressive Strength (ASTM D695)	18.0 ksi
Short Beam Shear (ASTM 2344)	2.5 ksi
Glass Transition Temperature (ASTM D4065)	320° F (min)

\* Results based on four ply laminates having 0/90 orientation.

TABLE 2.

MECHANICAL PROPERTIES OF CONDITIONED SPECIMENS

## Tensile Properties (ASTM D3039)

Tensile Strength	43.8 + 1.6 ksi
------------------	----------------

Tensile Modulus	2.87 + .17 msi
-----------------	----------------

## Flexural Strength (ASTM D790)

Flexural Strength	35.0 + 4.8 ksi
-------------------	----------------

Flexural Modulus	3.59 + .23 msi
------------------	----------------

## Compressive Properties (ASTM D3410)

Compressive Strength	16.0 + 2.1 ksi
----------------------	----------------

Compressive Modulus	2.12 + .45 msi
---------------------	----------------

## Through-Thickness Compressive Properties (ASTM D695)

T-T Compressive Strength	67.7 + 8.8 ksi
--------------------------	----------------

T-T Compressive Modulus	710 + 62.0 ksi
-------------------------	----------------

## Inplane Shear Properties (ASTM D4255)

Shear Strength	9.24 + .16 ksi
----------------	----------------

Shear Modulus - Compression	567 + 150 ksi
-----------------------------	---------------

Shear Modulus - Tension	303 + 61 ksi
-------------------------	--------------

## Short Beam Shear Strength (ASTM D2344)

Shear Strength	2.19 + .37 ksi
----------------	----------------

## Bearing Strength (ASTM D953)

Fastener Torque

Maximum Bearing Stress

0 in-lbs	33.4 + 2.1 ksi
----------	----------------

36 in-lbs	45.2 + 1.3 ksi
-----------	----------------

72 in-lbs	50.4 + 2.2 ksi
-----------	----------------

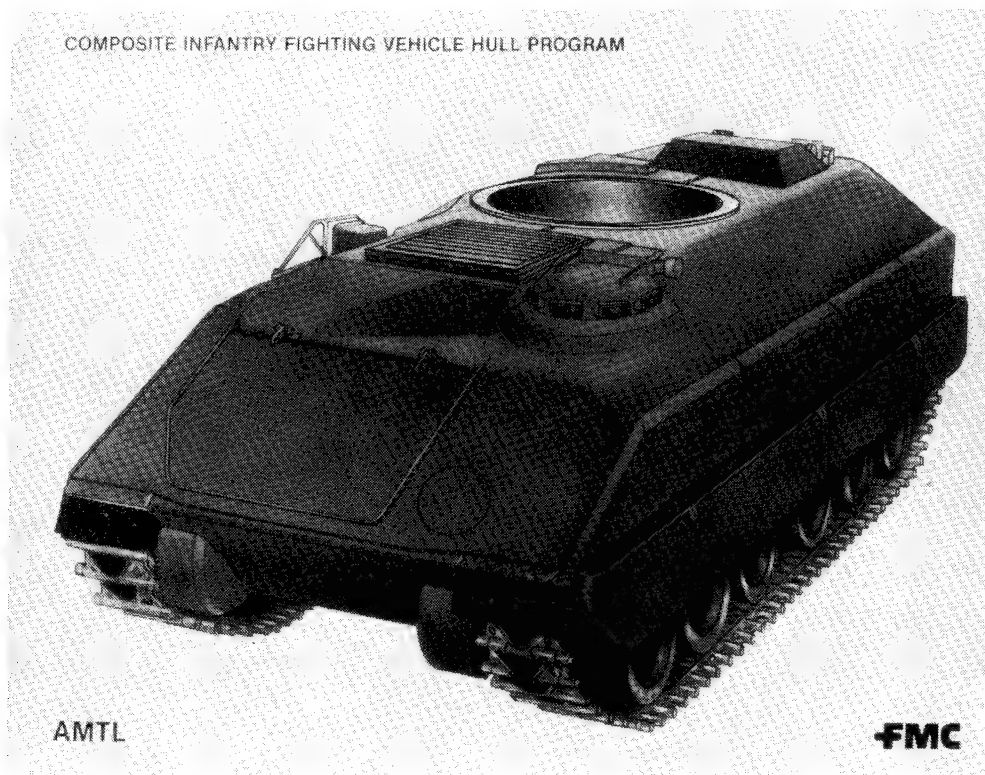


Figure 1. CIFV Concept, Phase I and II

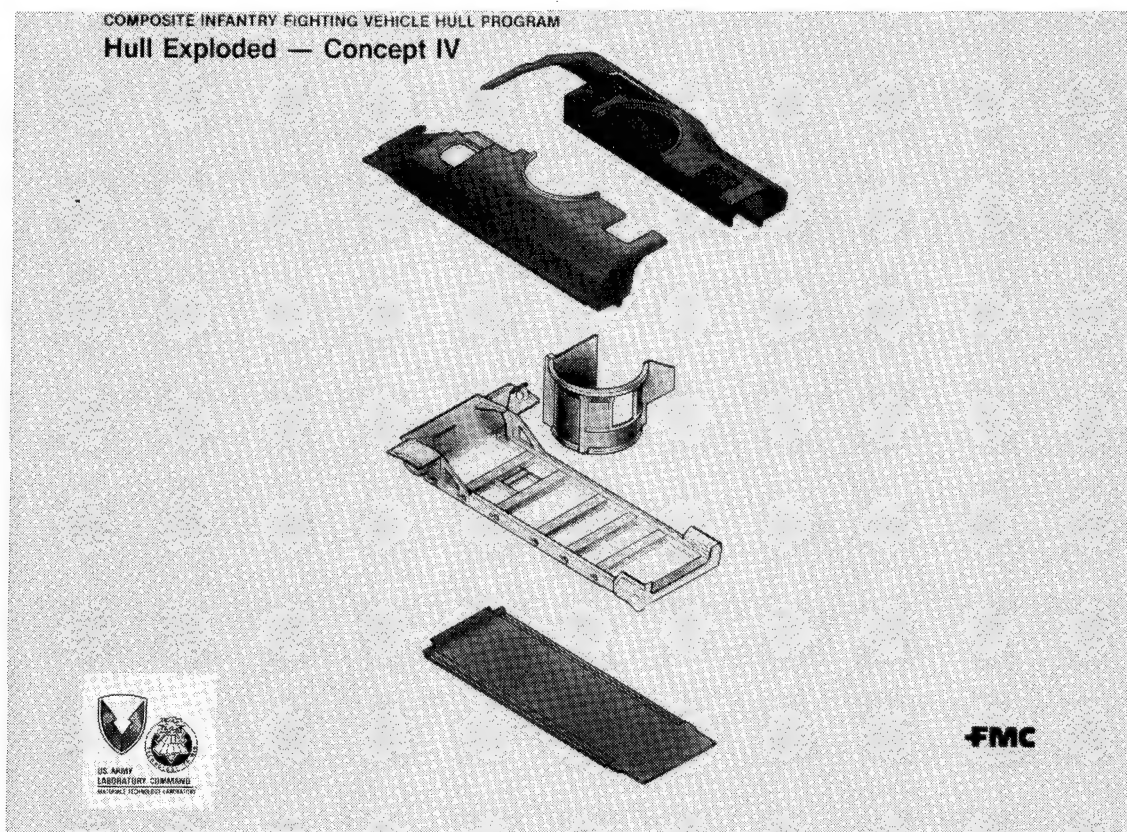


Figure 2. CIFV Exploded View



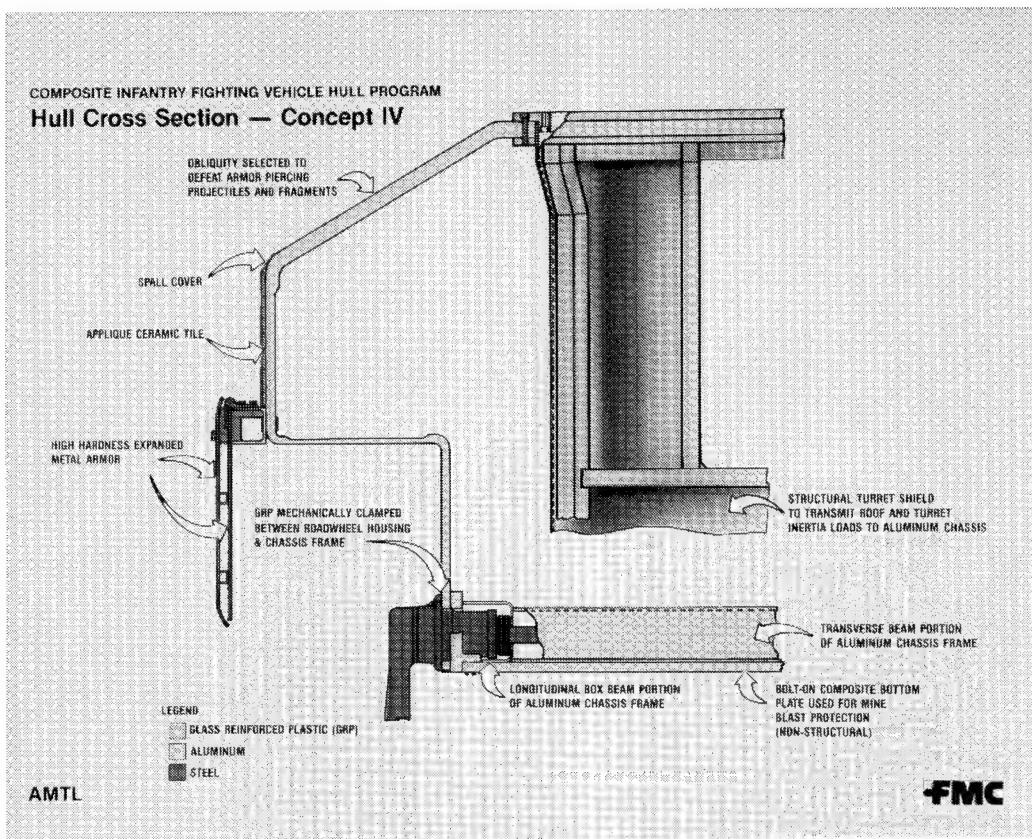


Figure 3. Wall-Ply Count

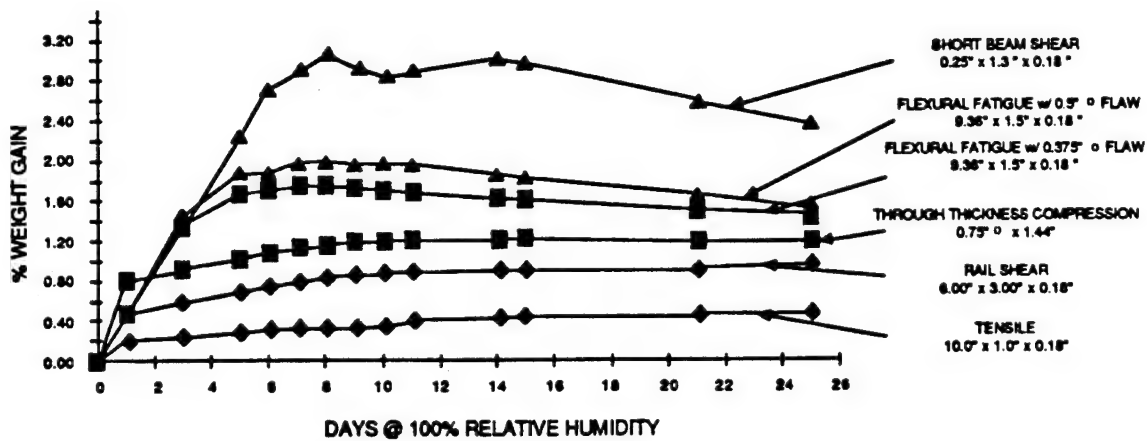


Figure 4. Weight Gain Versus Immersion Time

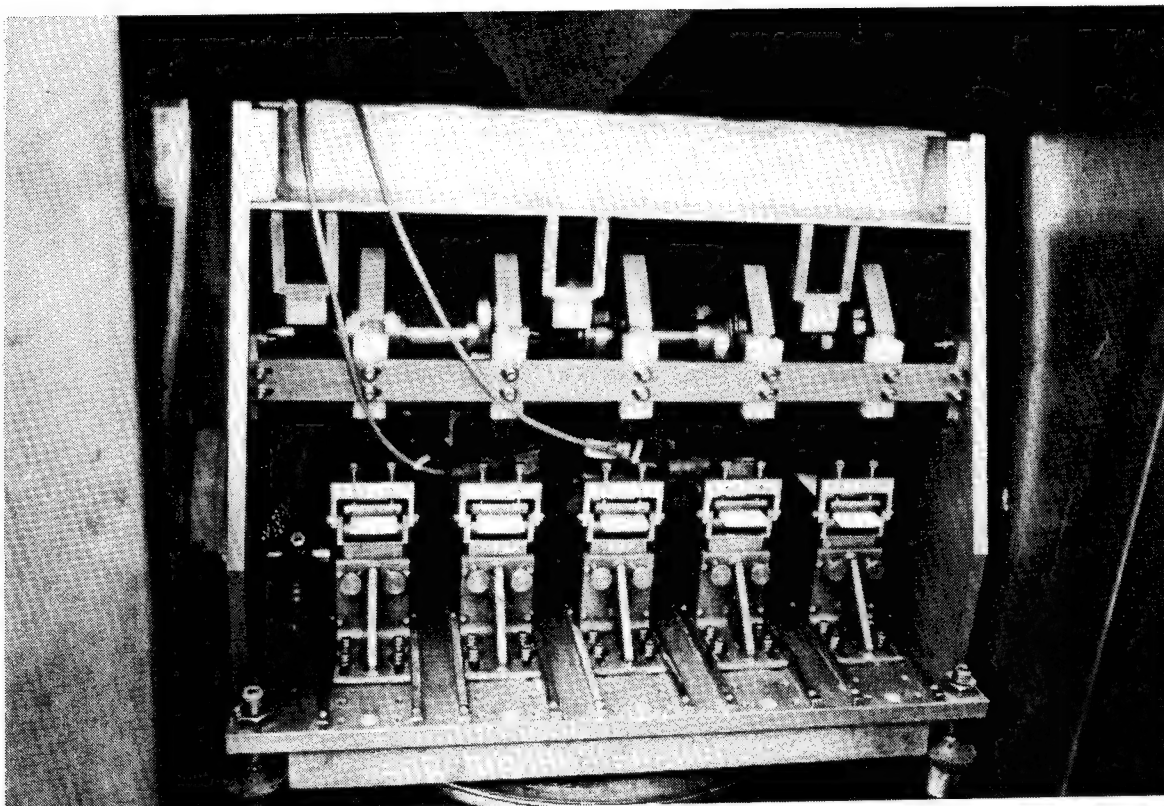
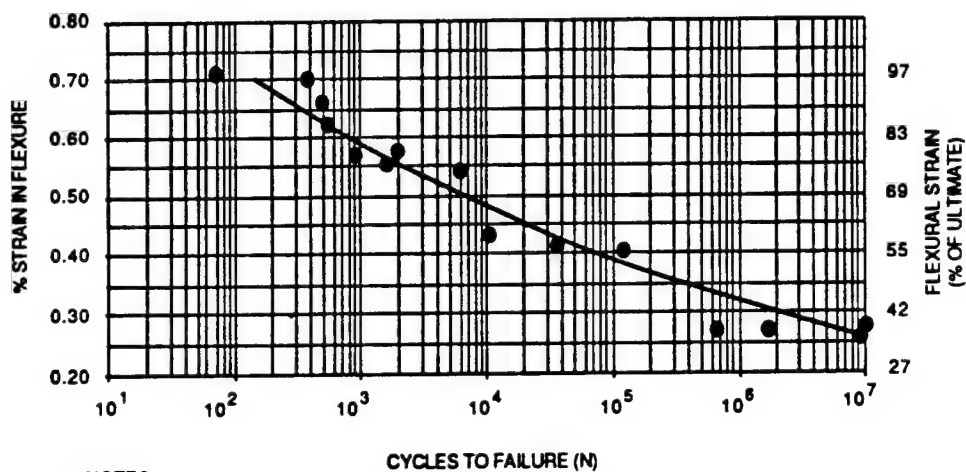


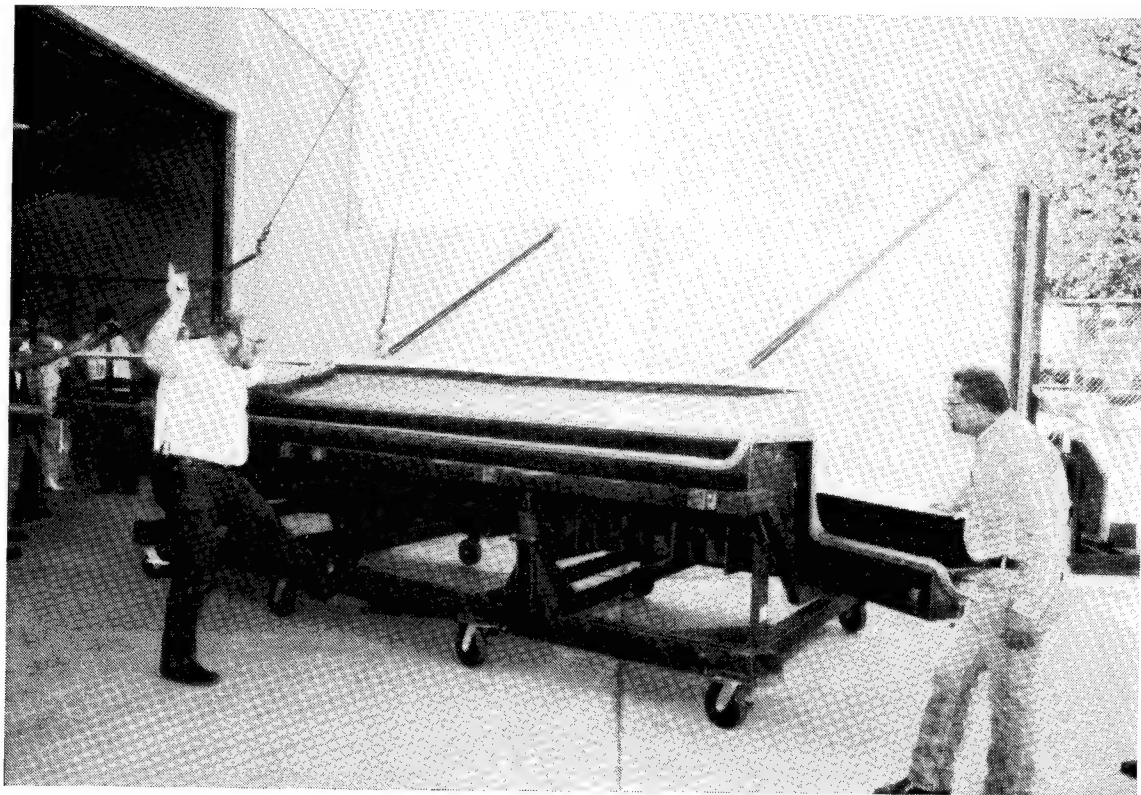
Figure 5. Flexural Fatigue Machine



NOTES:

1. 24 oz/yd<sup>2</sup> Woven Roving S2 Glass/Polyester Resin
2. Displacement Controlled 3-Point Flexural Fatigue with Displacement Ratio of -1.0 at 3 Hz.
3. 8-Ply Laminates [0°, 90° ± 45]s
4. Curve represents data fitted to the power function interpolation method,  $y = a x^b$

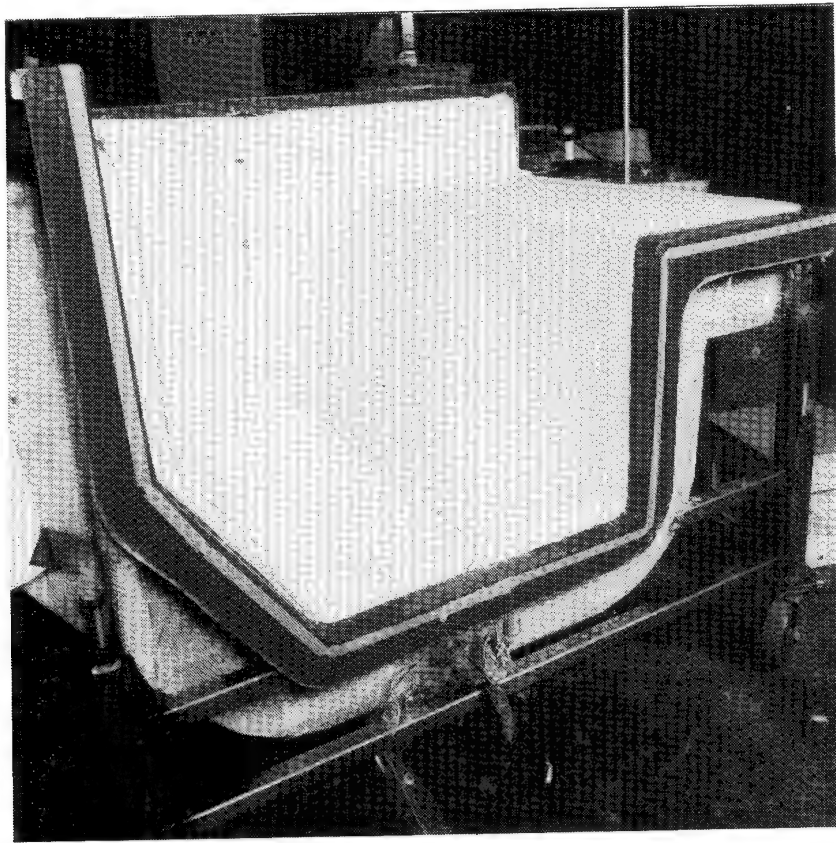
Figure 6. Flexural Fatigue Results



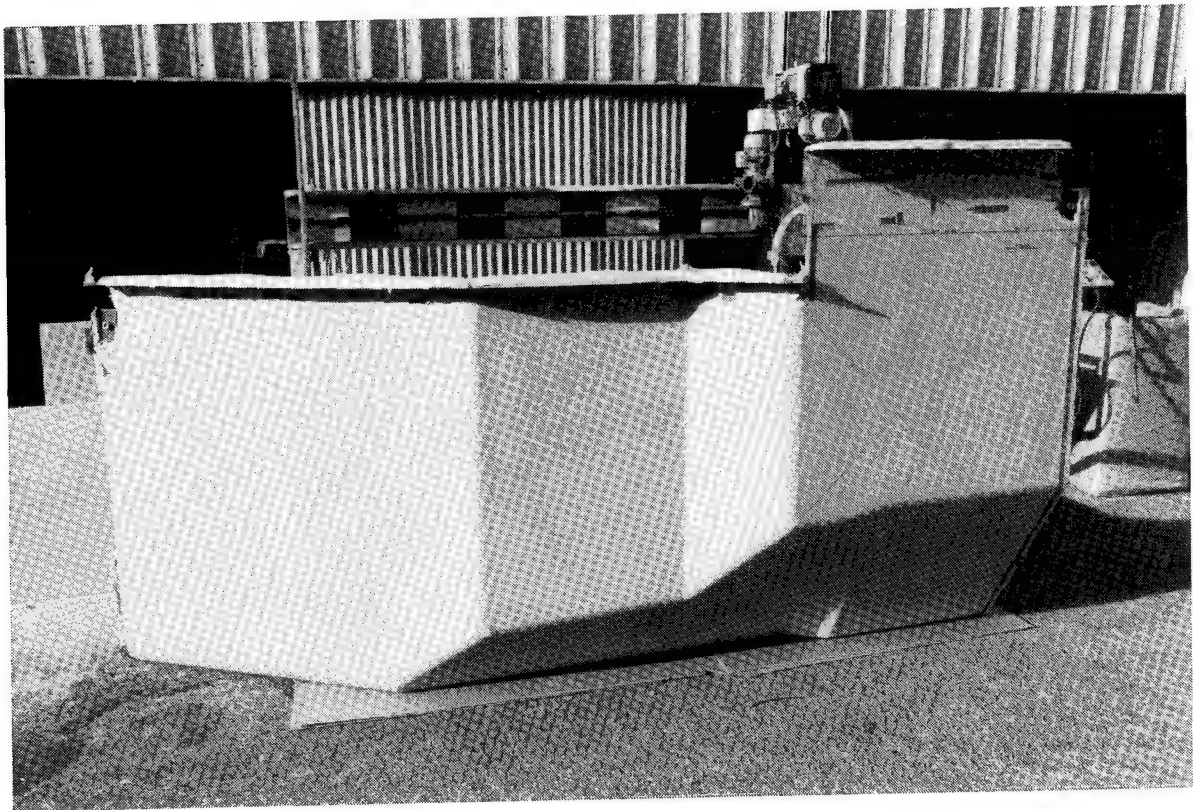
**Figure 7. Left Composite Hull Section**



**Figure 8. Right Composite Hull Section**



**Figure 9. Prepeg Screening Tool**



**Figure 10. Eleven Foot Process Development Specimen**



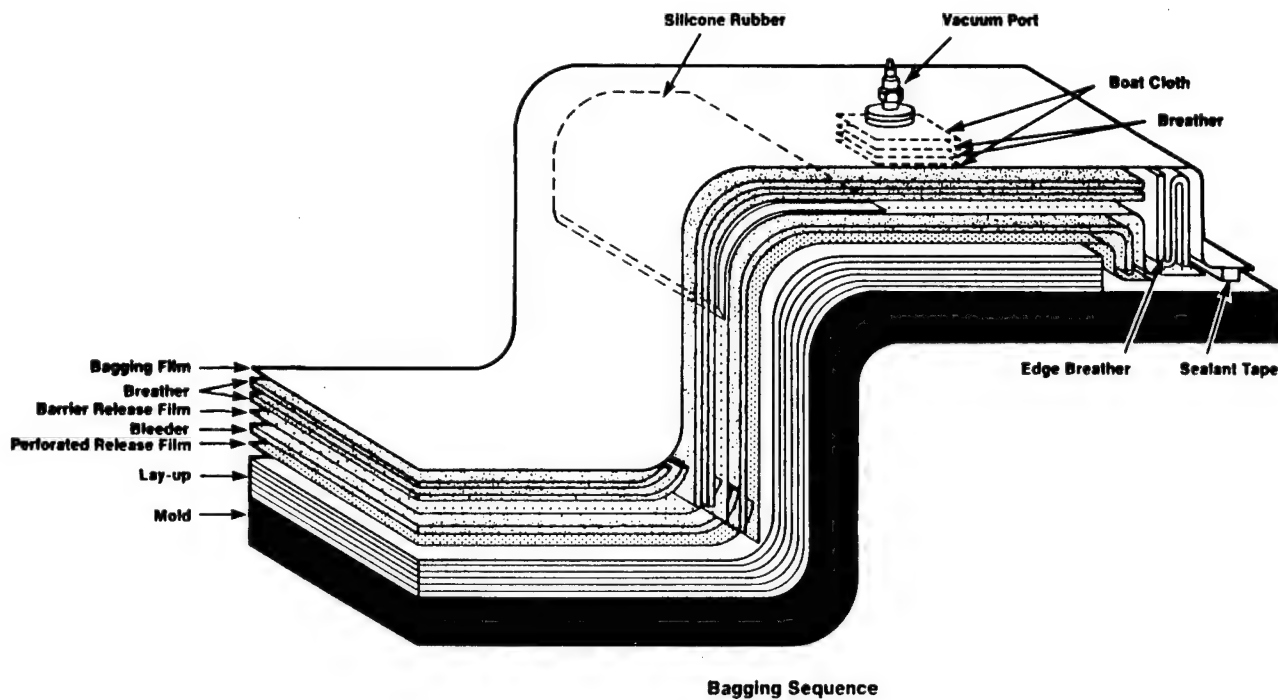


Figure 11. Vacuum Bagging Sequence

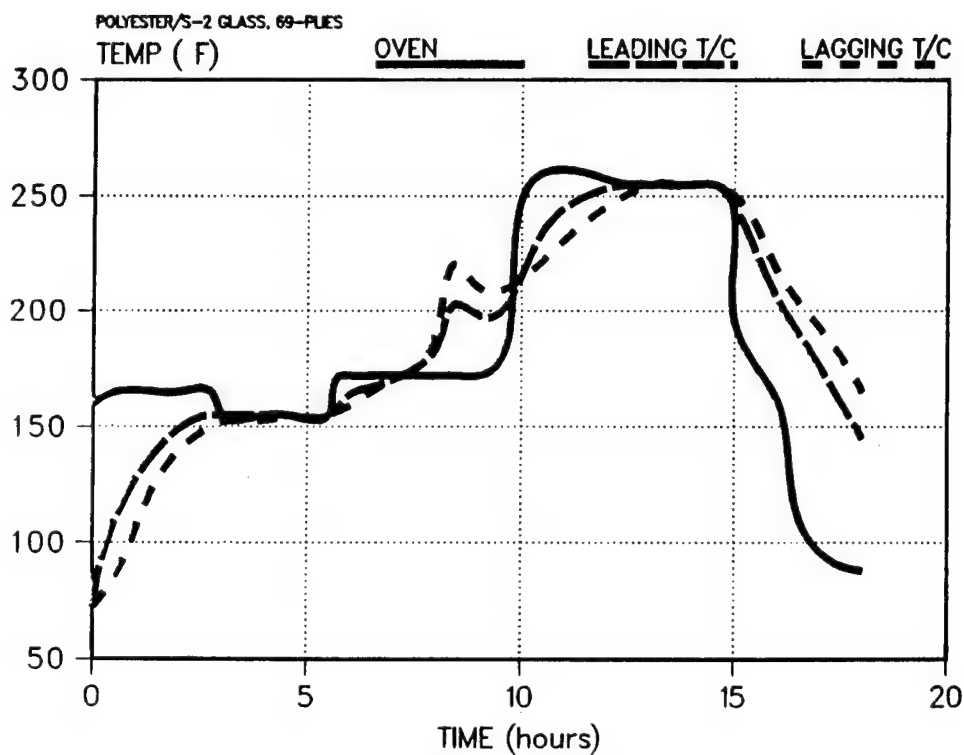
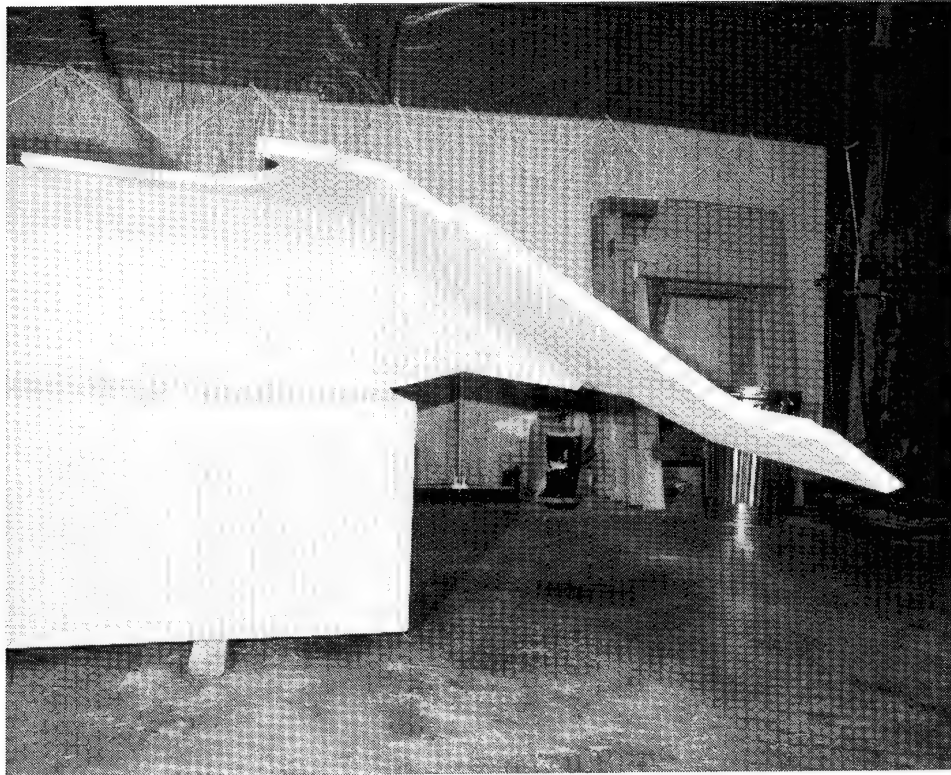
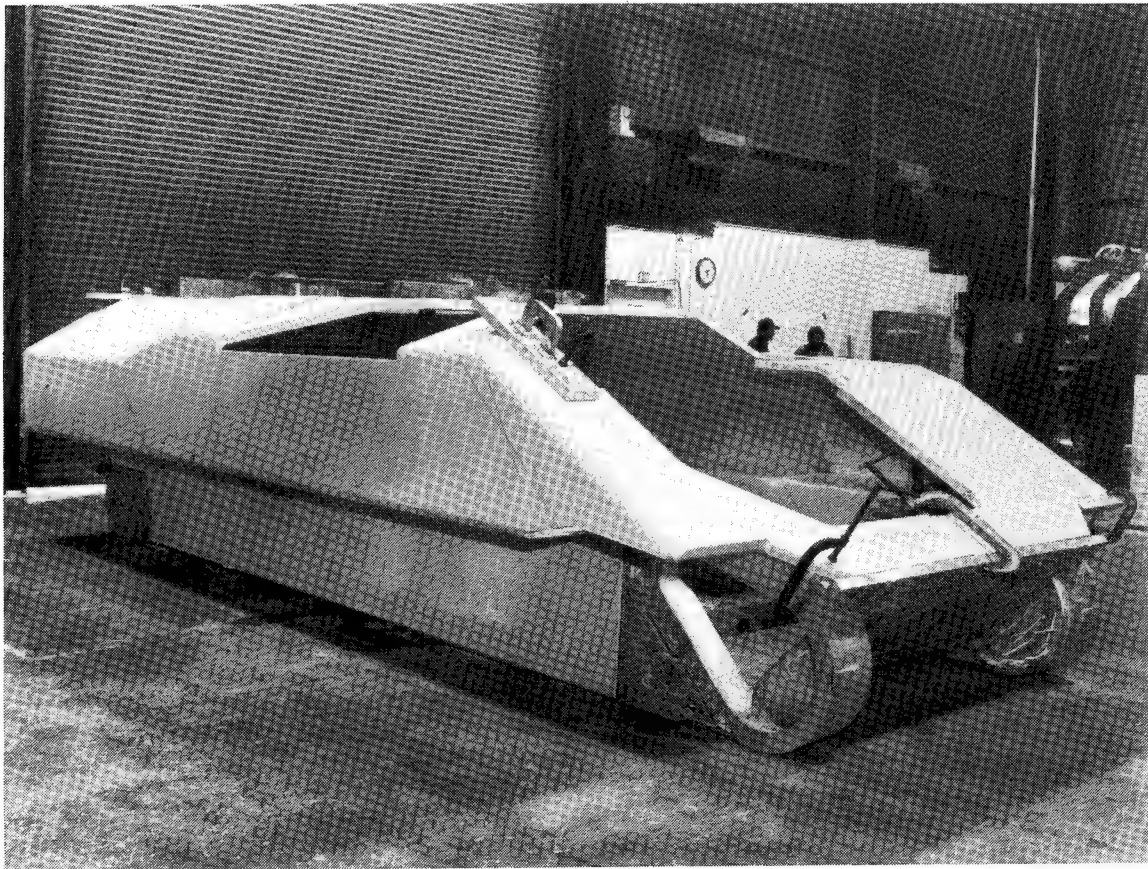


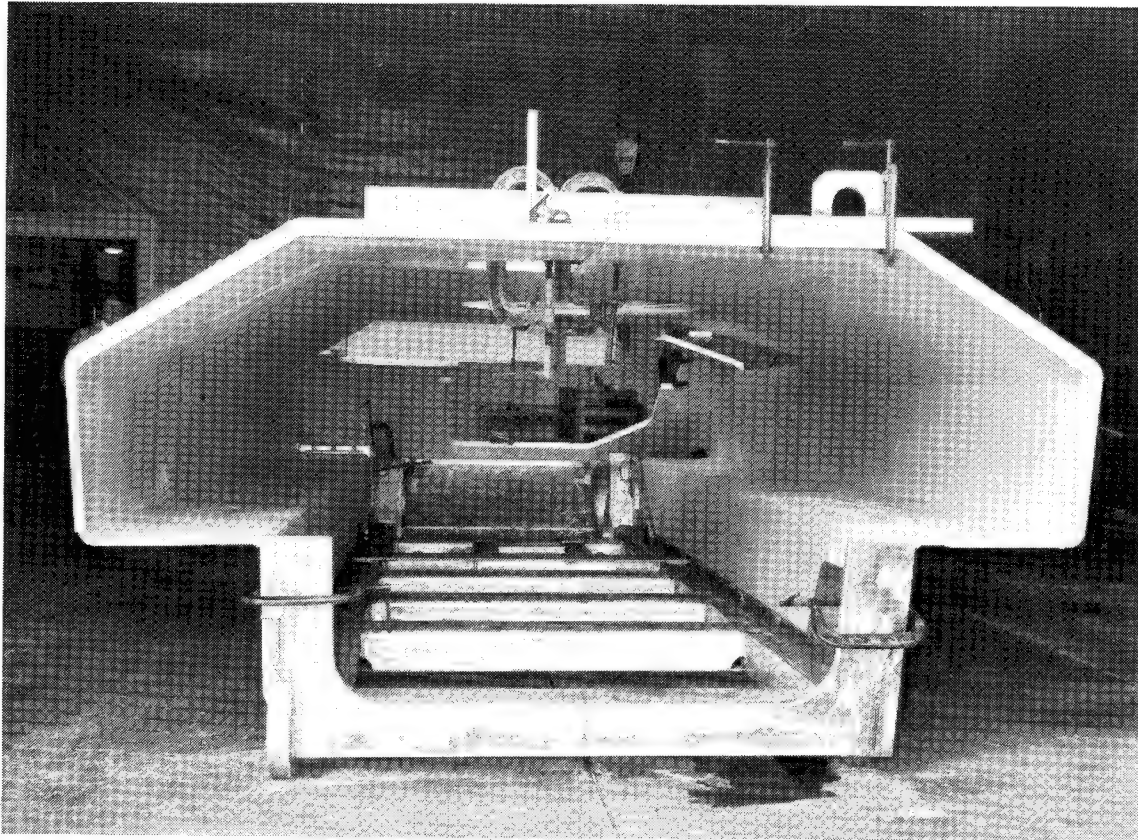
Figure 12. Cure Cycle



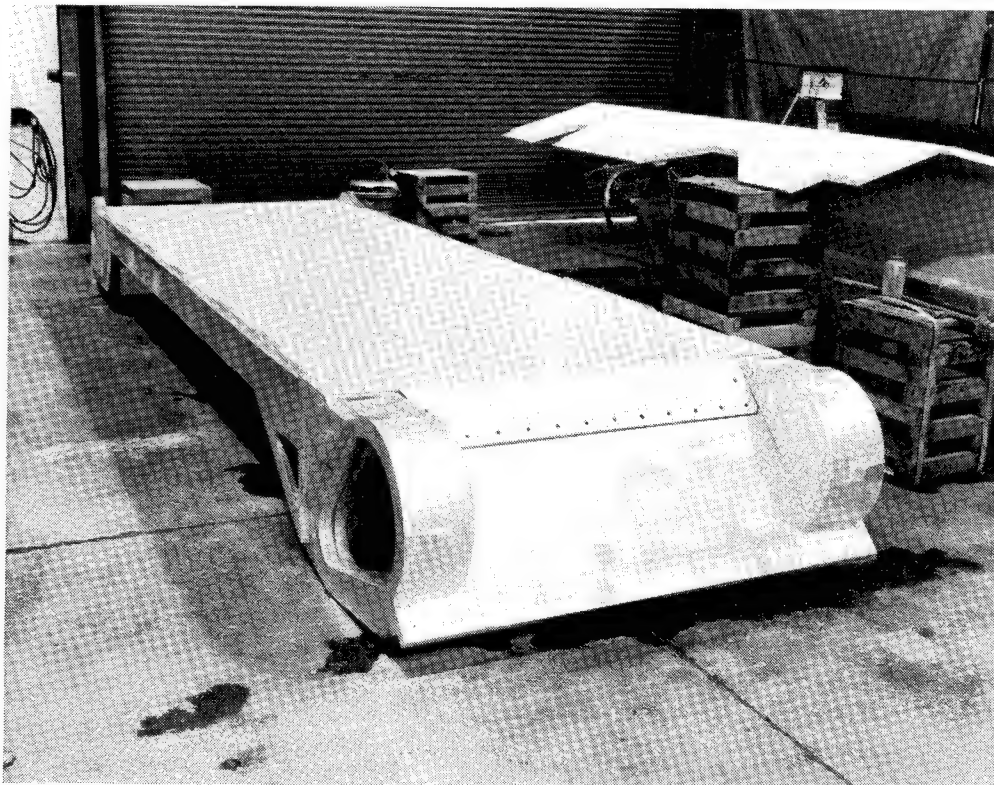
**Figure 13. Machined Edges**



**Figure 14. Fitup to Chassis**

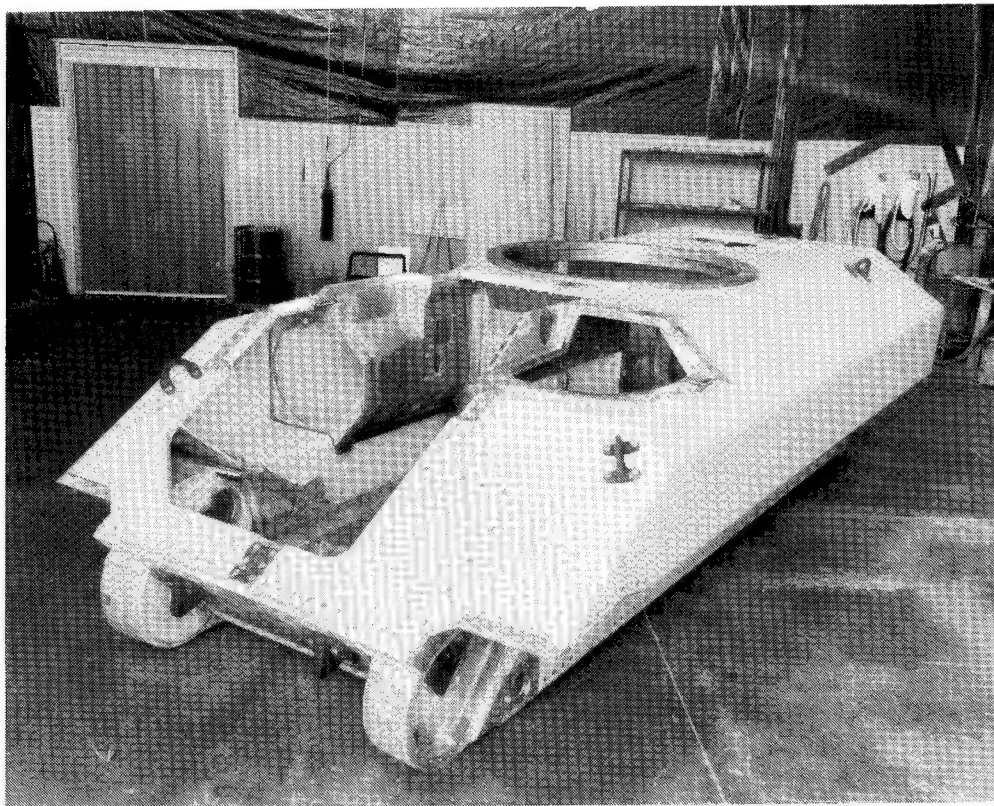


**Figure 15. End View, CIFV**



**Figure 16. Composite Bottom Plate**





**Figure 17. CIFV Hull Assembly**



**Figure 18. Left Side View**



**Figure 19. Right Side View**

## APPLICATIONS OF COMPOSITES TO ARMAMENTS

D. W. Oplinger

Army Materials Technology Laboratory  
Watertown MA, 02172

### ABSTRACT

The US Army Materials Technology Laboratory (MTL) has been engaged in investigating the feasibility of applying composite materials to the lightening of artillery structural components since about 1982. In this period a number of efforts have been carried out either in-house at MTL or by supporting organizations, including Benet Laboratory and the Oak Ridge National Laboratory, aimed at investigating applications to various components of towed artillery. This paper will describe salient features of these efforts and some important conclusions that have come out of them. In addition to organic matrix composites, discontinuously reinforced metal matrix composites appear to have great potential for weight reduction in this type of application.

### INTRODUCTION

The Army interest in composites is wide-ranging in scope, as illustrated in Table 1 which is a summary of Army programs described at a recent mechanics meeting [1] .

It can be seen, in particular, that the composites activities at the US Army Materials Technology Laboratory (MTL) place a major emphasis on technology demonstration activities in which a variety of potential applications are pursued by development of representative subsystems or components. In addition to the subject of this particular paper, that of another paper to be presented at this meeting [2] is a case in point. It should be noted that, as illustrated in these examples, applications of interest for ground-based Army operations form the major thrust of the MTL program.

For the last twenty or so years, MTL has repeatedly pursued a strategy of selecting previously unexplored areas for investigating applications of composite materials so as to establish a level of technology which was sufficient for demonstrating the payoffs that existed in these areas. In addition, the MTL efforts were aimed at showing that such payoffs could be successfully realized by applying viable composites technology for their exploitation. By default, these application efforts have been most frequently directed at non-flight Army hardware, since flight applications have been vigorously pursued in other quarters, while, except for weapon applications, little effort has been expended on the non-flight applications outside of those in which MTL has been engaged.

# **TABLE 1** **ARMY APPLICATIONS OF COMPOSITE MATERIALS**

## **AVIATION SYSTEMS COMMAND(AVSCOM)/FT KUSTIS/LANGLEY**

- HELICOPTER AIR FRAMES (ACAP)
- ROTOR BLADES
- POWER SHAFTING
- BALLISTIC SURVIVAL
- IMPACT DAMAGE
- IMPROVED STRUCTURAL CONCEPTS

## **ARMY RESEARCH OFFICE (ARO)**

- ROTOR BLADES
- HELICOPTER AIRFRAMES
- "INTELLIGENT" STRUCTURES FOR VIBRATION CONTROL
  - IMBEDDED TRANSDUCERS
  - " SHAPE MEMORY DEVICES
  - ELECTORRHEOLOGICAL DEVICES
- POWER SHAFTING
- ROBOTICS
- IMPACT DAMAGE CONTROL
- IMPROVED MANUFACTURING METHODS
- FAILURE
- CONSTITUTIVE RELATIONS

## **BALLISTIC RESEARCH LABORATORY (BRL)**

- 3D CONSTITUTIVE RELATIONS
- WEAPON APPLICATIONS
- ARMOR

## **BENET WEAPONS LABORATORY**

- COMPOSITE GUN TUBE REINFORCEMENT
- EM GUN APPLICATIONS
- APPLICATIONS TO GUN FABRICATION -- REINFORCED PLATING ELECTRODES
- BRAIDING TECHNOLOGY
- PERIPHERAL DEVICES FOR WEAPONS -- COMPOSITE BORE EVACUATOR
- FILAMENT WINDING SOFTWARE DEVELOPMENT

## **MISSILE COMMAND (MICOM)**

- MISSILE COMPONENTS
- LAUNCHERS/LAUNCH TUBES
- ROCKET MOTOR CASINGS
- MECHANICAL CHARACTERIZATION METHODS FOR FILAMENT WOUND COMPONENTS
- MATERIAL CHARACTERIZATION FOR FILAMENT WINDING

## **MATERIALS TECHNOLOGY LABORATORY (MTL)**

- THICK COMPOSITE HULLS FOR ARMORED VEHICLES
- TOW BARS FOR HEAVY VEHICLE BATTLEFIELD RECOVERY
- LIGHTENED ARTILLERY
- SHELTERS
- MECHANICS OF COMPOSITES, BOLTED & BONDED JOINTS
- MIL-HDBK-17
- FABRICATION/PROCESSING R&D
- NDE

In the present paper, one such application, that of structural components for artillery, will be described. The MTL program on lightened components for towed artillery illustrates the various phases that such an effort may encounter.

This paper can be considered to be a summing up of what has been accomplished to date regarding the applications of composites to artillery. Important issues which were brought to light by the present effort will be clarified here.

## **THE MTL LIGHTWEIGHT HOWITZER PROGRAM**

### **BACKGROUND**

Since early in 1982, MTL has been investigating the application of composite materials to towed artillery for weight reduction. Fig. 1 illustrates the primary motivation which has driven Army support of the Lightweight Howitzer project, that of reducing the weight of 155mm towed artillery so as to allow this level of firepower to become available to units of the Army which do not normally have access to helicopters having adequate lifting capability for dealing with such weapons as they are currently fielded. The existing situation is represented by the M198 155mm towed howitzer which weighs slightly under 16,000 lbs. and requires either a CH 47 or, in the case of the Marines, a CH 53, for air transport. Light Divisions of the Army normally have access to helicopters such as the Blackhawk with a worst-case (hot-day, high altitude) lift load of less than 5000 lb, and therefore are not able to deliver the M198 to battlefield locations of interest. Early in the Lightweight Howitzer program it was envisioned that some aircraft such as an upgraded version of the Blackhawk would become available which could manage to provide transportation capability for loads on the order of 9000 lbs, and this was the original target weight of the overall Army Lightweight Howitzer effort.

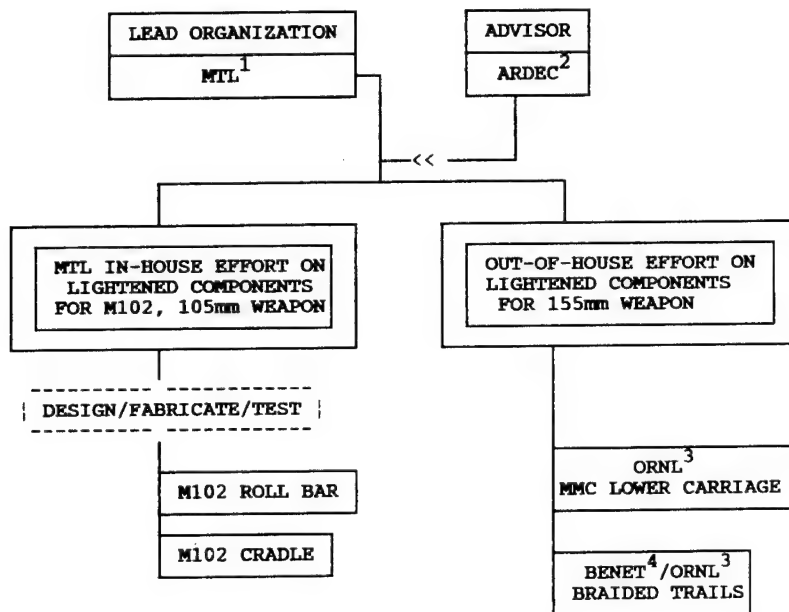
It was assumed that composite materials would have a significant role in providing a lightened 155mm weapon to meet this need. Accordingly, MTL undertook a component development effort in which various components of typical towed howitzer systems were examined for weight reduction potential obtained from replacing metals by composites.

It should be understood that there is a broader objective in the MTL effort than the achievement of a specific system development, however. The application of composites can be considered a relatively mature art in the case of aircraft, in which the major issues have been addressed over a period of more than twenty years. However, in ground-breaking applications such as those of both armored vehicles as exemplified by system to be discussed by W. Haskell[2] as well as the Lightweight Howitzer program, which is the subject of this paper, the challenges are primarily connected with the introduction of composites technology into a new application by a group (the weapons development community) whose experience has been limited mostly to homogeneous metals. This is certainly a familiar situation in the history of the composites industry over the last 20 years and indeed is probably not unrepresentative of the dilemma faced by the aircraft industry

when composites were introduced there for primary structure in the late 60's.

TABLE 2 shows the format which the MTL program has assumed over the period of 1982 to the present. Contributions were made at various stages by outside organizations including Oak Ridge National Laboratory (ORNL) and Benet Weapons Laboratory under MTL funding. In addition, the Armament Research, Development and Engineering Center (ARDEC) at Picatinny Arsenal, which has responsibility for the development of artillery for the Army, acted as an advisor for technical issues related to artillery performance requirements. TABLE 3 shows the team of individuals from various organizations who contributed to the effort.

TABLE 2  
FORMAT OF MTL LIGHTWEIGHT  
HOWITZER PROJECT



MTL¹ -- US ARMY LABORATORY COMMAND  
MATERIALS TECHNOLOGY LABORATORY

ARDEC² -- US ARMY ARMAMENT RESEARCH,  
ENGINEERING AND DEVELOPMENT  
COMMAND

ORNL³ -- OAK RIDGE NATIONAL LABORATORY

BENET⁴ -- ARDEC/BENET WEAPONS LABORATORY

In addition to the MTL effort, ARDEC (Picatinny Arsenal, Dover NJ) conducted a contractual effort aimed at developing a 9000 lb., 155mm weapon. Three contractors, shown in TABLE 4, were involved. An important part of the ARDEC contracted effort was the development of innovative approaches to retention of stability in lightened weapons, a problem which will be discussed below. Various approaches taken in the contracted effort are described in TABLE 4; these will be clarified later.

The ORNL and Benet efforts involved investigation of the applications of composites to components for 155mm towed artillery, as exemplified

**TABLE 3**  
**MTL LIGHTWEIGHT HOWITZER TEAM**

PROJECT LEADER  
D. Oplinger

**ARDEC \* ADVISORY TEAM**

ARDEC POC**	-- H. Liberman
TECHNICAL CONSULTANTS	-- R. Becker, N. Lionetti, S. Floroff

**MTL \* EFFORT (COMPOSITE ROLL BAR AND CRADLE FOR M102 HOWITZER)**

STRUCTURAL ANALYSIS ENGINEER	-- K. Gandhi
DESIGN ENGINEER	-- P. Cavallaro
DESIGN-DETAIL TESTING AND FABRICATION LIASON ENGINEER	-- G. Piper
COMPOSITES FABRICATION ENGINEERS	-- J. De Luca, S. Ghiorse
DATA AUTOMATION ENGINEER	-- J. Beatty
STRUCTURAL TESTING ENGINEERS	-- W. Bethoney, W. Crenshaw R. Pasternak

**OUT-OF-HOUSE SUPPORTING ACTIVITIES**

OAK RIDGE NATIONAL LABORATORY POC**	-- G. T. Yahr
BENET WEAPONS LABORATORY POC**	-- G. Friar

---

\* ARDEC -- see Organizational Designations, Table 1

\*\* POC -- "Point of Contact"

**TABLE 4**  
**ARDEC 9000 LB SYSTEM DEVELOPMENT EFFORT (1984-1988)**

• CONTRACTED EFFORT TO DEVELOP 9000 LB 155mm LIGHTWEIGHT  
TOWED HOWITZER

- FMC NORTHERN ORDNANCE -- SUPER LOW PIVOT HEIGHT,  
LONG RECOIL STROKE, ACCOMPLISHED BY  
"STILT-LIKE" SUPPORTING STRUCTURE
- BMY -- STABILITY ACHIEVED BY CURVILINEAR  
(UPWARDLY CURVED) RECOIL PATH
- AAI -- EFFECTIVE LONG RECOIL STROKE BY  
USE OF "FOLDED" (TELESCOPING) RECOIL  
STRUCTURE

by the M198 towed howitzer shown in Fig. 2(A). Although as stated above, the Army objective was toward lightening of 155mm weapons, the MTL effort was directed toward design, fabrication and testing of components for a lighter system, the M102 (105mm) shown in Fig. 2(B), which was selected as a test bed for experimenting with composite components.

Fig. 3 shows further details of systems of interest. Fig. 3(A) illustrates a typical air transport operation with the M102 howitzer. The



self-propelled M109 howitzer, Fig. 3(B), in which the gun is mounted on a tracked vehicle is included to emphasize the difference between towed and vehicle-mounted artillery.

The major consideration in this regard is the challenge of maintaining dynamic stability of towed weapons during firing operations. In the case of a vehicle-mounted weapon such as the M109 self propelled howitzer shown in Fig. 3(B), the total weight of the system will typically amount to 30 tons or greater. Obviously, this weight is available for providing stability to the gun with regard to motion induced by recoil forces. Incentives for weight reduction of gun components for such systems are not significantly impacted by stability issues, in contrast with the situation in the case of towed artillery. This will be discussed in some detail subsequently.

Fig. 4 summarizes the components which have been of interest in the present effort. In the case of the M102 howitzer which, as noted above, was used as a test bed, a composite roll bar was included in the effort. A rollbar is of interest because of a tendency for these weapons to overturn during either air drop (Fig. 3(A) ) or ground transport maneuvers, leading to a loss of optical fire control equipment needed for sighting the weapon.

In the case of the 155mm M198, the main effort was on trail and bottom carriage components. Details of interest for these components will be described later.

## CHARACTERISTICS OF TOWED ARTILLERY

### Description of Components

A few remarks are in order regarding the nature of towed artillery and resulting performance requirements which affect opportunities for weight reduction.

Fig. 5 shows an expanded view of the M198 howitzer shown in Fig. 4. Here the weapon is separated into recoiling and non-recoiling parts for convenience with regard to subsequent discussion. In Fig. 6 the non-recoiling (supporting structure) components are shown individually. These include (1) the "cradle" which supports the weight and recoil loads produced by the recoiling parts, i.e. the cannon together with the recoil mechanism, shown at the top of Fig. 6; (2) the "upper carriage" which provides for vertical movement of the gun and cradle; (3) the "lower carriage" which supports the previously mentioned components and allows for horizontal (azimuthal) motion of the gun, and ; (4) the "trails" which serve the dual functions of helping to resist backward tipping of the gun during recoil, and providing an attachment point for towing during ground transport in which the weight exerted on the towing vehicle is reduced by the effect of leverage provided by the length of the trails. Components shown in Fig. 6 include a firing platform which is removed from the storage position shown here and installed under the bottom carriage during firing, together with "spades" which are attached to the rear end

of the trails and driven into the supporting terrain to prevent rearward motion of the gun.

### Dynamic Performance Requirements

Certain performance characteristics of towed howitzers having to do with behavior during recoil have an important bearing on the extent to which weight reduction can be undertaken. These relate to the factors controlling the magnitude of the recoil forces and the dynamic stability, i.e. the tendency of the howitzer to "hop" during recoil.

Hop is objectionable because its presence tends to result in a disturbance to the sighting of the gun, relating to accuracy of target acquisition. While this is not a factor in the case of vehicle-mounted artillery such as that shown in Fig. 3(B) in which the mass of the vehicle provides more-than-adequate stability, in the case of towed howitzers which depend on the mass of the non-recoiling supporting structure (Fig. 5) for stabilization, stability exerts an overriding influence on the configuration of the system.

The magnitude of the recoil forces produces two effects which make it desirable to limit them. First of all, the magnitude of the recoil force is a crucial factor in determining whether or not the weapon is stable against hop. In addition, their magnitude should be kept low in order to avoid excessive wear on the recoil mechanism. Low weight of recoiling components per se, together with low total system weight, tends to cause both large recoil forces and severe hop. The factors which control these two effects are illustrated in Fig. 7 to 9.

Fig. 7 indicates the relationships which govern the recoil force magnitude. These include (1) the projectile momentum, which is the basic performance requirement of the weapon and corresponds to the payload of the projectile which governs its mass, together with the desired firing range which governs the projectile velocity; (2) conservation of momentum which determines the relation between projectile momentum and momentum absorbed by the recoiling parts, and; (3) conservation of energy which determines the work that the recoil mechanism has to do in bringing the recoiling parts to a stop, equivalent to the kinetic energy of the recoiling mass which corresponds to its momentum.

In conventional howitzers in which the gun is at rest before firing, the recoiling momentum is equal in magnitude to that of the projectile. Experimental systems (called "soft recoil" systems) have been tried, in which a spring mechanism is used to impart an initial forward velocity to the gun which, as deduced from the conservation-of-momentum relationships shown in Fig. 7, reduces the recoiling momentum significantly. This is one approach which has been considered for reducing recoil forces and maintaining stability in lightened weapons.

The relationship shown at the bottom of Fig. 7 implies that the **average** recoil force is given by (see notation of Fig. 7):

$$\bar{F}_{rec} = gP_{rec}^2 / 2L_r W_{rec} \quad (1)$$

Note that large  $P_{rec}$  together with small  $L_r$  and  $W_{rec}$  will lead to large values of the average recoil force. In addition, as indicated in Fig. 8, characteristics of the recoil mechanism (typically a hydraulic/spring/pneumatically actuated system) which cause the resistance characteristic to vary during the recoil stroke, will cause the **peak** force to be considerably above the average value. This will aggravate the problem since the peak force is the determining factor for both stress on the recoil mechanism and stability.

Fig. 9 illustrates the relationships which govern weapon stability. These can be summarized fairly simply in terms of the vector denoted as " $F_{res}$ " in Fig. 9. This is the resultant of the horizontal recoil force,  $F_{rec}$ , acting through the trunnion, (ie. the pivot about which the gun is rotated vertically) and the vector corresponding to the total weight,  $W$ , acting through the CG of the system. The distance  $L_{res}$ , shown in Fig. 9 near the end of the trail, represents the lever arm of the resultant vector about the anchor point produced by the spade attached to the rear end of the trail. If  $L_{res}$  is such that the line of action of  $F_{res}$  lies below the tip of the spade, as is the case in Fig. 9, then all tendency toward hop will essentially be eliminated, since there will be a clockwise moment tending to push the front end of the gun into the ground throughout the recoil stroke. On the other hand if any combination of large  $F_{rec}$  and  $h_{piv}$  is present which rotates the line of action of  $F_{res}$  so that it lies above the spade tip, a counterclockwise moment will result, tending to produce definite hop. The fundamental condition described by the last equation in Fig. 9, which is required to avoid hop, is determined by the magnitude and lever arm of the recoil force and total weight vector as follows:

CONDITION FOR AVOIDANCE OF HOP (see Fig. 7 for notation)

$$WL_{cg} > F_{rec})_{max} h_{piv} \quad (2)$$

Taking into account the relationship between maximum and average recoil force shown in Fig. 8, which is described by a magnification parameter denoted as  $\eta$  in Fig. 9, then when equation (1) for the magnitude of average recoil force is taken into account, Eq(2) reduces to

$$L_{cg} L_{rec} / h_{piv} > gP_{rec}^2 \eta / 2W_{rec} W \quad (3)$$

where

$$\eta = F_{rec})_{max} / \bar{F}_{rec}$$

$P_{rec}$  = momentum of recoiling mass

$W_{rec}$  = recoiling weight

$W$  = total system weight

$L_{cg}$  = horizontal distance from spade tip to system CG

$L_{rec}$  = length of recoil stroke

$h_{piv}$  = height of trunnion (pivot)

TABLE 5 summarizes the effects which control recoil force magnitude and stability. The message here is that we can change various dimensions in the weapon (increasing the trail length and length of recoil stroke, decreasing the pivot height) to compensate for the adverse effects of reduced weight on both the magnitude of recoil forces and the tendency toward hop during recoil. However, practical considerations tend to limit the extent to which advantage can be taken of such dimensional changes. For example, if the pivot height is lowered, firing with the gun elevated becomes awkward, since there

**TABLE 5**  
**OBSERVATIONS FROM DYNAMIC ANALYSIS**

RECOIL FORCE **DECREASES WITH --**

- INCREASING RECOIL STROKE

RECOIL FORCE **INCREASES WITH --**

- DECREASING WEIGHT OF RECOILING PARTS

STABILITY **INCREASES WITH --**

- INCREASING TRAIL LENGTH
- " RECOIL STROKE
- DECREASING TRUNNION (PIVOT) HEIGHT

STABILITY **DECREASES WITH --**

- DECREASING **TOTAL SYSTEM WEIGHT** (LINEAR EFFECT)
- DECREASING **RECOILING WEIGHT** (QUADRATIC EFFECT)

will be a loss of clearance with respect to the ground level as the gun recoils, for high elevations. Even with existing gun designs, there is a tendency for the gun to "dig a hole" at high elevations. The only approach to compensating for this situation is shortening the recoil stroke, which then increases  $F_{rec}$  and therefore works against the desired performance characteristics.

TABLE 6 describes various approaches which may be considered for lowering recoil forces and recovering stability in a lightened weapon. As noted in TABLE 5, some of these ideas were incorporated in the contractual efforts funded by ARDEC. Of particular interest was the approach of BMY which involved an upwardly curving recoil path which helped to stabilize the weapon particularly in the early stages of recoil during which the forces are greatest. Other particularly innovative ideas include the spring-catapulted gun, mentioned previously, in which the initial momentum of the gun significantly reduces that which is imparted by the projectile. Methods such as the use of add-on ballast (e.g. heaping earth or other debris onto the base of the gun) are objectionable from the standpoint of ease of setup, and are not looked on with favor by artillery users. The last item noted in TABLE 6 refers to the "muzzle brake" which is a device attached to the front end of the gun tube and produces a deflection of the muzzle blast which helps to absorb momentum. In a properly designed muzzle brake, the blast deflection may produce an upward component of flow which produces a downward force component at the front end of the gun. A particularly important consideration in weight reduction attempts is

the difficulty in reducing the weight of recoiling parts per se. As indicated at the bottom of Table 6, in studies to date there has been a tendency to retain much of the recoiling weight of existing howitzers such as the M198, and to concentrate on reducing the weight of the supporting structure. The reason for this is that the recoil force, according to Eq(1), is affected by the weight of recoiling parts, and a reduction in recoiling weight aggravates not only the stability problem but also the structural burden on the recoil mechanism. The weight distribution in the M198 155mm howitzer is roughly 7500lbs of recoiling weight vs. 8500 lbs of non-recoiling support structure. Under typical firing conditions, the recoiling parts may be

**TABLE 6**  
**APPROACHES TO STABILIZING LIGHTENED GUN**

- LONG TRAILS (LIMITED BY DIMENSION ENVELOPE FOR AIR TRANSPORT)
- LOW  $h_{piv}$  (LIMITED BY NEED FOR RECOIL CLEARANCE AT ELEVATED FIRING)
- LARGE RECOIL STROKE (LEADS TO AWKWARD OPERATING CHARACTERISTICS)
- USE OF SPRING CATAPULTED (MUNITION QUALITY PROBLEMS)
- USE OF CURVED RECOIL PATH PER BMY (COMPLICATED MECHANISM)
- USE OF ADD-ON BALLAST, e.g. EARTH, ETC. (OBJECTIONABLE FROM STANDPOINT OF SET-UP TIME)
- UPWARD DEFLECTION OF MUZZLE BLAST BY "TUNED" MUZZLE BRAKE

CONCLUSION
EMPHASIS OF LIGHTENING EFFORTS PLACED ON NON-RECOILING COMPONENTS IN CONSERVATIVE EFFORTS TO DATE

receding with velocities on the order of 40-50 ft/sec, ie. 25-35 mph. In order to bring the 7500 lbs of recoiling weight to a stop in distances in the range of 3-6 ft. which represents practical stroke lengths for typical hydraulic mechanisms, **average** force levels on the order of 50-100,000 lbs are encountered, according to Eq(1), with peak values possibly lying 30-50% higher. This is not necessarily a difficulty for the supporting structure, but may be for the typical hydraulic recoil devices that tend to be used in howitzers. Weight

reduction studies that have been conducted on towed artillery by the Army have generally tended to confine their attention to the supporting structure.

In terms of the lightening of guns per se, conventional technology involves the use of gun steels, and consideration of other materials involves a technical challenge of great difficulty because of the combination of severe structural loading, thermal environment and chemical environment which are encountered. Fig. 10 illustrates an example, from a program by Benet Laboratory, of how composites can be used successfully to improve gun performance, although in this case, lighter weight was not sought or achieved. In this example the desire was to lengthen the gun barrel for better accuracy, and a filament wound graphite epoxy over-wrap was used to increase the stiffness-to-weight ratio of the barrel in bending, to compensate for the tendency of a longer barrel to "droop" which would reduce the achieved accuracy. The resulting lengthened barrel was designed to be dynamically equivalent to the original all-steel barrel, by a judicious relocation of mass which would not have been possible if an all-steel construction had been used with the lengthened barrel.

In general, it is clear that in the case of towed artillery, there are basic limitations to the extent by which lightened designs can be developed for a given payload range and weight which the weapon is required to deliver. Although challenges to the use of composites are significant, it should be kept in mind that they are not necessarily the main barrier to achieving significant weight reduction. However, many options for addressing the stability problem are available, so that in the long run this should not be a major obstacle to the introduction of composites.

In the subsequent sections the issue of what can be accomplished through the use of composites will be addressed.

## **COMPONENT DEVELOPMENT ACTIVITIES**

### **GENERAL REMARKS**

In this section we will describe a series of studies which have been carried out on various towed howitzer components to illustrate some of the technical challenges and solutions which are encountered with composites. The component development studies undertaken under the MTL Lightweight Howitzer Program are summarized in Table 7.

### **COMPONENTS FOR 155mm HOWITZER**

#### **Trails**

The trail of the towed howitzer appears to be the component with the greatest weight savings potential through composites from several standpoints. Here it is feasible to utilize almost 100% of the weight saving potential of composites because attachment problems demanding any use of metals are minor.



In general, hollow, rectangular box beam shapes can be used with considerable effectiveness. Both filament winding and braiding have been considered as appropriate fabrication methods for such structures. These methods allow tapering along the length of the trail to be used.

An idea of the weight savings potential for composites can be obtained from a simple optimized box beam design for the generic load system shown in Fig. 11, which represents a worst-case situation for horizontal firing where the gun is rotated horizontally so as to lie in line with one trail. Structural consideration here is restricted to bending in the trail due to a vertical load component at the spade end, whose magnitude corresponds to the moment about the firing base produced by

**TABLE 7**  
**COMPONENT DEVELOPMENT EFFORTS IN**  
**MTL LIGHTWEIGHT HOWITZER PROGRAM**

**155mm HOWITZER COMPONENTS**

- TRAILS (MTL, BENET LAB, OAK RIDGE)
- BOTTOM CARRIAGE (OAK RIDGE)

**M102 COMPONENTS**

- ROLL BAR
- CRADLE

the recoil load acting through the pivot height. It should be kept in mind that firing at azimuthal positions not in line with either trail will tend to generate torsional loading on the trails which is ignored here but which would have to be accounted for in an actual design.

Such a load is considered to act on the hollow box beam shown in Fig. 12. The moment of inertia for section rotation about the x-axis in Fig. 12 is  $I_x$  which, for a thin-walled box, is approximately

$$I_x \approx A_f d^2 / 2 \quad (4)$$

leading to an upper flange compressive stress given by

$$\sigma_f^C \equiv M_T d / 2 I_x \approx M_T / d A_f \quad (5)$$

on allowing for Eq(4). When the expressions for  $M_T$  and  $F_y$  given in the lower sketch of Fig. 12 are combined with Eq(5), then in terms of an assumed ultimate compressive stress in the flange denoted as  $\sigma_f^{cu}$ , we get a requirement for a minimum value of flange area given by

$$A_f \geq \frac{L_T}{L_{CG}} \frac{F_{rec}}{\sigma_F^{cu}} \left( \frac{h_{piv}}{d} \right) \quad (6)$$

i.e. as inversely proportional to the web height,  $d$ . For the webs, it will be found that the optimized design generally leads to a shear-buckling critical condition, rather than shear stress failure of the webs. In addition, it is found that the flanges should be close to compression-buckling critical at the stress for which compressive failure occurs. Table 8 gives appropriate classical buckling predictions for long narrow orthotropic strips with simply supported edges, which apply here to a satisfactory degree. (These tend to be conservative since they ignore the restraining effect of one wall on lateral rotation of the neighboring wall corresponding to the buckling deformation.) For shear buckling of the webs due to a stress  $\tau_w$  given by

$$\tau_w = F_Y / 2A_w \quad (7)$$

then freedom from shear buckling requires that

$$K_w^S (t_w/d)^2 \geq \tau_w \quad (8)$$

which, when combined with Eq(7), can be transposed to give a requirement on the web area,  $A_w$  (given by  $dt_w$  in accordance with the notation of Fig. 12), as follows

$$A_w \geq (F_Y / 2K_w^S)^{1/3} d^{4/3} \quad (9)$$

Note that a minimum-weight design requires that the box-beam section area,  $2(A_w + A_f)$  be minimized. Taking account of Eq(6) and (9) and setting

$$c_1 = (F_Y / 2K_w^S)^{1/3} \quad (10.1)$$

$$c_2 = \frac{L_T}{L_{CG}} \frac{F_{rec}}{\sigma_F^{cu}} h_{piv} \quad (10.2)$$

then leads to

$$A_f + A_w = c_1 d^{4/3} + c_2/d \quad (11)$$

which is minimized with respect to  $d$  for  $d = d_{opt}$  given by

$$d_{opt} = (0.75c_1/c_2)^{3/7} \quad (12)$$

Once  $d_{opt}$  is determined from Eq(12), the remaining dimensions of the box beam can be solved inversely from the proceeding equations. The result is

$$t_w = (F_Y / 2K_w^S d_{opt}) \quad ; \quad A_w)_{min} = t_w d_{opt}$$

$$A_f)_{min} = \frac{L_T}{L_{CG}} \frac{F_{rec}}{\sigma_F^{cu}} \left( \frac{h_{piv}}{d_{opt}} \right)$$

$$b_{opt} = [A_f)_{min} (K_f^C / \sigma_f^{cu})^{1/2}]^{1/2} \quad ; \quad t_f = A_f)_{min} / b_{opt}$$

(The last two equations insure that the flange is simultaneously buckling and stress critical, which is a requirement for a minimum weight design.)

Table 9 shows the application of the above equations to a weight tradeoff study for loads and dimensions equivalent to the M198 howitzer. For the composite material systems (glass and graphite epoxy), generic unidirectional properties representative of S-glass/5208 and T300/5208 were assumed and used as inputs for a conventional laminate analysis which provided in-plane and bending properties for the box-beam walls. Moreover, a filament-wound construction was assumed in which the flanges were equivalent to a  $0_8/\pm 45^\circ$  layup while the webs were assumed to be all  $\pm 45^\circ$ . The compression-failure strengths,  $\sigma_F^{cu}$  were assumed to represent damage-tolerance allowables in which strains

**TABLE 8**  
**BUCKLING RELATIONS FOR LONG NARROW STRIP**  
(Simply Supported Edges)

$$\tau_{xy}|_{web} < K_w^S \left(\frac{t_w}{d}\right)^2 \qquad \sigma_x|_{flange} < K_f^C \left(\frac{t_f}{d}\right)^2$$

where

**FOR ISOTROPIC STRIPS**[3] ( $E$ =Young's modulus, Poisson ratio = 0.3)

$$K_f^C \approx 3.61E \qquad ; \qquad K_w^S \approx 4.84 E$$

**FOR ORTHOTROPIC STRIPS** [4]

$$K_f^C = \frac{\pi^2}{6} \left[ \frac{(E_x E_y)^{1/2} + \nu_y E_x}{1 - \nu_x \nu_y} + 2G_{xy} \right]$$

$$K_w^S = \frac{1}{3} \left[ \frac{\nu_x E_x E_y}{(1 - \nu_x \nu_y)^{1/2}} + \frac{2E_y G_{xy}}{1 - \nu_x \nu_y} \right]^{1/2} f(\theta)$$

where

$$\theta = \frac{(E_x E_y)^{1/2}}{\nu_y E_x + 2(1 - \nu_x \nu_y) G_{xy}}$$

and

$$f(\theta) = 11.7 + 0.532\theta + 0.938\theta^2$$

were limited to 0.004. For the metal components, generic yield strength values were assumed.

The weight comparisons which were obtained are felt to be representative of what would be obtained even if more optimistic values for the yield strengths of the metals were assumed, since the analysis provides a sensitivity to compression yield strength which is less than linear. It is thus apparent that in such a direct tradeoff, composites show a considerable weight savings, percentage wise in terms of the trail weights, vis-a-vis metals.

These results must be accepted with some reservations, however. The inclusion of metal attachments at the forward ends of the trails could significantly jeopardize the weight savings offered by composites, for example. However, an attachment concept devised by the Oak Ridge Team which will be discussed later shows considerable promise for minimizing the weight penalty of trail attachments.

An additional consideration is the need for torsional stiffening of the trails beyond that provided by the construction shown at the top of Table 9 for the composite systems. Fig. 13 shows the results of buckling analysis of the M198 aluminum trails by the Oak Ridge Team [5] The numbers which are included with the mode shapes represent bending stress levels in the flanges at which each mode occurs.

**TABLE 9**  
**WEIGHT TRADEOFFS FOR OPTIMIZED BOX BEAM**

(Composites:  $0_8 \pm 45^\circ$  flanges,  $\pm 45^\circ$  webs: Metals -- isotropic)

$F_{rec} = 100 \text{ klb} ; h_{piv} = 48" ; L_T^* = 200" ; L_{cg} = 250"$
--

	STEEL	ALUMINUM	GRAPHITE EPOXY	GLASS EPOXY
$\sigma_f^{cu} \text{ (ksi)}$	100	50	50	50
$K_w^s (10^6 \text{ psi})$	147	48	39	24
$K_f^c ( " " )$	109	36	16.6	12.3
DENSITY, $\text{lb-in}^{-3}$	0.28	0.10	0.055	0.072
$d_{opt}, \text{in}$	18.9	19.2	18.6	17.4
$b_{opt}, \text{in}$	8.19	10.35	8.67	10.82
$t_w, "$	0.107	0.156	0.166	0.191
$t_f, "$	0.249	0.386	0.475	0.407
$A_f)_{min}, \text{in}^2$	2.03	3.99	4.12	4.41
$A_w)_{min}, "$	2.03	3.01	3.09	3.32
Trail Weight*, lb	227	140	79.3	111

\* based on an effective trail length of  $1/2 L_T$  due to assumed tapering of the box beam along its length

The design of the M198 trails includes transverse bulkheads which can be expected to provide significant torsional stiffening. It can be seen that even with such stiffening, the warp-buckling seen in the

third mode occurs as a load not much above that of the first mode which appears to be pure vertical bending. In addition, other modes which occur at loads not far removed from that of the first mode give lateral deflection, presumably corresponding to column buckling about the bending axis with the lowest moment of inertia, due to the load equivalent to  $F_{REC}$  in Fig. 11 applied at the spade end of the trail.

Since these global buckling modes are sensitive to the moments of inertia of the box beam, detailed design efforts would have to insure that these moments of inertia (two bending plus one polar moment of inertia) are high enough to prevent the global modes from degrading the structural performance of the beam. Minimum weight designs in such cases might require some kind of stiffening or sandwich construction to achieve the maximum performance of the composite systems.

As part of the Lightweight Howitzer program, the Benet Laboratory Team (Table 2) undertook the development of a braided concept which is shown in Fig. 14. Braiding has a number of potential advantages over filament winding, including lower production costs for sufficiently large production runs and improved damage tolerance. The 1/6th scale trail shown in Fig. 14 took advantage of an improved resin delivery system resulting from MTL's SBIR program[6].

#### **Trail Attachments**

The bottom carriage of the M198 towed howitzer is shown at the top of Fig. 15. Massive steel "door hinges" are used in the M198 design for attachment of the trails. (Horizontal articulation of box trails is normally required so that the trails can be repositioned for towing and storage.) In this case the weight of the trail attachments amounts to several hundred pounds.

The lower sketch in Fig. 15 illustrates a concept developed by the Oak Ridge Team as an alternative to the door-hinge approach. This approach builds the trail attachment horizontally into the body of the bottom carriage. This allows much greater spacing of the load points in the attachment, possibly twice the vertical spacing of the typical door-hinge design, thus lowering the bearing loads corresponding to a given reaction moment which the attachment has to sustain. In addition, for rectangular box trail designs, the loads can be borne as in-plane loads on the box-beam web walls which, as discussion of the MTL composite cradle design below will indicate, is an excellent way to provide for load transfer in composite structures. The ORNL imbedded trail concept for the attachment at the bottom carriage shows great promise for eliminating nearly all weight penalty introduced by the attachment.

#### **MMC Bottom Carriage Effort**

Material tradeoff studies were carried out on a bottom carriage component for a 155mm howitzer having performance characteristics similar to those of the M198 by the ORNL Team (Table 2), to determine weight savings that can be anticipated from various materials. Conventional metals, organic composites and metal matrix composites were considered. Results of the tradeoff which are summarized in Fig. 16 indicate that:(1) aluminum and titanium, i.e. conventional light metals, would provide a component of around 800 lbs., as opposed to

1500 lbs for the current steel bottom carriage of the M198 howitzer;(2) organic composites, due to the presence of severe bearing loads and hard-contact points, would require the inclusion of metal inserts in various locations which would tend to negate the lightening advantage of organic composites over conventional metals; (3) **particulate reinforced metal matrix composites gave a considerable weight reduction over conventional metals and organic composites**, due, mainly, to the high stiffness/weight ratio of particulate reinforced aluminum together with the fact that the design tends to be stiffness(i.e. buckling) critical. An idea of the construction which was visualized is indicated in Fig. 17 which represents an FE model of the ORNL MMC carriage concept used to carry out the tradeoff studies.

This highlights the difficulty of realizing maximum weight savings with organic composites in some components where shapes are complex and numerous heavily loaded attachment points have to be dealt with. It should be recognized that this conclusion ought to be tempered with the recognition that the study was short term and did not allow time for creative solutions which might have eliminated some of the problems caused by bearing loads in organic matrix composites.

On the other hand the bottom carriage tradeoff study did surface the attractiveness of particulate reinforced MMC for many applications. More mundane applications of such materials such as in bolts which are lightly loaded but make up an appreciable fraction of the lower carriage weight appear attractive, for example. Studies[7] have indicated that conventional threading techniques can be successfully used with particulate reinforced metal matrix composites.

The present program hardly scratched the surface for potential applications of MMC's for lightening of howitzer components. A potential problem which surfaced in the course of the present study, however, is that of low dynamic toughness of particulate reinforced MMC's. Data obtained on contract[8] indicated that with materials initially considered for the ORNL bottom carriage design, Charpy impact energies were limited to only 10% of those of typical aluminum alloys. Moreover, ballistic impact experiments [9] indicated that significant cracking around holes produced by hostile projectiles can occur which would constitute considerable degradation of structural loading capability and might render the weapon inoperable for relatively minor battlefield damage. This concern motivated a subsequent effort by DWA[10] which indicates that significant improvement in ductility over that of the earlier materials can be obtained. The materials initially considered had elongations on the order of 1-2%, whereas the materials produced in the Ref. [10] study exhibited elongations as high as 5.5 %. In addition, revolutionary new approaches to toughening[11] of particulate reinforced composites appear to offer impressive improvements specifically in dynamic fracture toughnesses, resulting in Charpy energy capabilities equal to or greater than those of typical aluminum alloys.

The end result is that there appears to be considerable optimism for the use of particulate reinforced MMC's in howitzer components, although the issue of fracture toughness in the presence of battle

---

\*Private communication



damage must be addressed before accepting them completely. If this turns out to be not a limiting obstacle, then the opportunities for lightening using MMC's appear to be extensive.

## **MTL EFFORTS ON M102 HOWITZER COMPONENTS**

### **ROLLBAR FOR M102 HOWITZER[12]**

The rollbar which was developed at MTL for the M102 howitzer is visible in Fig. 2(B). The need for a rollbar grew out of roll-over incidents which have occurred both in air drop activities and in ground towing of the M102, although they have not been unheard-of with other towed howitzers. Such events can cause serious damage to crucial components such as the fire control optics, tending to disable the howitzer if it is far removed from supply facilities. As described in [12], the composite rollbar development was undertaken to provide a replacement for a field fix which resulted in a steel rollbar weighing over 150 lbs; because of its weight, the steel rollbar was too awkward to remove during firing operations, causing great inconvenience. The MTL-developed composite rollbar whose construction is indicated in Fig. 18 weighed 40 lbs and could be detached in a matter of seconds.

As in Fig. 18, the composite rollbar involved straight tubular sections consisting of S2 glass-epoxy ( $\pm 20$  deg) wound over a thin aluminum sleeve which served both as a winding mandrel and a structural element, together with cast aluminum elbows which were bandage-wrapped with woven glass tape and subsequently impregnated with resin and cured. Welded joints were used between the straight aluminum sleeves and the case elbows.

The effort described in [12] included structural analysis, design, fabrication and structural testing which verified that the composite rollbar was capable of loading considerably in excess of any that could be conceived as likely to occur in planned applications.

In addition, a program of bend testing of the straight tubular sections which included the 0.625" aluminum sleeve together with the filament wound composite overwrap (0.25" thick) was devised and carried out by the ORNL Team (Table 2) in which 30 specimens were tested to failure. These tests provided a reliability data base for the hybrid material concept, as well as verifying that the straight sections had strength capability considerably in excess of what was required in the rollbar.

### **COMPOSITE CRADLE FOR M102 HOWITZER**

#### **General Remarks**

As seen in the upper drawing of Fig. 4, the cradle is the component of a large caliber weapon which contains the recoiling components, including the cannon and the recoil mechanism. The cradle provides a

surface over which the gun slides during recoil, together with guiding ways which keep the recoil motion straight. In typical weapons the recoil loads are born by the cradle at its front end and transmitted to the supporting structure through the trunnion located at the rear of the cradle.

Fig. 19 shows a preliminary version of the MTL graphite epoxy cradle for the M102 howitzer, together with the details of construction, while Fig. 20 and 21 show the load system that the cradle has to sustain. Fig. 22 indicates various attachment design efforts that were undertaken and shows the most recent version of the elevation mechanism attachment and front end design. Table 10 gives a description of the effort that was undertaken in support of the composite cradle development. As of this time, the basic concept has been subjected to over 150% limit loading statically together with simulated firing loading at limit load, representative of 20,000 rounds; in addition, except for the trunnion (rear end of cradle) attachment design, all of the details of the MTL design have been subjected to static structural verification loading to considerably greater than 150% of limit load and have proven more than adequate.

The following is a review of various aspects of the Composite Cradle Development.

#### **Concept Formulation**

The original design for the M102 howitzer, an all-aluminum concept, was developed in the pre-Vietnam era of the early 1960's. The currently fielded version of the aluminum cradle which is generally similar to the MTL composite version weighs 81 lbs. For the composite cradle, expectations are that the final weight will be less than 60 lbs, possibly as low as 55 lbs, although detailing is not yet complete.

The construction of the aluminum cradle involves extruded shapes which are welded up to form a box construction that is quite similar to the "U" and "V" inner and outer walls of the composite cradle. In addition, some aluminum versions include tubular members welded into the lower U-wall corners similar to the tubes seen in the bottom sketch of Fig. 19, although in the aluminum cradle the tubes are smaller and do not contact the V wall as they do in the MTL design.

It is obvious that since the MTL cradle was intended to be a working model which would fit on an M102 howitzer and be subjected to firing tests, it had to be made to fit the same attachment points as the aluminum cradle. Accordingly, it was felt to be useful to copy as many features of the latter as possible. For example, many of the overall dimensions are close to those of the aluminum cradle. This highlights the well recognized difficulty of retrofitting an existing system with composite hardware. In particular, some of the major challenges encountered with the composite cradle, mainly those having to do with loads on attachment points, could have been avoided in a totally redesigned howitzer, although they served to provide a good model for the usual activities involved in a composite hardware development effort.

The construction for the MTL composite cradle, as summarized in the upper right part of Table 10, includes (1) autoclave molded inner and outer walls of Hercules AS-4/3501 prepreg in a quasi-isotropic layup; (2) filament wound tubes (wet wound [ $\pm 15/\pm 45/\pm 15/90$ ]<sub>S</sub> Hercules As-4 epoxy) which were large enough in diameter to bridge the gap between the U and V walls; (3) autoclave-molded channels of AS-4/3501 which were reinforced predominately 90 degrees to the long axis to provide high bending stiffness and strength at the corners (to provide strength for the uplift loads shown in Fig. 20 and 21) and ; (4) a foam insert seen in the section (lower) view of Fig. 19, to provide restraint against local buckling of the lower U wall surface under column loading of the cradle by recoil loads. The channels together with the U and V walls were laid up as separate pieces over aluminum tooling and autoclave cured. The final component consisting of the U wall, tubes, V wall and channels were assembled by bonding with

**TABLE 10**  
**DESCRIPTION OF CRADLE EFFORT**

<u>DESIGN</u>	<u>FABRICATION</u>
<ul style="list-style-type: none"> <li>• CONCEPT SELECTION</li> <li>• ATTACHMENT DESIGN <ul style="list-style-type: none"> <li>-FRONT END</li> <li>-ELEVATION ATTACHMENT</li> <li>-TRUNNION ATTACHMENT</li> </ul> </li> <li>• PATRAN/ABAQUS ANALYSIS</li> </ul>	<ul style="list-style-type: none"> <li>• AS4-3501-6 OVERALL, ALUMINUM ELEVATION BRACKET INSERTS, GLASS EPOXY TRUNNION ATTACH DOUBLER</li> <li>• DOUBLE WALL COMPOSITE LAYUP <ul style="list-style-type: none"> <li>-FILAMENT WOUND TUBULAR ELEMENTS,</li> <li>-BONDED ASSEMBLY</li> </ul> </li> <li>• BOLTED ELEVATION BRACKET CONCEPT</li> </ul>
<u>TESTING</u>	
<ul style="list-style-type: none"> <li>• LIVE FIRE TESTING OF M102 FOR DYNAMIC LOADS ASSESSMENT</li> <li>• IN HOUSE TESTING OF SUB-LENGTH COMPONENT <ul style="list-style-type: none"> <li>-STATIC COLUMN LOADING (150% OF LIMIT LOAD VERIFIED)</li> <li>-CYCLIC COLUMN LOADING (LIMIT LOAD)</li> <li>-ELEVATION BRACKET VERIFICATION TESTING (200% OVERLOAD, NO FAILURE)</li> </ul> </li> <li>• "COUPON" TESTING <ul style="list-style-type: none"> <li>-BOLTED JOINTS FOR ELEVATION BRACKET</li> <li>-UPLIFT LOADS ON GRAPHITE EPOXY CHANNELS</li> <li>-FRONT END CONCEPT VERIFICATION (ACHIEVED &gt; 200% OF LIMIT LOAD)</li> </ul> </li> </ul>	

American Cyanimide FM97 film adhesive. In the most recent version of the cradle design, the U wall, V wall and tubes are 0.062" thick while

the webs and upper flange of the channels are 0.28", with the lower flange tapered from 0.56" at the web to 0.28" at the free edge.

The use of the foam insert shown in the section view of Fig. 19 was found to be necessary to avoid under-strength buckling resistance of the lower U-wall surface. Fig. 23 illustrates the situation under consideration. A classical buckling analysis was performed to determine the spring constant of the insert required to force a full sine wave buckling pattern in the lateral direction, i.e. the middle pattern shown in Fig. 23. A half wave pattern which would have resulted in the absence of a restraint (upper buckling pattern of Fig. 23) would have lowered the buckling strength to an intolerably low level. However, by forcing a pattern with zero displacement along the mid-span axis, more than adequate strength against local buckling can be anticipated. The spring restraint indicated along the mid-span line of the lower surface in Fig. 23 would produce either the lower symmetric buckling pattern, or, for excessively large spring stiffness, the antisymmetric middle pattern of Fig. 23.

Since the cradle walls were quasi-isotropic, the analysis follows that outlined by sect. 9.4 of Timoshenko and Gere[3] for isotropic plates, (although this is not strictly correct since the quasi-isotropic laminate will not quite be isotropic in bending properties as a rule) and leads to a buckling deflection pattern given by

$$w(x,z) = \sin \pi \frac{x}{\lambda} \left[ \sin \beta \pi \frac{z}{\lambda} - \frac{\beta}{\alpha} \frac{\cos \beta \frac{\pi b}{2\lambda}}{\cosh \alpha \frac{\pi b}{2\lambda}} \sinh \alpha \pi \frac{z}{\lambda} \right] \quad (13)$$

where

$x$  = lateral coordinate (see Fig. 23)

$z$  = axial coordinate along cradle

$\lambda$  = axial half-wave length of buckling pattern

and where  $\alpha$  and  $\beta$  are related to the applied compression load as follows:

$$\beta = \{ [(\sigma_z)_{cr} t / E'] 12 \lambda^2 / \pi^2 t^2 ]^{1/2} - 1 \}^{1/2}$$

$$\alpha = (\beta^2 + 2)^{1/2}$$

in which

$$E' = E / (1 + \nu^2)$$

with

$E, \nu$  = Young's modulus and Poisson ratio for assumed isotropic plate

As in the the discussion related to Table 8, the critical compressive stress,  $(\sigma_z)_{cr}$  can be expressed in terms of the square of the thickness-to-span ratio of the lower surface as follows:

$$(\sigma_z)_{cr} = k (12 / \pi^2) E (t^2 / b^2) \quad (14)$$

in which  $k$  is a parameter expressing the effect of restraint on the plate; for example, for the long strip with simply supported edges and no center restraint (upper buckling pattern of Fig. 23) we get the

well-known result of  $k=4$ , while for the antisymmetric pattern (middle pattern of Fig. 23) we get  $k=16$ . The intent of the foam insert is to force a pattern comparable to the lower pattern in Fig. 23 for which  $k$  is at least 16. The effect of the spring constant produced by the foam for vertical deflection of the lower surface can be expressed in terms of a parameter  $\Lambda$ , given by

$$\Lambda = 24\lambda^3 K_f / \pi^3 E_f t^3 \quad (15.1)$$

with

$$K_f = E_f h_f / w_f \quad (15.2)$$

in which

$E_f$  = Young's modulus of foam

$h_f, w_f$  = height and width of foam insert (as seen in the section view of Fig. 19)

The relationship between  $k$  and  $\Lambda$  is indicated in the curve at the bottom of Fig. 23. The bottom line of the design effort for the foam is to determine a value of the foam restraint parameter,  $\Lambda$ , which produces a  $k$  value of at least 16, i.e. comparable to that for the antisymmetric pattern, which represents the highest value that can be achieved with a line of restraint along the center line of the lower wall, since for values of  $\Lambda$  producing higher  $k$  values, the antisymmetric pattern, being of lower  $k$ , would prevail. The curve of  $k$  vs.  $\Lambda$  shown in Fig. 23 indicates that a value of  $\Lambda$  equal to 16 will produce a  $k$  value of 16 and represents the appropriate design condition.

In the aluminum cradle an internal bulkhead is present at the location of the foam insert; it was found cost effective in terms of manufacturing labor and tooling to use the foam for this purpose in the case of the composite cradle, however.

Generally speaking, the overall configuration constitutes a sandwich concept with the tubes acting as the core. In addition, considerable extra strengthening is provided by the channels due to their relatively heavy gage. The latter served as particularly vital elements for bolted connections which were used in the elevation and trunnion attachments.

The front end assembly seen at the left side of Fig. 22 and in detail in Fig. 23, was possibly the most crucial feature of the cradle design. The flat end plate used in the early version of the cradle shown in Fig. 19 for reacting the recoil loads led to insurmountable problems. The nature of the situation is illustrated schematically in Fig. 24. This model represents a beam supported on four springs which represent the inner and outer walls of the cradle in terms of axial deflection with respect to the long axis of the cradle. If the inner springs are stiff relative to the bending stiffness of the part of the beam lying between them, then the beam will deform as shown in Fig. 24, with reverse deflection at the outer springs. Not only do the outer springs not support compressive load, but they develop tension if their connection with the beam remains intact, leading to extra compressive load on the inner springs. A simple analysis in which the end plate is modelled as a beam and the U and V walls are treated as springs shows that they are too rigid under axial load to deform



enough to prevent pull-away at the outer edge. When this happens, all load is born by the V wall. It was desirable to have a loading system which would load both walls, in addition to the tubes, so that the full structural capability of the structure was available. It was estimated that an aluminum plate 3" thick (and weighing 15 lbs.) would have been required to provide a workable end plate.

The final front end design which constituted an edge-loaded plate beam gave completely satisfactory structural capability for this requirement. It took advantage of the in-plane loading capability of composite plates, as opposed to the transversely loaded end plate in which the composite is loaded in its weakest mode. In the aluminum cradle design, what was essentially a flat-plate front end with a center buildup for accepting bearing loads is made workable by the use of horizontal corner gussets which serve as interior buttresses to the front end. For the composite cradle, the plate-beam approach was found to be the most attractive fix to the problems generated by attempts to use unsupported transversely loaded end plates, since introduction of any kind of gussets of the type used in the aluminum cradle did not appear to be feasible.

An important feature of the plate beam is seen in Fig. 23 (side view). The plates were slotted at their lower edges where they bear on the front end of the cradle. This insures that the load will be introduced at the outer edges of the front end, since any deflection of the plates under recoil load will fail to allow contact at the inner part of the front end.

The elevation mechanism attachments were originally thought to be subjected only to dead weight loading by the gun and recoil mechanism, and were intended to be of bonded construction. As discussed below, instrumented firing tests on the M102 howitzer showed that severe dynamic loads are, in fact, present in the elevation brackets which make bonded attachment impractical. The final design involved bolting the aluminum inserts to the channels. Testing to be described later showed that the bolted connections were more than adequate structurally.

The trunnion bracket attachment is similar to that used on the aluminum cradle, i.e. an area built up to a thickness of 1" at the rear of the cradle to which the trunnion attachment brackets are bolted.

### Loads

Values of the loads shown in Fig. 20 (upper sketch) were initially obtained from available design documentation on the M102 howitzer. The major loads correspond to the recoil load which is reacted at the front end of the cradle. This results from withdrawal of a piston from the hydraulic recoil cylinder which is attached to the underside of the gun tube and moves rearward with it during recoil. Note that the system has to be moment-free at the trunnion pivot point, so that the moment generated from the offset of the recoil load with respect to the center of the trunnion axis has to be reacted between the gun and cradle, resulting in a tendency toward transverse loads passed between

them through the rails attached to the gun and the channels ("ways") of the cradle, seen in the lower sketch of Fig. 20. The location of the uplift loads is clarified in Fig. 21 which shows that the uplift load is initially located at the forward edge of the cradle, and remains there until the forward edge of the rails has moved past the forward end of the cradle, at which point the uplift load position moves rearward with the forward edge of the rails.

One feature which was discovered in the course of the effort was that of dynamic loading in the elevation attachment. The available documentation indicated that only static loading of the cradle corresponding to dead weight loading by the gun tube was present in the elevation mechanism attachment. The configuration of the gun relative to the cradle, with the center line of the gun passing through the trunnion pivot axis, led to the assumption that dynamic moments due to the offset of the recoil load from the trunnion were accommodated by self-equilibrating forces between the rails and channels.

However, firing tests conducted with the elevation and trunnion attachment brackets instrumented with strain gages showed that there were, in fact, severe dynamic loads present in the elevation brackets. It was eventually concluded that these were due to "give" of the channel flanges which allowed enough downward movement of the gun to take place early in the recoil cycle to cause the gun to bear against the elevation strut. Since the latter are much more rigid than the channel flanges, the lateral loads indicated in Fig. 20 do not initially develop, so that the moment about the pivot has to be taken out through the elevation bracket. This raises the loads in these brackets from about 1500 lbs for assumed dead-weight loading to over 6000 lbs of dynamic loading. The latter value was finally assumed as the design limit load.

An additional point with regard to the lateral loads on the cradle is the role they play in the structural response of composite channels. As seen in the lower sketch of Fig. 20, uplift of the gun rails against the channel flanges invokes special concern about their ability to sustain the resulting bearing loads, since we are dealing with a composite plate loaded transversely, i.e. in its weakest direction. This issue, as with several similar ones having to do with attachment design, led to the need for careful testing of various components for their ability to resist bearing loads associated with attachment performance.

### **Design Analysis**

Much of the design could be carried out without extensive finite element analysis. The buckling analysis mentioned previously in connection with the foam insert connecting the lower U wall face to the trough of the V wall is an example of the type of effort encountered in the early stages. Later in the effort considerable modelling was done using PATRAN (PDA Engineering) in combination with the ABAQUS (Hibbitt, Karlson & Sorenson, Inc.) general purpose finite element code. This was particularly useful for evaluating details around the trunnion attachment doubler. In the course of the program, finite element analyses were carried out to check special details of the

cradle design, including:

- RESPONSE OF THE CRADLE STRUCTURAL CONCEPT IN THE VICINITY OF THE TRUNNION BRACKET
- RESPONSE OF THE UPPER CHANNEL FLANGES TO UPLIFT LOADS BY THE RAILS
- STRENGTH ANALYSIS OF THE FRONT END PLATE BEAM FOR EDGE LOADING OF THE PLATES

Fig. 25 illustrates two of the FE analyses which were carried out. A sublength model of the overall structure (lower sketch) was developed using PDA Engineering's PATRAN preprocessor capability and solved on ABAQUS , followed by postprocessing with PATRAN. The main interest was to investigate the extent to which stress concentrations were present around the trunnion attachment. A simulated doubler using high-stiffness plates with transverse bar elements for connection to the cradle body were used to avoid the need for a detailed description of load introduction from the trunnion bracket. Results of the analysis indicated that the stress concentrations were not severe enough to be of special concern. A problem of particular interest in this regard has to do with load diffusion from the doubler region to the main cradle structure. In view of the relative massiveness of the channel, it is visualized that most of the load should go directly into the channel from the doubler. How the load diffuses from the channel into the U wall, V wall and tubes remained an issue. The problem is somewhat aggravated because of a horizontal lateral offset of the load from the trunnion bracket which leads to opposing side moments on the two doublers. Again, the plate and bar model for the doubler was used to focus attention on this mode of behavior and to clarify whether or not high stresses would result in the thin gage structural elements of the cradle. As stated above, the stresses were found to be manageable for this type of behavior.

The analysis indicated in the upper sketch of Fig. 26 highlights a concern with localized bearing loading of the channel flanges. Several phenomena are generated by loading of the flanges by the rails:(1) considerable upward deflection of the flanges (as much as 0.2" for ultimate loads) due to bending of the channel webs:(2) corresponding to the deflection of the flanges is a concern about bending stresses near the corners of the channel where the flanges contacts the webs;(3) as illustrated in Fig. 21, the forward ends of the rail recede past the front ends of the channels in the later stages of the recoil stroke; in that situation the uplift loads are produced by an 0.5" radius fillet making up the front edge of the rails, leading to the possibility of punch-through of the flange by the rail. One phase of the testing program (discussed below) involved a simulation of this action by pressing of an 0.5" diameter steel pin against the flange and determining if bearing failure (i.e. punch through) could be expected. The FE analysis of this issue was somewhat sketchy as it was eventually realized that a 3d stress analysis was needed to get credible results for this kind of loading, and the time was felt to be more

effectively spent by the simulated loading test. However, the flange deflection results were important in terms of highlighting the inability of the flanges to resist downward motion of the gun in the early stages of recoil, thereby allowing the earlier discussed tendency for dynamic loading of the elevation bracket to occur. In addition, results having to do with bending stresses at the root of the flanges are shown in Fig. 27. Here a plot of stress concentration with respect to beam bending stresses in the webs vs. fillet radius of the flange-web corner is shown. This illustrates the selection of a minimum radius shown by the vertical dashed line in Fig. 27 which was chosen for the channel design. In addition to providing a selection of the fillet radius, the analytical results provided motivation for selecting a stacking sequence in the channels in which the fibers were predominately vertical in the channel webs, i.e. normal to the long axis of the cradle.

For the other analysis mentioned above, no details will be given here, but it should be mentioned that the design of the plates used for the front end plate beam was thoroughly checked by 2d stress analyses on plates of various shapes under edge loads comparable to those the front end is expected to see, i.e. an edge loaded plate with the load over a narrow central band and two opposing supports. The results indicated that a rectangular plate of 0.4" thick x 12.75" long x 3.75" deep (see Fig. 24 for the comparable dimensions) was more than adequate for sustaining the recoil loads. A limited effort aimed at optimizing the shape of the plates led to the selection of plates having inclined lateral edges for minimum weight, although this was somewhat academic since the weight saving with respect to a rectangular plate was minor when compared with the total cradle weight.

#### **Testing Effort[13,14]\***

The testing effort which was carried out on the M102 composite cradle is described in the lower part of Table 10. The effort was divided between "coupon" testing[13] which included, in addition to routine material property evaluation, testing of a number of details of the cradle design, such as:

- Structural verification testing on the front end plate beam (Fig. 22,28)
- Tests for bearing strength of the channels used for the rail ways to insure that there was sufficient corner strength for bend loading due to the uplift loads, in addition to strength against punch-through for the 0.5" radius of the forward edge of the rails (Fig. 29)
- Bolted joint coupon specimens (Fig.22,30) related to design of the elevation attachment, **INCLUDING SPECIMENS DESIGNED TO CHECK FOR HEAD PULL-THROUGH STRENGTH** with flush head fasteners
- Structural verification testing of the bolted elevation bracket assembly (Fig. 22)

---

\*Reports in preparation (see REFERENCES)

and the testing outlined in Table 10 which had to do with evaluation of a sub-length version of the cradle prototype[14] (Fig. 31-34). In that effort (described in detail in Fig. 32), static testing to 150% of required limit load (limit load = 24,000 lbs of axial load) applied statically, in addition to 100% of limit load applied dynamically, using the test machine seen in the photograph of Fig. 31, were applied. The dynamic load pulse seen in Fig. 34 which was well within the capability of the test machine, represents a worst-case scenario since it represents a steady load equal to the peak expected recoil load, whereas as discussed previously, a practical recoil load pulse would show considerable droop over the width of the pulse. The pulse width of approximately 0.1 sec is representative of a typical recoil mechanism, however. In these tests, multiple strain gaging (see strain gage array described in Fig. 33) was emphasized. Data collection was implemented with a computerized system (Optim Electronics) capable of reading 20,000 channels/sec, either singly or disbursed among a number of instrumentation outputs.

Among the significant results of the test effort are the following:

- As indicated previously, structural testing results indicated that the design details have been more than satisfactorily addressed, other than those of the trunnion bracket attachment area at the rear of the cradle. Preliminary calculations indicate that there is more than adequate strength available in that area since the constraints of the design allow for about a 1" buildup of the structure in that area without incurring either violation of dimensional requirements or significant weight penalty. However, verification testing of the trunnion bracket attachment to confirm the final design is a vital step.

- Static and dynamic testing of the 24" long sublength model of the cradle indicates that the components fit well together in providing vital structural integrity. In particular, the 20,000 round simulated firing test indicated that no special problems will arise in the gun firing environment, and that static bench testing is reasonably representative of what the cradle will experience dynamically.

- The front-end plate beam appears to be a very attractive concept for avoiding the problems that arose in the original flat plate front end.

#### **Future Plans**

The design of the composite cradle for the M102 howitzer appears to be successful at this point, and no new problems are anticipated. At the present time the M102 cradle effort is dormant due to funding constraints. The following is a description of the effort which is needed to complete the program.

In order to complete the design, detailed testing to confirm the trunnion attachment design is needed. Once that is accomplished, construction of a full-scale prototype with attachments installed needs to be undertaken, followed by in-house static and simulated firing tests to insure that the integrated structure does not incur



unanticipated problems. With the design adequately confirmed, effort will be undertaken to allow for installation on an M102 howitzer, involving primarily precision machining of required mating points with respect to the howitzer. (This will include installation of appropriate bearing strips to allow proper recoil motion of the gun.) The effort will culminate in live firing tests of the howitzer to demonstrate the structure under in-use conditions.

## CONCLUSIONS

The MTL effort shows that many opportunities exist for applying composites to the lightening of artillery, and results indicate that no insurmountable technical barriers to fabricating these components from composites will be encountered. The usual questions encountered at the end of any technical feasibility study for demonstrating the application of composites to military hardware, related to damage tolerance, repairability and cost penalties remain to be addressed.

Although the emphasis of efforts to date at lightening of artillery has been on non-recoiling parts, considerable headway has been made in the ARDEC contractual effort to indicate a number of attractive solutions to the stability problem which should allow greater emphasis on lightening of recoiling parts, including the gun tube, breech mechanism and recoil energy absorption system. Current efforts are indeed underway by one contractor, Royal Ordnance, to exploit the curvilinear recoil path concept introduced by BMY as part of the ARDEC program.

The future for application of particulate reinforced metal matrix composites to the lightening of weapons in general and artillery in particular looks reasonably bright. Significant strides appear to have been made in overcoming drawbacks related to low fracture toughness and structural integrity, and although not of as great technical benefit as filament wound MMC's, the discontinuously reinforced materials avoid the cost penalties of the fiber reinforced metals which can be extreme in today's technological environment.

Although the Army effort toward lightening of artillery through application of advanced materials has been at a relatively low level in the recent past, concrete continuing interest has been demonstrated on the part of the Marines by their funding of a program to evaluate a 8900 lbs 155mm howitzer, primarily titanium, designed and built by Vickers. There is an indication that the effort will be revived more generally in the early-to-mid 90's. In the meantime, programs such as those which have been conducted by MTL and ARDEC will have pointed the way to early solution of important problem areas.

## ACKNOWLEDGMENTS

Numerous individuals contributed to this effort.

First of all the excellent work of the individuals cited in Table 3



who constituted the Lightweight Howitzer Team, both in house at MTL as well as at the supporting organizations, should be noted. Major in-house contributors included: K. Gandhi (Structural Design Analysis), P. Cavallaro (Structures and Test Design Engineering), G. Piper (Testing and Fabrication Liason) and J. de Luca, together with S. Ghiorse (Fabrication Engineering). A number of other individuals provided support for the major part of assembly structural testing, including W. Crenshaw, W. Bethoney and R. Pasternak.

The excellent effort at Oak Ridge National Laboratory was managed by G. T. Yahr, with the support of colleagues R. C. Gwaltney, C. R. Lutrell and J. Mayhall (design, material tradeoff studies and finite element analysis ) together with D. O'Connor who conducted important testing effort on the MTL rollbar material concept.

The Benet Laboratory effort (design and fabrication of braided trails) was conducted by P. O'Hara, T. O'Brien, K. Miner and P. Wheeler, under the direction of G. Friar. Important Management support at Benet was provided by Dr. G. D'Andrea.

Advise and consultation by a number of individuals of the Future Weapons Branch at Picatinny Arsenal Dover NJ (ARDEC) has to be likewise acknowledged. These include R. Becker, H. Liberman, N. Lionetti and S. Floroff.

Finally, the extensive help provided by personnel of the US Army Ballistic Research Laboratory (BRL) including Rick Murray and Ned Patten under the direction of Dr. Bruce Burns, in conducting instrumented firing tests on the M102 howitzer for the purpose of evaluating elevation bracket loads, is gratefully acknowledged.

#### REFERENCES

1. Oplinger, D. W. ARMY OVERVIEW, FOURTEENTH ANNUAL AIR FORCE MECHANICS OF COMPOSITES REVIEW, Dayton OH, (Oct. 1989).
2. Haskell, W., "COMPOSITE STRUCTURAL ARMOR FOR COMBAT VEHICLE APPLICATIONS", EIGHTH CONFERENCE ON FIBROUS COMPOSITES IN STRUCTURAL DESIGN, Norfolk, VA, (Nov., 1989)
3. Timoshenko, S. and Gere, J., THEORY OF ELASTIC STABILITY, Mc Graw Hill (1961)
4. Lekhnistkii, S. ANISOTROPIC PLATES, Gordon and Breach (1968)
5. Gwaltney, R. Oak Ridge National Laboratory Report ORNL/TM 10401 (1987)
6. Contract DAAG46-85-C-0059, "Computer Controlled Resin Impregnation for Composite Braiding", US Composites Corp.

7. \* Private communication, DWA Composite Specialties, INC to D. Oplinger, 1987
8. Contract DAAG46-82-C-0031, DWA Composite Specialties, INC. (1982)
9. Muldoon, R. "Ballistic Protection Provided by DWAL Aluminum Metal Matrix Composite Plate when Disposed at Normal Obliquity to Assault by CAL 0.30 AP-M2 Projectile", MTL Technical Report MTL TR 87-34 (1987)
10. Harrigan, W. "Metal Matrix Materials for Improved Ballistic Toughness", MTL Technical Report MTL-TR-89-106 (1989)
11. Nardone, V. C., Annual Contract Report#2, Contract N00014-87-C-0406, United Technologies Research Laboratory (1989)
12. Gandhi, K. et al, "Light Weight Composite Rollbar for Army Towed Howitzer", Proceedings of 36th International SAMPE Conference (November 1990)
13. \*\* Piper, G. "Mechanical Testing Support for the M102 Composite cradle" (1990)
14. \*\* Cavallaro, P. C. et al, "Structural Testing Efforts for M102 Howitzer Sub-length Composite cradle" (1990)

---

\* Reference not available

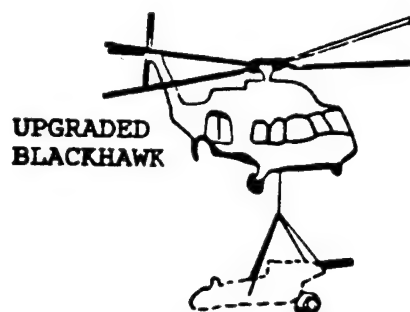
\*\* MTL Technical Reports in preparation

**CURRENT  
ARMY CAPABILITY**



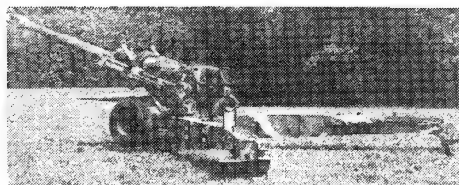
**M198 155mm HOWITZER  
(16,000 LB)**

**DESIRED  
CAPABILITY**

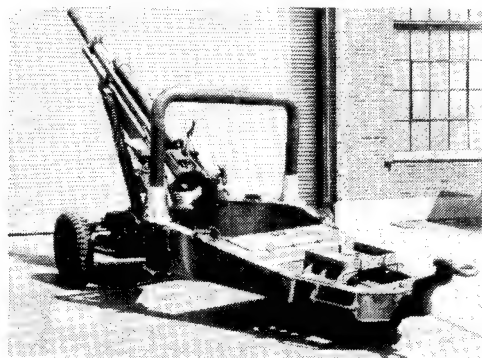


**9000 LB 155mm  
LIGHT HOWITZER**

**Figure 1. Objective of the lightweight howitzer program**



**(A) M198 (155mm) towed howitzer**

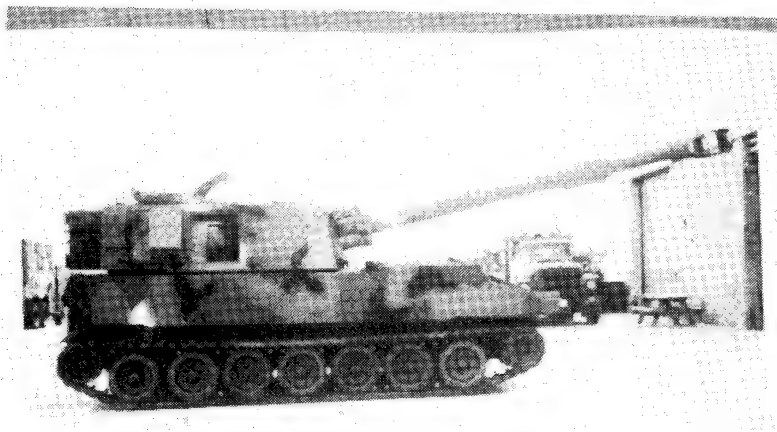


**(B) M102 (105mm) towed howitzer  
with MTL rollbar attached**

**Figure 2. US towed howitzers in current inventory**

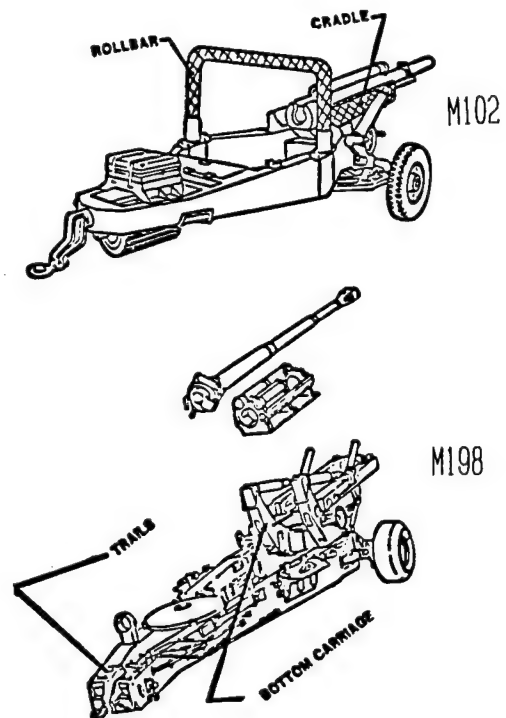


**(A) Blackhawk helicopter in airlift operation  
with M102 howitzer**

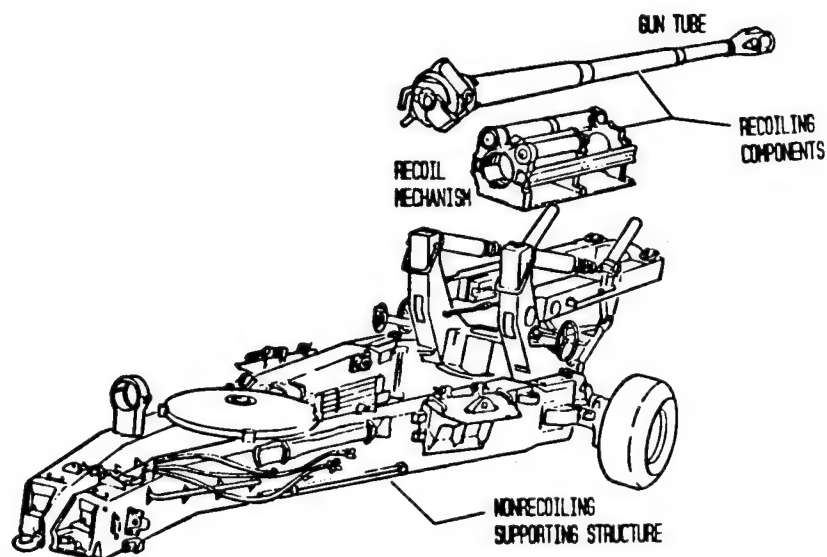


**(B) M109 self propelled howitzer**

**Figure 3. Howitzer operations**



**Figure 4. Towed howitzer components for application of composites**



**Figure 5. Main subsystems of towed howitzer**

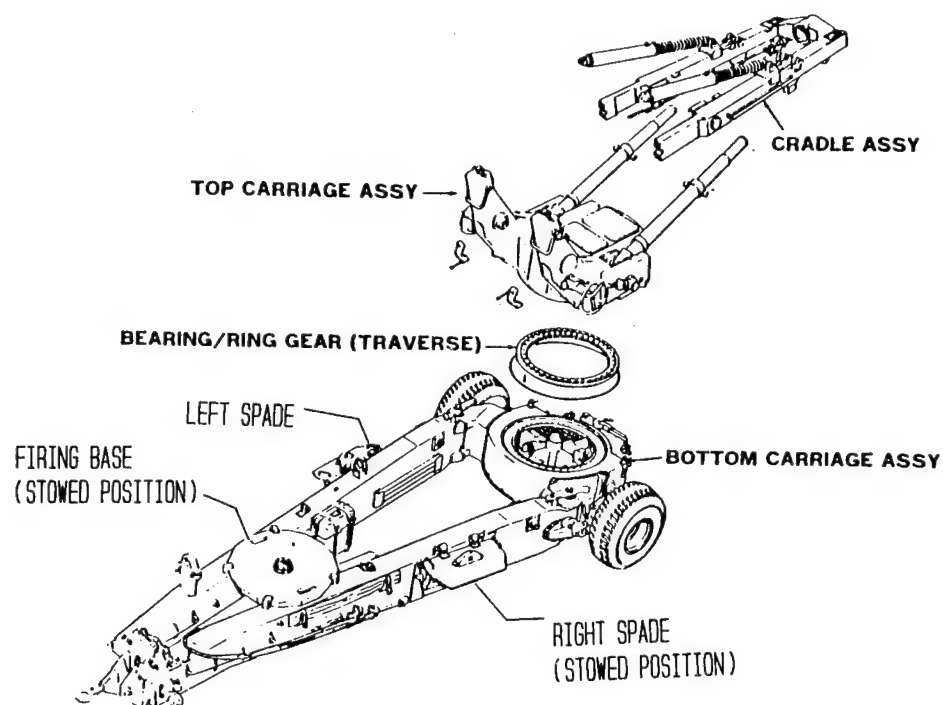


Figure 6. Towed howitzer supporting structure

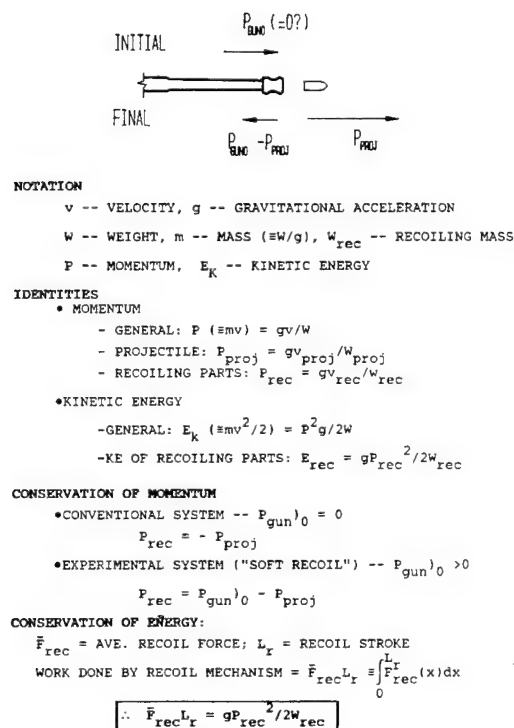


Figure 7. Basic physics of gun recoil



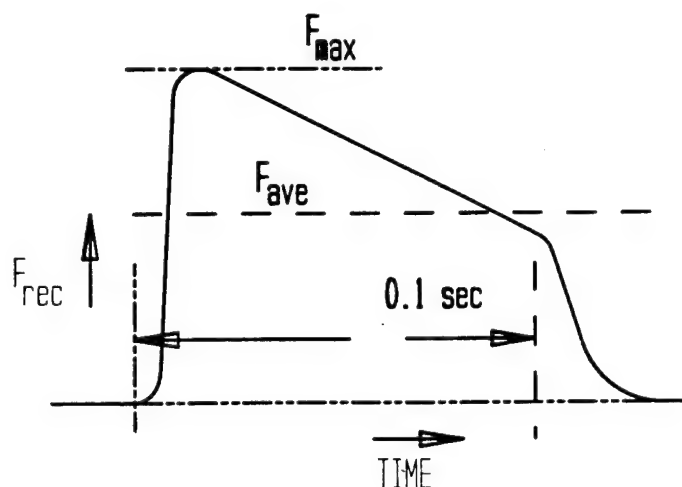
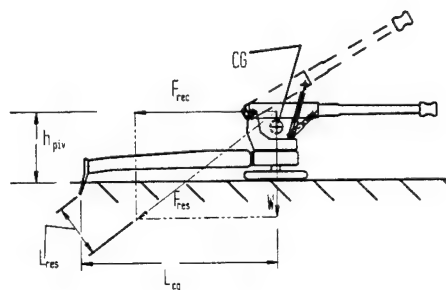


Figure 8. Typical recoil force-vs.-time characteristic



#### EQUATIONS

##### RELATIONSHIP FOR RECOIL LOAD

$$F_{rec}^{(max)} = \eta g P^2 / 2 L_{rec} W_{rec}$$

##### WHERE

$\eta$  = RECOIL LOAD MAGNIFICATION FACTOR

$$\equiv F_{rec}^{(max)} / \bar{F}_{rec}$$

$P$  = PROJECTILE MOMENTUM

$L_{rec}$  = RECOIL STROKE LENGTH

$W_{rec}$  = RECOILING WEIGHT

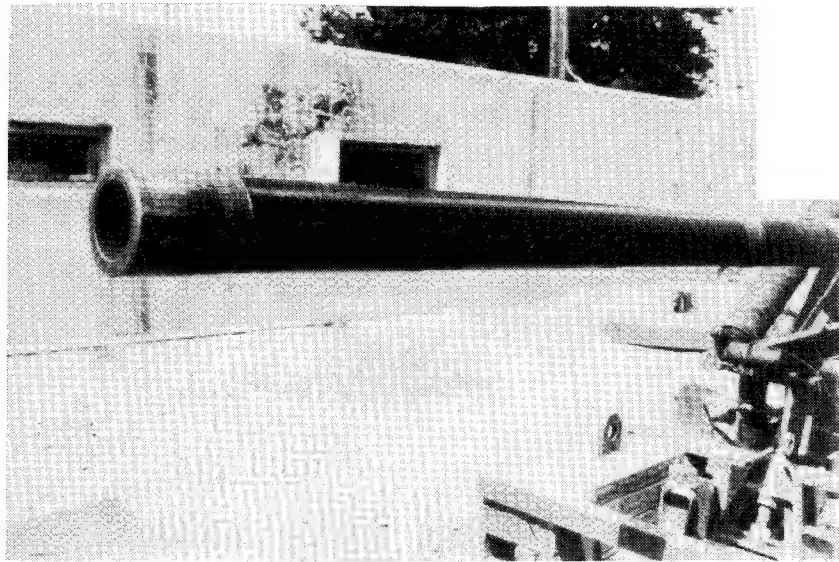
##### STABILITY CRITERION

$$W L_{cg} > F_{rec} h_{piv}$$

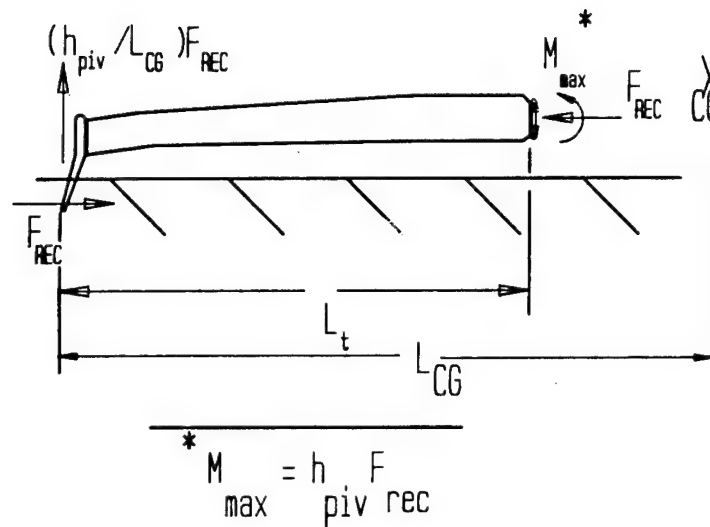
##### LEADING TO

$$L_{cg} L_{rec} / h_{piv} > (\eta / 2 W W_{rec}) g P^2$$

Figure 9. Relations for recoil stability



**Figure 10. Benet laboratory graphite overwrapped gun concept**



**Figure 11. Loads on howitzer trail**

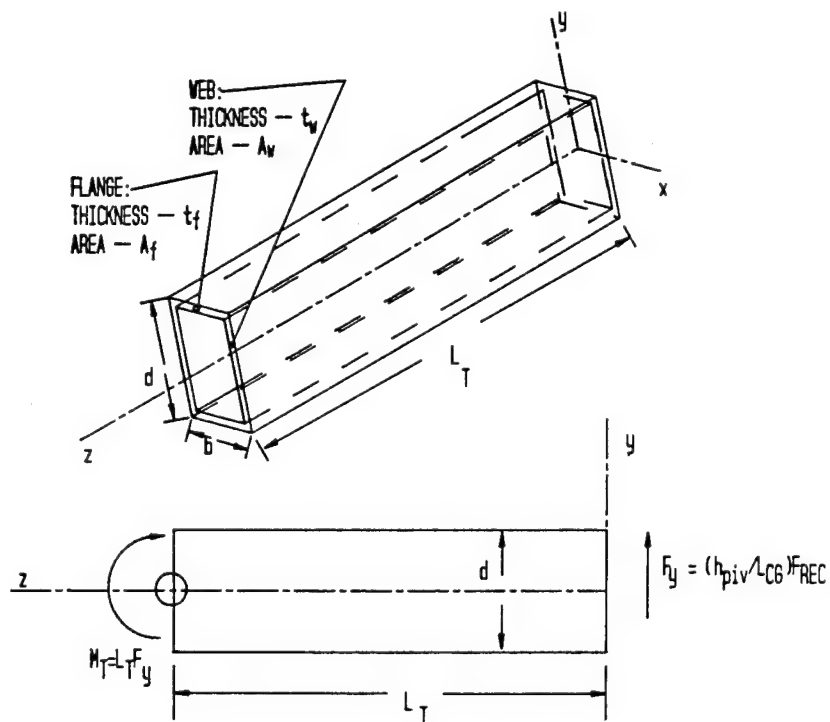


Figure 12. Box beam parameters

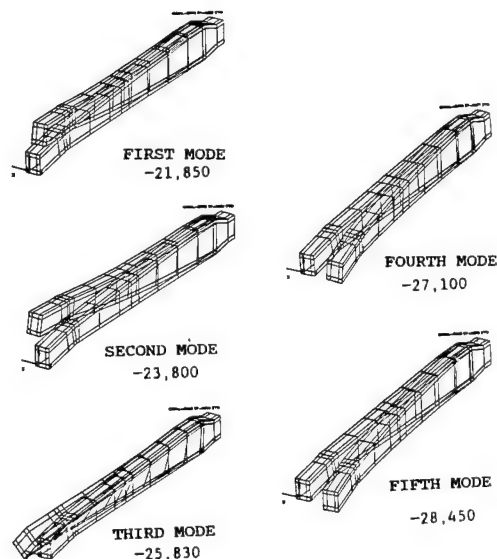
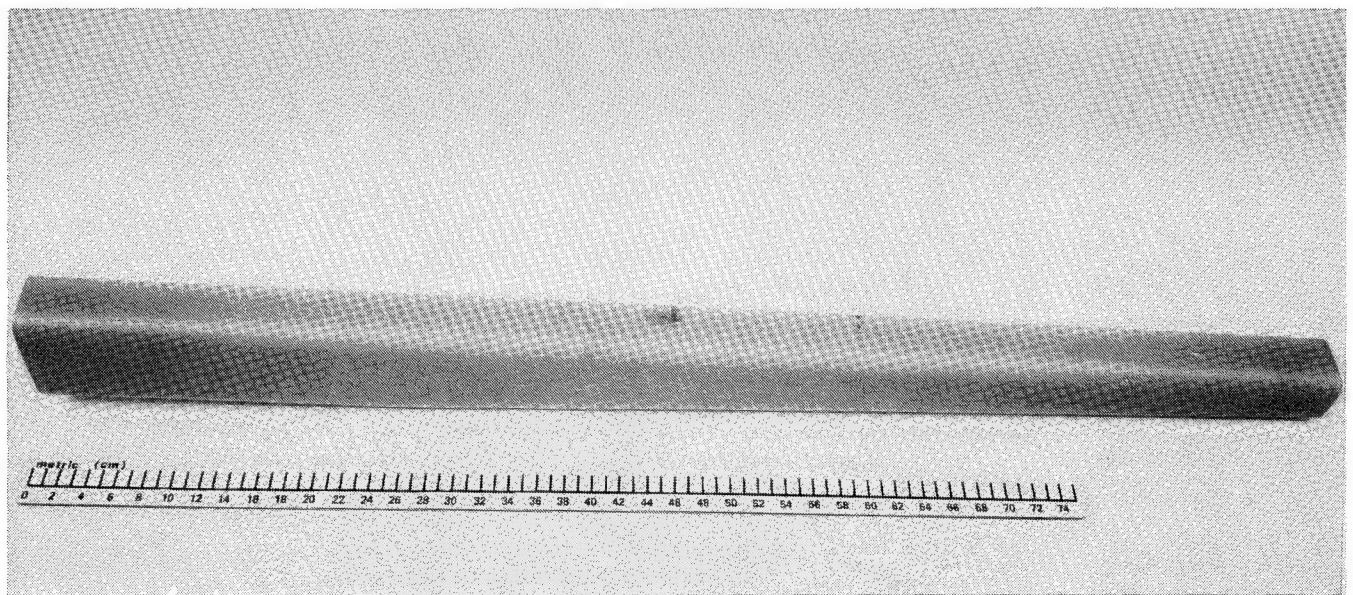
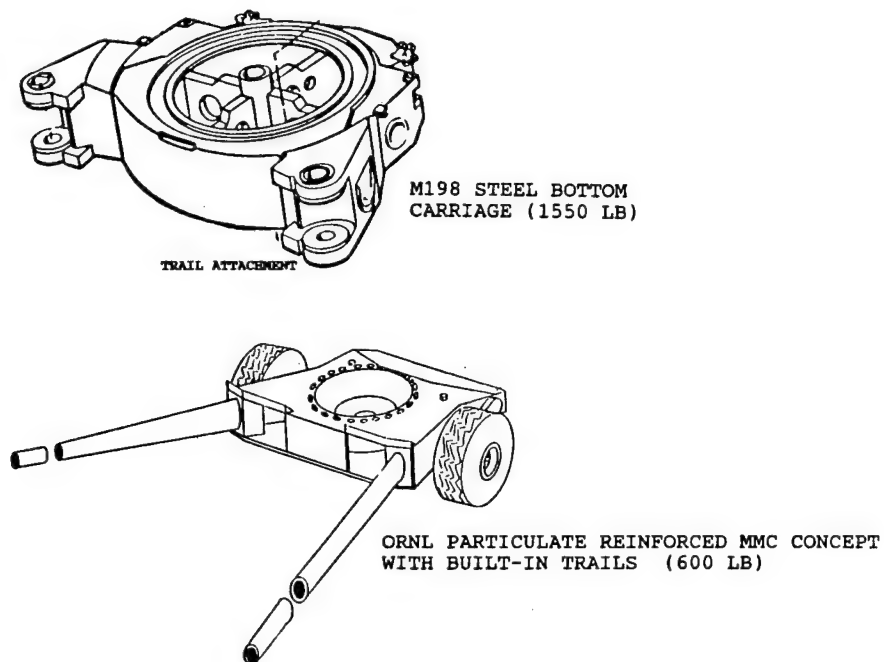


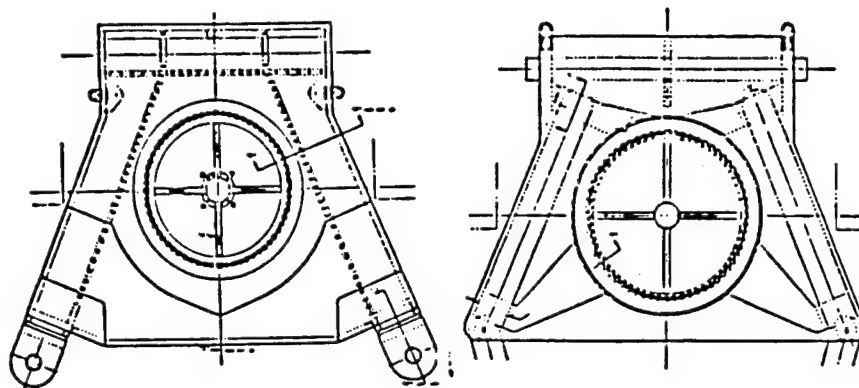
Figure 13. ORNL FE analysis results—buckling analysis of M198 trials (numerical values = flange bending stress at buckling)



**Figure 14. Benet braided trail concept for 155mm howitzer (1/6 scale)**



**Figure 15. Comparison of bottom carriage designs**



#### COMPOSITE/METAL HYBRID

ORGANICS (graphite epoxy, -- 331 lb  
glass epoxy,  
adhesives)

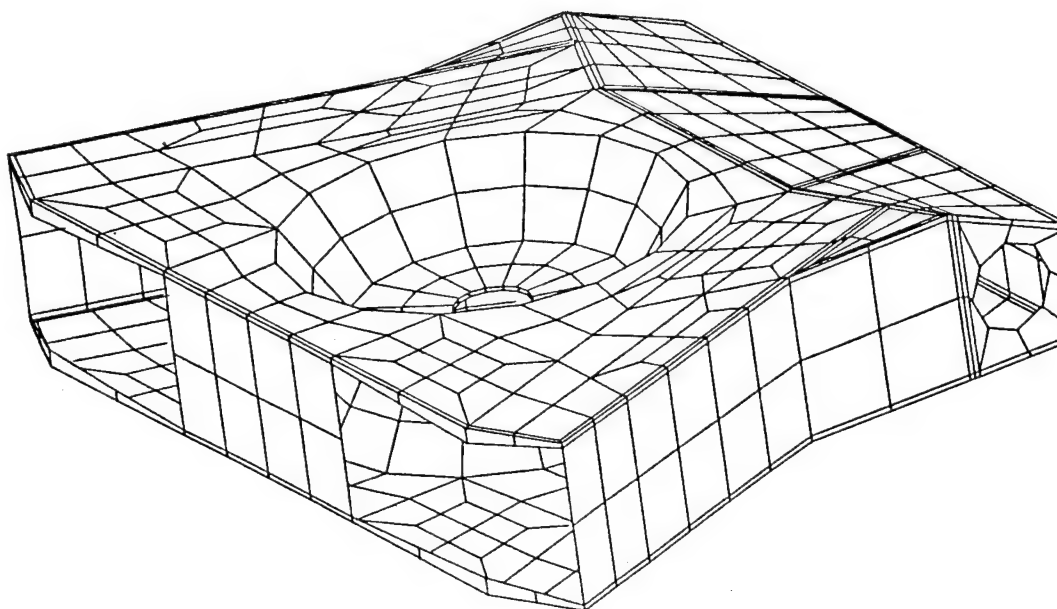
METAL  
-- 449 lb  
780

#### ALL-METAL DESIGN

(STIFFNESS/BUCKLING CRITICAL)

TITANIUM DESIGN	-- 780 LB
ALUMINUM DESIGN	-- 820 LB
PARTICULATE REINFORCED MMC DESIGN	-- 620 LB

**Figure 16. Lower carriage tradeoff studies**



**Figure 17. Model for FE study of MMC lower carriage**

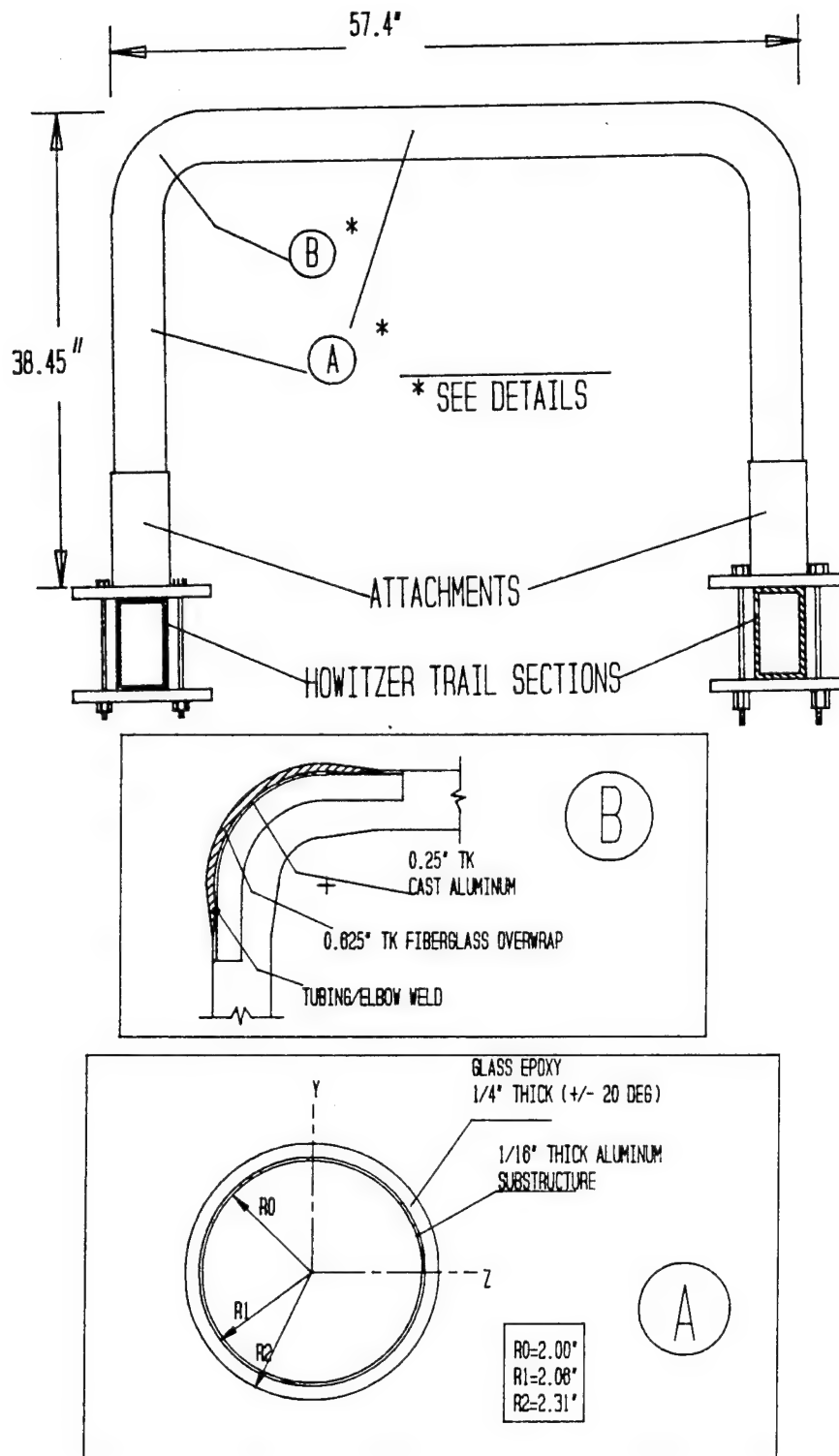


Figure 18. Construction of MTL composite rollbar for M102 howitzer



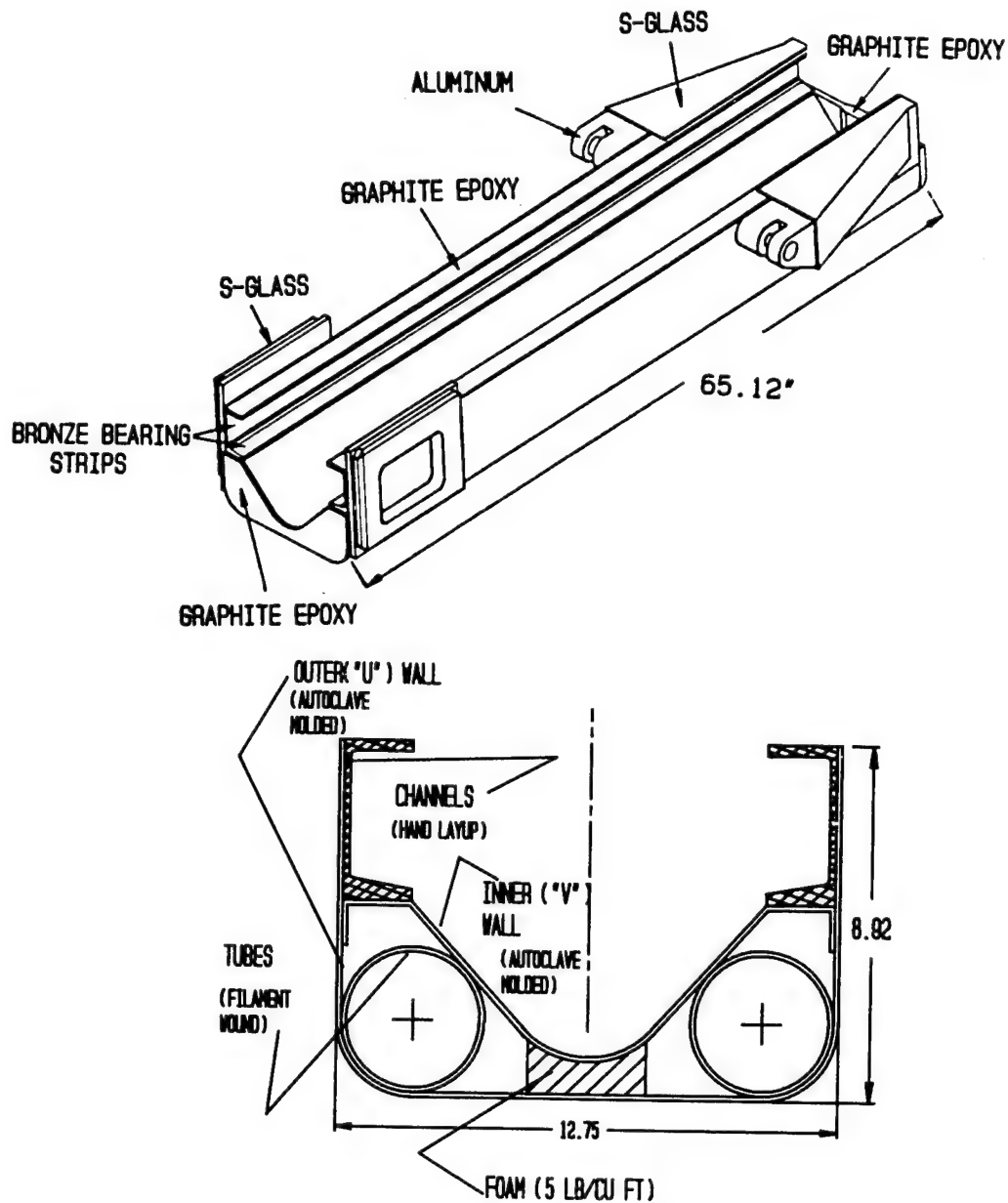
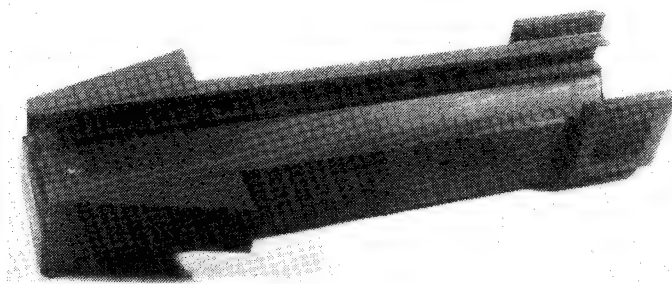


Figure 19. MTL composite cradle for M102 howitzer

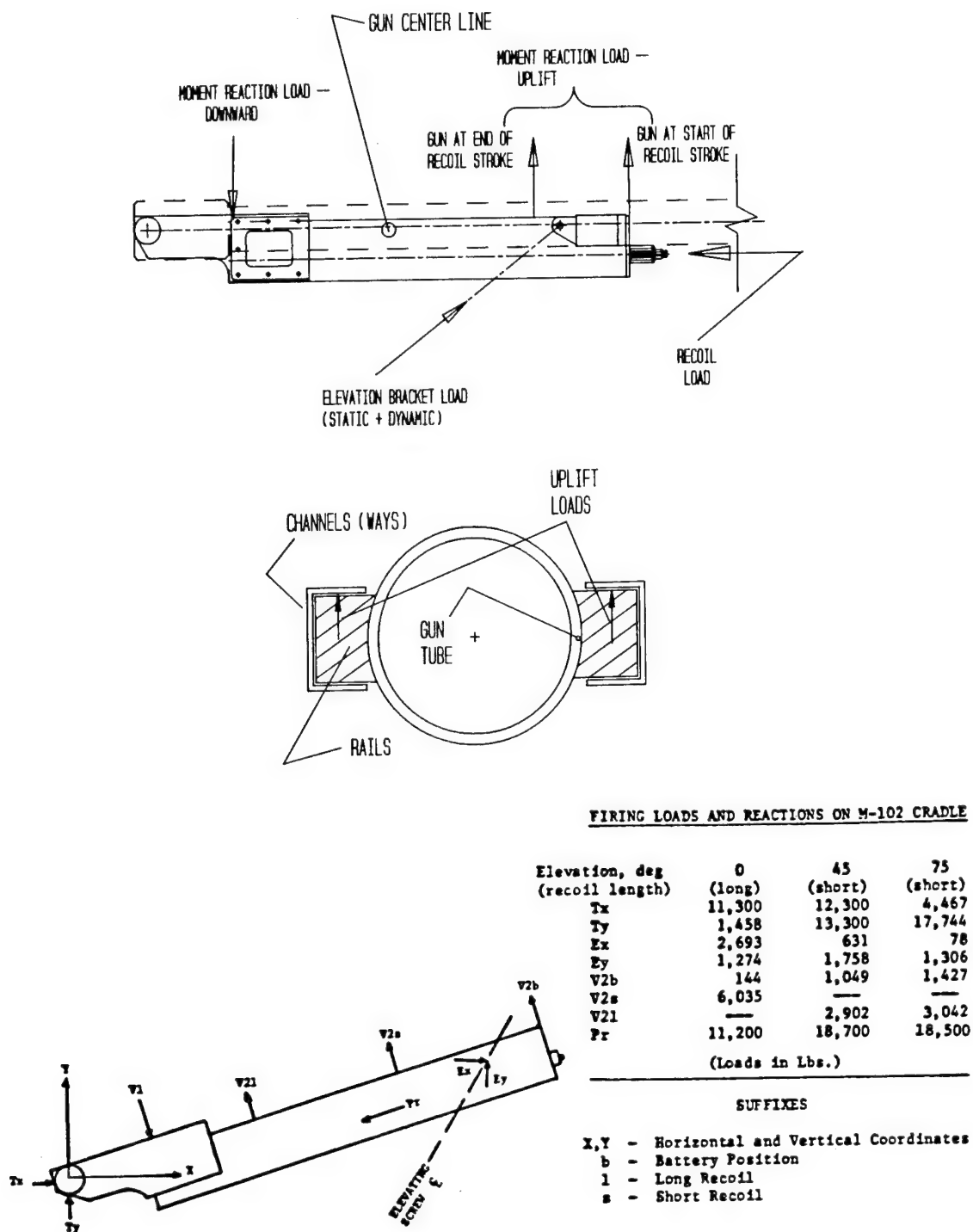


Figure 20. Loads on cradle of M102 howitzer



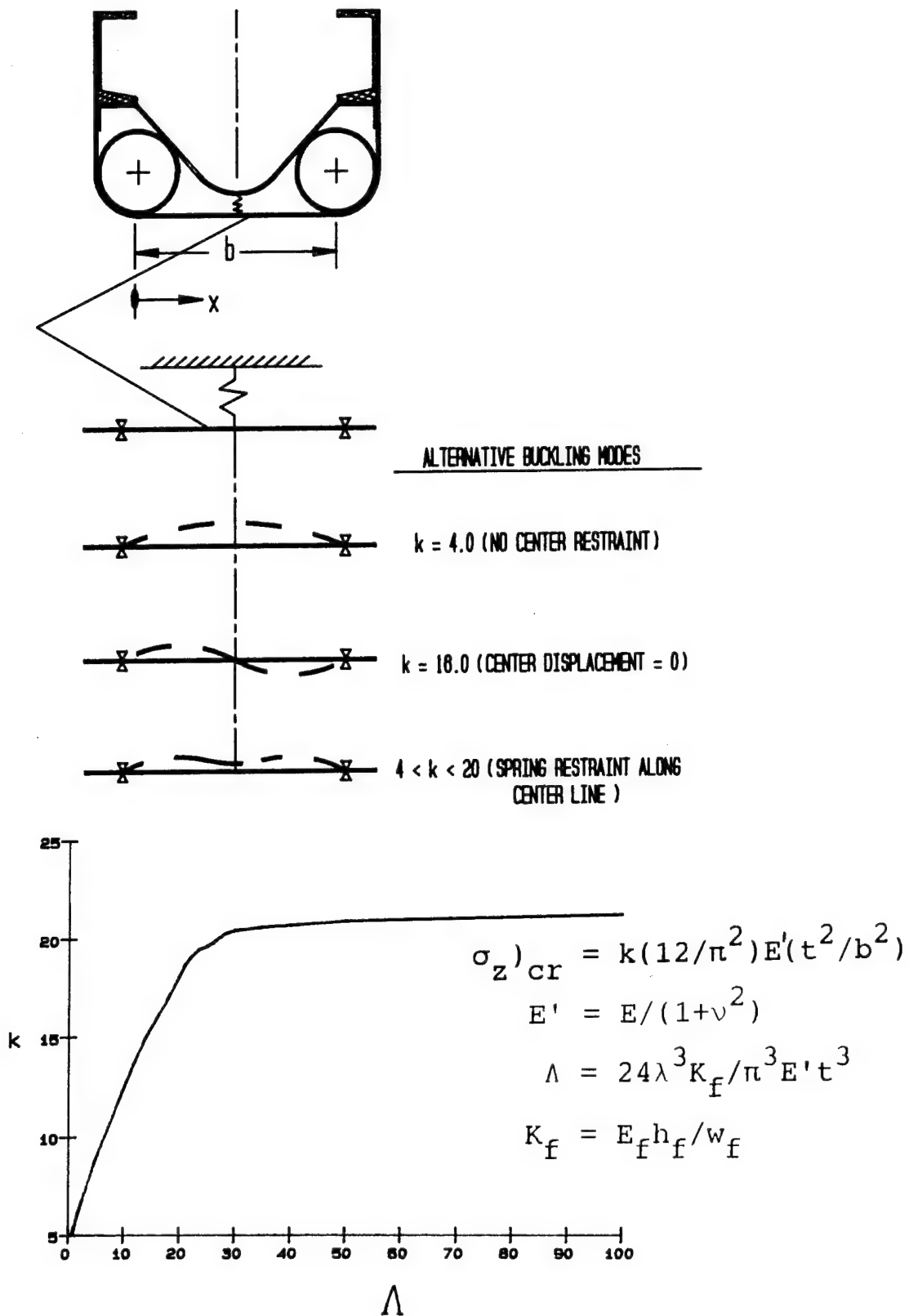
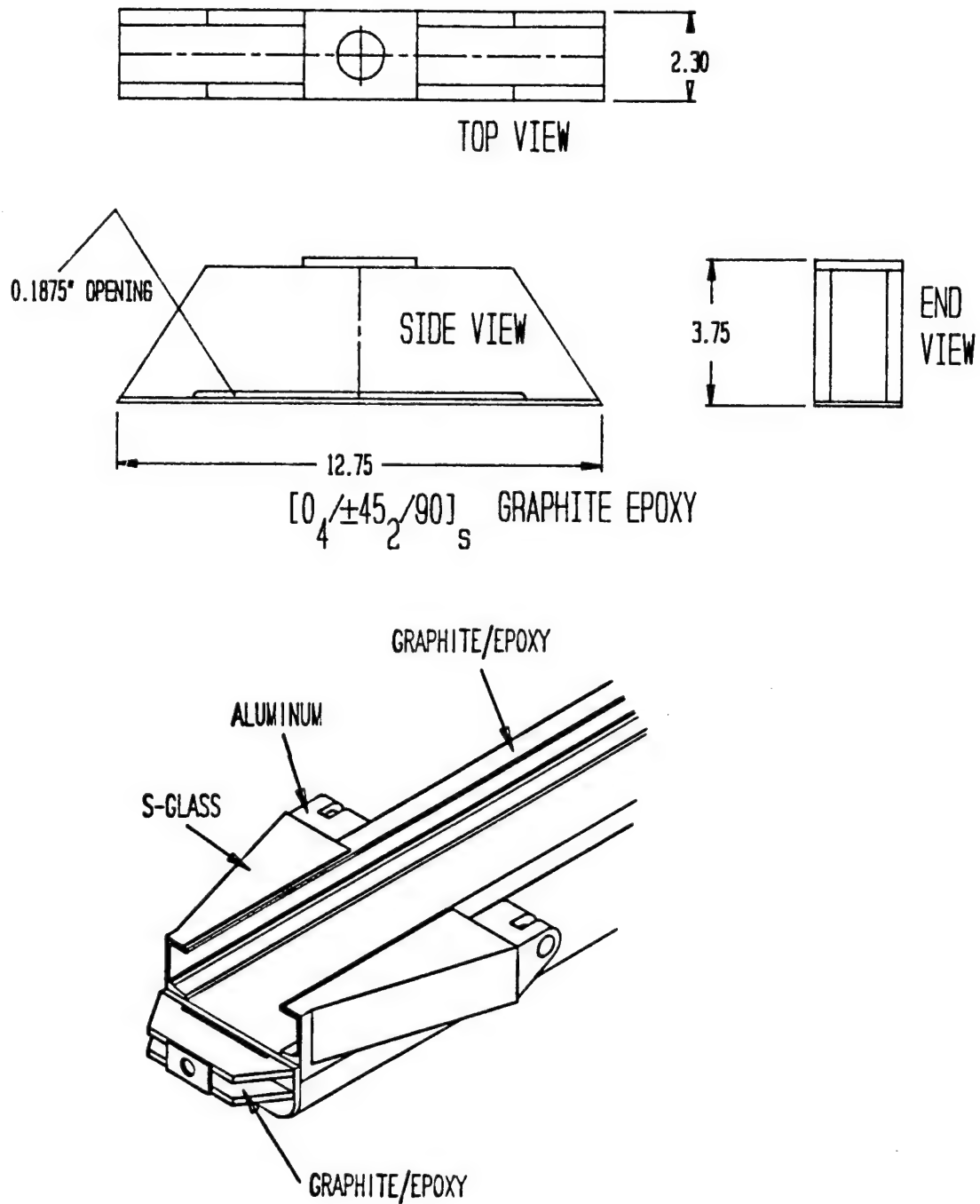


Figure 23. Buckling considerations for U wall lower surface



**Figure 24. Plate beam front end concept**

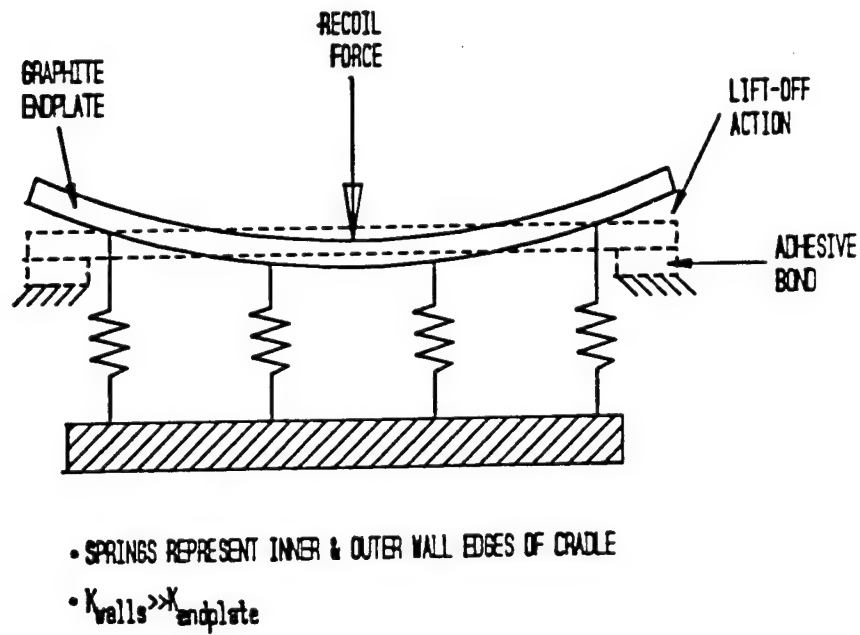


Figure 25. Model for visualization of flat plate front end support

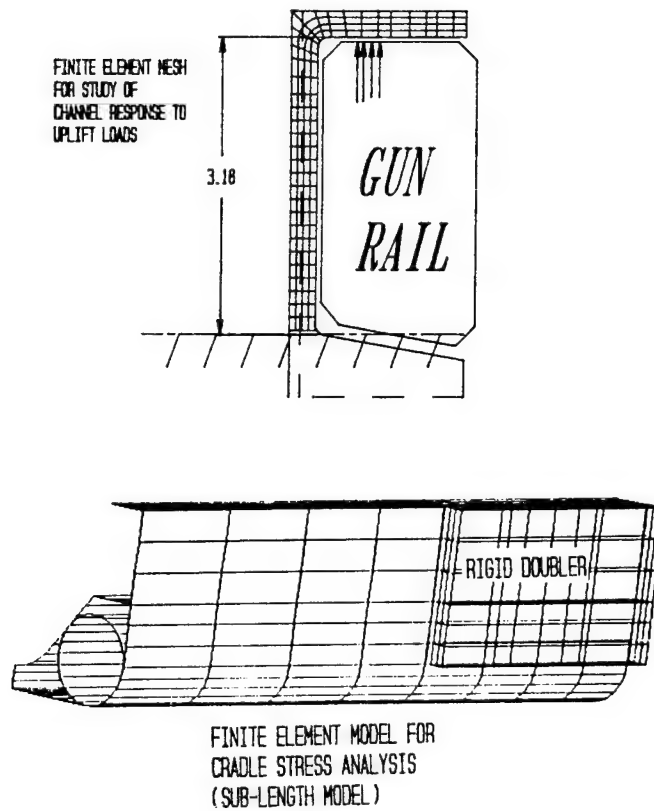
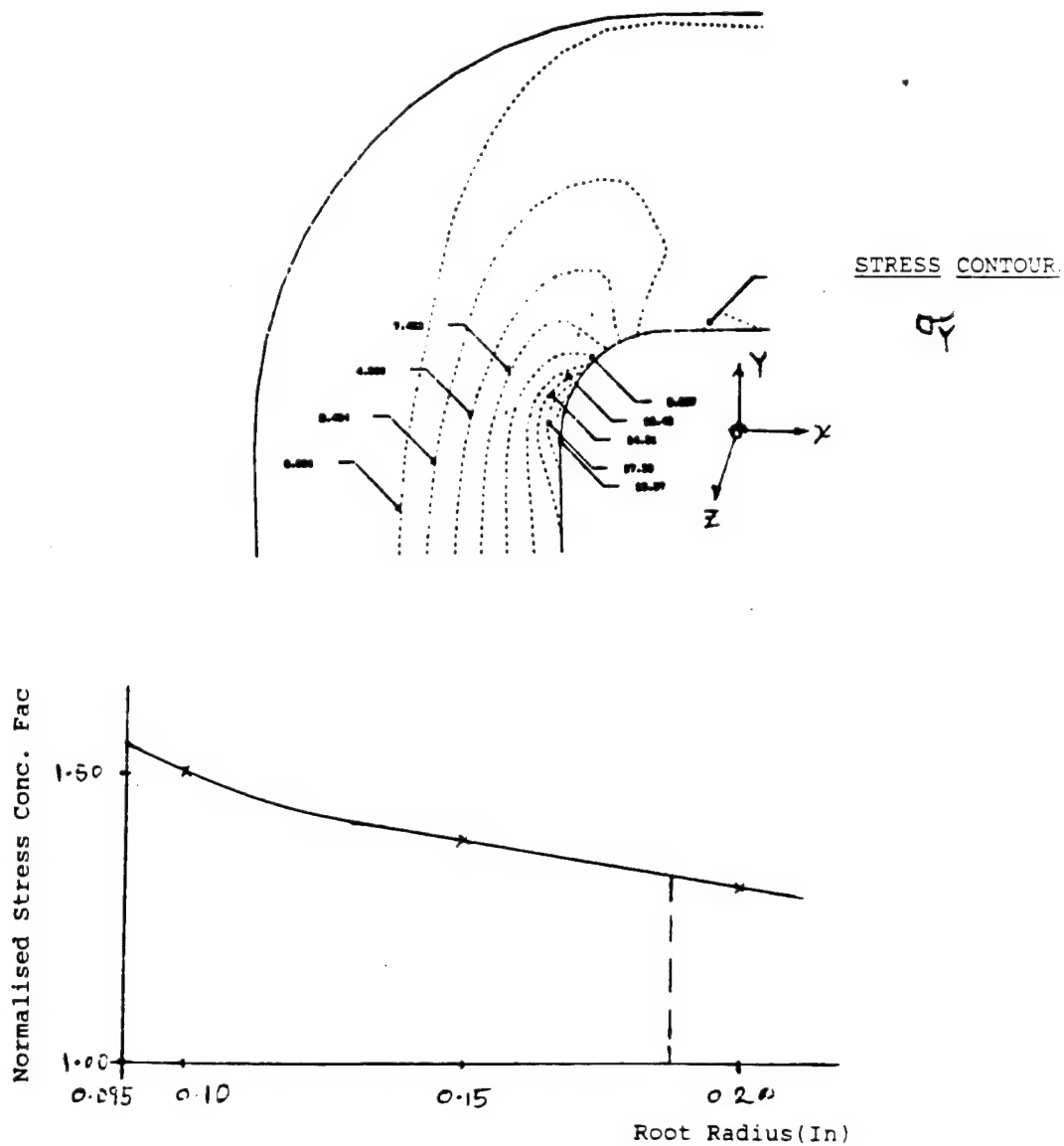


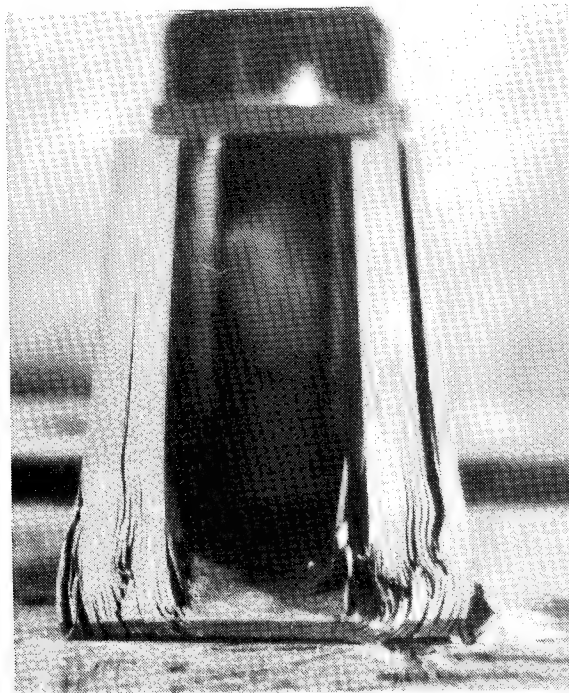
Figure 26. Finite element analysis models



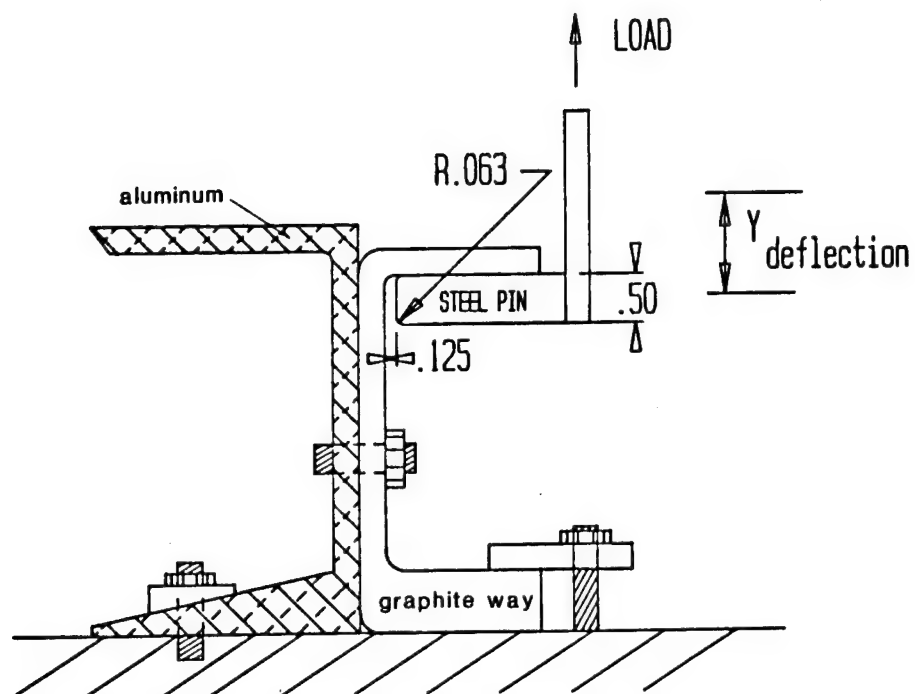
# STRESSES IN THE KNEE REGION



**Figure 27. Stress concentration factor vs. corner radius for channel uplift loading**



**Figure 28. Post-test view of failed front-end plate beam**



**Figure 29. Test fixture for channel bearing strength determination**

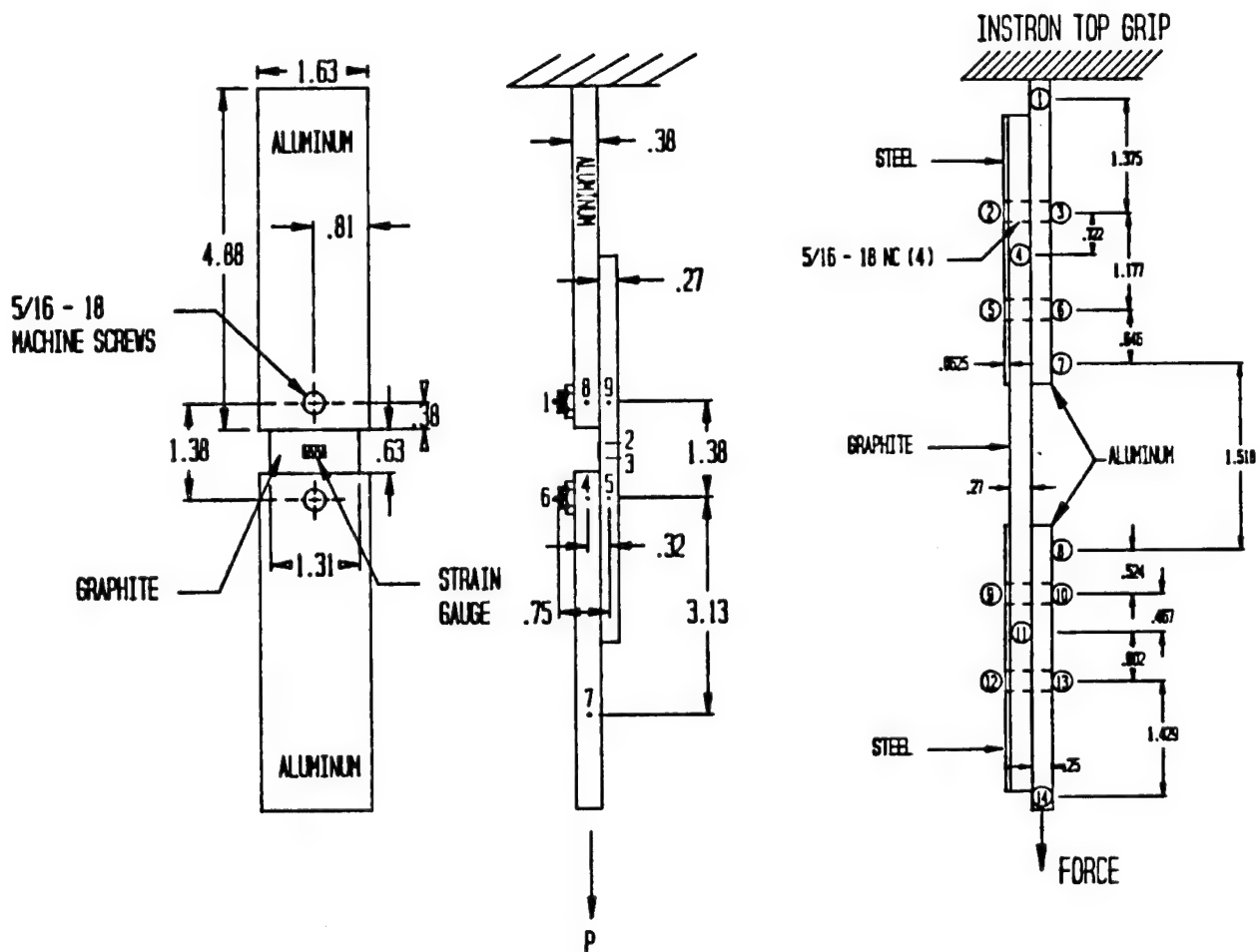
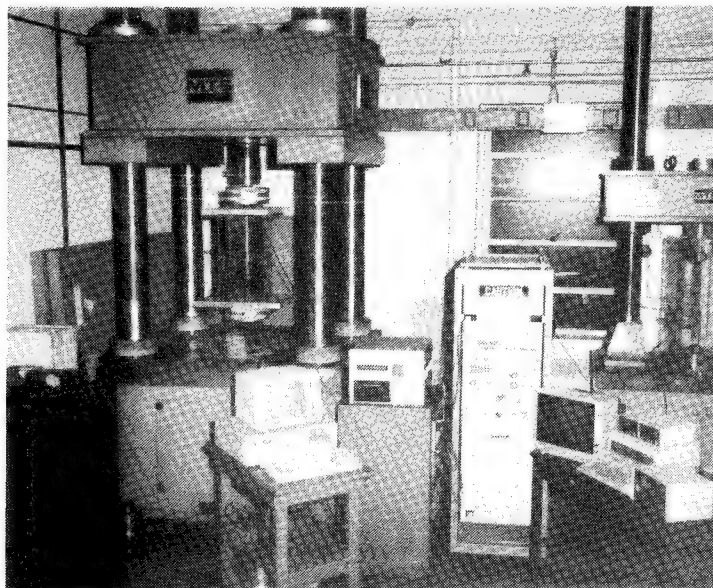
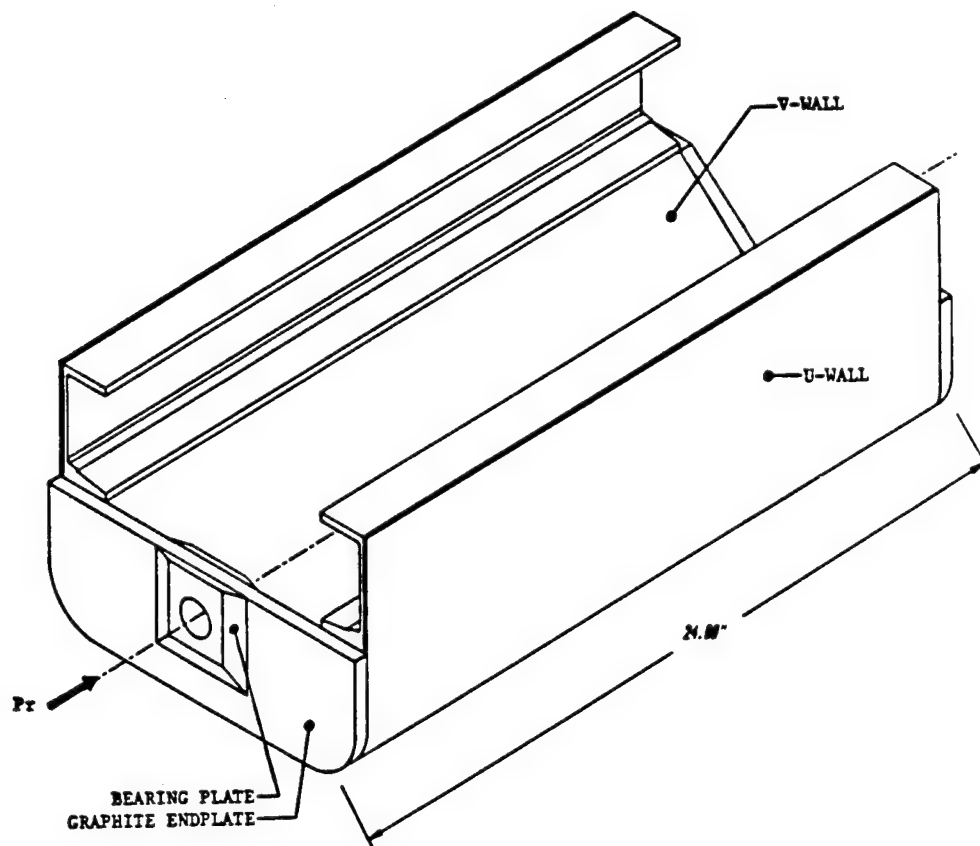


Figure 30. Bolted joint test specimens



**Figure 31. Sublength cradle and test facility**

TEST TYPE	LOADING	RESULTS
#1 Static	Concentrated load applied to graphite endplate.	Graphite endplate debonded from cradle at 10% required load.
#2 Static	Concentrated load applied to 1" thick Al 6061-T6 plate on top of graphite endplate.	Significant plastic bending deformation of aluminum plate. Max load = 45 kips No damage to cradle.
#3 Static	Platen loading	Max load = 40 kips No damage evident.
#4 Fatigue	Platen loading	Cradle withstood 20,000 cycles of simulated firing. Max load = 25 kips. No damage evident.

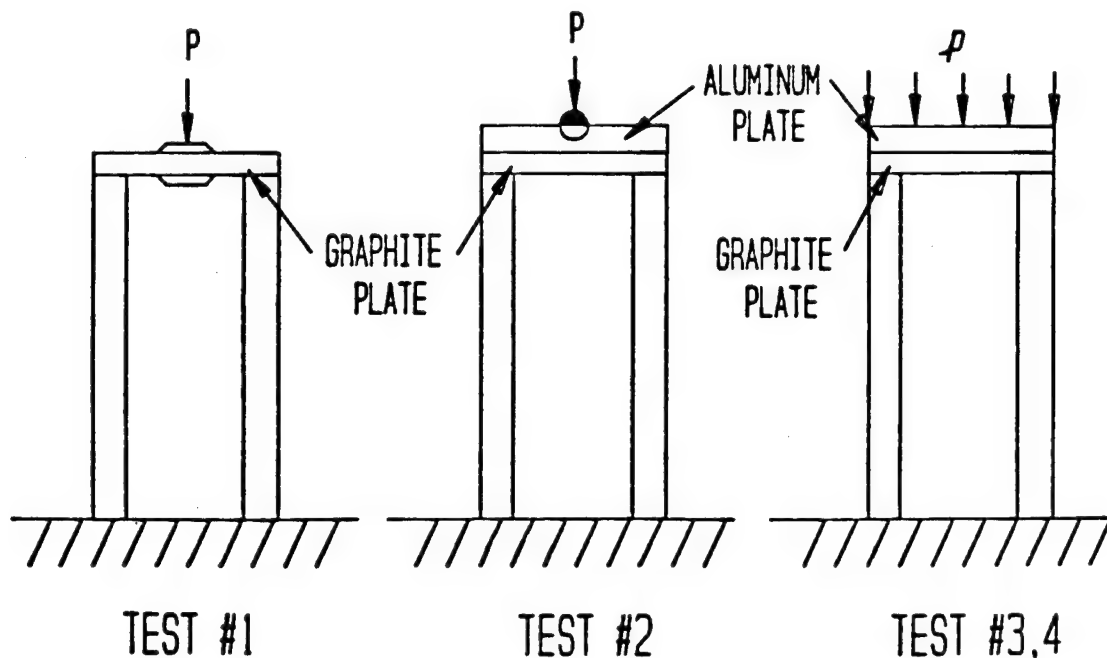


Figure 32. Test plan for sub-length cradle assembly test

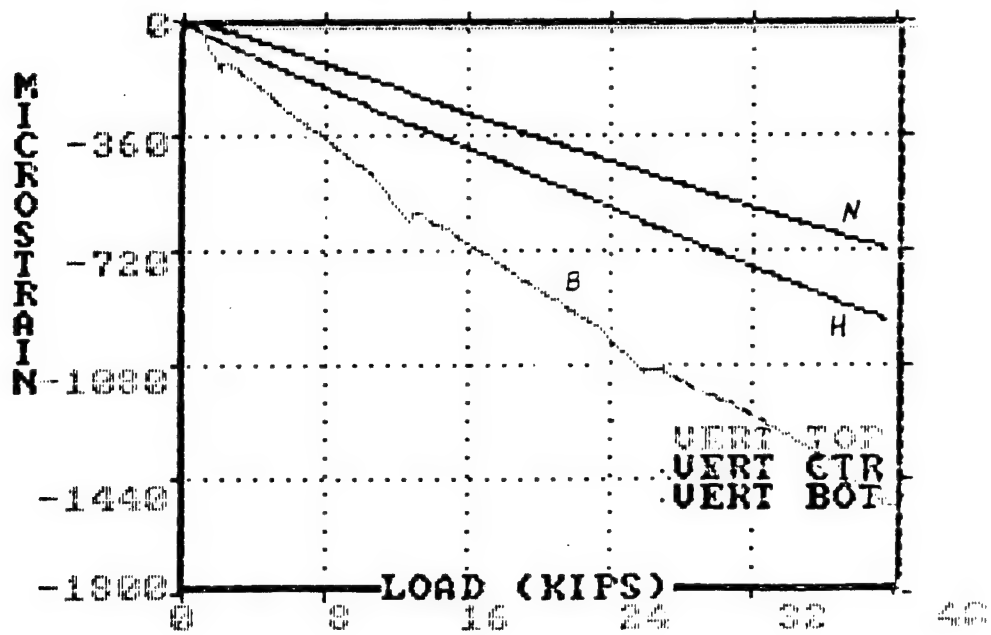
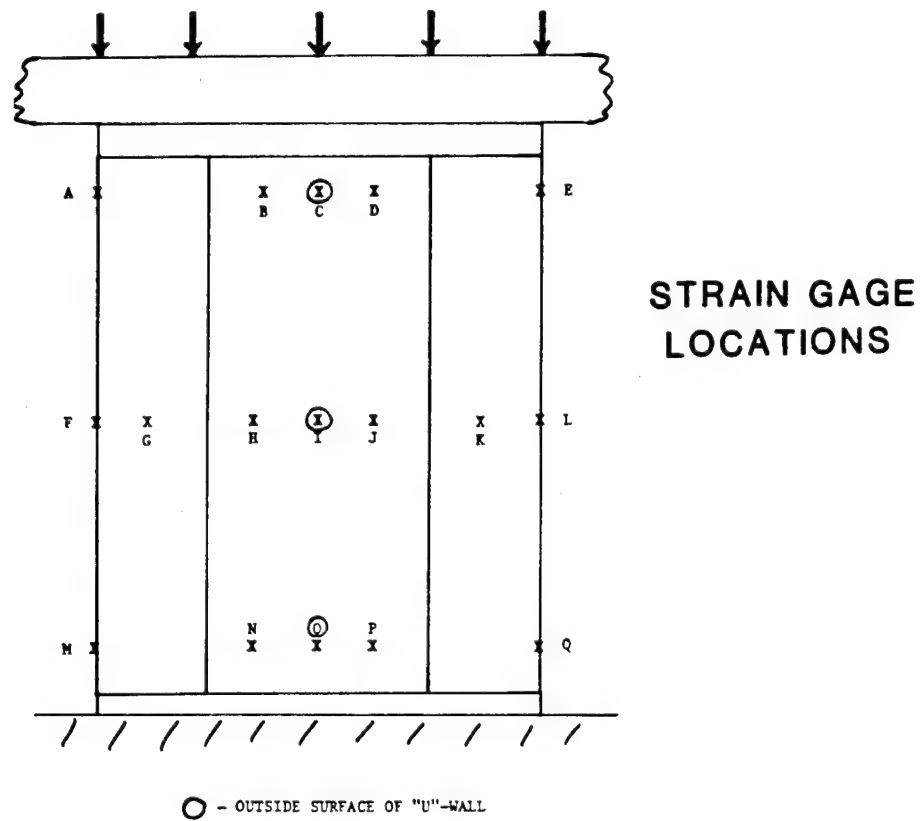


Figure 33. Strain gage layout and typical strain-vs.-load results



# 20,000 CYCLE CRADLE FATIGUE TEST SUMMARY

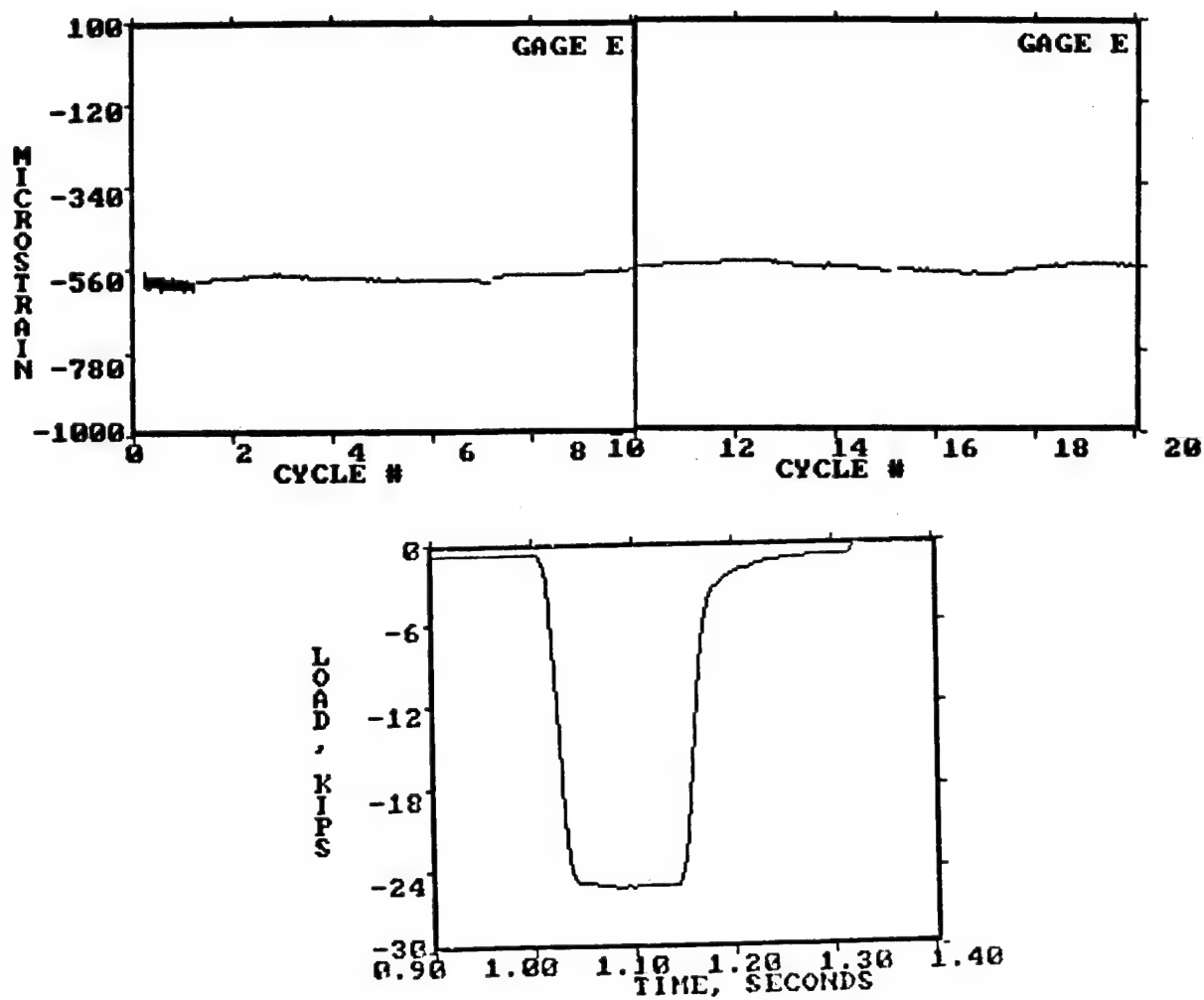


Figure 34. Cyclic loading test results and typical loading pulse

# THE WEIGHT OPTIMIZATION OF AN ARMORED CRASHWORTHY CREWSEAT THROUGH THE USE OF ADVANCED COMPOSITES AND DESIGN

Howard A. Lindsay and Stephen M. Motoyama  
Simula Inc.  
Phoenix, Arizona

Kent F. Smith  
Aviation Applied Technology Directorate (AATD)  
Fort Eustis, Virginia

## SUMMARY

The development of composites-related technology applicable to armored crashworthy helicopter crewseats is discussed. The main objective of the program was to achieve a significant weight reduction relative to the first-generation seats exemplified by the UH-60A and the AH-64A designs. This weight reduction was achieved while maintaining full compliance with the most recent version of the military crashworthy crewseat specification, MIL-S-58095A. The technology developed during this effort is intended to apply to the next generation of Army helicopters, such as LHX. This Small Business Innovation Research (SBIR) program was sponsored by the U.S. Army Aviation Applied Technology Directorate (AATD).

## INTRODUCTION

Armored crewseats have been in use since the mid 1960's when AATD (known then as AVLABS), designed, fabricated, and delivered "bolt-on" crewseat armor kits for the UH-1 and OV-1 fleets operating in the Republic of Vietnam. Since that time energy-absorbing capability has been added to crewseats for enhanced crash survival. The U.S. Army's introduction of armored energy-absorbing crashworthy crewseats in the UH-60A Black Hawk in the late 1970's ushered in a new era of aviator protection. The energy absorption characteristics of these seats have been demonstrated repeatedly in high-energy ground impacts in which injuries were prevented and/or lives saved. The AH-64A Apache has been fielded with crashworthy crewseats having even more armor protection than that of the UH-60A crewseats. The U.S. Navy has led the way in retrofitting armored and unarmored crashworthy crewseats in some of its older fleet of helicopters, such as the CH-53 A/D/E, SH-3, and UH-1.

The U.S. Army's next advanced helicopter, the LHX, is to achieve rotorcraft superiority in the late 20th and early 21st centuries. The LHX is expected to have a maximum empty weight of 7,500 lbs and a maximum flyaway cost of \$7.5 million, based on FY 1988 dollars. The need to emphasize weight reduction, while still maintaining high levels of performance at reasonable cost, is clear.

Anticipating the need for advanced lightweight armored crewseats, AATD began the Advanced Crashworthy Crewseat (ACWCS) program in 1985. Composite materials and advanced armor technology were to be used to design a crashworthy crewseat meeting LHX requirements. The program demonstrated that weight savings of 50 lbs per aircraft (two seats) was possible when compared to current UH-60A and AH-64A crewseat technology. Many of the advances that

contributed to this accomplishment, and particularly those implementing advanced composites technology, are described in this paper. The focus is on the general design approach used to optimize the weight of the ACWCS design.

## DESIGN APPROACH

The design approach entailed examining the major components of the seat and determining which components might be optimized through the use of advanced composite materials. Three components--the armored bucket liner, guide tube, and main strut--were identified for optimization and will be detailed in this paper. These components are commonly used in typical armored crashworthy crewseats, such as the one for the UH-60A Black Hawk shown in Figure 1. The case studies include a discussion of the multiple (and sometimes conflicting) design requirements that influenced the individual components. The design requirements which applied to the entire seat included ballistic performance, static and dynamic structural loading, and damage tolerance.

### Armored Bucket Liner

The armored bucket liner is a reinforced composite laminate that performs two primary functions. The first is to stop fragments in a ballistic impact, and the second is to provide the main load path for reacting the occupant's inertial loads during a crash. These two functions result in drastically different, and often conflicting, design requirements. The most significant parameter for determining the liner's configuration involves the choice of materials. The ballistic requirement for the armor system had the most impact on the weight of the liner, and also influenced the design of the liner much more than the structural requirements. The threat level was specified as that of LHX, as defined in January 1988, which was more stringent than that of either the UH-60A or AH-64A crewseats.

The prime consideration in the design of the armor system was to defeat the specified threat and provide adequate structural capability to meet the loading conditions, while yielding the lightest possible system. To do this, an extensive materials selection process was undertaken to investigate the relative performance of several candidate armor systems against the known requirements. The ballistic performance of the candidates was evaluated empirically by the fabrication and testing of armor panels in Simula's ballistic range. Several systems capable of meeting the ballistic requirement emerged, and each had a different areal density. Figure 2 shows a comparison of their relative areal densities when normalized against the LHX threat.

The armor system's ability to defeat the threat was not the only issue involved in the selection process. A phenomenon referred to as tangential, transient, or dynamic deflection is also a critical performance criterion. The problem relates to the amount of deflection that occurs directly behind the impact area, as illustrated in Figure 3. It is an important criterion because even when a projectile is defeated, the deflection with some armor systems is enough to cause severe injury to the occupant. This factor drove the design of the composite liner to the S-2 Glass® based system, which resulted in the lowest possible weight armored bucket. The alternate systems

---

®S-2 Glass is a registered trademark of Owens-Corning Fiberglas Corp.

required an additional section to stand the occupant off from the back of the armor system. An example of this approach is shown in Figure 4, with a crushable foam core used to absorb the energy of the deflecting armor panel. This requirement added weight to the other candidate armor systems which eliminated them from further consideration.

The resin system selected for use in the armored liner was a proprietary system which Simula had developed for use in other armor applications. It possessed the desired ballistic, mechanical, flammability, and fabrication related characteristics sought for this design.

The next step was to optimize the configuration of the liner to enable it to meet the remaining functions at the least possible weight. A configuration similar to that used on the Apache seat was selected for several reasons:

- It was consistent with the baseline seat design and established a convenient reference to make comparisons with
- It provided sufficient armor coverage for the seated occupant.

The basic liner shape was now defined, but the mounting locations of the various interfacing attachments had yet to be determined. The attachments included the restraint system components, the frame, and auxiliary equipment such as side arm controllers and wing panels. Many of these attachments were highly loaded and their positions were critical to the weight of the liner.

A finite element modeling (FEM) program, NISA-II, was used to optimize the final positions and check the entire liner for compliance with expected loading as well. This program also enabled accurate predictions of the deflections of the various parts of the seat to ensure there was no interference that might prevent the seat from performing its energy absorption function.

Once the strength requirements of the structure were well defined, a check was made on the mechanical allowables for the S-2 Glass liner to verify compliance with expected loads. A complete mechanical test program had been performed during the initial material study to quantify the structural performance of each candidate armor system. The results of those tests were used as the allowables for the final analysis.

The composite liner of an armored bucket usually exhibits poor structural characteristics because the laminate has been optimized for ballistic performance. A ballistically tolerant laminate tends to have fairly low resin content. Unfortunately, this normally yields a structurally inferior composite structure. Figure 5 illustrates the general trends of how these two performance features are affected by resin content. The selection of an S-2 Glass based armor system minimized the penalty normally attributed to using armor laminates to carry high structural loads. Figure 6 presents a comparison of the flexural strength and stiffness of the candidate material systems.

By using the S-2 Glass based system for the composite liner, the ACWCS program was able to meet both the ballistic and structural requirements. Also, the structural capability of the laminate provided the additional benefit of reducing the strength requirements of several frame components.

## Composite Guide Tube

The second component redesigned for the ACWCS seat was the guide tube. This component is the main structural element that reacts the forward and lateral crash loads. They are called guide tubes because they guide the bucket as it moves down relative to the frame in a crash. Figure 7 shows how the guide tubes are cantilevered above the main strut mount and how they support the inertial loads of both the occupant and the armored seat bucket. The principal design drivers for this component are high bending loads, concentrated point loading at interfacing fittings, and the need for a benign failure mode. In other seat designs these requirements have been met by using high-strength steel structures, which have performed very well. A composite version was designed solely to reduce weight.

The first step in redesigning the guide tube as a composite structure was to conduct an extensive evaluation of suitable material systems. The material candidates included both thermoset and thermoplastic matrices and were examined using various ply orientations. The goal was to arrive at a final design that possessed the same performance as the baseline steel guide tube, yet saved weight. The Finite Element Model (FEM) of the entire seat was first used to determine the reactions on the guide tubes. A detailed FEM effort on just the guide tube was then done to determine which materials and ply orientations would best meet the expected design requirements, while keeping the weight at a minimum. Several iterations of this process resulted in five potential candidate designs. The individual designs included definition of the material system, ply orientation and sequence, and fabrication approach.

The candidate material systems that Simula believed were well suited to the guide tube application were then included in a complete mechanical test program. The test coupons were fabricated and the testing completed with the results shown in Table I.

The materials were then evaluated by fabricating actual prototype sections and testing them for compliance with the expected bending requirements. The test setup is shown in Figure 8. The load-versus-deflection data for the candidate systems revealed a great deal of information concerning their suitability to the guide tube application. Figure 9 shows the relative performance of all five candidates against the baseline steel guide tube.

The results of this testing were very informative. It had been hoped that many of the systems would duplicate the "ductile" failure mode of the steel tube, thereby maintaining the desirable noncatastrophic failure mode of the baseline structure. However, only System 2 exhibited the desired response. Several of the candidate designs had identical layup sequences, so the response appears highly dependent on the material system itself. The actual failure of System 2 showed the compression side of the tube failing very controllably, while the tension side remained intact. This allowed the tube to bend approximately as it would if the tension side were stretching. The other tube concepts failed to meet the minimum load requirement or experienced a very undesirable brittle failure when the compressive stresses exceeded the strength of the tube.

Based largely on the results of these tests, System 2 was selected for use in the guide tubes. It possessed an excellent combination of strength, pseudo-plastic failure mode, and acceptable processing characteristics.

The guide tube was developed as an autoclave-cured assembly and was built in a split shell female mold. The O.D. was therefore controlled to provide a smooth finish to reduce friction loading during seat stroke.

The composite guide tube met all the design requirements. Its structural capability was verified when the ACWCS passed all of test requirements of MIL-S-58095A. When the two steel guide tubes required per seat were replaced with two composite tubes, a weight savings of 6.82 lbs, or 54.6 percent, was realized. This was a significant reduction in weight on a highly loaded, complex structural element of the crashworthy seat.

### Composite Strut

The final component case study was for the diagonal strut which is used in a floor-mounted seat to react forward and aft loading. There are several struts of this type on a typical crashworthy seat, which are normally designed as pure tension/compression members. Spherical rod ends are used at each end to eliminate any bending loads. Previous generation seat designs have used both thin-walled aluminum and steel tubing, depending on the loading requirements. This approach has produced efficient, economical structures which have successfully met all of the known design requirements.

A variety of composite and metallic materials was considered for the body of the strut. Simula elected to pursue two distinctly different approaches in the redesign. Both involved using the same graphite material selected for use in the composite guide tube. That material had been fully characterized and had demonstrated its ability to meet both the demanding structural requirements and the required processing considerations. These designs were then compared to a thin-walled aluminum strut which was chosen as the baseline.

One approach was to design a strut that met all of the anticipated loading conditions, yet was as light as possible. This was done by designing the composite strut with a minimum wall thickness and an optimized ply layup sequence. The greatest possible weight savings, 70.6 percent, was achieved by this approach when compared to the baseline design, yet the same structural requirements were met.

The second approach considered was to design a composite strut of equivalent weight to the baseline design, which possessed superior strength and damage tolerance. This was a viable alternative because of the strut's physical location on the seat (Figure 7) and its susceptibility to incidental impact damage, such as denting. Because the strut must perform as a compression member under forward loading, any dents in the tube could initiate a buckling failure which could allow the seat to collapse. This situation is magnified in that the seat is designed for crash loads and therefore experiences the ultimate design load only once. Therefore, a dent in a key member might not be a problem under flight loads, but could be disastrous in a crash. This approach produced a design that was more resistant to dents and several times stronger than required, yet had no weight penalty compared to the baseline design.



The final design Simula selected was a compromise of the two designs. Table II shows the different options that were considered along with the pertinent engineering data defining their capability. The graphite composite tube with a .073 wall thickness was ultimately chosen because it offered a significant weight savings while also providing enhanced impact damage resistance. As indicated in Table II, that selected design demonstrated a 20 percent weight savings over the baseline design.

The strut sections were fabricated using a Simula-proprietary processing technique which controls both the I.D. and O.D. surfaces to acceptable standards. The ends of the tube are cut to length and fitted with permanent metallic inserts which accept the threaded spherical rod ends. Figure 10 shows a cutaway view of a completed strut assembly.

#### CONCLUDING REMARKS

The ACWCS that Simula designed and developed during this program was verified in a test program conducted in accordance with the current revision of MIL-S-58095A. The test program involved the completion of both static and dynamic testing, with the seat design passing all of the required tests.

A series of ballistic tests was also conducted as part of the test program, and the design again demonstrated its ability to meet the specified requirements. This testing was done at Simula's ballistic test facility, but because the threat and test results are classified, they have been omitted from this paper.

Because the main purpose of the ACWCS program was to reduce the weight of existing technology armored crewseats, a detailed weight analysis was done on the prototype seats used in the structural test program. This weight was then compared to a baseline AH-64A Apache seat design. The weight of the baseline Apache seat was adjusted for the comparison to provide the performance capability equivalent to that of the ACWCS design. This correction was necessary to make an accurate comparison due to the different performance levels of the energy absorption and ballistic features between the ACWCS and AH-64A seat designs. The corrections included

- Scaling up the existing Apache armor system to meet the new threat level because the Apache ballistic requirement was less severe than that for the ACWCS
- Making a weight allowance to compensate for the Apache's fixed-load energy absorber limitation because the ACWCS has a variable-load energy absorption system (The variable-load energy absorber compensates for differences in occupant weight)
- Allotting weight to the Apache seat to allow more adjustment range since it does not have seat adjustment capability for 5th-percentile female pilots
- Adding 4.3 in. to each Apache guide tube because the Apache seat has 7.7 in. of stroke in the full-down position whereas the ACWCS has 12 in.

The weight of the current Apache seat was adjusted to provide these additional features so an accurate weight comparison could be made. The amount of weight added for each category was calculated on a very conservative basis. For example, there was no attempt to add weight for the crashworthy frame components even though they would need to carry more load due to additional armor weight. Therefore, the weight allowance added to the actual Apache seat was not exaggerated. A breakdown of the demonstrated weight savings indicated that

- 72 percent of the demonstrated weight savings was due to material usage and/or substitutions. This included advances in armor technology as well as replacing metallic structures such as guide tubes and struts with composite versions.
- 22 percent of the savings was due to the selection of advanced design concepts. This related primarily to the configuration of eventual seat design selected for the ACWCS program, the location of key structural components, and the elimination of redundant members.
- 6 percent of the weight saved was due to reductions in a corresponding airframe structure. This value was based on a hypothetical aircraft structure which was designed to carry the loads of the baseline design, yet could have been lightened to react the loads for the ACWCS design.

The weight savings achieved by the ACWCS design will establish the benchmark for future armored crashworthy helicopter seating systems. Figure 11 illustrates how the ACWCS design compares to the two U.S. Army helicopter crew-seat designs currently in service, the UH-60A and AH-64A, and the Navy's CH-53E, as well as the projected baseline Apache seat that had equivalent performance capability to the ACWCS design. This chart illustrates that as much as 50 lbs per aircraft can be saved in future helicopter designs if the technology developed during this program is implemented.

TABLE I. MECHANICAL PROPERTIES TEST MATRIX

Test Methods	Candidate Material Systems				
	System 1	System 2	System 3	System 4	System 5
Bell-Boeing 299-947-330					
Rev. G					
0 <sup>0</sup> Tensile Strength (ksi)	212.3	287.3	323.0	189.2	292.8
0 <sup>0</sup> Tensile Modulus (Msi)	17.0	22.9	20.1	21.7	22.0
Bell-Boeing 299-947-330					
90 <sup>0</sup> Tensile Strength (ksi)	3.8	9.8	13.4	8.7	10.9
90 <sup>0</sup> Tensile Modulus (Msi)	0.7	0.9	1.1	1.0	0.9
Bell-Boeing 299-947-330					
0 <sup>0</sup> Compression -					
Strength (ksi)	85.2	163.9	112.3	142.4	162.8
Modulus (Msi)	16.2	21.3	26.3	18.8	20.0
Bell-Boeing 299-947-330					
90 <sup>0</sup> Compression -					
Strength (ksi)	16.3*	68.5	7.6*	29.0*	26.5*
Modulus (Msi)	1.0	1.3	1.4	1.4	1.2
Bell-Boeing 299-947-330					
Open Hole Tension (ksi)	40.9	66.7	69.6	52.1	62.8
Bell-Boeing 299-947-330					
Open Hole Compression (ksi)	23.0	34.0	43.3	36.6	36.4

\*Indicates suspect data due to tab failure.

ksi = Thousand lb/in.<sup>2</sup>

Msi = Million lb/in.<sup>2</sup>

TABLE II. VARIOUS DESIGN OPTIONS FOR MAIN STRUT

Option	Wall Thickness (in.)	Tension Load (lb)	Compression Load (lb)	Buckling Load (lb)	Safety Factor			Weight (lb)	Weight Saving (%)
					Tension	Compression	Buckling		
Aluminum	.049	7,223	6,299	11,345	0.85	0.97	1.80	.165	N/A
"Baseline"									
Aluminum	.058	7,223	6,299	12,013	1.00	1.15	1.90	.194	-
Graphite Composite	.033	7,223	6,299	9,038	1.43	1.79	1.44	.057	70.6
Graphite Composite	.073	7,223	6,299	40,564	13.10	1.79	6.44	.155	20.1
Composite	.099	7,223	6,299	54,171	4.85	3.46	8.60	.194	0

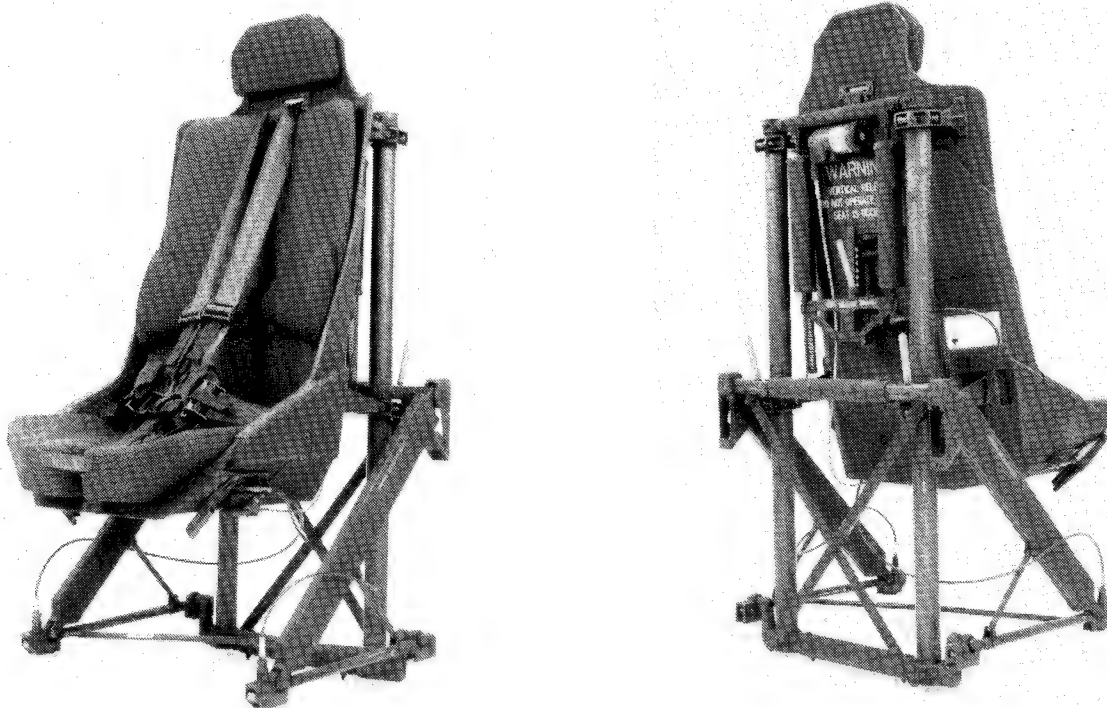


FIGURE 1. ENERGY-ABSORBING CREWSEAT FOR UH-60 BLACK HAWK.

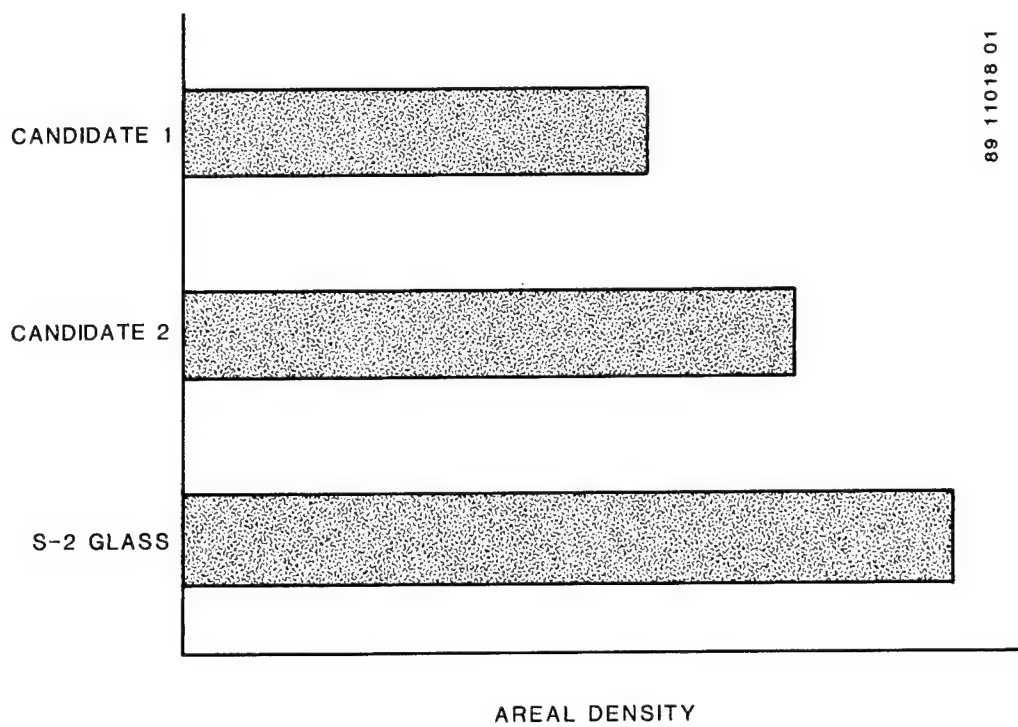


FIGURE 2. NORMALIZED BALLISTIC PERFORMANCE VERSUS A SPECIFIC THREAT.

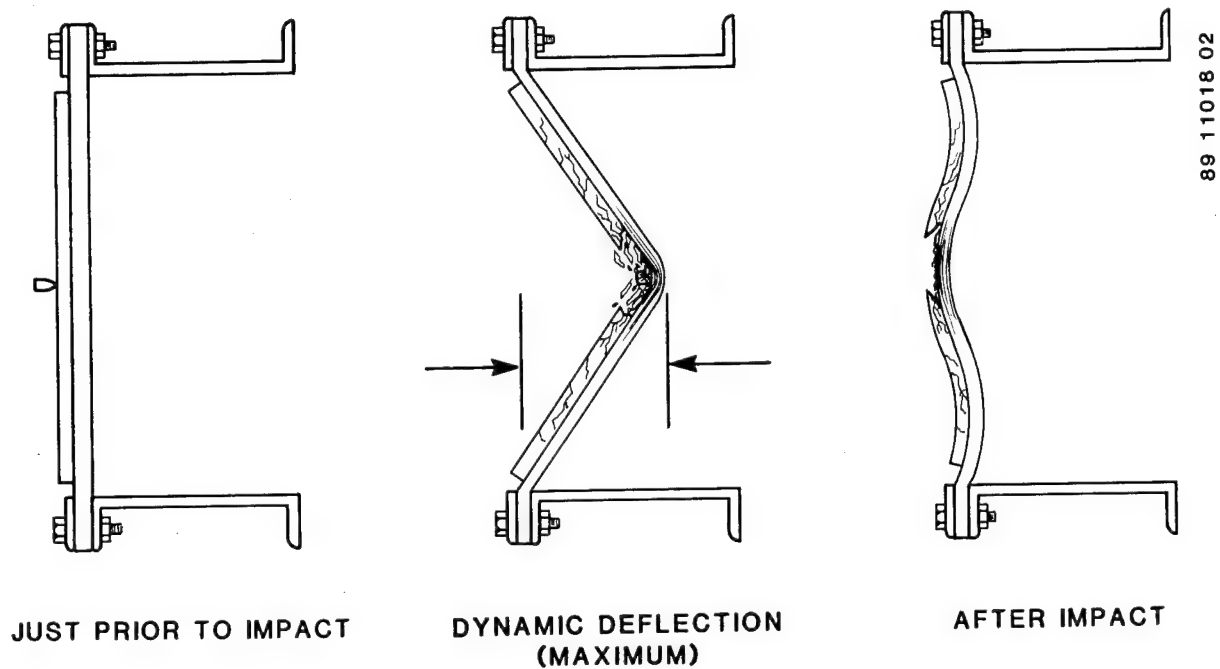


FIGURE 3. BALLISTIC IMPACT SEQUENCE FOR AN ARMOR TEST COUPON.

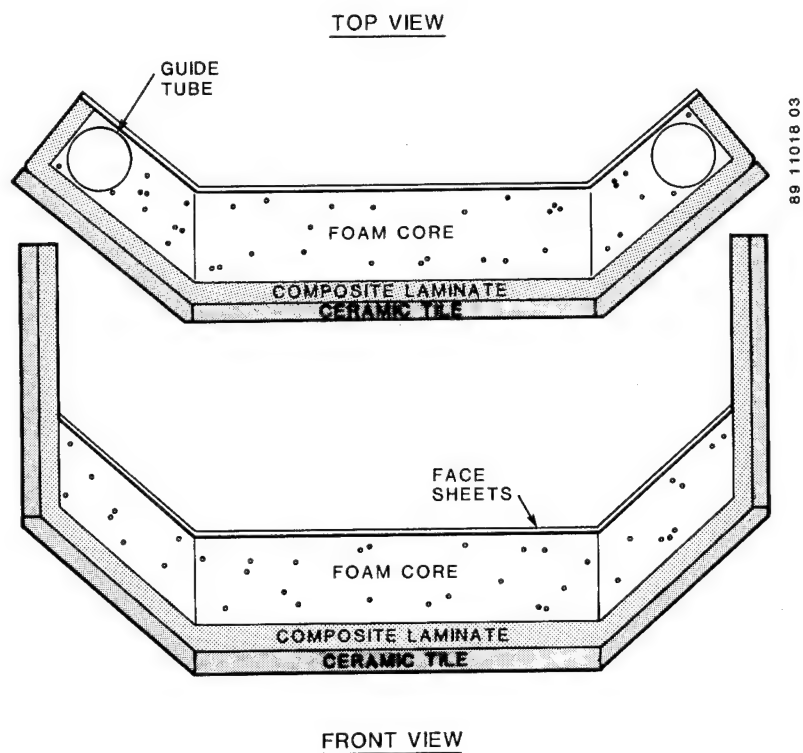


FIGURE 4. CROSS SECTIONS OF ARMOR SYSTEM WITH STANDOFF FEATURE.



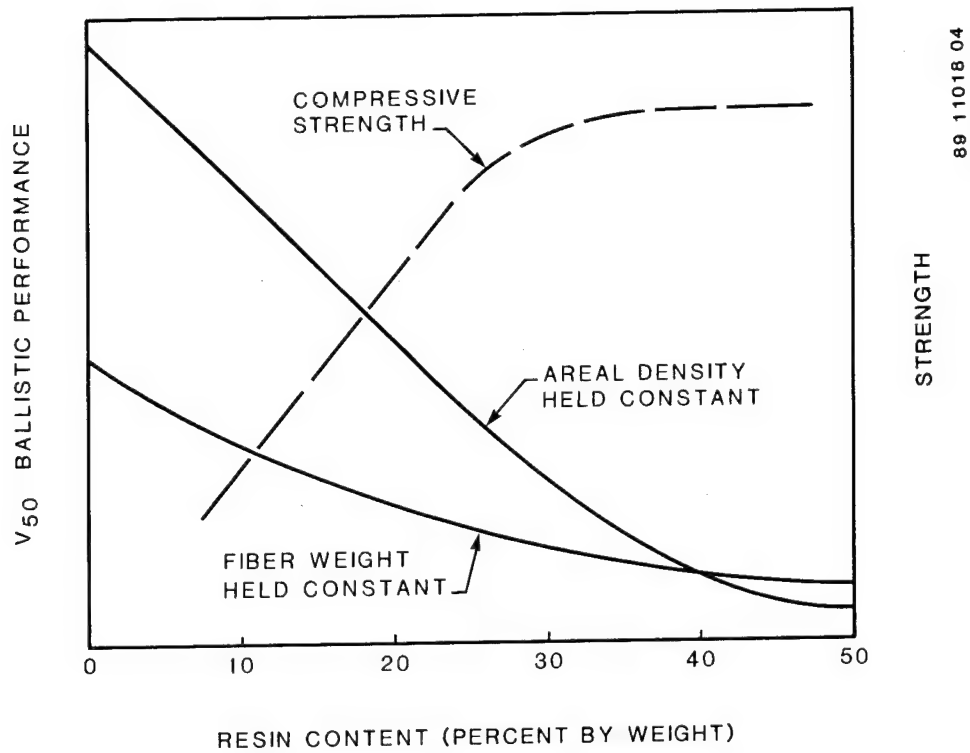


FIGURE 5. EFFECT OF RESIN CONTENT ON LAMINATE STRUCTURAL AND BALLISTIC PERFORMANCE.

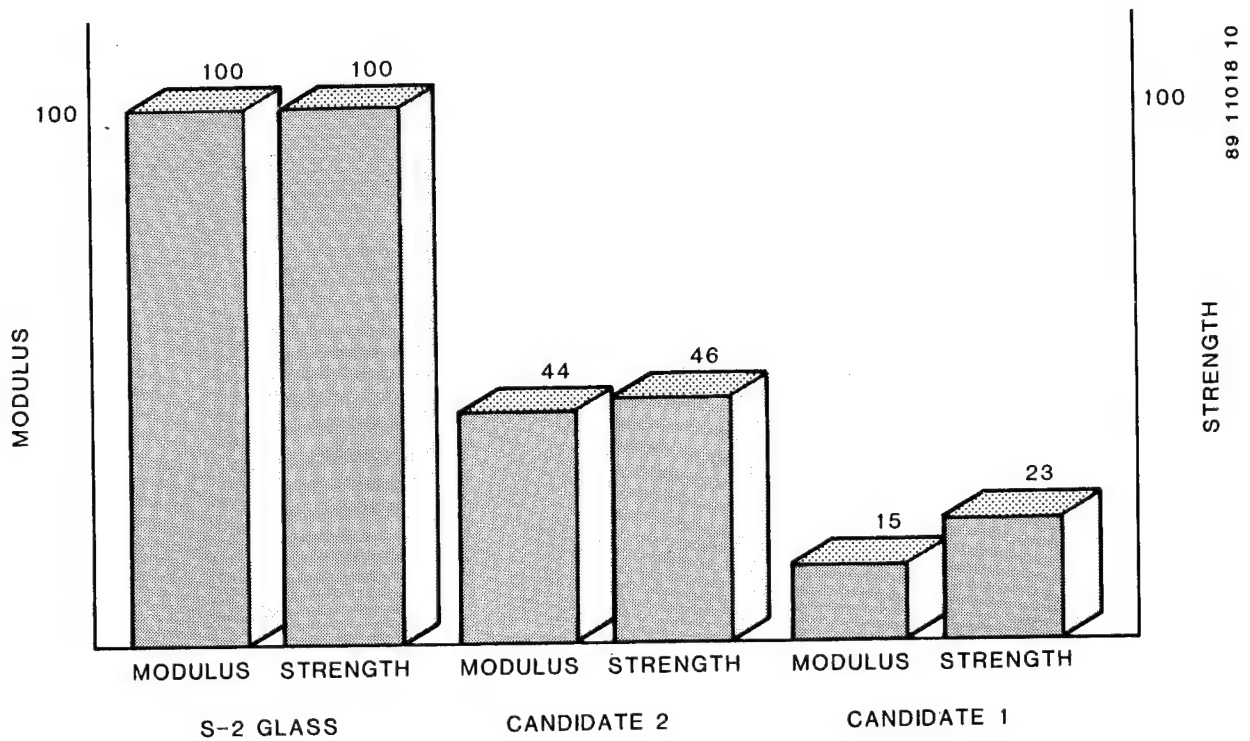


FIGURE 6. FLEXURAL PROPERTIES OF CANDIDATE ARMOR SYSTEMS.

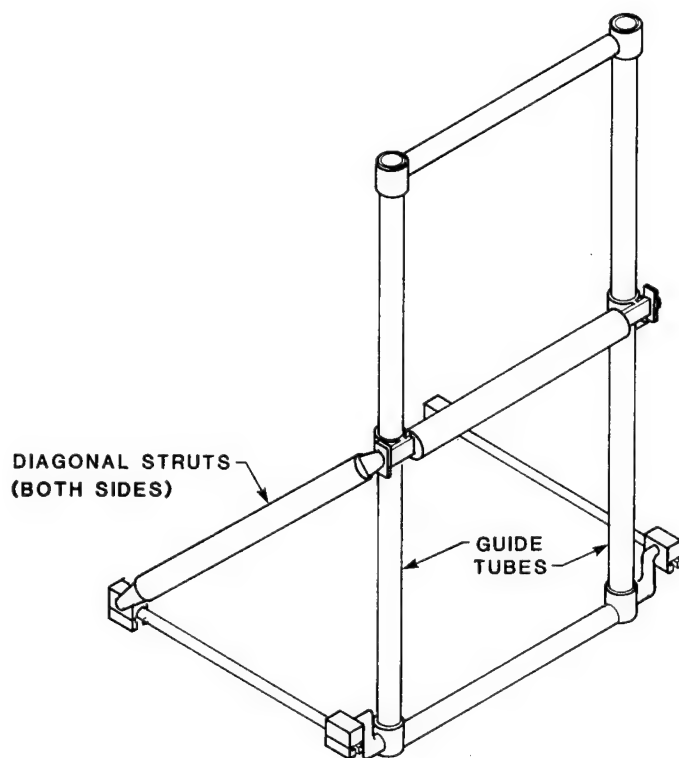


FIGURE 7. UH-60A BLACK HAWK CRASHWORTHY FRAME.

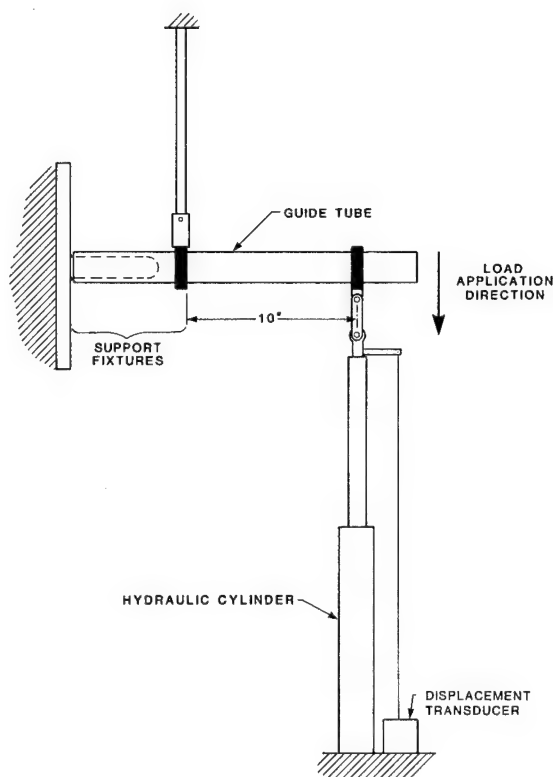


FIGURE 8. GUIDE TUBE BENDING STRENGTH TEST FIXTURE.

86 01002 177

89 11018 06

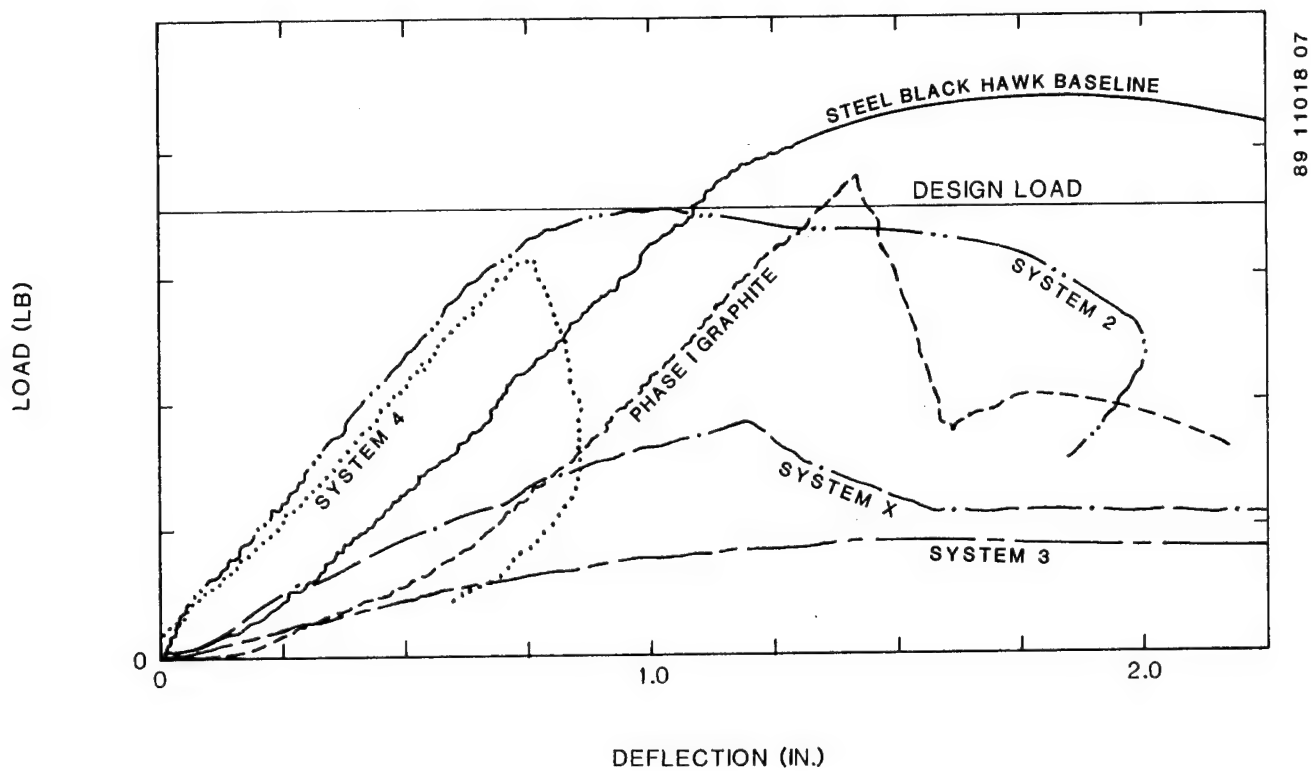


FIGURE 9. LOAD-VERSUS-DEFLECTION PLOT FOR CANDIDATE GUIDE TUBE CONCEPTS.

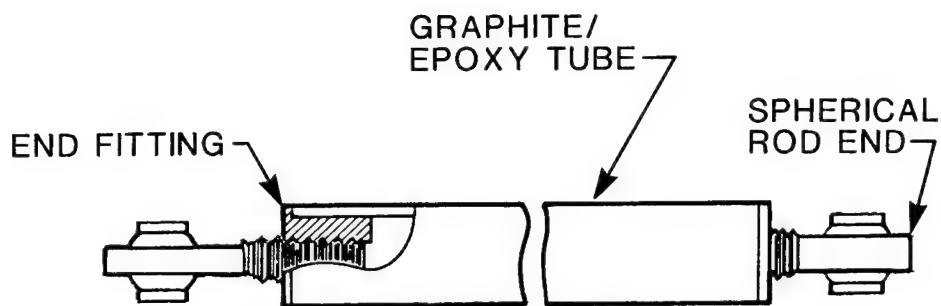


FIGURE 10. CUTAWAY VIEW OF MAIN STRUT.

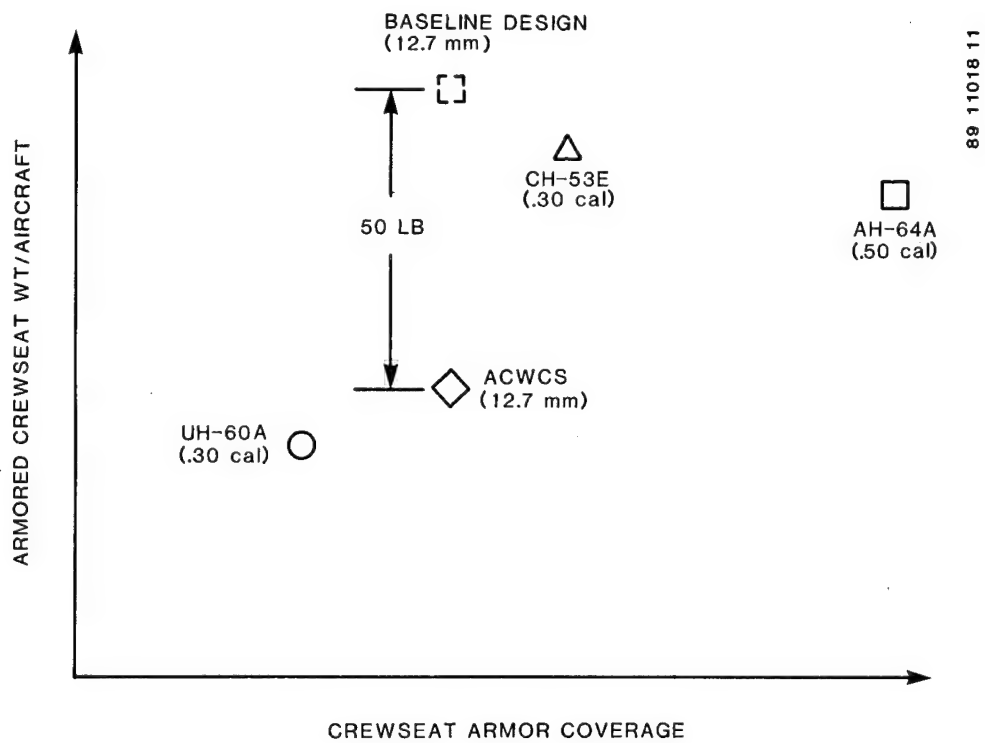


FIGURE 11. ACWCS WEIGHT COMPARED TO CURRENT TECHNOLOGY SEAT WEIGHT.

# DESIGN, ANALYSIS, AND TESTING OF A REUSABLE WINGBOX FOR BALLISTIC EVALUATION OF COMPOSITE STRUCTURES

W.G. BARON  
J.D. OETTING

Wright Research and Development Center  
Wright-Patterson Air Force Base  
Ohio

## INTRODUCTION

Future fighter aircraft will continue to be subjected to severe mechanical loading and ballistic impact. In the past aircraft primary wing structure was constructed predominantly with aluminum, but with increasing aircraft performance the need for more structurally efficient materials is necessary. In an attempt to achieve structural efficiency requirements aircraft designers have begun using an increasing amount of composite materials. Composite materials have been indicated to have a low level of ballistic tolerance in some applications. Composite materials possess the characteristic of structural tailoring, which has been utilized to demonstrate that survivability can be designed into a structure.

The combat flight environment subjects fighter aircraft wing structures to the effects of combined loading during ballistic impact. These loads have previously been demonstrated independently i.e., the application of structural load (Reference 1), hydrodynamic ram damage (Reference 2), and the effects of airflow (Reference 3). The objective of this program was to design a reusable test fixture for the ballistic evaluation of advanced composite structures under all the effects of combined loading.

The fixture that has been developed provides a test bed that can completely simulate the flight environment of a generic fighter aircraft wing, but can be used for an indefinite number and variety of tests. It is intended that this fixture will provide a standardized method of ballistically evaluating an advanced composite primary wing structure. This fixture will be used to accomplish the development of designs and/or advanced concepts that lead to a survivable composite wing structure.

## AIRFLOW TEST FIXTURE DESIGN DISCUSSION

In order to provide a feasible means of ballistically evaluating materials and survivable concepts, the fixture had to be easy to use and quick to repair so that valuable test range time was not needlessly expended. If the fixture was to be accepted as a baseline for testing it was necessary that it be designed with the ability to tailor test section specimens. This would allow the fixture to accommodate the testing of wing skin panels of variable thicknesses with incorporated damaged arrestment features or the use of an entire wing box test section which would include skin and substructure. The only limitation that would be imposed on the test component structure is the geometrical dimensions of the test section.

The overall design of the test fixture was driven by the need to represent a generic fighter aircraft wing under accurately simulated combat flight loads. These loads included the application of airflow, structural bending load, ballistic impact of realistic threats and the effect of hydrodynamic ram. To size the test section of the fixture, a baseline for a generic fighter aircraft was selected. A schematic of the airflow fixture layout and the method of load application is shown in Figure 1.

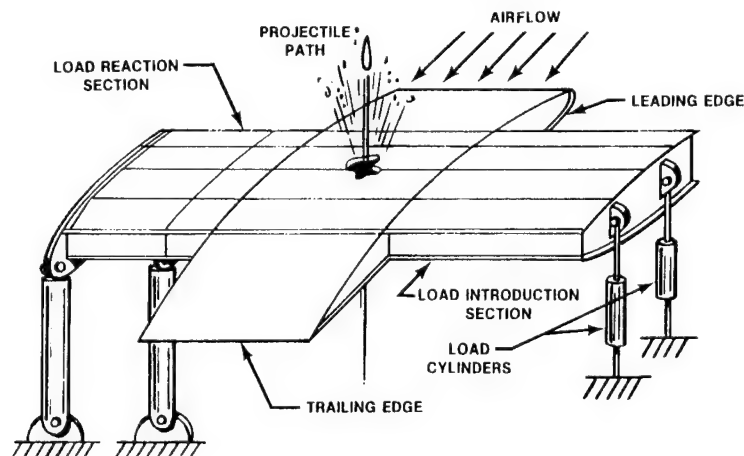


Figure 1. Combined Loading

The fixture was configured with three entirely separate component sections. This included a load introduction section, test section and a load reaction section. With this approach any skin or substructure damage that occurs in the test section during ballistic testing could be replaced without having to dismantle and rebuild the load introduction or the load reaction sections of the test fixture. This allows turn-around of specimens for testing in a more expedient and cost effective method.

The dimensions of the fixture were driven by the geometrical requirements of the test section and the test range limitations. For the test section to simulate realistic fighter aircraft structure, a multi-bay configuration was selected. This would provide multiple load paths so that after ballistic impact the redistribution of load could be quantified, and the failure mechanism understood. For effective wingbox representation, a four-bay, five-spar test section configuration was utilized. The substructure of the airflow fixture is shown in Figure 2.



Figure 2. Substructure of the Fixture

The substructure of all three component sections of the airflow fixture was designed entirely with 7075-T6 aluminum. All of the ribs in the fixture were machined from plate stock. The upper and lower spar caps were machined to specification from T-section extrusion. The spar caps in the test section are mechanically fastened with the webs and are attached to the test section close-out ribs with the use of clips. The base of the spar caps extends over the inboard and outboard ribs and are assembled as part of a splice plate joint. The load reaction section consists of an inboard close-out rib, which has a load reaction lug attached to the forward and aft intermediate spars. A set of four partial ribs form the outboard load reaction rib, which is located 21.25 inches from the inboard end and provides the hard point for the two outboard load reaction lugs. The load introduction section is also attached to the test section with the use of a splice joint. The load introduction lugs are located on the outboard end of this section on the forward and aft intermediate spars.

The position of each spar is located on 7.0-inch centers, therefore establishing the size of each bay and the overall width of the test section. The length of the test section was set to 36 inches to correspond with the fighter wingbox configuration selected. The test section uses a curved wing skin cover; therefore, the test section depth is variable but has a maximum depth of 7.5 inches occurring at the center span. The overall airflow test fixture measures 110 inches from the root of the load reaction section to the outboard end of the load introduction section. The test fixture is shown in Figure 3, assembled for testing in the loading structure.



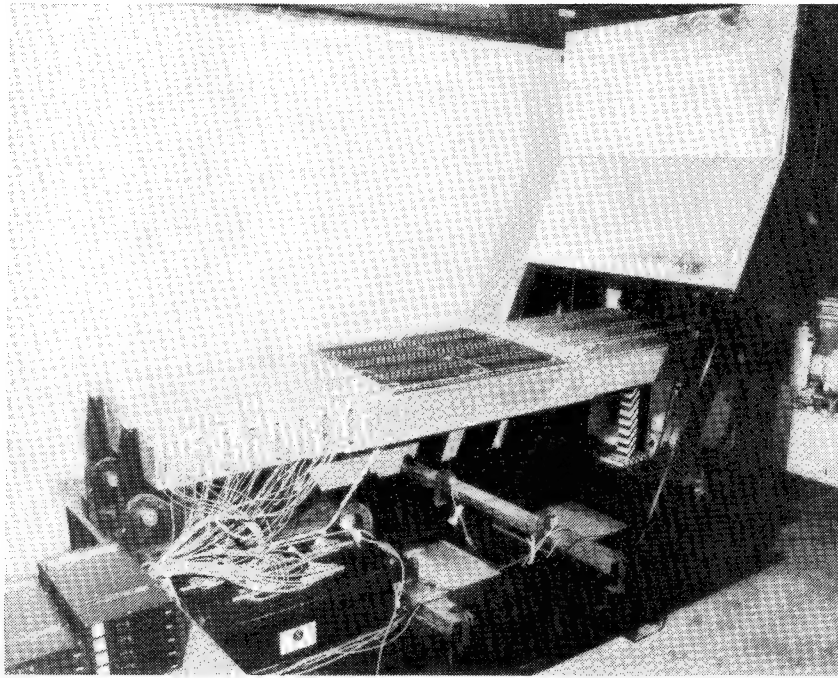


Figure 3. Airflow Fixture in Loading Structure

Since the airflow test fixture will be used in a simulated flight environment, airflow is a loading mechanism to which the test fixture will be subjected. In order to provide a method of applying airflow the test section had to be designed with a mold-line contour. Therefore a leading and trailing edge for the airflow over the test section was designed with a theoretical chord length of 100 inches. These leading and trailing edges have been installed and are shown in Figure 4 with the upper covers removed.

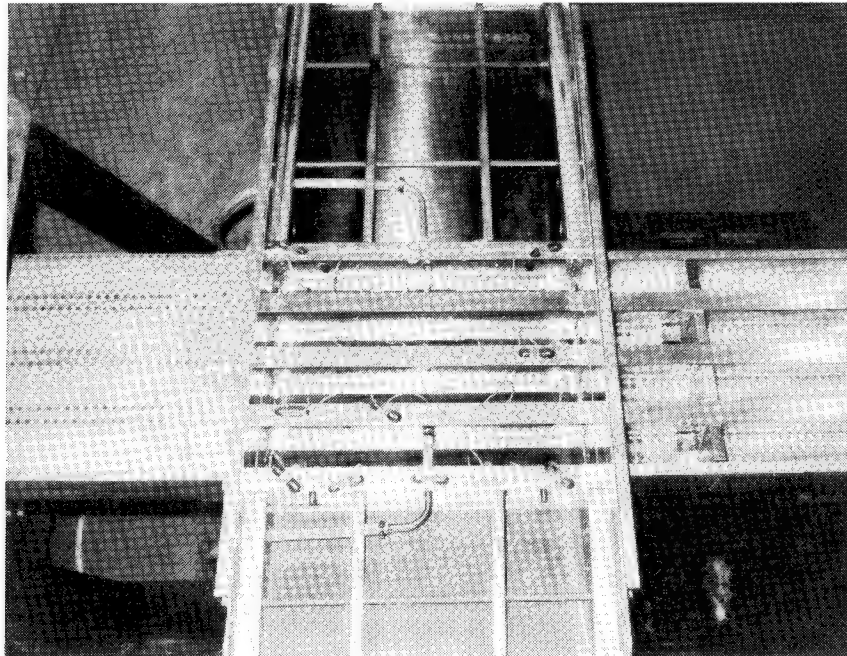


Figure 4. Leading and Trailing Edge Installed

### TEST SECTION COMPOSITE PANELS

The panels used for the fixture evaluation test series were fabricated in the WRDC/FIBCA composites facility. The material used for all of the evaluation tests was AS4/3501-6 graphite/epoxy prepreg tape manufactured by Hercules, Incorporated. This was selected because its structural properties are well characterized and a great deal of engineering confidence exists in its applications.

The test section composite skin designed for the tests was a 32-ply hard skin. These panels consisted of the following percentage ply orientations:

37.5% 0 degree plies (spanwise)  
50.0% 45 degree plies  
12.5% 90 degree plies (chordwise)

This laminate is laid up with the following symmetric stacking sequence:

( $\pm 45, 0_2, \pm 45, 0_2, 90, \pm 45, 0_2, \pm 45, 90$ )<sub>s</sub>

This panel design was used for all of the structural and ballistic baseline evaluation tests.

### BASELINE TEST INSTRUMENTATION

All airflow tests conducted were fully instrumented in order to accurately characterize the load transfer mechanism in the fixture and verify the NASTRAN computer model. The extensive use of instrumentation was to aid in understanding the ballistic impact phenomenon which needs to be quantitatively recognized before survivable structures can be designed.

The test database that has been compiled includes experimental data such as structural static and dynamic strain surveys, hydraulic ram pressure transients, deflection, real time video, high speed film and nondestructive investigation results. This data has been reduced using graphical illustrations and classical structural analysis methods.

The airflow fixture was instrumented with six deflection potentiometers to identify the bending and torsion that occurred to the fixture. The 32-ply graphite/epoxy wing skin panels were instrumented with an array of three gage rectangular rosettes. Each of the rosettes were positioned in the center of the four bays between the spars, so that the strain field was less inhibited by the stress concentrations induced from the bolted attachment. Twenty rosettes were applied to the inside surface of each wing skin panel. Two rosettes were attached to the outside surface on the top (compression surface) skin and placed back to back with two internal rosettes to determine the level of bending. Dynamic strain data was acquired during the ballistic impact event on the selected rosettes adjacent to the target location and at the root of the test section.

Pressure transducers have been located in each bay of the wingbox in the inboard and outboard close-out ribs so that the hydraulic ram effect could be recorded during impact. The transducers have been mounted in a rubber bushing to isolate them from the structure.

### **BASELINE TESTING PROCEDURE**

Ballistic impact, structural load and airflow were required for these tests so they were conducted in range three at the Aircraft Survivability Gun Range at Wright Patterson AFB. The airflow fixture is shown in Figure 5 installed in the loading structure and in the test range.

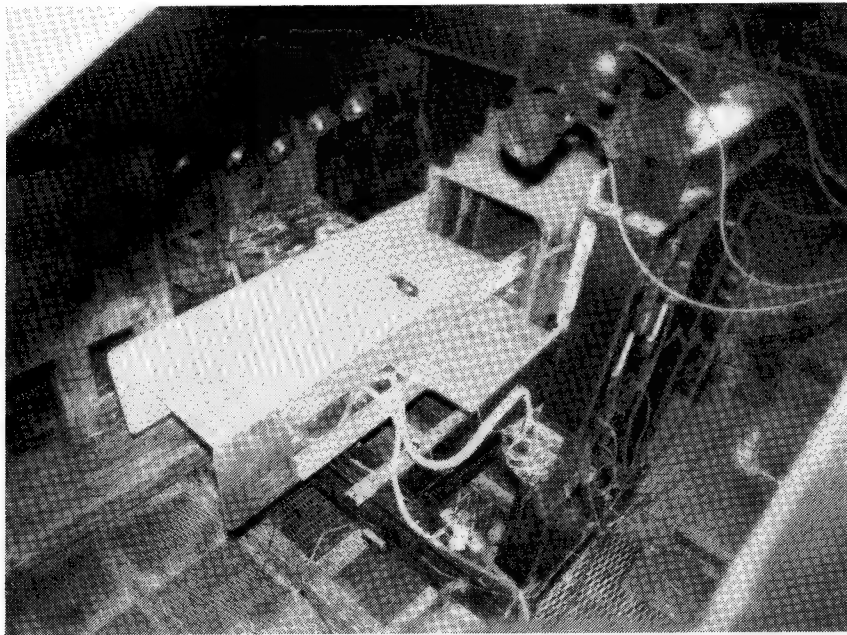


Figure 5. Test Range Configuration

Each test was conducted in three separate stages:

1. Undamaged evaluation
2. Ballistic impact evaluation
3. Damaged evaluation

Each undamaged test was initiated by first applying a load equal to the fifty-percent design limit load to set the structure. The test fixture was loaded in four consecutive cycles up to the fifty-percent design limit load with strain surveys conducted at every 10 percent increment. Deflection readings were also acquired at these load increments. After completion of the four undamaged loading cycles, a statistical analysis program was run to reduce the data from the four load cycles to identify any strain gage anomalies.

During the ballistic impact stage of testing, load was applied up to the test level and a strain survey was completed. Additional strain

surveys were also conducted before and after the impact event while the airflow was maintained.

A final series of structural tests were performed to assess the level of damage that occurred to the test component. This was done in an identical manner as the four undamaged load cycles were completed. After this was done a statistical analysis was completed on the acquired strain gage surveys.

## **STRUCTURAL AND BALLISTIC TESTING**

The objective of the testing which has been completed and is reported herein was to establish a baseline database of the airflow fixture's structural integrity. The test series was designed to assess the airflow test fixture's structural and ballistic limitations. The baseline data generated from this test series is intended for use to influence designs of survivable structure for evaluation using the airflow test fixture.

Five separate tests have been conducted and were completed in the following order:

1. Structural verification test
2. Full-up proof test
3. Baseline 23 mm API\* test
4. Baseline 23 mm HEI† test 1
5. Baseline 23 mm HEI test 2

The structural verification test was completed to determine the load distribution and identify structural components that were critically stressed. Full-up proof testing was then accomplished in order to demonstrate the use of the fixture under airflow load, structural load, hydraulic ram and ballistic impact. These two tests directed several minor structural modifications which were completed to the prototype airflow fixture at that time. These modifications were then later incorporated into the initial fabrication of the four additional airflow fixtures fabricated for quick turn-around of test articles.

## **BASELINE TEST SUMMARY**

The data from each of the three structural baseline evaluation tests has been reviewed and summarized. The intention of this assembled data reduction is to provide an understanding of the magnitude of damage, the lethality of the threat and the load redistribution mechanism.

The first baseline test conducted was with full-up loading conditions as done in the proof test. This included the use of structural load application of 25-percent design limit load at the root of the test section, a 75-percent full tank of water for hydraulic ram, 500 knots of airflow and ballistic impact with a 23-mm API round. The damaged test section skins are shown in Figure 6, with the exit panel (compression skin) on the left.

\*armor-piercing incendiary (API).

†high-explosive incendiary (HEI).

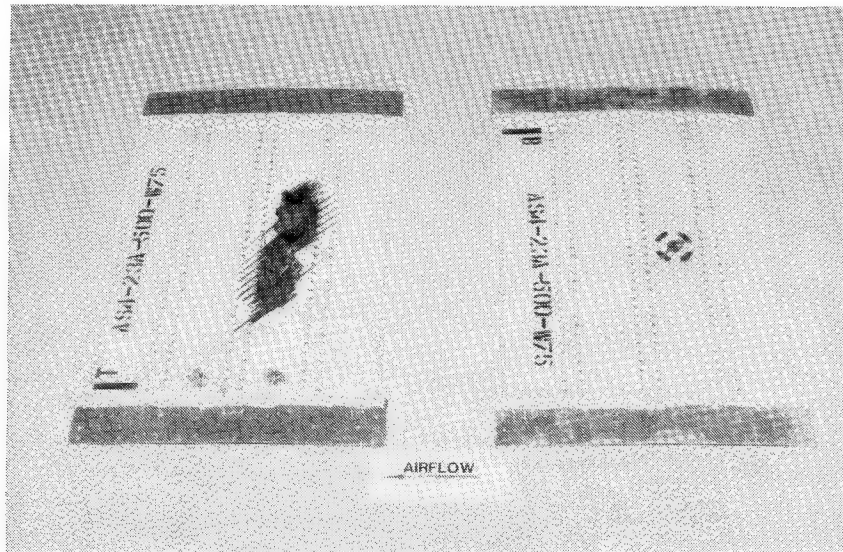


Figure 6. Damaged Skins Baseline Test 1

The entrance panel survived with minimal damage. The target location experienced a 1/2-inch diameter hole punched out by the penetrating projectile. Delamination extended between the impacted bay's closeout spars, which was observed using a simple "coin tap" test. The composite panel also experienced bolt pull-through at the spar attachments which extended approximately 8 inches; this can be attributed to the hydraulic shock wave. The exit panel experienced much more extensive damage which also extended between the spars. Surface plies were lost 18 inches spanwise which was caused by the compression stress state and the projectile bending the skin material into the airflow. Bolt pull-through also occurred on the exit surface but was not as severe as the entrance panel, which was partially buffered by the 25-percent ullage above the water. The substructure was also damaged, which is attributed to the hydraulic ram effect. The forward intermediate spar was not visibly damaged but the center upper and lower spar were both damaged. The compression cap was split at the radius of the T-section over its entire span, and the tension cap split in a similar fashion but traversed 20 inches.

Observing the static strain data before and after the impact it was determined that the load in the panel was transferred into the substructure. The strain on either side and outboard of the impact location on both the tensile and compression panels was actually reduced in the post test strain surveys. This load was redistributed into the forward intermediate and aft intermediate spars, which are the primary load paths.

As a result of the damage the fixture incurred a 3.13-percent reduction in stiffness. The pressures in the impacted bay reached the highest magnitude. The inboard pressure transducer had a peak pressure of 60.9 psi at 7.74 msec after the event, and the outboard transducer recorded 77.0 psi at 5.7 msec. These pressures are recorded 18 inches from the impact site and are much lower than the pressure that caused the substructure damage. The dynamic strain data acquired also reached the highest magnitude in the impacted bay as expected. This data was relative to the static load that was applied to the panel at the time of impact. At



the inboard end of the exit test panel the internal spanwise leg of the gage in this bay recorded an oscillation between a compressive strain of 849 micro in/in and a tensile strain of 870 micro in/in. The gage placed back-to-back on the outside surface recorded a maximum compressive strain of 1395 micro in/in and a maximum tensile strain of 1384 micro in/in. This demonstrates the excessive bending occurring in the exit panel.

The second baseline ballistic evaluation was completed with identical test parameters as used in baseline test 1 except that the round used was a 23 mm HEI. The damaged test section skins resulting from this test are shown in Figure 7, with the exit panel shown on the left.

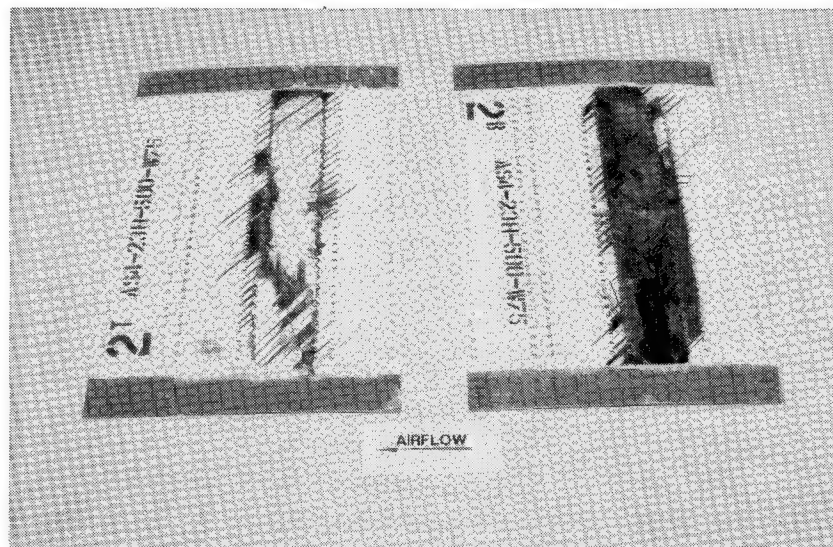


Figure 7. Damaged Skins Baseline Test 2

The damage in both the upper and lower test section skins was very extensive and, as seen in the Figure 7, extends over the entire impacted bay. Although visible damage was arrested by the bolted spar attachment, delamination was indicated to have extended into the skin of both adjacent bays by using the "coin tap" test. The exit skin also exhibited a surface buckling in the forward bay. The fasteners on the aft intermediate spar pulled-through the exit skin which could be attributed to the failure of the center spar cap. This spar cap split at its root radius across the entire length. The lower spar cap fractured and was bent 8 inches out of the skin plane. The forward intermediate spars also had extensive damage. The upper cap split along its radius over its entire length, and the lower cap fractured along its aft bolt-line but did retain some load carrying capability. The detonation of the high explosive is believed to have occurred in the 25-percent ullage. This is due to the localized fragmentation damage that was observed on the center spar cap, which extended over a 4-inch region.

The static strain contours for the these skins were analyzed to assess the load carrying capability that remained in the skin. The entrance panel retained more ability to carry load than the exit panel. This was a result of the local forward bay skin buckling and the aft intermediate bolt pull-through damage on the compression skin. Although

the remaining structural skin did show an increase in the level of strain the primary load was redirected into the substructure.

As a result of the ballistic damage the fixture incurred a reduction in stiffness of 33.41 percent. Unfortunately the pressures in the impacted bay were much higher than originally anticipated and the gain on the transducer amplifiers was not set appropriately and this data was lost. The dynamic strain data collected has revealed a preliminary understanding of the failure mechanism. Data was collected on selected gages adjacent to the impact site and the inboard end. On the gages that were damaged during the event, data was acquired up to the level at which the gage was damaged. For comparison with test 1, the internal spanwise leg referenced for the API test, recorded a much higher level of strain. The gage experienced a tensile strain of 840 micro in/in, at 0.734 msec and maximum compressive strain at gage failure of 4071 micro in/in at 1.274 msec. The back-to-back gage at this location never experienced a tensile fluctuation and reached a maximum compressive strain at gage failure of 6275 micro in/in at 1.133 msec.

After observing the extensive damage that was precipitated by the impact with the 23-mm HEI in test 2, it was decided not to increase the threat to 30-mm HEI as originally planned. Since a set of panels had been fabricated for this third test, it was decided to use these panels in a test 2 replication to study the variability of the HEI. Therefore the third test conducted was done with identical parameters as in test 2. The damaged panels from this test are shown in Figure 8.

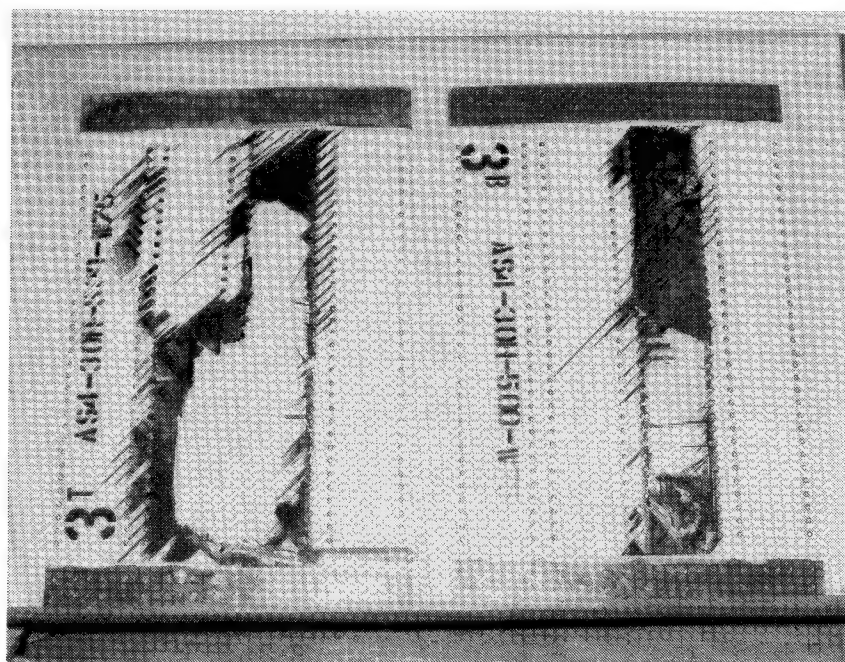


Figure 8. Damaged Skins Baseline Test 3

The damaged skin was much more extensive than was seen in test 2. The exit panel skin damage extended to the aft intermediate bay, but the entrance skin was confined to the impacted bay. The substructure failed in a very similar manner as in test 2, but the forward intermediate spars upper and lower caps did remain structural load carrying members. The primary failure difference of the structure could be attributed to two



observed variables. The explosive round detonated much earlier than in test 2. This is evidenced by the fragmentation damage on the web which was located from the web center to the spar cap; this would indicate a detonation within the water of the bay. Detonation within the water would result in a much higher level of hydraulic ram. Also the impact site was missed approximately 1 inch closer to the center spar; therefore, the forward intermediate spars were not affected as severely by the fragmentation damage. The center compressive spar was subjected to the full effect of the HEI and when it failed the skin remained bolted to the spar and destroyed all load carrying capability of the intermediate aft bay skin.

The ballistic damage caused a stiffness reduction of 22.62 percent. This was 10.79 percent less than the reduction occurring in test 2 because most of the forward intermediate spar remained structural. The dynamic strains observed in this test were similar in magnitude to those that occurred in test 2. The pressures observed in the impacted bay were much larger than observed in the API test. The outboard transducer recorded a pressure of 1960 psi at 1.5 msec, and the inboard transducer recorded 2000 psi at 0.78 msec, which was the maximum calibrated for recording.

### DEVELOPMENTAL CONCLUSIONS

The airflow fixture has demonstrated that it can be utilized as a baseline structure for the testing and development of advanced survivable composite structures. This fixture provides a test bed that can completely simulate the flight environment of a generic fighter aircraft wing. The fixture can be used for an indefinite number of tests which has been shown by the ability to rebuild the damaged structure. The completed testing has shown that the fixture can be used for the evaluation of structures subjected to a 23 mm HEI threat. If larger threats such as the 30 mm HEI were tested it would be suggested that a fixture with the same ability to tailor the test section be developed but with additional load paths. Since the airflow fixture was designed with a five spar configuration, the lethality of the 30 mm HEI threat would probably catastrophically fail the test section and very little load redistribution data could be recovered. The experimental data that has been acquired in this test series has defined the lethality of the 23 mm API and 23 mm HEI threats when subjected to this fixture. Using the airflow fixture and the test data as baseline, survivable structure will be developed in follow-on efforts.

### REFERENCES

1. M.R. Allen, D.T. Sawdy, S.J. Bradley, & J.G. Avery, "Survivability Characteristics Of Composite Compression Structures," AFWAL-TR-88-3014, JTCG/AS-87-T-005, May 1988.
2. M.J. Jacobsen, R.M. Heitz, & F. Hill, "Survivable Composite Integral Fuel Tanks," AFWAL-TR-85-3085, January 1986.
3. Gregory Czarnecki, "High-Speed Airflow Effects On Battle-Damaged Composite Surfaces," AFWAL-TR-87-3090, April 1987.

# DEVELOPMENT OF COMPOSITE WING CARRYTHROUGH BULKHEADS FOR FIGHTER AIRCRAFT<sup>1</sup>

J. C. Goering and R. S. Behrens  
McDonnell Aircraft Company  
McDonnell Douglas Corporation, St. Louis, MO

M. Libeskind  
Naval Air Development Center, Warminster, PA

## SUMMARY

Potential weight savings due to the use of composite materials for highly loaded primary structures are being demonstrated through the design, fabrication, and test of an all composite wing carrythrough bulkhead for the F/A-18 fighter aircraft. A one piece composite design which results in a 24% weight savings, relative to the existing aluminum bulkhead, has been developed. Critical details of this design have been evaluated through element tests, and a full scale prototype component has been fabricated. The structural integrity of this design will be demonstrated in a comprehensive full scale test program.

## INTRODUCTION AND BACKGROUND

The use of composite materials in fighter aircraft structure has increased steadily over the past few decades. The first production aircraft, manufactured by McDonnell Aircraft Company (MCAIR), to make substantial use of composites was the F-15 Eagle. Introduced in the early seventies, composites account for 2% of the structural weight of this aircraft. During the mid-seventies, composite usage increased to nearly 10% of the F/A-18 Hornet structure. This trend continued through the late seventies and into the eighties with the AV-8B Harrier II. Measured by weight, over 26% of the structure in the AV-8B is fabricated from composite materials. It is anticipated that composites will account for as much as half of the structural weight of the next generation of fighter aircraft.

The majority of the composite materials utilized in these aircraft have been incorporated into wing and tail structures (Figure 1). Although composites have been included in fuselage structures, these applications have been limited to lightly loaded fuselage panels. The objective of this work is to demonstrate that significant weight reductions can be achieved through the use of composite materials for more highly loaded primary fuselage structure, specifically, wing

1. This work was performed by McDonnell Aircraft Company for the Naval Air Development Center, under Contract No. N62269-87-C-0216, "Development of Composite Carrythrough Bulkhead."

carrythrough bulkheads.

Bulkheads are typically used to redistribute large concentrated loads, such as wing and landing gear loads, into the surrounding fuselage structure. These bulkheads provide an application for composite materials which shows considerable promise in eliminating recurrent structural problems while reducing weight. In addition, the corrosion resistance and fatigue insensitivity of these materials can be exploited to reduce high life cycle costs associated with such limited access structures.

Composite fuselage subcomponents from several existing and future aircraft have been fabricated and tested [refs. 1-9]. Composite bulkheads of varying degrees of complexity were addressed in these programs. Bulkhead issues considered by these researchers included the design of highly loaded lugs, moldline flanges, and stiffener intersections. Each program addressed one or more of these issues but no program addressed all of them, and only one considered composite lugs.

In more recent work, MCAIR designed, fabricated, and tested an integral composite fuselage fuel tank for a supersonic, fighter/attack, V/STOL aircraft [refs. 10,11]. This fuel tank included two composite closure bulkheads and a composite wing carrythrough bulkhead. Even though the main emphasis of this work was to demonstrate survivability and crash resistance, the carrythrough bulkhead demonstrated a 17% weight reduction relative to an aluminum baseline. This bulkhead included thick highly loaded wing attach lugs and stitched stiffeners. The design and fabrication of this component provided a solid foundation for the development of more complex bulkheads which carry landing loads as well as wing loads.

## BULKHEAD DESIGN AND FABRICATION

### Baseline Bulkhead and Design Criteria

The baseline component for this study was the existing aluminum bulkhead at fuselage station 453 in the F/A-18 (Figure 2). This component was selected because it includes structural complexities that are representative of bulkheads in general, and because a large amount of manufacturing, service, and test data is already available. This existing database permits a direct comparison of the benefits and risks for the same bulkhead made from composites.

The primary function of this bulkhead is to carry wing loads and support the main landing gear. In addition, it carries fuel pressure loads and is located at the manufacturing splice between the forward and aft sections of the center fuselage. The baseline is machined from 6 in. 7050-T73651 aluminum plate and weighs 264 lb. The upper dorsal section is made separately and mechanically fastened to the lower section. Cutouts in the center web area permit fuel system plumbing to pass through. This plumbing is joined at the web by fittings.

Structure is provided in the lower section, below the inlet ducts, to

support the forward trunnion of the main landing gear. The main landing gear pivots about an axis that is canted approximately 38 degrees away from a line parallel to the centerline of the aircraft. The forward trunnion is therefore rotated by this same amount relative to the plane of the bulkhead. Bushings are included in the trunnion to provide a wear resistant surface, as shown in Figure 2.

Fuel tank areas which interface with the bulkhead are shown in Figure 3. On the forward side of the bulkhead a flange is provided to support the fuel tank floor. Bulkhead flanges also support the center fuselage side panels and dorsal deck forming the sides and top of the tank. On the aft side, the floor of another tank is supported by a horizontal flange. Additional flanges support the inlet duct liners, upper outboard fuel beam, crease skins, and dorsal deck panel which form the sides and top of the tank.

The primary design requirement for the composite bulkhead was that it would have the form and function of this baseline bulkhead and would be capable of carrying all loads currently applied to the metal baseline. Specific requirements were that it must be able to withstand static ultimate loads (1.5 times limit load) without failure for critical design conditions, and that it must be capable of withstanding 2 lifetimes (12000 spectrum flight hours) of fatigue loading. In addition, the bulkhead was designed for -65°F to +160°F service temperature with moisture equivalent to 10 years on Guam.

The main goal of the program was to develop a composite bulkhead which met these requirements and weighed at least 20% less than the metal baseline. Secondary goals were to minimize cost, reduce maintenance, and improve survivability. Survivability requirements were that the bulkhead be able to withstand peak spectrum loads after low velocity impact and that the aircraft be able to return to base with only the loss of the bulkhead after ballistic impact.

### Trade Studies

Ten preliminary design concepts were defined and evaluated with respect to weight, cost, supportability, and fabricability. These concepts are shown in Figure 4. Selection of the best overall concept was made, based on the results of this evaluation. Weight was the most important consideration in the selection of the preferred concept, followed by cost, producibility, and supportability, in that order.

Relative measures of the weight, cost, and supportability of the ten concepts, normalized to the values for concept 1, are shown in Figure 5. As shown in this figure, concepts 1, 7, and 10 result in the lightest weight and lowest cost bulkheads. Concepts 7 and 10 have a 1 to 2% weight and cost penalty, relative to concept 1, but provide a slight benefit in supportability. Taking producibility into account, concept 10 is heavily favored over concepts 1 and 7, since these two concepts each have three fixed tooling surfaces, namely the flanges at the inlet ducts, nacelles, and forward fuselage. Concept 10 has only the nacelle and inlet duct flanges cocured, while the forward fuselage

flange is secondarily attached. Concept 10 was therefore selected for further development, since it provided the best balance between weight, cost, and producibility.

Along with structural trade studies, candidate material systems were surveyed to identify the most appropriate material for this application. Primary considerations for the selection of a material were that it provide sufficient strength, stiffness, and toughness at a reasonable cost. In addition, it had to process simply, have a use temperature of at least 160°F, and have sufficient durability and damage tolerance to meet the survivability requirements.

A number of thermoset, both epoxy and bismaleimide, and thermoplastic matrices were considered. Critical properties for the selection of a matrix were the elevated temperature wet compressive strength, the residual strength after low velocity impact, and its resistance to microcracking. Based on these parameters 8551-7 toughened epoxy, produced by Hercules Aerospace Co., was selected as the most appropriate matrix. AS4 and IM7 carbon fibers, also produced by Hercules Aerospace Co., were selected to reinforce this matrix. The high modulus IM7 fibers were used in unidirectional tape, wherever practical, to satisfy stiffness requirements with minimum weight, and AS4 cloth was used for web plies that wrapped around corners to form flanges. Subsequent to this survey, Hercules modified the 8551-7 resin to improve tack and increase use temperature. The modified resin was labeled 8551-7E. This resin was further modified to improve out time and is designated as 8551-7A.

A refined design for structural concept 10, which utilized the modified toughened epoxy material system, was developed and analyzed using detailed finite element models. The refined design is shown schematically in Figure 6. This design differs slightly from the original concept 10 in two areas. First, only the portion of the forward fuselage flange that intersects the carrythrough beam is secondarily attached, the majority of this flange is cured with the main web of the bulkhead. Second, the portions of the duct flanges which intersect the carrythrough beam are secondarily attached. These modifications were made to reduce tooling costs, since they allow the carrythrough beam to be tooled with relatively inexpensive monolithic graphite tools.

Referring to Figure 6, wing bending loads are carried by the 2.3 in. thick beam near the top of the bulkhead. These concentrated loads are introduced into the bulkhead through four integral composite lugs. Away from these lugs, pockets with .25 in thick webs were included to lighten the carrythrough beam. Landing loads are introduced through 1 in. thick webs in the lower portion of the bulkhead. The out of plane geometry of these webs is a modified sine wave with an extended flat, oriented at an angle of 38 degrees relative to the plane of the bulkhead, that accepts the main landing gear. The loads carried by these webs are sheared into the surrounding fuselage structure through the nacelle and duct flanges. A short distance away from the end of the modified sine wave, the trunnion web thickness tapers down to approximately .2 in., which is the thickness of the remainder of the bulkhead web. The weight of this bulkhead was calculated to be 201



1b., including the trunnion hardware, which represents a 24% reduction, relative to the aluminum baseline.

### Element Test Program

Coupons and critical structural elements were fabricated and tested to demonstrate fabrication methods, determine static strength and fatigue life and to validate critical design details. The structural elements represented specific areas of the bulkhead, as shown in Figure 7. Various elements were static and fatigue tested in room temperature dry and elevated temperature wet environments. In addition, some specimens were tested after low velocity impact damage had been introduced. Test conditions and results are summarized in Figure 8.

With the exception of the trunnion specimen (TR-1), all static specimens failed at loads higher than the design ultimate, and all fatigue specimens demonstrated better than the required life. In addition, there was no growth in the delamination area of any impacted specimen during fatigue testing. The majority of the bulkhead design was therefore considered to be sound. However, due to a premature failure in the trunnion test component, additional investigation of the trunnion area was required.

The initial trunnion failure was determined to be an interlaminar failure of the web which led to crippling of the upper cap. The failure was due to a combination of high interlaminar stresses because of the out of plane geometry and lower than anticipated interlaminar strengths for the toughened epoxy in the hot wet condition. The trunnion areas of the bulkhead were therefore redesigned. This redesign consisted of increasing the radius of curvature of the out of plane web and defining a new stacking sequence that improves the web's ability to shear loads into the caps. The web thickness remained unchanged, so the change in weight due to the redesign was negligible. Additional element tests to validate the redesigned trunnion are currently in progress.

### Bulkhead Fabrication

Following completion of the element test program, work began on the fabrication of a full scale bulkhead which utilized the refined design with the redesigned trunnion. Tooling that would provide the required bonding forces were designed using a variety of materials and tool types. The complete bulkhead bond tool is shown in Figure 9. The majority of this tooling utilized MCAIR proprietary conformal tooling. This is a type of inflatable tool that provides autoclave pressure in three directions. These tools could therefore be used to cocure horizontal and vertical stiffeners with webs. All of the tools were set on a carbon/epoxy slip plate that was supported by a steel base. The slip plate was fabricated with plies oriented in directions similar to those in the bulkhead, thereby minimizing thermal expansion problems.

The design of the bulkhead was such that it could be fabricated as an assembly of subcomponents. These subcomponents consisted of 1) the carrythrough beam, 2) trunnion webs, 3) stiffeners, 4) the forward web plies, and 5) the aft web plies. The carrythrough beam, trunnion webs, and stiffeners were all made up of unidirectional tape plies. The carrythrough beam and trunnion webs were similar, in that each consisted of two complementary ply packs that sandwiched the main web of the bulkhead. The plies for each pack were cut, collated, room temperature debulked, and held under vacuum until ready for final assembly.

The fore and aft web subcomponents were made of cloth plies that formed the main web of the bulkhead as well as the centermost plies of the carrythrough beam and trunnion webs. In addition, these plies were folded perpendicular to the plane of the bulkhead to form the innermost plies of the duct and moldline flanges. As with the other subcomponents, the web plies were room temperature debulked before final assembly.

Final assembly of the subcomponents followed a specific sequence. The aft plies of the carrythrough beam were located first, followed by the aft stiffeners, aft conformal tools, and aft plies of both trunnions. These subcomponents were then debulked to reduce assembly gaps and irregularities. All aft fillets were filled with adhesive, and the aft web plies were installed. Assembly of the forward half of the bulkhead followed the same sequence in reverse order. Finally, unidirectional plies in the duct and moldline flanges were assembled. These plies were debulked as they were collated to reduce wrinkles and bridging in the assembly. The final assembly was then vacuum bagged for cure in an autoclave.

After completion of the cure cycle, the assembly was removed from the autoclave, debagged, and the conformal tools were removed. The resulting untrimmed bulkhead is shown in Figure 10. Final machining of this part consists of trimming the duct and moldline flanges to width, machining the lug and upper duct flange contours into the carrythrough beam, and machining a variety of holes in the main web, lugs, and trunnions. Final assembly of the bulkhead then consists of installing landing gear trunnion hardware and mechanically attaching the upper duct and forward fuselage flange sections. The weight of the untrimmed part shown in Figure 10 was 213 lb., which compares well with the predicted weight for the complete assembled bulkhead. It is anticipated that the additional weight of the trunnion hardware and mechanically attached flange sections will be more than compensated for by the weight removed during final machining.

## RESULTS AND DISCUSSION

During the cure, there was a failure of the bladder in the conformal tool that forms the upper left moldline flange and a leak in the stem that connected the fore and aft conformal tools for the center pocket in the carrythrough beam. Because of these failures, the vacuum was removed and the autoclave pressure was reduced from 140 psi to 10 psi. The majority of the cure was therefore performed at this reduced



pressure. This loss of pressure resulted in a part with a high degree of porosity.

Porosity in the bulkhead was concentrated primarily in the upper portion of the carrythrough beam and between the trunnions in the lower portion of the main web. The porosity in the upper carrythrough beam was mainly due to the tool failures which left the tools in this critical area unpressurized. Porosity in the lower portion of the bulkhead was due to a debulking problem. The room temperature debulk used in the assembly of the subcomponents did not adequately compact the material for final assembly. This problem was compounded by the use of conformal tools that had been sized to nominal dimensions. As a result, the tools were difficult to install in the final assembly and did not seat properly.

In spite of these problems, many difficult details formed very well. In general, stiffeners were good quality laminates that were within dimensional tolerances throughout most of the bulkhead, and intersections between stiffeners cured well. The lug areas and lower portion of the thick carrythrough beam were good, even though the upper portion contained porosity. Center portions of the trunnion webs cured well, but there was porosity in the duct and moldline flanges that connected to them. These details are shown in Figure 11.

Because of the amount of porosity in the prototype composite bulkhead, it will not be used as a test article. Current work is directed toward the fabrication of a second bulkhead that can be used to validate the design through full scale testing. Fabrication of the first bulkhead exposed two major problems that are being solved before this second bulkhead is built. First, more reliable conformal tools will be developed. This is being accomplished by identifying more durable bladder materials and more compliant stem designs. These new bladders and stems will be evaluated by fabricating a full scale component that represents approximately one half of the lower portion of the bulkhead. Secondly, sub-assemblies must be more thoroughly debulked before final assembly. This will be accomplished through the use of hot rather than room temperature debulk cycles.

Following the successful fabrication of a second bulkhead, a full scale test program will be initiated. In this program the bulkhead will be tested in a free standing condition, but will be loaded to match peak strains predicted for the bulkhead installed in a fuselage. The test plan includes both static and fatigue loads. The bulkhead will be loaded statically to design ultimate for both wing and landing gear loads. Fatigue tests will only be conducted with wing loads, but will be performed both before and after the introduction of low velocity impact damage.

The bulkhead being developed in this program is one of the more complex one piece composite structures ever attempted. The geometry of this bulkhead, coupled with the use of a new material system and an advanced tooling concept, has provided a substantial technical challenge. While not perfect, the prototype component has met this challenge and represents a significant step forward in the development of composite bulkhead technology.

## REFERENCES

1. Fant, J. A., "Advanced Composite Technology Fuselage Program. Vol. 6 - F-5 Mid Fuselage Component - Design and Test," Air Force Materials Lab. Report No. AFML-TR-71-41, October, 1973.
2. Eves, J., "Advanced Composite Bulkhead Concepts for Wing-to-Fuselage Trunnion Joints," 22nd. National SAMPE Symposium, San Diego, CA, April, 1977.
3. Roberts, R. H., "Advanced Development of Conceptual Hardware for the Lightweight Fighter," Air Force Flight Dynamics Lab. Report No. AFFDL-TR-77-67, October, 1977.
4. Watson, J. C., "Composite Forward Fuselage Development. Vol. 1 - Design, Fabrication, and Test," McDonnell Aircraft Co. Report No. MDC-A6398, November, 1980.
5. Corvelli, N., "Advanced Composite Fuselage Study. Center Fuselage," Naval Air Development Center Report No. NADC-77059-30, November, 1981.
6. Borstell, H., "Manufacturing Technology for Complex Composite Fuselage Shapes - Phase I," Air Force Wright Aeronautical Labs Report No. AFWAL-TR-83-4035.
7. Pimm, J. H., Rogers, J. B., and Cooper, W. C., "Advanced Composite Fuselage Study - Aft Fuselage," Naval Air Development Center Report No. NADC-84084-60, April, 1984.
8. Eves, J., et al., "Composite Wing/Fuselage Program - Interim Technical Report Nos. 1 - 11," AFWAL Contract No. F33615-79-C-3203, November, 1979 through October, 1984.
9. Lonas, F. R., et al., "Manufacturing Technology for Complex Composite Fuselage Structures - Interim Report Nos. 1- 15," AFML Report Nos. IR-469-0(1) through IR-469-9(15), October, 1981 through April, 1985.
10. Behrens, R. S., Ellis, D. A., and Koch, L. C., "Development of Survivable, Crash Resistant, Integral Fuel Tank Composite Fuselage Structure," Naval Air Development Center Report No. NADC-81130-60, August, 1984.
11. Behrens, R. S., "Composite Fuselage Integral Fuel Tank Structure Test," Naval Air Development Center Report No. NADC-89096-60, December, 1987.

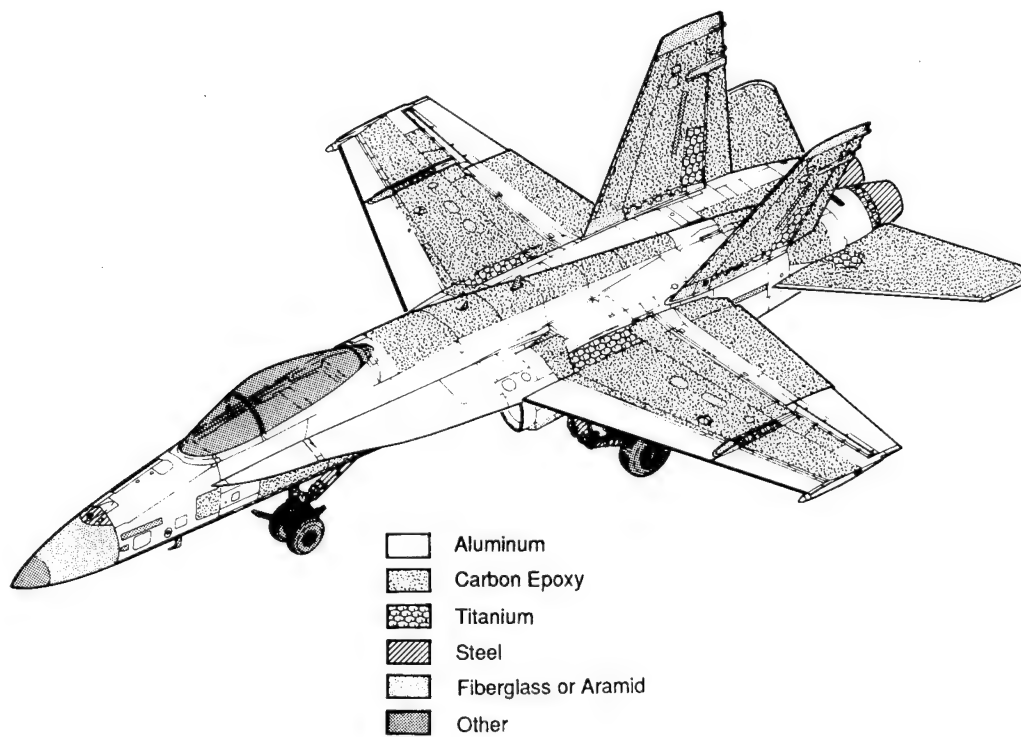


Figure 1. F-18 Material Usage

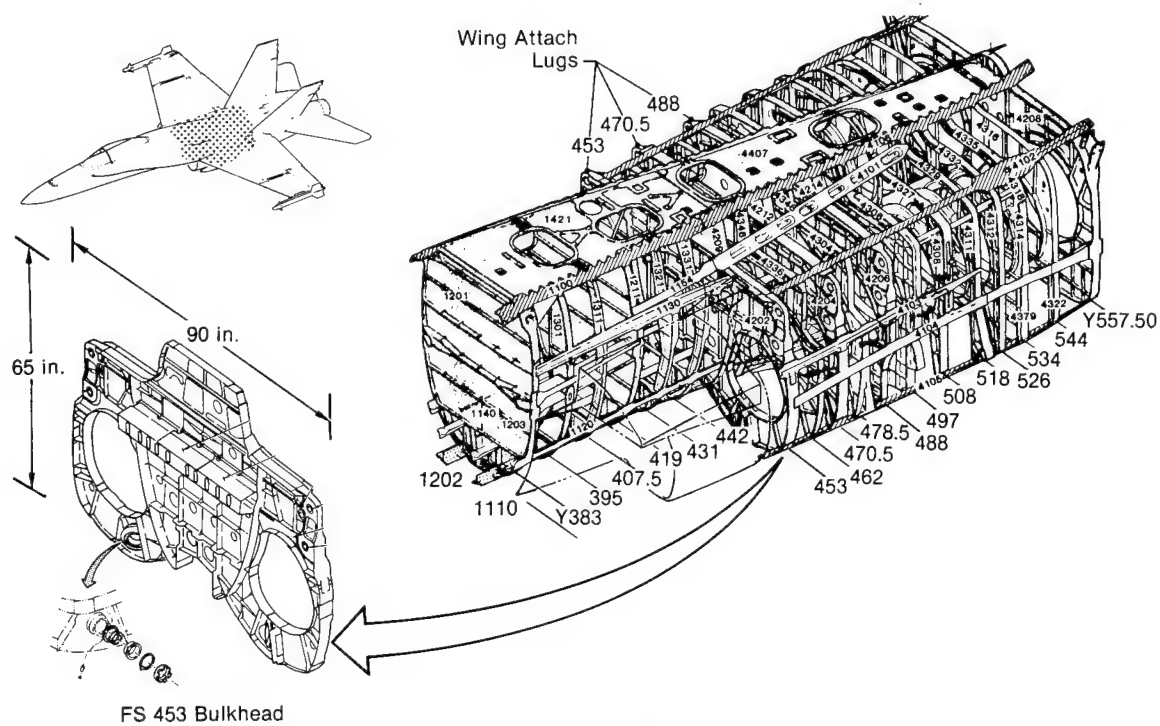
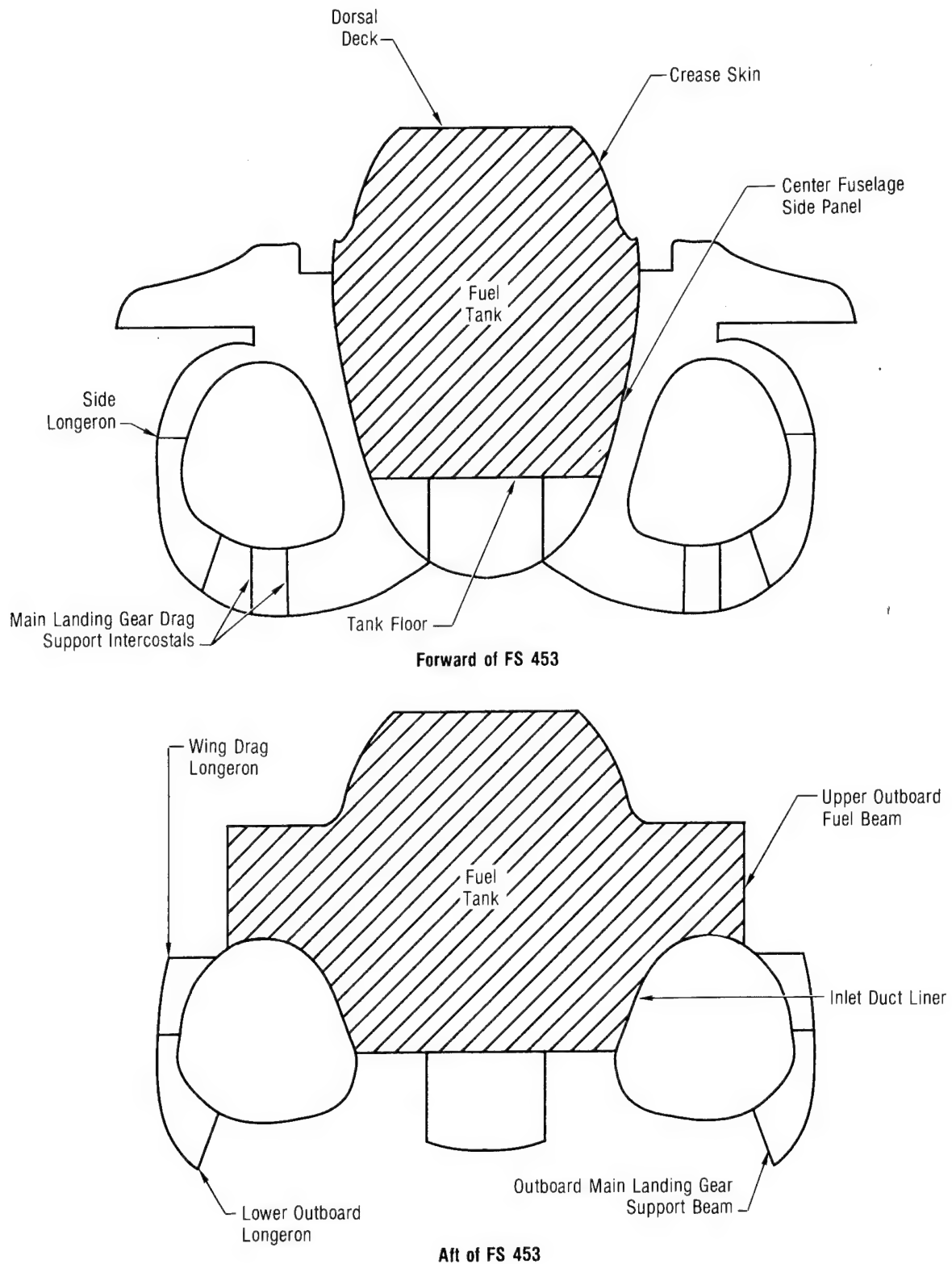
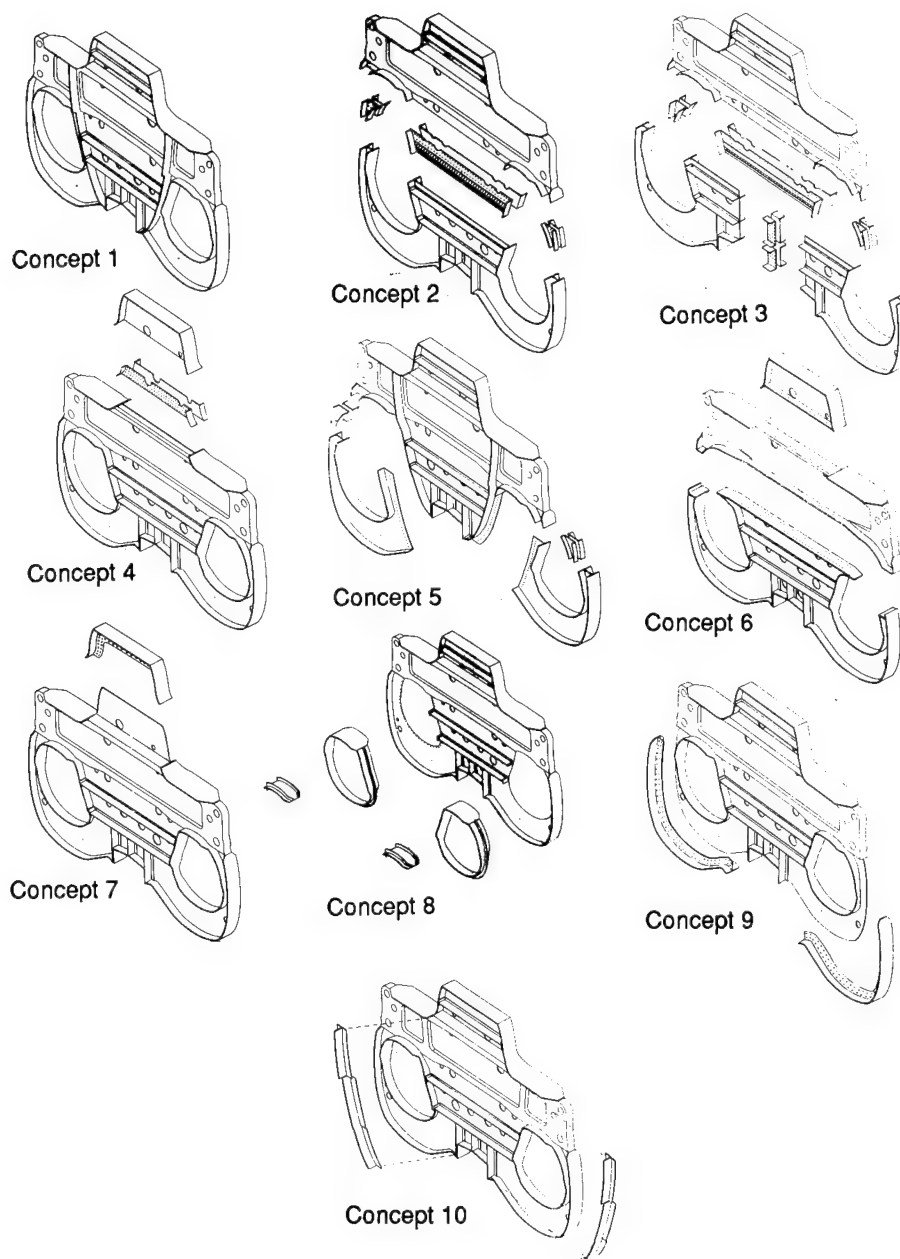


Figure 2. Baseline Airplane and Bulkhead



**Figure 3. F-18 Center Fuselage Shear Structure**

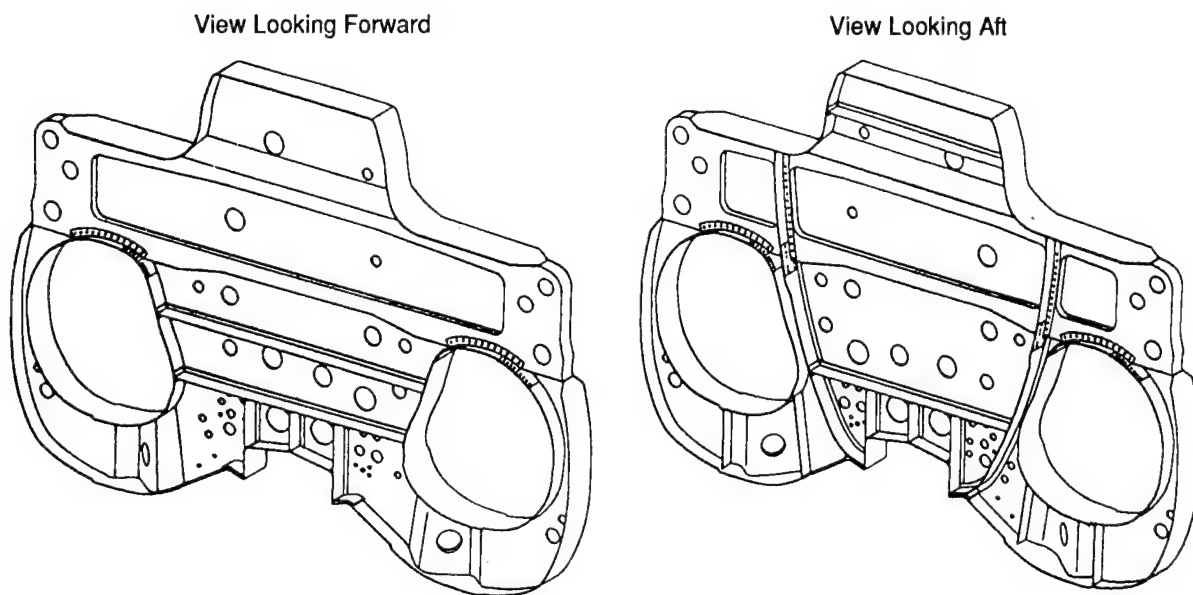


**Figure 4. Bulkhead Concepts**

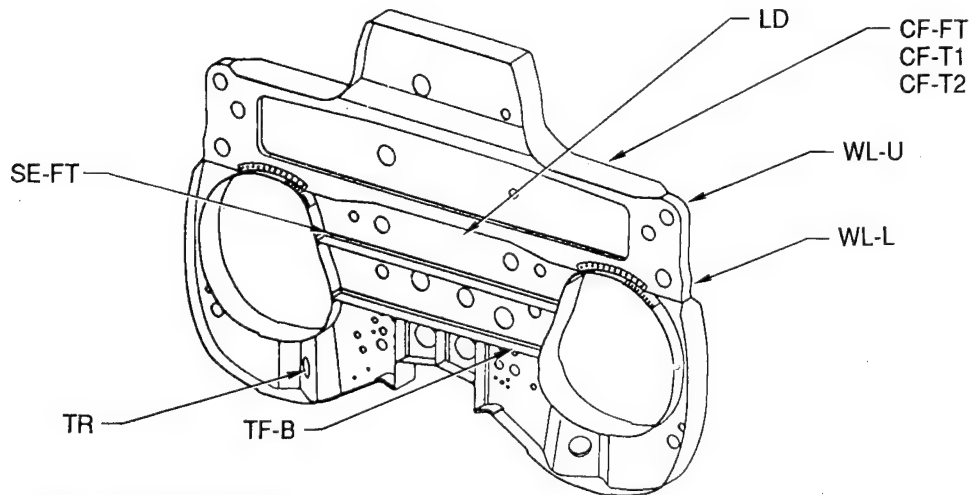
Concept	Relative Weight	Relative Cost	Relative Supportability
1	1.00	1.00	1.00
2	1.08	1.17	0.85
3	1.11	1.11	0.70
4	1.03	1.05	0.96
5	1.05	1.08	0.75
6	1.12	1.05	0.80
7	1.01	1.02	0.98
8	1.05	1.05	0.92
9	1.03	1.05	0.90
10	1.02	1.02	0.94

Note: Low value is goodness

**Figure 5. Trade Study Summary**



**Figure 6. Final Composite Bulkhead Design**



**View Looking Forward**

Specimen	Region Represented	Loading	Test Load (kips)	No. of Tests	Environment	Remarks
LD	Web Area Between Inlet Ducts	Spectrum Fatigue	14.0	2	RTD	Tested for 1 Lifetime at DLL Following LVID
TF-B	Tank Floor Support, Bending	Static Shear	0.8	1	ETW1	Bending of Tank Floor Support Flange After LVID
		Spectrum Fatigue	0.5	1	ETW2	
		Spectrum Fatigue	0.5	1	RTD	
SE-FT	Stiffener End Tie-In, Flatwise Tension	Static Tension	2.1	1	ETW1	After LVID
		Static Tension	2.1	1	RTD	
		Spectrum Fatigue	1.3	2	ETW2	
		Spectrum Fatigue	1.3	1	RTD	
		Spectrum Fatigue	1.3	1	RTD	
WL-U	Wing Attach Lug-Upper	Static	307	1	ETW1	Full Scale
WL-L	Wing Attach Lug-Lower	Static	308	1	ETW1	Full Scale
CF-FT	Carrythrough Beam Flange Flatwise Tension	Static	2.2	1	ETW1	
		Spectrum Fatigue	1.5	1	ETW2	
CF-T1	Carrythrough Beam Flange Inboard/Outboard Tension	Static	-12.0	1	ETW1	
		Spectrum Fatigue	-8.0	1	ETW2	
CF-T2	Carrythrough Beam Flange Fore/Aft Tension	Static	12.4	1	ETW1	
		Spectrum Fatigue	8.3	1	ETW2	
TR	Trunnion Attach Lug	Static	140 Inbd 160 Vert	1	ETW1	

**Notes:**

1. ETW1: 200°F, saturation after 75 days. Used for static tests.  
ETW2: to be determined, based on fuel temperature analysis. Used for fatigue tests.
2. All static tests will be to failure except specimen TR, which will be tested to ultimate load at the two most critical design conditions.
3. All fatigue tests will utilize the F-18 wing root spectrum.
4. All fatigue tests except those for LVID specimens will be tested to failure.
5. LVID specimens will be impacted, and then spectrum fatigue tested at DLL for one lifetime, while monitoring damage growth.

**Figure 7. Element Test Matrix**



Specimen ID	Test Requirement		Design Requirement		Test		Comments
	Type	Temperature	Load (lb)	Life (SFH)	Load (lb)	Life (SFH)	
LD-1	SF After LVID	RTD	4,700	6,000	4,700	6,000	No Growth in Delamination Area
LD-2	SF After LVID	RTD	5,577	6,000	5,577	6,000	No Growth in Delamination Area
LD-3	SF After LVID	RTD	6,455	6,000	6,455	6,000	No Growth in Delamination Area
TF-B-1	Static	200°F Wet	284	Static Ultimate	525	Static	First Load Drop – Failure at 1,286 lb
TF-B-2	SF	160°F Wet	217	12,000	217, 260, 290, 320, 370	12,000 at Each Load Level	No Failure
TF-B-3	SF After LVID	RTD	217	6,000	217	6,000	No Growth in Delamination Area
SE-FT-1	Static	RTD	2,550	Static Ultimate	5,387	Static	Separation of Stiffener End From Flange
SE-FT-2	Static	200°F Wet	2,100	Static Ultimate	4,948	Static	Separation of Stiffener End From Flange
SE-FT-3	SF	RTD	1,584	12,000	1,584, 3,700, 4,000, 4,200, 4,700, 5,000	12,000 SFH Each	Failure at 5,000 lb, 7,661 SFH
SE-FT-4	SF After LVID	RTD	1,584	6,000	1,584, 1,800, 1,985, 2,620	6,000 SFH Each Load	Failure at 2,620 lb, 897 SFH
SE-FT-5	SF	160°F Wet	1,266 (80% DLL)	12,000	1,266, 2,200, 2,500, 2,800	12,000 SFH Each Load Except Failure	Failure at 2,800 lb, 2,784 SFH
SE-FT-6	SF	160°F Wet	1,740 (110% DLL)	12,000	1,740, 2,200, 2,500, 2,650	12,000 SFH Each Load Except Failure	Failure at 2,650 lb, 10,300 SFH
WL-U	Static	200°F Wet	307,000	Static Ultimate	310,800 lb	Static	Shear Failure, No Bearing Failure
WL-L	Static	200°F Wet	308,000	Static Ultimate	400,000 lb	Static	Reached Test Machine Capability With No Failure
CF-FT-1	Static	200°F Wet	2,960	Static Ultimate	6,718	Static	Flange Peeled From Cap
CF-FT-2	SF	160°F Wet	1,960	12,000	1,960, 2,160	12,000, 1,535	Failure at 2,160 lb, 1,535 SFH. Start of Flange Peel
CF-T2-1	Static	200°F Wet	12,400	Static Ultimate	13,425	Static	Fasteners Failed. No Specimen Failure
CF-T2-2	SF	160°F Wet	9,360	12,000	9,360, 13,325	12,000 SFH Each Load Level	No Failure
TR-1	Static	200°F Wet	160,000 Vertical	Static Ultimate	126,000	Static	Interlaminar Shear Failure (Web Delamination). Crippling Failure of Upper Cap

SF denotes Spectrum Fatigue  
LVID denotes Low Velocity Impact Damage  
RTD denotes Room Temperature Dry  
SFH denotes Spectrum Flight Hours

**Figure 8. Summary of Element Test Results**

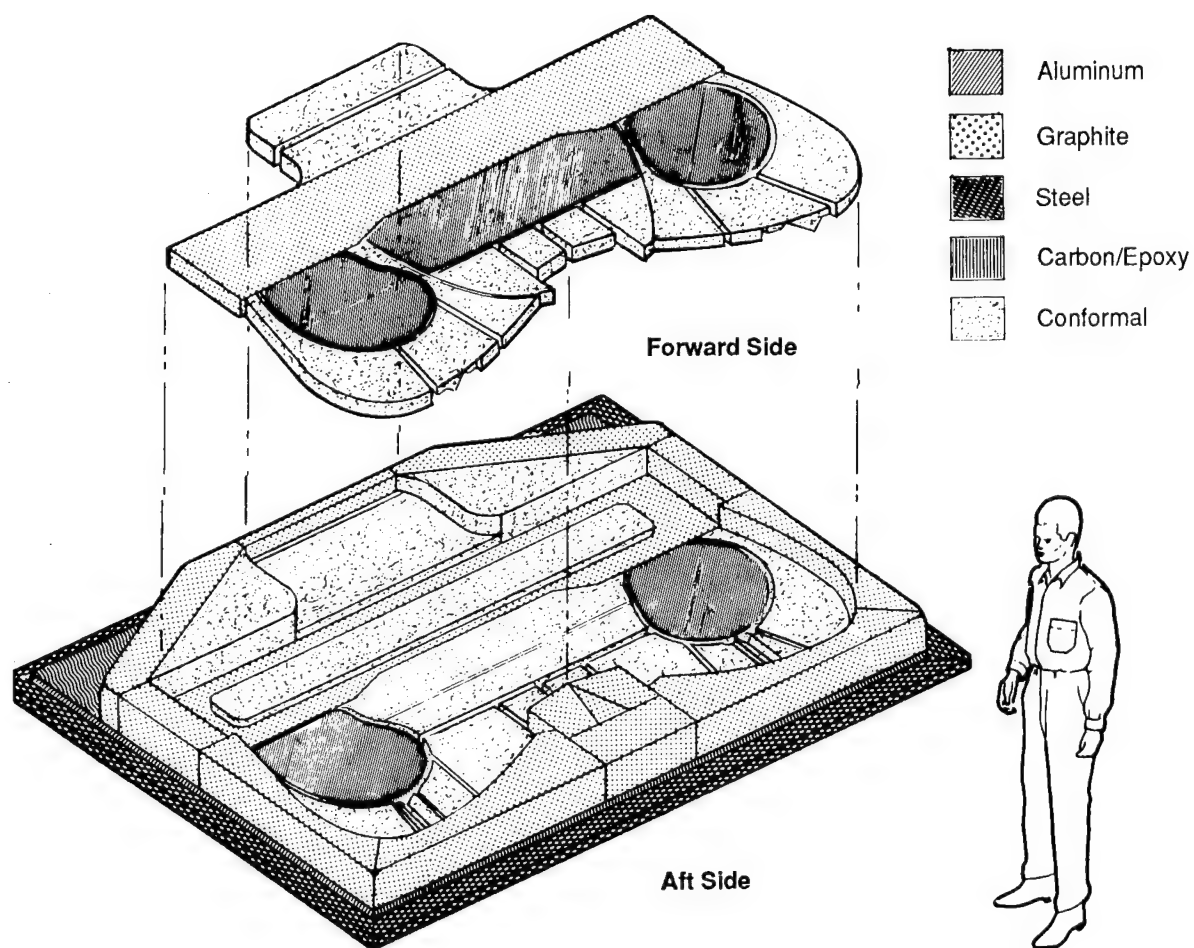
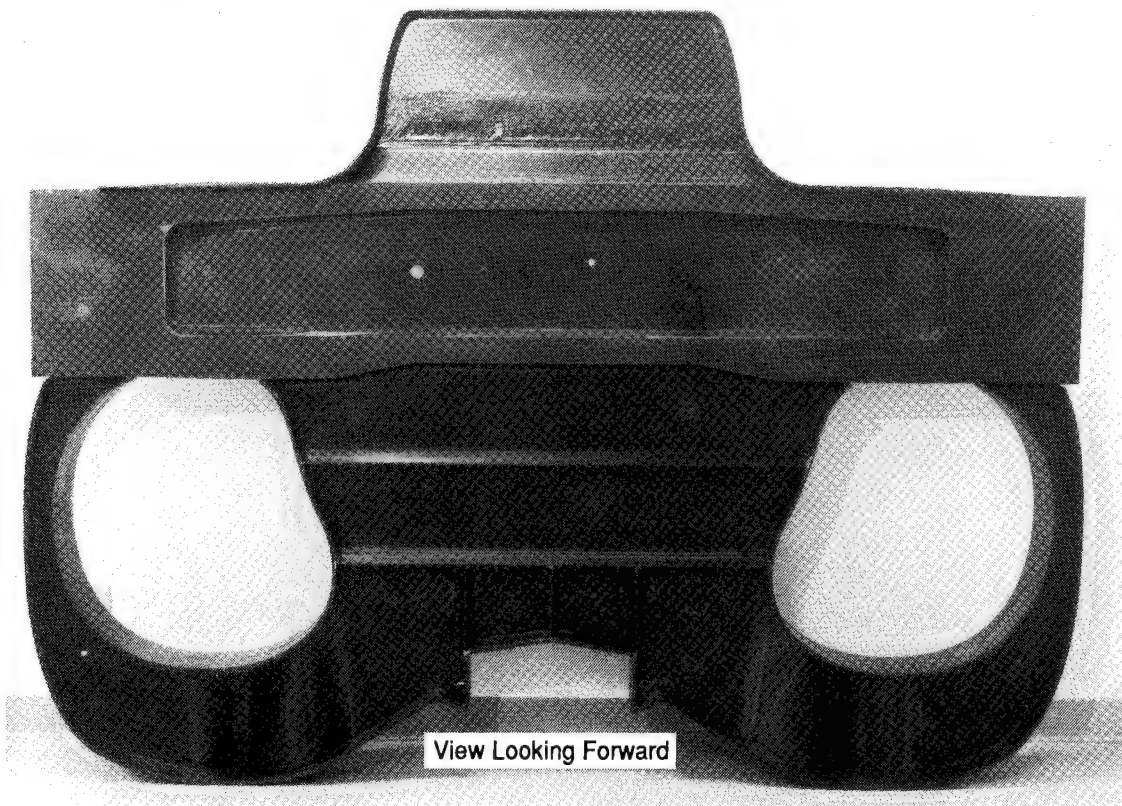
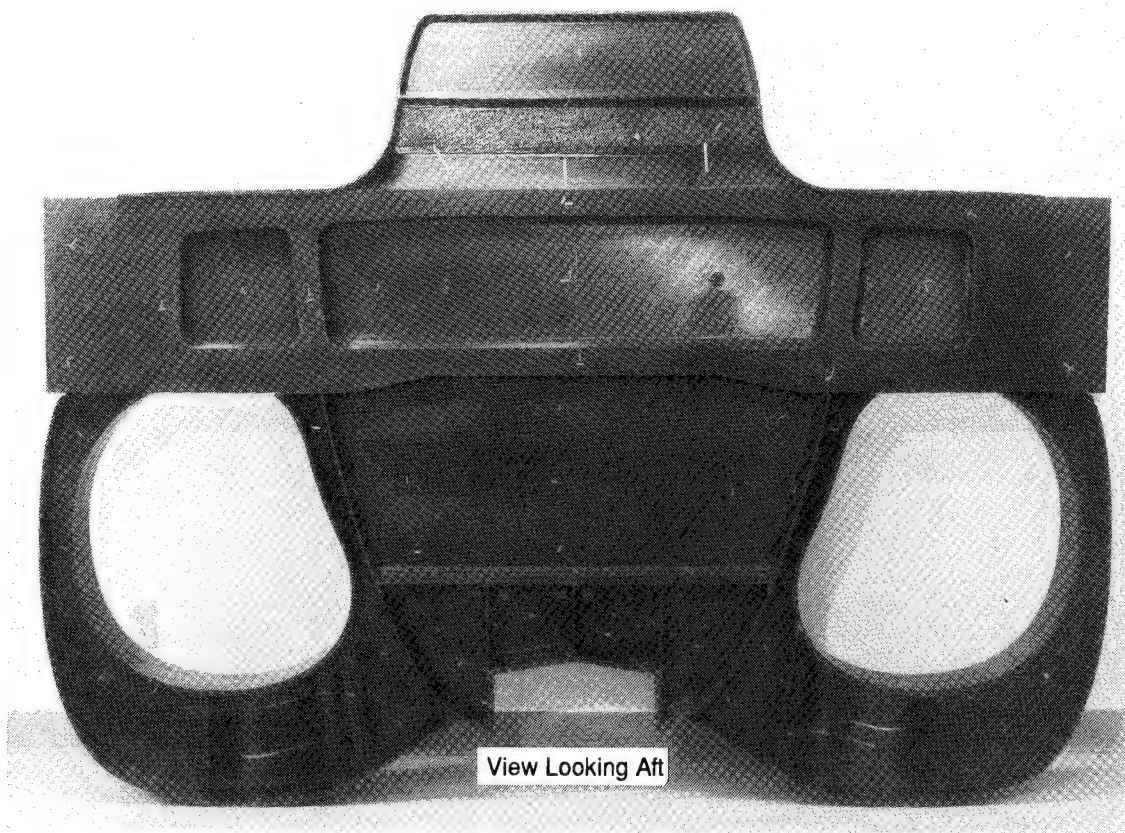
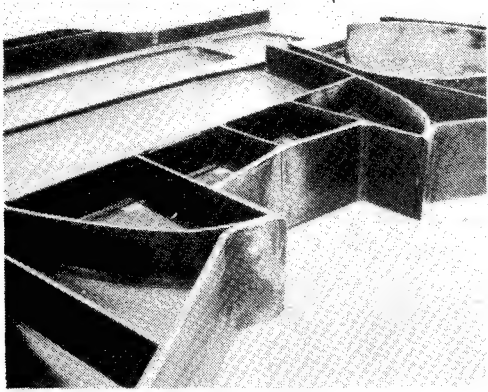


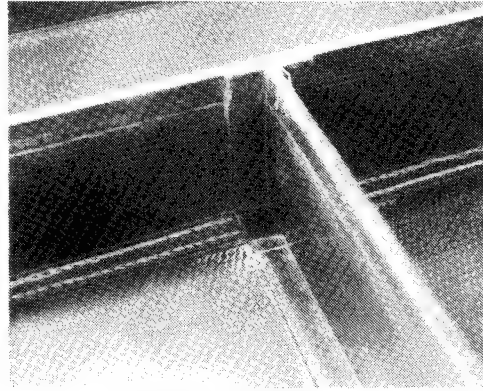
Figure 9. Composite Bulkhead Bond Tool



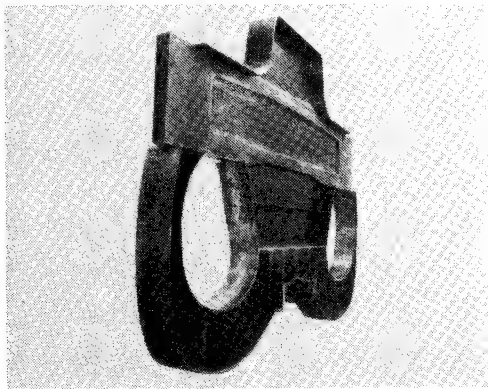
**Figure 10. Prototype Composite Bulkhead**



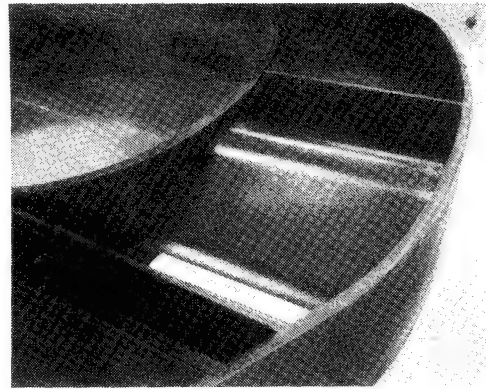
Deep Pockets



Complex Intersections



Thick Beam



Sinewave Webs

**Figure 11. Complex Design Details in the Composite Bulkhead**

# **Concepts in Design**

Chairman: Dave Oetting  
Wright Research and Development Center

## BRAIDED COMPOSITE BORE EVACUATOR CHAMBERS

### FOR TANK CANNONS

Philip C. Wheeler  
U.S. Army Armament Research, Development, and Engineering Center  
Close Combat Armaments Center  
Benet Laboratories  
Watervliet, NY

### SUMMARY

Typically, continuous filament composite components are fabricated using a filament winding technique. In this operation, fibers are introduced to a rotating mandrel while a guide holding the material traverses back and forth to place the material in a helical pattern over the surface of the mandrel. This procedure is continued until complete coverage is obtained.

An alternative method for fabricating continuous filament composite components is braiding. In the braiding operation a mandrel is traversed through the center of the braider while 144 strands of material traverse around a carrier ring. As the fibers are applied to a mandrel surface, 72 carriers holding the fibers travel clockwise, while another 72 carriers travel counterclockwise to interlock fibers. An additional 72 carriers located on the back of the braider introduce longitudinal fibers to the composite giving the composite lateral strength.

The goal of using the braider is to reduce production time by simultaneously applying 144 strands of material onto a mandrel as opposed to the four-strand wrapping most filament winding techniques offer.

Benefits to braiding include the ability to (1) introduce longitudinal fibers to the composite structure; (2) fabricate non-symmetric components without using complex functions to produce full coverage; and (3) produce a component with a higher degree of damage tolerance due to the interlocking of fibers.

This paper investigates the fabrication of bore evacuator chambers for a tank cannon system by utilizing a 144 carrier braiding machine, an industrial robot, and a resin applicator system.

### INTRODUCTION

An alternative method for fabricating continuous filament composite components is the 144 carrier braiding machine (Figure 1). The advantage of using the braider is reduced production time by simultaneously applying 144 strands of material onto a mandrel as opposed to

the four-strand wrapping the filament winding technique offers.

Other benefits include the ability to (1) introduce longitudinal fibers to the composite while braiding; (2) fabricate non-symmetric components without using complex winding functions to produce full coverage; and (3) produce a component which displays a higher degree of damage tolerance and good resistance to crack propagation.

### BRAIDING MACHINE

The braiding machine contains 216 carriers: 144 carriers on the front face apply helical wraps (72 of which travel clockwise about the face of the braider while 72 simultaneously travel counterclockwise to interlock a pattern), and an additional 72 carriers placed at the back of the braider introduce longitudinal fibers. Each carrier holds a spool of material 5 3/4 inches long by 1 1/2 inches wide containing approximately 0.48 pound of material. Carriers on the carrier ring move in an over- and under-type movement to interlock fibers as a braided sock is applied to a mandrel as shown in Figure 1. The braiding machine is 9 feet 5 inches high by 9 feet 3 inches wide. The carrier ring containing the carriers is 6 feet in diameter.

A smaller ring 2 feet in diameter, called the braid ring, sits 2 feet forward and coaxial with the carrier ring. Yarn travels over the braid ring and is braided into a sock at the center. This ring serves as a guide and gives tension to the fibers as they are applied to the mandrel. Each carrier is spring-loaded to give steady tension to the fibers. These springs are removable so that different tensioning springs can be added. Typical spring tensions range from 2 to 10 ounces.

A reversing ring, also located coaxial to the braider, sits slightly forward of the braid ring. This ring allows braiding to take place at the proper location when reversing directions. The reversing ring prevents fibers from lifting off the braid ring and braiding at a more forward distance from the braider. Both the braid ring and the reversing ring act together to retain and support fibers for proper placement onto the mandrel.

The braid ring and reversing ring diameter should be no more than a few inches larger than the finished diameter of the fabricated component. Keeping the rings close to the mandrel maintains the location of the braiding close to the braider and also allows steep angles to be braided over the mandrel at a distance closer to the braider.

One must be careful when reversing the mandrel while braiding. Since the carriers are able to take up only a few inches of material, by pulling the fibers a large distance between the braid ring and the component upon reversing, there is excess material that the carriers are unable to retrieve. Loose fibers hang between the carriers and the mandrel. If this occurs while the braiding machine is running,



the loose fibers may tangle with carriers traveling in opposite directions.

Insulated springs are located every 30 degrees around the circumference of the carrier ring. These springs are electrically connected to a relay which turns the braiding machine off if a yarn or roving breaks (roving refers to a group of untwisted longitudinal fibers opposed to a group of twisted fibers as found in yarn). Each carrier is grounded to the braider. Should a yarn break, the lower guide of the carrier (the lower guide changes direction and gives tension to the fibers) is pushed down, thus making contact with one of these springs as the carrier crosses it. The longitudinal carriers also have a mechanism which shuts the braider off if a yarn breaks. The carrier guide comes in contact with an electrically charged spring which is connected in series with all 72 longitudinal carriers on the back ring. Upon grounding any of these springs, the braider turns off. A switch on the back left-hand side of the braider turns this capability on or off.

The braiding capacity (diameter of component which is to be braided) depends largely on the diameter of the braid ring. It must be kept in mind that the larger the diameter to be braided, the steeper the angle of the braid must be to give complete coverage. Another factor which affects coverage is the fiber bandwidth.

The smallest diameter of a structure which can be braided is limited and is determined by the number of carriers. A fully loaded braider tightly knits a sock approximately 1 1/2 inches in diameter. This is the smallest size possible. Smaller components can be fabricated by simply removing specific spools from the carrier ring. For example, removing every other set of spools from the carrier ring gives the equivalent of a 72-carrier braiding machine. Using this setup, a smaller diameter sock can now be braided.

Located on the control console is a dashpot which operates the speed of the braider. This dashpot is calibrated from 0 to 100, indicating percentage of power output to the braider. A dial setting less than 10 percent does not give the braider enough power to move the carriers. A dial setting of 10 percent is required just to get the carriers moving. Dial settings greater than 10 percent will increasingly speed up the carriers. A dial setting of 100 percent gives the carriers a maximum rotational speed around the carrier ring of 3.258 revolutions per minute (R.P.M.).

## MATERIALS

A material commonly used in braiding is the 6-ended S2-glass yarn (see Figures 2 and 3). Each end consists of three twisted strands, each strand containing 204 filaments roughly 0.00038 inch in diameter. A variety of packages can be ordered containing from 1 to as many as 20 ends. Approximately 1200 feet of yarn is wound on each.

Other materials that can be incorporated in the braiding system are S2-glass fiber, graphite fiber, and Aramid fiber. Steel wire can also be supplied on spools.

Braiding with graphite can be difficult. When braiding with graphite roving, individual fiber strands tend to break loose and wrap around various parts of the carriers. Broken fibers can also become air-bound and hazardous if inhaled. These particles may short out electrical circuits in computers.

Pre-impregnated roving fibers (already coated with the proper volume fraction of B-staged resin) can be supplied on packages for the braider. B-staged resin is a term which refers to the partial cure of a resin. A resin at this stage is no longer in a liquid state and does not flow off the fibers. When prepreg material is heated, the resin turns back into a liquid and flows through the fibers. The resin fully cures upon subsequent heating. Manufacturers of prepreg material supply curing curves indicating time, temperatures, and autoclave pressures for curing their material. An autoclave is a vessel which places a composite specimen under high pressures and regulates its temperature and pressures during the cure cycle. Typical autoclave pressures run around 100 psi. Autoclave parameters are important in the cure of both prepreg and wet-braided components. The objective of autoclaving is to compact the fibers to achieve an optimum fiber-volume fraction of 60 percent. Reduction of void content is also an added advantage.

There is a vast array of resins which can be used. Each resin must be studied for its application. Viscosity, physical properties of the cured resin, and time and temperature for cure are areas of interest when deciding on types of resin.

Resins come in two groups: thermoplastics and thermosets. The components made from thermoset resins retain their form after curing and do not change shape even when heated up to their curing temperature. At temperatures higher than the curing temperature, the resin begins to degrade and the modulus of elasticity drops rapidly. Thermoplastics retain their form at temperatures lower than their cure temperature but can be reshaped at higher temperatures. The application of each resin depends on the properties the designer is looking for in a specific case.

When braiding with some of these materials, it is important to be aware of breathing hazards. For example, with graphite, fibers break and fray while braiding and are dispersed into the air. Proper ventilation should encompass the braiding machine to draw these air-bound fibers out of the working area and through a filtering system. Some resins may also be hazardous. Resins give off volatiles which can make a person ill if inhaled for a long period of time. Adequate ventilation should also be placed over the mandrel while braiding. Information pertaining to the health hazards of various resins can be acquired through the manufacturer of the resin used.

## ROBOT

To braid over a mandrel at some given angle of wrap, two variables must be controlled: (1) the braider speed which is controlled by the dashpot setting, and (2) the mandrel traverse speed (the rate at which the mandrel is traversed through the braid ring). By setting the dashpot of the braider to give the carriers a fixed rotational speed around the carrier ring, the mandrel feed rate can be adjusted to give various angles of wrap. For example, a dashpot setting of 58 percent corresponding to 1.74 R.P.M. and a mandrel traverse speed of 10.9 inches per minute gives a 45-degree angle of wrap over a 2-inch diameter mandrel.

To control the mandrel locations and feed rates, a four-axis robot was purchased (see Figures 4 and 5). All motions are controlled by the point-to-point type controller through one of two methods: (1) typing information in directly using a key pad or (2) by entering data using a "teach pendent." The teach pendent allows the operator to physically move the arm to a desired location. By depressing the enter button, information giving the location of the arm is stored into the controller's memory. The sequence is automatically advanced to accept any new coordinates.

The braiding machine is hard-wired to the robot's controller. The controller can be programmed to turn the braider on and off automatically while the robot is operating. This allows the operator to braid down the length of a mandrel then stop the braider at some given point while allowing the robot to reposition the mandrel at some new position before continuing to braid.

## RESIN APPLICATOR

Components are easily "wet"-braided using a resin applicator (see Figures 6 and 7). The resin applicator impregnates fibers as they sweep across a cover plate before being applied to the mandrel. Roughly 10,000 laser-drilled holes through the cover plate serve as ports to allow resin to flow from a reservoir located behind the cover plate to its face in a uniform manner.

Figure 7 shows stainless steel resin and hardener tanks. These tanks have a capacity of 6 and 3 gallons, respectively. Resin is usually contained in the 6-gallon tank since larger amounts of resin than catalyst are generally used when mixing the two components. These tanks can be pressurized to a maximum pressure of 80 psi to aid in the transfer of resin and catalyst from the holding tanks to the resin applicator pumps which, in turn, transfer the resin and catalyst to the resin applicator ring. Typical operating pressures for these tanks range between 10 and 20 psi. Pressures lower than 10 psi may not be sufficient to push thicker resins to the pump inlet. Higher pressures may damage components of the resin applicator. These resin tanks can be heated to 100°C to lower the viscosity of the resin before being pumped. This enables the operator to braid with a more viscous resin system.

A tube is inserted through a channel in the back of the resin applicator. When hot water runs through this tube, it heats up and conducts heat to the resin located in the reservoir, thus lowering the resin's viscosity. Heating elements can also be inserted through this channel to allow heating through an electrical source. Heating of the resin, however, shortens its gel time.

Resin levels can be observed in the applicator as the resin fills the reservoir and flows through each of the small holes in the resin applicator cover plate. Mixed resin begins to form beads at the bottom of the cover plate and continues up both sides of the applicator as the resin fills the reservoir ring. When the reservoir is completely filled, resin flows out of all the small holes in the resin applicator cover plate.

Void contents between 1.7 and 3.7 percent in structures fabricated using the resin applicator have been discovered. In addition, fiber-volume fractions of parts fabricated using the resin applicator ranged from 56.8 to 63.9 percent.

#### BRAIDING BORE EVACUATORS

The bore evacuator chambers were fabricated using the 144 carrier braiding machine. Figures 8 and 9 show one of the bore evacuator chambers. A collapsible mandrel was used for its fabrication. This mandrel has rounded edges which allow smooth braiding over angled surfaces. A mandrel with sharp edges may lead to slippage and incomplete coverage.

Longitudinal fibers, or warp fibers as they are sometimes called, were introduced into the braided structure. This not only added lateral strength to the composite, but also helped to interlock fibers and prevent fibers from spreading.

A recommended fiber for this application is the S2-glass yarn with 12 ends or higher. A 12-ended yarn has a larger bandwidth than a 6-ended yarn; a 12-ended yarn allows braid angles closer to 45 degrees and still gives complete coverage of the mandrel. Yarns with smaller bandwidths require wrap angles closer to 90 degrees for complete coverage. With modifications to the carrier mechanism, S-glass roving can be used. S-glass roving has a significantly larger bandwidth than the yarns and aids in mandrel coverage.

A braided layer was applied to the mandrel, starting at the small diameter end and continuing over the sloped region to the larger diameter. Braiding continued over the large diameter, down the opposite slope, and finished at the collar on the small diameter closest to the robot. The mandrel was jogged back and forth by a small amount while the braider continued to run. Jogging the mandrel allowed a braided layer to slowly braid up to the collar. As the braid approached the collar, its angle of wrap approached 90 degrees. Once the braid reached the collar, the mandrel reversed and a second layer of braid was applied in the opposite direction.

The mandrel should be rotated a couple of degrees upon reversal. Indexing the mandrel allows the longitudinal fibers to lay down next to the longitudinal fibers from the previous layer of braid. This distributes longitudinal fibers around the circumference of the mandrel instead of stacking them one on top of the other.

As the mandrel reverses direction during braiding, the braid folds over onto itself. At this point, the tension given to the fibers by the carriers may cause the braid to slide back towards the braid ring. The hoop wrap applied at the collar tends to clamp down onto the mandrel and prevent slippage.

Since the final thickness of the smaller diameter of the bore evacuator is thicker than the larger diameter, more material has to be applied to the smaller diameter region. This is done by reversing the direction of the mandrel before braiding over the sloped region. A third layer is now braided over the small diameter. As the braid approaches the collar, the mandrel is jogged back and forth again until the braid reaches the collar. The mandrel is reversed once again and braiding is continued over the small diameter and up the sloped region to the large diameter. The small diameter now has four layers of braid and the large diameter has two. The braid continues over the large diameter and down the slope to the small diameter end closest to the braider. The doubling of layers is now performed on this smaller diameter end. This method of doubling is done until the proper thickness is obtained.

While braiding up the slope of the mandrel, fibers tend to slip and spread over the surface leaving regions vacant of fibers. Filament-wound inserts were laid down between braided layers to fill in these voids. A possible way to control fiber spreading is a wrist rotation to the robot arm so the mandrel can be manipulated in the X-Z plane. Cantering the mandrel such that the sloped surface is as close as possible to the horizontal plane enables the braider to braid over this surface more easily. The braider functions very well over horizontal surfaces.

When braiding was completed the braided bore evacuator was removed from the robot arm and placed in a rotisserie where heat lamps applied heat. Aluminum foil was placed around the lamps and the composite to reflect heat and maintain high temperatures. The bore evacuator was rotated until the resin hardened. Finally, the bore evacuator was placed into an oven to finish curing. Since this mandrel had a large volume of material, it required additional heating to bring the mandrel and inner layers of the composite up to proper curing temperatures.

When braiding up to the collar on the mandrel and then reversing direction, the braid forms small grooves along the face of the collar and O-ring sealing surface. These grooves are formed by the braid folding over onto itself (see Figure 10). During curing, the resin heats up and becomes less viscous. Resin may then drain out from these grooves. When the composite cures, the grooves remain as part of the final structure. One method of eliminating this would be to

modify the mandrel by removing the collar (see Figure 11). The composite material is now braided over the O-ring sealing surface at a distance approximately 3 inches from this point. When the bore evacuator is finished and cured, this excess length is faced off to its proper dimension.

## CONCLUSION AND RECOMMENDATIONS

A disadvantage of braiding compared to filament winding is the time required to load all 144 half-pound cops of glass yarn onto the braiding carriers, as opposed to the four 10-pound creels the filament winding technique requires. This installation of material onto the braider requires one person roughly 2 hours to accomplish, whereas the filament winding process takes just several minutes. A second disadvantage is the frequent loading of the braider. Only two or three bore evacuators can be braided per loading depending on the wall thickness of the bore evacuator. The lag time between actual construction of these components adds up to a substantial amount over the course of manufacturing many bore evacuator chambers.

The advantages of braiding over the filament winding technique are time savings in actual fabrication time; increased damage tolerance of the final component attributed to the interlocking of fibers during braiding; introduction of longitudinal reinforcements while braiding; and crack arrest characteristics of braided laminates.

Many components made in private industry utilize the damage tolerance characteristics that braided composite structures offer. Drive shafts for land vehicles, airplanes, and helicopters can be made from braided structures with this damage tolerance nature in mind. One area of concern for drive shafts in military helicopter applications is the possibility of a projectile or shrapnel penetrating the shaft and causing the torsional forces to twist or unravel the shaft in much the same way a paper towel roll unravels when twisted. In experiments, shafts under load with high torsional forces have been pierced with small arms projectiles without degradation in performance.

The disadvantage of braiding is the lag time between braiding a pair of bore evacuators. Due to the small carrier design and close tolerance between moving carriers, it is impossible to add larger spools to the existing machine. Presently, 0.5-pound spools make it possible to braid two or three bore evacuators before a complete reloading of the braiding machine is required. As a result, the operation must be shut down to allow reloading before the next set of bore evacuators can be fabricated.

One way to deal with the lag time problem between braiding operations is to operate two braiding machines. While one braider is operating to fabricate components, the other braider could be reloaded and readied for the next braiding operation.

Another recommendation to the braiding operation is for the robot to have wrist rotation in the vertical plane (X-Z plane). Using this rotation, the bore evacuator can be positioned such that the angled surface of the mandrel is as close as possible to the horizontal plane. The braider, a machine which braids very well over surfaces perpendicular to its braid ring, is apt to braid over these angled surfaces with little or no slippage.

Modifications to the carrier design should be conducted to allow pre-impregnated material and dry roving to flow through the carrier mechanism with little trouble.



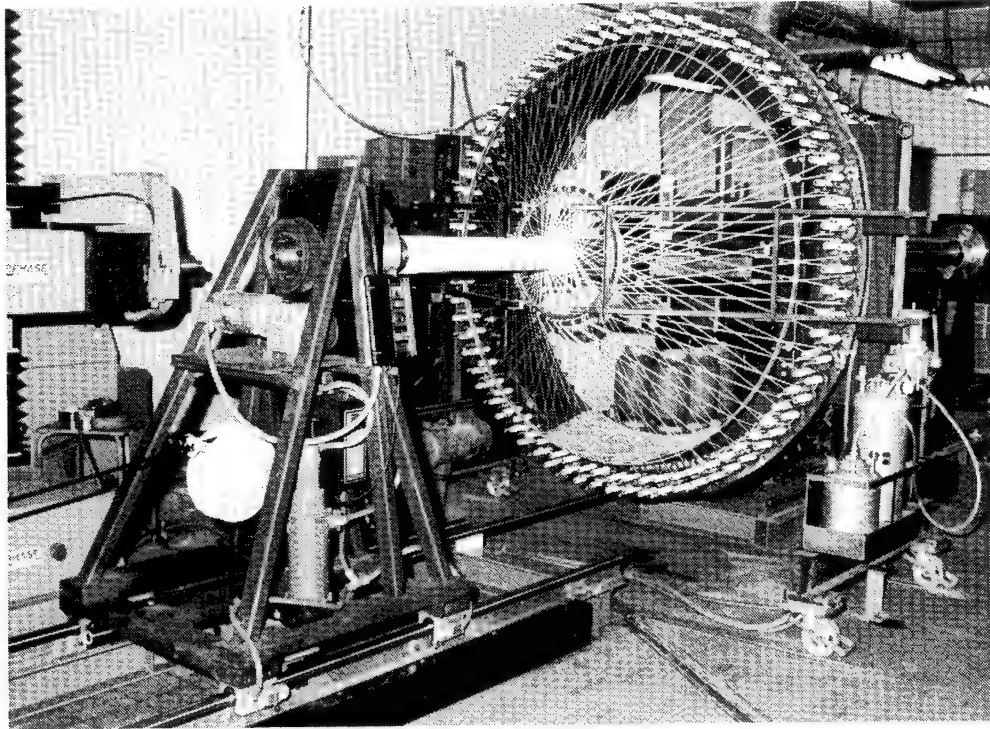


Figure 1. 144 carrier braiding machine braiding over a mandrel.

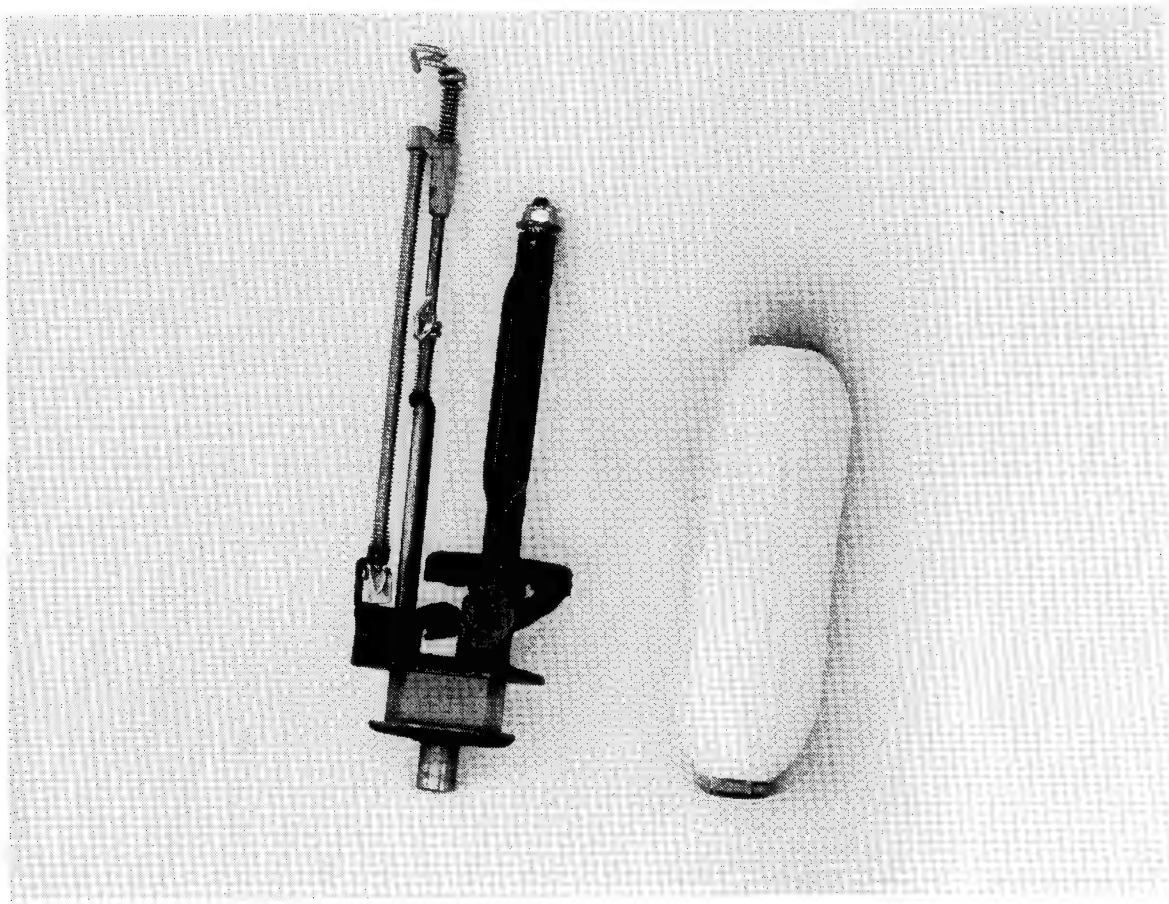


Figure 2. S2-glass yarn on a spool.

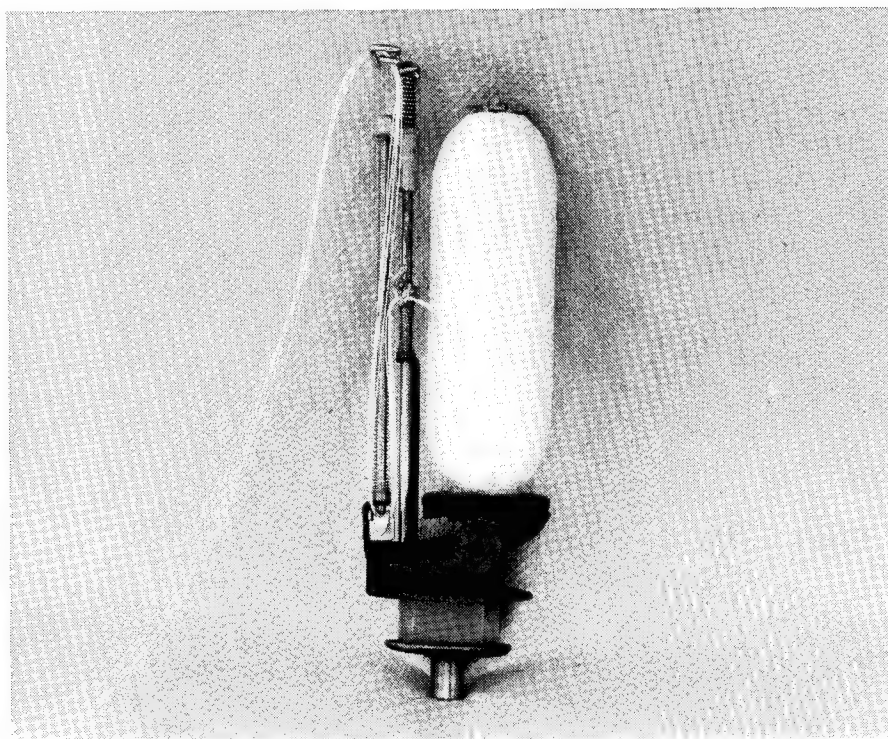


Figure 3. S2-glass yarn on a spool and loaded on a braider carrier.

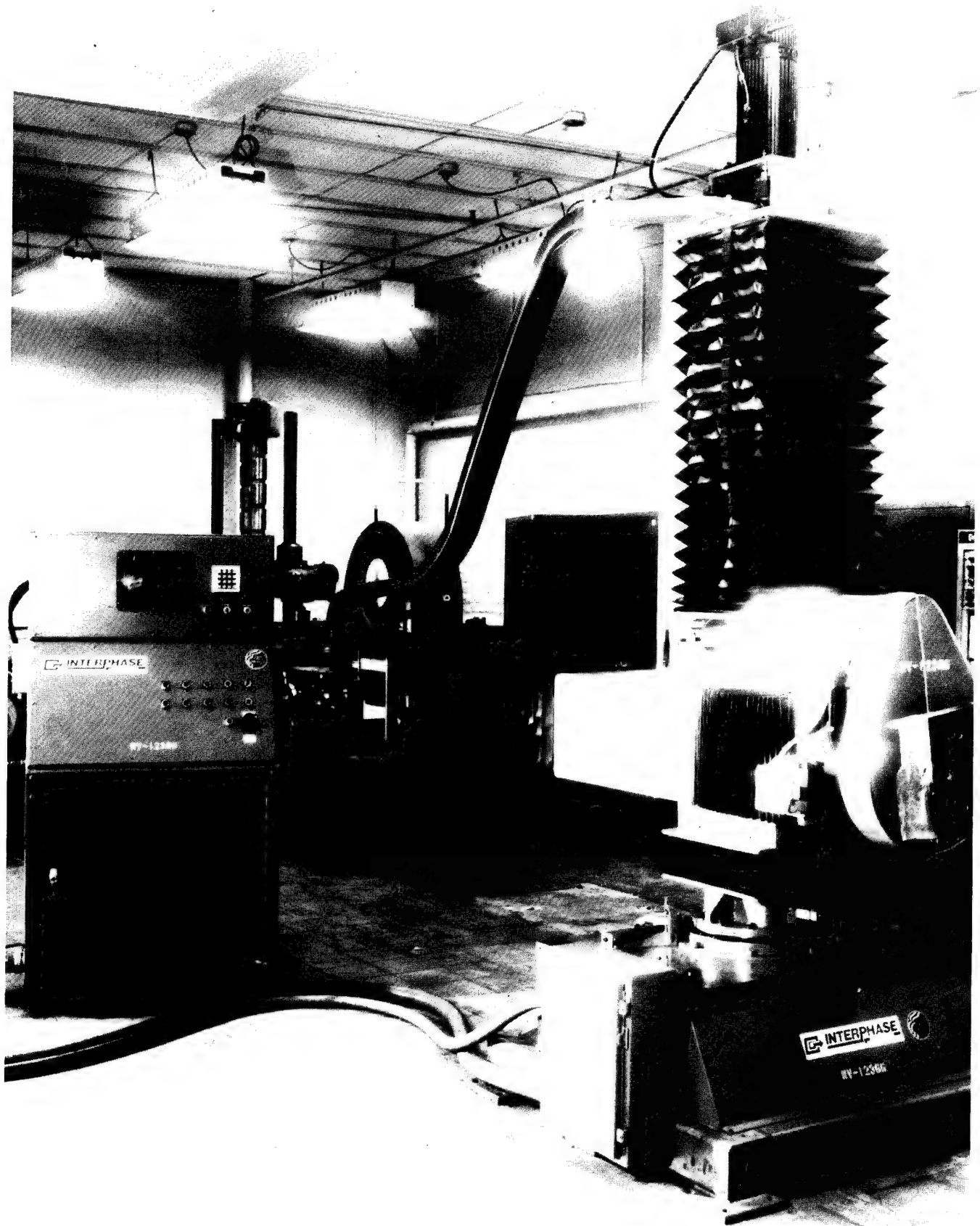


Figure 4. Industrial robot and controller.

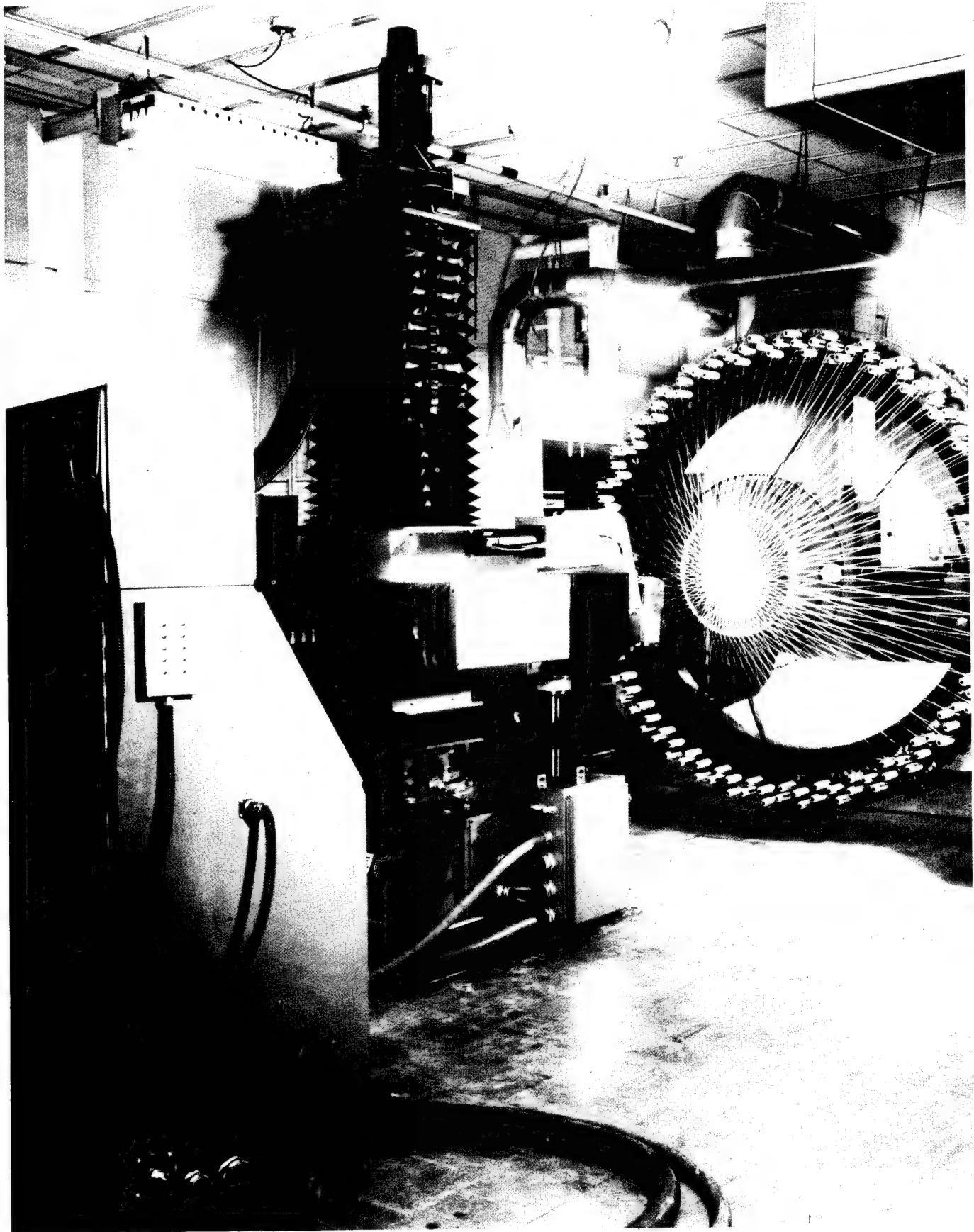


Figure 5. Industrial robot, controller, and braiding machine.



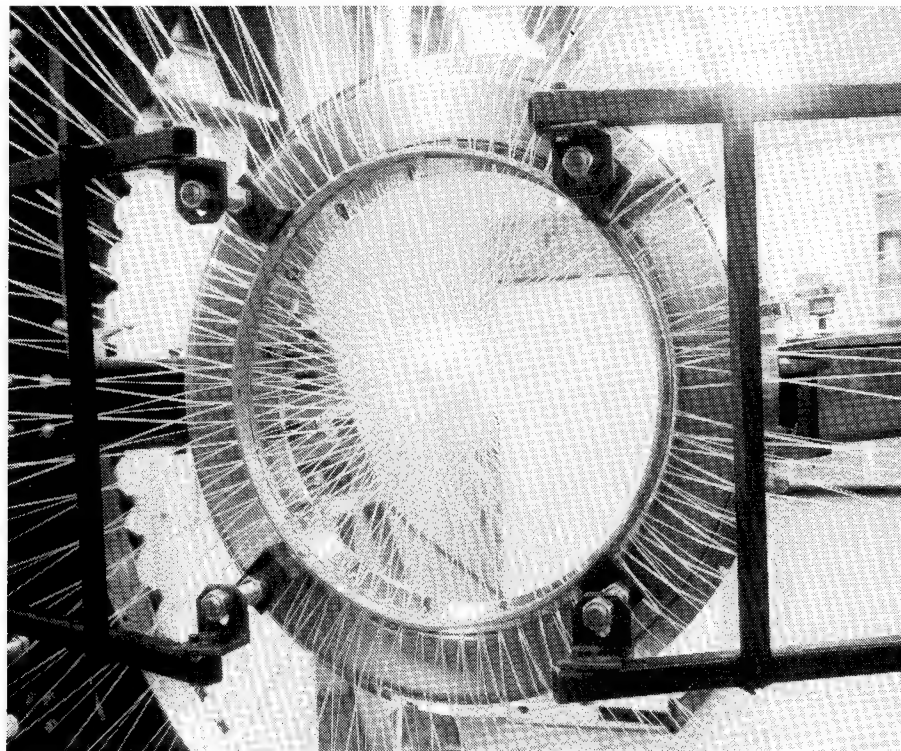


Figure 6. Resin applicator.

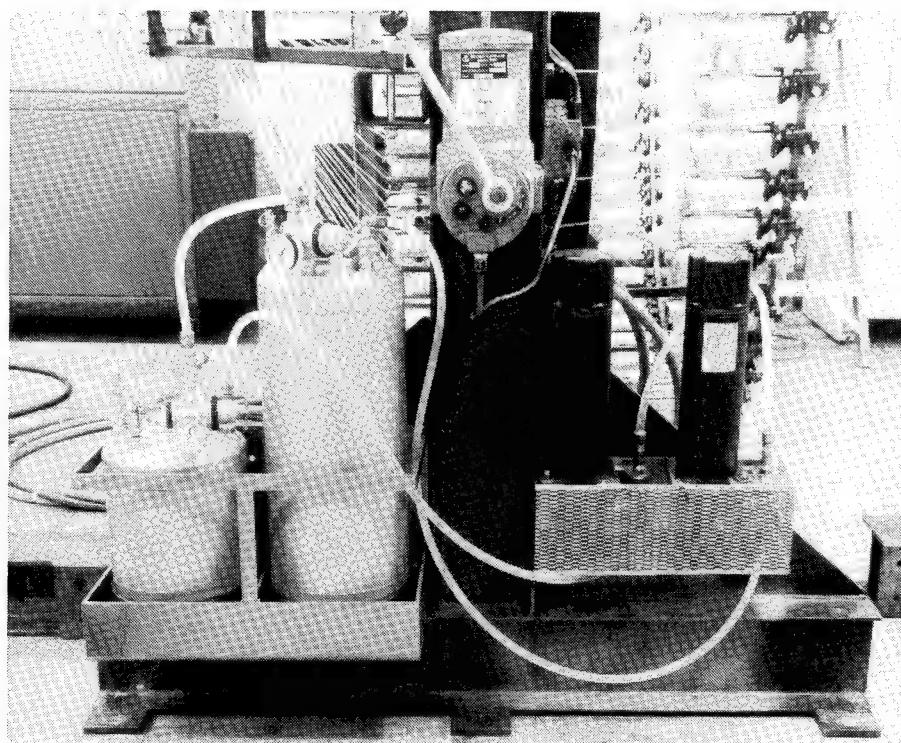


Figure 7. Storage tanks for the resin applicator.

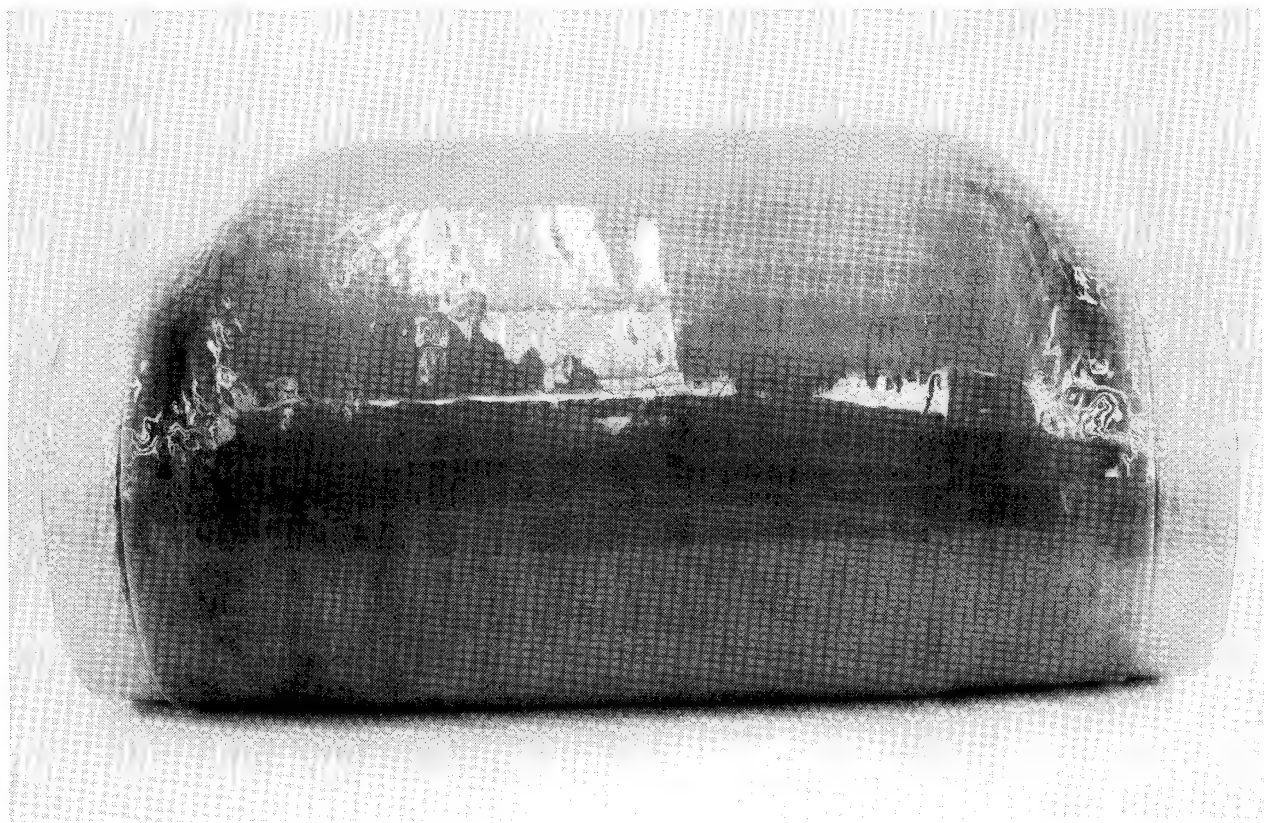


Figure 8. Bore evacuator chamber.

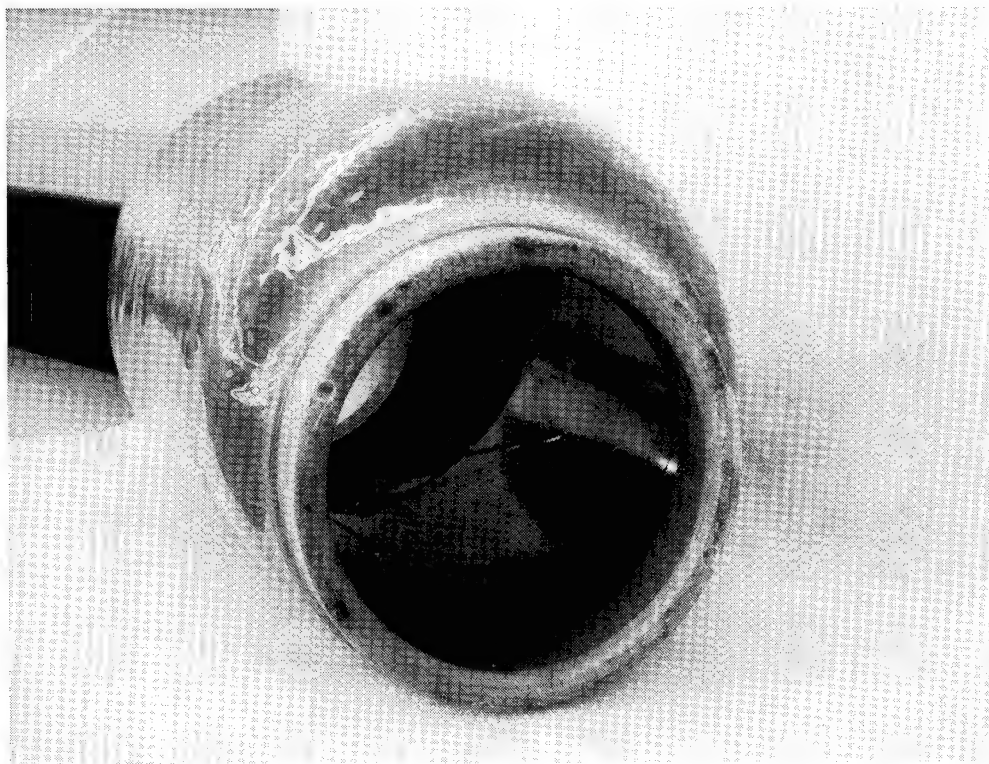


Figure 9. Bore evacuator chamber.

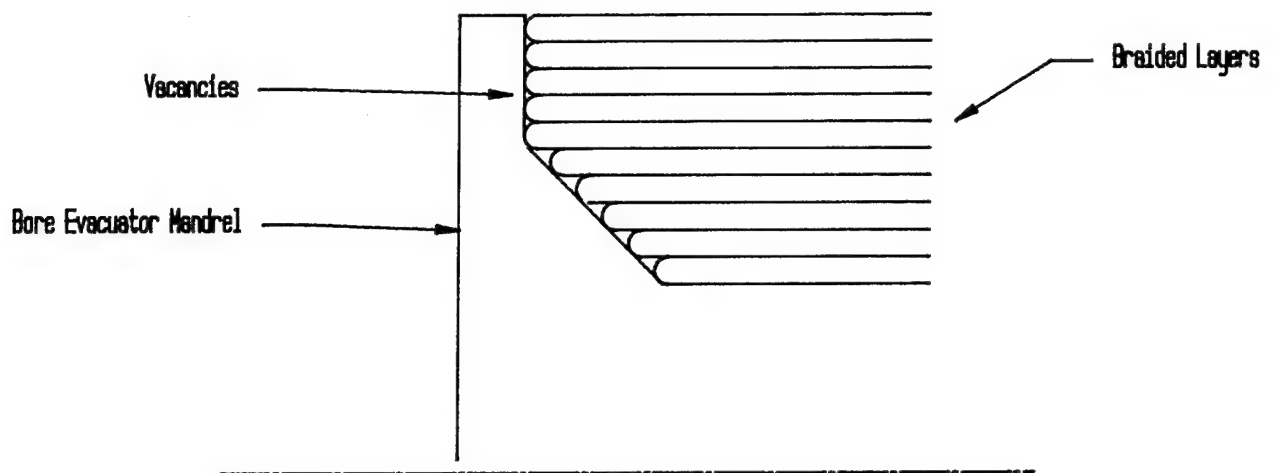


Figure 10. Grooves at end of braid layer.

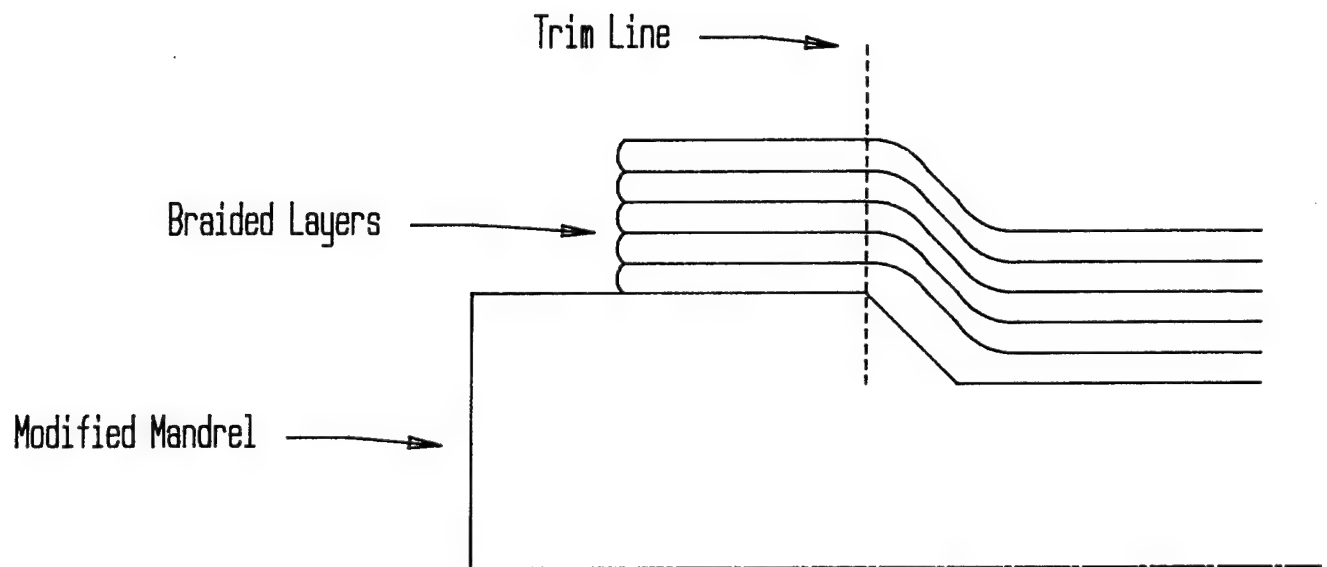


Figure 11. Modified bore evacuator mandrel.



# **The Use of Curvilinear Fiber Format to Improve Buckling Resistance of Plates with Central Circular Holes<sup>1</sup>**

H.H. Lee<sup>2</sup>

M.W. Hyer<sup>3</sup>

Department of Engineering Science and Mechanics  
Virginia Polytechnic Institute and State University  
Blacksburg, VA

## **INTRODUCTION AND BACKGROUND**

Conventional design philosophies for fiber-reinforced composite structures are based on the idea of using multiple layers of fibers embedded in a matrix, the fibers in each layer being straight and aligned in a particular direction. Though each layer may have its own unique fiber orientation, the idea of allowing the fiber orientation within a layer to vary from point to point has not been seriously considered. Fabrication techniques and analysis procedures have precluded this form of fiber usage, herein referred to as a curvilinear format, and have emphasized the use of fibers in a straight line. Contemporary fiber handling techniques, however, make the issue of a curvilinear format less of an obstacle. This paper explores the potential gain in buckling resistance by using the curvilinear format with a plate containing a centrally located circular hole and subjected to a uniaxial compressive load. This work is considered a follow-on to earlier work [1] directed at improving the tensile load capacity of a plate with a centrally located circular hole using the curvilinear fiber concept. (See also refs. 2 and 3.) In that previous work, using the maximum strain criterion, the tensile capacity of a plate with a stacking arrangement denoted as  $(\pm 45/C_0)_S$  was shown to have a load capacity greater than an equal-weight conventional straightline design. The notation C in the stacking sequence signifies a layer in the laminate that has a fiber direction that varies from point to point within the plate. In the above laminate, then, the central 12 layers have the curvilinear format. In the tension study, the fiber orientations within the layers with the curvilinear format were determined by aligning the fibers in those layers with the principal stress directions in those layers. This should not be confused with aligning the fibers with principal stress directions of the laminate. Principal stress directions of a laminate are somewhat meaningless.

Ideally, with the curvilinear format the fiber directions would vary continuously from point to point. For the tension problem the fiber directions would everywhere be aligned with the principal stress directions of the particular layers. However, a finite-element discretization was used in the analysis of the tension problem. Thus instead of having the fiber directions varying continuously, they were assumed to be constant within each element of the finite-element model, but they varied from element to element. With 120 elements in a quarter

---

<sup>1</sup> Funded by Grant NAG-1-665 with NASA Langley Research Center, Grant Monitor M.P. Nemeth

<sup>2</sup> Graduate Research Assistant

<sup>3</sup> Professor

plate model, this approximation was not a detriment. Since principal stress directions depend on the fiber orientations, aligning the fibers with the principal stress directions required iteration. Usually within 4 or 5 iterations the fibers were aligned with the principal stress directions in each element and the performance of the curvilinear designs was compared with conventional straightline format designs. Figure 1 shows the fiber orientations of the curvilinear layers that resulted from the iteration process. For this curvilinear case, a  $(\pm 45/0_6)_s$  is considered the straightline counterpart. The tensile strength of the curvilinear  $(\pm 45/C_6)_s$  was shown to have capacity 1.25 times greater than this straightline counterpart. Relative to a conventional quasi-isotropic design, the curvilinear design was 1.60 times stronger in tension. The baseline quasi-isotropic, the curvilinear, and the straightline counterpart designs were all predicted to fail due to fiber tension near the net-section hole edge. Though the curvilinear design had the same failure mode, it was shown that the primary effect of the curvilinear design was to move the load around the hole in a more effective manner than the straightline designs did. Material near the hole edge, where the stresses were highest in all designs, was not stressed as highly in the curvilinear design as in the other designs. Hence the tensile load capacity was greater.

The increased tension capacity of the curvilinear designs could well come at the expense of a degradation in buckling load. Thus the buckling loads of the baseline, curvilinear, and straightline counterpart designs were computed and compared. In particular, the buckling loads for a uniform stress loading and simple support boundary conditions were examined. The baseline quasi-isotropic design exhibited the highest buckling load, presumably due to the fact that half layers were in a  $\pm 45$  orientation. The curvilinear design buckling capacity was generally 5-15% less than the baseline quasi-isotropic design, and as good or better than the straightline counterpart. Thus the study concluded that though the improved tensile performance was at the expense of buckling performance, the penalty was no worse, and in fact less, than other non-quasi-isotropic straightline designs.

The studies related to buckling immediately raised the question: Can buckling performance be improved by utilizing the curvilinear concept? How many layers should have the curvilinear format? What is the basis for comparison to measure improvements in buckling resistance? Is the tensile strength of these designs degraded? It seems certain that working with the principal stress directions is not the approach to take. However, as in the principal stress direction method of improving tensile strength, it seems logical to consider the fiber angle at each point in the plate (or, in the present analysis, in each finite-element) as a variable that can be used to control buckling load. The principal question is How do we determine these fiber angles so as to result in the maximum buckling load? As alluded to above, of equal importance is the influence of these fiber angles on the tensile load. Improved buckling performance could well come at the expense of degraded tensile capacity.

The approach taken here is similar to the approaches used in optimization studies, namely, sensitivity studies and finding the conditions that lead to a maximum of a performance measure. The sections that follow focus on these issues and provide details of the approach. The next section briefly outlines the method of analysis for this buckling improvement study. The section after that further discusses the method of analysis and presents several designs that represent an improvement over a baseline quasi-isotropic design, a design, as mentioned above, that is quite good for buckling resistance. The section following that discusses the tensile load capacity of these designs. The paper concludes with a recommended design that not only shows an improved buckling capacity, but also shows improved tensile performance. Follow-on activities are also discussed at the close of this paper.

## METHOD OF ANALYSIS

The finite-element method is used throughout the study. The presence of the hole requires a prebuckling analysis to determine the inplane stress resultants. This is accomplished with an 8-node isoparametric element. The buckling analysis, of course, uses the prebuckling stress resultants to compute the level of those resultants that causes the plate to buckle. The finite element used for the buckling analysis is also an 8-node element.

The material properties used in the study represent typically available polymer matrix graphite composite. The properties are as follows:

$$\begin{aligned} E_1 &= 137 \text{ MPa (19.9 Msi)}; E_2 = 8.8 \text{ MPa (1.28 Msi)} \\ G_{12} &= 7.1 \text{ MPa (1.03 Msi)}; \nu_{12} = 0.298 \\ \text{layer thickness} &= 0.1 \text{ mm (0.005 in.)} \end{aligned} \quad (1)$$

The failure strains used to evaluate tensile load are as follows:

$$\begin{aligned} \text{tensile failure in fiber direction} &: 10.5 \times 10^{-3} \\ \text{compressive failure in fiber direction} &: 10.5 \times 10^{-3} \\ \text{tensile failure perpendicular to fiber} &: 5.8 \times 10^{-3} \\ \text{compression failure perpendicular to fiber} &: 23.0 \times 10^{-3} \\ \text{shear failure in plane of layer} &: 13.1 \times 10^{-3} \end{aligned} \quad (2)$$

## SENSITIVITY STUDIES

With a sensitivity study, as it applies here, the fiber angles at each point are considered as design variables. For a finite-element representation, wherein the fiber angle is constant within each element, element fiber angles are considered the design variables. Here, the sensitivity of the buckling load to the design variables is examined. In the previous study to improve tensile capacity, 120 elements were used. If this many elements were used for the buckling study being discussed here, there would be 120 design variables. Determining the sensitivity of the buckling load to each of the 120 fiber angles would be an impossible task. Hence, for the buckling study, less fiber angles are used. This, in effect, prescribes that a given fiber angle be fixed over a larger region of the plate than if 120 fiber angles were used. Though 120 finite-elements could be used to compute the lowest buckling load, far fewer elements produced the same result, and obviously required far less computation. A convergence study indicated that no more than 18 elements in a quarter plate were necessary to accurately compute the lowest buckling load. As a first step at studying sensitivity, then, 18 different fiber angles in a quarter plate are considered. Though it is well known that the presence of the  $D_{16}$  and  $D_{26}$  terms prevents quarter plane symmetry [4], a quarter plate analysis provides a good estimate of the effectiveness of the curvilinear format for improving buckling resistance. A schematic of the quarter plate divided into 18 regions is illustrated in fig. 2. The numbering scheme for the regions is shown in the figure. Here only square plates are studied, in particular, square plates with a hole diameter to width ratio of 0.3. Specifically, the plate dimensions considered are chosen for purposes of possible small-scale verification experiments. The plate length and width are 254 mm (10 in.) and the hole diameter is 76.2 mm (3 in.). Only 16 layer plates are studied. The plate is assumed to be simply supported on all four edges. The loading used is actually a displacement loading, rather than the uniform stress loading discussed in the INTRODUCTION, a displacement

loading more closely representing an experimental set-up. The laminate used to begin this sensitivity study is a  $(\pm 45/0_6)_s$ . Shown in fig. 2 is the fact that the sensitivity study is based on allowing the  $0^\circ$  fiber angle in one of the 18 regions of the plate to vary. In this one region the laminate could be considered a  $(\pm 45/\theta_6)_s$  laminate. The sensitivity study examines the influence of this variable fiber angle on the buckling load by computing the buckling load as a function of  $\theta$ . This variation is allowed on a region-by-region basis. For each region there is a fiber angle,  $\theta^*$ , that results in the greatest buckling load. The sensitivity of the buckling load to the fiber angle in each region is illustrated in fig. 3. In this figure the buckling load is normalized by the buckling load of the  $(\pm 45/0_6)_s$  laminate. Hence, for each region, when  $\theta = 0^\circ$ , the buckling load is in unity because the laminate is actually the original  $(\pm 45/0_6)_s$  laminate.

By studying fig. 3, two important facts can be learned. First, it is clear that the buckling load is not sensitive to the fiber angle in some regions of the plate. For example, along the centerline, regions 1, 2, and 3, fiber angle is not overly important. By contrast, around the hole, regions 7, 10, 13, and 16, improvements in the buckling load can be made by changing the fiber angle. In a similar vein, the sensitivity study indicates that the buckling load can be degraded by changing the fiber angles in regions 9, 12, 15, and 18.

As a second point, fig. 3 indicates that if effects are additive, there can be significant improvements in buckling resistance if fiber angles are chosen properly in the various regions of the plate. To that end, if a plate design is considered that uses the angle in each region that results in the maximum buckling load, a considerable increase in buckling resistance is achieved. Such a design is illustrated in fig. 4, the angles in each region being the angle from fig. 3 that results in the maximum buckling load when the fiber angles were varied one region at a time. The buckling load is 2.26 times the buckling load of the original  $(\pm 45/0_6)_s$  laminate, indeed a significant improvement. It should be noted that for a uniform displacement loading of a plate simply supported on all four sides, the buckling load of a quasi-isotropic laminate and  $(\pm 45/0_6)_s$  laminate are practically identical. This is opposed to the stress-loaded simply supported case discussed in the INTRODUCTION where the quasi-isotropic laminate was 15% more resistant to buckling. Hence the buckling loads being discussed in this buckling improvement study can be considered as being normalized either by the quasi-isotropic baseline, or by the original  $(\pm 45/0_6)_s$  straightline design. Herein, the normalized buckling load will be denoted by  $\bar{P}_{cr}$  and hence for the design of fig. 4,  $\bar{P}_{cr} = 2.26$ .

Though the sensitivity study results in a design with improved buckling resistance, the approach may be somewhat misleading. In reality, the fiber orientation in each region that maximizes the buckling load more than likely depends on the fiber orientation in other regions...that is, the regions interact. In the sensitivity study, it is assumed that the fiber orientations in the other regions were  $0^\circ$ , the only nonzero fiber angle being the one in the region being studied. To allow for interaction between regions, the fiber angle in each of the 18 regions is considered an unknown, and a gradient-search [5] technique is used to find the combination of angles in the 18 regions that maximizes the buckling load. As used here, there is no guarantee the technique will find the absolute maximum. The maximum in the neighborhood of the initial angles given the gradient-search algorithm is what the technique will find. This concern in mind, if the gradient-search technique is applied, the design illustrated in fig. 5 results. This design has a buckling load 2.96 times the baseline case ( $\bar{P}_{cr} = 2.96$ ). This is an improvement over the baseline case, and an improvement over the sensitivity analysis design. Comparing figs. 4 and 5 it can be seen that the sensitivity anal-

ysis and the gradient-search method result in different fiber angles in the 18 regions, the fiber angle distribution, however, being generally the same.

One of the first concerns that comes to mind when examining either fig. 4 or 5 is the issue of manufacturing. The change in fiber angle between adjacent regions is large, for example, between regions 7 and 8, or between regions 10 and 11. Such discontinuities in fiber directions are not possible for even the most advanced manufacturing methods. Dividing the plate into more regions may reduce the discontinuity of fiber angles between regions. And with more design variables, the improvement in buckling load could be expected to increase. As stated above, the computational effort becomes quite large with more regions. The approach taken here is to use fewer design variables, or other geometric arrangements of fiber angles. A variation on the geometric arrangement of regions is shown in fig. 6, the plate being divided into 6 radially oriented regions. There are still 18 finite elements in the discretization but there are only 6 different fiber angles. The results of the sensitivity study, based on the  $(\pm 45/0_6)_S$  laminate, are shown in fig. 7. Except for region 1, the region along the centerline of the plate, and the region that corresponds to regions 1, 2, and 3 in the 18 region scheme, each region has an influence on the buckling load. Fiber orientations within this 6 region scheme can lead to improvements in buckling resistance. The sensitivity analysis design is shown in fig. 8. This value of  $\bar{P}_{cr}$  for this design is 1.83. The design resulting from the gradient-search technique is shown in fig. 9. For the gradient-search design,  $\bar{P}_{cr} = 1.85$ . These designs, where the fibers are grouped along radial regions, are referred to herein as a  $(\pm 45/RG_6)_S$  designs. Compared to the factor of 2.96 for the gradient-search 18-region design, the buckling resistance is not as great. However, this near factor of 2 in improvement is significant, and the design is much more manufacturable.

### TENSILE STRENGTH CONSIDERATIONS

Since in a normal operating environment both compressive and tensile loads are present, it is of paramount importance to evaluate the tensile strength of the designs that improve the buckling load. For a tensile load the stresses of concern are the prebuckling stresses with the sign reversed. Thus a tensile analysis is available as part of the buckling analysis.

The principal material direction strains  $\epsilon_1$ ,  $\epsilon_2$ , and  $\gamma_{12}$  in each layer are computed and the maximum strain criterion applied using the strains in eq. 2. The strains as computed at the finite-element Gauss points are used. (The prebuckling compressive strains are quite small compared to the failure strains and thus it is clear compressive loading causes buckling rather than material failure.)

Table 1 summarizes the tensile failure loads of the laminates discussed so far, in addition to a laminate to be discussed. For completeness, buckling loads are included in the Table. In the Table both the buckling load and the tensile failure load are normalized by the respective load for the quasi-isotropic laminate. For the curvilinear designs, only the designs determined by the gradient-search method are included. For the tensile failure, the failure mode and the location of this failure are indicated. As a reference, the buckling load of a 10 in. by 10 in. 16 layer displacement loaded quasi-isotropic simply supported laminate with a 3 in. hole is calculated to be 6.00 kN (1.35 kips) and the tensile failure load is 105 kN (23.6 kips). Tensile failure is predicted to occur due to fiber failure at the net section hole edge.



TABLE 1

**Buckling and Tensile Load Capacities of Laminates**

Laminate	Buckling Load	Tensile Load	Tensile Failure Details
quasi-isotropic	1.00 <sup>1</sup>	1.00 <sup>2</sup>	fiber failure at hole edge
$(\pm 45/0_6)_S$	1.01	1.88	fiber failure at hole edge
$(\pm 45/C_6)_S$	2.97	-	not considered <sup>3</sup>
$(\pm 45/RG_6)_S$	1.85	0.62	shear at loaded edge
$(\pm 45/0/90/RG_4)_S$	1.30	1.35	fiber failure at hole edge

1 - 6.00 kN (1.35 kips)

2 - 105 kN (23.6 kips)

3 - Since this design was judged to be too difficult to manufacture, it was not pursued.

Immediately obvious in Table 1 is the fact that the  $(\pm 45/RG_6)_S$  design, a manufacturable design, is about 40% weaker in tension than the baseline quasi-isotropic laminate, and considerably weaker in tension than the  $(\pm 45/0_6)_S$  design. Failure is predicted to occur in shear at the loaded edge. Specifically, referring to fig. 6, failure is predicted to occur at the loaded edge of region 3. In this region, due to the fiber angle of  $-44^\circ$ , the laminate is effectively a  $(+45/-45_7)_S$  laminate. This laminate, while strong in inplane shear in the plate coordinate system, is extremely weak in inplane shear in a coordinate system rotated at  $45^\circ$  to the plate coordinate system. Needed is reinforcement in the 0 and/or  $90^\circ$  direction in the plate coordinate system to overcome this weakness in shear. As a step in this direction, four of the curvilinear layers are re-oriented so as to form a  $(\pm 45/0/90/RG_4)_S$ . The fiber angles in the curvilinear layers as found by the gradient-search technique for this laminate are not quite the same as in the  $(\pm 45/RG_6)_S$  laminate. Effectively, the  $(\pm 45/0/90/RG_4)_S$  laminate is a 'sandwich', the curvilinear layers being sandwiched between two quasi-isotropic laminates. As can be seen from the Table, the tensile strength is significantly improved, and in fact, exceeds the baseline quasi-isotropic laminate. This is presumable due to the load being transferred around the hole more effectively, as discussed in the INTRODUCTION. The buckling load has decreased relative to the original  $RG_6$  design. However, overall, the  $(\pm 45/0/90/RG_4)_S$  laminate is better than a quasi-isotropic laminate.

**CURRENT AND FUTURE ACTIVITIES**

The results obtained to date in this area are quite encouraging. Though the number of regions that can have unique fiber angles, and the number and arrangements of the layers within those regions would appear to be infinite, there is a practical limit to what can be fabricated. Tow placement devices must work with smooth fiber trajectories, and the fiber trajectories in one area of the plate have to be able to blend in a continuous fashion with the fiber trajectories in other areas of the plate. In addition, there are volume fraction considerations. Thus there is not an endless array of possibilities. Some other possibilities have been considered but have not been thoroughly investigated. For example, using circumfer-

entially grouped regions rather than radially grouped regions could lead to high buckling loads. And what of post-buckling? The buckled plates must eventually fail. It is important to know whether their post-buckling strength is improved or degraded. Material failure will most likely occur in the post-buckled range and this must be investigated. These areas are currently under investigation and will be reported on at a later date.

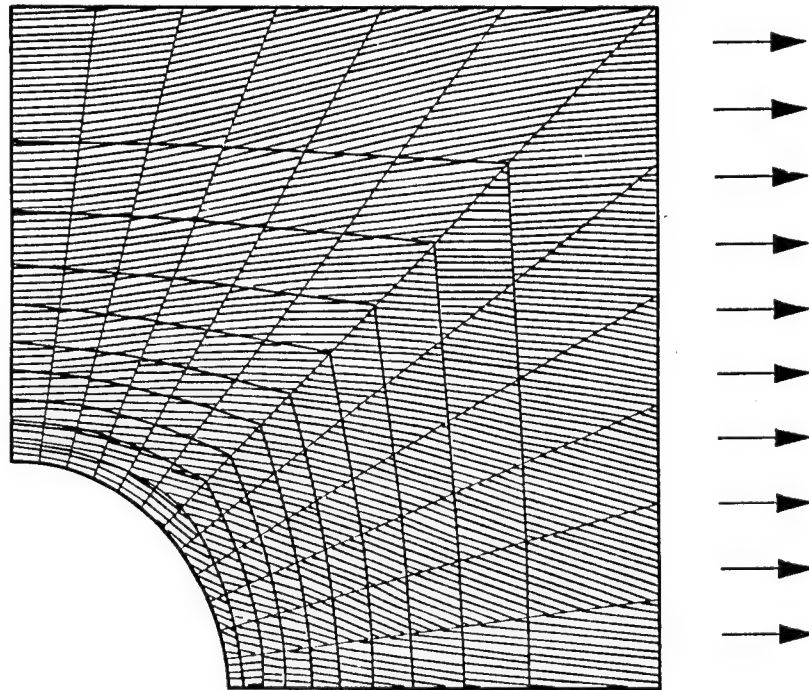
### ACKNOWLEDGMENTS

The work reported on here was supported by Grant NAG-1-665, "Innovative Design of Composite Structures," with the Structural Mechanics Branch of the NASA Langley Research Center. The Grant Monitor is Dr. M.P. Nemeth. The financial support and technical advice and encouragement from Dr. Nemeth are appreciated by both authors.

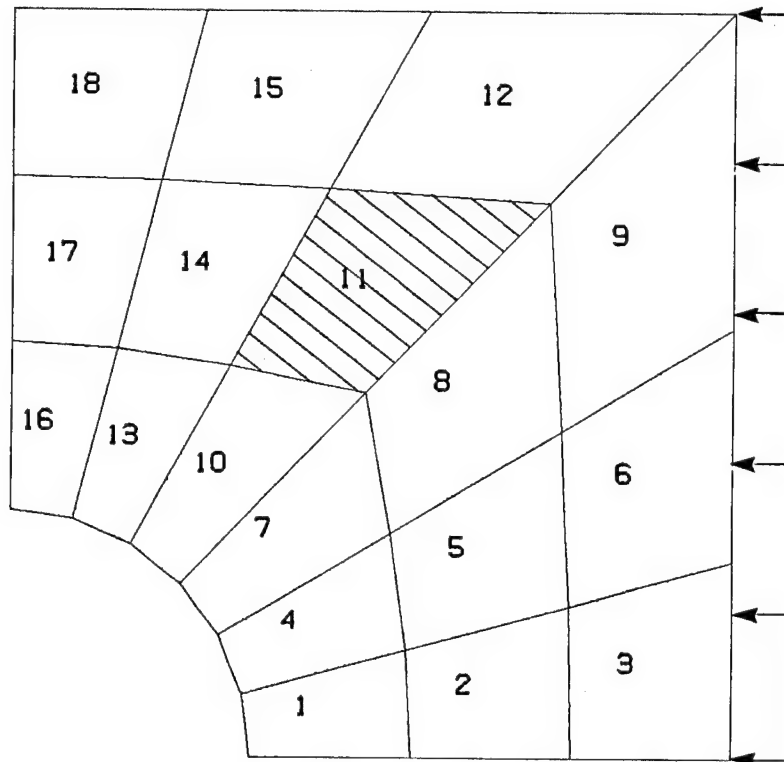
### REFERENCES

1. Hyer, M.W. and Charette, R.F., "The Use of Curvilinear Fiber Format in Composite Structure Design," AIAA Paper No. 89-3105, presented at the 30th AIAA SDM Conference, Mobile, AL, April 1989.
2. Hyer, M.W. and Charette, R.F., "Innovative Design of Composite Structures: Further Studies in the Use of a Curvilinear Fiber Format to Improve Structural Efficiency," Virginia Tech College of Engineering Report VPI-E-88-8, March 1988.
3. Hyer, M.W. and Charette, R.F., "Innovative Design of Composite Structures: Use of Curvilinear Fiber Format to Improve Structural Efficiency," University of Maryland Department of Mechanical Engineering Technical Report 87-5, May 1987.
4. Nemeth, M.P., "Importance of Anisotropic Bending Stiffness on Buckling of Symmetrically Laminated Plates Loaded in Compression," AIAA Journal, vol. 24, pp. 1831-35, Nov. 1986.
5. Miura, H. and Schmitt, L.A., "NEWSUMT - A Fortran Program for Inequality Constrained Function Minimization - Users Guide," NASA CR 159070 June 1979.

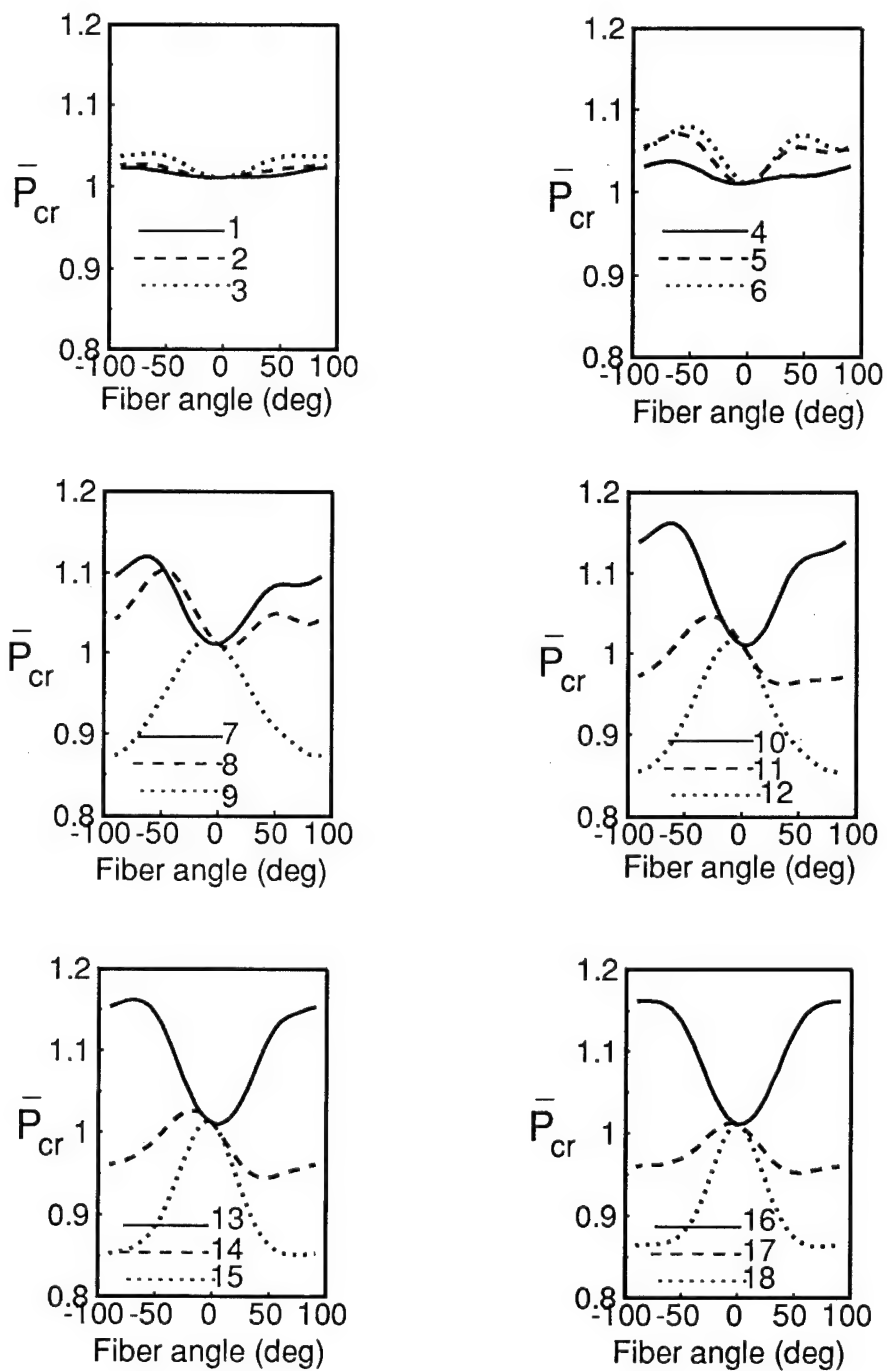




**Fig. 1** Fiber orientations in the curvilinear layers of the  $(\pm 45/C_6)_s$  tensile design. (ref 1.)



**Fig. 2** Quarter plate divided into 18 regions.



**Fig. 3 Sensitivity of buckling load to fiber angle in each of the 18 regions of a  $(\pm 45/0_6)_s$  laminate.**

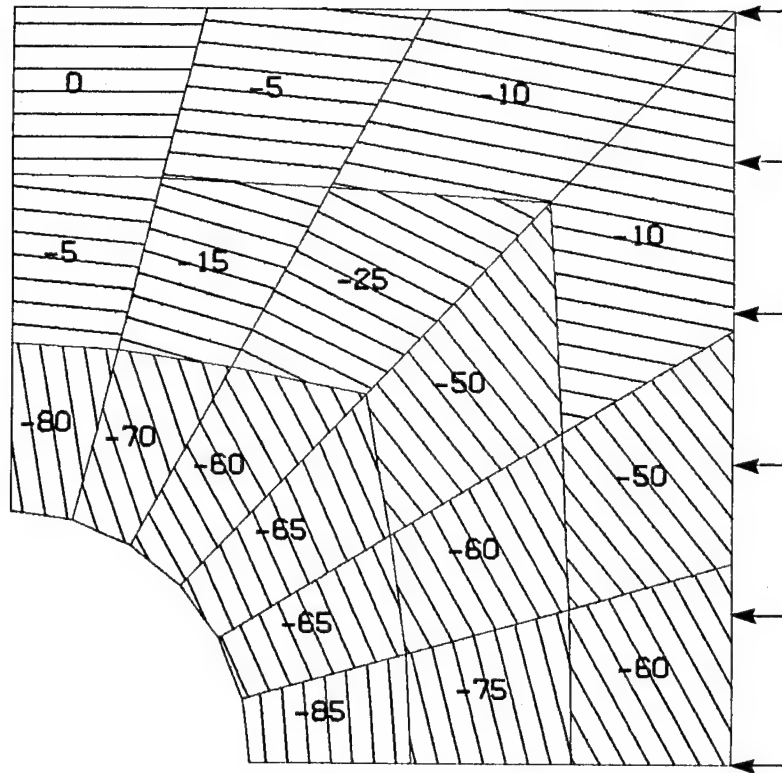


Fig. 4 Fiber angles in the curvilinear layers that maximize buckling load in a  $(\pm 45/C_6)_s$  plate, sensitivity design with 18 regions,  $P_{cr} = 2.26$ .

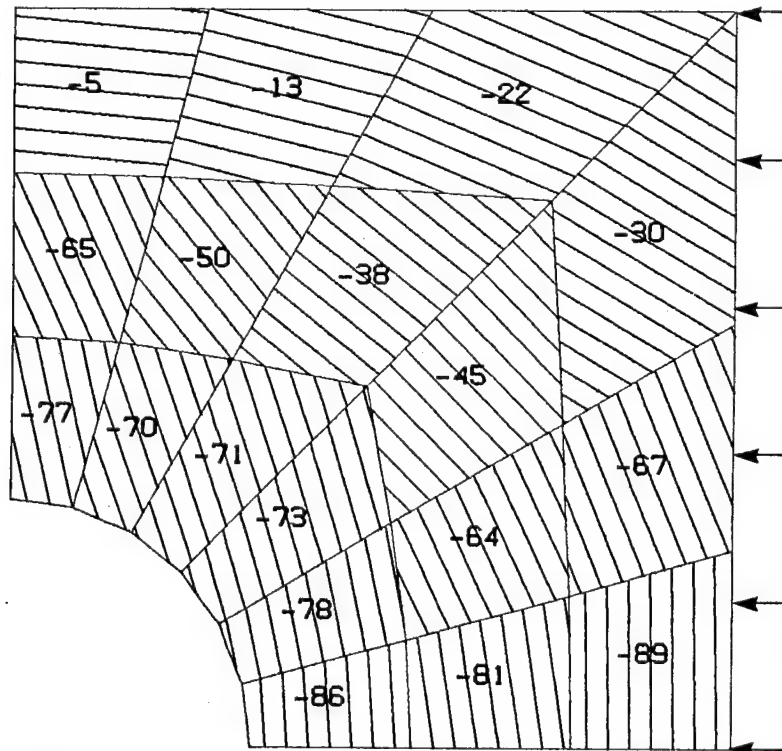


Fig. 5 Fiber angles in the curvilinear layers that maximize buckling load in a  $(\pm 45/C_6)_s$  plate, gradient-search design with 18 regions,  $\bar{P}_{cr} = 2.96$ .

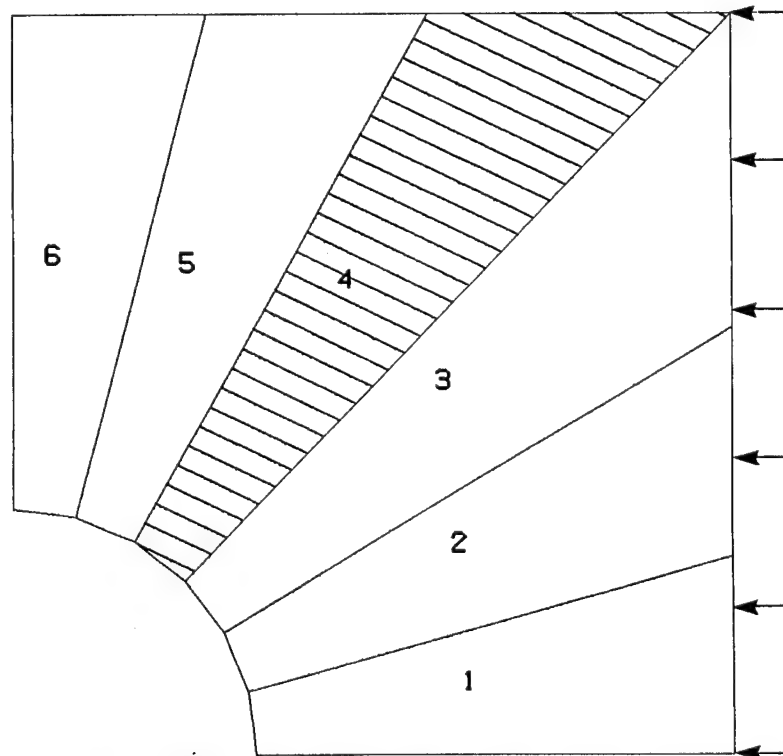


Fig. 6 Quarter plate divided into 6 radial regions.

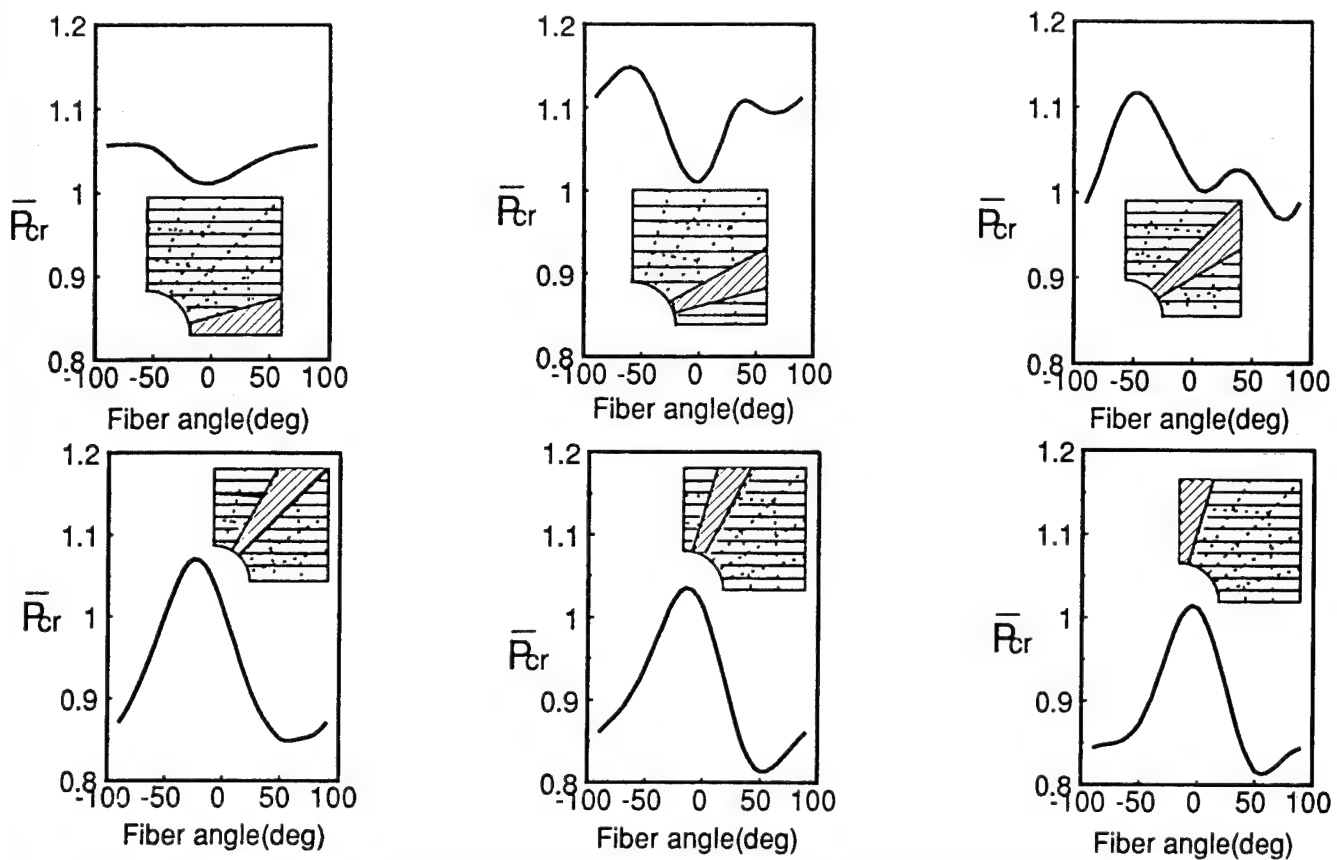
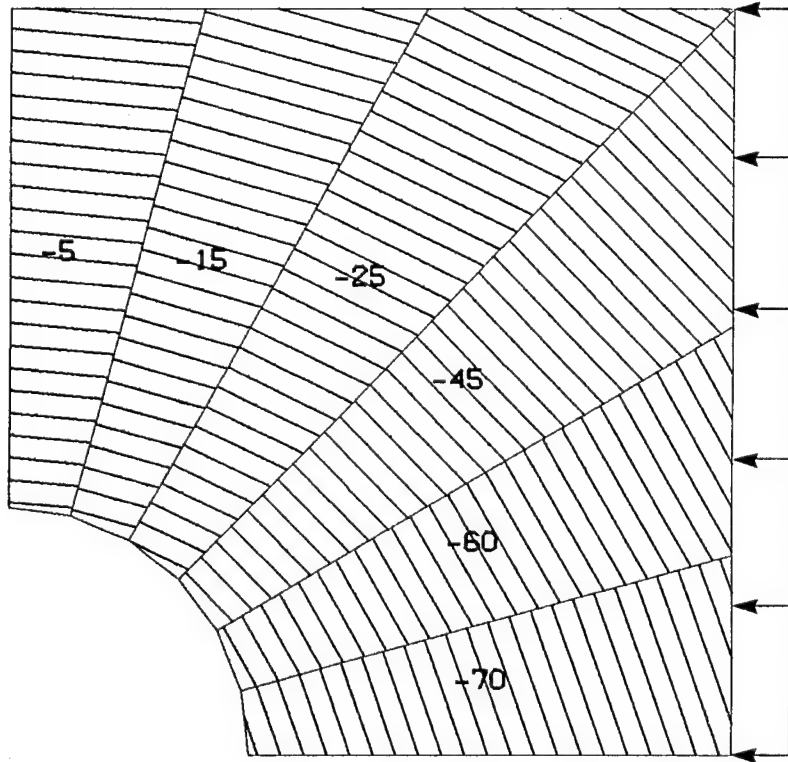
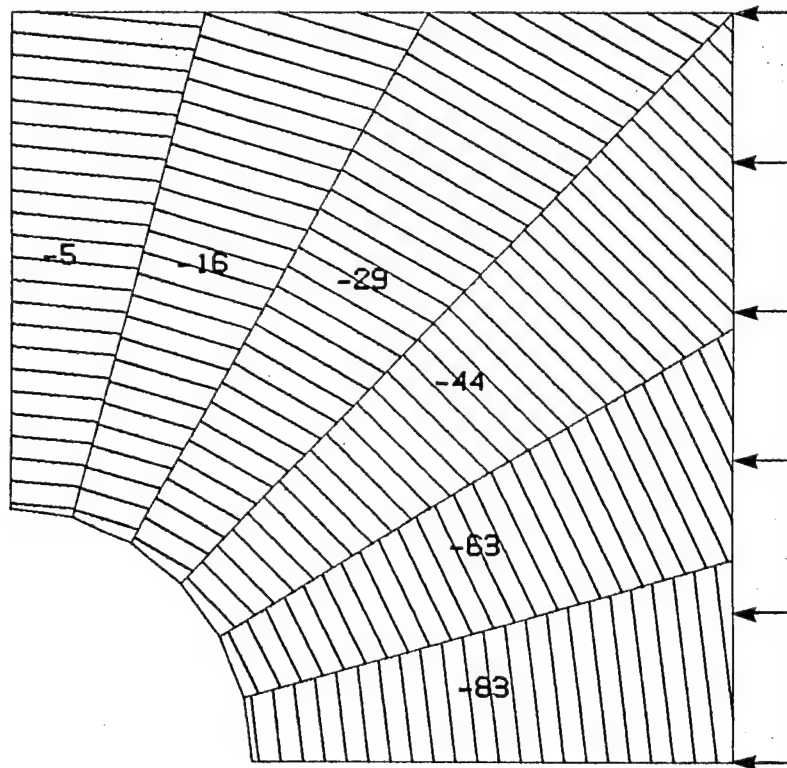


Fig. 7 Sensitivity of buckling load to fiber angle in each of the 6 regions of a  $(\pm 45/0_6)_s$  laminate.



**Fig. 8** Fiber angles in the curvilinear layers that maximize buckling load in a  $(\pm 45/C_6)_s$  plate, sensitivity design with 6 regions,  $\bar{P}_{cr} = 1.83$ .



**Fig. 9** Fiber angles in the curvilinear layers that maximize buckling load in a  $(\pm 45/C_6)_s$  plate, gradient-search design with 6 regions,  $\bar{P}_{cr} = 1.85$ .

# **DEVELOPMENT OF THERMOPLASTIC COMPONENTS FOR STRUCTURAL VALIDATION**

John G. Avery  
Gary G. Cassatt

Boeing Military Airplanes  
MS K80-30, P.O. Box 7730  
Wichita, Kansas

## **SUMMARY**

Recent activity directed toward advancing the development and validation of graphite reinforced thermoplastic primary and secondary structure are described. The efforts discussed include the design, manufacture and test of a highly-loaded multi-spar wing-box component, and the development of a flight-worthy article that is form, fit and functionally replaceable with the nose landing gear door of the V-22 Osprey.

## **INTRODUCTION**

Thermoplastic composites such as PEEK reinforced with graphite fibers offer promising producibility and performance characteristics for both primary and secondary structure applications. A key element in capturing potential benefits is the structural validation of full-scale components fabricated using the forming and fusion bonding processes that are being developed for thermoplastics. Toward this goal, recent work was focussed on a multi-spar wing-box test article and a nose landing gear door.

Both articles employed APC-2 prepreg material purchased from ICI. The wing-box component incorporated planked soft-skin upper and lower covers and C-channel spars produced by press forming. Test validation included limit load demonstration followed by combat damage tolerance testing. These results provide enhanced confidence in the capability to produce high-performance structure using fabrication methods that can capture the cost-reduction potential of thermoplastics.

The nose landing gear door demonstrated several features that are critical for thermoplastic payoffs, including integrally stiffened diaphragm-formed skins and fused assembly. Formed bead-stiffening was used to provide stiffness without employing sandwich construction, and is well-suited for thermoplastic fabrication. A structural qualification program was completed that includes coupon testing, damage tolerance evaluation, and full-scale static testing.

## WING-BOX TEST ARTICLE

The objective of developing the wing-box test article was to confirm the structural integrity of a large, highly loaded full-scale structure fabricated of thermoplastics using nonautoclave processes. The work was undertaken in mid-1986 and completed with full-scale testing in 1987.

The material system employed was APC-2 (AS4 graphite fibers reinforcing PEEK matrix) purchased from ICI as 9-inch wide unidirectional tape. The box-configuration contained some of the design features of the graphite/epoxy replacement wing developed by Boeing for the Navy's A-6 aircraft. These features included planked wing covers (ie., a soft-skin design) for both the upper and lower skins, and C-channel spars bolted to the planks.

Figures 1 and 2 are pictorial representations of the article which has a constant cross-section, and is 34-inches wide by 98-inches long. Figure 3 shows the box prior to installation of the lower cover. Overall design features include the following:

- planked, soft skins
- five C-channel, nontapered spars, spaced at 8-inches
- 8-inch depth, constant section

Figure 4 shows the spar-to-skin attachment and some details of the planked skin design. The planks contain a high percentage of 0-degree plies and provide bending and axial stiffness. The region between planks (referred to as the web or skin) provides torsional stiffness and internal pressure resistance. Most significantly, the  $\pm 45$  dominated skin region provides improved notch-sensitivity relative both low-energy impact damage (LEID), and the high-energy impact damage to impact (HEID) induced by combat projectile threats that perforate the structure.

The design cut-off strain used for sizing the structural members was 0.006-in/in ultimate. This value was selected from the standpoint of a developmental goal for high-strain design concepts using tough polymers. This goal has also been employed by Grumman and McDonnell-Douglas for high-strain wing development programs sponsored by the Naval Air Development Center (Reference 1). An allowable substantiation test program was not undertaken for the wing-box test article described herein because of the limited objectives of the project.

A combat damage tolerance criteria was employed in addition to the 0.006-in/in ultimate strain cut-off, based on the multiple fragment threat described in Reference 2. This criteria requires sustaining a 3-fragment impact while the wing is loaded at 25-percent limit strain followed by an application of limit-strain without catastrophic failure.

Grade 145 tape was used for all fabrication. Nine-inch wide tape was edge-seamed to form sheets of appropriate size for the skin and spar laminates. The



sheet and strip materials for the planked panels were stacked onto a heated platen, wrapped in heating blankets, and consolidated using autoclave pressure.

The spar beams were press-formed in a conventional brake press using the tooling indicated in Figure 5 consisting of an aluminum female tool and a rubber male tool. Flat laminates were first consolidated under vacuum pressure using heating blankets for thermal control. Following consolidation, the laminates were trimmed to form blanks for the C-channel sections. The blanks were then heated to forming temperature, transferred to the cold tooling and pressed to final shape. After several minutes, the press was opened and the formed channels removed, as indicated in Figure 6. A total of nine 100-inch long channels were formed. C-scanning of the parts indicated good quality.

Only one wing-box article was fabricated. Structural testing consisted of demonstrating the 0.004-in/in design limit strain without evidence of degradation, followed by a ballistic test to verify the combat damage tolerance criteria. Figure 7 shows the testing performed for verification and Figure 8 shows the 4-point beam loading fixture and ballistic test apparatus. Following the limit-load strain demonstration with no damage, the article was loaded to 0.001-in/in strain and impacted in the center spar with three fragments launched simultaneously at 2500 feet per second. The fragments were 250-grain steel cylinders.

The article successfully sustained the applied load at impact. The applied loads were then increased until failure occurred. The maximum strain at failure in the covers was 0.004-in/in, providing verification of limit load strain following ballistic damage.

## **NOSE LANDING GEAR DOOR**

The nose landing gear door development work was initiated in 1987. Advanced reinforced thermoplastic composite technology was demonstrated through the design, fabrication, and test of a full-scale thermoplastic component for possible flight evaluation. The nose landing gear door of the V-22 Osprey aircraft was selected for this demonstration. IM7/PEEK unidirectional tape was used in a rapid, nonautoclave, thermoforming process which exhibited significant cost reduction over the thermoset honeycomb baseline design. The validation effort included, in addition to coupon and element tests, a full-scale structural loads demonstration. The door has been fit-checked by installation onto a V-22 aircraft.

The approach chosen was to redesign a baseline thermoset article using thermoplastic composites and nonautoclave fabrication processes. The right hand door of the nose landing gear door set (see Figure 9 and 10) was selected. The redesigned component was required to weigh no more than the baseline door. Four door assemblies were fabricated. Two were used for structural evaluation, and one is reserved for potential flight test.

The baseline door is a conventional minimum gage facesheet over honeycomb core design, employing graphite/epoxy as shown in Figure 11. The door is 54.1-inch by 12.6-inch and has a mild compound curvature. The facesheet material used is T300/5208 graphite epoxy and the core is 4.1 PCF Nomex ®. An elastomeric edge attached by a fiberglass retainer strip and small diameter mechanical fasteners completes the door assembly.

In addition, the inboard forward corner of the door has a bulge required for tire clearance during the operation of landing gear extension/retraction. In the baseline design, the bulge area is a separate piece attached to the door proper by mechanical fasteners.

The manufacturing approach for the baseline thermoset door is hand layup followed by a cocure/bond cycle in the autoclave at 350°F. Fabrication labor was 45.7 manhours per door average for the first five shipsets produced. For the 4.9 pound weight of the baseline door, this equates to 9.3 manhours per pound of delivered composite hardware.

Loads experienced by the door include both aerodynamic forces and ground handling loads. Both positive and negative pressures occur on the door surface when the door is closed during normal flight. An out-of-contour deflection limit of 0.18-inches is associated with those conditions. In addition, two ultimate load conditions occur with the door open: 1) a side condition of 100 knots and 2) a 50 pound ground handling load.

The thermoplastic redesign consists of the bonded assembly of an outer skin and an inner skin/doubler as indicated in Figure 12. Figure 13 is a photograph of the completed thermoplastic door. The inboard forward bulge area was made integral to the basic door which reduced part count. Honeycomb core was eliminated by employing a beaded inner panel to provide the required door stiffness. Both the inner panel and the outer skin use IM7/PEEK unidirectional prepreg tape and thermoformed consolidation. The basic layup consisted of eight plies each, for the skin and beaded doubler. Padups were added in the areas of hinge and actuator arm attachments.

The unidirectional prepreg tape was supplied by ICI in 12-inch widths. The material grade was 145 grams/meter<sup>2</sup> which provides a ply thickness of 0.0055-inches.

The dual diaphragm forming process was used to form both the outer skin and the inner doubler. The tooling mandrel material used was aluminum and the diaphragm material was 0.065-inch thick aluminum alloy. The approach as shown in Figure 14 consisted of 1) placing the dry ply stack between the two diaphragms, 2) inserting the assembly into the chamber, 3) closing the press to facilitate perimeter clamping, 4) heating to forming temperature, 5) applying positive pressure into the chamber cavity above the diaphragms to force the diaphragm and composites against the tool surface, and 6) cool-down and removal.

Bonding the inner doubler to the outer skin was accomplished by a dual polymer fusion process using Ultem 1000 between the assembly elements. For the bonding operation, the parts were placed on the outer skin tool and heated under pressure to melt the Ultem 1000 and form the bond.

Figure 15 shows the testing performed to support design development and verification. Compression-after-impact, filled hole compression, lap shear and fastener pull-through strengths were determined for the parameters of the door design. Selected properties were obtained at elevated temperature wet and after soak with MEK solvent. From this data, neither the MEK or humidity exhibited any greater reductions in bond strength over that experienced by co-cured joints without the Ultem layer.

Once a repeatable process was established, four doors were fabricated and the time required for each step was recorded. A significant reduction in the manhour requirement compared to the baseline thermoset production doors was demonstrated. 24.9 hours were required for fabrication through the bond assembly compared to an average of 45.7 hours for the seven thermoset doors fabricated for the V-22. Figure 16 shows a breakdown of the labor hours.

The second door was used as an impact survey door to determine the energy levels required to create clearly visible damage for the static test. Three regions of the door assembly were impacted:

1. Skin away from a bead (16 plys).
2. Skin region under a bead (8 plys).
3. The intersection of a bead and the outer skin (concern for peel).

In all three cases, clearly visible damage was achieved only when the impactor fully penetrated the door. Based on this survey, the static test door was impacted at these levels.

The third door was assembled with hinges and actuator fitting, mounted in a test rig representing the aircraft installation and static tested to verify the capability to sustain critical handling loads of 50 lbs (limit) on the bottom edge of the door in the open position. Static testing consisted of applying handling loads to the test article in three locations while recording critical strains and deflection. The door was then removed from the fixture, impacted in three critical locations, and the static test was repeated. This static test resulted in no failures. Strain and deflection measurements were used to validate the finite element model which was then used to substantiate the structure for the remaining load conditions.

The fourth door was assembled into a flight ready configuration (hinges, actuator fitting, and perimeter seals) and installed on the unit #4 aircraft opposite a baseline door for form, fit, and function checks as shown in Figure

17. Prior to installation, the thermoplastic and thermoset doors were weighed providing the following comparison:

Thermoset door	7.2 lb.
Thermoplastic door	5.5 lb.

This represented a 24-percent weight reduction for the fully assembled thermoplastic door.

## **RESULTS AND CONCLUSIONS**

The wing-box article development provided increased confidence in the structural integrity of large, highly loaded thermoplastic assemblies. Specific capability demonstrated included

- Press-formed spars and ribs
- Fabrication of a tailored skin laminate
- Static strength to 0.004-in/in strain
- Ballistic impact tolerance under load
- Limit strain capability with significant ballistic damage

The developmental thermoplastic door met or exceeded project goals, including reduction of both fabrication labor and weight. The door demonstrated the feasibility of features that are critical to achieving the potential payoffs envisioned for thermoplastic composites, including

- Thermal formed integrally stiffened parts
- Fusion bonded subassemblies

## REFERENCES

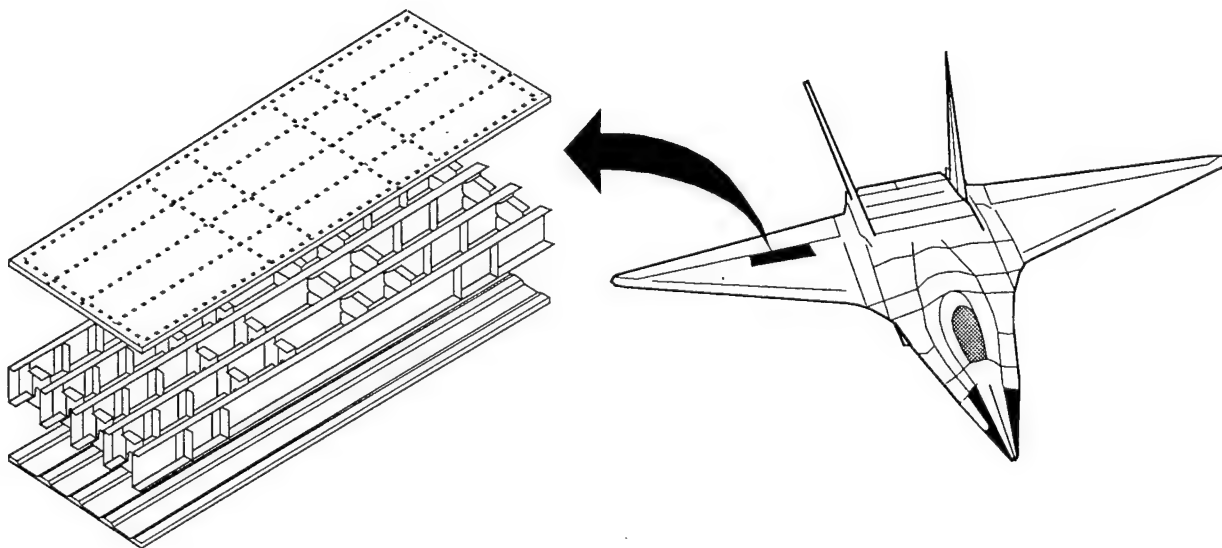
1. Bruno, J., "*Conceptual Design of a Composite High Strain Wing For Multi-mission Type Aircraft*," NADC-81088-60, February 1981.
2. Allen, M., "*Survivability Characteristics of Composite Compression Structures*," Final Report AFWAL-TR-88-3014, JTCG/AS-87-T-005, May 1988.

## ACKNOWLEDGMENTS

The projects described were achieved through the dedicated efforts of S. Schuessler, Jeff King, R. Kysar, Bob Brock, John Pilla, J. Thomas, M. Linhardt, and Jim Westerman.

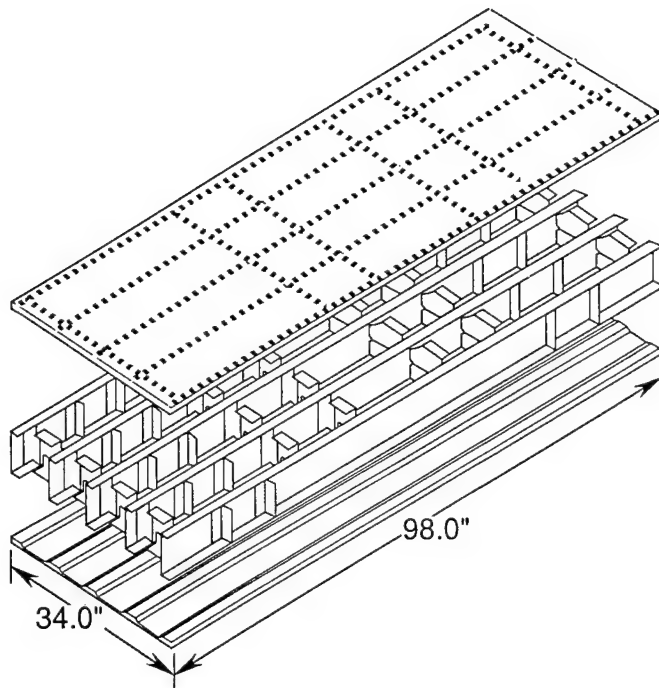
# WING - BOX TEST ARTICLE

OBJECTIVE: DEMONSTRATE STRUCTURAL INTEGRITY OF  
HIGHLY-LOADED THERMOPLASTIC COMPONENT



Thermoplastic Wing-Box Test Article  
Figure 1

# CONFIGURATION



- INTEGRALLY STIFFENED, SOFT SKINS
- 5 C-CHANNEL SPARS
- 6 RIBS
- 20-IN TEST SECTION
- 8-IN BOX DEPTH
- 8-IN SPAR SPACING
- BOLTED ASSEMBLY

Configuration Details  
Figure 2



Article With Cover Removed  
Figure 3



# SPAR/SKIN DETAIL

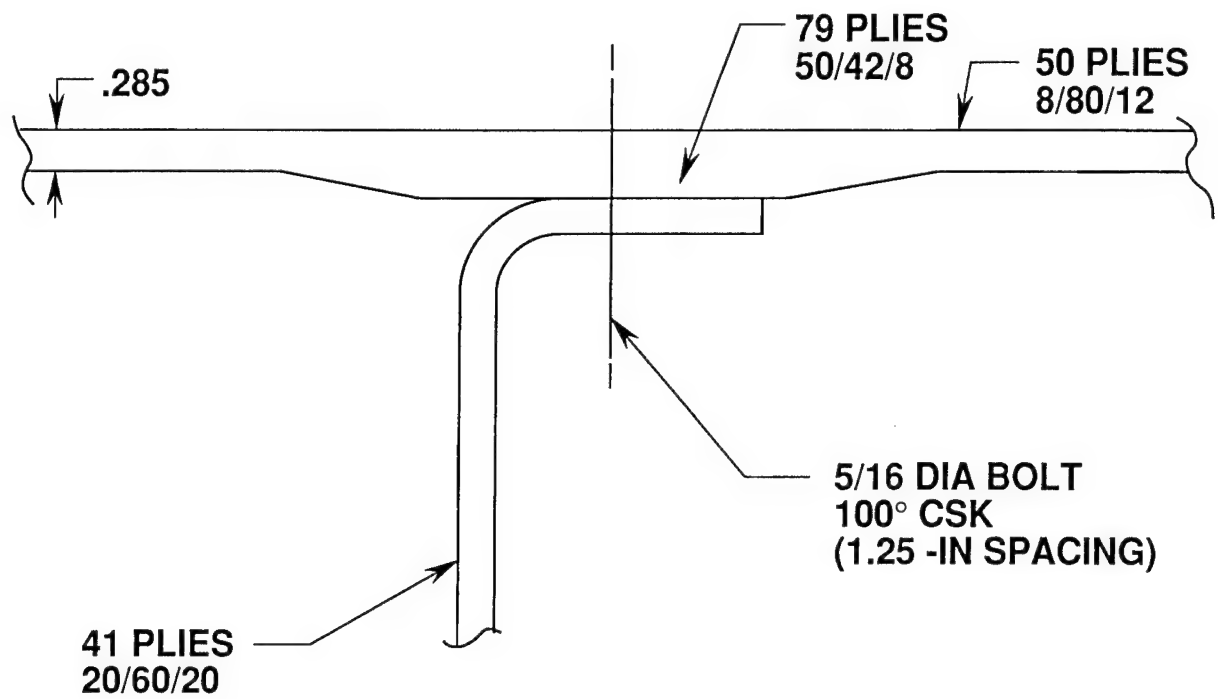
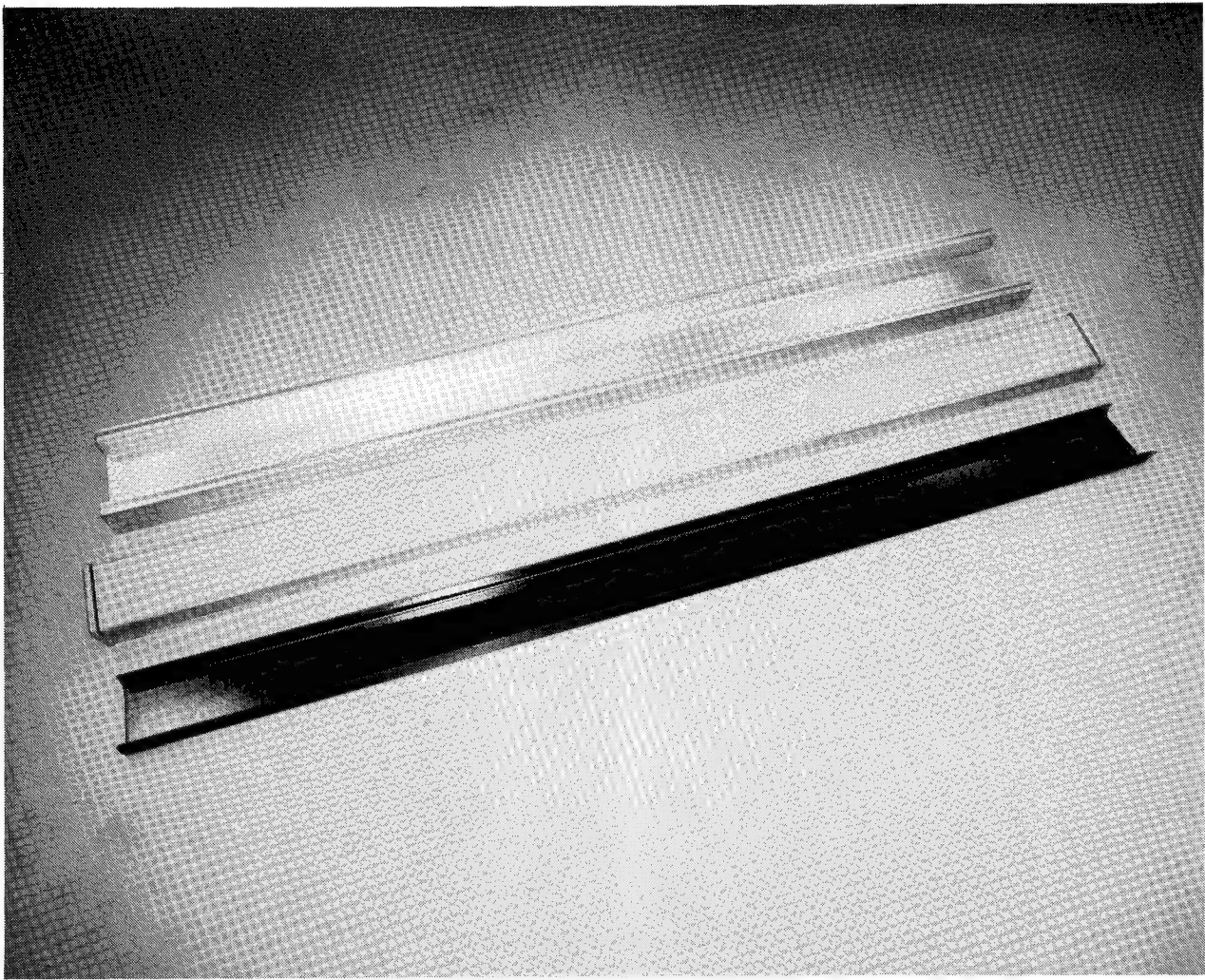


Figure 4

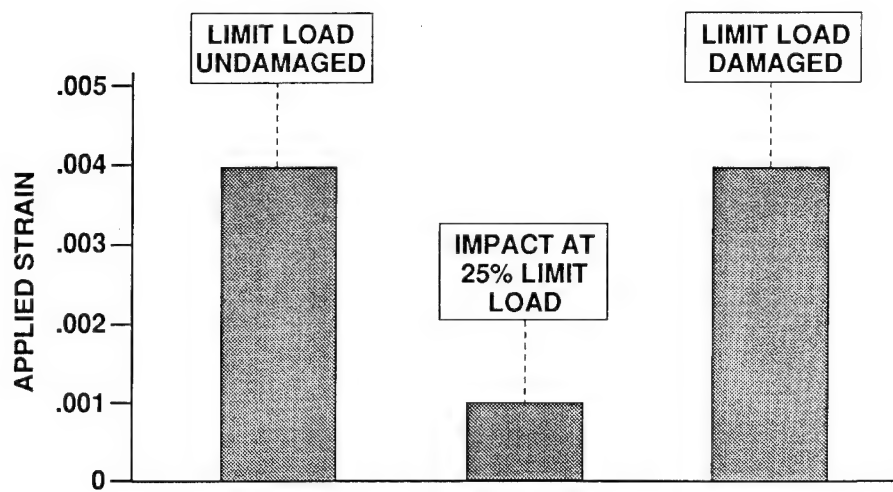


Tooling for Press Formed Spar Beams  
Figure 5

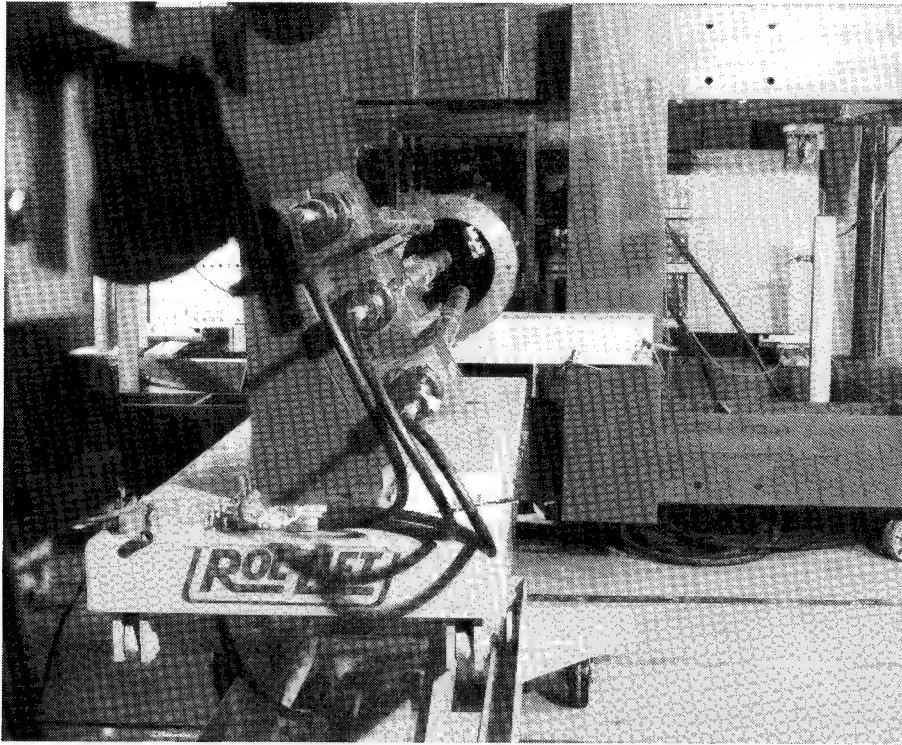


Brake Press Forming of Spar Beams  
Figure 6

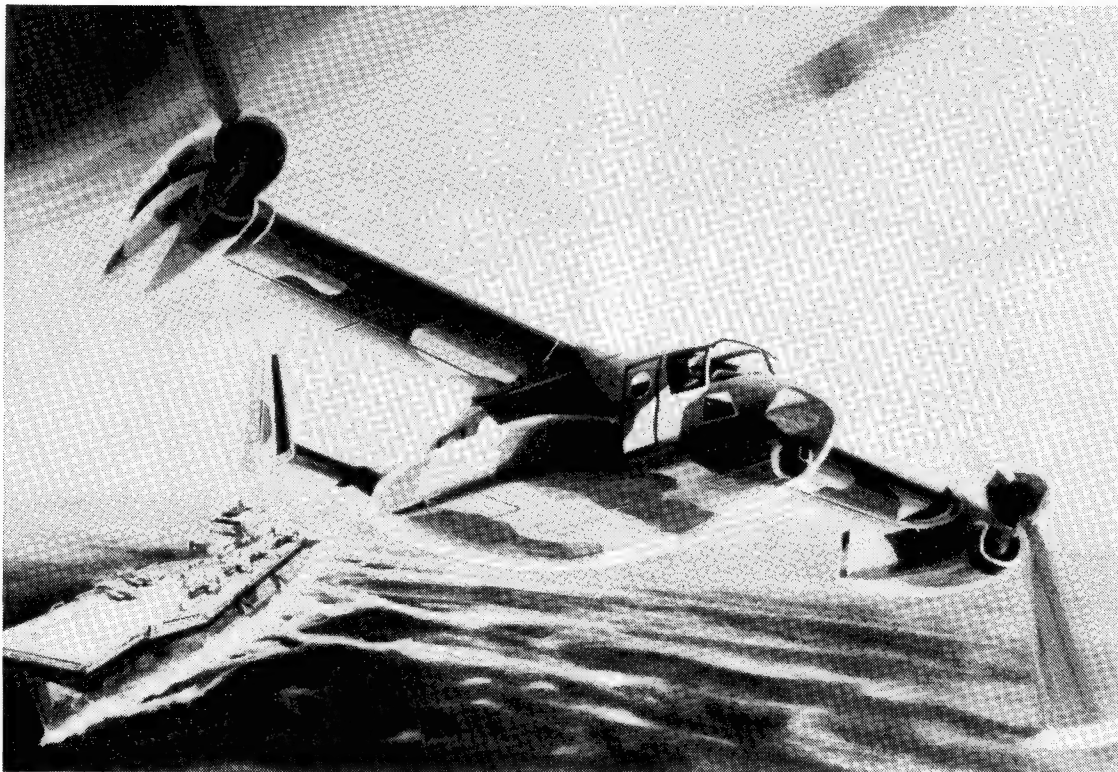
## TEST VERIFICATION



Structural Test Summary  
Figure 7

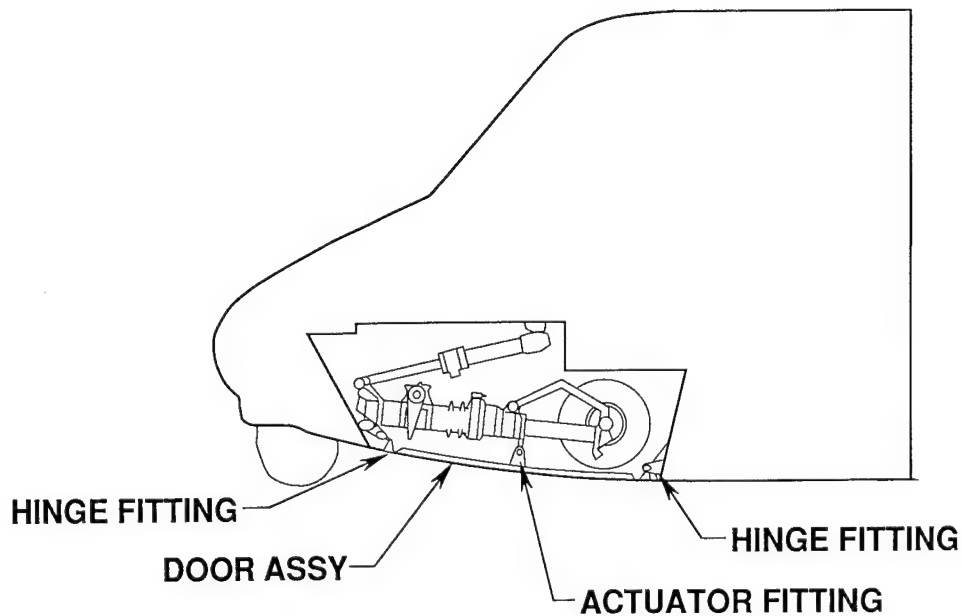


Static Test Arrangement  
Figure 8



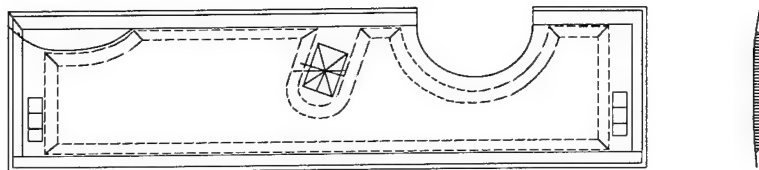
V-22 Osprey Tiltrotor Aircraft  
Figure 9

# NOSE LANDING GEAR DOOR

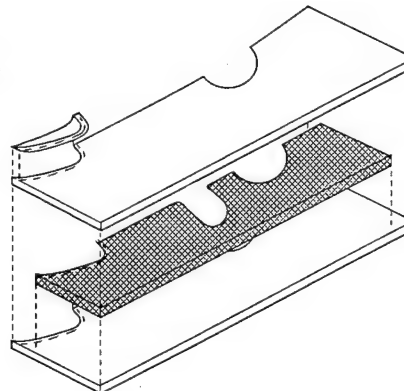


Nose Landing Gear Door Arrangement  
Figure 10

## CURRENT PRODUCTION DESIGN

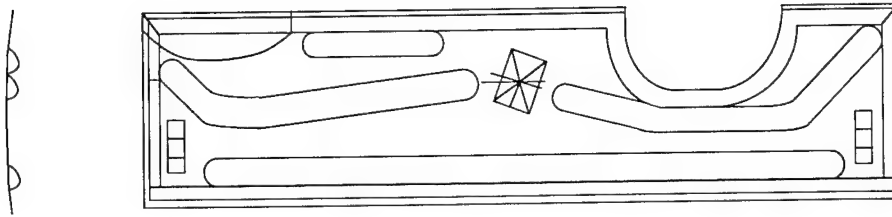


- GRAPHITE EPOXY FABRIC
- 4.1 PCF NOMEX HONEYCOMB CORE
- AUTOCLAVE CURE



Baseline Graphite/Epoxy Door  
Figure 11

# THERMOPLASTIC REDESIGN



- IM7/PEEK TAPE
- INTEGRAL BEAD STIFFENED
- DIAPHRAGM FORMED OUTER SKIN
- DIAPHRAGM FORMED INNER DOUBLER
- DUAL POLYMER BONDED ASSEMBLY

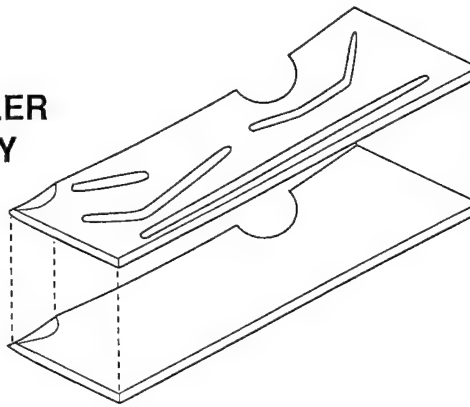
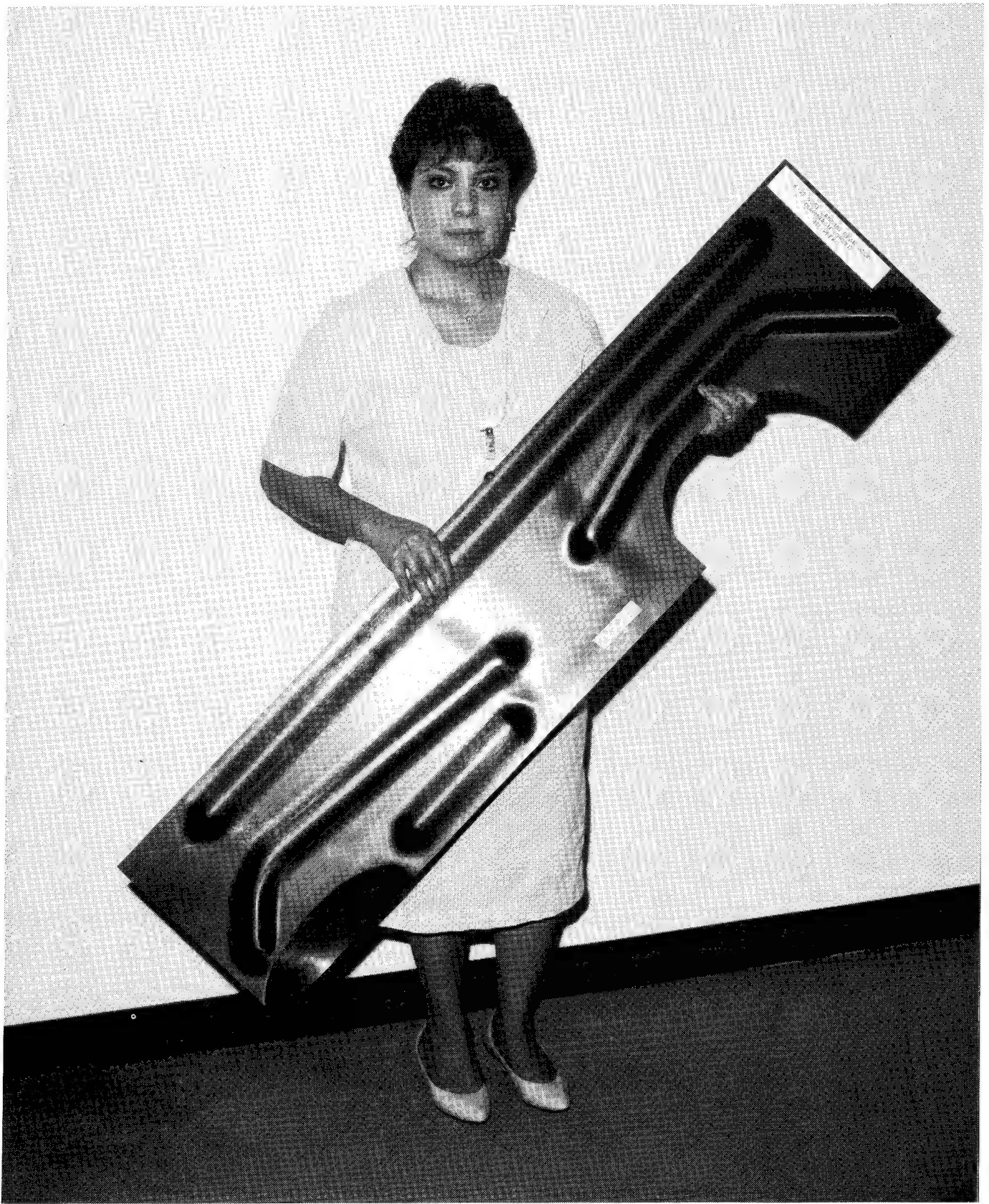


Figure 12

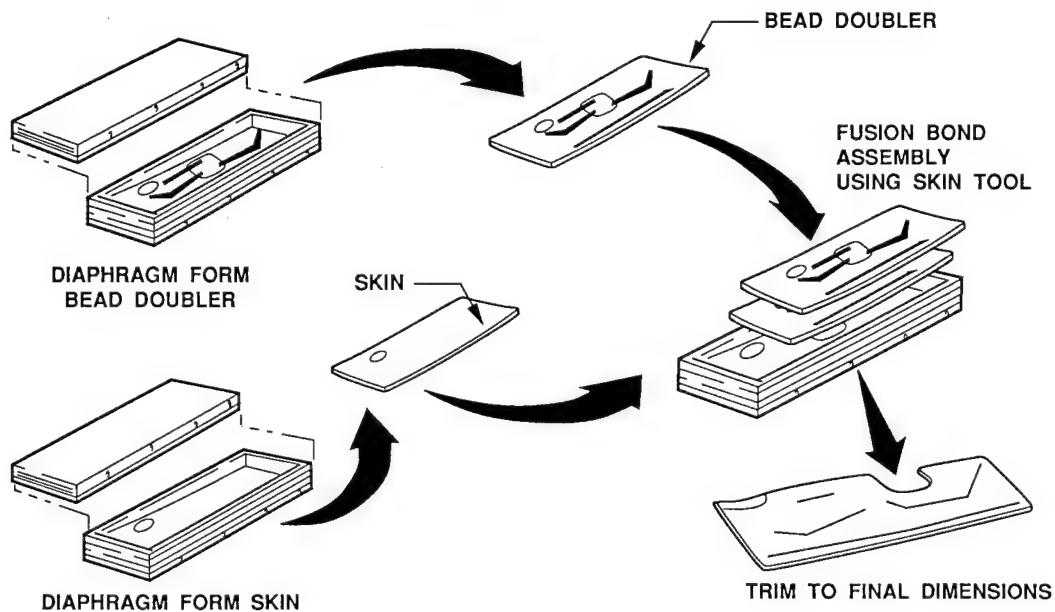




Completed Thermoplastic Door Assembly  
Figure 13

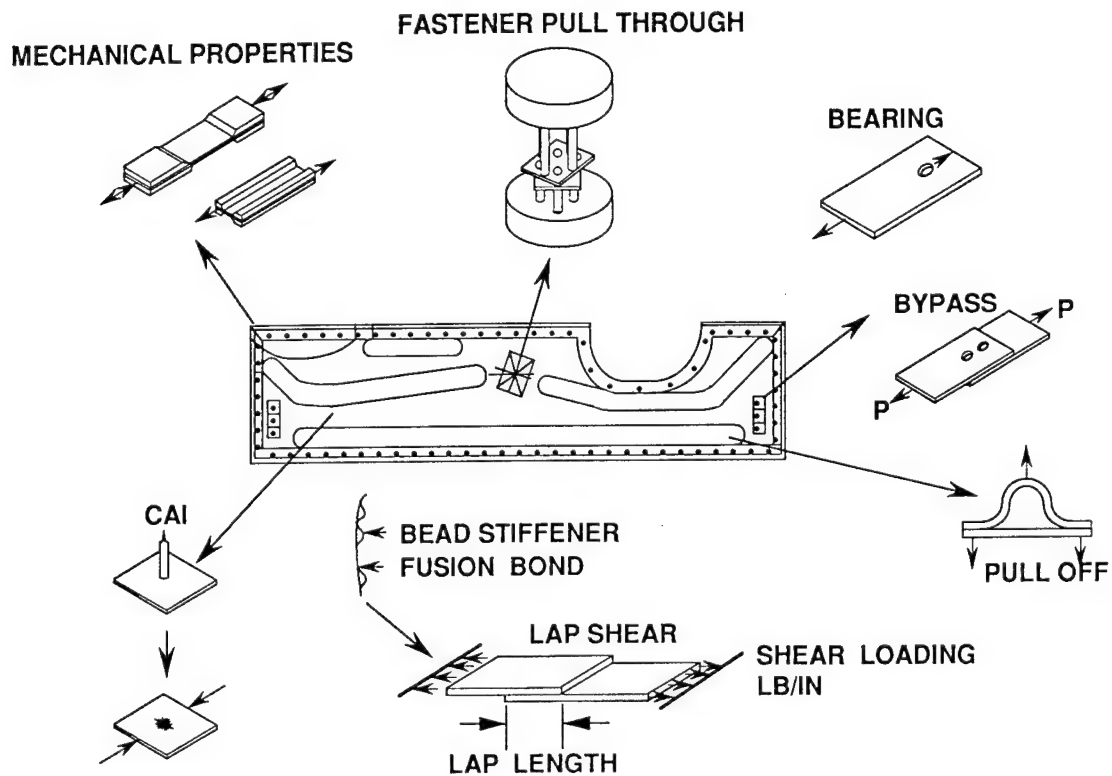


# THERMOPLASTIC LANDING GEAR DOOR



Manufacturing Approach  
Figure 14

# DESIGN DEVELOPMENT TESTING



Design Development Testing  
Figure 15

# FABRICATION LABOR COMPARISON

THERMOPLASTIC (PEEK/IM7)	BASELINE (3501/AS4)
<ul style="list-style-type: none"> <li>• SEAM BY HAND</li> <li>• CUT PLIES MANUALLY</li> <li>• STACK PLIES LOOSELY</li> <li>• PLACE BETWEEN ALUMINUM SHEETS (INNER AND OUTER PANELS FORMED SEPARATELY)</li> <li>• DIAPHRAGM FORM IN PRESS</li> <li>• FUSION BOND IN PRESS</li> <li>• TRIM</li> </ul>	<ul style="list-style-type: none"> <li>• STABILIZE CORE</li> <li>• TRIM CORE</li> <li>• CHAMFER CORE</li> <li>• AUTO CUT PLIES</li> <li>• FORM AND STACK PLIES</li> <li>• INSERT CORE</li> <li>• FORM AND STACK REMAINING PLIES</li> <li>• VACUUM BAG</li> <li>• FORM IN AUTOCLAVE</li> <li>• TRIM</li> </ul>
MANHOURS = 24.9	MANHOURS = 45.7

Fabrication Labor Comparison  
Figure 16



Fit-Check Installation  
Figure 17

## A PROTECTION AND DETECTION SURFACE (PADS) FOR DAMAGE TOLERANCE

M. J. Stuart  
NASA Langley Research Center  
Hampton, Virginia

C. B. Prasad  
AS&M, Inc.  
Hampton, Virginia

S. B. Biggers\*  
Lockheed Aeronautical Systems Co.  
Burbank, California

### ABSTRACT

A protection and detection surface (PADS) concept has been studied for application to composite primary aircraft structures. A Kevlar-epoxy woven face sheet with a Rohacell foam core was found to be the most effective PADS configuration among the configurations evaluated. The weight of the PADS configuration was estimated to be approximately 17 percent of the structural weight. The PADS configuration was bonded to graphite-epoxy base laminates, and up to a 70 percent improvement in compression-after-impact failure strains was observed.

### INTRODUCTION

Cost-effective, weight efficient composite structures should also be damage tolerant. Damage tolerance for composite structures has been achieved using a materials approach (e.g., tough material systems [1-3]) and/or a structures approach (e.g., structural concepts having redundant load paths [4]). These approaches minimize the structural performance degradation due to damage by minimizing the extent of damage propagation. However, these approaches do not contribute to damage detectability during routine inspection. The undetectability of damage can dominate the design criteria for some structural components. A simple approach is needed that both minimizes performance degradation and indicates the location of potential damage.

The current investigation was conducted to study a protection and detection surface (PADS) concept for application to composite primary aircraft structures. This PADS concept utilizes a lightweight sandwich construction that can be applied to the outer surface of a structure. The PADS concept protects a structure from critical impact events by absorbing impact energy and enables simple and reliable detection of the location of potential point-source damage. A preliminary study was conducted to identify effective PADS constituents and to evaluate the behavior of composite laminates with the PADS concept. The PADS constituents' performance was evaluated on the basis of damage visibility and damage

---

\* Currently Associate Professor, Clemson University.

protection. The best performing design was selected for use in a structural evaluation of the PADS concept. The structural evaluation tests were conducted to quantify the effects of the PADS concept on the compression-after-impact behavior of graphite-epoxy laminates. Laminate strength and failure strain are reported as a function of impact energy for both a brittle-matrix material system and a toughened-matrix material system.

## TEST SPECIMENS

Two types of test specimens were used in this study. PADS constituent specimens were impacted to evaluate the performance of several face-sheet/core combinations. PADS concept evaluation specimens were compression loaded to determine the effects of the PADS concept on a laminate's compression-after-impact behavior.

Identification of commercial products and companies in this report is used to describe adequately the test materials. The identification of these commercial products does not constitute endorsement, expressed or implied, of such products by the National Aeronautics and Space Administration.

### Constituent Specimens

The constituent specimens were fabricated using a face-sheet material, a core material, and a base laminate material. Four commercially available thermosetting materials were chosen as face-sheet candidates. These materials were DuPont Kevlar-49/Fiberite MXM-7714, Ferro S-glass/293, Hercules AS4/3501-6, and Hercules AS4/American Cyanamid HST-7. These materials were selected because they represent a tough fiber, a cost-effective fiber, a brittle graphite-epoxy, and a toughened graphite-epoxy, respectively. The first three materials were 10-mil-thick, plain-weave preimpregnated cloth, and the AS4/HST-7 material was 5.5-mil-thick, unidirectional preimpregnated tape. Each cloth material was laid-up to form 3-ply laminates approximately 0.030 in. thick. The stacking sequence for these laminates was  $[+45/0/-45]_t$ . The unidirectional tape was laid-up to form 6-ply laminates approximately 0.033 in. thick. The stacking sequence for these laminates was  $[\pm 45/0/90/\mp 45]_t$ . Preliminary testing with 0.020-in.-thick face sheets indicated that 0.030-in.-thick face sheets were needed to achieve significant damage reduction.

Four commercially available materials were chosen as PADS core candidates. These materials were aluminum honeycomb and DuPont Nomex honeycomb (each 8.0 lbs/ft<sup>3</sup> (pcf)), Rohr 110 WF Rohacell foam (6.9 pcf), and multiple layers of American Cyanamid FM-73 adhesive (total weight 8.0 pcf). The aluminum core was chosen because it offered plastic deformability. The Nomex core was chosen because of its common usage in composite structures. The Rohacell core was chosen because of its uniform small cell size and ease of machining. The layered FM-73 adhesive was chosen because of its compactness. The core was 0.25 in. thick except for selected cases with a 0.125-in.-thick core and layered FM-73

adhesive. In the latter case the thickness was chosen to provide a weight approximately equal to the 0.25-in.-thick core materials. Preliminary testing on lower density core materials indicated the need for core densities at least in the 7 to 8 pcf range.

The base laminate material was AS4/3501-6 graphite-epoxy preimpregnated tape. These tapes were laid-up to form 48-ply laminates approximately 0.25 in. thick, and the laminate stacking sequence was  $[+45/0/-45/90]_{6S}$ .

All laminates were cured in an autoclave using the manufacturers' recommended procedures. Following cure, the laminates were ultrasonically C-scanned to establish specimen quality. The face sheets and cores were cut to 4 in. squares; the base laminates were cut to 5.0 in. squares. Each face-sheet/core combination was centered on a base laminate, and the face sheet, core, and base laminate were bonded using FM-73 adhesive. The PADS constituent specimens evaluated in this study are summarized in Table 1. A total of 105 constituent specimens were tested.

### Concept Evaluation Specimens

The concept evaluation specimens consist of base laminates with the test section protected by a PADS concept. The PADS concept was the same for all the evaluation specimens and was selected based on the constituent specimen results. The PADS concept covered a 4-in.-square area. The base laminates were fabricated using either AS4/3501-6 or AS4/HST-7 graphite-epoxy materials. Pre-impregnated tapes were laid-up to form 48-ply laminates. The stacking sequence for all the AS4/3501-6 and for most of the AS4/HST-7 laminates was  $[\pm 45/0_2/\mp 45/90_2]_{3S}$ . Some of the AS4/HST-7 laminates were inadvertently fabricated as  $[\pm 45/0_2/\mp 45/90_2/\pm 45/90_2/\mp 45/90_2/\pm 45/0_2/\mp 45/90_4/\pm 45/90_2/\mp 45/90_2/\pm 45/90/0/\mp 45/90_2/\pm 45/90_2/\mp 45]_t$  laminates. The stacking sequence for these unsymmetric laminates was determined using a deply technique [5]. The AS4/3501-6 and AS4/HST-7 laminates were nominally 0.25 in. thick and 0.31 in. thick, respectively. All the AS4/3501-6 and most of the AS4/HST-7 laminates were 10.0 in. long and 5.0 in. wide. Some of the AS4/HST-7 laminates were 10 in. long and 7.0 in. wide. Concept evaluation specimens having AS4/3501-6 base laminates are subsequently referred to herein as 3501-6 specimens, and concept evaluation specimens having AS4/HST-7 base laminates are subsequently referred to as HST-7 specimens. A total of 74 concept evaluation specimens were tested.

## APPARATUS AND TESTS

### Impacts

Specimens were impacted on the PADS-protected region using either a projectile from a compressed air gun or a dropped weight. A procedure for air-gun impacting graphite-epoxy components is detailed in reference 6, and this procedure was used in the current investigation. Aluminum spheres 0.5 in. in diameter were used



as impact projectiles. These spheres were propelled by a compressed air gun equipped with an electronic detector to measure projectile speed. A schematic drawing of the air gun and a description of its operation are also given in reference 6. For convenience, this type of impact is subsequently referred to as a projectile impact. Projectile impacts were performed at speeds ranging from approximately 100 ft/s to 500 ft/s which correspond to impact energies of 1.0 ft-lb to 25.5 ft-lbs, respectively. Dropped-weight impacts were performed using a 10-lb weight with a 0.5-in.-diameter hemispherical head at energy levels ranging from 4.0 to 50.0 ft-lbs. The projectile and dropped weight were directed normal to the plane of the specimen, and all specimens were impacted at the center of the PADS-protected region. Specimen edges were supported by fixtures during impacting. An example of such a fixture is the test fixture shown in Figure 1.

### **Compression Loading**

Concept evaluation specimens were loaded in axial compression using a 300-kip-capacity hydraulic testing machine. The loaded ends of the specimen were clamped by fixtures during testing and the unloaded sides were simply supported by restraints to prevent the specimen from buckling as a wide column. All specimens were tested to failure by gradually applying a compressive load to simulate a static loading condition. A typical specimen mounted in the support fixture is shown in Figure 1.

Electrical resistance strain gages were used to monitor strains, and direct-current differential transformers were used to monitor longitudinal displacements of the specimen ends. Electrical signals from the instrumentation and the corresponding applied loads were recorded on magnetic tape at regular time intervals during the test.

## **RESULTS AND DISCUSSION**

This section describes results from the constituent tests and from the concept evaluation tests. Combinations of the PADS constituents were evaluated on the basis of damage visibility and damage protection to determine the most effective PADS configuration. This PADS concept was evaluated to determine the effects of impact damage on the compression-after-impact response of composite laminates.

### **Constituent Tests**

*Impact Site Damage Visibility* - The ease with which a critical impact site can be located was the first criterion by which the PADS designs were evaluated. The PADS designs were qualitatively rated visually, and the indentation depths were measured.

Photographs of impacted surfaces are shown in Figure 2 for a woven Kevlar-Rohacell foam PADS configuration. These photographs illustrate the impact site visibility for five impact energy levels. Labels having energy levels accompanied by speeds are for specimens with air-gun projectile impacts. Labels having only

energy levels are for specimens with dropped-weight impacts. The woven fiberglass face sheets provided visibility at the lowest impact levels due to surface crazing. The woven graphite-epoxy face sheets provided slightly inferior visibility. All core materials performed acceptably well with the exception of the layered FM-73 adhesive core which gave only marginal visibility improvement compared to a specimen without PADS. The impact sites for the specimens without PADS were not visible at an energy level.

Surface indentation depths were measured and are categorized by core material and impact energy level in Figure 3. The impact sites were visually classified qualitatively and then related to the indentation depths as shown below:

Indentation Depth, in.	Visibility
<.008	Not Visible
>.008 and <.040	Barely Visible
>.040 and <.080	Visible
>.080	Easily Visible

The height of the bar in Figure 3 represents the range of indentation depths measured for the four face-sheet materials. The layered FM-73 adhesive core material is ineffective for improving damage visibility. The other three core materials perform about equally well with the aluminum honeycomb being slightly more effective than the other two.

The surface indentation data are also affected by the PADS face-sheet material. These data are plotted in Figure 4. The height of the bars on this figure represents the range of indentation depths measured for the three acceptable core materials. The data for the layered FM-73 adhesive specimens are not plotted. In all but one case, the woven Kevlar face sheet provided the most damage visibility when indicated by indentation depth.

Damage Protection - Average damage areas were measured from C-scans of constituent specimen base laminates. Micrographs of selected specimens confirmed the C-scan results. The measured damage areas are summarized in Figure 5 where they are categorized with respect to core material versus impact energy level. The height of the bars in this figure represents the range of damage measured for the four face sheet materials. The data show that the layered FM-73 adhesive core and the thinner (0.125 in.) Rohacell and Nomex cores are ineffective in reducing damage to the base laminate. The 0.25-in.-thick Rohacell, Nomex, and aluminum honeycomb cores all performed well. The Nomex and the Rohacell cores were slightly more effective than the aluminum honeycomb core since both of these cores eliminated damage at the intermediate impact energy levels and reduced damage area by approximately 50 percent at the highest impact energy level.

The damage area data are also affected by a configuration's face sheet material, and these data are plotted in Figure 6. The data for the layered FM-73 adhesive core and the thin (0.125 in.) cores are not included due to their poor performance. The height of the bars in this figure represents the range of damage for the acceptable core materials. The four face-sheet materials have essentially equal performance with respect to damage protection. The AS4/HST-7 tape and the Kevlar cloth face-sheet materials appear to be slightly more effective for minimizing damage area when compared to the other face-sheet materials.

In summary, significant damage protection was achieved with any of the face sheets combined with the Nomex or Rohacell cores. The aluminum honeycomb core was only slightly less effective.

*PADS Design for Compression-After-Impact Testing* - Since many of the PADS designs proved to be effective in both increasing impact-site visibility and in providing damage protection to the structural laminate, the selection of a design for further evaluation was based somewhat on secondary considerations. Kevlar cloth was selected as the face sheet material because of its excellent performance in both primary evaluations and because of its low weight and ease of fabrication. Rohacell foam (0.25 in. thick, 110 WF) was selected as the core material because of its excellent performance, its ease of fabrication and its slight weight advantage compared to the honeycomb cores.

### **Concept Evaluation**

Failure data for the concept evaluation specimens indicate a significant effect of the PADS concept on a laminate's compression-after-impact (CAI) behavior. Results are presented in Tables 2-8 and Figures 7-10 for specimen strength and failure strain. The failure data do not appear to be a function of the method used to impact the specimen. Also, the unsymmetric stacking sequence for some laminates does not appear to affect the failure results. The strength and failure strain data are plotted as a function of impact energy for the 3501-6 specimens in Figures 7 and 8 and for the HST-7 specimens in Figures 9 and 10. The symbols on the figures correspond to the experimental data, and the solid lines are lower bounds for these data. The results on the figures show that the laminates without the PADS concept have CAI failure strains that approach 0.40 percent for the 3501-6 specimens in this study and 0.50 percent for the HST-7 specimens in this study as the impact energy increases. The laminates with the PADS concept have CAI failure strains greater than 0.60 percent for the 3501-6 specimens in this study and greater than 0.85 percent for the HST-7 specimens in this study for the impact energies considered. These failure strain data demonstrate a 50 percent improvement in CAI failure strain for the 3501-6 specimens and a 70 percent improvement in the CAI failure strain for the HST-7 specimens. These improvements are a direct result of the PADS concept.

The structural efficiency of the selected PADS concept for AS4/HST-7 laminates is shown in Figure 11. Results are presented for a weight index  $W/AL$  (where  $W$  is the structural weight,  $A$  is the cross-sectional area, and  $L$  is the laminate length)

versus a load index  $N_x/L$  (where  $N_x$  is the compressive stress resultant). These results were obtained using the PASCO panel analysis and sizing computer program [7]. The 0.003 in./in. strain has been used as a maximum design strain for brittle-matrix composite structures. The 0.006 in./in. strain is a typical design strain for heavily loaded wing structures. A simple conservative calculation to approximate the weight of a composite structure with the PADS concept indicates that the weight of the PADS concept is approximately 17 percent of the structural weight. This calculation is based on considering a flat, 48-ply (0.31-in. thick) laminate. The laminate has an areal weight of 2.68 lbs/ft<sup>2</sup>, and the PADS concept has an areal weight of 0.46 lbs/ft<sup>2</sup>. The analytical structural efficiency results shown on the figure reflect the 17 percent increase in structural weight for structures with the PADS concept and with a 0.006 maximum design strain. The results on the figure show that the heavily-loaded structures with the PADS concept are more structurally efficient than the heavily-loaded structures with a 0.003 maximum design strain and without the PADS concept. The weight of the PADS concept for structures loaded by  $N_x/L > 250$  lbs/in.<sup>2</sup> is more than offset by the structural weight savings from using a 0.006 in./in. maximum design strain. The PADS concept appears to be an effective damage tolerant concept that will allow higher ultimate strain designs for heavily loaded composite structures without significant weight increases.

#### CONCLUDING REMARKS

A protection and detection surface (PADS) concept has been studied for application to composite primary aircraft structures. The PADS concept utilizes a lightweight sandwich construction, and combinations of four face sheets and four cores were evaluated on the basis of damage visibility and damage protection. The [+45/0/-45]<sub>t</sub> Kevlar-epoxy woven face sheet with a 110-WF Rohacell foam core was found to be the most effective PADS configuration among those configurations evaluated. This PADS configuration was bonded to AS4/3501-6 and AS4/HST-7 base laminates to assess the effect of the PADS concept on a laminate's compression-after-impact (CAI) behavior. For the impact conditions studies, the failure strain data demonstrate a 50 percent improvement in CAI failure strain for the 3501-6 specimens and a 70 percent improvement in the CAI failure strain for the HST-7 specimens. These improvements are a direct result of the PADS concept. A simple conservative calculation to approximate the weight of a composite structure with the PADS concept indicates that the weight of the PADS concept is approximately 17 percent of the structural weight. The weight of the PADS concept for heavily-loaded composite structures is more than offset by the structural weight savings that results from increased maximum design strains. The PADS concept appears to be an effective damage tolerant concept that will allow higher ultimate strain designs for heavily-loaded composite structures without significant weight increases.

## REFERENCES

1. Williams, J. G.; O'Brien, T. K.; and Chapman, A. J.: Comparison of Toughened Composite Laminates Using NASA Standard Damage Tolerant Tests. ACEE Composite Structures Technology, NASA CP-2321, August 1984, pp. 51-74.
2. Dexter, H. B.; and Funk, J. G.: Impact Resistance and Interlaminar Fracture Toughness of Through-The-Thickness Reinforced Graphite/Epoxy. AIAA Paper No. 86-1020-CP.
3. Johnston, N. J.; and Hergenrother, P. M.: High Performance Thermoplastics: A Review of Neat Resin and Composite Properties. SAMPE, Vol. 32, February 1987, pp. 1400-1412 (Also available as NASA TM 89104).
4. Haftka, R. T.; Starnes, J. H., Jr.; and Nair, S.: Design for Global Damage Tolerance and Associated Mass Penalties. Journal of Aircraft, Vol. 20, January 1983, pp. 83-88.
5. Freeman, S. M.: Characterization of Lamina and Interlaminar Damage in Graphite/Epoxy by the Deply Technique. Composite Materials: Testing and Design (6th Conference), ASTM STP 787, I. M. Daniel, ed., American Society for Testing and Materials, 1982, pp. 50-62.
6. Starnes, J. H., Jr.; Rhodes, M. D.; and Williams, J. G.: Effect of Impact Damage and Holes on the Compressive Strength of a Graphite/Epoxy Laminate. Nondestructive Evaluation and Flaw Criticality for Composite Materials, ASTM STP 696, R. B. Pipes, ed., American Society for Testing and Materials, 1979, pp. 145-171.
7. Anderson, M. S.; and Stroud, W. J.: A General Panel Sizing Code and Its Application to Composite Structural Panels. AIAA Journal, Vol. 17, No. 8, August 1979, pp. 892-897.

Table 1. PADS configurations for constituent tests.

Specimen Number	Face Sheet Material <sup>a</sup>	Face Sheet Lay-up	Core Thickness, in.	Core Material <sup>b</sup>
C1	Kevlar	[+45/0/-45] <sub>t</sub>	0.25	A
C2	.	.	0.25	N
C3	.	.	0.25	R
C4	.	.	0.035	AD
C5	Glass	.	0.25	A
C6	.	.	0.25	N
C7	.	.	0.25	R
C8	.	.	0.035	AD
C9	Graphite	.	0.25	A
C10	.	.	0.25	N
C11	.	.	0.25	R
C12	.	.	0.035	AD
C13	Tape	[±45/0/90/∓45] <sub>t</sub>	0.25	A
C14	.	.	0.25	N
C15	.	.	0.25	R
C16	.	.	0.035	AD
C17	Tape	.	0.125	N
C18	Tape	.	0.125	R
C19	Kevlar	[+45/0/-45] <sub>t</sub>	0.125	N
C20	Kevlar	.	0.125	R

<sup>a</sup> Kevlar: Ke/MXM-7714, 10 mil, plain-weave cloth  
 Glass: S-glass/293, 10 mil, plain-weave cloth  
 Graphite: AS4/3501-6, 10 mil, plain-weave cloth  
 Tape: AS4/HST-7, 5.5 mil, tape

<sup>b</sup> A: aluminum honeycomb, 8.0 pcf  
 N: Nomex honeycomb, 8.0 pcf  
 R: 100 WF Rohacell, 6.9 pcf  
 AD: multiple layers of FM 73 adhesive, 8.0 pcf

Table 2. Failure data for AS4/3501-6 specimens without PADS impacted using a dropped weight.

Specimen Number	Impact Energy, ft-lbs	Strength, ksi
DW1-1	20.0	25.7
DW1-2	20.0	25.5
DW1-3	20.0	26.5
DW1-4	31.3	20.1
DW1-5	31.3	23.7
DW1-6	31.3	21.2
DW1-7	50.0	18.5
DW1-8	50.0	18.9
DW1-9	50.0	19.5

Table 3. Failure data for AS4/3501-6 specimens without PADS impacted using a projectile from a compressed air gun.

Specimen Number	Impact Energy, ft-lbs	Strength, ksi	Failure Strain, percent <sup>a</sup>
G1-1	4.1	56.6	b
G1-2	4.2	58.8	b
G1-3	4.0	48.4	b
G1-4	8.9	30.5	b
G1-5	9.3	26.8	b
G1-6	9.2	30.9	b
G1-7	17.2	25.5	0.45
G1-8	16.5	25.3	0.47
G1-9	16.3	26.0	0.46
G1-10	25.3	19.8	0.41
G1-11	24.8	19.7	0.41
G1-12	25.1	21.2	0.41

<sup>a</sup> Failure strain calculated using laminate end-shortening and original length rather than measured by strain gages.

<sup>b</sup> Failure strain data unavailable.



Table 4. Failure data for AS4/3501-6 specimens with PADS impacted using a projectile from a compressed air gun.

Specimen Number	Impact Energy, ft-lbs	Strength, ksi	Failure Strain, percent <sup>a</sup>
G1-13	16.1	63.4	1.08
G1-14	16.5	60.7	1.06
G1-15	16.7	64.9	1.09
G1-16	24.4	39.2	0.69
G1-17	25.2	40.4	0.68
G1-18	24.8	32.1	0.64

<sup>a</sup> Failure strain calculated using laminate end-shortening and original length rather than measured by strain gages.

Table 5. Failure data for AS4/HST-7 specimens without PADS impacted using a dropped weight.

Specimen Number	Impact Energy, ft-lbs	Strength, ksi	Failure Strain, percent <sup>a</sup>
DW2-1	0.	58.2	1.24
DW2-2	14.1	63.6	b
DW2-3	14.1	57.4	1.22
DW2-4	14.1	53.9	1.07
DW2-5	16.9	59.3	1.38
DW2-6	22.6	41.9	b
DW2-7	22.6	41.5	b
DW2-8	24.0	49.9	1.07
DW2-9	31.3	33.2	0.69
DW2-10	31.3	35.1	0.71
DW2-11	31.3	34.1	0.70
DW2-12	50.0	25.8	0.53
DW2-13	50.0	25.5	0.51
DW2-14	50.0	27.2	0.54
DW2-15	50.0 <sup>c</sup>	26.1	0.56
DW2-16	50.0 <sup>c</sup>	26.7	0.57
DW2-17	50.0 <sup>c</sup>	28.2	0.55

<sup>a</sup> Failure strain calculated using laminate end-shortening and original length rather than measured by strain gages.

<sup>b</sup> Failure strain data unavailable.

<sup>c</sup> Impact event: 9.0 ft-lbs followed by 50.0 ft-lbs.

Table 6. Failure data for AS4/HST-7 specimens with PADS impacted using a dropped weight.

Specimen Number	Impact Energy, ft-lbs	Strength, ksi	Failure Strain, percent <sup>a</sup>
DW2-18 <sup>b</sup>	22.6	54.2	1.28
DW2-19 <sup>b</sup>	22.6	51.0	1.19
DW2-20 <sup>b</sup>	22.6	50.7	1.20
DW2-21 <sup>b</sup>	31.3	56.4	1.34
DW2-22 <sup>b</sup>	31.3	57.2	1.36
DW2-23 <sup>b</sup>	31.3	40.9	0.92
DW2-24	50.0	42.7	0.87
DW2-25	50.0	49.8	1.02
DW2-26	50.0	44.6	0.92

<sup>a</sup> Failure strain calculated using laminate end-shortening and original length rather than measured by strain gages.

<sup>b</sup> Base laminate unsymmetric.

Table 7. Failure data for AS4/HST-7 specimens without PADS impacted using a projectile from a compressed air gun.

Specimen Number	Impact Energy, ft-lbs	Strength, ksi	Failure Strain, percent <sup>a</sup>
G2-1	0.	71.0	b
G2-2	5.6	62.9	b
G2-3	5.7	64.9	b
G2-4	9.2	59.0	b
G2-5	9.3	48.2	b
G2-6	9.2	59.6	b
G2-7	9.2	57.7	b
G2-8	9.4	59.6	1.24
G2-9	9.5	61.1	1.31
G2-10 <sup>c</sup>	15.8	47.2	0.97
G2-11 <sup>c</sup>	15.6	42.7	0.85
G2-12 <sup>c</sup>	16.0	41.2	0.75
G2-13 <sup>c</sup>	25.4	37.1	0.68
G2-14 <sup>c</sup>	25.0	37.3	0.70
G2-15 <sup>c</sup>	25.0	39.0	0.74

<sup>a</sup> Failure strain calculated using laminate end-shortening and original length rather than measured by strain gages.

<sup>b</sup> Failure strain data unavailable.

<sup>c</sup> Specimen dimensions: 7 in. long by 10 in. wide; specimens buckled prior to failure.

Table 8. Failure data for AS4/HST-7 specimens with PADS impacted using a projectile from a compressed air gun.

Specimen Number <sup>b</sup>	Impact Energy, ft-lbs	Strength, ksi	Failure Strain, percent <sup>a</sup>
G2-16	16.0	54.4	1.28
G2-17	16.2	53.2	1.25
G2-18	17.4	52.0	1.22
G2-19	24.8	55.8	1.33
G2-20	25.0	53.6	1.26
G2-21	24.3	56.4	1.34

<sup>a</sup> Failure strain calculated using laminate end-shortening and original length rather than measured by strain gages.

<sup>b</sup> Base laminate unsymmetric.

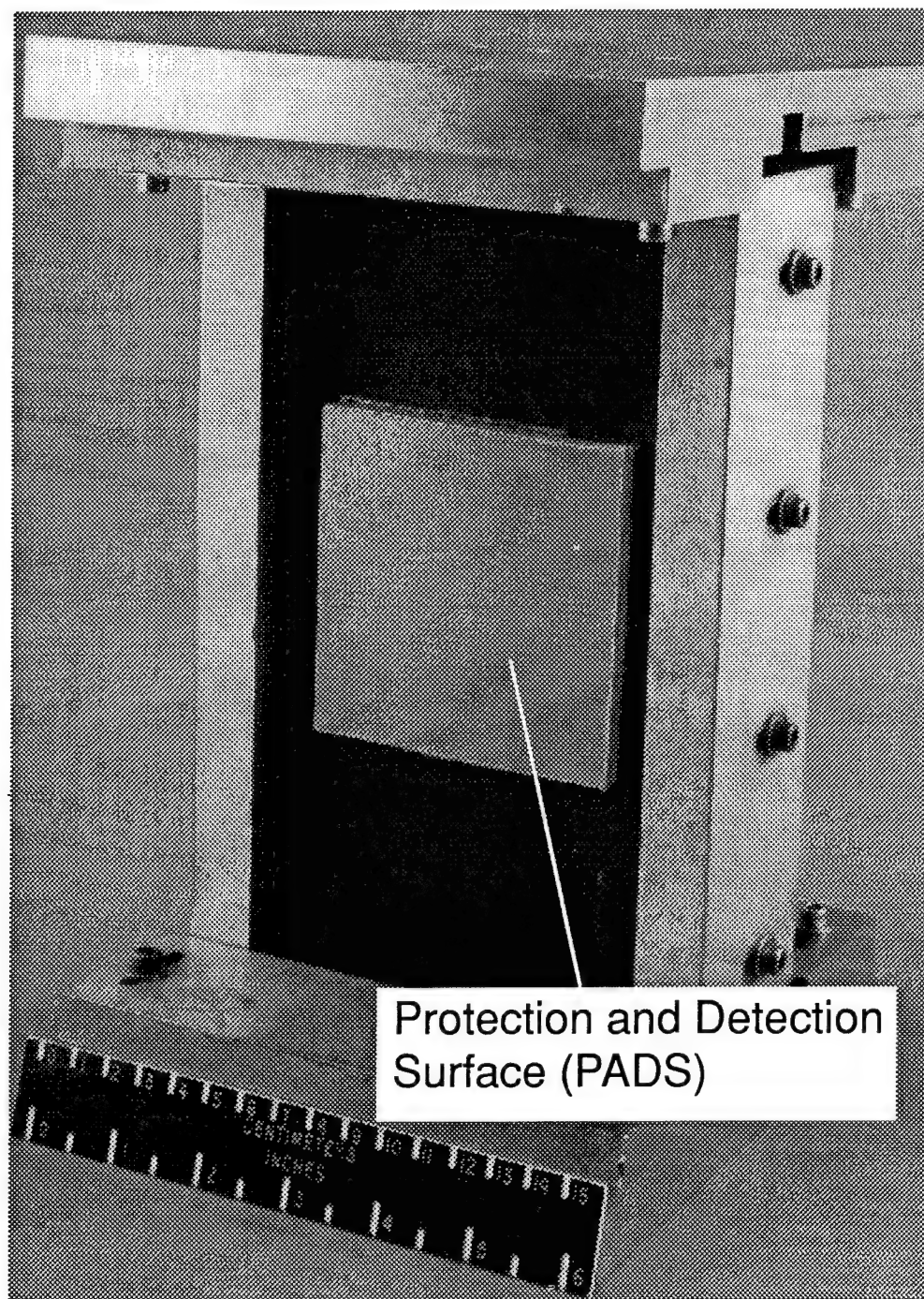


Figure 1. PADS concept evaluation specimen in test fixture.

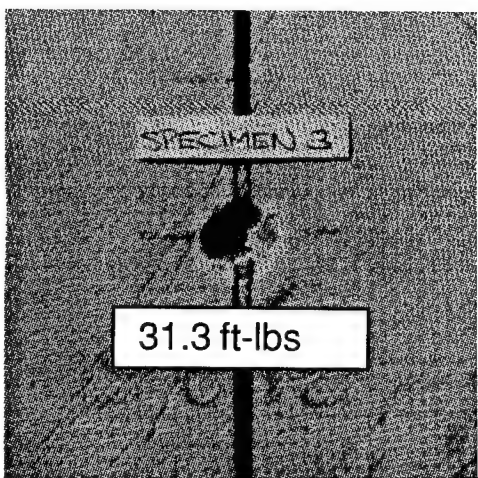
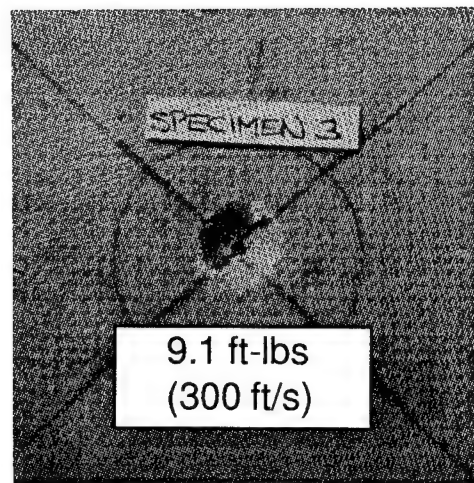
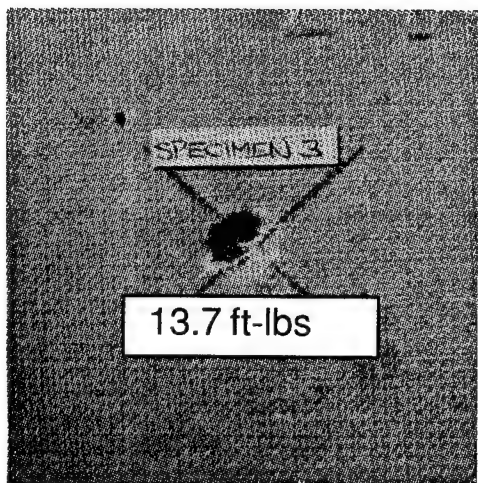
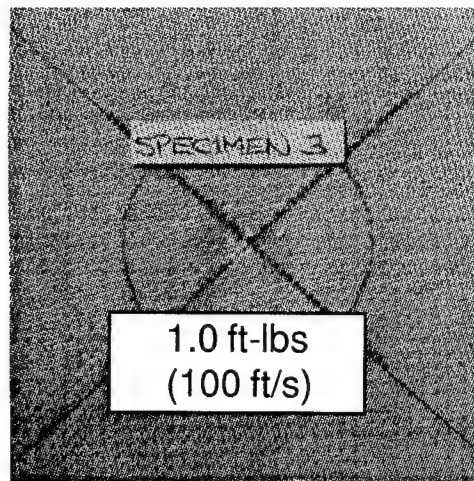
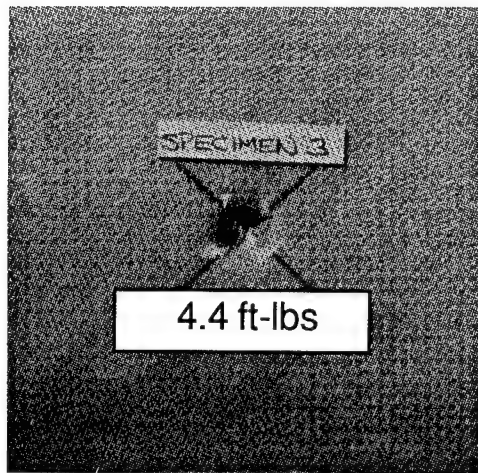


Figure 2. Impact site visibility for woven Kevlar - Rohacell PADS configuration.

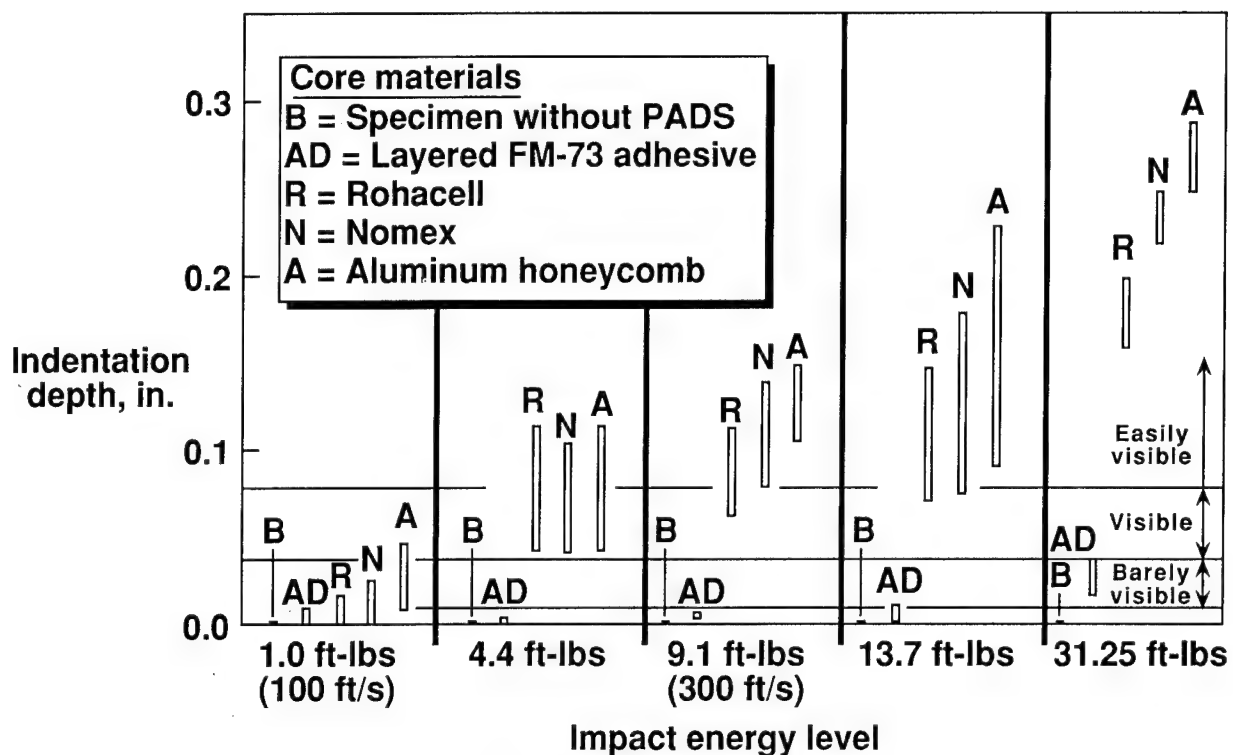


Figure 3. Surface indentation depths for core materials.

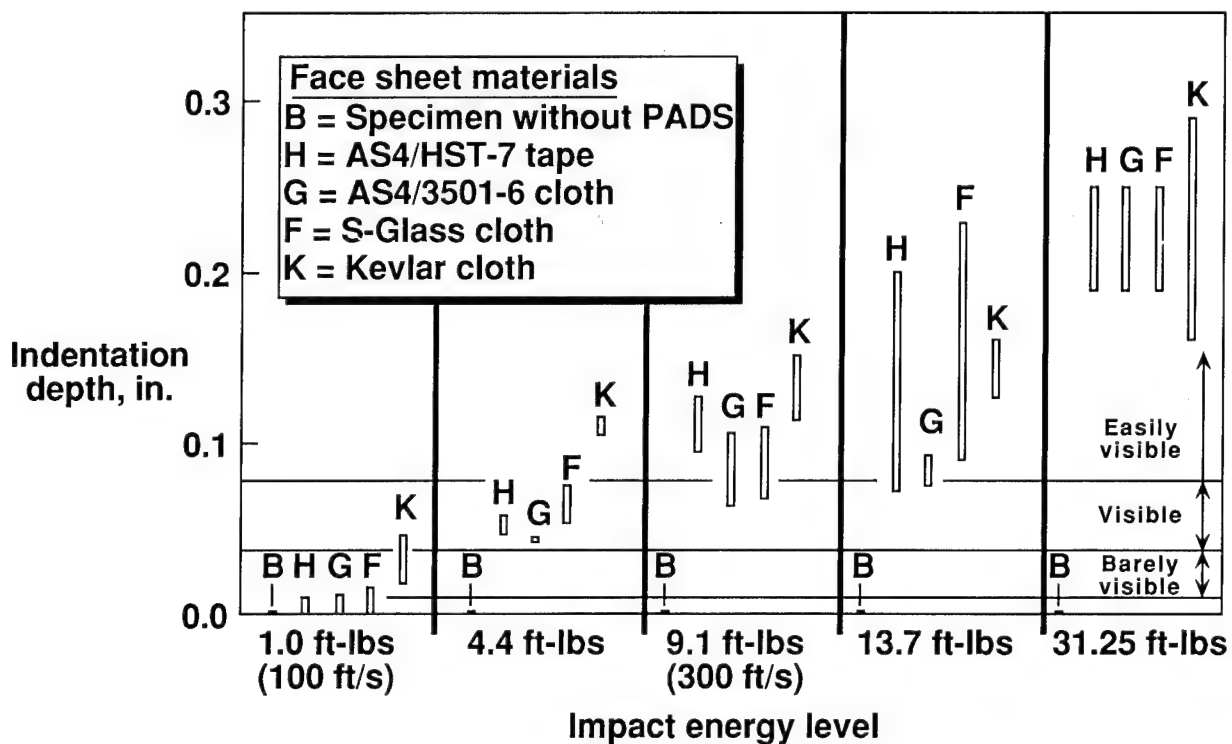


Figure 4. Surface indentation depths for face-sheet materials.

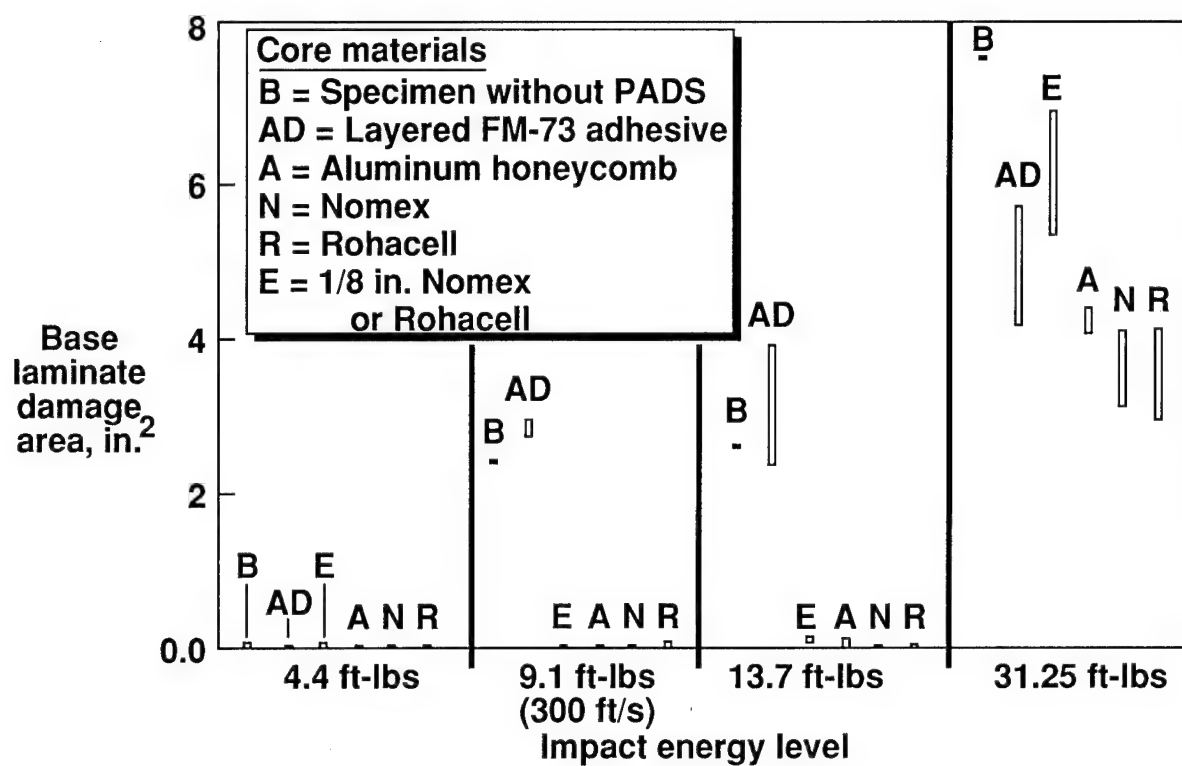


Figure 5. Effect of core materials on damage area for base laminate.



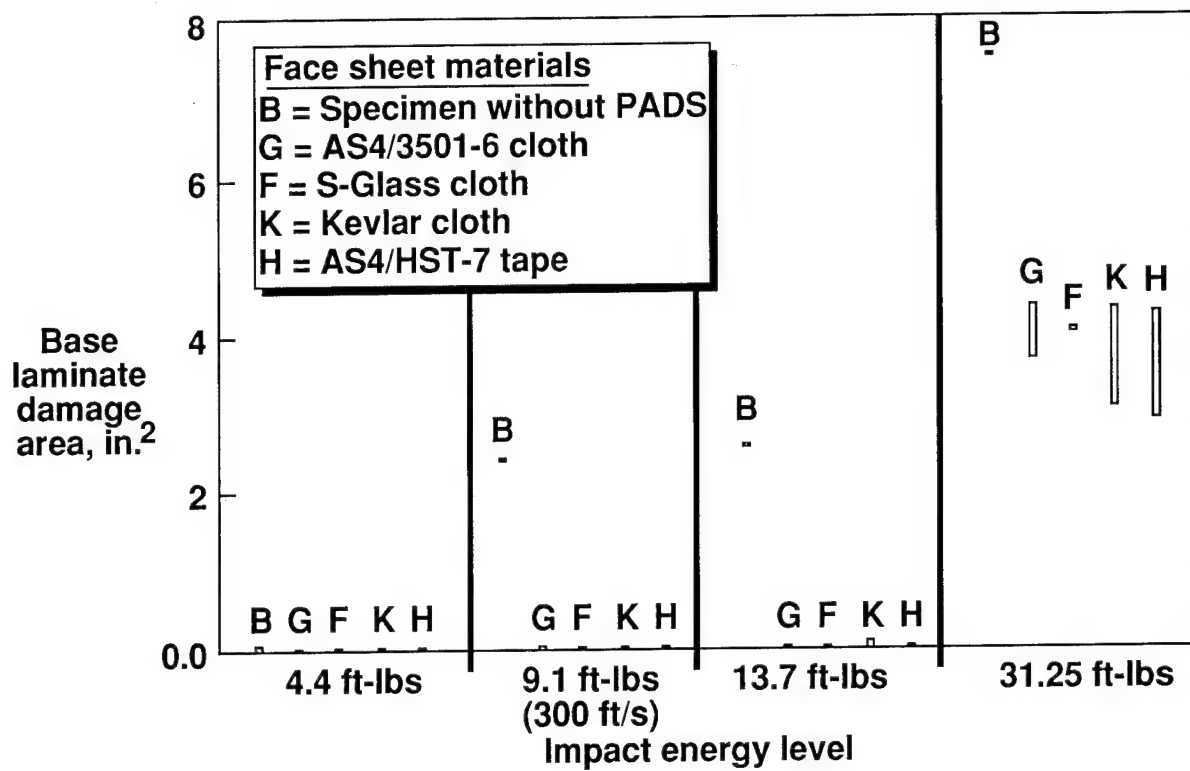


Figure 6. Effect of face-sheet materials on damage area for base laminate.

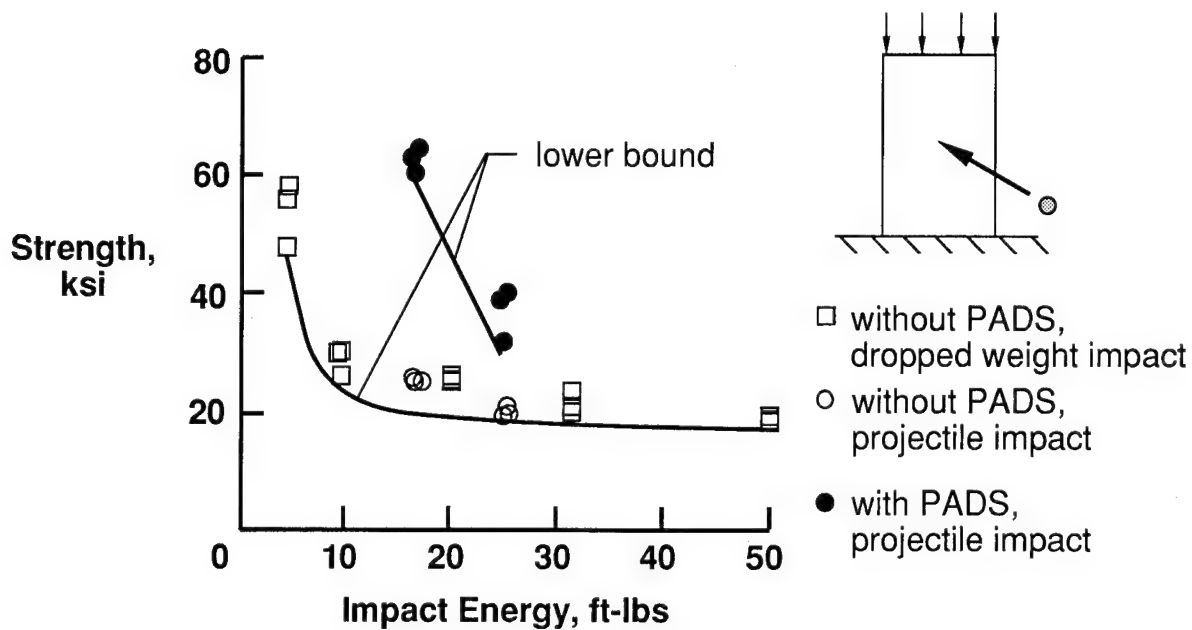


Figure 7. Strength results for impacted AS4/3501-6 specimens.

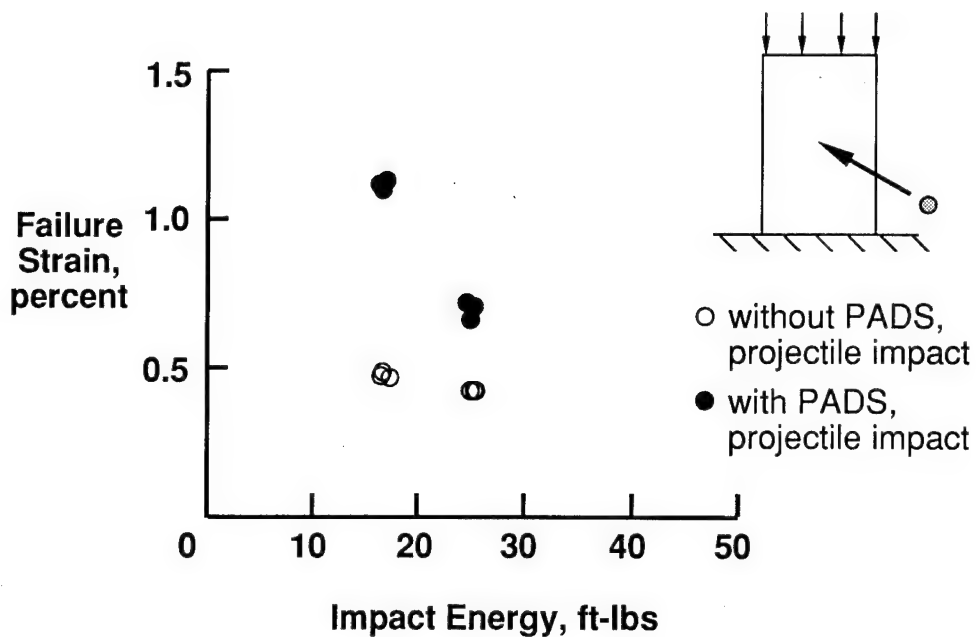


Figure 8. Failure strain results for impacted AS4/3501-6 specimens.

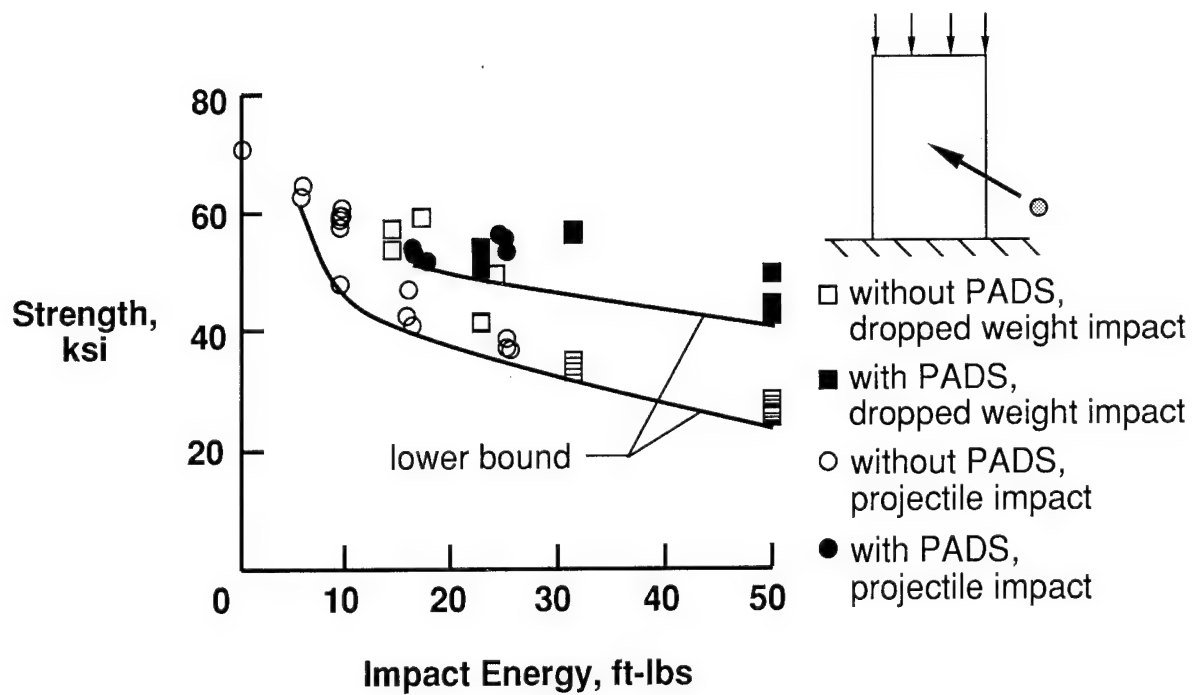


Figure 9. Strength results for impacted AS4/HST-7 specimens.

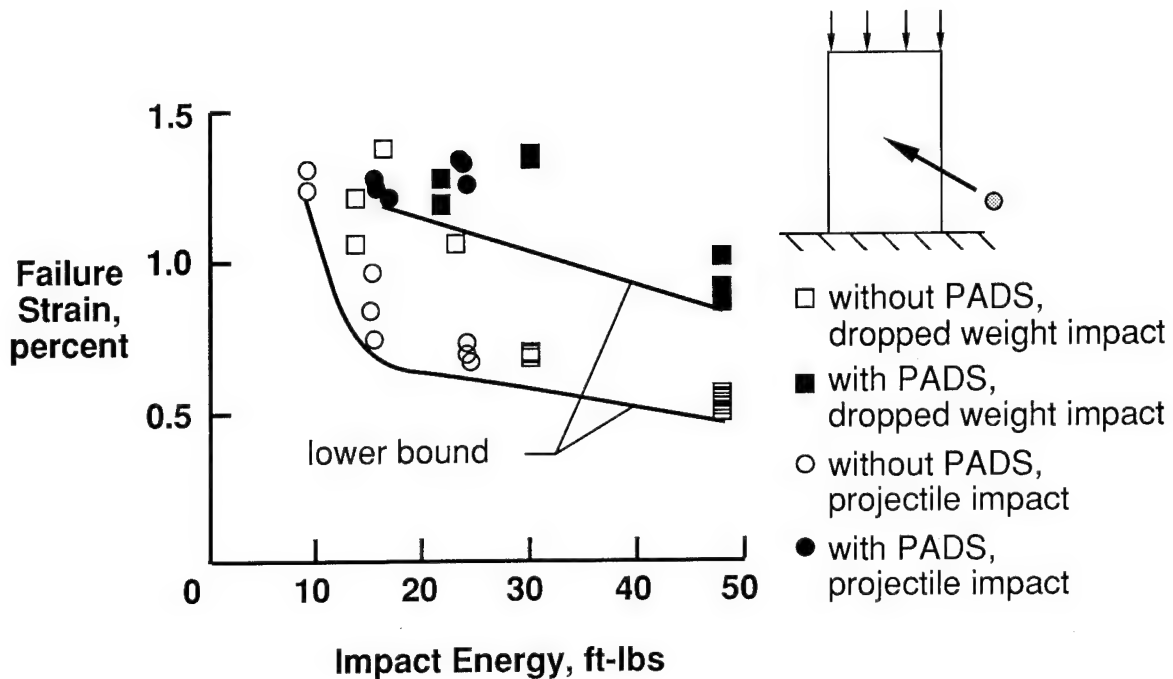


Figure 10. Failure strain results for impacted AS4/HST-7 specimens.

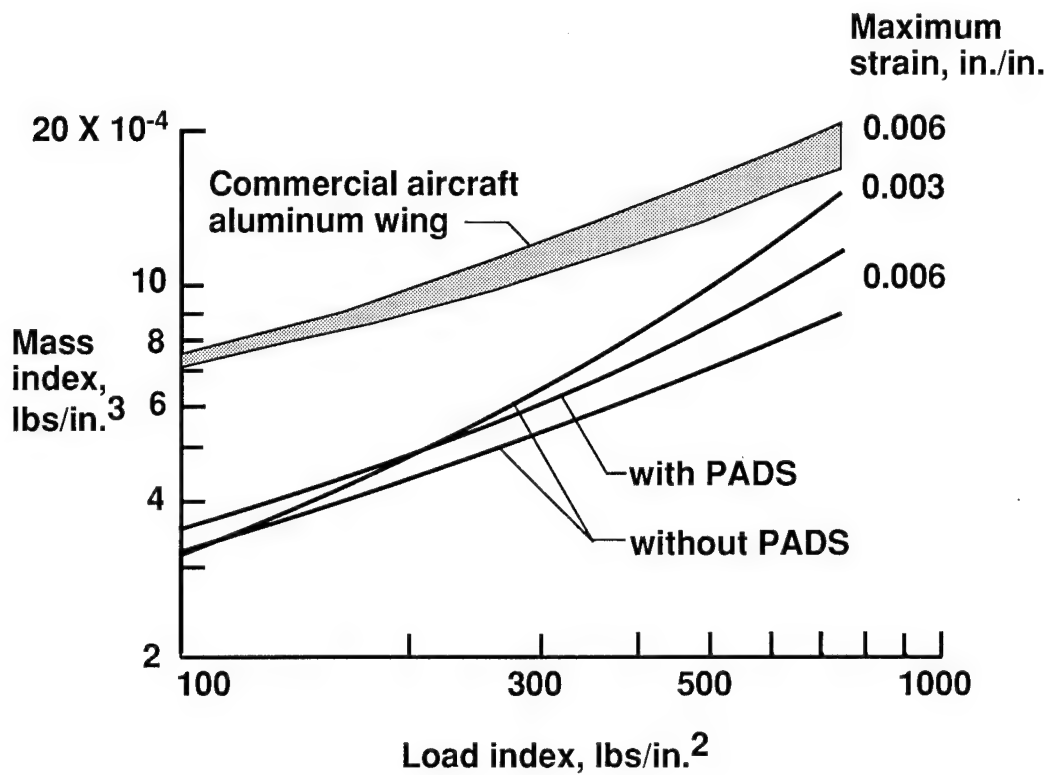


Figure 11. Effect of PADS concept on structural efficiency.

# INVESTIGATION INTO THE FABRICATION OF A COMPOSITE TOP ATTACK RECOILLESS RIFLE

Kevin R. Miner  
U.S. Army Armament Research, Development, and Engineering Center  
Close Combat Armaments Center  
Benet Laboratories  
Watervliet, NY

## SUMMARY

The fabrication of a lightweight, expendable recoilless rifle using composite materials was investigated. Filament winding and braiding were successfully employed in the construction of several of these shoulder-fired weapons.

## INTRODUCTION

A recoilless rifle concept has been proposed which is a man-portable, fire-and-forget antiarmor weapon. The proposed rifle can launch an 11-pound projectile utilizing a unique, polygon-shaped rifled barrel. The counterrecoil and countertorque are provided by canted, kidney-shaped exhaust ports. This concept offers low cost, simplicity, and minimal system weight.

The severe weight restrictions imposed on the rifle system necessitated the use of high-performance composite materials such as fiberglass or carbon-reinforced plastic. The high strength-to-weight ratios achieved through the use of these materials made the manufacture of lightweight and efficient structures as well as the ability to develop complicated geometrical shapes possible. These attributes are exploited in the development of various components of this weapon to meet the performance requirements.

## DESIGN AND FABRICATION

The rifle is designed to meet several key performance criteria including a system weight not to exceed 20 pounds. With a projectile weight of 11 pounds and 1.5 pounds of propellant, this leaves only 7.5 pounds for the rifle tube and supporting hardware. The physical dimensions include a 105-mm bore diameter, a 30-inch barrel length, and a total length of 40 inches. Also, a simple and inexpensive manufacturing process is required to economically produce large numbers of these expendable weapons. To meet the stringent weight requirements, several types of composite materials were examined as candidates for the rifle. They were audited in terms of their cost, processability, specific strength, and modulus. During firing, excessive bore dilation is undesirable; therefore, a high priority was

placed on stiffness as well as strength. Given these factors, an epoxy matrix coupled with a high-strength, intermediate modulus carbon-fiber reinforcement was selected.

A preliminary design was developed to meet the performance requirements as depicted in Figure 1. The 30-inch barrel portion of the rifle had a 12-sided, spiraled polygonal shape which provided the required spin to the projectile. The chamber zone was conical, approximately 10 inches in length expanding to about an 8-inch diameter. A nozzle plate constituted the rear of the rifle and contained four kidney-shaped exhaust ports. The projectile was inserted from the rear of the rifle followed by the propellant and the nozzle plate, which is affixed to the rifle using 12 cap screws passing through the laminate and threading into a ring called the nozzle seal.

The fabrication process involved filament winding the preimpregnated carbon/epoxy material onto an aluminum mandrel followed by curing under heat and pressure. The barrel portion of the mandrel had a 12-sided polygonal shape with a 150-degree twist over its 30-inch length. The distance between flats was 105 mm. The chamber portion was composed of seven radial segments grouped around a 3.25-inch diameter central shaft which was affixed to the barrel portion of the mandrel by a threaded rod passing through its center. These segments were held in place by a nozzle seal which is an integral part of the rifle and is wound into the structure. An end cap was used to hold the nozzle seal onto the segments.

To evaluate the concept of filament winding, several spiraled, polygon-shaped tubes were fabricated using the barrel portion of the mandrel alone. Both ends of the mandrel had a spherical end dome to facilitate the turnaround of the filament during the winding process. Two tubes were made using a laminate composed of hoop and helical layers. It was found that a moderate winding tension of about 5 pounds is optimal and that an external pressure is needed to compact the laminate which tends to bridge the gap between the points of the polygonal shape. During the curing process, the external pressure was exerted by enclosing the mandrel with the wound tube into a sealed bag and drawing a vacuum. This supplied enough pressure to compact the laminate and gave a uniform wall thickness of about 0.2 inch. Two tubes were also fabricated using wound hoop layers and longitudinal layers of unidirectional tape of the same material. These tubes were cured under pressure and compacted well.

A laminate of carbon/epoxy material was designed using a maximum pressure of 7000 psi and a torsional load of 100 lbs·ft. This laminate consisted of six hoop or 90-degree layers and four  $\pm 30$ -degree helical layers and was represented as  $[90_2, \pm 30, 90, \pm 30]_s$ . The approximately 0.125-inch thick laminate was consistent throughout the length of the rifle making it an inefficient but simple structure. The winding process was similar to that of the barrel, but included the chamber portion. The fiber path for the helical winding process started at the muzzle's end dome and followed a constant 30-degree helical path to the base of the chamber. As the fiber path progressed up the slope of the chamber, the helical angle increased to a

90-degree hoop passing over the edge of the nozzle seal to the boss on the end cap and returned to the muzzle end by a similar path completing an entire circuit. This was repeated many times while indexing the mandrel to develop the individual helical plies of the laminate. The hoop layers similarly started at the muzzle end, proceeded towards the nozzle end, and stopped at the rear portion of the chamber zone.

After winding, the laminate was covered with a peel-ply fabric to produce a matte finish. This was followed by a perforated halohydrocarbon release film which controlled the amount of excess resin absorbed by the following two layers of peel-ply. A breather blanket and nylon bagging film enclosed the part and a vacuum was drawn to allow a hydrostatic atmospheric pressure to compact the laminate. The assembly was then placed into an oven for a six-hour 250°F cure cycle with no additional pressure applied.

When the cure cycle was complete, the bagging material was removed. Using the lathe, the portion of the laminate extending over the muzzle end dome was detached and discarded. Removing the end cap and central shaft revealed the chamber segments which were collapsed and withdrawn leaving the chamber void. The barrel portion of the mandrel could then be removed by sliding it in either direction.

As mentioned earlier, the nozzle seal is an integral part of the structure, since it is part of the mandrel that is wound in during the fabrication stage. The nozzle plate was simply mated with the nozzle seal and affixed with 12 socket head cap screws. The portion of the laminate which was sandwiched between the nozzle plate and seal was of a precise thickness and was controlled during the fabrication stage just prior to bagging and curing. A plate was slid over the mandrel's end cap and bolted into position compressing the still soft prepreg material to the proper thickness and providing a flat molding surface eliminating the need for an additional machining operation.

As an exploratory assignment, the use of a 144-carrier braider was employed to fabricate two rifles, each identical in construction but using different resin application techniques. A six-layer triaxial braid containing 72 0-degree fiber yarns and 144 55-degree fiber yarns developing a laminate thickness of approximately 0.2 inch was braided upon the same filament winding mandrel. The first attempt used dry yarns with the resin brushed on, while the second attempt utilized an automatic resin applicator system which precisely controls the resin volume ratio. After braiding, the part was slowly revolved and gelled using heat lamps. This was followed by curing without pressure in an oven. By using the resin applicator, a much better rifle was quickly and easily produced, although the setup and cleanup times were extensive.

## CONCLUSIONS

The filament winding process provides an easy method of producing many inexpensive and lightweight rifles; however, the bagging process



is time-consuming. Alternative methods to provide external pressure during the curing process should be sought to reduce this time and material expense. This will make filament winding an attractive fabrication option. The braiding process coupled with a resin applicator system also provides a good quality rifle in a reduced processing time, but with an added weight penalty due to the inefficiencies inherent in the braid compared to filament winding.

The wound-in nozzle seal provides an excellent way to attach the nozzle plate to the rifle. The 12 cap screws used for attachment may be replaced by a method in which the nozzle plate is simply placed into position and rotated to lock it firmly to the seal providing convenient access to the propellant and projectile. The prototype nozzle is made of aluminum for ease of manufacture, but is much too heavy for this application. The combined weight of the 2.62-pound nozzle plate and the 4.39-pound nozzle seal is 7.01 pounds, in excess of the 3 pounds desired. Since the shape of the parts must be maintained, a less dense material must be used. One solution involves the use of random fiber-reinforced plastic, injection molded in quantity to lower costs. This would typically bring the total weight down to about 3.5 pounds. By removing all unnecessary material, the 3-pound weight can be met, but a complete analysis of the nozzle should be performed to ensure structural integrity.

The 7.5-pound weight limit for the rifle should be met with design optimization techniques possibly in conjunction with other materials or material hybrids. A 0.5-pound sight and a 0.5-pound trigger mechanism will be added to the launcher to bring the system weight to 20 pounds. The rifle, quickly and easily produced using either the filament winding or braiding process coupled with an injection-molded random fiber plastic nozzle and nozzle seal, provides an inexpensive lightweight system meeting the performance criteria and introduces a needed and formidable antiarmor weapon.

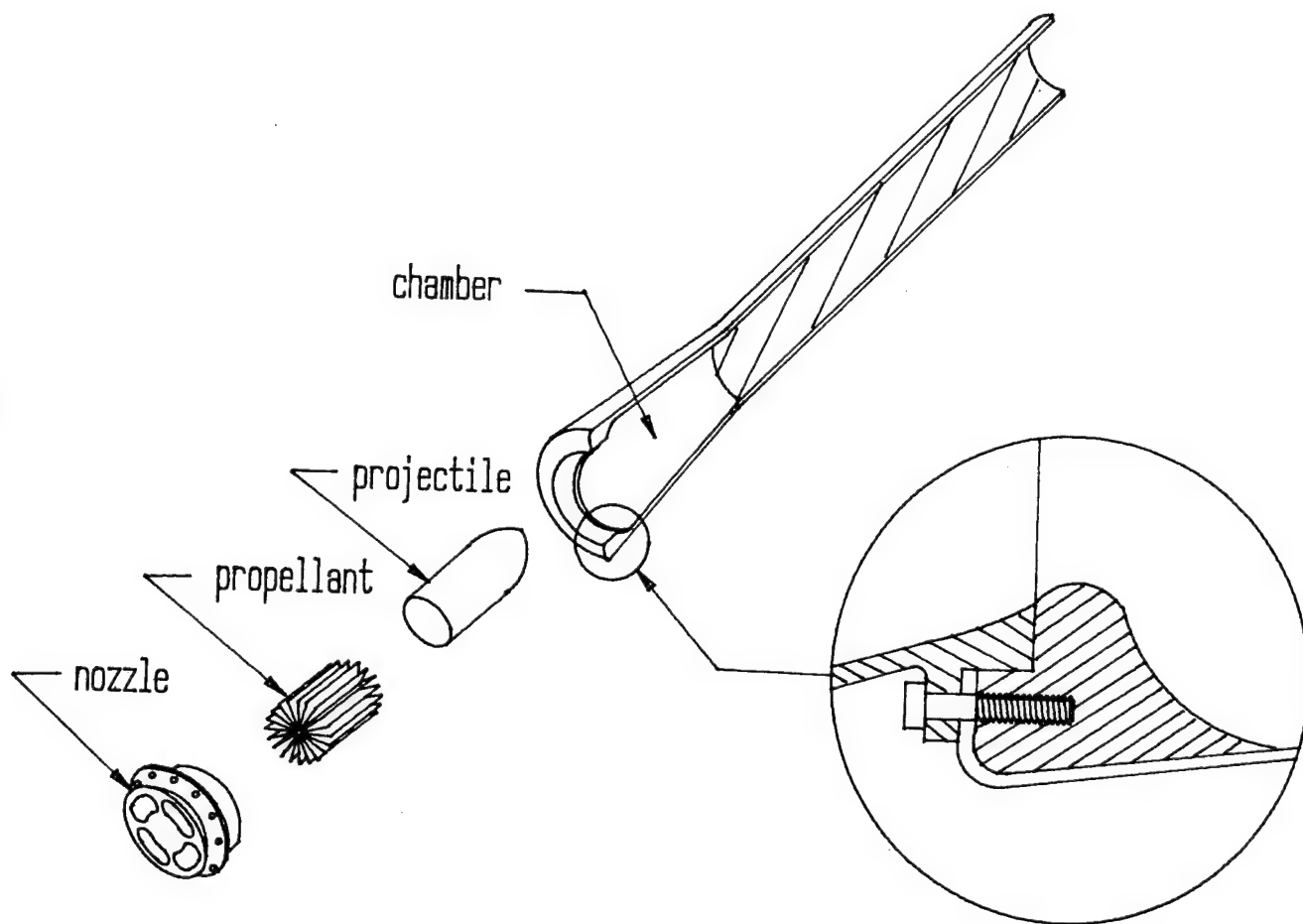


Figure 1. Preliminary design of recoilless rifle system.

# STRUCTURAL ASSESSMENT OF ULTRALIGHTWEIGHT COMPOSITES\*

D.M. Kane, M.A. Jankowski, and R.S. Whitehead  
Northrop Corporation

## SUMMARY

The potential weight savings of advanced ultralightweight (ULW) materials were investigated using the F/A-18 and 747 as baseline aircraft. Weight savings were calculated using a weight ratio methodology. Material properties used in the analysis were those projected for 1993 ULW production materials. The study results indicated that these ULW materials could save 30 percent airframe weight for both baseline aircraft studied.

## INTRODUCTION

Operational criteria for new, high performance aircraft, coupled with stringent performance/mission requirements, have placed greater emphasis on the development of advanced structures, materials, propulsion, avionics, and manufacturing techniques. A key driver in meeting these performance and mission requirements is airframe weight. The USAF has recognized this and is pursuing technology development in structural concepts, materials, and manufacturing processes to provide a new generation of aircraft structures offering significant weight savings over current designs. The potential weight savings of ULW materials were investigated using the F/A-18 and 747 as baseline aircraft. Weight savings were calculated using a weight ratio methodology. Material properties used in the analysis were those projected for 1993 ULW production materials.

## BACKGROUND

Northrop Corporation has a significant involvement in the USAF ULW airframe thrust (References 1 through 4). A roadmap of the four USAF/Northrop ultralightweight programs is presented in Figure 1. The combined objective of these programs is to develop and integrate ULW materials, innovative design concepts, sophisticated optimization methods, and cost-effective manufacturing technologies to reduce the structural weight of current state-of-the-art aircraft by as much as fifty percent. The state-of-the-art material mix is that used on the F/A-18, which is presented in Figure 2. The F/A-18 material mix is approximately 50 percent aluminum, 12 percent graphite epoxy, 9 percent titanium, 13 percent steel, and 16 percent other materials. All four programs shown in Figure 1 are currently in progress and one key effort conducted in Task I of Reference 1 (Contract F33615-88-C-5447) was to estimate the weight savings potential of advanced ULW materials. The contribution of improved material properties alone to the 50 percent airframe weight savings goal was determined in this task. The results are discussed in the following paragraph.

## APPROACH

The approach used to estimate the weight savings potential of the improved properties of ULW materials is summarized in Figure 3 and was to

1. Select F/A-18 and 747 as baseline aircraft
2. Select ten components from each baseline aircraft airframe
3. Define the failure mode breakdown for each component
4. Define ULW material properties for a 1993 production system

\* This work was performed under USAF Contract No. F33615-88-C-5447.

5. Calculate the weight savings in each component due to ULW material substitution only
6. Extrapolate the component weight savings to the total airframe.

### Component Selection

The ten F/A-18 airframe components selected are shown in Figure 4 and are

1. Vertical stabilizer skins
2. Vertical stabilizer torque box substructure
3. Rudder assembly
4. Inner wing torque box
5. Outer wing torque box
6. Wing attachment bulkhead
7. Fuselage skin panels
8. Main strut landing gear door
9. Outboard longerons
10. Pressure bulkhead.

These components were selected because they represented a wide range of airframe geometries and load carrying requirements.

The ten 747 fuselage components selected are presented in Figures 5 and 6 and are

1. Side skin stringers
2. Side skin bulkheads
3. Side skin formers
4. Middle side skin with window cutouts
5. Lower side skin without window cutouts
6. Side skin window frame assembly
7. Underfloor frame
8. Upper bonnet tension skin
9. Lower bonnet compression skin
10. Cargo door upper sill.

The 747 components selected were restricted to the fuselage. This part of the 747 airframe was designed and is manufactured by Northrop Corporation under subcontract to the Boeing Company.

### Failure Mode Breakdown

For each component, the breakdown of the different structural failure modes that governed local sizings was identified. A summary of the failure mode breakdowns, for the ten F/A-18 components, shown in Figure 4, is presented in Table 1. Table 2 summarizes the baseline weights of the ten F/A-18 components. Table 3 presents the failure mode breakdown for the ten 747 fuselage components and Table 4 summarizes the calculated baseline weights of these components.

## Ultralightweight Material Properties

The weight savings potential of ULW materials was estimated using projected 1993 production material properties. In order to qualify as a 1993 production ready material, it was assumed that the material would need to be available in development quantities in the 1990 time frame. The three years from 1990 are needed for material technology transition, scale-up, and batch-to-batch verification testing.

Following a comprehensive vendor survey and a review of extensive Northrop in-house test data, production material properties were selected for the 1993 time frame. The projected 1993 ULW material properties are presented in Table 5 and Figure 7, along with typical properties used on the F/A-18. Figure 7 shows that the 1993 ULW material has a 38 to 40 percent increase in tension and compression modulus, a 115 percent increase in tension strength, and a 21 percent increase in compression strength. The strength properties account for the presence of a 0.25-inch fastener hole.

### Weight Savings Prediction

The "Weight Ratio Methodology" described in References 5 and 6 was used to estimate the material substitution weight savings potential of the 1993 ULW material. This methodology consists of a set of mathematical equations that combine material density and governing material properties to arrive at a weight difference for material substitutions. The weight ratio equations are given in Table 6.

The philosophy behind using this method is to estimate weight reductions associated with material substitutions without affecting the baseline margins of safety. This is a primary consideration to assure an unbiased projection of weight savings due to material substitutions. Basically, substitution of materials in an already sized structural component can affect the baseline weight in two ways:

1. Weight reductions due to different material densities
2. Weight reductions due to different part thicknesses.

The second consideration is based on the assumption that, with the exception of part thickness, the areal geometry of the baseline components remains unchanged during material substitutions. This is required for the evaluation of ULW composites, since it provides the study with weight reductions due to improved material properties, independent of modifications in baseline structural concepts and manufacturing techniques.

It should be noted that the overall validity of this approach was based on the following key assumptions:

1. All candidate components under consideration are producible with ULW composite materials.
2. Substitution of ULW composites for baseline metallic structures is based on weight where cost and supportability are not considered.
3. Weight estimates are based on static loading checks. Fatigue considerations were ignored due to the insensitivity of composite materials to fatigue-related failures.
4. The baseline failure modes presented in Tables 1 and 3 remained unchanged after material substitutions.

The weight ratio methodology equations presented in Table 6 are existing relationships developed for metal-to-metal substitutions. In order to calculate weight savings for composite substitutions, Northrop modified the equations in Table 6 to account for anisotropic composite properties and composite failure criteria. These modified equations were used in conjunction with the component failure mode breakdowns shown in Tables 1 and 3 to calculate component weight savings. The component weight savings were then extrapolated to calculate total airframe weight savings.

## RESULTS

The calculated weight savings for a 1993 production ULW material system are presented in this section.

### F/A-18 Airframe

The weight savings results for the ten F/A-18 components are given in Table 7. Weight savings range from 9 percent for the rudder assembly to 46 percent for the inner wing torque box and the outboard longerons. The overall average weight savings for the ten components were 42 percent. The results of the component weight savings were extrapolated to the overall F/A-18 airframe to assess weight savings at the total airframe level. Figure 8 presents the structural weight breakdown of this vehicle with and without the landing gear/engine section. The total wing group weight is 3,419 lbs which is approximately 36.8 percent of the total structural weight excluding landing gear/engine section. A summary of the extrapolation methodology for the wing group is presented in Figure 9.

Figure 9 shows that the weight of the two wing components used in the study was 1,760 lbs or 51.5 percent of the total wing weight. However, since the weight savings estimates in the study were based on material substitutions only, the joints, splices, and fasteners can be excluded. As a result, the two wing components comprise 55 percent of the total wing weight without joints, splices, and fasteners. The average ULW material savings were 45.6 percent for the two wing components (Table 7) and, adjusting the weight savings for the unconsidered areas to 40 percent, the total F/A-18 wing weight savings were 1,371 lbs and 40 percent as shown in Figure 9.

The same approach shown in Figure 8 was used to calculate the total weight savings for the tail group and body (fuselage) group. These were calculated to be 17 percent for the tail group and 29 percent for the body group.

Based on these extrapolations, the combined wing, body and tail group weight savings were calculated to be 2,980 lbs, which is 32 percent of the total structural weight of the F/A-18 vehicle (8,304 lbs).

### 747 Fuselage

The weight savings results for the ten 747 components are given in Table 8. Weight savings range from 38 percent for the lower side skin with window cutouts and the lower bonnet skin to 68 percent for the side skin stringers. The overall average weight savings were 47 percent. Figure 10 shows the approach to the 747 center fuselage weight savings extrapolations. The estimated weight savings of the components (Table 8) were used to determine weight savings for each skin panel assembly, using geometric failure mode similarity for the selected components, representing detail parts of the outer side skin assemblies. A total of three different panel groups, namely, side skin panels, upper bonnet skin panels, and lower bonnet skin panels, was used since they were representative of typical panel groups. These weight savings were applied to all common panel groups. These data were then extrapolated to the center fuselage and full airframe.

Based on these extrapolations, a weight saving of 42 percent was calculated for the complete airframe. The higher airframes' weight savings for the 747 (42 percent) compared to the F/A-18 (32 percent) are due to the differences in material mix. The 747 has significantly lower composite weight fraction than the F/A-18.

## Discussion

The F/A-18 weight savings study projected a 32 percent airframe weight savings for a 1993 production ULW material. This value is in agreement with the preliminary material driven weight savings estimates of 30 to 35 percent identified in an original Forecast II projection on "Ultralightweight Airframes" (PT-22). This confirms the significant role improved material properties will play in achieving a 50 percent weight savings goal. Indeed, additional material property improvements should be available after 1993, which will further increase the weight savings potential of ULW materials in the 2000 time frame.

The study conducted here assumed that the ULW material would be competitively priced, be producible, and cost effective. It should be noted that satisfying these very important criteria may reduce the calculated weight savings. However, material property improvements are only one facet of the ULW airframe goal. The key is to integrate advanced ULW materials, innovative design concepts, sophisticated structural optimization methods, and novel cost effective manufacturing methods together to achieve the 50 percent airframe weight savings goal.

## WEIGHT SAVINGS SENSITIVITY STUDY

A weight savings sensitivity study was conducted to determine the influence of compression strength on the ULW material weight savings calculated for the ten F/A-18 components. This study was conducted for the following reasons:

1. Post-1993 candidate ULW materials are polyphenylenebenzobisoxazole (PBO) fibers and molecular composites.
2. These materials offer significant density advantages, significantly improved specific tension modulus, and tension strength over the 1993 ULW materials.
3. PBO fiber composites and molecular composites have significantly lower specific compression strength than 1993 ULW materials.
4. The impact of reduced compression strength on ULW material weight savings was needed to establish a target compression strength for these materials.

The study was conducted using the 1993 ULW material properties shown in Table 5 and Figure 7. All properties were constrained except the notched compression strength, which was varied from 2,500 micro-in./in. to 7,500 micro-in./in.

Typical results for the sensitivity of ULW material weight savings to compression strain allowable are shown in Figure 11 for the vertical stabilizer substructure, inner and outer wing torque boxes, and the main landing gear strut door. The average weight savings sensitivity to compression strain allowable, for all ten F/A-18 components, is presented in Figure 12. For the 1993 ULW compression strain allowable of 4,840 micro-in./in., the weight savings are 42 percent. If the AS1 (original F/A-18 fiber) compression strain allowable of 4,000 micro-in./in. is used, the weight savings reduce to approximately 40 percent. For a compression strain allowable of 2,400 micro-in./in. (the value for current PBO fibers), the weight savings further reduce to 30 percent.

It appears, therefore, that the weight savings provided by the higher specific modulus and tension strength of the PBO fiber would be significantly offset by the 12 percent loss in weight savings due to its (current) low compression strength.

An interesting feature, shown in Figure 12, is the influence of increased compression strain allowable above the 1993 ULW value of 4,840 micro-in./in. The trend in weight savings with increased compression strength, in this regime, is relatively flat. For a compression strain allowable equal to 7,000 micro-in./in., the weight savings are approximately 46 percent, which represents only a 4 percent increase in weight savings. It can be concluded that a compression allowable target of 5,000 micro-in./in. is adequate for ULW materials.

Figure 13 presents the weight savings sensitivity of a typical structural panel subjected to combined tension, compression, and shear loading. For strength design, the panel thickness (and weight) is sensitive to the compression strain allowable, as expected. In contrast, design for buckling is insensitive to compression strain allowable, again as expected. However, the key feature of Figure 13 is that the panel thickness, and, therefore, weight, is controlled by satisfying buckling requirements rather than strength requirements. The same trend was also observed with other combinations of combined loading. Thus, compression modulus is an important property in determining the weight of composite airframes.



## CONCLUSIONS

1. Projected 1993 ULW production materials properties have the potential to save 32 percent airframe weight for the material mix used on the F/A-18 airframe.
2. Density and compression modulus are the material property drivers for weight savings.
3. A compression strength equivalent to current AS4 composites is required for next generation ULW materials.
4. The 50 percent airframe weight savings goal should be achieved by the integration of ULW materials, innovative design concepts, sophisticated optimization methods, and cost effective manufacturing methods.

## REFERENCES

1. Beck, A., et al., "Development of ULW Materials," USAF/Northrop Contract No. F33615-88-C-5447.
2. Bohner, R., et al., "ULW Trade Studies," USAF/Northrop Contract No. F33615-88-C-3202.
3. Kane, D. et al., "ULW Structures," USAF/Northrop Contract No. F33615-88-C-3205.
4. Luzar, J., et al., "ULW Technology Component Demonstration," USAF/Northrop Contract No. F33615-89-C-3223.
5. Ekval, J.C., et al., "Methodology For Evaluating Weight Savings From Basic Material Properties," Proceedings from ASTM E09/E24 Symposium, November 1980, Bal Harbor, Florida.
6. Taylor, R.J., "High Temperature Airframe Weight Estimation," presented at 24th Conference of SAWE, Denver, Colorado, 19 May 1965.

Table 1. F/A-18 Component Failure Mode Breakdowns

COMPONENTS		CRITICAL FAILURE MODES (PERCENT)							
NO.	NAME	BUCKLING	CRIPPLING	TORSIONAL STIFFNESS	TENSILE STRENGTH	COMP. STRENGTH	BEARING STRENGTH	MIN. GAGE	MISC.
1	Vertical Stabilizer Skins (WF = 7.13%)	63	---	30	3	---	---	4	---
2	Vertical Stabilizer Torque Box Substructure (WF = 5.19%)	18	22	6	7	---	37	---	10
3	Rudder Assy. (WF = 1.78%)	43	---	---	41	---	10	---	6
4	Inner Wing Box (WF = 57.23%)	16	8	---	25	29	17	---	5
5	Outer Wing Box (WF = 12.52%)	16	13	5	14	18	29	---	5
6	Wing Attach Bulkhead (WF = 8.52%)	19	44	---	3	---	34	---	---
7	Fuselage Skin Panels (WF = 1.66%)	80	---	---	---	---	20	---	---
8	Main Landing Gear Door (WF = 1.55%)	---	---	20	68	12	---	---	---
9	Longerons Upper Lower (WF = 2.3%)	---	10 90	---	80 ---	---	10 10	---	---
10	Pressure Bulkhead (WF = 2.1%)	---	70	---	9	---	2	19	---
<b>TOTAL</b>		20.3	14.4	3.4	19	19	19	0.7	4.2

T89-25/44/A

Table 2. F/A-18 Component Weights

COMPONENT	BASELINE WEIGHT* (LB)	PERCENT OF TOTAL STRUCTURAL WEIGHT**
Vertical Stabilizer Skins	180	2
Vertical Stabilizer Substructure	131	1.4
Rudder Assembly	45	0.5
Inner Wing Torque Box	1,444	15.5
Outer Wing Torque Box	316	3.4
Main Landing Gear Strut Door	39	0.4
Upper & Keel Longerons	58	0.6
Fuselage Skin Panel	42	0.5
Pressure Bulkhead	53	0.6
Wing Attach Bulkhead	215	2.3
<b>TOTAL WEIGHT</b>	<b>2,523</b>	<b>27.2</b>

\*Where Applicable, Weights Include L/R.

\*\*Excluding Landing Gear Engine Section

T89-25/25/B

Table 3. 747 Component Failure Mode Breakdowns.

Component	Percent Weight Sized by Failure Mode						Part Weight
	Tension	Compression	Buckling	Crippling	Bearing	Misc.	
Upper Bonnet Skin	87				10	3	268.0
Side Skin w/o Window Cutout	10		84		6		139.5
Side Skin w/ Window Cutout			100				239.5
Frame FS 1220 (S-12 to Wing)	19	35	45		1		20.5
Bulkhead FS 1140	42	35	22		1		77.0
Stringers							
- Roll Formed Sheet (S-1, S-19)	100						10.5
- Extrusion (S-23, S-49)				100			17.5
Window Support Frame	100						14.0
Lower Bonnet Skin			90		10		369.5
Floor Frame FS 1980	29	10	41	17		3	25.0
Cargo Door Upper Sill		79	21				18.5

\*Based on Calculated Weights

T89-25/26/8

Table 4. 747 Component Weights

CANDIDATE COMPONENT	CALCULATED BASELINE WEIGHT (LB)
Upper Bonnet Skin	268
Side Skin w/o Window Cutout	139
Side Skin With Window Cutout	239
Frame FS 1220 (S-12 to Wing)	20
Bulkhead FS 1140	77
Stringers	
- Roll Formed Sheet	10
- Extrusion	18
Window Support Frame	14
Lower Bonnet Skin	370
Floor Frame FS 1980	25
Cargo Door Upper Sill	19

T89-25/27/8

Table 5. Comparison of 1993 ULW and AS/3501-6 (F/A-18) Material Properties.

ULW Composite Material	Conventional Composites (AS Series)
$E_1^t = E_1^c = 25 \text{ ksi}$	$E_1^t = 18.1 \text{ ksi}$
$E_2 = 1.6 \text{ ksi}$	$E_2 = 1.9 \text{ ksi}$
$G_{12} = 0.9 \text{ ksi}$	$G_{12} = 0.85 \text{ ksi}$
$\epsilon^t$ (unnotched) = 14,300 $\mu\text{in./in.}$	$\epsilon^t$ (unnotched) = 11,070 $\mu\text{in./in.}$
$\epsilon^t$ (notched) = 8,460 $\mu\text{in./in.}$	$\epsilon^t$ (notched) = 4,000 $\mu\text{in./in.}$
$\epsilon^c$ (unnotched) = 8,600 $\mu\text{in./in.}$	$\epsilon^c$ (unnotched) = 15,025 $\mu\text{in./in.}$
$\epsilon^c$ (notched) = 4,840 $\mu\text{in./in.}$	$\epsilon^c$ (notched) = 4,000 $\mu\text{in./in.}$
$F_{bru} = 100 \text{ ksi}$	$F_{bru} = 90 \text{ ksi}$

T89-25/28/A

Table 6. Weight Ratio Methodology Equations

CATEGORY NUMBER	FAILURE MODE	WEIGHT RATIO ( $W_2/W_1$ )
1	TENSILE STRENGTH	$\rho_2/\rho_1 \times F_{tu1}/F_{tu2}$
2	COMPRESSIVE STRENGTH	$\rho_2/\rho_1 \times F_{cy1}/F_{cy2}$
3	CRIPPLING	$\rho_2/\rho_1 \times (E_1/E_2)^{0.25} \times (F_{cy1}/F_{cy2})^{0.25}$
4	COMPRESSION SURFACE COLUMN & CRIPPLING	$\rho_2/\rho_1 \times (E_1/E_2)^{0.4} \times (F_{cy1}/F_{cy2})^{0.2}$
5	BUCKLING COMPRESSION OR SHEAR	$\rho_2/\rho_1 \times (E_1/E_2)^{0.33}$
6	AEROELASTIC STIFFNESS	$\rho_2/\rho_1 \times (E_1/E_2)$
7	DURABILITY AND DAMAGE TOLERANCE CUTOFF	$\rho_2/\rho_1 \times (F_1/F_2)$
8	GENERAL INSTABILITY	$\rho_2/\rho_1 \times (E_1/E_2)^{0.5}$
9	MINIMUM GAGE	$\rho_2/\rho_1 \times (t_2/t_1)$

760.12

Table 7. F/A-18 Weight Savings Summary.

CANDIDATE COMPONENT	BASELINE WEIGHT (LB)	ULW WEIGHT (LB)	PERCENT SAVINGS
Vertical Stabilizer Skins	180	139.5	22.5
Vertical Stabilizer Substructure	131	73.4	44
Rudder Assembly	45	41	9
Inner Wing Torque Box	1,444	779.8	46
Outer Wing Torque Box	316	177.0	44
Main Landing Gear Strut Door	39	24.6	37
Upper & Keel Longerons	58	31.3	46
Fuselage Skin Panel	42	28.1	33
Pressure Bulkhead	53	29.2	45
Wing Attach Bulkhead	215	148.4	31
<b>TOTAL WEIGHT</b>	<b>2,553</b>	<b>1,472.3</b>	<b>42</b>

T89-25/29A

Table 8. 747 Weight Savings Summary.

CANDIDATE COMPONENT	BASELINE WEIGHT (LB)	ULW WEIGHT (LB)	PERCENT SAVINGS
Upper Bonnet Skin	268	99	63
Side Skin w/o Window Cutout	139	81	42
Side Skin With Window Cutout	239	148	38
Frame FS 1220 (S-12 to Wing)	20	12	41
Bulkhead FS 1140	77	33	57
Stringers			
- Roll Formed Sheet	10	3	68
- Extrusion	18	12	68
Window Support Frame	14	5	63
Lower Bonnet Skin	370	229	38
Floor Frame FS 1980	25	11	55
Cargo Door Upper Sill	19	10	50
<b>TOTAL WEIGHT</b>	<b>1,199</b>	<b>635</b>	<b>47</b>

T89-25/30/B

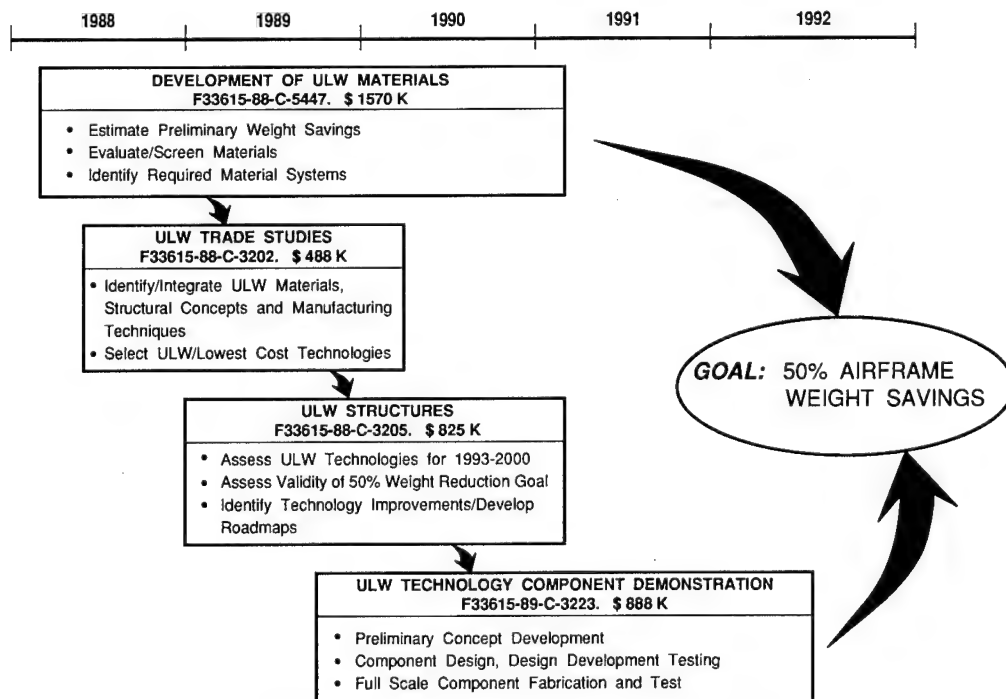


Figure 1. Roadmap of USAF/Northrop Ultralightweight Programs

T89-25/31/A

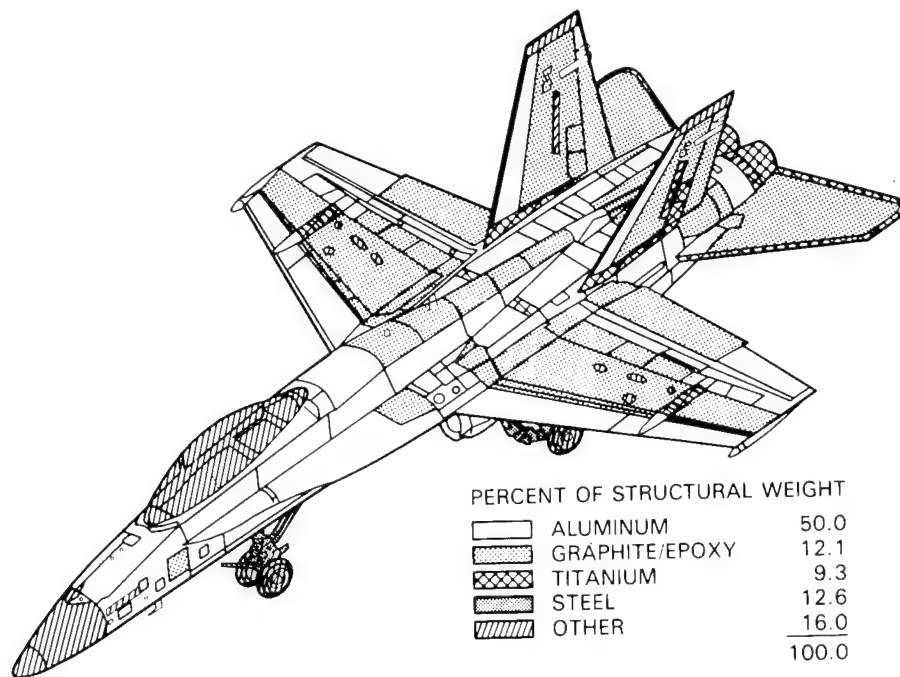


Figure 2. F/A-18 Airframe Material Mix

T89-25/32/A

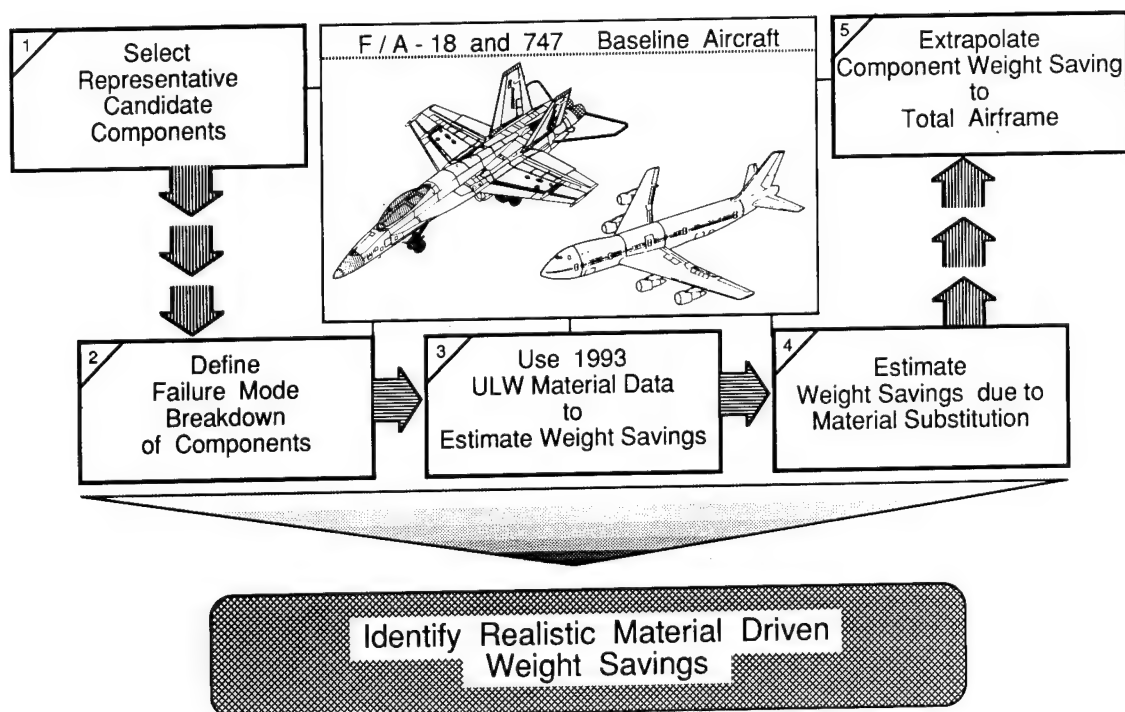


Figure 3. Approach to Caculate Weight Savings Potential of 1993 ULW Materials

T89-25/33/A



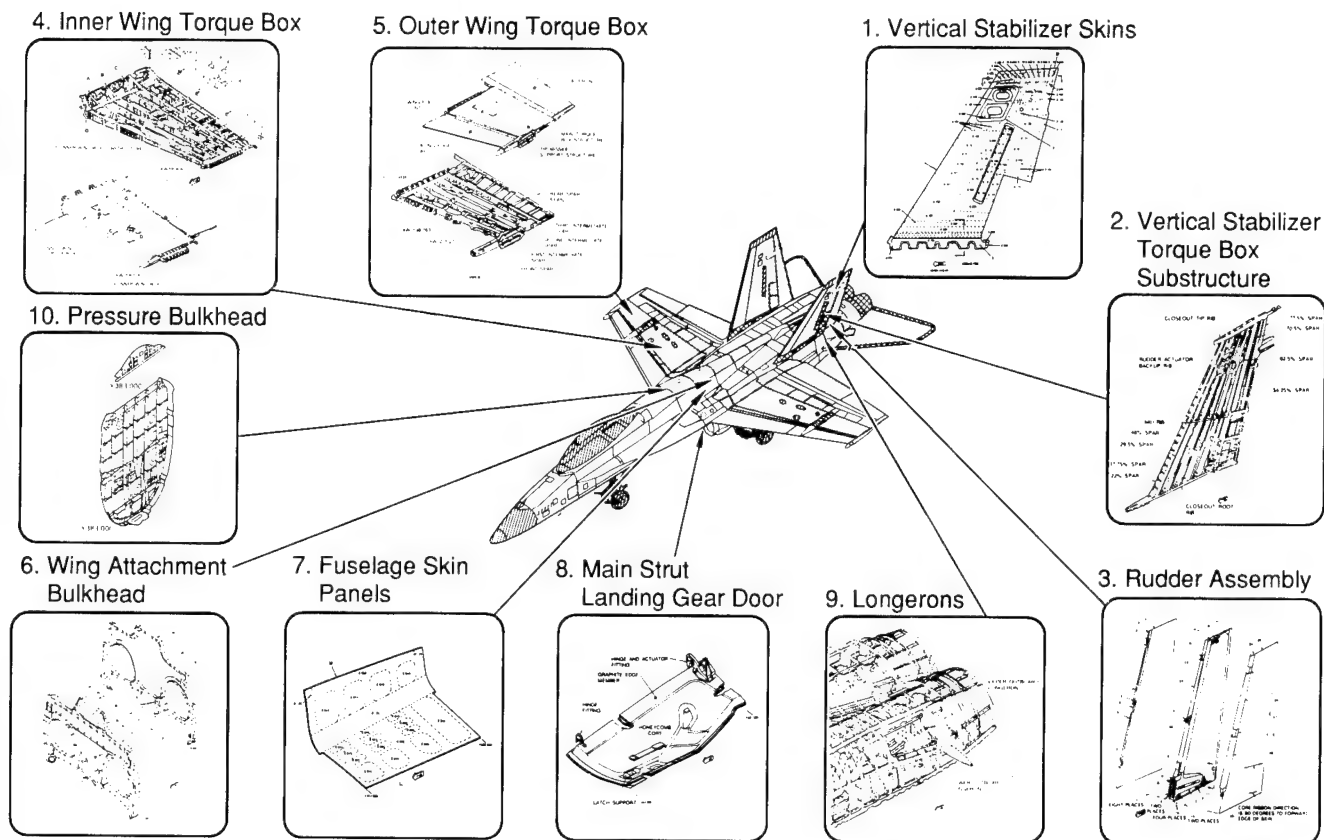


Figure 4. F/A-18 Components

T89-25/34/A

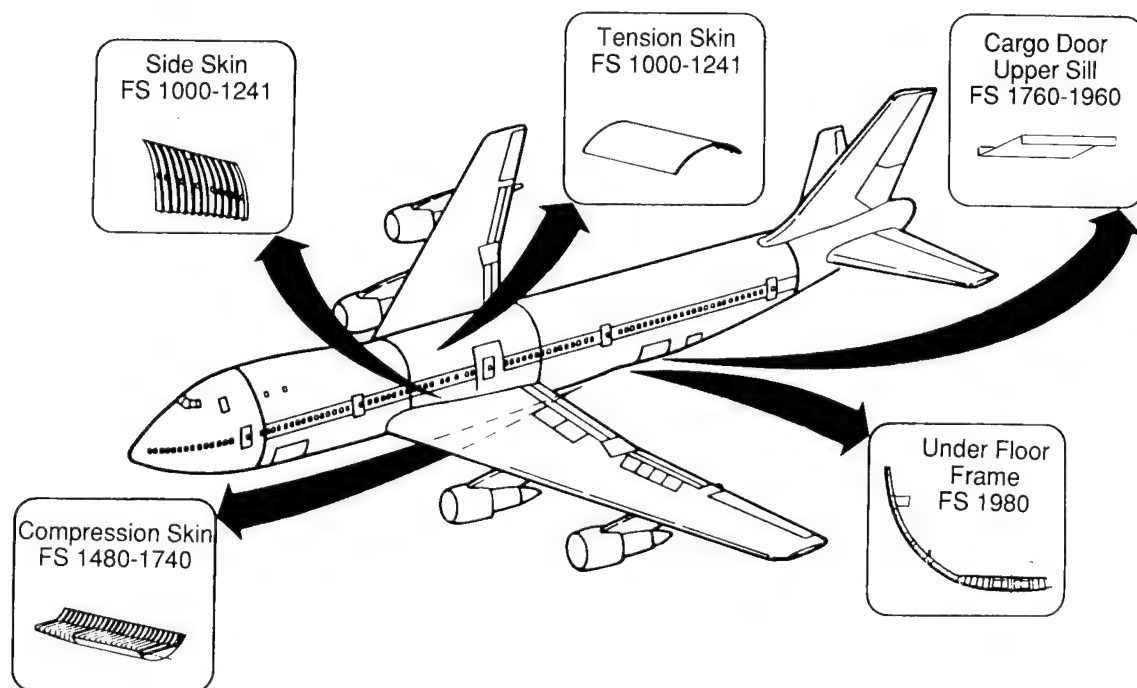


Figure 5. 747 Fuselage Components

T89-25/35/B

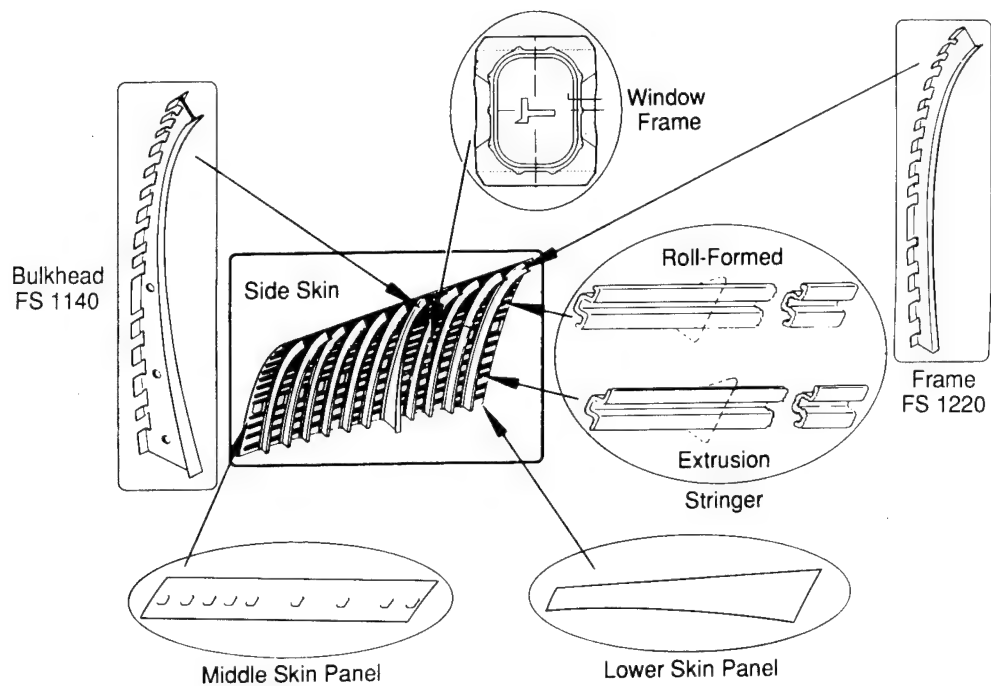


Figure 6. 747 Fuselage Side Skin Components

T89-25/36/8

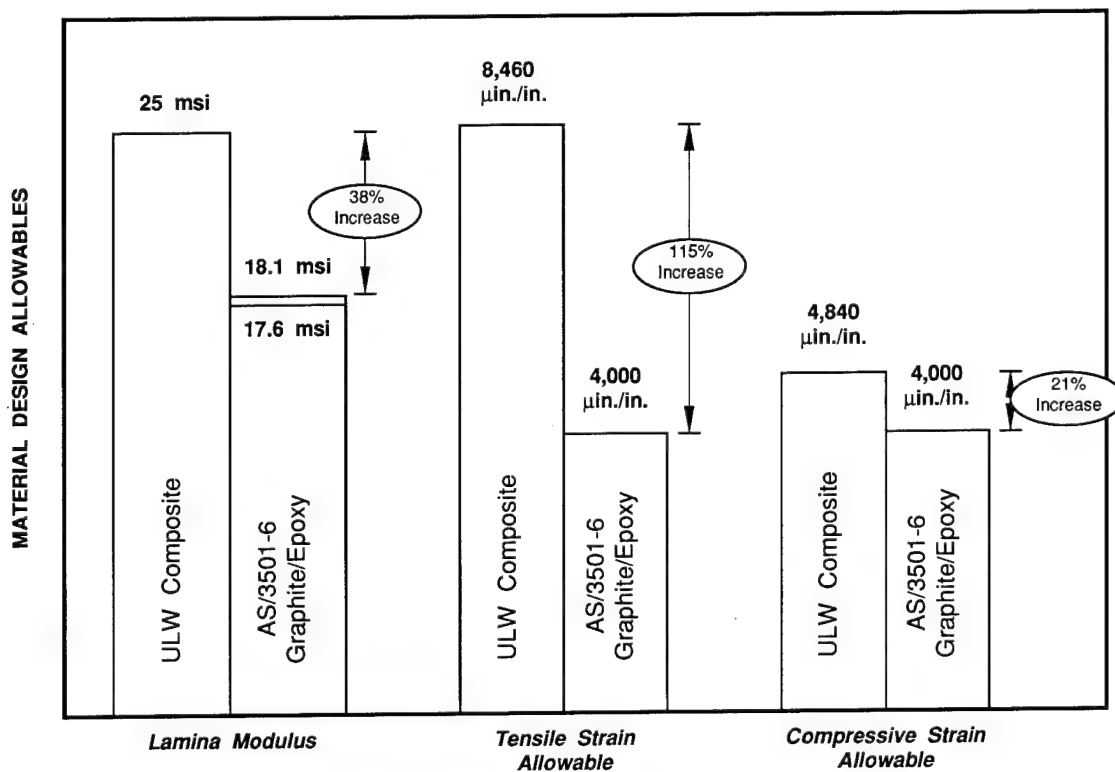
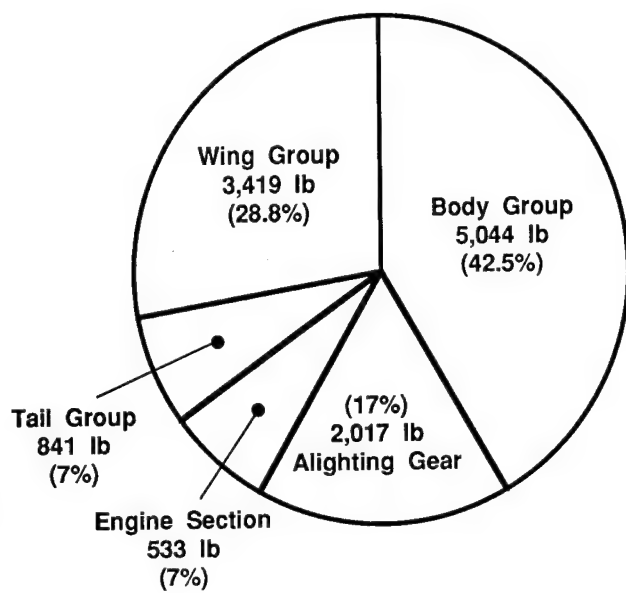
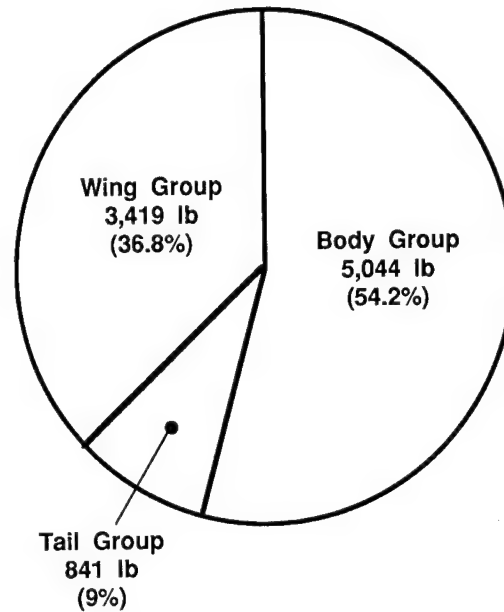


Figure 7. Comparison of 1993 ULW and AS/3501-6 (F/A-18) Material Properties

T89-25/37/A



Total Structural Weight = 11,874 lb



Total Structural Weight = 9,304 lb  
(Excluding Landing Gear & Engine Section)

T89-25/38/A

Figure 8. F/A-18 Structural Weight Distribution

**Wing Group (Wt = 3,419 lb)**

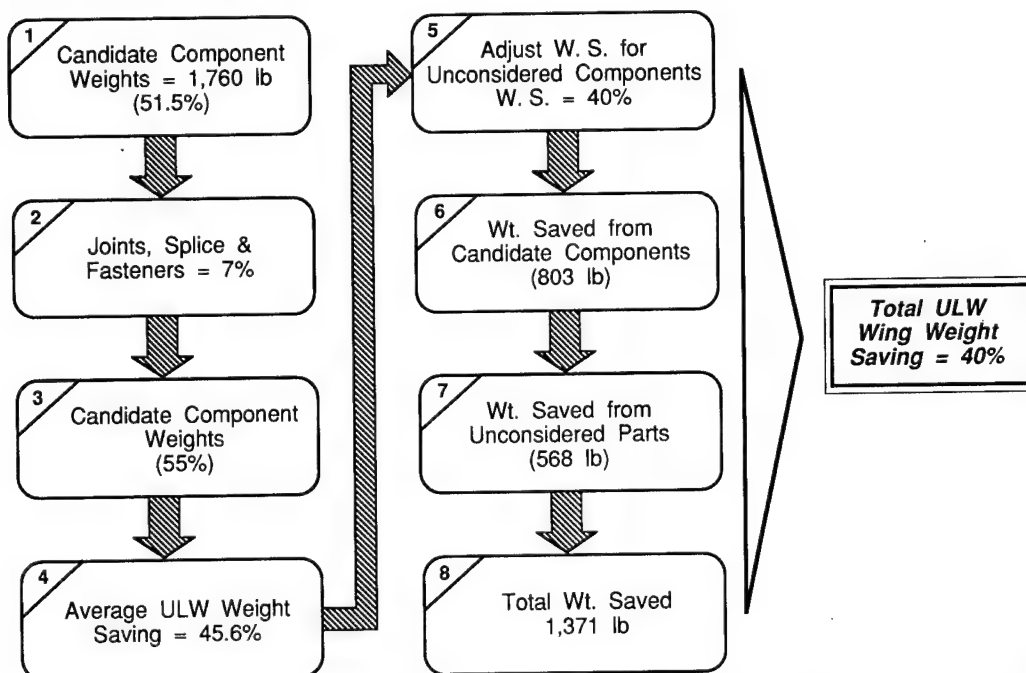


Figure 9. Extrapolation of Component Weight Savings to Total F/A-18 Airframe Weight Savings

T89-25/39/A

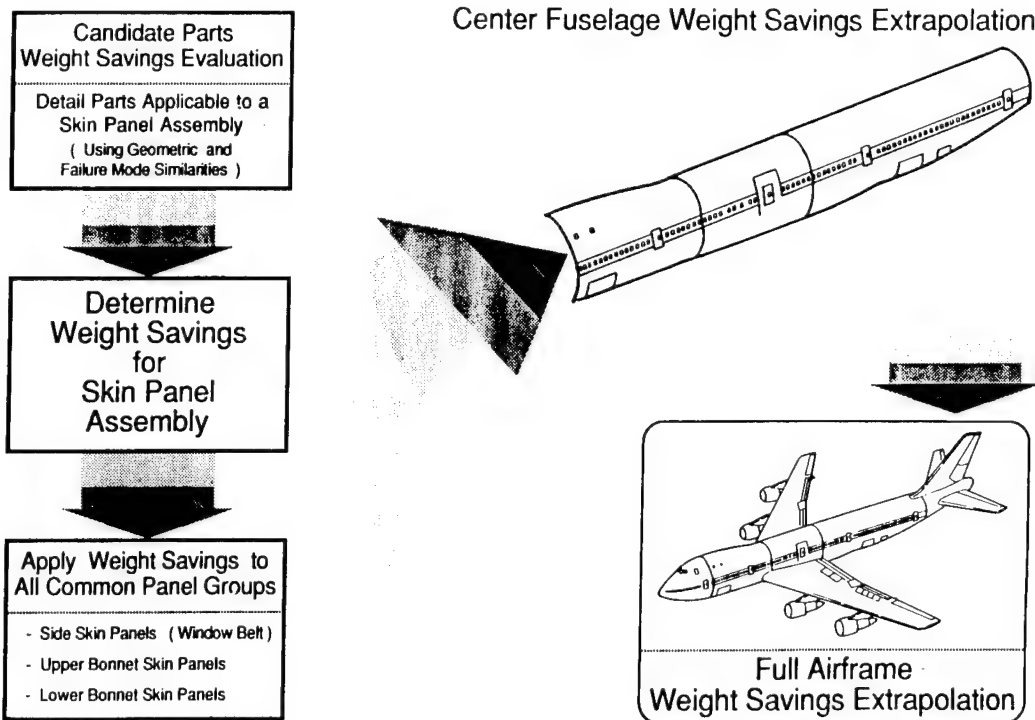


Figure 10. 747 Center Fuselage Weight Savings Estimate Approach

T89-25/40/A

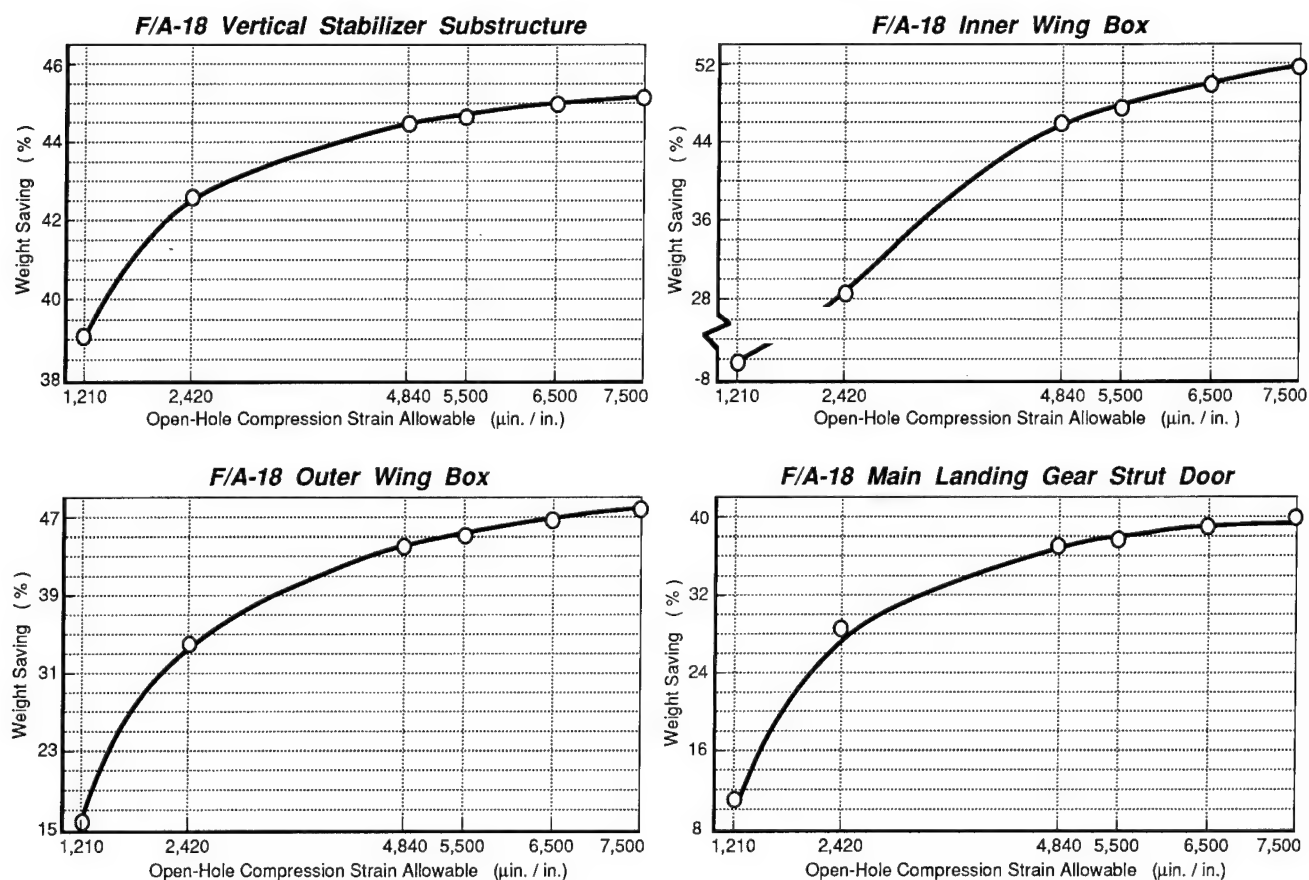


Figure 11. Impact of Compression Strength on F/A-18 Component Weight Savings

T89-25/41/A

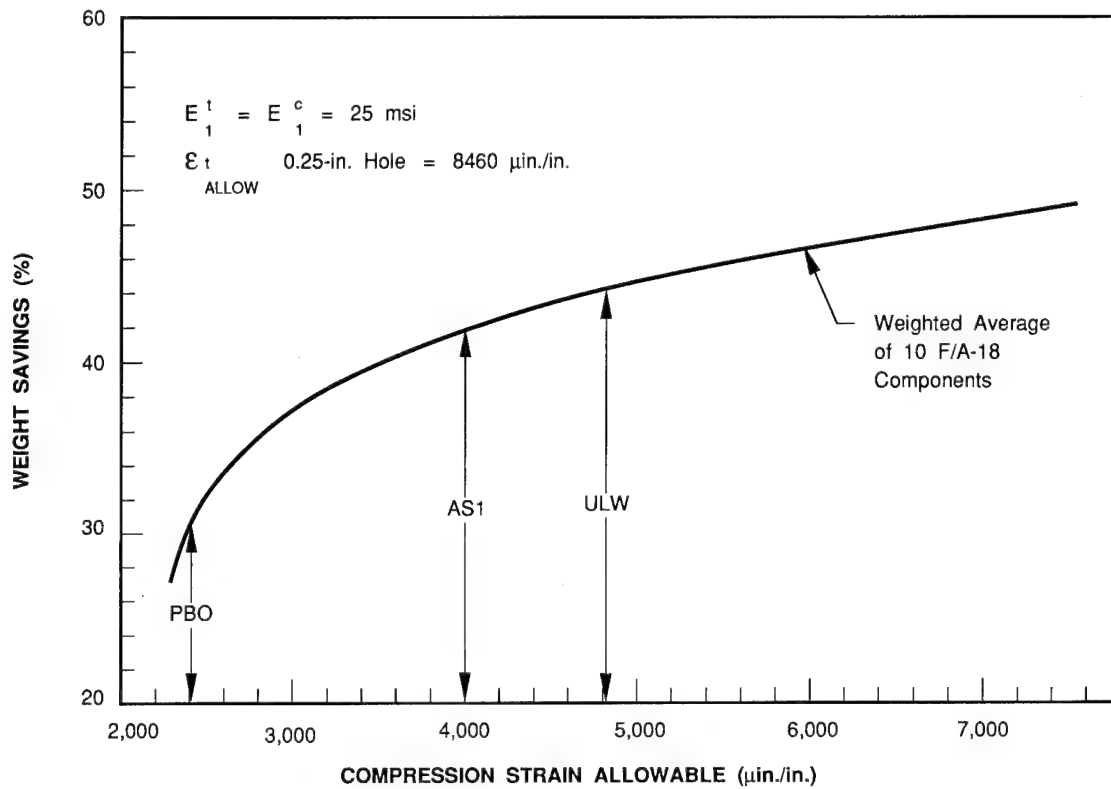


Figure 12. Impact of Compression Strength on F/A-18 Overall Component Weight Savings

T89-25/42/A

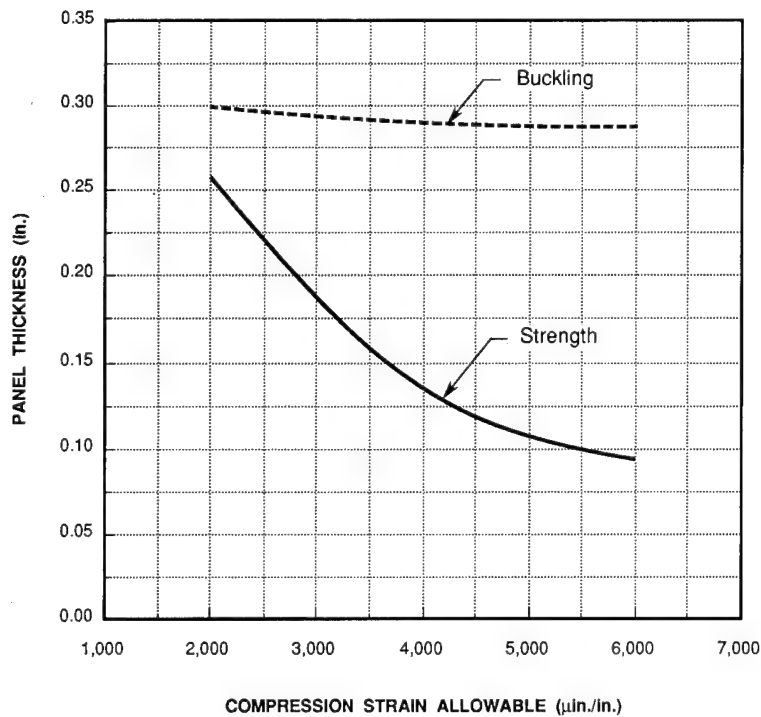
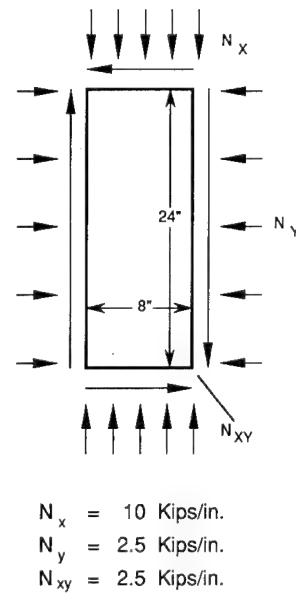


Figure 13. Impact of Compression Strength Versus Stability

T89-25/43/A



# **Methodology in Design (A)**

Chairman: Don Oplinger  
Army Materials Technology Laboratory

A CURVED BEAM TEST SPECIMEN FOR DETERMINING THE  
INTERLAMINAR TENSILE STRENGTH OF A LAMINATED COMPOSITE

Clement C. Hiel, Mark Sumich, and David P. Chappell  
NASA Ames Research Center  
Moffitt Field, California

SUMMARY

A curved beam type of test specimen is evaluated for use in determining the through-the-thickness strength of laminated composites. Two variations of a curved beam specimen configuration (semi-circular and elliptical) were tested to failure using static and fatigue loads. The static failure load for the semi-circular specimens was found to be highly sensitive to flaw content, with the specimens falling into two distinct groups. This result supports the use of proof testing for structural validation. Static design allowables are derived based on the Weibull distribution. Fatigue data indicates no measured increase in specimen compliance prior to final fracture. All static and fatigue failures at room temperature dry conditions occurred catastrophically. The elliptical specimens demonstrated unusually high failure strengths indicating the presence of phenomena requiring further study. Results are also included for specimens exposed to a wet environment showing a matrix strength degradation due to moisture content. Further testing is under way to evaluate a fatigue methodology for matrix dominated failures based on residual static strength (wearout).

INTRODUCTION

As composite structures enter service in more demanding roles, the successful designer must have a clear understanding of the characteristics peculiar to fiber reinforced materials. The anisotropy of composites results in exceptional performance along fiber directions, but comparatively poor properties orthogonal to the fibers. The failure modes observed in composites are also substantially different from those seen in metallics. Delamination is one failure mechanism unique to laminated composites, which is often characterized by high rates of propagation and catastrophic consequences. Numerous occurrences of delamination failures during the development of composite hardware have been documented (refs. 1,2).

Delamination is caused by excessive stress within the matrix of a composite material. This stress has been referred to as interlaminar tensile stress (ILTS), short transverse stress, or through-the-thickness stress. Primary fiber-carried loads in regions of part curvature, ply dropoffs (ref. 3), or ply waviness can create secondary stresses within the matrix which tend to pull the plies of the laminate apart. Most practical composite structures contain a number of these and other features which can encourage delamination. Since the strength of the matrix may be two orders of magnitude less than the strength of the fiber, even low levels of interlaminar tension (6.89 Mpa, 1.00 ksi) may jeopardize the ability of the laminate to sustain its design load. Serious consideration must always be given to evaluating the magnitude of the



interlaminar stresses and reducing them by appropriate modifications early in the design phase.

In the literature, little design data exists on the through-the-thickness properties of laminated composites. Some of the specimen configurations that have been used to determine interlaminar tensile strength include the diametrical compression specimen (ref. 4) and variations of the flatwise tension test specimen (refs. 5,6). Although some success has been achieved with the flatwise tension test specimen, this configuration has inherent limitations. Testing under extreme environmental conditions such as elevated temperature and moisture content is complicated by the presence of a failure-prone adhesive bond between the test specimen and the grips. Forcing the failure to occur within the laminate requires that the interlaminar tensile stress be concentrated by some means such as necking the specimen down at the test section. This requires relatively thick specimens, measuring 1.27 cm (0.5 in.) or more in depth, which may not be adequately representative of a particular composite structure. This paper describes the development of two variations of a new type of interlaminar tension test specimen and the application of an analytical-experimental approach to determine design allowables for interlaminar tensile strength.

#### SYMBOLS

Values are given in both SI and U.S. Customary Units. The measurements and calculations were made in U.S. Customary Units.

$\sigma_{zz\max}$	peak interlaminar tensile stress, Mpa (psi)
P	applied load, N (lbs)
L	moment arm, cm (in.)
b	width at test section, cm (in.)
t	thickness at test section, cm (in.)
$R_i$	inside radius of laminate at test section, cm (in.)
$R_o$	outside radius of laminate at test section, cm (in.)

#### TEST SPECIMEN CONFIGURATION

##### Theory

Two test specimen configurations are shown in figures 1A and 1B. Both are curved beams with all plies oriented around the circumferential direction (100% 0° layup). This type of ply schedule eliminates the free edge ILTS intensification that would occur for cross-ply laminates as load is applied or during cooldown from the cure temperature. The load P is applied at the free ends of each beam (flat section), tending to pull them apart. This load acting over moment arm L generates maximum ILTS within the laminate at the apex (test

section) of each specimen. Note that with curved beam geometries, the applied load can be introduced well away from the test section. The peak interlaminar tensile stress at the apex may be closely estimated by the following equation from reference 2.

$$\sigma_{zz\max} = \frac{3 P L}{2 b t \sqrt{R_i R_o}} \quad (1)$$

This equation has been shown to give a very good estimation of the peak ILTS for simple geometries with small deflections, such as the semi-circular curved beam specimen shown in figure 1A. The peak ILTS at failure for the semi-circular specimens was calculated by substituting experimentally measured failure loads into equation (1). A more detailed analysis using classical elasticity (continuum) theory and multilayer (discrete) theory is given in reference 7.

More complicated and compliant curved beam configurations such as the elliptical specimen in figure 1B would not be expected to conform as closely to the behavior predicted by equation (1). Consequently, a NASTRAN finite element analysis was performed on the elliptical specimen configuration to provide a mathematical expression relating the applied load to the peak ILTS. Figure 2 compares the non-linear response determined by NASTRAN to the linear response predicted by equation (1). Relatively large deflection of the elliptical specimen under load (exceeding 2.54 cm total at the load application points) causes a reduction of the effective moment arm and curvature at the apex, resulting in slightly non-linear behavior. The peak ILTS at failure for the elliptical specimens was calculated by substituting experimentally measured failure loads into the following polynomial curve fit of NASTRAN results.

$$\sigma_{zz\max} = (-0.0905)P^2 + (107.6)P + 23.1 \quad (2)$$

The 2-D NASTRAN model utilized 22 CQUAD8 elements through-the-thickness (one per ply) and provided for increasing mesh refinement in the circumferential direction when approaching the apex of the ellipse (symmetric boundary condition). The non-linear analysis used five load increments to account for geometric changes due to large deflections and required approximately 500 seconds of run time on a CRAY Y-MP. Figure 3 shows the ILTS contours near the apex of the elliptical specimen configuration. As predicted by elasticity theory, the maximum ILTS occurs at the apex location (section A-A), slightly inboard of the mean geometric radius. Figure 4 is a photograph of a failed semi-circular and elliptical specimen which highlights the radius along which each type of specimen fails and confirms that we are looking at failures originating at the region of maximum interlaminar tension.

#### Manufacture

The semi-circular specimens were fabricated from carbon/epoxy (G40-600/5245C) prepreg utilizing a male tooling approach. One long part

resembling a channel is produced from which about twenty 2.54 cm (1.00 in.) wide specimens are cut. The plies were periodically debulked during layup using vacuum compaction, and the entire assembly was vacuum bagged and cured in an oven at 177°C (350°F). Ultrasonic non-destructive inspection was used to ascertain global part quality and some specimens were cut up and inspected under a microscope, revealing a significant amount of scattered porosity. The relatively thick semi-circular specimens were difficult to manufacture with consistent quality and typically exhibited variations in thickness and poor consolidation.

In an effort to improve the laminate quality and further localize the region of peak ILTS, the manufacturing method was changed and the specimen configuration was modified into an ellipse. The elliptical specimens were fabricated from carbon/epoxy (T300/934) prepreg in a female tool using a lock mold process which provided high compaction pressure and excellent geometric tolerances (ref. 8). Generally, when the thicknesses of the elliptical specimens were within  $0.279 \pm 0.005$  cm ( $0.110 \pm 0.002$  in.), no discernible flaws could be found when inspecting cutup sections with the microscope. The elliptical shape allows for a very small local radius at the test section which permits the use of a thinner, more producible laminate while maintaining low fiber stresses due to bending and forcing the specimen to fail first by delamination. Since local radius increases away from the apex, the highest ILTS is concentrated into a narrower circumferential region.

#### TEST SETUP

Figure 5 shows a photograph of an elliptical specimen ready to be loaded to failure. The load originates from an MTS\* servohydraulically operated ram at the bottom, which moves downward during the test. The downward movement is transferred to the lower clevis, which is connected to a male rod end that is bolted to one of the flat ends of the specimen. A similar arrangement carries the load from the specimen to the upper clevis, which is attached to a load cell with a capacity of 9060 N (2000 lbs). The use of rod ends allows the specimen to better align itself with the direction of the applied load, reducing out-of-plane moments that can cause the specimen to twist.

The position of the ram, and consequently the specimen's opening displacement, is monitored using a locally mounted clip gauge for the circular specimens and the MTS-LVDT gauge for the elliptical specimens. A load versus displacement plot, the slope of which is defined as the stiffness, is obtained during each test. Since the delamination of both types of specimens occurs catastrophically (as it does in full scale structural testing), the applied load at the event of delamination failure is determined precisely.

#### RESULTS

##### Semi-Circular Specimens (Unscarfed)

Ten semi-circular specimens with a uniform width of 2.54 cm (1.00 in.) were statically loaded to failure at room temperature dry (RTD) conditions. The total applied deflection was increased at a rate of 0.5 mm/min. (0.02 in./min.) until delamination occurred. The cumulative probability of failure  $P(x)$  is

\*Materials Test System (MTS).

plotted against the obtained interlaminar tensile strength in figure 6. The data displays a mean strength of 36.85 Mpa (5.38 ksi), which is only 63% of the in-plane transverse strength value for the 5245C family of composite materials (unpublished RSRA/X-Wing program data). The standard deviation is 8.56 Mpa (1.25 ksi), and consequently the coefficient of variation is 23%, which is a rather disappointing result since we had hoped to effectively develop a test specimen with no more than the 10%-15% scatter (which is typical for the in-plane properties of composites). The solid line is the cumulative distribution function fitted through the data with a Weibull scale parameter of 40.01 Mpa (5.85 ksi) and a shape parameter of 5.26. Using the analytical expression for the Weibull distribution (ref. 9), one obtains 16.72 Mpa (2.44 ksi) for the A-allowable and 26.13 Mpa (3.81 ksi) for the B-allowable. Both allowables are fairly low, which is a reflection of the effect of poor specimen quality on interlaminar tensile strength.

To quantify poor specimen quality, we can idealize the cross section at the apex as a flat 2.54 cm (1.00 in.) wide and 0.91 cm (0.36 in.) long panel with side cracks, to which the maximum interlaminar tensile stress is being applied in the lengthwise direction. Using a value for the fracture toughness ( $K_{IC}$ ) of  $1.324 \times 10^6 \text{ N/m}^{1.5}$  (1183 lb/in<sup>1.5</sup>) from reference 10, we find that the critical crack size for the specimens represented in figure 6 ranges from approximately 1.00 mm (0.039 in.) for the specimen that has the lowest strength (20.55 Mpa, 3.00 ksi) to 0.165 mm (0.006 in.) for the specimen that has the highest strength (50.69 Mpa, 7.40 ksi). These calculated critical crack sizes are globally in accord with flaw sizes observed on cut and polished cross sections viewed under the microscope.

Equation (1) indicates that the ILTS is directly proportional to the applied force times the moment arm. Since the moment arm does not decrease significantly until well away from the apex, much of the circumference near the apex of the specimen is subjected to high ILTS. This effect has been confirmed by finite element analysis (ref. 2). Failure can consequently initiate at any weak spot or flaw which is located within a rather broad circumferential region. The presence of flaws distributed throughout the laminate has been established by looking at cross sections and free edges with a microscope. The exact location of failure initiation, therefore, could not be determined with our current test methods due to the catastrophic nature of the failure event.

#### Semi-Circular Specimens (Scarfed)

In order to focus the ILTS into a more narrow region, the semi-circular specimens were necked down (scarfed) at the test section. Equation (1) shows the ILTS as being inversely proportional to specimen width, indicating that a reduction in width at the test section would serve to intensify and localize the region of peak ILTS. The width at the apex was reduced from 2.54 cm (1.00 in.) to 0.60 cm (0.24 in.) using a gradual, linear taper. Figure 7 presents the cumulative probability of failure  $P(x)$  versus the static interlaminar tensile strength for the nine scarfed specimens that were tested at RTD conditions. The specimens separated into two distinct groups, turning out to be either "weak" or "strong." The "strong" specimens cluster around an average strength of 57.95 Mpa (8.46 ksi) with a coefficient of variation of 7.6%. This average represents 99% of the in-plane transverse strength for this material. The "weak" specimens cluster around 32.49 Mpa (4.74 ksi) with a coefficient of

variation of 11.8%. The two curves are the cumulative distribution functions for the "strong" (curve #1) and "weak" (curve #2) specimens. Curve #1 has Weibull parameters of 59.8 Mpa (8.73 ksi) and 15.78 and may be considered as the intrinsic interlaminar tensile strength distribution of the material in ideal conditions. Curve #2 has Weibull parameters of 34.04 Mpa (4.97 ksi) and 9.67 and may be considered as a processing and flaw size induced horizontal shift of the ideal distribution. The difference in strength between both curves effectively gauges the quality of the material and the fabrication process. Ideally, as the quality of processing improves, curve #2 should shift to the right until it coincides with curve #1. It can also be seen from figure 7 that the overlap between both curves is minimal indicating that either a flaw was present in the necked down test section resulting in a low failure stress, or that no such flaw was present resulting in a high failure stress. This suggests that one can discriminate the "strong" specimens from the "weak" specimens by proof-testing them to some intermediate load level.

### Elliptical Specimens

To improve the laminate quality and further concentrate the ILTS even more than in the scarfed semi-circular test specimens, an elliptically shaped specimen was developed for which both the analysis and the fabrication procedures were described earlier. Static interlaminar tensile strength data obtained on thirteen elliptical specimens at RTD conditions from two different batches having a uniform width of 2.54 cm (1.00 in.) is plotted against the cumulative probability of failure  $P(x)$  in figure 8. The mean strength is 107.06 Mpa (15.63 ksi), which is 194% of the published in-plane transverse strength of T300/934 (ref. 10), and the coefficient of variation is 9.8%. The solid line is the cumulative distribution function calculated for both batches of specimens pooled together. The Weibull scale and shape parameters are 111.9 Mpa (16.34 ksi) and 10.05, respectively. The circles in figure 8 represent a very high quality batch, whereas the squares represent a lower quality batch. It was found that an excellent indication of batch quality could be obtained by measuring the specimen thickness and its variability at the apex location.

The extremely high interlaminar tensile strength obtained on these specimens is a most striking result. We currently speculate that this is because only a very small volume located at the specimen apex is subject to the peak ILTS. This may represent a size effect that has not yet been reported in the literature and which needs further investigation. Another factor which needs further clarification is the effect of double (anticlastic) curvature at the apex location, since the elliptical specimens may be behaving more like curved plates than curved beams due to their width being over nine times their depth. Additional tests are planned on narrower elliptical specimens and the NASTRAN analysis shall be extended into 3 dimensions to account for width effects. This may result in a different failure stress being calculated from the experimentally measured failure load.

### Moisture Effects

Eight 2.54-cm (1.00 in.) wide elliptical specimens were put in a 100% relative humidity environment at 60 C (140° F) for a period of 3 months. After being statically tested to failure at room temperature, the specimens were

weighted regularly during desorption and this data indicated that 1.7% by weight of moisture was present in the laminate at the time of the test. The test results are shown in figure 9, on which the data and cumulative distribution function from figure 8 (dotted line) are plotted for comparative purposes. The solid line is the cumulative distribution function for the moisture conditioned specimens, with a Weibull scale parameter of 107.9 Mpa (15.75 ksi) and a shape parameter of 7.86. The mean strength is 101.5 Mpa (14.82 ksi) and the coefficient of variation is 15.4%. As can be seen, absorbed moisture has the effect of broadening the strength distribution. The load displacement plots obtained on the wet laminate revealed initial cracking beginning at about 60% of the ultimate failure load, followed by increases in load until final, complete fracture occurred. Such behavior was not observed for the dry specimens.

### Fatigue Testing

Fatigue data at RTD conditions was obtained on seven 2.54-cm (1.00 in.) wide elliptical specimens. The tests were conducted at  $R=0.1$  and a frequency of 1 Hz. The stiffness of each specimen was evaluated every 100 load cycles to check for changes in compliance that could indicate crack initiation or matrix degradation. The data has very low scatter, as seen in figure 10. The plot suggests about a 50% reduction in fatigue life for  $10^6$  cycles. As with the RTD static tests, the fatigue failures occurred catastrophically with no stable crack growth observed or any measured increase in specimen compliance prior to final fracture. Further fatigue testing is planned, which will include more frequent measurements of stiffness to determine if compliance increases in the few cycles before catastrophic delamination.

### DISCUSSION AND CONCLUSIONS

Designers of composite structures must be aware that primary fiber-carried loads passing through regions of curvature or discontinuity can cause small but significant secondary stresses which have a tendency to delaminate the component. The situation is complicated by the fact that a design allowable for interlaminar tensile stress is difficult to obtain due to its sensitivity to processing methods and flaw types, sizes, and locations. Often extensive coupon, subscale, and full scale testing must be performed to qualify the specific fiber/matrix system and manufacturing techniques for a particular design. This paper demonstrates that curved beam test specimens are useful for determining interlaminar tensile stress allowables under realistic manufacturing, environmental, and loading conditions. A database can be established which should allow the designer to increase the safety of composite components and structures.

An analytical study was undertaken for two curved beam test specimen configurations: a semi-circular type beam and an elliptically shaped beam. The theoretical relationship between interlaminar tensile stress (ILTS) and applied load was first established. Each geometry was fabricated using very different manufacturing methods and tests were conducted at room temperature conditions to determine matrix static and fatigue strength and the effects of moisture content. The tests indicated that it was not possible to achieve stable crack growth. For all but the moisture conditioned specimens,

delaminations occurred suddenly and were of a catastrophic nature.

It was found that the scarfed (necked down) version of the semi-circular type specimen was very well suited to obtaining static A- and B-allowables for design. The mean interlaminar tensile strength obtained was 99% of the value published for the in-plane transverse strength. Additionally, the specimen proved to be useful for evaluating the quality of the manufacturing method and determining the effect of manufacturing deficiencies on the interlaminar tensile strength. The data supports the use of proof testing for structural validation.

It was found that the elliptical geometry could sustain static delamination stresses of up to 199% of the inplane transverse strength. The reason for this very high strength warrants further examination. The fatigue strength of the elliptical specimens decreased by approximately 50% for  $10^6$  cycles. Static tests conducted on moisture-conditioned specimens indicated a degradation in mean static strength and increased scatter.

Further investigations are focusing on the development of a fatigue methodology for matrix-dominated failures based on residual static strength (wearout). Experimental measurements of the actual ILTS at the free edges of the test section will be performed using Moire techniques. Additional tests are planned that will examine the effects of spectrum loads and hostile environments. It appears that the test results derived from curved beam geometries shall continue to improve the fundamental understanding of interlaminar tensile strength.

#### ACKNOWLEDGMENTS

The authors express their appreciation to the NASA-Ames Basic Research Council for providing Director's Discretionary Fund (DDF) support. Thanks are due to Mladen Chargin and Ken Hamm for the finite element analysis and to Dr. William Ko for his analytical support. Gratitude is extended to Manuel Fontes (retired) and Susan Praskins Suffel for their manufacturing expertise and to Mike Adamson for performing the moisture conditioning of the specimens.

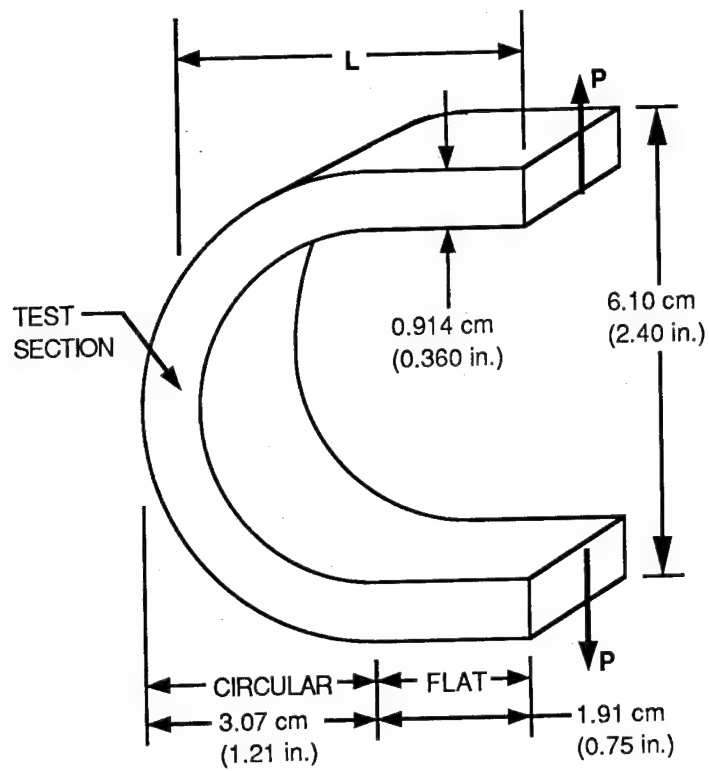
#### REFERENCES

1. Lane, J. W.; and Sumich, M.: The RSRA/X-Wing Experiment: A Status Report. 1987 SAE International Powered Lift Conference & Exposition, Santa Clara, CA.
2. Kedward, K. T.; Wilson, R. S.; and McLean, S. K.: The Flexure of Simply Curved Composite Shapes. Composites, vol. 20, no. 6, November 1989, pp. 527-536.
3. Hoa, S. V.; Daoust, J.; Du, B. L.; and Vu-Khanh, T.: Interlaminar Stresses in Tapered Laminates. Polymer Composites, vol. 9, no. 5, October 1988, pp. 337-344.
4. Mao, T. H.; and Owen, M. J.: Through-the-Thickness Tensile Strength of Fiber-Reinforced Plastics. Composite Materials: Testing and Design

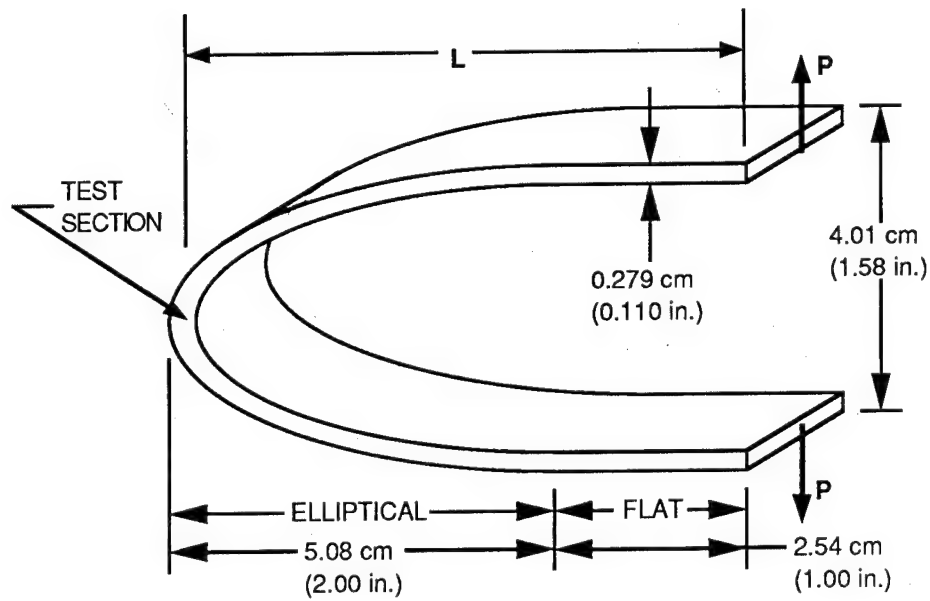


(Sixth Conference), ASTM STP 787, American Society for Testing and Materials, 1982, pp. 5-18.

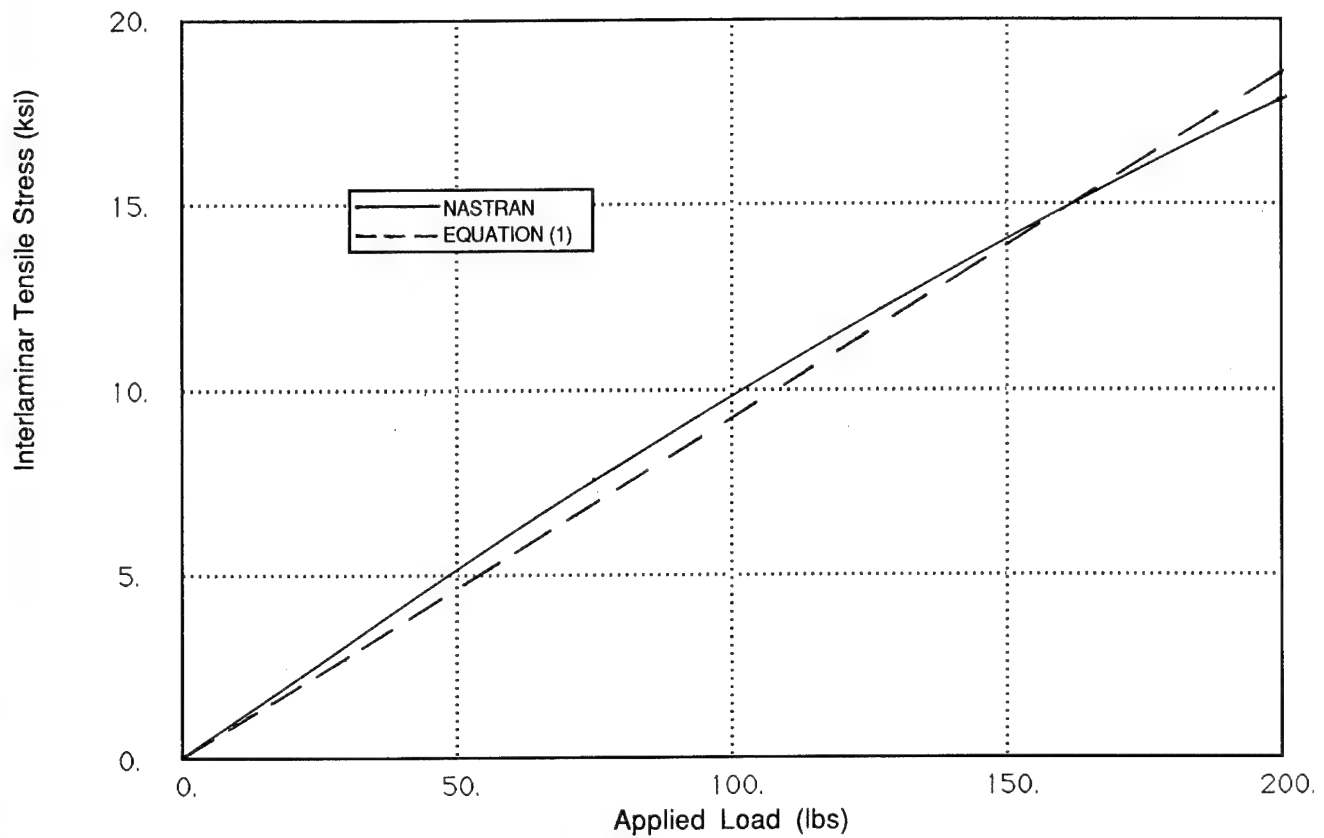
5. Lagace, P. A.; and Weems, D. B.: A Through-the-Thickness Strength Specimen for Composites. Second ASTM Symposium on Test Methods and Design Allowables, Phoenix, AZ, 1986.
6. Mandell, J. F.; McKenna, G. B.; and McGarry, F. J.: Interlaminar Strength and Toughness of Fiberglass Laminates. 29th Annual Technical Conference, The Society of the Plastics Industry, 1974, Paper 13-C.
7. Ko, W. L.; and Jackson, R. H.: Multilayer Theory for Delamination Analysis of a Composite Curved Bar Subjected to End Forces and End Moments. NASA Technical Memorandum 4139, September 1989.
8. Sumich, M.: Manufacture of Composite Test Specimens for Delamination Studies. Experimental Techniques, October 1989, pp. 20-22.
9. Mil Handbook-17B: Polymer Matrix Composites. Naval Publications and Forms Center, 5801 Tabor Avenue, Philadelphia, September 1987.
10. Wu, Hsi-yung T.; and Springer, George S.: Impact Induced Stresses, Strains, and Delaminations in Composite Plates. Journal of Composite Materials, vol. 22, June 1988, pp. 533-560.



1A) Semi-circular specimen configuration



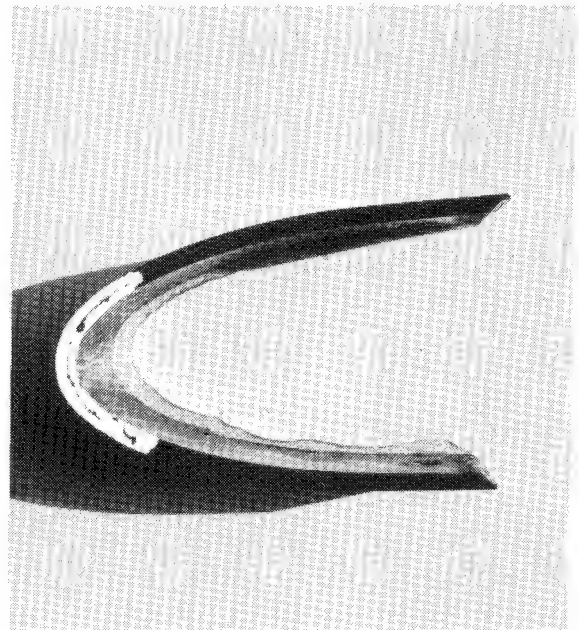
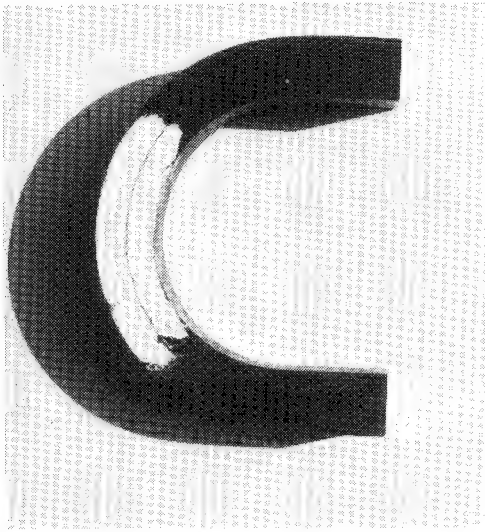
1B) Elliptical specimen configuration



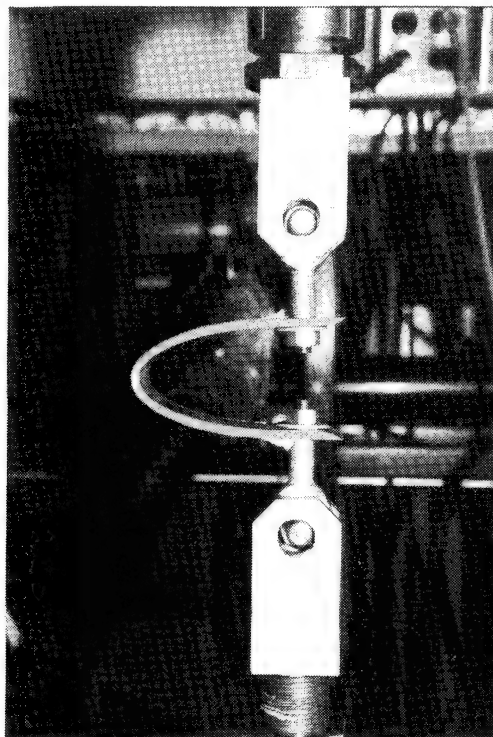
2) Predicted Peak ILTS vs Applied Load for the elliptical specimen



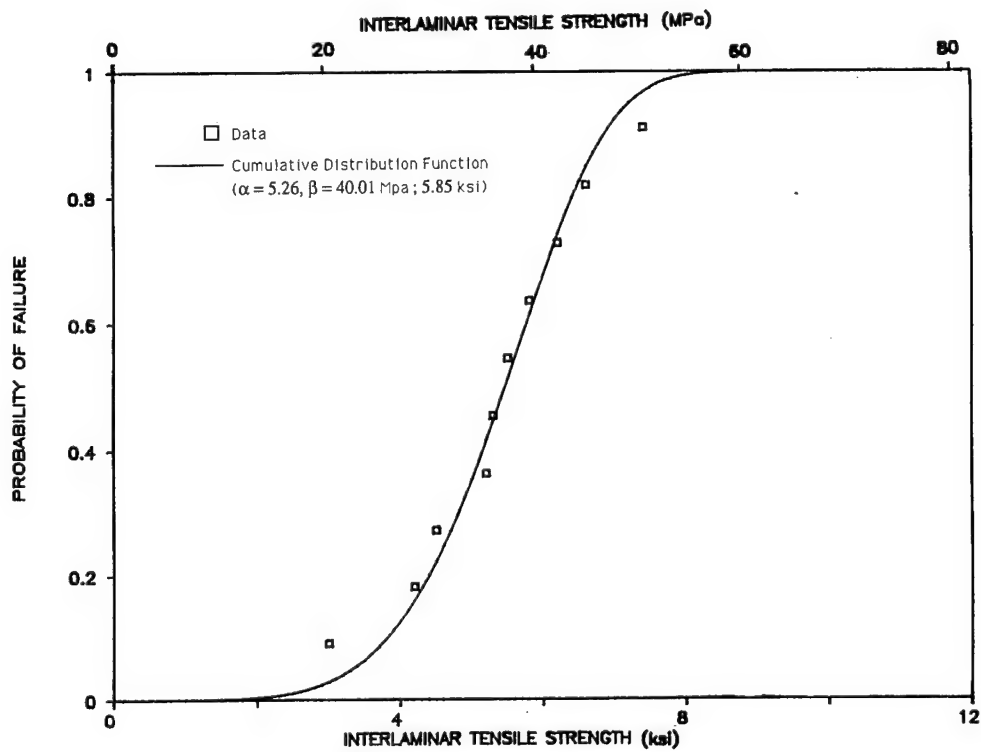
3) NASTRAN ILTS contours near the apex (section A-A) for the elliptical specimen



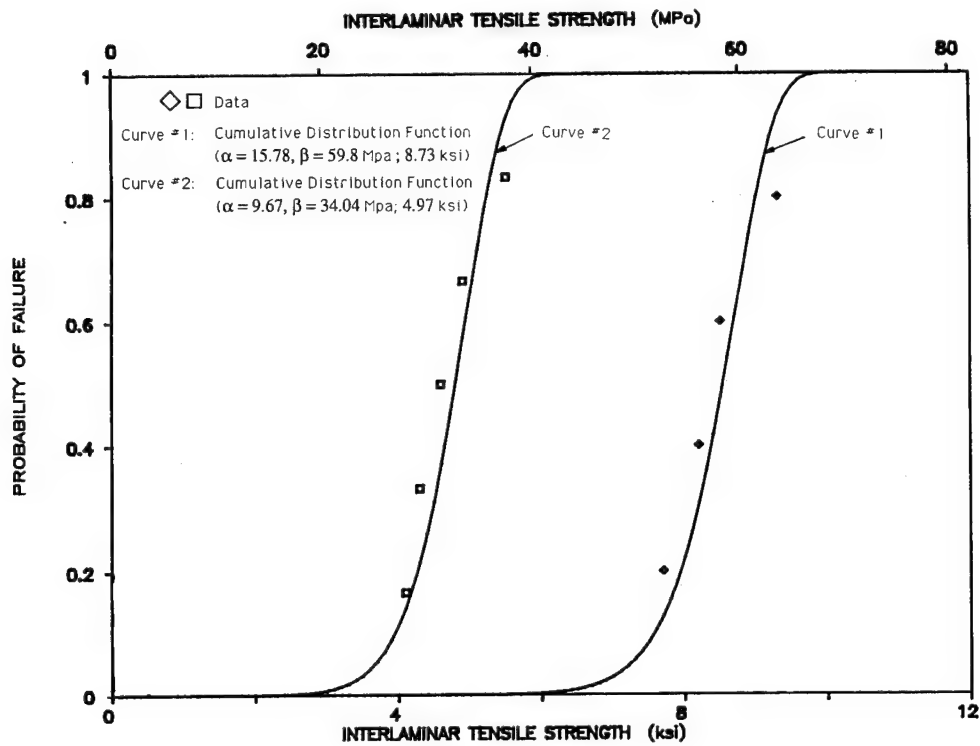
4) Photograph of a failed semi-circular and elliptical specimen



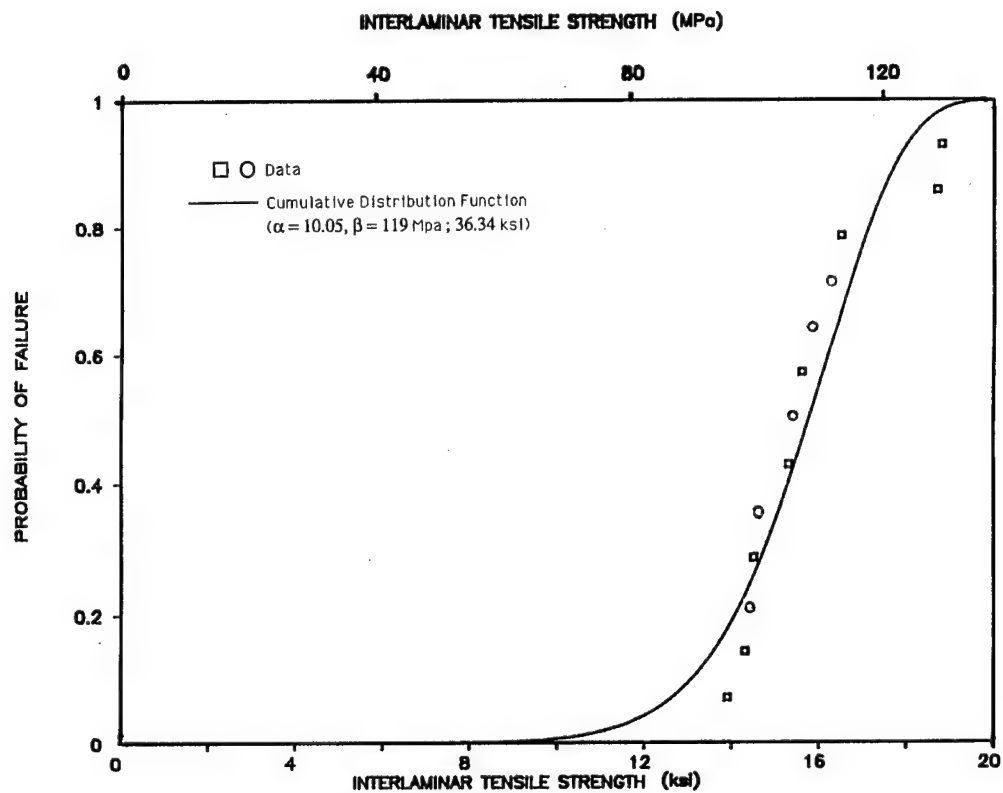
5) Elliptical specimen mounted in the testing machine



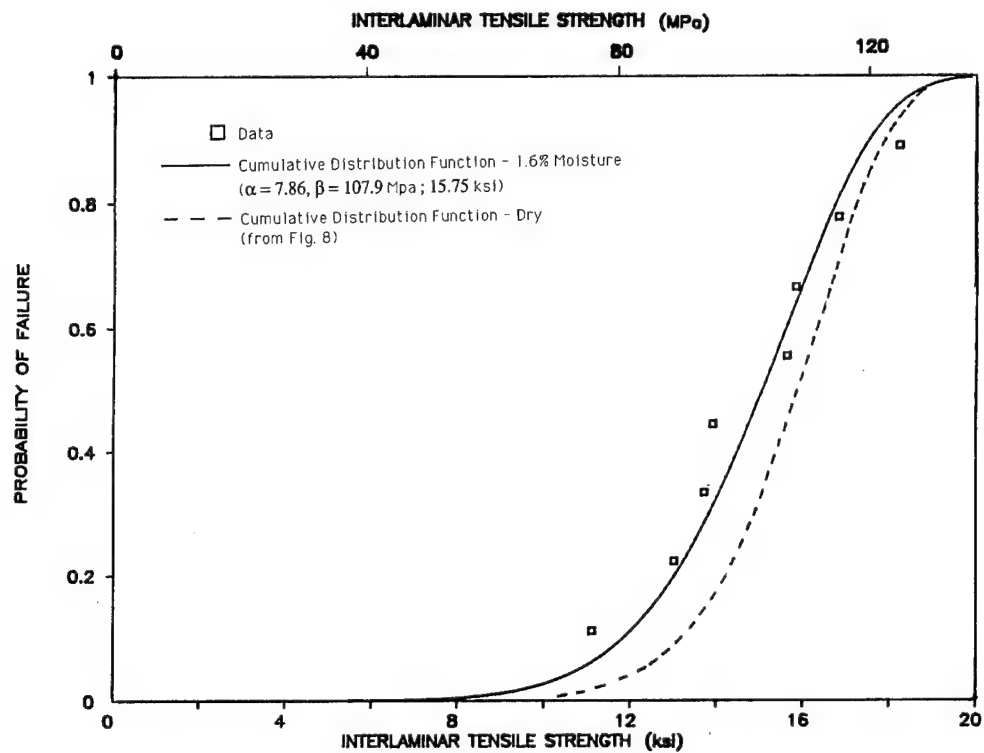
6) Cumulative probability of failure for the semi-circular specimen (unscarfed)



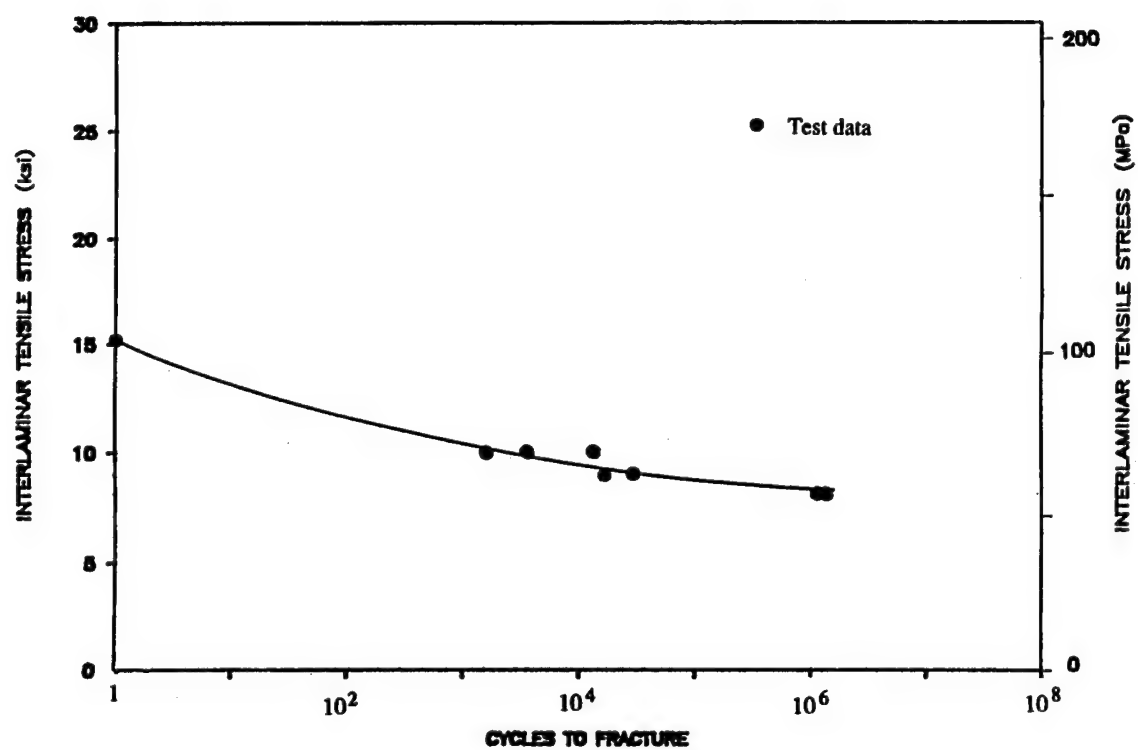
7) Cumulative probability of failure for the semi-circular specimen (scarfed)



8) Cumulative probability of failure for the elliptical specimen



9) Cumulative probability of failure for the moisture conditioned elliptical specimen



10) Fatigue test results for the elliptical specimen



# OUT OF PLANE ANALYSIS FOR COMPOSITE STRUCTURES<sup>1</sup>

P.C. Paul and C.R. Saff  
McDonnell Aircraft Company  
McDonnell Douglas Corporation, St. Louis, MO

K.B. Sanger  
McDonnell Douglas Technologies, Inc., San Diego, CA  
McDonnell Douglas Corporation, St. Louis, MO

M.A. Mahler and H.P. Kan  
Northrop - Aircraft Division, Hawthorne, CA

E.F. Kautz  
Naval Air Development Center, Warminster, PA

Introduction - The ability to predict stresses and failures due to out of plane loads has gained importance as airframe manufacturers begin to use integral (cocured or bonded) composite structures to maximize performance by minimizing weight. Rapid and accurate analysis methods are needed to reduce the amount of testing required to ensure confidence in integral composite structures. The use of postbuckled composite structures will make these analyses even more important. While three dimensional finite element methods can be used to analyze such structures, they require too much time for preliminary structural sizing.

The matrix properties of today's laminates in conjunction with cocured composite construction can produce delaminations under modest levels of out of plane loads. In addition, out of plane loads are only beginning to be considered during the design, development testing, and certification phases of airframe development.

Under a joint Navy/FAA Contract (Reference 1), the problems resulting from out of plane loads were investigated, and ways were presented for avoiding failures that are caused by these loads. A literature search and a survey of industry contacts were used to identify the failure modes and their causes. Simple two dimensional analysis methods were developed to predict the out of plane failure strengths of composite airframe structures. Element test data were used to verify the analyses. Application of these methods to aircraft structure was demonstrated by predicting the ultimate strength of the McDonnell Aircraft High Strain Wingbox test article. The methods and experience from this program were used to compile a set of design guidelines for designers and analysts.

Review of Out of Plane Structural Failures - The difficulties inherent in predicting failures precipitated by out of plane loads are demonstrated in a number of recent test failures of composite structures. A literature search and a survey of industry contacts revealed several examples of these failures: the Lockheed L-1011

composite vertical fin, test articles from the Northrop Composite Wing/Fuselage Program, the MCAIR AV-8B rudder, the Northrop F-20 horizontal stabilizer, and the Messerschmitt/Grumman Composite Panel Repair Program demonstration component.

Failures due to out of plane stresses were also encountered during development tests of the MCAIR AV-8B horizontal stabilizer. This stabilizer consists of an all carbon/epoxy torque box with separate leading edge, trailing edge, and tip components. Several possible failures resulting from out of plane loads induced by buckling were identified for the torque box, as shown in Figure 1. A combination of out of plane loads and moments caused failures of both the upper and lower covers of the torque box. Failure of the upper panel of the torque box, in excess of 150% design limit load, was attributed to a combination of out of plane loads and moments, caused by buckling, that caused fasteners to pull through the carbon/epoxy closure spar.

The review of out of plane structural failures identified several failures and their causes. These failures are a result of high interlaminar tensile and shear stresses relative to low interlaminar strengths. These high out of plane stresses and subsequent failures result either directly from the application of out of plane loads or indirectly as a result of laminate geometry under in plane loads. Examples of these loadings are

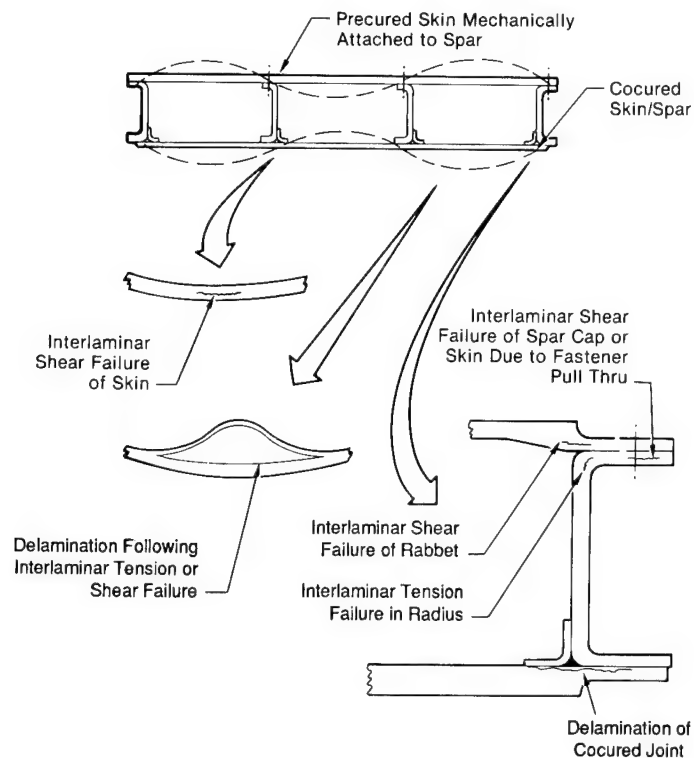
- indirect stresses in laminate corner radii
- indirect stresses due to thickness changes
- indirect stresses due to panel buckling deformations
- direct stresses due to fuel pressure loads
- indirect stresses due to irregular load paths

These potential loading situations must be examined when designing, analyzing, and certifying composite structures.



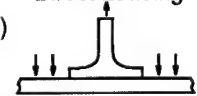

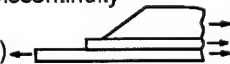
Analysis Development and Verification - In Reference 1, methods were developed to minimize the stresses identified above. While these techniques can be used to address a great variety of out of plane loading conditions, they were primarily derived to address the failure sources summarized in Figure 2.

The Curved Laminate Analysis (CLA) is a mechanics of materials formulation that can be used to predict the interlaminar stresses in laminate corner radii. Previous curved laminate analyses were based only on the effects of pure bending. CLA extends this capability to include the effects of applied axial, shear, and pressure loads.

In CLA it is assumed that the curved laminate exhibits linear elastic behavior, and plane sections remain plane. Equilibrium conditions for an angular differential element were used to determine the stress state



**Figure 1. Possible Postbuckling Related Out-of-Plane Failure Modes in AV-8B Torque Box**

Problem	Solution Method
 (1) Load Path Eccentricity	Curved Laminate Analysis (CLA)
 (2) Variable Thickness Ply Drop-Off	Design Procedure
 (3) Direct Loading	Elasticity Method (WEBSTER) Interfacial Stress Field Model (ISFM)
 (4) Indirect Loading	Elasticity Method (WEBSTER) Interfacial Stress Field Model (ISFM)
 (5) Geometric Discontinuity	Elasticity Method (WEBSTER)

GP93-0007-508-D

**Figure 2. Analysis Methods**

of the curved laminate. CLA loads are defined at the center of curvature, as shown in Figure 3. Stresses are then computed at several user-specified angular positions to find the location that provides the critical stress combination at each ply interface. The Tsai-Hill failure criterion (Reference 2) is used to determine this critical combination of radial and shear stresses.

The Curved Laminate Analysis was evaluated and verified by analyzing carbon/bismaleimide (C/BMI) angle specimen test data. The test specimens were manufactured with a variety of radii and laminate thicknesses and tested to failure under four different environmental conditions. Comparisons of the predicted and actual failure loads are shown in Figure 4.

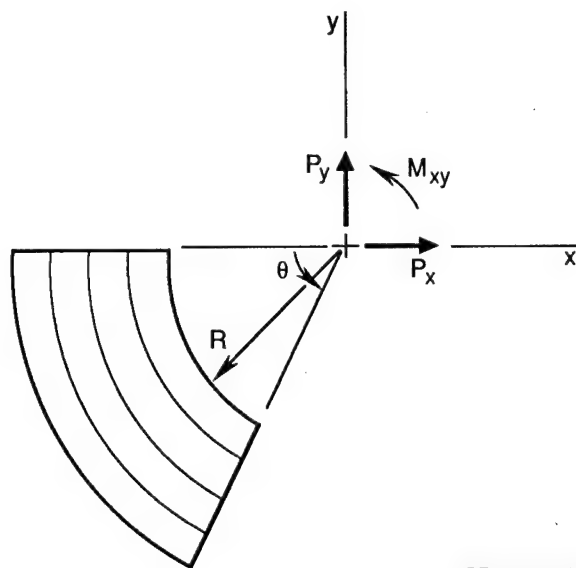
A fracture mechanics approach (Reference 3) for predicting the initiation and propagation of a delamination in front of a ply drop off was used to conclude that gradual changes in laminate thickness and stiffness generally do not initiate delamination growth. Therefore, out of plane loads due to thickness changes can be minimized and controlled by using established ply drop off design procedures. These design procedures are discussed in more detail in the Design Guidelines section of this paper.

Stresses in integral composite joints due to direct loads (e.g. fuel pressure) or due to indirect loads (induced by out of plane deformations of buckled panels) can be predicted using the Interfacial Stress Field Model (ISFM). This mechanics of materials method models the stiffener flange and the skin as beams, with the cocured or adhesively bonded joint acting as a common elastic foundation, as shown in Figure 5. A set of eight boundary conditions coupled with the governing differential equations of equilibrium establishes a system of eight linearly independent equations that are solved simultaneously. This provides the coefficients that describe the skin and flange deflections. The interfacial normal stress state is determined by the difference of the deflections of the skin and flange at any point along the interface. A shear lag analysis is used to predict the interfacial shear stress state caused by differences in the skin and flange membrane loads. The Tsai-Hill failure criterion is used to couple both the interfacial normal and shear stresses and provide the strength prediction.

ISFM was formulated to analyze the direct and indirect load cases separately by assuming two sets of boundary conditions. A shear load and moment can be applied to the stiffener flange for the direct load case. The buckle deflection needs to be specified for the indirect load case.

The ISFM method was verified for both load cases by correlating the strength predictions with test results. Postbuckling tests of flat composite panels (Reference 4) were used to verify the indirect load case. Figure 6 shows the correlation between the predicted and test separation loads for a range of combined axial and shear load cases.

The WEB Stiffener Termination (WEBSTER) model offers a more general



GP93-0386-60-D

Figure 3. Curved Laminate Analysis Geometry

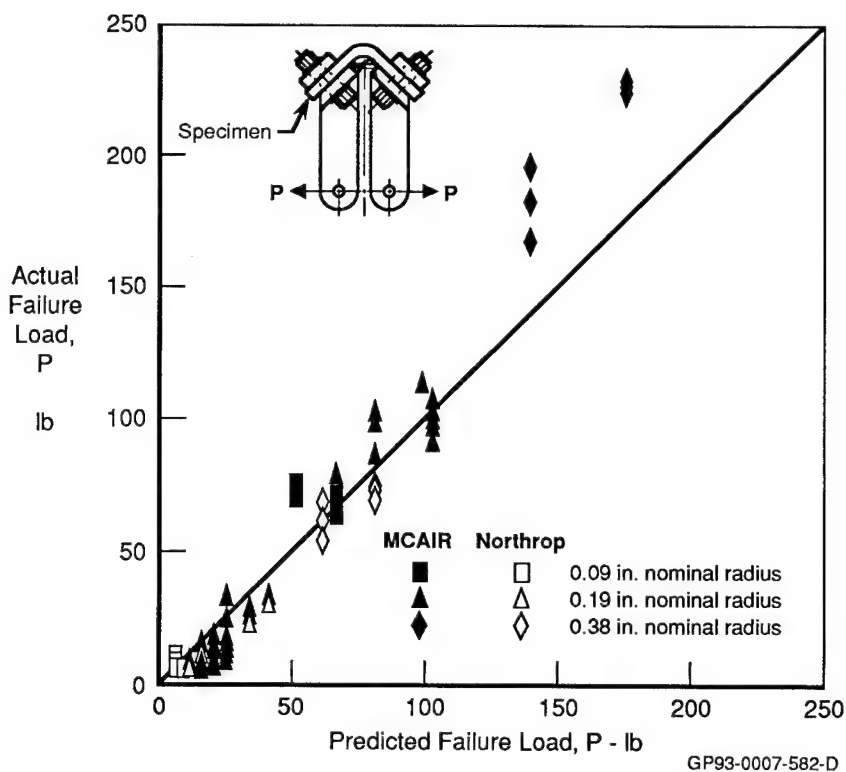
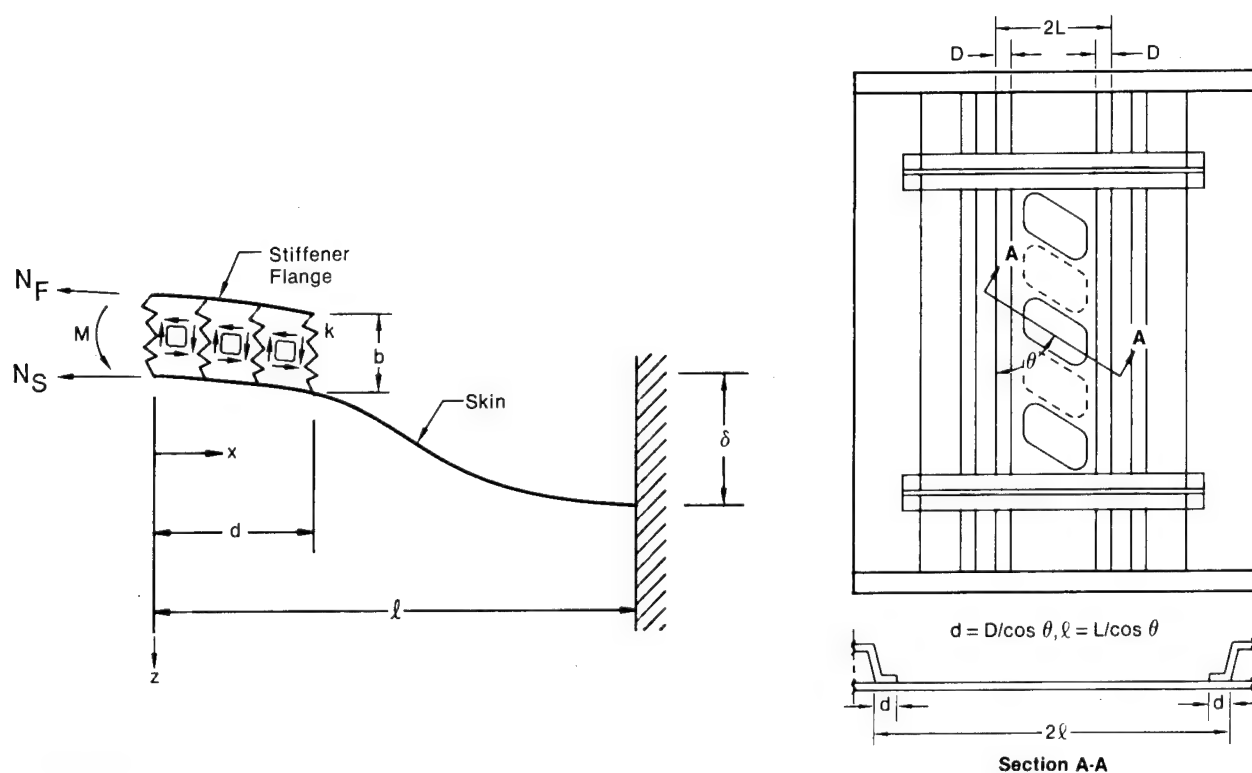
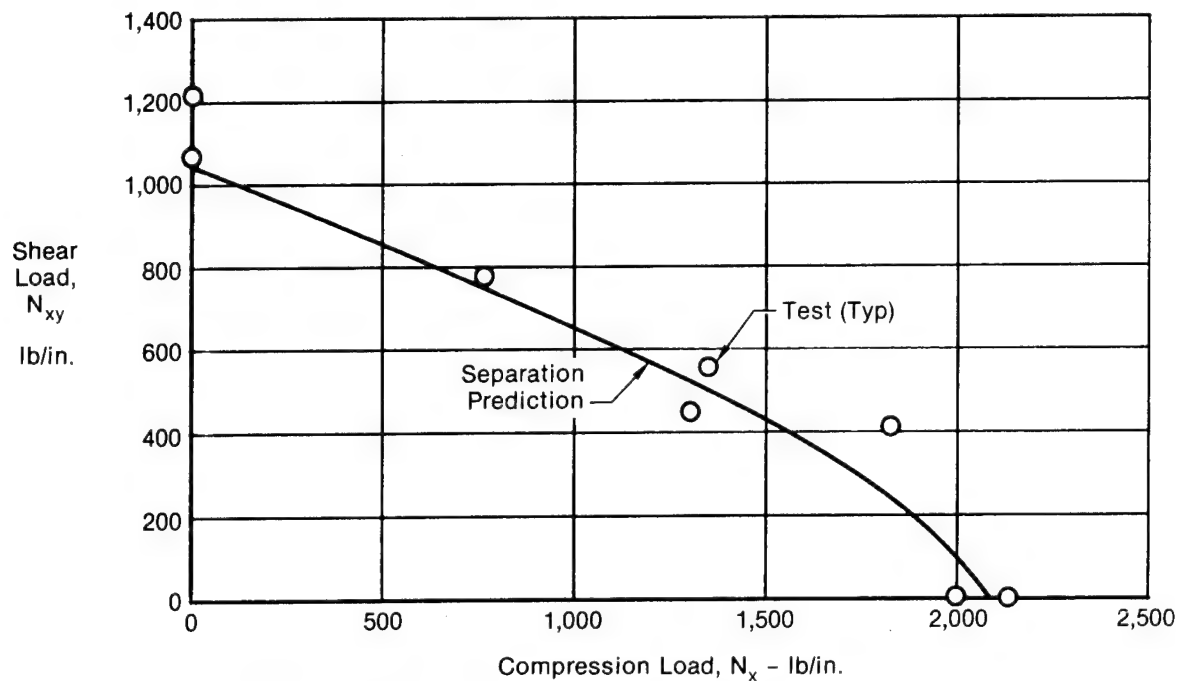


Figure 4. Curved Laminate Analysis Verification



GP93-0386-15

**Figure 5. Interfacial Stress Field Model for Indirect Load Cases and Its Application to a Buckled Panel**



GP93-0386-17

**Figure 6. Correlation of ISFM and Test Data of Panels Subjected to Combined Loads**

method to assess the strength of integral composite joints subjected to direct loads or indirect loads caused by panel buckling. WEBSTER can also be used to predict stresses in composite structures at discontinuities in the geometry, such as the termination of a stiffener or other reinforcement. Figure 7 illustrates the application of the WEBSTER.

In the WEBSTER method the stiffener flange and the adjacent structure (skin) are modeled as separate orthotropic plates that are bonded together with a bondline of zero thickness. The problem is formulated as a generalized plane deformation problem. Boundary stresses are applied to the local region to determine the constants that describe the stress components. The failure function is calculated by averaging the normal and shear stresses over a characteristic distance and applying these values to the Tsai-Hill failure criterion.

The stiffener runout capabilities of WEBSTER were validated using compression panel data. Three specimen configurations were tested to determine the effects of varying the type of stiffener runout. The results of this correlation are shown in Figure 8. Because the Tsai-Hill type failure function is proportional to the square of the applied load, the error in the failure function, shown in Figure 8, is considerably greater than the actual error in the predicted failure load.

An important point to make is that the applicability of each analysis method is dependent on the accuracy of the assumed boundary conditions to the structure being modeled. Figure 9 summarizes the boundary conditions assumed for both the ISFM and the WEBSTER analyses.

**Methodology Demonstration** - These analyses were used to predict the ultimate strength of the McDonnell Aircraft High Strain Wingbox as a demonstration of the applicability of the techniques to aircraft structural analysis. This structure was a full scale integral composite wingbox, representing that of a next generation fighter structure (Figure 10). Innovative concepts such as integral stiffening and postbuckling were employed to reduce weight and to demonstrate durability and low velocity impact damage tolerance.

An extensive test program was conducted to validate the High Strain Wingbox. Figure 11 summarizes the durability, damage tolerance, and residual strength phases of the test program. Internal fuel pressure and four point bending loads were combined in both static and fatigue tests. Initial static strain surveys were conducted to measure load redistribution due to skin buckling and damage growth. The durability portion of the test program consisted of internal fuel pressure loads and 16000 spectrum fatigue hours (SFH) of bending loads. Nonvisible impact damage and a simulated battle damage repair caused very little degradation of structural response, even after an additional 8000 SFH, for the damage tolerance phase. The residual strength phase of the test program consisted of ultimate bending loads and wing tank pressures for a symmetrical pull up (SPU) maneuver and a rolling pull out (RPO) maneuver. Failure occurred during the RPO condition at the design ultimate load, when the compression cover failed catastrophically. Top and side views of the failure are depicted in Figure 12.



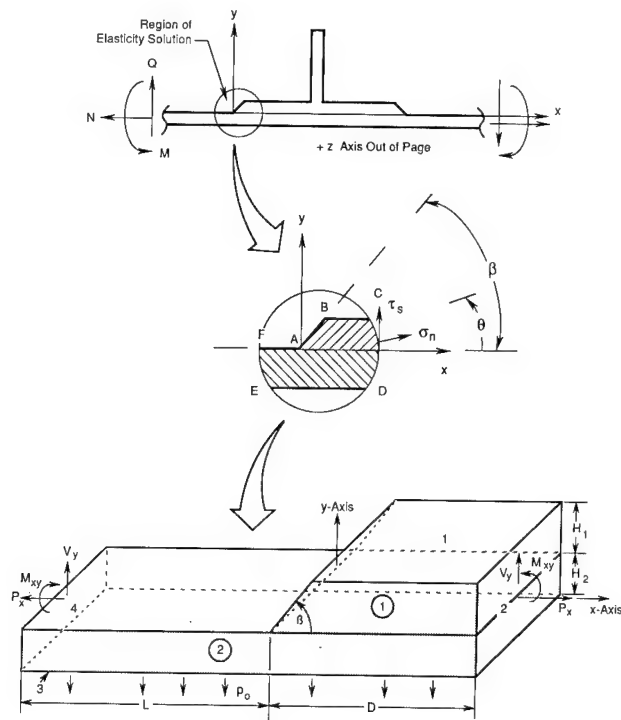


Figure 7. Local Elasticity Model for Stiffener Termination Analysis

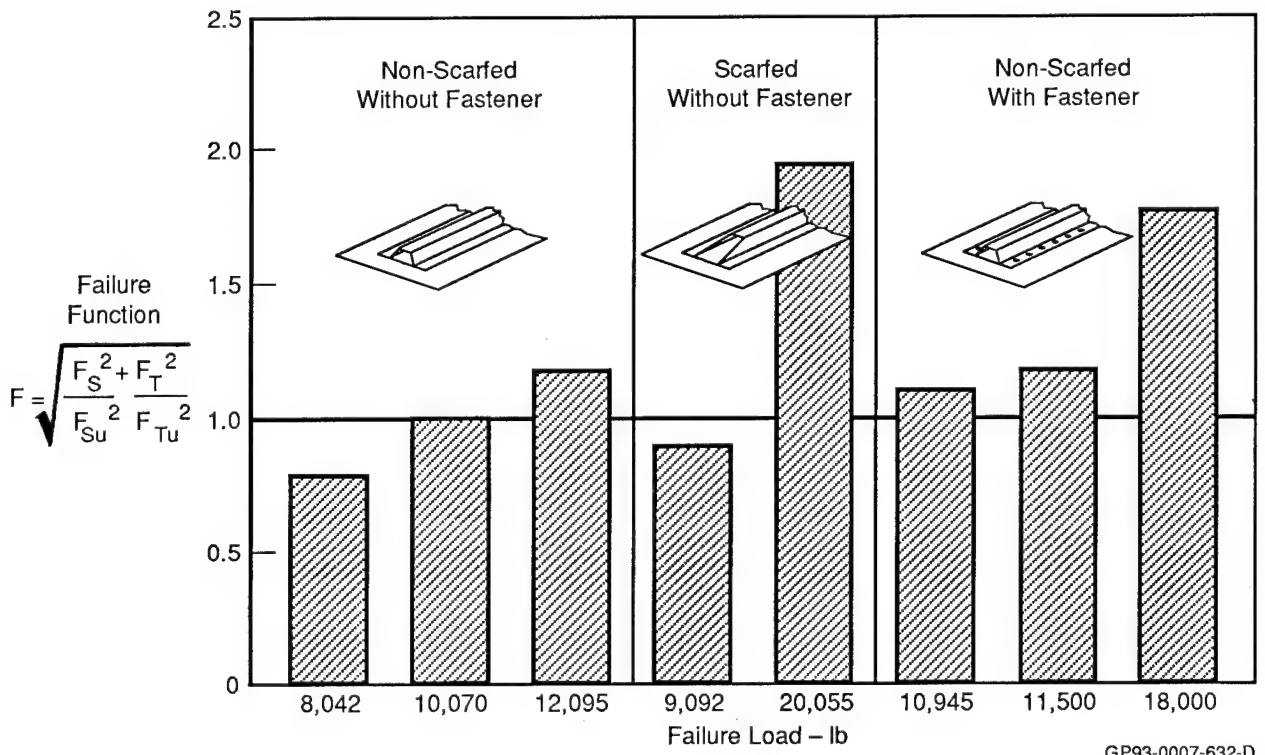
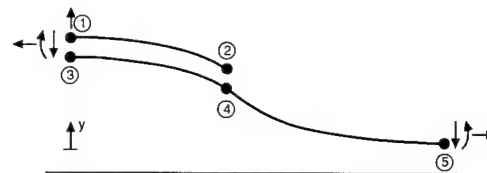


Figure 8. Compression Hat Stiffener Runout Specimen Failure Correlation



Location	Boundary Condition	Prescribed Boundary Value				
		ISFM		WEBSTER		
		Direct	Indirect	Case 1	Case 2	Case 3
1	Deflection	-	$\delta^*$	-	-	-
	Slope	-	-	-	-	-
	Moment	$M^*$	0	$M^{**}$	-	$M^{**}$
	Shear Load	$P^*$	-	$V^{**}$	$P^*$	$V^{**}$
	Axial Load	-	-	$N^{**}$	-	$N^{**}$
2	Deflection	-	-	-	-	-
	Slope	-	-	-	-	-
	Moment	0	0	0	0	0
	Shear Load	0	0	0	0	0
	Axial Load	-	-	0	0	0
3	Deflection	-	-	-	-	-
	Slope	0	0	-	-	-
	Moment	-	-	$M^{**}$	$M^{**}$	$M^{**}$
	Shear Load	0	0	$V^{**}$	-	$V^{**}$
	Axial Load	-	-	$N^{**}$	-	$N^{**}$
4	Deflection	$\delta^{**}$	$\delta^{**}$	-	-	-
	Slope	$\theta^{**}$	$\theta^{**}$	-	-	-
	Moment	-	-	-	-	-
	Shear Load	-	-	-	-	-
	Axial Load	-	-	-	-	-
5	Deflection	$0^{**}$	$0^{**}$	-	0	-
	Slope	$0^{**}$	$0^{**}$	-	0	-
	Moment	-	-	$M^*$	-	$M^*$
	Shear Load	-	-	$P^*$	-	$P^*$
	Axial Load	-	-	$N^*$	-	$N^*$
Bottom Surface	Pressure	-	-	-	-	$p$

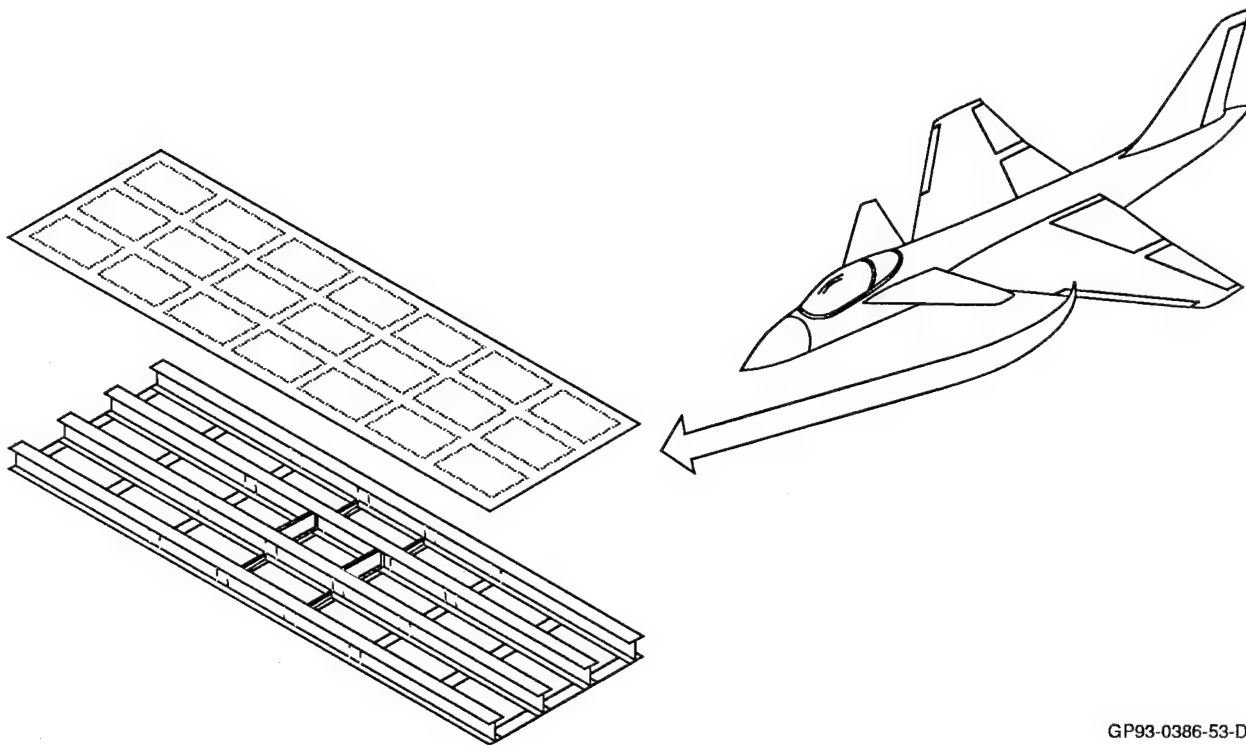
\* Denotes applied boundary condition

\*\* Assumed boundary condition - a function of derivation

GP93-0007-584-D

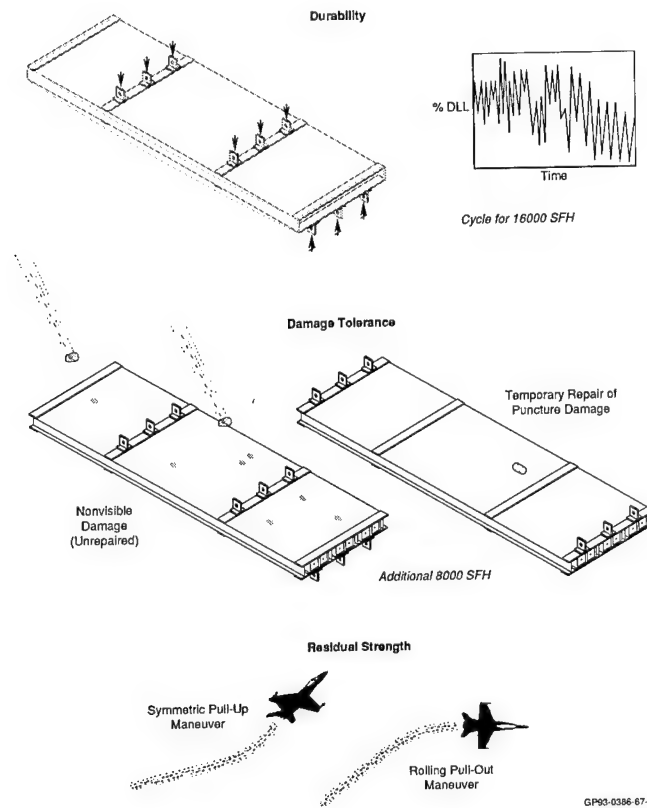
Figure 9. Summary of Boundary Conditions of Skin/Stiffener Joint Analyses

Figure 9. Summary of Boundary Conditions of Skin/Stiffener Joint Analyses

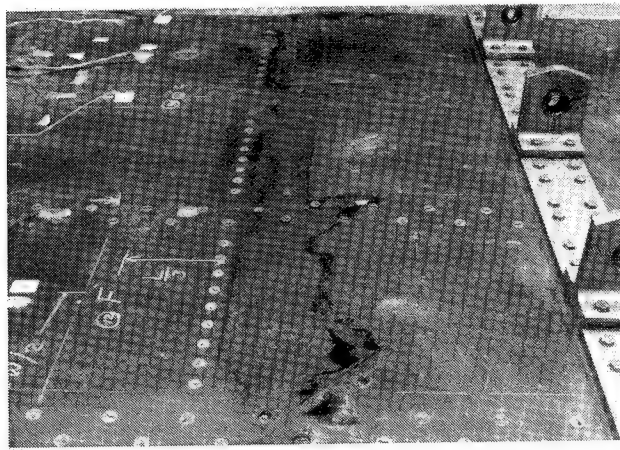


GP93-0386-53-D

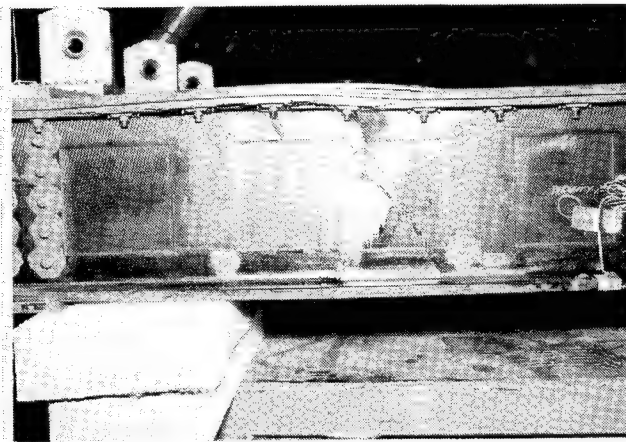
Figure 10. MCAIR High Strain Wingbox Concept



**Figure 11. Test Program for the High Strain Wingbox**



**a) Across Compression Skin**



**b) Side View**

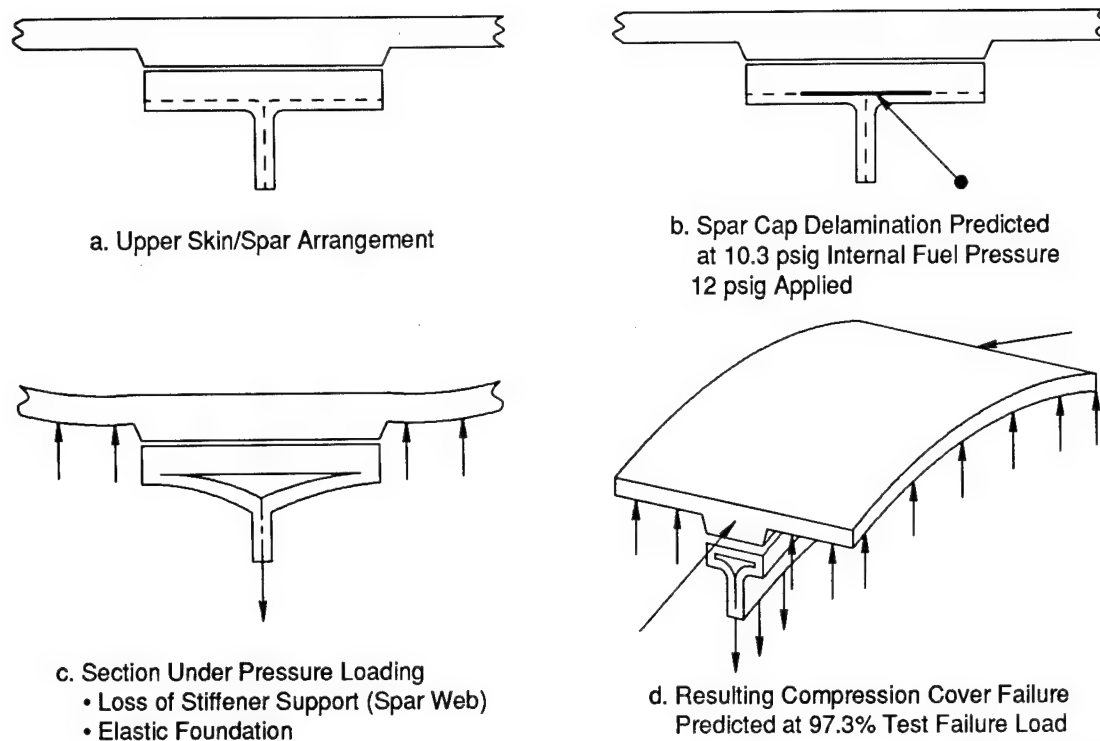
**Figure 12. High Strain Wingbox Failure**

The MCAIR High Strain Wingbox was subjected to an extensive structural analysis as part of the methodology demonstration. The purpose of this analysis was to demonstrate that the out of plane methods previously described could have been used to predict the failure of the wingbox, had they been available. These methods could also have been used to improve designs to provide substantially higher strengths.

The analysis of the wingbox was focused on the spar to skin attachments, since the spars provide the reaction for the skin pressure loads and support for postbuckled skins. Failure progression in the wingbox is depicted in Figure 13. The ISFM method was used to predict that the spar cap to web joint would delaminate at internal fuel pressures greater than 10.3 psig. During the durability phase of the test program, a maximum of 12 psig fuel pressure was applied. Therefore, fuel pressure is predicted to cause a delamination in the spar cap. This delamination changed the support of the skin, exchanging a stiff support (the spar web) for a weaker elastic foundation (the delaminated wrapped plies). The reduced stiffness of this joint led to catastrophic failure of the compression cover under wingbox bending loads. The predicted failure load with delaminated spar caps was 97.3% of that measured in test. These analyses show that the box strength was limited by the early failure of the spar caps. The box was predicted to take at least 50% more load without failure if the spar joint does not delaminate.

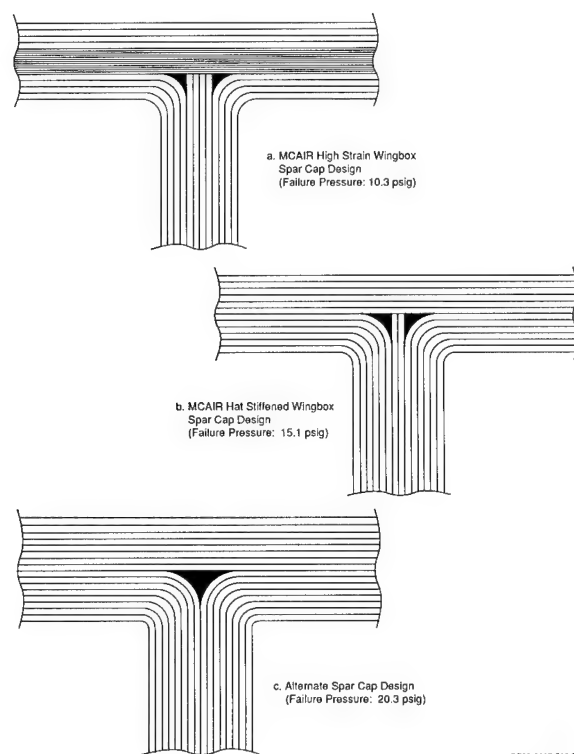
The methodology demonstration was completed by defining an improved spar cap to web joint design. Figure 14 shows the design and the predicted fuel pressure at failure for three of these joints. The design of the joint used in the High Strain Wingbox (Figure 14a) mandated that the pressure load reactions be transferred from the upper skin to the spar webs through both the web plies that wrap into the cap, and the web plies that butt against the cap. MCAIR test data indicates that the strength of butt joints is very low, making them undesirable. Analysis shows that wrapped plies transfer the pressure reaction loads more effectively. A subsequent wingbox, the MCAIR Hat Stiffened Wingbox, featured a spar cap design with fewer plies in the butt joint, and more wrapped plies (Figure 14b). This joint is predicted to fail at 15.1 psig fuel pressure. The third configuration (Figure 14c) represents a spar cap design that features all the web plies wrapped into the spar cap. This joint is strongest and is predicted to fail at 20.3 psig fuel pressure.

The High Strain Wingbox was reanalyzed using CLA, replacing the existing spar cap design with the alternate design shown in Figure 14c. The redesigned spars, and the subsequent lack of delaminations in the spar caps, significantly affect the behavior of the wingbox. The spar caps maintain the stiff support provided by the spar webs, instead of the flexible support provided by the delaminated spar flange. The compressive strength and moment carrying capability of the spar cap/upper skin region is greatly improved for the redesigned wingbox. The predicted load at failure was determined to exceed the RPO maneuver ultimate load by more than 50% when subjected to the same loading conditions.



GP93-0007-585

**Figure 13. Failure Progression of the High Strain Wingbox**



GP93-0007-585-D

**Figure 14. Spar Cap Designs**

Design modifications accounting for out of plane loads using the techniques developed in this program would have significantly increased the failure load of the MCAIR High Strain Wingbox. These analysis techniques can be used in the future to provide stronger integrally stiffened composite structures.

Design Guidelines- These methods and the experience gained in this program provide valuable information for the designer/analyst to reduce the risk of out of plane failures of composite parts. The potential for failures due to out of plane stresses can be minimized through proper design, analysis, and test verification. The design guidelines given in Figure 15 will help to further reduce this potential for failure.

As stated previously, out of plane loads caused by thickness changes can be minimized by using established ply drop off design procedures. These have been based on many years of experience at both MCAIR and Northrop, as well as other aircraft companies. The procedures listed in Figure 16 have been proven to produce durable thickness variation in composite structures.

Element test data are required to validate the out of plane analysis methods and to provide data for the determination of stress allowables. Two small elements and one small subcomponent are recommended for this purpose, and are summarized in Figure 17. The curved laminate test specimen (Figure 17a) is similar to those analyzed for verification of the CLA method. This test is recommended for aircraft design development programs whenever curved laminates are used as primary load paths. The laminate layup, thickness, and radius at the corner of the specimen should be designed to satisfy the range of design applications of the specific structure. The test environment should simulate the service environment of the actual structure. A minimum of five specimens should be tested for each specimen configuration and environment.

The stiffener pull off specimen, shown in Figure 17b, is recommended for future tests to verify skin/stiffener separation strength. This configuration is suggested for determining the pull off strength using a failure mode induced by the buckle shape of the skin, rather than direct pull off as has been performed previously. The length and loading conditions of the specimen are selected to match the wavelength of the skin buckle as closely as possible. Previous tests that use transversely cut sections of the stiffener and skin section produce considerable transverse skin bending. This large bending moment at the skin/stiffener joint is not representative of the local loads in actual postbuckled panels.

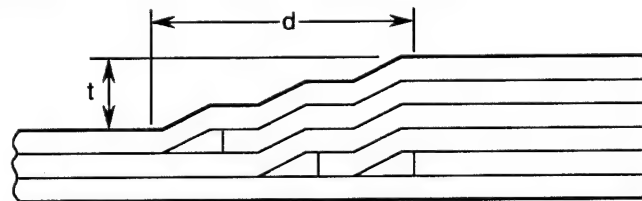
The stiffener runout specimen is shown schematically in Figure 17c. The purpose of this test is to evaluate designs that attempt to reduce interfacial stresses and to avoid out of plane failures. This test is used to verify the design and WEBSTER predictions. Tests should include a sufficient range of termination angles ( $\alpha$ ) to optimize the structural design. Design features being considered for application to



- Avoid sudden load path changes within a structure.
- Avoid sudden stiffness changes. Design stiffener runouts so that bending stiffness is continuously runout into the skin.
- If out of plane loads cannot be reduced to acceptable levels, an arrestment mechanism for interfacial failures (fasteners or stitching) should be provided.
- Follow ply drop off procedures in thickness variations (Figure 16).
- Avoid sharp corners ( $R < 2t$ ) to reduce interlaminar stresses.
- Avoid differences in attachment stiffnesses greater than a factor of 2 in joints.
- Increase skin thicknesses by adding soft plies near discontinuities.
- Optimize skin to stiffener stiffness ratio in postbuckled panels to reduce pull off loads.

GP93-0007-511-D

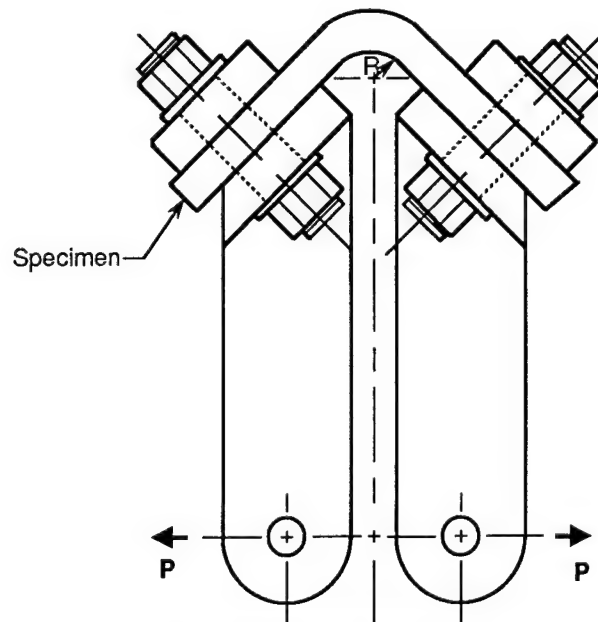
**Figure 15. Recommended Design Guidelines**



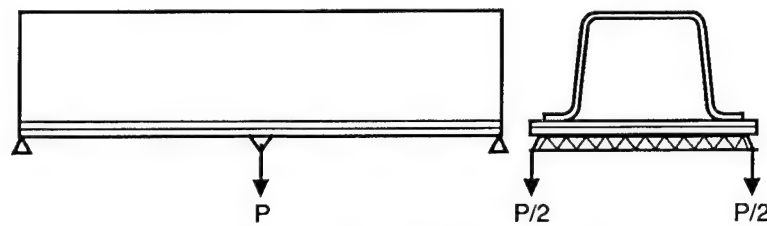
- Maintain symmetry about laminate mid-plane in all constant thickness areas whenever possible
- Maintain  $d/t > 20$  in primary load direction and  $d/t > 10$  in secondary load direction
- Maintain continuous plies on both inner and outer moldline surfaces
- Maintain  $+45^\circ/-45^\circ$  ply combination or  $45^\circ$  cloth ply at inner and outer moldline surfaces
- Stack  $+45^\circ$  and  $-45^\circ$  plies adjacent to each other whenever possible
- Stack  $90^\circ$  plies adjacent to  $+45^\circ/-45^\circ$  pairs whenever possible
- Avoid stacking multiple  $0^\circ$  plies together
- Avoid dropping a  $0^\circ$  ply when adjacent to a  $90^\circ$  ply
- Drop off inner plies first
- Do not terminate plies at fastener patterns

GP93-0386-29-D

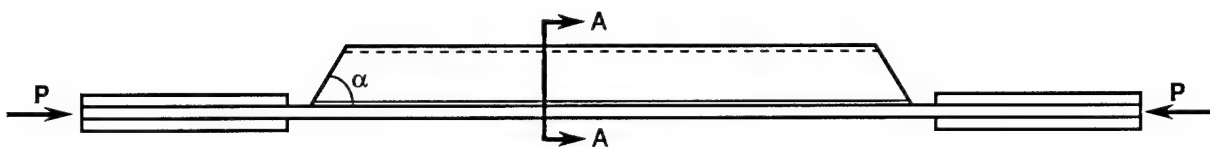
**Figure 16. MCAIR/Northrop Ply Drop Off Design Procedures**



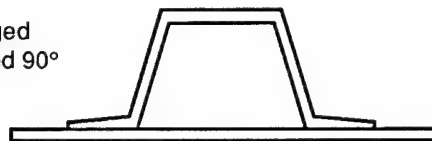
a. Curved Laminate Test Configuration



b. Stiffener Pull Off Test Configuration



A-A Enlarged  
Rotated 90°



c. Stiffener Runout Test Configuration

GP93-0007-587-D

Figure 17. Recommended Test Configuration

structure must be examined in the design development testing. One such option is to place "chicken rivets" (mechanical fasteners that provide a redundant load path for cocured or bonded joints) around the termination region such that an out of plane failure can be arrested. Other options include stitching the stiffener flanges to the skin, scarfing (tapering the stiffener termination) and increasing the skin thickness near the termination site. Design features like these must be included in the test article.

Summary - Simple two dimensional analysis techniques were developed to aid in the design of strong joints for integrally stiffened/bonded composite structures subjected to out of plane loads. It was found that most out of plane failures were due to induced stresses arising from rapid changes in load path direction or geometry, induced stresses due to changes in geometry caused by buckling, or direct stresses produced by fuel pressure or bearing loads. While the analysis techniques were developed to address a great variety of out of plane loading conditions, they were primarily derived to address the conditions described above.

The methods were developed and verified using existing element test data. The methods were demonstrated using the data from a test failure of a high strain wingbox that was designed, built, and tested under a previous program. Subsequently, a set of design guidelines were assembled to assist in the design of safe, strong integral composite structures using the analysis techniques developed.

Acknowledgment - This work was jointly funded by NADC and the FAA under Contract N62269-87-C-0226, with technical monitoring provided by NADC.

#### References

1. Paul, P.C., et al., "Out-of-Plane Analysis of Composite Structures," Final Report on NADC Contract N62269-87-R-0226, Submitted August 1989.
2. Jones, R.M., Mechanics of Composite Materials, Hemisphere Publishing Corporation, New York, 1975, pp. 76-80.
3. McCarty, J.E., et al., "Damage Tolerance of Composites," Interim Reports 1-8, Contract No. F33615-82-C-3213, March 1983 - September 1986.
4. Ogonowski, J.M. and Sanger, K.B., "Postbuckling of Curved and Flat Stiffened Composite Panels Under Combined Loads," NADC-81097-60, December 1984.

# GLOBAL/LOCAL METHODS RESEARCH USING THE CSM TESTBED

Norman F. Knight, Jr.\* and Jonathan B. Ransom\*

NASA Langley Research Center  
Hampton, Virginia

O. Hayden Griffin, Jr.\*\* and Danniella M. Thompson†

Virginia Polytechnic Institute and State University  
Blacksburg, Virginia

## Abstract

Research activities in global/local stress analysis are described including both two- and three-dimensional analysis methods. These methods are being developed within a common structural analysis framework. Representative structural analysis problems are presented to demonstrate the global/local methodologies being developed.

## Introduction

Discontinuities and eccentricities, which are common in practical structures, increase the difficulty of accurately predicting detailed local stress distributions, especially when the component is built of a composite material, such as a graphite-epoxy material. The use of composite materials in the design of aircraft structures introduces added complexity due to the nature of the material systems and complexity of the failure modes. The design and certification process for aerospace structures requires an accurate stress analysis capability. Detailed stress analyses of complex aircraft structures and their subcomponents are required, and these analyses can severely tax even today's computing resources. Embedding detailed "local" finite element models within a single "global" finite element model of an entire airframe structure is usually impractical due to the computational cost associated with the large number of degrees of freedom required for such a detailed global model. If the design load envelope of the structural component is extended, new regions of the component may be discovered with high stress gradients. In that case, the entire analysis with embedded local refinements may have to be repeated with a new model.

---

\* Aerospace Engineer, Structural Mechanics Branch, Structural Mechanics Division.

\*\* Associate Professor, Engineering Science and Mechanics Department.

† Graduate Research Assistant, Engineering Science and Mechanics Department.

The phrase global/local analysis has a myriad of definitions among analysts (*e.g.*, refs. [1,2]). The concept of global and local may change with every analysis level, and also from one analyst to another. An analyst may consider the entire aircraft structure to be the global model and a fuselage section to be the local model. At another level, the fuselage or wing is the global model, and a stiffened panel is the local model. Laminate theory is used by some analysts to represent the global model, and micromechanics models are used for the local model. The global/local stress analysis methodology, herein, is defined as a procedure to determine local, detailed stress states for specific structural regions using information obtained from an independent global stress analysis. A separate refined local model is used for the detailed analysis.

Existing global/local methods generally require that the analyst know where the critical region is located before performing the global analysis (see refs. [3-12]). However, a global/local methodology which does not require a priori knowledge of the location of the local region(s) requiring special modeling could offer advantages in many situations by providing the modeling flexibility required to address detailed local models as their need is identified.

Within NASA Langley's Computational Structural Mechanics or CSM activity (see ref. [13]), methodology is being developed for both two-dimensional and three-dimensional global/local stress analysis procedures. The two-dimensional global/local analysis methods are being developed at Langley (see ref. [14-15]), and the three-dimensional methods are being developed at Virginia Polytechnic Institute and State University under NASA Grant NAG1-675 (see refs. [16-18]). The overall goal of these CSM activities in global/local stress analysis is to develop a computational strategy for obtaining detailed stress states of composite structures. The objectives of this research include developing methodology for performing global/local stress analysis of composite structures, developing criteria for defining the global/local interface regions and local modeling requirements, and demonstrating the computational strategy on representative structural analysis problems. The paper concludes by identifying global/local methods research directions.

### Global/Local Methodology

Global/local stress analysis methodology is defined as a procedure to determine local, detailed stress states for specific structural regions using information obtained from an independent global stress analysis. The local model refers to any structural subregion within the defined global model. The global stress analysis is performed independent of the local stress analysis. The interpolation region encompassing the critical region is specified. A surface spline interpolation function is evaluated at every point in the interpolation region yielding a spline matrix and vector of unknown coefficients. The global field is used to compute the unknown coefficients. An independent, more refined local model is generated within the previously defined interpolation region. The global displacement field is interpolated producing a local displacement field which is applied as a "boundary condition" along the boundaries of the local model. Then, a complete local finite element analysis is performed which may be either two- or three-dimensional.

The development of a global/local stress analysis capability for structures generally involves four key components. The first component is an "adequate" global analysis. In this context, "adequate" implies that the global structural behavior is accurately determined and that local structural details are at least grossly incorporated. The second component is a strategy for identifying, in the global model, regions requiring further study. The third component is a procedure for defining the "boundary conditions" along the global/local interface boundary. Finally, the fourth component is an "adequate" local analysis. In this context, "adequate" implies that the local detailed stress state is accurately determined and that compatibility requirements along the global/local interface are satisfied. The development of a global/local stress analysis methodology requires an understanding of each key component and insight into its interaction.

In practice, the global analysis model is "adequate" for the specified design load cases. However, these load cases frequently change in order to extend the operating envelope of the structure or to account for previously unknown effects. In these incidents, the global analysis may identify new critical areas or "hot spots" that require further study. The methodology presented herein provides an analysis tool for these local analyses.

### Terminology

The terminology of the global/local methodology presented herein is depicted in figure 1 to illustrate the components of the analysis procedure. The global model, figure 1a, is a finite element model of an entire structure or a subcomponent of a structure. A region requiring a more detailed interrogation is subsequently identified by the structural analyst. This region may be obvious, such as a region around a cutout in a panel, or not so obvious, such as a local buckled region of a curved panel loaded in compression. Because the locations of these regions are usually unknown prior to performing the global analysis, the structural analyst must develop a global model with sufficient detail to represent the global behavior of the structure. An interpolation region is then identified around the critical region as indicated in figure 1b. The interpolation region is the region within which the generalized displacement solution will be used to define the interpolation matrix. An interpolation procedure is used to determine the generalized displacements used to define "boundary conditions" for the local model. For two-dimensional local models, these generalized displacements correspond to displacements and rotations along the global/local interface region. For three-dimensional local models, these generalized displacements are used to define kinematically consistent, three-dimensional fields from the two-dimensional displacements and rotations. The global/local interface boundary, indicated in figure 1c, coincides with the intersection of the boundary of the local model with the global model. The definition of the interface boundary may affect the accuracy of the interpolation and thus the local stress state. The local model lies within the interpolation region as shown in figure 1c and is generally more refined than the global model in order to predict more accurately the detailed state of stress in the critical region. However, the local model is independent of the global finite element model as indicated in figure 1d. The coordinates or nodes of the local model need not be coincident with any of the coordinates or nodes of the global model.

The global/local interpolation procedure consists of generating a matrix based on the

global solution and a local interpolated field. The local interpolated field is that field which is interpolated from the global analysis and is valid over the domain of the local model. Local stress analysis involves the generation of the local finite element model, use of the interpolated field to impose boundary conditions on the local model, and the detailed stress analysis.

### **Global Modeling and Analysis**

The development of a global finite element model of an aerospace structure for accurate stress predictions near local discontinuities is often too time consuming to impact the design and certification process. Predicting the global structural response of these structures often has many objectives including overall structural response, stress analysis, and determining internal load distributions. Frequently, structural discontinuities such as cutouts are only accounted for in the overall sense. Any local behavior is then obtained by a local analysis, possibly by another analyst. The load distribution for the local region is obtained from the global analysis. The local model is then used to obtain the structural behavior in the specified region. For example, the global response of an aircraft wing is obtained by a coarse finite element analysis. A typical subcomponent of the wing is a stiffened panel with a cutout. Since cutouts are known to produce high stress gradients, the load distributions from the global analysis of the wing are applied to the stiffened panel to obtain the local detailed stress state. One difficulty in modeling cutouts is the need for the finite element mesh to transition from a circular pattern near the cutout to a rectangular pattern away from the cutout. This transition region is indicated in figure 2 and will be referred to as a transition square (*i.e.*, a square region around the cutout used to transition from rings of elements to a rectangular mesh). This transition modeling requirement impacts both the region near the cutout and the region away from the cutout. Near the cutout, quadrilateral elements may be skewed, tapered, and perhaps have an undesirable aspect ratio. In addition, as the mesh near the cutout is refined by adding radial "spokes" of nodes and "rings" of elements (see figure 2), the mesh away from the cutout also becomes refined. For example, adding radial spokes of nodes near the cutout also adds nodes and elements in the shaded regions (see figure 2) away from the cutout. This approach may dramatically increase the computational requirements necessary to obtain the detailed stress state. Alternate mesh generation techniques using transition zones of triangular elements or multipoint constraints may be used; however, the time spent by the structural analyst will increase substantially.

The global modeling herein, although coarse, is sufficient to represent the global structural behavior. The critical regions have been modeled with only enough detail to represent their effect on the global solution. This modeling step is one of the key components of the global/local methodology since it provides an "adequate" global analysis. Although the critical regions are known for the numerical studies discussed in a subsequent section, this *a priori* knowledge is not required but may be exploited by the analyst.

### **Local Modeling and Analysis**

The local finite element modeling and analysis is performed to obtain a detailed analysis of the local structural region(s). The local model accurately represents the geometry



of the structure necessary to provide the local behavior and stress state. The discretization requirements for the analysis are governed by the desired accuracy of the solution. The discretization of the local model is influenced by its proximity to a high stress gradient.

One approach for obtaining the detailed stress state is to model the local region with an arbitrarily large number of finite elements. Higher-order elements may be used to reduce the number of elements required. Detailed refinement is much more advantageous for use in the two- or three-dimensional local model than in the global model. The local refinement affects only the local model, unlike embedding the same refinement in the global model which would propagate to regions not requiring such a level of detailed refinement. A second approach is to refine the model based on engineering judgment. Mesh grading, in which smaller elements are used near the gradient, may be used. An error measure based on the change in stresses from element to element may be used to determine the accuracy in the stress state obtained by the initial local finite element mesh. If the accuracy of the solution is not satisfactory, additional refinements are required. The additional refinements may be based on the coarse global model or the displacement field in the local model which suggests a third approach. The third approach is a multi-level global/local analysis. At the second local model level, any of the three approaches discussed may be used to obtain the desired local detailed stress state. A two- or three-dimensional local model may be used at this level. Detailed refinement is used for local modeling in the studies performed to date.

### **Global/Local Interface Boundary Definition**

The definition of the global/local interface boundary is problem dependent. Herein, the location of the nodes on the interface boundary need not be coincident with any of the nodes in the coarse global model. The distance that the local model must extend away from a discontinuity is highly dependent upon the coarse model used [7]. The more accurate the coarse model displacement field is, the closer the local model boundary may be to the discontinuity. This conclusion is based on the results of a study of a flat, isotropic panel with a central cutout subjected to uniform tension, and extends to other structures with high stress gradients.

Stresses are generally obtained from a displacement-based finite element analysis by differentiation of the displacement field. For problems with stress gradients, the element stresses vary from element to element, and in some cases this change,  $\Delta\sigma$ , may be substantial. The change in stresses,  $\Delta\sigma$ , may be used as a measure of the adequacy of the finite element discretization. Large  $\Delta\sigma$  values indicate structural regions where more modeling refinement is needed. Based on this method, structural regions with small values of  $\Delta\sigma$  have obtained uniform stress states away from any gradients. Therefore, the global/local interface boundary should be defined in regions with small values of  $\Delta\sigma$  (i.e., away from a stress gradient). Exploratory studies to define an automated procedure for selecting the global/local interface boundary for two-dimensional problems have been performed using the strain energy per unit area since it represents a combination of all the stress components instead of a single stress component. Regions with high stress gradients will also have changes in this measure of strain energy from element to element. For three-dimensional problems, the interlaminar stress fields are of interest; however, these stresses are generally

excluded from the global two-dimensional analysis. Locating the global/local interface is then more difficult and currently is assessed by imposing kinematically consistent displacements from the two-dimensional model along the boundaries of the local three-dimensional model.

### **Global/Local Interpolation Procedure**

The global/local analysis method is used to determine local, detailed stress states using independent, refined local models which exploit information from less refined global models. A two-dimensional finite element analysis of the global structure is performed to determine its overall behavior. A critical region may be identified from the results of the global analysis. The global solution may be used to determine an applied displacement field along the boundary (*i.e.*, boundary conditions) of an independent local model of the critical region. This step is one of the key components of the global/local methodology; namely, interpolation of the global solution to determine boundary conditions for the local model. For the two-dimensional analyses, the interpolation is performed using a surface spline approach (see refs. [14,15]). A surface spline is used to interpolate a function of two variables and removes the restriction of single variable schemes which require a rectangular array of grid points. The derivation of the surface spline interpolation function used herein is based on the principle of minimum potential energy for linear plate bending theory. This approach incorporates a classical structural mechanics formulation into the spline interpolation procedure in a general sense. Using an interpolation function which also satisfies the linear plate bending equation provides inherent physical significance to a numerical analysis technique. The spline interpolation is used to interpolate the displacements and rotations from a global analysis and thereby provides a functional description of each field over the domain. The fields are interpolated separately which provides a consistent basis for interpolating global solutions based on a plate theory with shear flexibility effects incorporated. That is, the out-of-plane deflections and the bending rotations are interpolated independently rather than calculating the bending rotations by differentiating the interpolated out-of-plane deflection field.

The procedure for interpolation between the two-dimensional global finite element analysis and the three-dimensional local analysis currently relies on having a one-to-one in-plane nodal correspondence. That is, the local models are created by simple expansion of the global grid in the third dimension. For finer local models without this correspondence, interpolation functions representing the response of the global model along the global/local interface can be used. This method would eliminate the need to predict the three-dimensional response a priori. The displacements would then continue to be applied in a kinematically admissible manner in the third dimension along the interface. Although this approach may result in slightly larger local models so that the three-dimensional response can be fully developed, the potential for incorrect assumptions about the response has been eliminated.

### **Computational Strategy**

A schematic which describes the overall solution strategy is shown in figure 3. The computational strategy described herein is implemented through the use of the Computa-

tional Structural Mechanics (CSM) Testbed (see refs. [19-20]). The CSM Testbed is used to model and analyze both the global and local finite element models of a structure. Two computational modules or processors were developed to perform the global/local interpolation procedure. Processor SPLN evaluates the spline coefficient matrix. Processor INTS solves for the interpolation coefficients and performs the local interpolation to obtain the "boundary conditions" for the local model. Various other Testbed processors are used in the stress analysis procedure. The overall computational strategy for the global/local stress analysis methodology is controlled by a high-level procedure written using the command language of the Testbed (see ref. [21]). The command language provides a flexible tool for performing computational structural mechanics research.

### Numerical Results

The effectiveness of the computational strategy for the global/local stress analysis outlined in the previous sections is demonstrated by obtaining the detailed stress states for a blade-stiffened graphite epoxy panel with a discontinuous stiffener and the interlaminar stresses of a cross-ply composite plate with a hole. The first problem was selected to demonstrate the two-dimensional global/local analysis capabilities while the second problem was selected to demonstrate the three-dimensional global/local analysis capabilities. The objective of these numerical studies is to demonstrate the global/local stress analysis methodology.

All numerical studies were performed on a Convex C220 minisupercomputer. The computational effort of each analysis is quantified by the number of degrees of freedom used in the finite element model, the computational time required to perform a stress analysis, and the amount of auxiliary storage required. The computational time is measured in central processing unit (CPU) time. The amount of auxiliary storage required is measured by the size of the data library used for the input/output of information to a disk during a Testbed execution.

#### Composite Blade-Stiffened Panel with Discontinuous Stiffener

Recent interest in applying graphite-epoxy materials to aircraft primary structures has led to several studies of postbuckling behavior and failure characteristics of graphite-epoxy components (*e.g.*, ref. [22]). One goal of these studies has been the accurate prediction of the global response of the composite structural component in the postbuckling range. In one study of composite stiffened panels, a blade-stiffened panel was tested (see ref. [23]). This composite blade-stiffened panel was proof-tested and used as a "control specimen". The panel was subsequently used in a study of discontinuities in composite blade-stiffened panels. The global structural response of these composite blade-stiffened panels presented in reference [13] correlate well with the earlier experimental data. The composite blade-stiffened panel with a discontinuous stiffener shown in figure 4 is representative of a typical aircraft structural component and will be used to demonstrate and assess the global/local methodology. This problem was selected because it has characteristics which often require a global/local analysis. These characteristics include a discontinuity, eccentric loading, large displacements, large stress gradients, high inplane loading, and a brittle material system. This problem represents a generic class of laminated composite structures with

discontinuities for which the interlaminar stress state becomes important. The local and global finite element modeling and analysis needed to predict accurately the detailed stress state of flat blade-stiffened graphite-epoxy panel loaded in axial compression is described in this section.

The overall panel length  $L$  is 30 in., the overall width  $W$  is 11.5 in., the stiffener spacing  $b$  is 4.5 in., the stiffener height  $h_s$  is 1.4 in., and the cutout radius  $r_0$  is 1 in. The three blade-shaped stiffeners are identical. The loading is uniform axial compression. The loaded ends of the panel are clamped and the sides are free. The material system for the panel is T300/5208 graphite-epoxy unidirectional tapes with a nominal ply thickness of 0.0055 in. Typical lamina properties for this graphite-epoxy system are 19,000 ksi for the longitudinal Young's modulus, 1,890 ksi for the transverse Young's modulus, 930 ksi for the shear modulus, and 0.38 for the major Poisson's ratio. The panel skin is a 25-ply laminate ( $[\pm 45/0_2/\mp 45/0_3/\pm 45/0_3/\mp 45/0_3/\pm 45/0_2/\mp 45]$ ) and the blade stiffeners are 24-ply laminates ( $[\pm 45/0_{20}/\mp 45]$ ).

End-shortening results are shown in figure 5 for the "control specimen" and for the configuration with a discontinuous stiffener. These results indicate that the presence of the discontinuity markedly changes the structural response of the panel. The structural response of the "control specimen" is typical of stiffened panels. Two equilibrium configurations are exhibited; namely, the prebuckling configuration and the postbuckling configuration. The structural response of the configuration with a discontinuous stiffener is nonlinear from the onset of loading due to the eccentric load path associated with the discontinuous stiffener and the cutout. The blade-stiffened panel with a discontinuous stiffener was tested to failure. Local failures occurred prior to overall panel failure as is evident from the end-shortening results shown in figure 5.

**Global Analysis.** A linear global stress analysis of the composite blade-stiffened panel with a discontinuous stiffener was performed for an applied load corresponding to  $P/EA$  of 0.0008 (i.e., an applied compressive load  $P$  of 19,280 pounds normalized by the extensional stiffness  $EA$ ). At this load level, the structural response of the panel is essentially linear. Out-of-plane deflections are present, however, due to the eccentric load path caused by the discontinuous stiffener. Several global finite element models are considered as indicated in Table 1 to determine a converged solution for comparison purposes since a theoretical solution is not available. The value of the longitudinal stress resultant at the edge of the cutout changed less than 2% between Models G2 and G4. Therefore, Model G1 will be referred to as the "coarse" global model (see figure 6), Model G2 will be referred to as the "refined" global model, and Model G4 will be referred to as the "converged" global model.

The distribution of the longitudinal stress resultant  $N_x$  normalized by the average applied running load  $(N_x)_{avg}$  (i.e., applied load divided by the panel width) as a function of the lateral distance from the center of the panel normalized by the radius of the cutout is shown in figure 7 for both the "coarse" (G1) and the "refined" (G2) global models. The maximum longitudinal stress resultants  $(N_x)_{max}$  normalized by the average applied running load  $(N_x)_{avg}$  are given in Table 1. The results obtained using the coarse global model adequately represent the distribution away from the discontinuity but underestimate (by 24%) the stress concentration at the edge of the discontinuity.

The change in the strain energy per unit area within the transition square indicates that a high stress gradient exists near the discontinuity and rapidly decays away from the discontinuity. These results are consistent with the structural analyst's intuition, and the local models described subsequently will further interrogate the region near the discontinuity. For this load level, the skin-stiffener interface region has not yet become heavily loaded. However, this region will also be studied further to demonstrate the flexibility of the global/local stress analysis procedure presented herein.

**Local Analyses.** A global/local analysis capability provides an alternative approach to global mesh refinement and a complete solution using a more refined mesh. For this example, one "critical" region is easily identified as the region near the cutout and discontinuous stiffener. A second critical region that may require further study is indicated by the slight gradient near the intersection of the outer blade-stiffeners and the panel skin at the panel midlength. Skin-stiffener separation has been identified as a dominant failure mode for stiffened composite panels (see ref. [22]). The global model, the interpolation regions and the local models considered are shown in figure 8. The global model corresponds to the "coarse" global model (G1) and the shaded regions correspond to the interpolation regions which are used to generate the spline coefficient matrix and to extract boundary conditions for the local model. As indicated in figure 8, two different critical regions are considered. One region is near the discontinuity, and a circular local model is used. The boundary of the circular model is inscribed in the transition square. That is, the outer radius of the circular model is equal to half the length of a side of the transition square. The other region is near the skin-stiffener interface region at the panel midlength for one of the outer stiffeners. The global/local interpolation for the local models is performed from the data obtained from the "coarse" global model analysis. Two interpolation regions were used in each of the local analyses. The first interpolation region, specified in the plane of the panel skin, is used to obtain the boundary conditions on the global/local interface boundary of the panel skin. The second interpolation region, specified in the plane of the stiffener, is used to obtain the boundary conditions on the global/local interface boundary of the stiffener. The boundary conditions for the panel skin and the stiffener were interpolated separately. Compatibility of displacements and rotations at the skin-stiffener intersection on the global/local interface boundaries was enforced by imposing the boundary conditions obtained for the panel skin.

The local model (Model LC1 in Table 1) of the first critical region near the discontinuity has 576 4-node quadrilateral shell elements, 612 nodes, and 3456 degrees of freedom. This local model has only 56% of the elements used in the refined global analysis. The distribution of the longitudinal stress resultant  $N_x$  at the panel midlength normalized by the average running load  $(N_x)_{avg}$  is shown in figure 9 as a function of the lateral distance from the cutout normalized by the cutout radius. These results indicate that the global/local analysis based on the coarse global solution accurately predicts the stress concentration at the cutout as well as the distribution at the global/local interface boundary.

The second critical region near the intersection of the outer blade-stiffener and the panel skin at the midlength has been studied in greater detail. Three different local finite element models of this critical region are considered as indicated in Table 1. The first,



Model LR1, has the same number of nodes (25) and number of elements (16) within the critical region as the coarse global model (G1). The second, Model LR2, has the same number of nodes (45) and number of elements (32) within the critical region as the refined global model (G2). The third and most refined model, Model LR3, has 117 nodes, 96 elements and 462 degrees of freedom. The longitudinal stress resultant  $N_x$  distributions obtained for the local models (LR1 and LR2) correlate well with the  $N_x$  distributions for the coarse and refined global models (Models G1 and G2). However, these models are not sufficiently refined in the skin-stiffener interface region to accurately predict the gradient at the skin-stiffener intersection. The distribution of the longitudinal stress resultant  $N_x$  normalized by the applied running load as a function of the lateral distance from the center of the panel normalized by the radius of the cutout is shown in figure 10. These results indicate that the global/local analysis using the local model Model LR3 predicts a higher gradient at  $y/r_0 = -4.5$  in the skin-stiffener interface region than the other global and local analyses. A third global model, Model G3, is used to investigate the local structural behavior predicted by Model LR3. The global analysis performed with Model G3 predicts the same local behavior as the analysis performed with Model LR3 as indicated in figure 10. The local analysis revealed local behavior at the skin-stiffener interface region that was not predicted by either of the global models. In addition, the global modeling requirement for examining the skin-stiffener interface region is substantial. Because the global models were generated to predict the stress distribution around the discontinuity, additional radial "spokes" in the transition square are required to refine the panel skin in the skin-stiffener interface region in the longitudinal direction. The global/local analysis capability provides the analyst with the added modeling flexibility to obtain an accurate detailed response at multiple critical regions (*i.e.*, at the discontinuity and at the skin-stiffener interface region) with minimal modeling and computational effort.

**Computational Requirements.** A summary of the computational requirements for the global and local analyses of the graphite-epoxy blade-stiffened panel with the discontinuous stiffener is given in Table 2. The computational cost in CPU seconds of the local analyses around the discontinuity is approximately 57% of the CPU time of the refined global analysis. The CSM Testbed data libraries for the local analyses are half of the size of the data library for the refined global analysis. The local models have 55% and 16% of the total number of degrees of freedom required for the refined model (G2) and converged global model (G4), respectively. The CPU time for the refined local analysis (LR3) of the skin-stiffener interface region is 24% of the CPU time required for the global analysis with Model G3. The size of the data library for the local analysis is 5% of the size of the data library required for the analysis with Model G3.

**Usage Guidelines.** Usage guidelines for the two-dimensional global/local analysis procedure described herein and derived from the global/local analysis of the blade-stiffened panel with a discontinuous stiffener are as follows. An "adequate" global analysis is required to ensure a sufficient number of accurate data points to provide accurate "boundary conditions" for the local model. When the global/local interface boundary,  $R_L$  is within the high stress gradient (*i.e.*, within a distance of two times the cutout radius from the cutout edge), the importance of an "adequate" global analysis in the high gradient region is increased. The interpolation region should coincide with or be larger than the local

model. To satisfy the compatibility requirements at the global/local interface boundary, the local model boundary  $R_L$  should be defined sufficiently far from the cutout (*i.e.*, a distance of approximately six times the radius from the cutout). For the blade-stiffened panel, two interpolation regions should be specified, one for the interpolation of the boundary conditions on the boundary of the panel skin and a second for the interpolation of the boundary conditions on the outer edges of the stiffeners.

### Cross-Ply Composite Laminates With Holes

Global/local finite element analyses of a laminated composite plate with a hole were presented in references [16-18] and summarized herein. The displacements of the global/local interface from the two-dimensional global model are applied to the edges of the three-dimensional local model. Three different hole diameters, one, three, and six inches, are considered in order to compare the effect of hole size on the three-dimensional stress state around the hole. All laminates are 0.1-inch thick, with planar dimensions of 18 by 12 inches, and loaded by uniform uniaxial compressive displacement of the ends. Typical properties for this T300/5208 graphite-epoxy system are 19,200 ksi for the longitudinal Young's modulus, 1,560 ksi for the transverse Young's moduli, 820 ksi, 820 ksi, and 540 ksi for the shear moduli ( $G_{12}$ ,  $G_{13}$ ,  $G_{23}$ , respectively), and 0.239, 0.239, and 0.45 for the Poisson's ratios ( $\nu_{12}$ ,  $\nu_{13}$ ,  $\nu_{23}$ , respectively).

To streamline the analysis so that adequate response predictions are obtained, a simplified analysis of the entire body (or global region) is performed using two-dimensional finite elements. However, near any geometric or material anomaly or near traction-free edges, the two-dimensional solution will not necessarily represent all the necessary information (see ref. [24]), and therefore a more detailed analysis is performed on a local region of interest with three-dimensional finite elements. In particular, this two-dimensional to three-dimensional global/local finite element analysis technique is applied to a laminated composite plate with a central circular hole. The local region of interest is the area around the hole, and the interlaminar stresses are examined in detail.

**Global Analysis.** The global model was generated using processor CSM1 of the CSM Testbed which produces a grid of plate elements. The plate consists of laminated  $[0_2/90_2]_S$  cross-plys. The plate had a total thickness of 0.1 inches and planar dimensions of 18 by 12 inches. The entire plate was loaded in compression by imposing a uniform  $x$ -displacement of 0.1 inches at the left edge, and restraining  $x$ -direction displacements at the right edge. All of the corner nodes were restrained from movement in the  $y$ -direction. No other  $y$ -direction displacements were imposed. The response is in the linear elastic range. A number of cases were considered in reference [18] including a study of the effect of varying hole size on stress distribution and comparing different stacking sequences for the cross-ply laminates. Only the effect of varying hole sizes on the interlaminar stress distribution is reported herein.

The grid generated by processor CSM1 was modified slightly to produce concentric rings of elements with specified thicknesses around the hole. Because interlaminar stresses are often confined to a region which is a multiple of the laminate thickness, two rings of elements of equal thickness were located within a one-laminate-thickness region near the



hole. The next two rings of elements were specified to be one and two laminate thicknesses away, respectively. The final ring of elements was allowed to vary in planar dimension in order to mate the curved elements of the hole region with the surrounding rectangular elements. A minimum element side length of 0.1 inches was maintained throughout this matching region. The number of radial spokes emanating from the hole was varied in order to obtain elements with relatively low aspect ratios and in-plane curvatures. Information about the grids for the various models with different hole sizes are presented in Table 3, and the undeformed grids are presented in figure 11. Because of the loading and stacking sequence, analysis of one-quarter of the global model would have been sufficient; however, the analysis was performed on the entire global model because of the way it was generated by processor CSM1. The 9-node assumed natural-coordinate strain element was utilized in the global model.

The deformed geometry plots with exaggerated deflections (scaled by a factor of 10) for each hole example with the  $[0_2/90_2]_S$  stacking sequence are shown in figure 11. Note that the left and right edges of each plate remained straight as specified by the boundary conditions. The circular holes became elliptical, and there is a bulging of the previously straight edges of the plates. As expected, the deformations and influence due to the hole extend farther into the plate with larger holes. The square around each hole exhibits concavity on its vertical sides and convexity on its horizontal sides. These are the global/local interfaces of interest.

**Local Analysis.** The local model was created by expanding the global model in three dimensions. Because a symmetric stacking sequence was used with an in-plane loading condition, only one-half of the laminate thickness would normally be modeled for the local analysis. Because a cross-ply laminate was considered, two additional planes of symmetry existed. This symmetry resulted in modeling only one-quarter of the curved edge area. Not all of these symmetry planes exist for more general ply orientations or loading conditions. In-plane displacement components from the global model were applied directly to the local model as applied displacements with the rigid-body translation of the  $yz$ -symmetry planes removed. A local coordinate system located at the center of the hole was chosen. As shown schematically in figure 12, along the  $xz$ -symmetry plane, the zero  $y$ -direction displacements ( $v=0$ ) were applied through the thickness of the model, while at the  $yz$ -symmetry plane, the zero  $x$ -direction displacements ( $u=0$ ) were applied. Along the two straight edges that were not symmetry planes, the midplane  $x$ - and  $y$ -direction displacements were applied through the thickness. The bottom of the local model, which is the midplane of global model, was constrained from moving in the  $z$ -direction ( $w=0$ ). No other  $z$ -direction displacements were applied in order to allow complete boundary layer development. Around the hole, no displacements were applied other than those at the symmetry planes. The three-dimensional models are shown for the hole sizes considered in figure 13, while Table 4 contains information about the local meshes.

The three-dimensional element utilized in this study is the BR20 element of the CSM Testbed (see ref. [19]). This element is from a family of serendipity (displacement formulation) elements installed in the CSM Testbed under NASA Grant NAG1-675. Varying degrees of integration level are allowed by the element implementation – a full integration

(27 Gauss point) rule is used herein. Griffin [16] concluded that two 20-node elements per ply thickness with full integration were sufficient to represent the response of a cross-ply composite plate subjected to in-plane loads.

The deformed local curved edge meshes for the  $[0_2/90_2]_S$  stacking sequence can be seen in figure 13 along with the undeformed local meshes for each of the plates. The displacements for each example were scaled individually (i.e., different scale factors) for viewing. The deformed mesh for each hole is compressed in the  $x$ -direction. The holes became elliptical as in the global case. Because of the scaling selected, the smaller holes appear to be more eccentric than the larger holes. For each of the hole cases, a noticeable thickening of the local model can be seen around the hole. This thickening is not constant for all hole sizes, nor is it uniform around the hole. A warping of the elements can also be seen near the same position and is strongest along the innermost rings of elements and extends outward. The diametrical changes are not constant through the thickness of the laminate, and vary with stacking sequence [18].

The displacements were post-processed to determine the stress fields around the hole at the laminate midplane. These interlaminar stress results were normalized by the absolute value of the average far-field stress  $\sigma_x$  (-56783 psi) for the laminate with a one-inch-diameter hole. The normalized interlaminar normal stress ( $\sigma_z/|\sigma_x|$ ) and interlaminar shear stresses ( $\tau_{rz}/|\sigma_x|$ ) as a function of the angle ( $\theta$ ) around the hole are presented in figures 14 and 15. The effect of hole size can be seen.

While there is some difference in the magnitude of interlaminar normal stress around the hole near the midplane, the principal difference is the location of the maximum as seen in figure 14. As hole size increases, the location of the maximum value tends to shift around the hole away from the axis of load application due to the relief of certain stress components by the proximity of the straight free edge of the laminate to the edge of the larger hole. Also, the magnitude of interlaminar normal stress  $\sigma_z$  is reduced for the larger hole, also due to the relief of stress by proximity to the straight free edge. The one-inch-diameter hole represents the worst case for interlaminar normal stress, exhibiting not only the highest negative value, but a positive (tensile) portion as well, due to the large distance between the hole edge and the free edge of the plate, resulting in a very small degree of stress relief.

The effectiveness of the two-dimensional to three-dimensional global/local finite element analyses to reduce computational requirements can be seen by comparing the solution times required to solve the global and local models as presented in Tables 3 and 4. The global model for the plate with a one-inch-diameter hole contains the largest number of elements and degrees of freedom considered. The use of global/local techniques for this case greatly reduced the time for solution as compared to a full three-dimensional model. Solution times for the global models do not decrease linearly because different equation solvers were used – both of which exploit the vector architecture of the CONVEX minisupercomputer. For the global solution, the incomplete Choleski preconditioned conjugate gradient (ICCG) iterative method implemented in processor ITER was selected. Each of the local models was solved using processor BAND, which contains a direct Choleski solver

designed for matrices stored in a variable-band format. The stiffness matrices, stored in a sparse-storage scheme in the CSM Testbed database files, are automatically converted to the variable-band storage scheme used by BAND. These solvers are described in reference [19].

**Usage Guidelines.** Usage guidelines for two-dimensional to three-dimensional global/local finite element analysis around the hole for cross-ply laminates with holes follow. The global solution need only be accurate in the global sense, representing the two-dimensional behavior of the midplane of the plate around the hole to a sufficient degree, recognizing that the two-dimensional solution cannot reveal the true three-dimensional character of the response around the hole. Placement of the global/local interface must be outside the region of suspected three-dimensionality in order to avoid unduly constraining the three-dimensional effects. All of the analyses performed to date have a one-to-one nodal correspondence between global and local models along the global/local interface. In-plane displacements are applied linearly through the thickness, based on the assumption that normals to the midsurface remain straight after deformation. For the loading and stacking sequence considered herein, the in-plane displacements are applied constant through the thickness. No out-of-plane ( $z$ -direction) displacements are applied, since the two-dimensional global model can only predict midsurface displacements in that direction. This approach maintains kinematic consistency between the models, because any out-of-plane deformations predicted by the global response are zero at the global/local interface.

### Current Research Topics

Global/local stress analysis continues to be an active research area in computational structural mechanics. Currently, alternate procedures to establish the global/local interface conditions are being developed in order to provide added flexibility for analyzing built-up structures and shell-type structures. These procedures are also needed in order to extend the methodology to geometrically nonlinear analyses. Automated procedures for locating the global/local interface boundary are also being studied. These procedures will aid the stress analyst and should provide a measure of reliability in the structural design since critical regions are readily identified. Procedures for locating the two-dimensional to three-dimensional modeling interface are more complicated than global/local (coarse-to-fine) models for either two-dimensional or three-dimensional models. Techniques for identifying this modeling interface and/or critical regions will benefit from the CSM research effort in adaptive refinement.

Consideration is also being given to the incorporation of "exact" analysis methods for the local stress analysis. This approach, however, may be effective only for a limited problem set. Coupling different analysis methods (*e.g.*, global finite element analysis; local elasticity solution) are also being investigated as part of the CSM research effort in partitioned analysis methods.

One final topic is developing strategies to exploit multiprocessor computers for concurrent multiple local analyses. With robust procedures for automating the location of the global/local boundaries (*i.e.*, multiple critical regions), multiple local analyses may be

performed concurrently on multiprocessor computers or sequentially on single-processor computers.

## Conclusions

Global/local analysis methodology for obtaining the detailed stress state of structural components is presented. The methodology presented is not restricted to having a priori knowledge of the location of the regions requiring a detailed stress analysis. The effectiveness of the global/local analysis capability is demonstrated by obtaining the detailed stress states of a blade-stiffened graphite-epoxy panel with a discontinuous stiffener and the interlaminar stresses of a cross-ply composite plate with a hole.

Although the representative global finite element models represent the global behavior of the structures, substantially more refined finite element meshes near the cutouts are required to obtain accurate detailed stress distributions. Embedding a local refined model in the complete structural model increases the computational requirements. The computational effort for the independent local analyses is less than the computational effort for the global analyses with the embedded local refinement.

The global/local analysis capability provides the modeling flexibility required to address detailed local models as their need arises. This modeling flexibility was demonstrated by the local analysis of the skin-stiffener interface region of the blade-stiffened panel with a discontinuous stiffener. This local analysis revealed local behavior that was not predicted by the global analysis.

The definition of the global/local interface boundary affects the accuracy of the local detailed stress state. For two-dimensional global/local analyses, the strain energy per unit area has been identified as a means for identifying a critical region and the location of the associated global/local interface boundary. The change in strain energy from element to element indicates regions with high stress gradients (*i.e.*, critical regions). A global/local interface boundary is defined outside of a region with large changes in strain energy. For three-dimensional global/local analyses, kinematically consistent displacement fields from the two-dimensional analysis are compared with the fields from a three-dimensional analysis to establish the global/local interface boundary.

The global/local analysis capability presented provides a general-purpose analysis tool for use by the aerospace structural analysis community by providing an efficient strategy for accurately predicting local detailed stress states that occur in structures discretized with relatively coarse finite element models. The coarse model represents the global structural behavior and approximates the local stress state. Independent, locally refined finite element models are used to predict accurately the detailed stress state in the regions of interest based on the solution predicted by the coarse global analysis.

## References

1. Knight, Norman F., Jr.; Greene, William H.; and Stroud, W. Jefferson: Nonlinear Response of a Blade-Stiffened Graphite-Epoxy Panel with a Discontinuous Stiffener. Proceedings of NASA Workshop on Computational Methods in Structural Mechanics

- and Dynamics, W. J. Stroud; J. M. Housner; J. A. Tanner; and R. J. Hayduk (editors), June 19-21, 1985, NASA CP-3034 - Part 1, 1989, pp. 51-66.
2. Noor, Ahmed K.: Global-Local Methodologies and Their Application to Nonlinear Analysis. *Finite Elements in Analysis and Design*, Vol. 2, No. 4, December 1986, pp. 333-346.
  3. Wilkins, D. J.: A Preliminary Damage Tolerance Methodology for Composite Structures. *Proceedings of NASA Workshop on Failure Analysis and Mechanisms of Failure of Fibrous Composite Structures*, A. K. Noor, M. J. Shuart, J. H. Starnes, Jr., and J. G. Williams (Compilers), NASA CP-2278, 1983, pp. 61-93.
  4. Han, Tao-Yang; and Abel, J. F.: Computational Strategies for Nonlinear and Fracture Mechanics, Adaptive Substructuring Techniques in Elasto-Plastic Finite Element Analysis. *Computers and Structures*, Vol. 20, No. 1-3, 1985, pp. 181-192.
  5. Clough, R. W.; and Wilson, E. L.: Dynamic Analysis of Large Structural Systems with Local Nonlinearities. *Computer Methods in Applied Mechanics and Engineering*, Vol. 17/18, Part 1, January 1979, pp. 107-129.
  6. Schwartz, David J.: Practical Analysis of Stress Raisers in Solid Structures. *Proceedings of the 4th International Conference on Vehicle Structural Mechanics*, Warrandale, PA, November 1981, pp. 227-231.
  7. Kelley, F. S.: Mesh Requirements of a Stress Concentration by the Specified Boundary Displacement Method. *Proceedings of the Second International Computers in Engineering Conference*, ASME, August 1982, pp. 39-42.
  8. Jara-Almonte, C. C.; and Knight, C. E.: The Specified Boundary Stiffness/Force SBSF Method for Finite Element Subregion Analysis. *International Journal for Numerical Methods in Engineering*, Vol. 26, 1988, pp. 1567-1578.
  9. Hirai, Itio; Wang, Bo Ping; and Pilkey, Walter D.: An Efficient Zooming Method for Finite Element Analysis. *International Journal for Numerical Methods in Engineering*, Vol. 20, 1984, pp. 1671-1683.
  10. Hirai, Itio; Wang, Bo Ping; and Pilkey, Walter D.: An Exact Zooming Method. *Finite Element Analysis and Design*, Vol. 1, No. 1, April 1985, pp. 61-68.
  11. Dong, Stanley B.: Global-Local Finite Element Methods. *State-Of-The-Art Surveys on Finite Element Technology*, A. K. Noor and W. D. Pilkey (editors), ASME, 1983, pp. 451-474.
  12. Stehlin, P.; and Rankin, C. C.: Analysis of Structural Collapse by the Reduced Basis Technique Using a Mixed Local-Global Formulation. *AIAA Paper No. 86-0851-CP*, May 1986.
  13. Knight, Norman F., Jr.; Lotts, C. G.; and Gillian, R. E.: Computational Structural Mechanics Methods Research Using an Evolving Framework. *AIAA Paper No. 90-1145*, 1990.

14. Ransom, J. B.; and Knight, N. F., Jr.: Global/Local Stress Analysis of Composite Panels. NASA TM-101622, 1989.
15. Ransom, J.B.: Global/Local Stress Analysis of Composite Structures. NASA TM-101640, 1989.
16. Griffin, O. Hayden, Jr.: Development and Verification of Local/Global Techniques for Laminated Composites. Proceedings of NASA Workshop on Computational Structural Mechanics - 1987, NASA CP-10012-Part 2, Nancy P. Sykes (Editor), 1989, pp. 653-682.
17. Griffin, O. Hayden, Jr.; and Vidussoni, Marco A.: Global/Local Finite Element Analysis of Composite Materials. Computer-Aided Design in Composite Material Technology, C. A. Brebbia, W. P. de Winkle, and W. R. Blain (editors), Proceedings of the International Conference for Computer-Aided Design in Composite Material Technology, Southampton, UK, April 13-15, 1988, pp. 513-524.
18. Thompson, D. M.; and Griffin, O. H., Jr.: 2-D to 3-D Global/Local Finite Element Analysis of Composite Laminates. Proceedings of the Fourth Technical Conference of the American Society for Composites, Blacksburg, VA, October 3-5, 1989, pp. 234-243.
19. Stewart, Caroline B., Compiler: The Computational Structural Mechanics Testbed User's Manual. NASA TM-100644, 1989.
20. Gillian, R. E.; and Lotts, C. G.: The CSM Testbed Software System - A Development Environment for Structural Analysis Methods on the NAS CRAY-2. NASA TM-100642, 1988.
21. Felippa, Carlos, A.: The Computational Structural Mechanics Testbed Architecture: Volume II-Directives. NASA CR-178385, 1989.
22. Starnes, James H., Jr.; Dickson, John N.; and Rouse, Marshall: Postbuckling Behavior of Graphite-Epoxy Panels. ACEE Composite Structures Technology: Review of Selected NASA Research on Composite Materials and Structures. NASA CP-2321, 1984, pp. 137-159.
23. Williams, Jerry G.; Anderson, Melvin S.; Rhodes, Marvin D.; Starnes, James H., Jr.; and Stroud, W. Jefferson: Recent Developments in the Design, Testing, and Impact-Damage Tolerance of Stiffened Composite Panels. NASA TM-80077, 1979.
24. Salamon, Nicholas J.: An Assessment of the Interlaminar Stress Problem in Laminated Composites. Journal of Composite Materials Supplement, Vol. 14, 1980, pp. 177-194.



**Table 1    Finite Element Models of Blade-Stiffened Panel  
with Discontinuous Stiffener.**

Model Designation	Number of Rings of Nodes <sup>b</sup>	Number of Radial Spokes of Elements <sup>b</sup>	Total Number of Elements	Total Number of Nodes	$\frac{(N_x)_{max}}{(N_x)_{avg}}$
G1	2	16	376	424	2.22
G2	16	32	1024	1088	2.88
G3	16	32	1408	1488	2.88
G4 <sup>a</sup>	32	80	3472	3584	2.94
LC1	16	32	576	612	2.92
LR1	-	-	16	25	-
LR2	-	-	32	45	-
LR3	-	-	96	117	-

<sup>a</sup> G4 is the converged model

<sup>b</sup> See Figure 2

**Table 2    Summary of Computational Requirements.**

Model Designation	Measures of Computational Effort		
	Total number of degrees of freedom	CPU, seconds	Size of data library, Mbytes
G1	2316	99.7	8.7
G2	6252	255.3	28.9
G3	8460	329.6	38.5
G4 <sup>a</sup>	21084	1006.0	140.6
LC1	3456	188.7	13.1
LR1	54	58.0	0.5
LR2	126	62.0	0.8
LR3	462	78.7	1.8

<sup>a</sup> G4 is the converged model



**Table 3 Two-Dimensional Global Finite Element Models of Plate with Hole.**

Hole Size, in.	Number of Nodes	Degrees of Freedom	Number of Elements		Spokes Around Hole	Average Solution Time, CPU sec.
			Total	Around Hole		
1.0	3208	19,248	768	160	64	488.9
3.0	2824	16,944	672	200	80	435.2
6.0	2240	14,640	576	240	96	242.2

**Table 4 Three-Dimensional Local Finite Element Models Near Hole.**

Hole Size, in.	Number of Nodes	Degrees of Freedom	Number of Elements	Average Solution Time, CPU sec.
1.0	1755	5,265	320	406.1
3.0	2157	6,471	400	514.3
6.0	2559	7,677	480	604.3

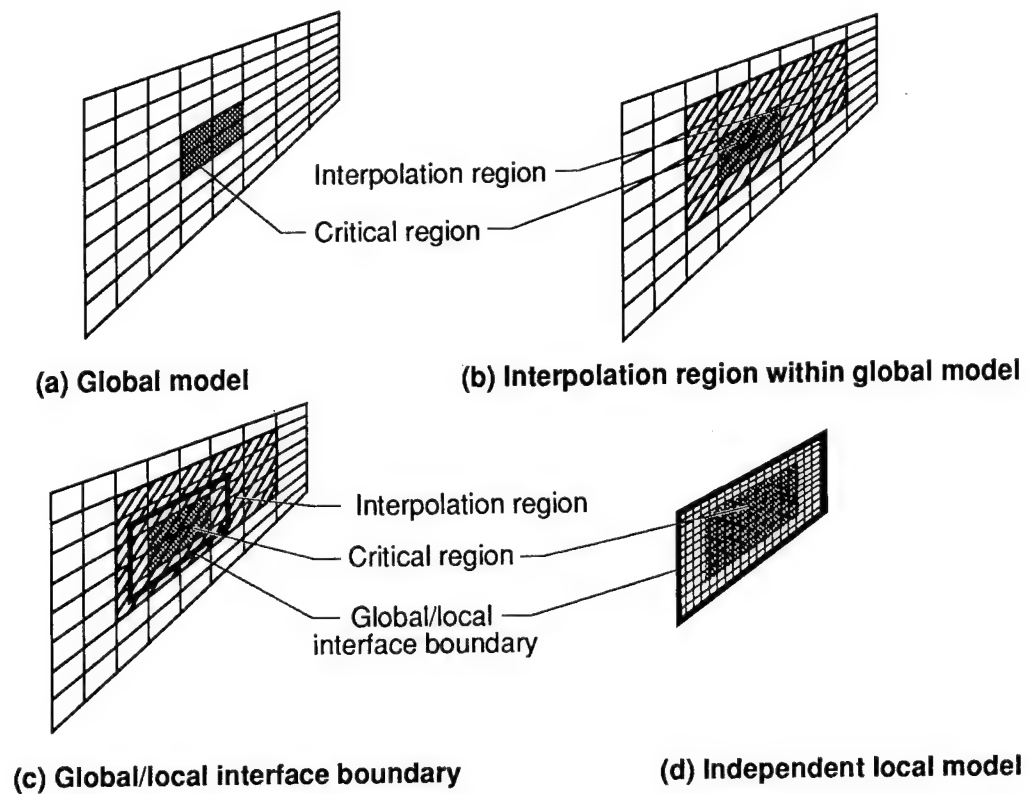


Figure 1. Terminology of the global/local methodology.

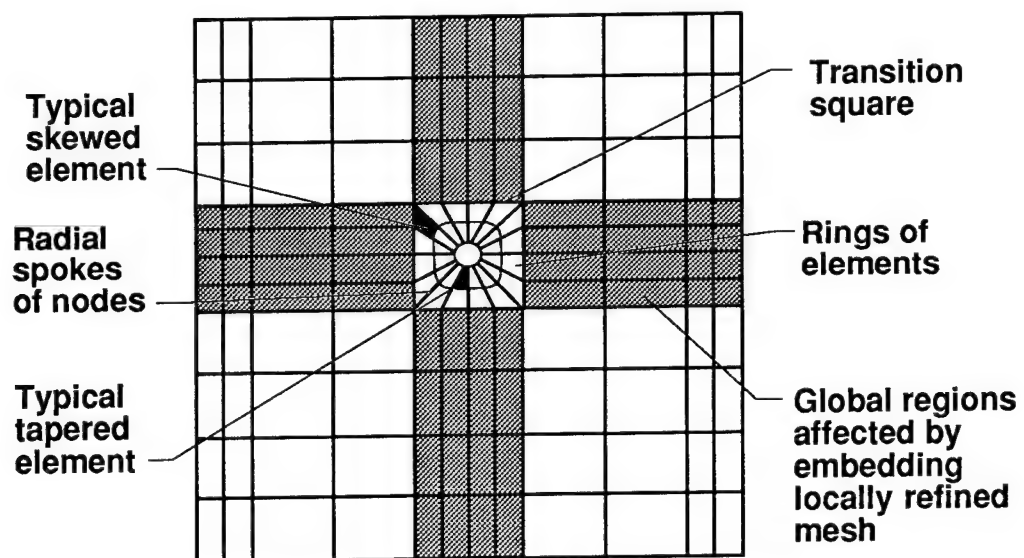


Figure 2. Terminology associated with modeling cutouts.

### Global modeling and analysis

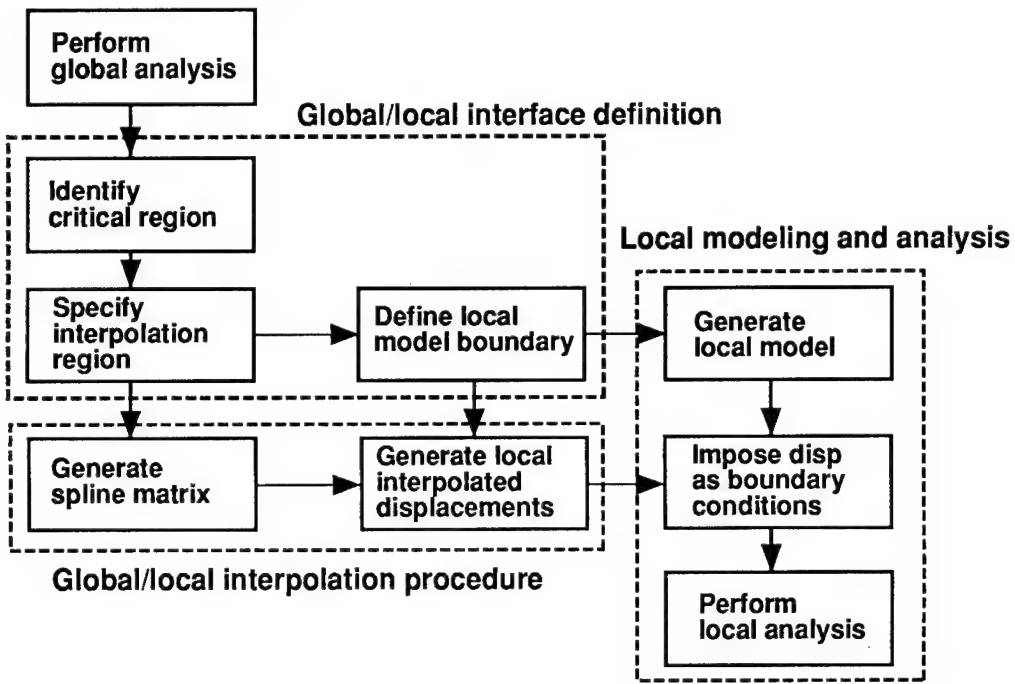


Figure 3. Schematic of overall 2-D global/local solution strategy.

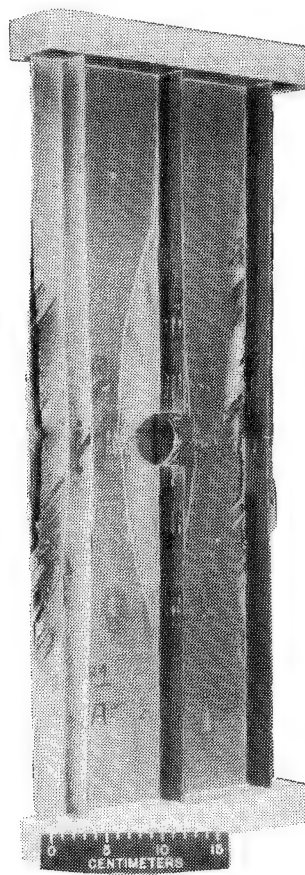


Figure 4. Composite blade-stiffened panel with a discontinuous stiffener.

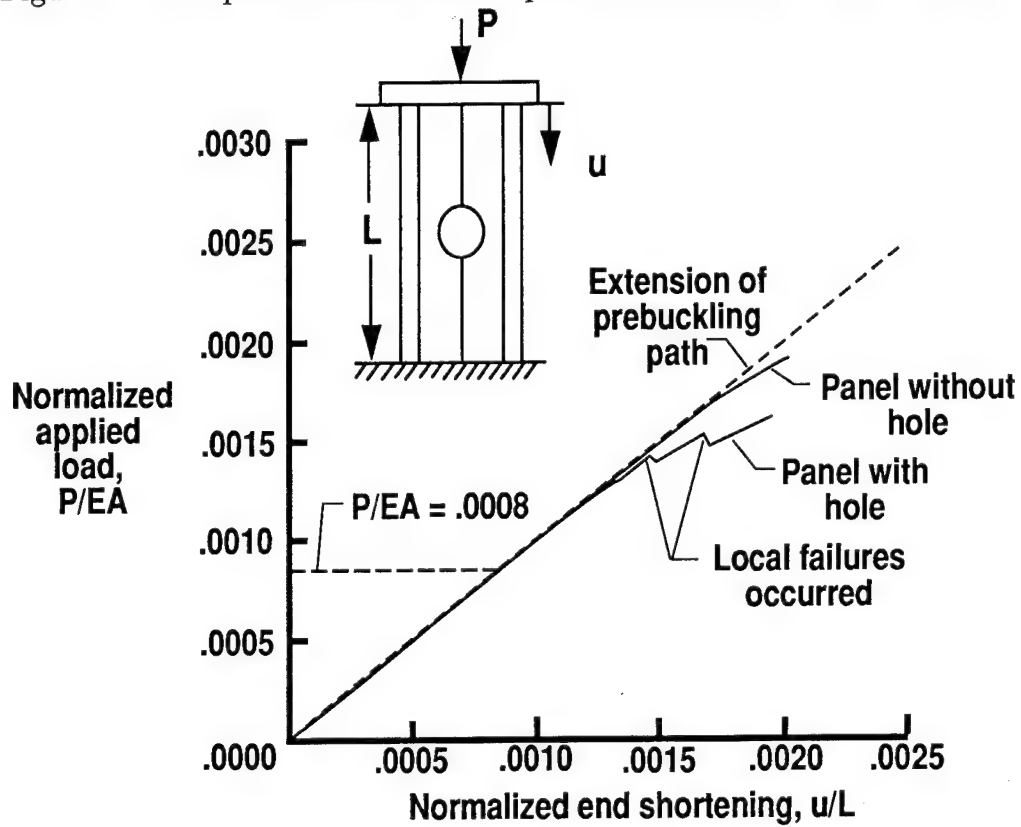


Figure 5. End-shortening results for composite blade-stiffened panel.

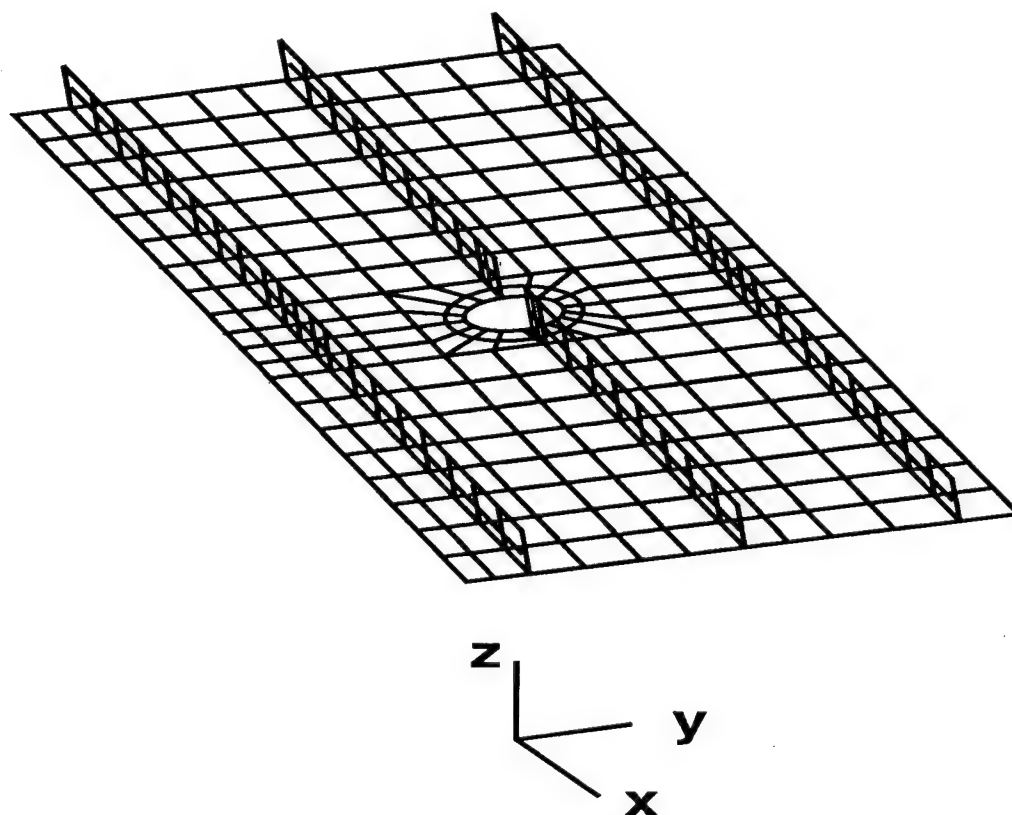


Figure 6. Global finite element model of blade-stiffened panel with discontinuous stiffener.

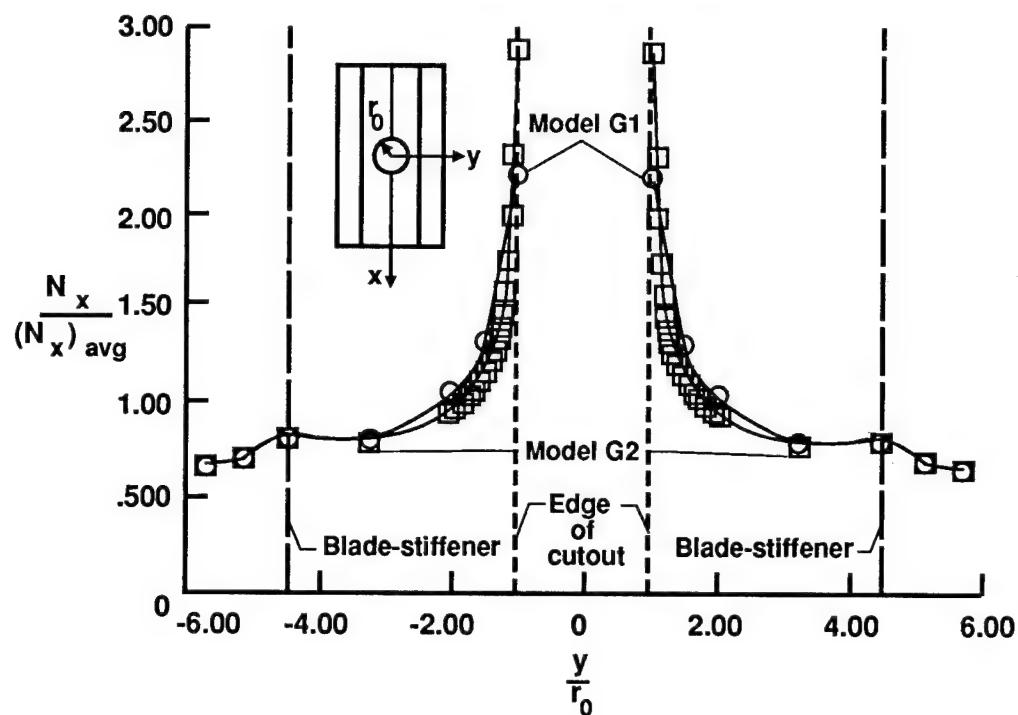


Figure 7. Longitudinal inplane stress resultant  $N_x$  distributions at panel midlength for coarse and refined global models.

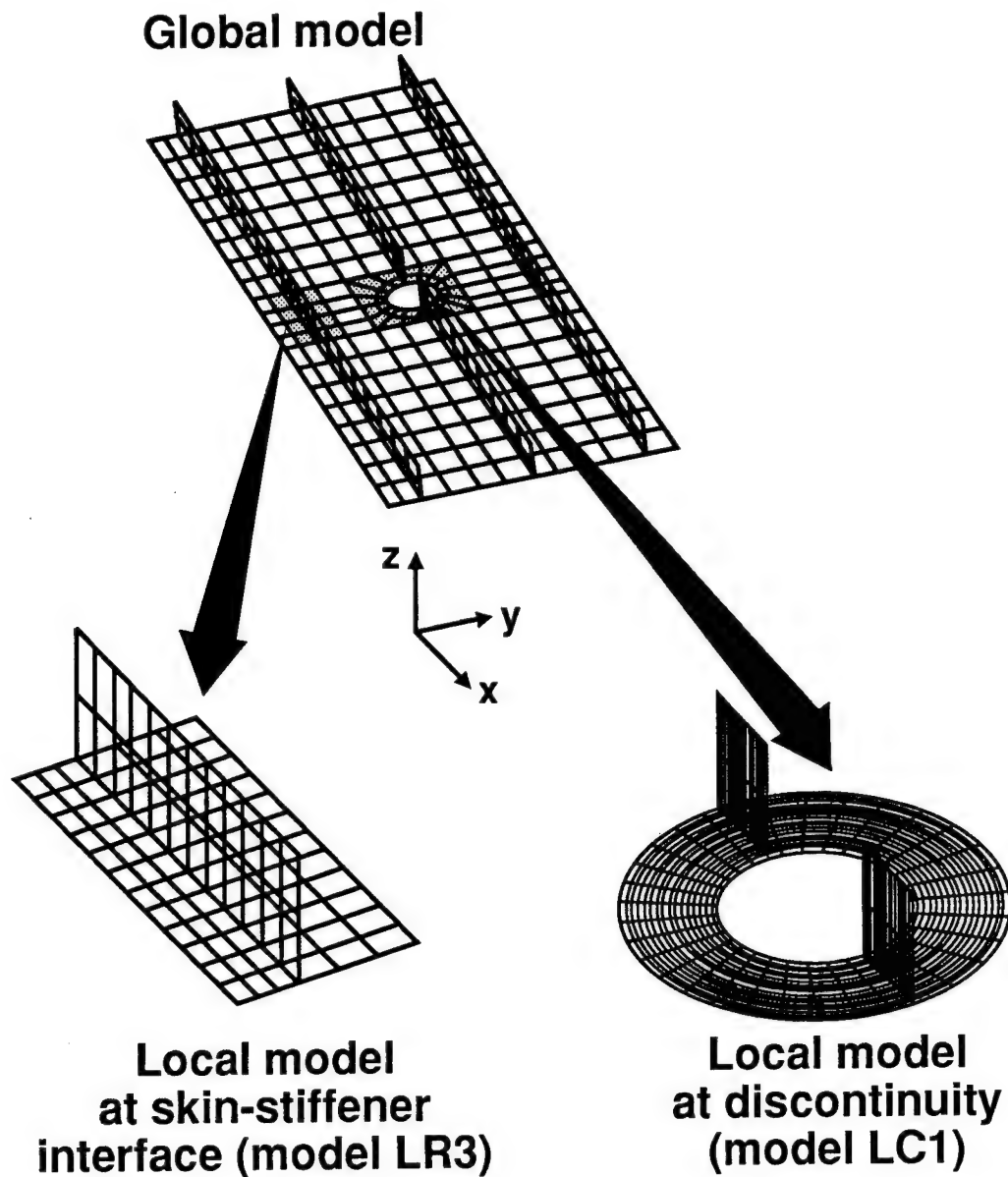


Figure 8. Global/local analysis models for blade-stiffened panel with discontinuous stiffener.

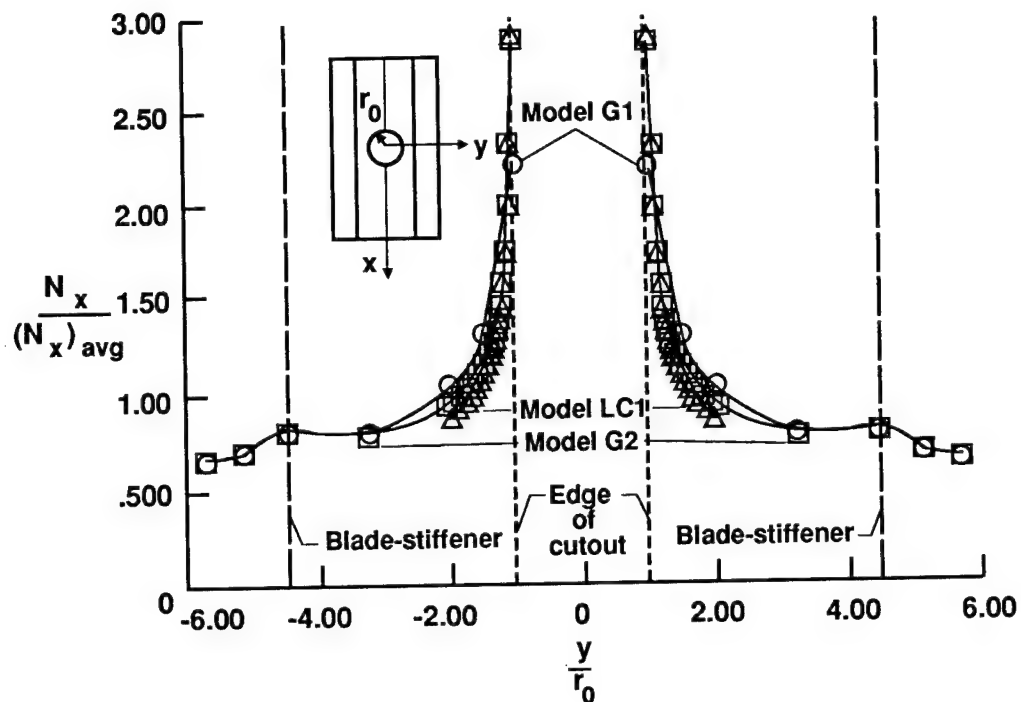


Figure 9. Longitudinal stress resultant  $N_x$  distributions for circular local finite element model of blade-stiffened panel with discontinuous stiffener.

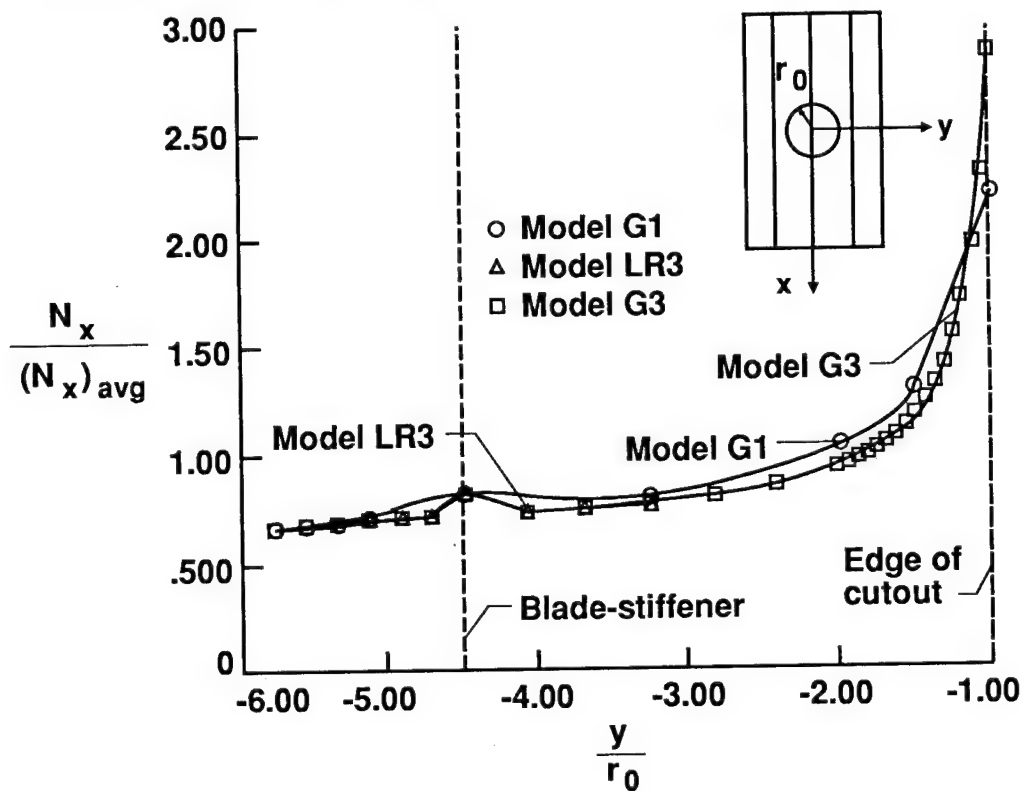
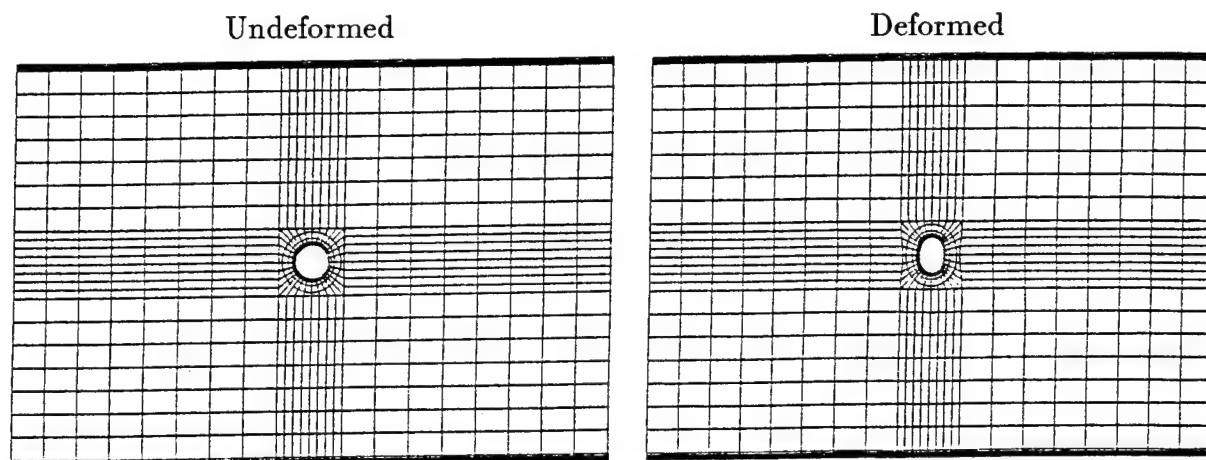
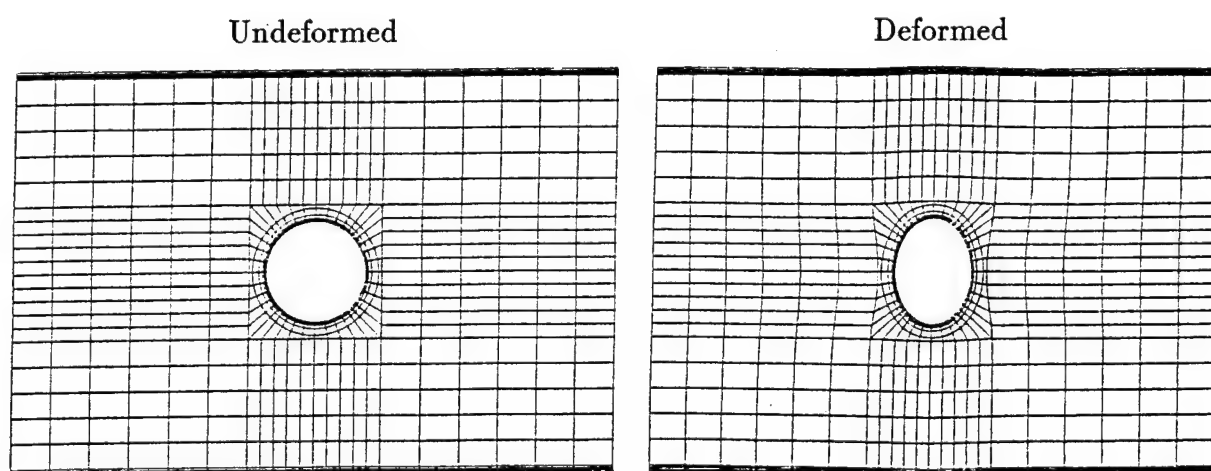


Figure 10. Longitudinal inplane stress resultant  $N_x$  distributions at panel midlength for skin-stiffener interface region.

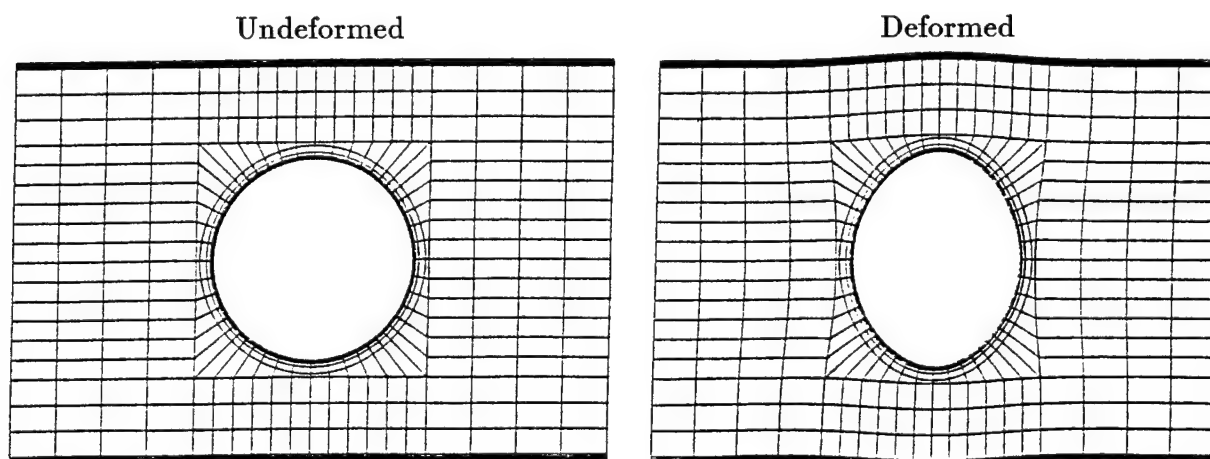




(a) Plate with 1-inch-diameter hole.



(b) Plate with 3-inch-diameter hole.



(c) Plate with 6-inch-diameter hole.

Figure 11. Global undeformed and deformed grids.

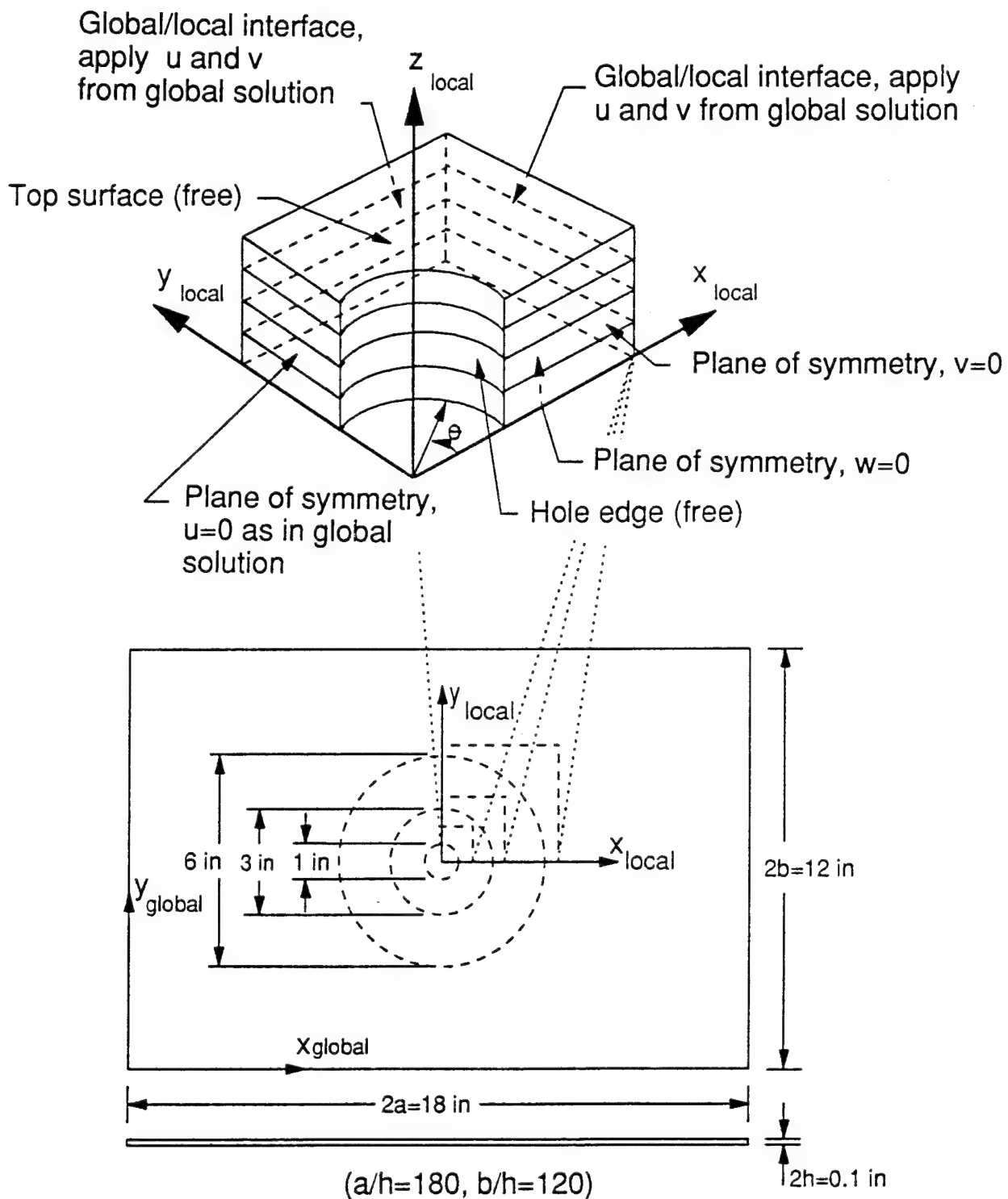
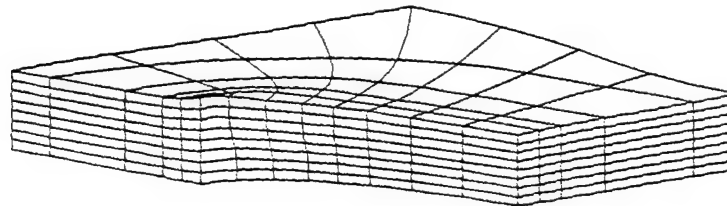
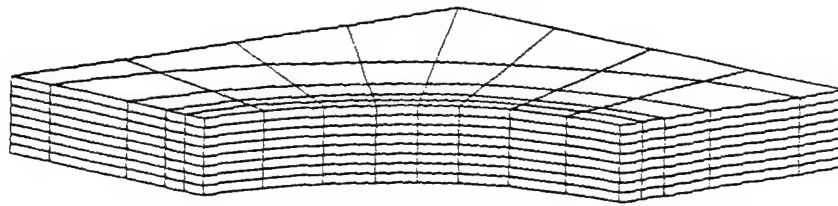
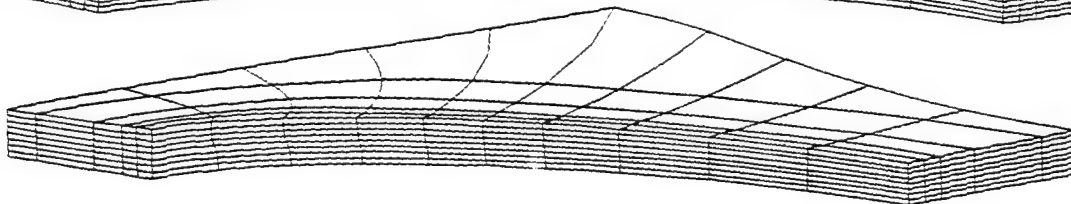
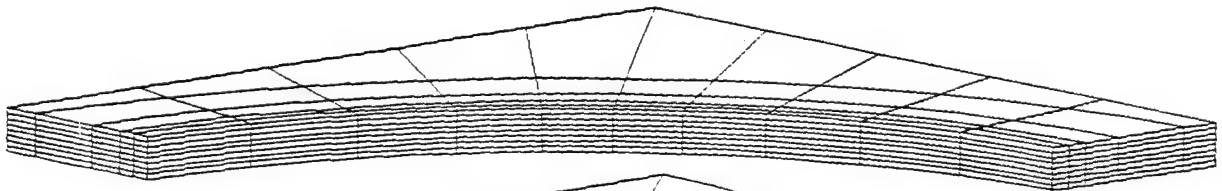


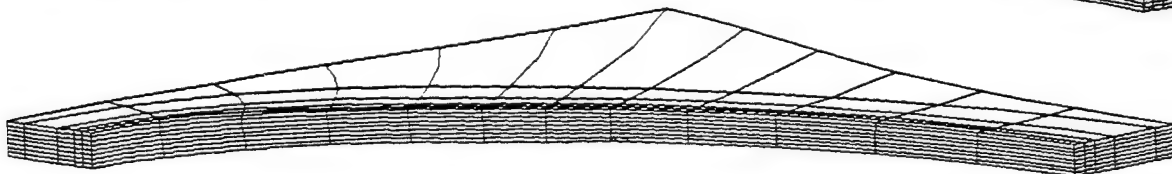
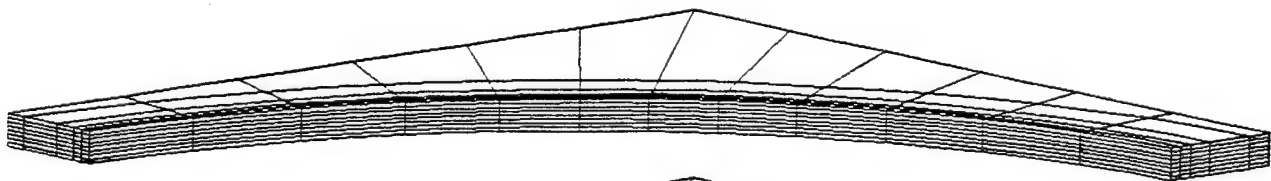
Figure 12. Global/local analysis of in-plane loading for cross-ply symmetric laminates.



(a) 1 inch Hole Meshes



(b) 3 inch Hole Meshes



(c) 6 inch Hole Meshes

Figure 13. Local undeformed and deformed meshes.

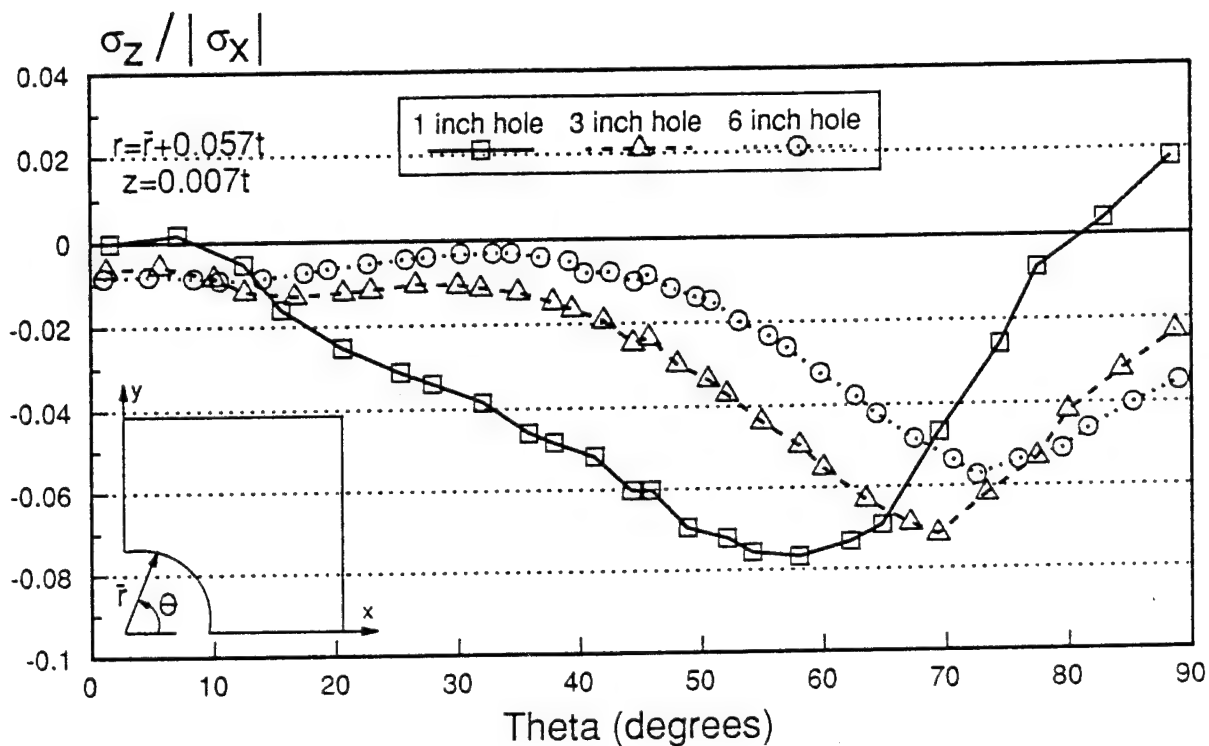


Figure 14. Normalized interlaminar normal stress  $\sigma_z$  around hole near midplane for  $[0/0/90/90]_S$

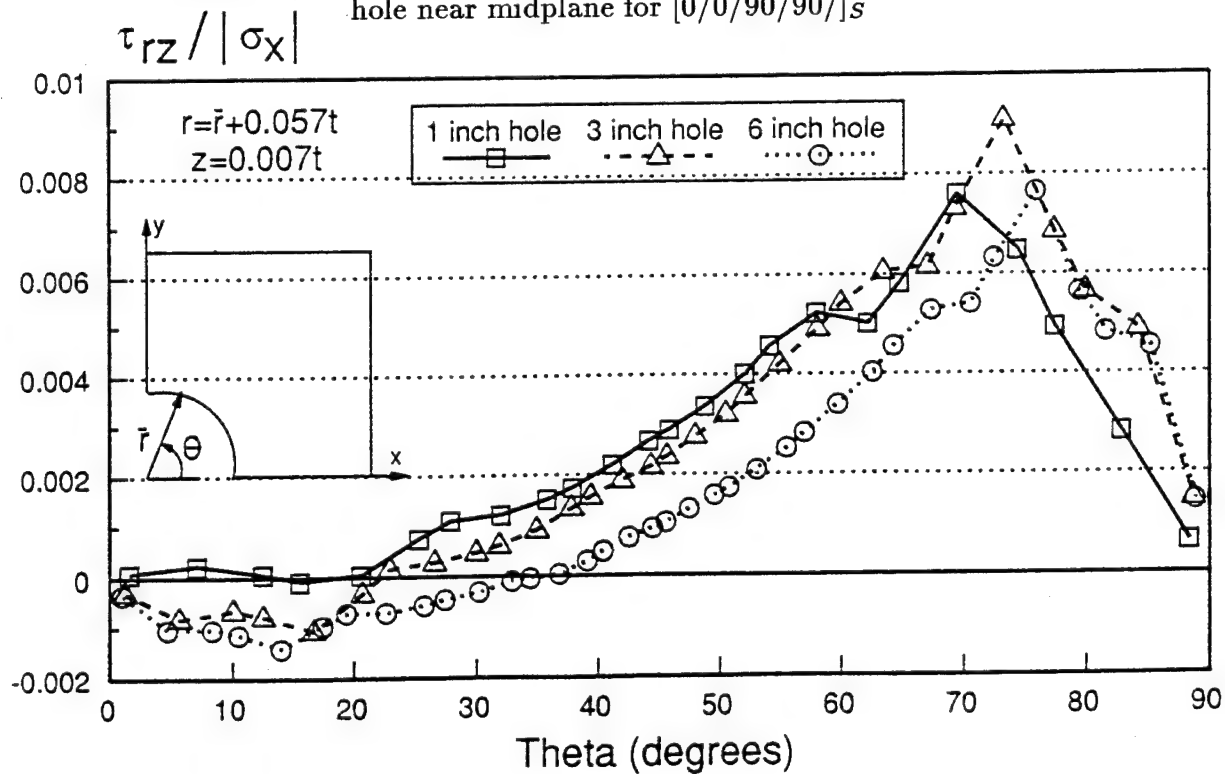


Figure 15. Normalized interlaminar shear stress  $\tau_{rz}$  around hole near midplane for  $[0/0/90/90]_S$

# EFFICIENT FINITE ELEMENT MODELING OF LAMINATED COMPOSITE PLATES BASED ON HIGHER-ORDER THEORY

Alexander Tessler and Erik Saether  
U.S. Army Materials Technology Laboratory  
Watertown, Massachusetts

## SUMMARY

A simple and efficient three-node plate bending element for the analysis of composite laminates is developed from a variational principle. The deformations due to transverse shear and transverse normal effects are accounted for, allowing accurate predictions in the range of thin to thick plates. The methodology incorporates  $C^0$ - and  $C^1$ -continuous displacement approximations and yields accurate ply-by-ply predictions of all displacement, strain, and stress variables.

## INTRODUCTION

With the increasing application of advanced composite materials in highly loaded structures, the ability to model the structural response and to predict accurately the stress field in thick laminates takes on a paramount role in the design process. The mechanical behavior of thick as well as moderately thick composite laminates is characterized by significant transverse shear and normal deformations which, for the same span (or wavelength of loading)-to-thickness ratio, are decidedly more pronounced than in homogeneous isotropic plates. This is due to a relatively low material compliancy in both transverse shear and normal material directions as compared to the axial fiber direction. Furthermore, composite laminates often exhibit much lower strength in the transverse directions as well as at the ply interfaces, thus permitting matrix cracking and delaminations.

A number of viable plate elements developed to date evolved from a shear-deformable displacement theory originally derived for homogeneous isotropic plates by Mindlin (e.g., refs. 1 and 2). Mindlin theory lends itself to the development of simple and efficient elements by virtue of the inherent  $C^0$  continuity prescribed for the approximation of the plate displacement variables. An earlier plate theory of Reissner (ref. 3) is based on stress approximations including the transverse normal stress component (which is neglected in Mindlin theory) and is somewhat more accurate as far as the stresses are concerned. Both the Mindlin and Reissner theories rely upon weighted-average displacement variables which assume linear variations across the thickness for the inplane displacements and a uniform transverse displacement. From a perspective of composite laminate analysis the displacement-based theories are generally preferred, allowing for discontinuous normal stresses which occur naturally in composite laminates.

Many higher-order plate theories have been proposed (e.g., see the reviews in refs. 4-6), which in addition to transverse shear also include the effect of transverse normal straining, and thus extend the range of applicability to thick plates. Regrettably, their adoptability to finite element approximations often presents insurmountable difficulties (ref. 7). Consequently, they attracted little interest in the finite element arena.

Recently, the senior author proposed a variational 10th-order theory for bending and stretching of homogeneous orthotropic plates (refs. 7 and 8) which includes both transverse shear and transverse normal deformations and embodies the simplicity and finite element suitability of Mindlin theory. Its kinematic assumptions include linear distributions for the inplane displacements and a parabolic variation for the transverse displacement. The theory was later extended by the present authors to laminated composites (refs. 9, 10).

A particularly attractive feature of this theory is that it allows for interelement discontinuous displacement approximations (i.e.,  $C^{-1}$  continuous) for a set of two higher-order displacements while relying upon  $C^0$ -continuous fields for the weighted-average displacements of the Reissner-Mindlin type (i.e., two inplane and one transverse displacements, and two normal rotations). The direct implication of  $C^{-1}$ -continuous higher-order displacements is that a static condensation of these variables is readily performed at the element level; hence, they do not contribute to the size of the global stiffness equations. An additional theoretical advantage of the present theory is that only physical Poisson-type conditions are prescribed at the plate edges as in shear-deformable theories of the Reissner-Mindlin type. (By comparison, other higher-order theories commonly involve nonphysical but variationally necessary higher-order boundary conditions.)

In this paper, we propose an efficient finite element formulation, specifically aimed at the analysis of thick laminated composite plates, which is based on the aforementioned laminate plate theory. The plate element presented herein is a three-node triangle based upon anisoparametric interpolations (refs. 11, 12) to ensure locking-free behavior in the thin regime. These interpolations were also found to satisfy one equilibrium equation identically. Each node possesses five standard displacement degrees-of-freedom, namely, three displacements and two normal rotations. Because both the inplane and transverse deformations are accounted for, the element can effectively model composite plate and shell structures subject to inplane and out-of-plane (transverse) loading.

In what follows, we will briefly describe the analytic basis of the formulation, some pertinent finite element issues, and present numerical results depicting typical behavior of the proposed finite element.

# ANALYTIC BASIS OF HIGHER-ORDER PLATE THEORY

In the present theory (refs. 9, 10), the Cartesian displacement components are expanded with respect to the dimensionless thickness coordinate  $\xi$ , with  $u_z$  having a special parabolic form:

$$\begin{aligned} u_x(x, y, z) &= u(x, y) + h\xi\theta_y(x, y) \\ u_y(x, y, z) &= v(x, y) + h\xi\theta_x(x, y) \\ u_z(x, y, z) &= w(x, y) + \xi w_1(x, y) + (\xi^2 - 1/5)w_2(x, y) \end{aligned} \quad (1)$$

where  $\xi=z/h=0$  designates the positions of the middle surface  $S_m$ , and  $2h$  is the total plate thickness.

The expansion coefficients  $u$ ,  $v$ ,  $\theta_y$ ,  $\theta_x$ , and  $w$  in equations (1) are weighted-average kinematic variables defined as:

$$u = \frac{1}{2h} \int_{-h}^h u_x dz, \quad v = \frac{1}{2h} \int_{-h}^h u_y dz \quad (2)$$

$$\theta_x = \frac{3}{2h^3} \int_{-h}^h u_y z dz, \quad \theta_y = \frac{3}{2h^3} \int_{-h}^h u_x z dz \quad (3)$$

$$w = \frac{3}{4h} \int_{-h}^h u_z (1 - \xi^2) dz, \quad (4)$$

where  $u$  and  $v$  denote the midplane displacements along the  $x$  and  $y$  directions, respectively;  $\theta_x$  and  $\theta_y$  denote the normal rotations about the  $x$  and  $y$  axes, respectively.

The inplane strain-displacement relations are obtained in the usual manner:

$$\varepsilon_x = u_{x,x}, \quad \varepsilon_y = u_{y,y}, \quad \gamma_{xy} = (u_{x,y} + u_{y,x}) \quad (5)$$

A major departure from a conventional displacement formulation is the way the transverse strains are introduced into the theory. Specifically, the through-thickness displacement gradients  $u_{x,z}$  and  $u_{y,z}$  are expanded up to order two, while  $u_{z,z}$  is taken to be cubic. This formally makes the present theory a mixed strain-displacement type. By adopting a weak (variational) form for the transverse strain compatibility, i.e., equating these higher-degree gradient expansions to the ones obtained directly from the displacements in the mean sense,



$$\min \int_{-h}^h \left[ \sum_{j=0}^m a_{ij}(x,y) \xi^j - u_{i,z} \right]^2 dz \quad (6)$$

$$i=x,y \text{ (m=2)}; \quad i=z \text{ (m=3)}$$

and satisfying a set of exact stress boundary conditions,

$$\left. \begin{aligned} \tau_{iz} &= \sigma_{zz,z} \\ &= 0 \quad (i=x,y) \end{aligned} \right|_{(\xi=\pm 1)} \quad (7)$$

there result appropriate  $a_{ij}$  coefficients in terms of the plate variables in equations (1). Consequently, the transverse shear strains and stresses vary parabolically across the plate thickness (satisfying traction-free boundary conditions) and the transverse normal strain and stress vary cubically. In the case of a homogeneous plate, this procedure enforces exact transverse equilibrium (ref. 7).

A general, three-dimensional Hooke's law is assumed to govern the behavior of each individual ply; i.e., for the k-th ply we have

$$\begin{bmatrix} \sigma_{xx} \\ \sigma_{yy} \\ \sigma_{zz} \\ \tau_{yz} \\ \tau_{xz} \\ \tau_{xy} \end{bmatrix}^{(k)} = \begin{bmatrix} \tilde{C}_{11} & \tilde{C}_{12} & \tilde{C}_{13} & 0 & 0 & \tilde{C}_{16} \\ & \tilde{C}_{22} & \tilde{C}_{23} & 0 & 0 & \tilde{C}_{26} \\ & & \tilde{C}_{33} & 0 & 0 & \tilde{C}_{36} \\ & & & \tilde{C}_{44} & \tilde{C}_{45} & 0 \\ \text{(Sym.)} & & & & \tilde{C}_{55} & 0 \\ & & & & & \tilde{C}_{66} \end{bmatrix}^{(k)} \begin{bmatrix} \epsilon_{xx} \\ \epsilon_{yy} \\ \epsilon_{zz} \\ \gamma_{yz} \\ \gamma_{xz} \\ \gamma_{xy} \end{bmatrix} \quad (8)$$

where the elastic constants  $\tilde{C}_{ij}^{(k)}$ , corresponding to the laminate x-y coordinates, are related to the ply principal direction constants  $C_{ij}^{(k)}$  as

$$\tilde{C}_{ij}^{(k)} = \alpha_{im} \alpha_{jn} C_{mn}^{(k)} \quad (9)$$

with  $\alpha_{ij}$  denoting appropriate cosine functions of the coordinate rotation between the ply principal material directions and laminate coordinates.

The laminate plate theory can then be derived from a modified

virtual work principle<sup>1</sup>, which includes all strain and stress components:

$$\iiint_V (\sigma_{xx} \delta \varepsilon_{xx} + \sigma_{yy} \delta \varepsilon_{yy} + \sigma_{zz} \delta \varepsilon_{zz} + \tau_{xy} \delta \gamma_{xy} + \tau_{xz} \delta \gamma_{xz} + \tau_{yz} \delta \gamma_{yz}) dv - \iint_{S^+} q^+ \delta u dx dy - \iint_{S^-} q^- \delta u dx dy = 0 \quad (10)$$

where  $\delta$  denotes the variational operator;  $S^+$  and  $S^-$ , respectively, denote the top and bottom plate surfaces which are taken free of shear tractions and loaded by normal pressures

$$\begin{aligned} \tau_{iz}(\xi=1) &= 0 \quad (i=x,y), \quad \sigma_{zz}(\xi=1) = q^+(x,y) && \text{on } S^+ \\ \tau_{iz}(\xi=-1) &= 0 \quad (i=x,y), \quad \sigma_{zz}(\xi=-1) = q^-(x,y) && \text{on } S^- \end{aligned} \quad (11)$$

Upon integrating equation (10) across the plate thickness, a two-dimensional (plate) variational statement is obtained:

$$\begin{aligned} \iint_{S_m} \left\{ N_x \delta u_{,x} + N_y \delta v_{,y} + N_{xy} (\delta u_{,y} + \delta v_{,x}) \right. \\ + M_x \delta \theta_{y,x} + M_y \delta \theta_{x,y} + M_{xy} (\delta \theta_{x,x} + \delta \theta_{y,y}) \\ + Q_x (\delta w_{,x} + \delta \theta_y) + Q_y (\delta w_{,y} + \delta \theta_x) + N_z \delta (w_1/h) + M_z \delta (w_2/h) \\ \left. - (q^+ - q^-) (\delta w + \frac{4}{5} \delta w_2) - (q^+ + q^-) \delta w_1 \right\} dx dy = 0 \end{aligned} \quad (12)$$

where  $N_{ij}$ ,  $M_{ij}$  and  $Q_i$  ( $i, j = x, y$ ) are the resultant membrane forces, bending moments and shear forces, all per unit length; also,  $N_z$  and  $M_z$  are the resultants associated with the transverse stress component.

The constitutive equations relating these plate stress resultants and their associated strains can be found in reference 10.

As discussed in the following section, the special form of equation (12) leads to simple and computationally efficient laminate plate finite elements incorporating both transverse shear and transverse normal deformations.

#### FINITE ELEMENT FORMULATION

The particular form of the variational statement (12) lends itself perfectly to the development of simple and efficient elements

---

<sup>1</sup>The term "modified principle of virtual work" is used here to signify the use of the transverse strains that are only "weakly" compatible.

comparable in computational efficiency to shear-deformable elements (refs. 11, 12). Indeed, the linear differential operator acting upon the five weighted-average kinematic variables is of order one (i.e., the highest spatial derivative is of order one). This implies that these variables need not exceed  $C^0$  continuity, as in Mindlin theory. Furthermore, in equation (12), there are no spatial derivatives associated with the two higher-order transverse displacements,  $w_1$  and  $w_2$ . This particular aspect allows the higher-order displacements to be approximated with  $C^{-1}$ -continuous functions (i.e., functions that are discontinuous at element interfaces). A further implication is that the degrees-of-freedom (dof) associated with the  $w_1$  and  $w_2$  element interpolations can be conveniently condensed out at the element equilibrium level and, therefore, they need not contribute to the size of the global stiffness equations.

It can further be shown that the variational principle (12) is of a penalty-constraint type (e.g., ref. 2). Hence, special finite element techniques should be employed to avoid thin-regime shear locking. In this regard, the anisoparametric interpolation strategy already established for Reissner-Mindlin plate elements (refs. 11, 12) is directly applicable for this higher-order theory formulation.

Having the simplest and most versatile element configuration in mind, we develop a three-node triangle based upon anisoparametric shape functions derived for a Reissner-Mindlin element (ref. 11):

$$\begin{aligned}
 \left. \begin{aligned}
 u &= \sum_{i=1}^3 \zeta_i u_i, & v &= \sum_{i=1}^3 \zeta_i v_i \\
 \theta_x &= \sum_{i=1}^3 \zeta_i \theta_{xi}, & \theta_y &= \sum_{i=1}^3 \zeta_i \theta_{yi}
 \end{aligned} \right\} \begin{array}{l} C^0 \text{ linear} \\ \text{interpolations} \end{array} \\
 \\
 \left. \begin{aligned}
 w &= \sum_{i=1}^3 [\zeta_i w_i + \theta_{xi}(b_k N_{i+3} - b_j N_{k+3})/8 \\
 &\quad + \theta_{yi}(a_j N_{k+3} - a_k N_{i+3})/8]
 \end{aligned} \right\} \begin{array}{l} C^0 \text{ quadratic} \\ \text{interpolations} \end{array} \quad (13) \\
 \\
 \left. \begin{aligned}
 w_1 &= w_1, & w_2 &= w_2
 \end{aligned} \right\} \begin{array}{l} C^{-1} \text{ constant} \\ \text{interpolations} \end{array}
 \end{aligned}$$

where  $N_i$  are quadratic shape functions

$$N_i = \zeta_i(2\zeta_i - 1), \quad N_{i+3} = 4\zeta_i\zeta_j \quad (13a)$$

and  $\zeta_i$  are the area-parametric coordinates

$$\zeta_i = (c_i + b_i x + a_i y)/2A \quad (A \text{ is the triangle area}) \quad (13b)$$

and where  $a_i$ ,  $b_i$ , and  $c_i$  are functions of nodal coordinates

$$a_i = x_k - x_j, \quad b_i = y_j - y_k, \quad c_i = x_j y_k - x_k y_j \quad (13c)$$

( $i = 1, 2, 3$ ;  $j = 2, 3, 1$ ;  $k = 3, 1, 2$ )

Upon introducing equations (13) into equation (12) and performing the necessary variations with respect to all seventeen dof, we obtain the element stiffness equilibrium equations. Because  $w_1$  and  $w_2$  are  $C^{-1}$  continuous, their dof can then be condensed out statically, thus becoming dependent upon the basic nodal dof, i.e.,  $\{u_i, v_i, w_i, \theta_{xi}, \theta_{yi}\}$  ( $i = 1, 2, 3$ ). The resulting plate element is, therefore, a three-node triangle having five basic dof at each node (see fig. 1).

#### COMMENTS ON STRESS CALCULATIONS

Due to their heterogeneous nature, laminated composite plates often exhibit ply-interface discontinuities in the inplane stresses as well as in the transverse strains. On the other hand, the inplane strains are continuous across the laminate thickness and the transverse stresses are also continuous, although their through-thickness gradients may be discontinuous at ply interfaces.

Since the present theory relies upon continuous strain distributions, as do all displacement-based theories, the inplane stresses can be effectively recovered from the ply constitutive law (8). The direct recovery of transverse stresses, however, may be grossly erroneous, as they evolve discontinuous at ply interfaces. In this theory, we were able to obtain rather accurate predictions for the transverse normal stress component accompanied with only insignificant ply-interface discontinuities (ref. 10). To compute accurate ply transverse shear stresses that are continuous across the plate thickness, we integrate the exact equilibrium equations once the inplane stresses are obtained from the constitutive relations (ref. 13), i.e.,

$$\begin{aligned} \sigma_{xz}^{(k)} &= - \int (\sigma_{xx,x}^{(k)} + \tau_{xy,y}^{(k)}) dz \\ \sigma_{yz}^{(k)} &= - \int (\sigma_{yy,y}^{(k)} + \tau_{xy,x}^{(k)}) dz \end{aligned} \quad (14)$$

Although within the context of analytic solutions this approach has been effective, the direct computation of stress/strain inplane gradients at the finite element level can be problematic. For instance, in the case of our simple triangular element, all strain gradients entering equation (14) vanish, simply because the strains are constant within the element domain. To overcome this difficulty, we employ a global smoothing procedure for each strain of interest (ref. 13, and \*). The procedure yields continuous solutions for the strains and their first derivatives across the entire plate domain.

\*Tessler, A.; Freese, C.: An Effective Global Penalty-Constraint Formulation for Strain/Stress Smoothing. MTL Technical Report (in review).

Once the first derivatives of the strains are obtained, the ply-by-ply stress computations in accordance with equations (14) are straightforward. For details on the global smoothing procedure the interested reader is referred to reference 14.

## DISCUSSION OF RESULTS

Numerical studies are carried out for the problem of cylindrical bending of a carbon/epoxy symmetric angle-ply ( $[30/-30]_s$ ) laminate subjected to a sinusoidal transverse pressure (fig. 2).<sup>s</sup> The ply material properties are taken as

$$\begin{aligned} E_\ell &= 25 \times 10^6 \text{ psi}, & E_t &= 10^6 \text{ psi} \\ G_{\ell t} &= .5 \times 10^6 \text{ psi}, & G_{tt} &= .2 \times 10^6 \text{ psi} \\ \nu_{\ell t} &= \nu_{tt} = .25 \end{aligned} \tag{15}$$

where  $\ell$  and  $t$  denote the longitudinal and transverse ply material directions, respectively.

The results are obtained analytically by way of the 10th-order theory (ref. 10, shown as PRESENT), an exact elasticity approach (ref. 15, designated as EXACT), the classical laminate plate theory (CPT), and the present finite element analysis designated as HMIN3. All displacement and stress quantities have been normalized in accordance with ref. 10.

Figure 2 depicts the finite element discretization of a narrow strip of HMIN3 elements spanning one quarter of the loading wavelength (i.e.,  $L/2$ ). Appropriate symmetric boundary conditions and multiple-point constraint equations are enforced to simulate the cylindrical bending features of this infinite plate. In fig. 3, a normalized value of the maximum midplane transverse displacement is plotted versus the half wavelength of loading-to-thickness ratio ( $L/2h$ ). As evidenced in the figure, extremely accurate results are obtained even in the truly thick regime of  $L/2h = 2$  due to the inclusion of both transverse shear and transverse normal deformability in the present theory. As the wavelength of loading-to-thickness ratio decreases, the observed deflection becomes dominated by these transverse deformations. The thick-regime improvement in accuracy afforded by the inclusion of both transverse shear and transverse normal deformations in the present theory over considering only shear deformation is demonstrated in fig. 4.

Figures 5 and 6 depict through-thickness distributions of the maximum normal ( $\epsilon_{xx}$ ) and inplane shear ( $\gamma_{xy}$ ) strains. Close agreement with the exact solution is obtained for  $L/2h = 10$ . For  $L/2h = 4$ , however, the present theory departs significantly from the exact solution in the outer plies. This is due to the linear approximations made for the inplane  $u_x$  and  $u_y$  displacements which, as evidenced by the elasticity solution, become increasingly nonlinear in the thick regime.

Figures 7 through 9 show through-thickness distributions of the transverse shear ( $\tau_{yz}$ ,  $\tau_{xz}$ ) and transverse normal ( $\sigma_{zz}$ ) stresses. As discussed previously, we employed two different methods to compute these quantities; the analytic stresses obtained directly from the constitutive relations are designated as PRESENT-1 and those computed by integrating the plate equilibrium equations are designated as PRESENT-2. Furthermore, the HMIN3 finite element results for the transverse shear stresses were obtained via a global smoothing technique.\* Evidently, the HMIN3 stresses are in excellent agreement with the corresponding analytic solutions.

#### CONCLUDING REMARKS

We have presented a simple and efficient three-node plate bending element for the analysis of composite laminates which includes the deformations due to transverse shear and transverse normal effects. The principal benefits of this type of higher-order plate analysis are: (a) the applicability range is extended further into the thick regime, (b) reliable three-dimensional distributions of displacements, strains and stresses are attainable, (c) there are no requirements for specifying composite shear correction factors, and (d) the cost of computations is practically the same as with Reissner-Mindlin type elements.

#### ACKNOWLEDGMENT

The authors wish to acknowledge the contribution of Colin Freese for utilizing the global smoothing technique (ref. 14) in computations of transverse shear stresses.

#### REFERENCES

1. Mindlin, R. D.: Influence of Rotatory Inertia and Shear on Flexural Motions of Isotropic, Elastic Plates. J. Appl. Mech., 18, 1951, pp. 31-38.
  2. Hughes, T. J. R.: The Finite Element Method: Linear Static and Dynamic Finite Element Analysis, Chapter 5, Prentice-Hall, Englewood Cliffs, NJ, 1987.
  3. Reissner, E.: On the Theory of Bending of Elastic Plates. J. Math. and Physics, 23, 1944, pp. 184-191.
  4. Lo, K. H.; Christensen, R. M.; and Wu, E. M.: A Higher-Order Theory of Plate Deformation, Part 1: Homogenous Plates. J. Appl. Mech., 44, 1977, pp. 663-668.
  5. Reissner, E.: Reflections on the Theory of Elastic Plates. Appl. Mech. Review, vol. 38, no. 11 Nov. 1985, pp. 1453-1463.
- \*Tessler, A.; Freese, C.: An Effective Global Penalty-Constraint Formulation for Strain/Stress Smoothing. MTL Technical Report (in review).

6. Noor, A. K.; and Burton, W. S.: Assessment of Shear Deformation Theories for Multilayered Composite Plates. Appl. Mech. Review, vol. 42, no. 1 Jan. 1989, pp. 1-12.
7. Tessler, A.: A Higher-Order Plate Theory with Ideal Finite Element Suitability. Comput. Meths. Appl. Mech. Engrg., 1990.
8. Tessler, A.: An Improved Higher-Order Theory for Orthotropic Plates. Proc. 13th Annual Mechanics of Composites Review, Nov. 1988, Bal Harbour, Florida.
9. Tessler, A.; and Saether, E.: A  $C^0/C^{-1}$  Higher-Order Displacement Theory for Laminated Composite Plates with Particular Finite Element Suitability. Proc. 14th Annual Mechanics of Composites Review, Nov. 1989, Dayton, Ohio.
10. Tessler, A.; and Saether, E.: A Computationally Viable Tenth-Order Plate Theory for Stress Analysis of Thick Composite Laminates. MTL Technical Report, 1990.
11. Tessler, A.; and Hughes, T. J. R.: A Three-Node Mindlin Plate Element with Improved Transverse Shear. Comput. Meths. Appl. Mech. Engrg., 50, 1985, pp. 71-101.
12. Tessler, A.: Shear-deformable Bending Elements With Penalty Relaxation, in Finite Element Methods for Plate and Shell Structures, Vol. 1: Element Technology, (eds. T.J.R. Hughes and E. Hinton), Pineridge Press, Swansea, U.K., 1986, pp. 266-290.
13. Lo, K. H.; Christensen, R. M.; and Wu, E, M.: Stress Solution Determination for Higher-Order Plate Theory. Int. J. Solids and Structures, 14, 1978, pp. 655-662.
14. Tessler, A.; Freese, C.; Anastasi, R.; Serabian, S.; Oplinger, D.; and Katz, A: Least-Squares Penalty-Constraint Finite Element Method for Generating Strain Fields from Moire Fringe Patterns. Proc. SPIE: Photomechanics and Speckle Metrology (ed. by F.P. Chiang), vol. 814, 1987, pp. 314-323.
15. Pagano, N. J.: Influence of Shear Coupling in Cylindrical Bending of Anisotropic Laminates. J. Comp. Mats., 4, 1970, pp.330-343.



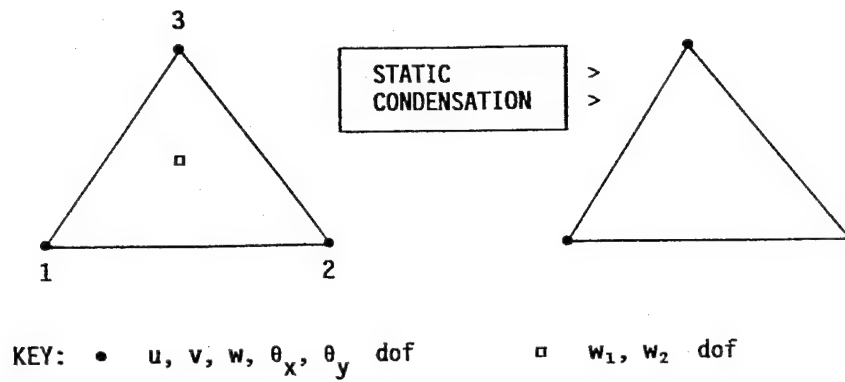


Fig. 1. HMIN3: A three-node stretching-bending plate element with transverse shear and transverse normal deformation.

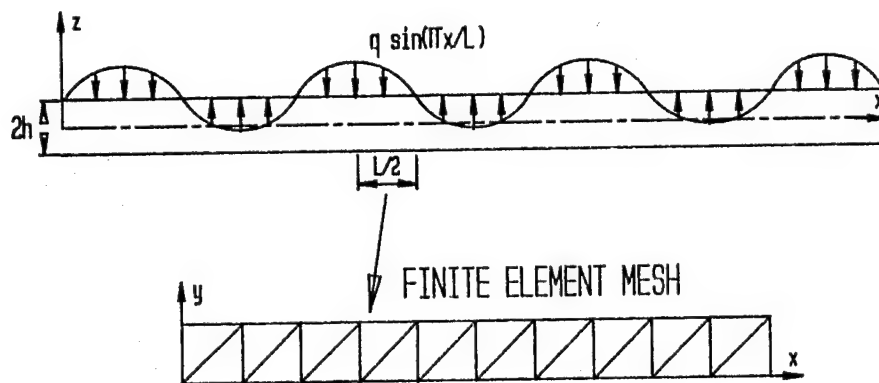


Fig. 2. Infinite [30/-30]<sub>s</sub> Gr/Ep laminate subject to sinusoidal pressure in cylindrical bending; finite element discretization.

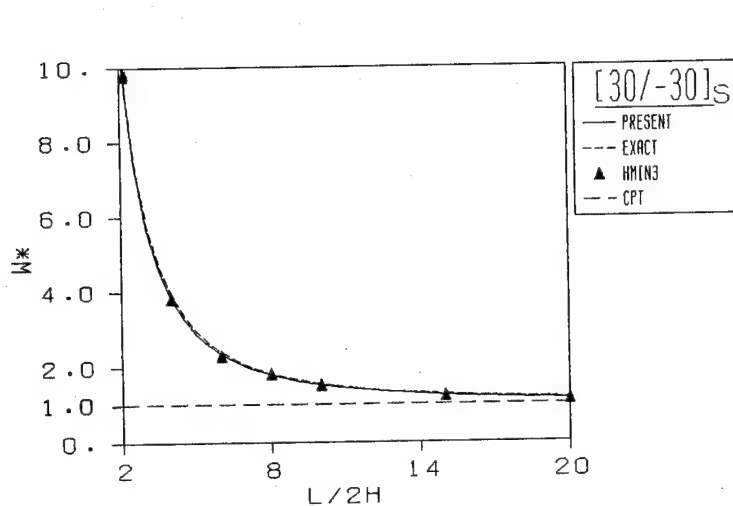


Fig. 3. Normalized maximum midplane deflection versus  $L/2h$  ratio.

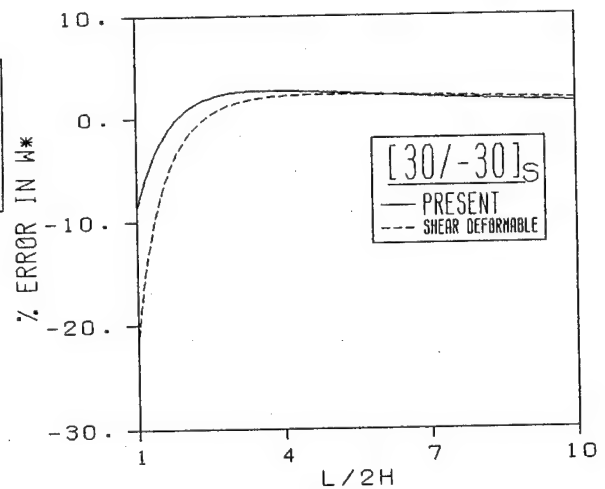


Fig. 4. Effect of transverse normal deformation on maximum midplane deflection.

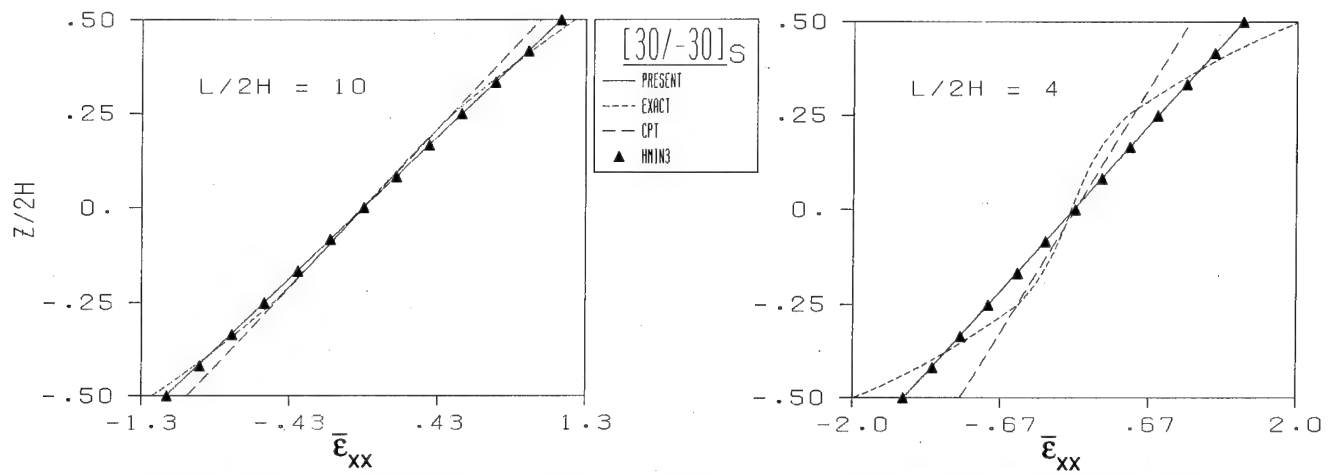


Fig. 5. Through-thickness distribution of normalized maximum normal strain ( $\bar{\epsilon}_{xx}$ ) for  $L/2h = 10$  and  $4$ .

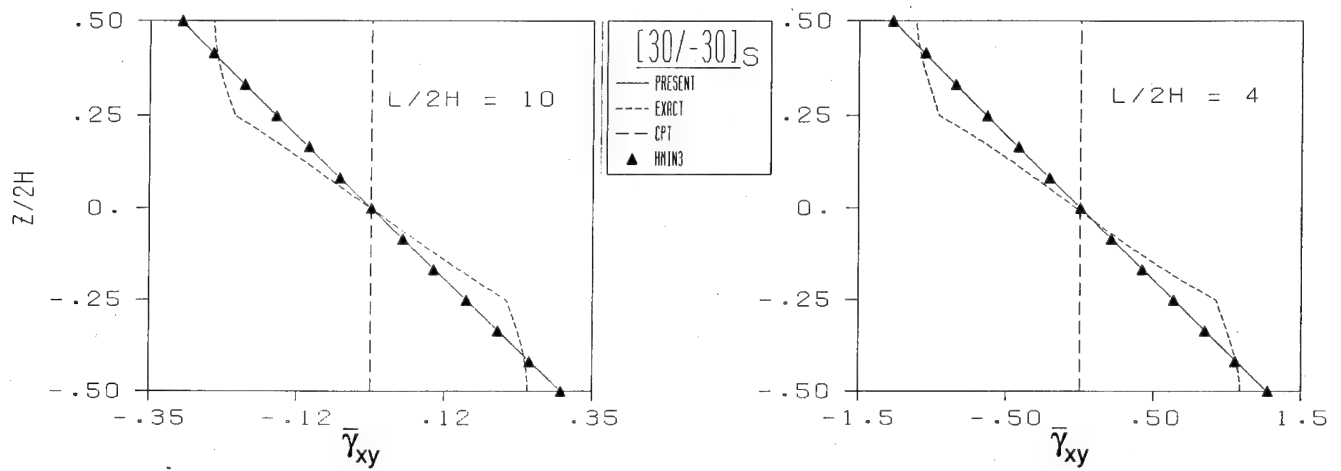


Fig. 6. Through-thickness distribution of normalized maximum inplane shear strain ( $\bar{\gamma}_{xy}$ ) for  $L/2h = 10$  and  $4$ .

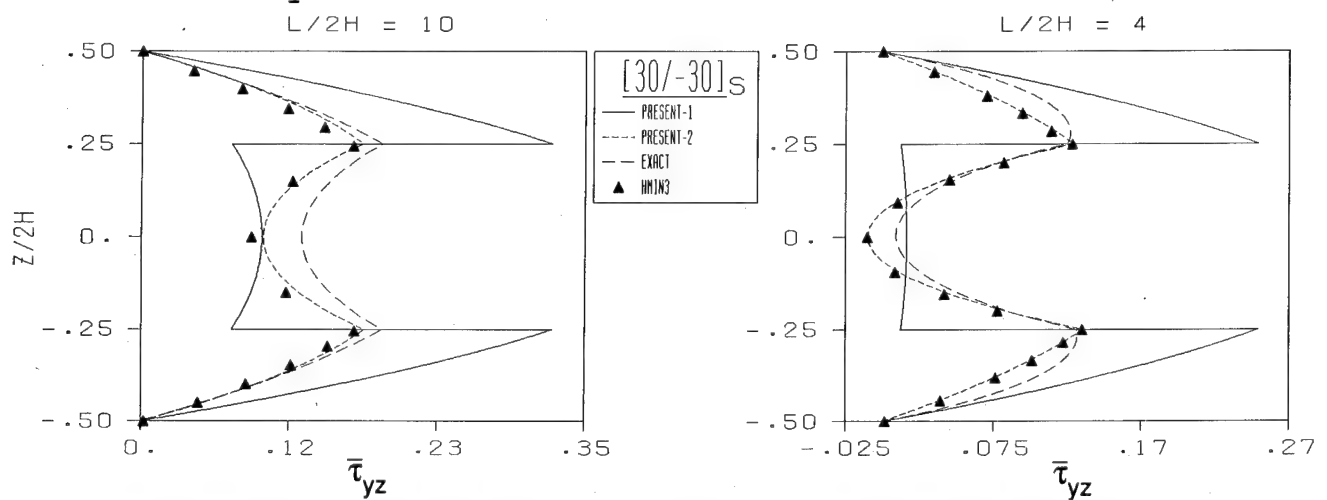


Fig. 7. Through-thickness distribution of normalized maximum transverse shear stress ( $\bar{\tau}_{yz}$ ) for  $L/2h = 10$  and  $4$ .

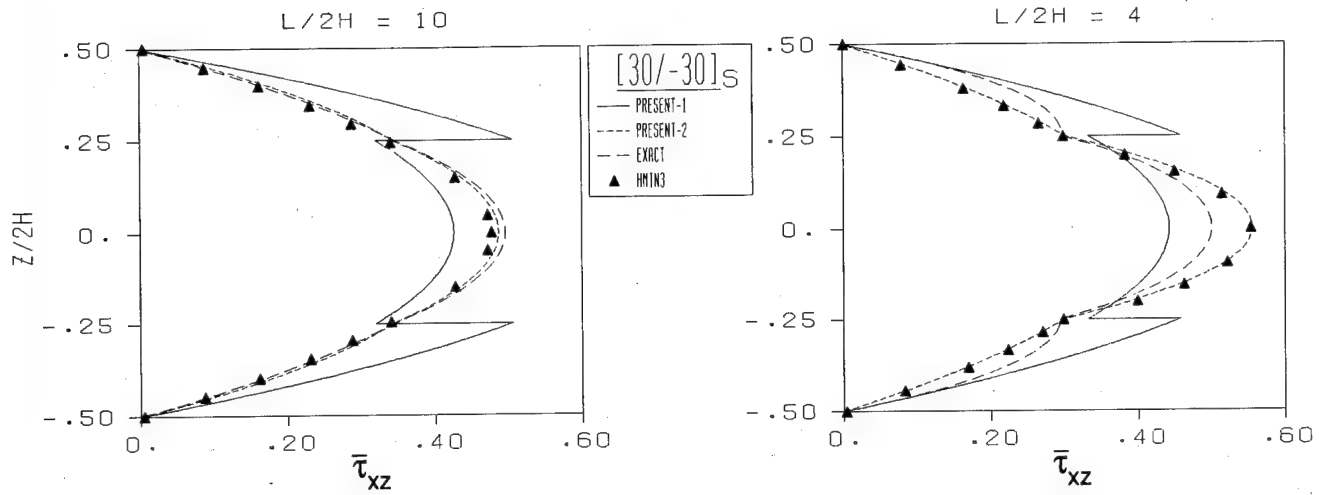


Fig. 8. Through-the-thickness distribution of normalized maximum transverse shear stress ( $\bar{\tau}_{xz}$ ) for  $L/2h = 10$  and  $4$ .

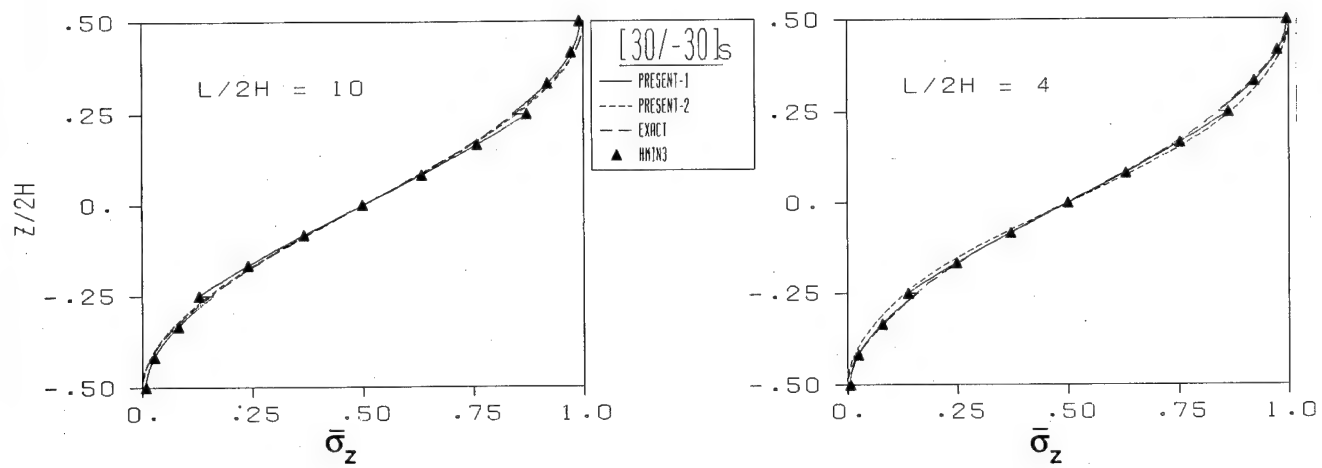


Fig. 9. Through-the-thickness distribution of normalized maximum transverse normal stress ( $\bar{\sigma}_{zz}$ ) for  $L/2h = 10$  and  $4$ .

# A NEW APPROXIMATE FRACTURE MECHANICS ANALYSIS

## METHODOLOGY FOR COMPOSITES WITH A CRACK OR HOLE

H. C. Tsai and A. Arocho  
Naval Air Development Center

### ABSTRACT

A new approximate theory which links the inherent flaw concept with the theory of crack tip stress singularities at a bi-material interface has been developed. Three assumptions were made: (1) the existence of inherent flaw (i.e., damage zone) at the tip of the crack, (2) a fracture of the filamentary composites initiates at a crack lying in the matrix material at the interface of the matrix/filament, (3) the laminate fails whenever the principal load-carrying laminae fails. This third assumption implies that for a laminate consisting of  $0^\circ$  plies, cracks into matrix perpendicular to the  $0^\circ$  filaments are the triggering mechanism for the final failure.

Based on this theory, a parameter  $K_0$  which is similar to the stress intensity factor for isotropic materials but with a different dimension was defined. Utilizing existing test data, it was found that  $K_0$  can be treated as a material constant. Based on this finding a fracture mechanics analysis methodology was developed.

The analytical results are correlated well with test results. This new approximate theory can apply to both brittle and metal matrix composite laminates with crack or hole.

### INTRODUCTION

The failure modes associated with fractures in fiber-reinforced composites differ considerably from those of homogeneous isotropic materials. The failure modes in composites are typically in the forms of transverse cracking, delamination, fiber breaks, matrix yielding, matrix cracking, fiber pull-out and fiber/matrix debonding. As a result, it is very difficult to predict the fracture behavior of composite materials exactly.

In the past, a great deal of effort has been expended to investigate the fracture behavior of composites. A number of fracture mechanics theories have been proposed. These theories have been reviewed and presented extensively in References 1 and 2.

\* In this paper a microscopic theory which was originally proposed by Mar and Lin<sup>9</sup> has been modified into a new theory. This new theory links the inherent flaw concept<sup>3-8</sup>, which postulates that a damage zone exists at the tip of crack, with the theory of crack singularities at a bi-material interface<sup>9-12</sup>. This combined theory can be used to predict the notched strength of organic and metal matrix composites with either a crack or a hole.

\*This paper cites references 1-20.

## THEORY

The stress distribution at the crack tip in a thin plate for a homogeneous, isotropic elastic solid in terms of the coordinates shown in Figure 1 is given by equation (1)

$$\begin{aligned}\sigma_x &= \sigma_N \left( \frac{a_0}{2r} \right)^{1/2} \left[ \cos \frac{\theta}{2} \left( 1 - \sin \frac{\theta}{2} \sin \frac{3\theta}{2} \right) \right] \\ \sigma_y &= \sigma_N \left( \frac{a_0}{2r} \right)^{1/2} \left[ \cos \frac{\theta}{2} \left( 1 + \sin \frac{\theta}{2} \sin \frac{3\theta}{2} \right) \right] \\ \tau_{xy} &= \sigma_N \left( \frac{a_0}{2r} \right)^{1/2} \left[ \sin \frac{\theta}{2} \cos \frac{\theta}{2} \cos \frac{3\theta}{2} \right]\end{aligned}\tag{1}$$

where

$\sigma_N$  = gross nominal stress

For an orientation directly ahead of the crack ( $\theta = 0$ )

$$\sigma_x = \sigma_y = \sigma_N \left( \frac{a_0}{2r} \right)^{1/2} \text{ and } \tau_{xy} = 0\tag{2}$$

Irwin<sup>13</sup> pointed out that equation (1) indicates that the local stresses near a crack depend on the product of the nominal stress and the square root of the half-flaw length. He called this relationship the stress intensity factor  $K$ , where for a sharp elastic crack in an infinitely wide plate,  $K$  is defined as

$$K = \sigma_N \sqrt{a_0}\tag{3}$$

In the approach using linear-elastic fracture mechanics (LEFM),  $K$  is a material parameter and may be determined from tests.

For a finite-width plate, equation (3) is modified to

$$K = Y \sigma_N \sqrt{a_0}\tag{4}$$

Where  $Y$  is a parameter that depends on the plate and crack geometry.

To develop similar concept for composite materials, the assumptions of references 3,9 were adopted in this paper; i.e.:

- The existence of an inherent flaw (also called a damage zone) at the edge of a hole or at the tip of a crack.
- Fracture of a filamentary composite initiates at a crack lying in the matrix material at the interface of the matrix/filament.
- A laminate fails whenever the principal load-carrying laminae fails. This implies that cracks in the matrix perpendicular to the  $0^\circ$  filaments are the triggering mechanism for the final failure.

Based on the above assumptions, the following theories are developed:

Using the same concept of stress intensity factor as is formulated above for isotropic materials, a material parameter similar to  $K$  is defined for composite material as

$$\overline{K} = Y \sigma_N (a_0)^m \quad (5)$$

where  $m$  is the order of singularity of a crack whose tip is at the interface of two different materials as shown in Figure 2. Calculations for determining  $m$  are presented in Reference 18.

Note that  $\overline{K}$  has a different dimension from  $K$ . ( $K$  has a dimension of "stress times length to the  $1/2$  power", while  $\overline{K}$  has a dimension of "stress times length to the  $m$  power".)

Although some composite materials (such as polymeric matrix composites) fail in a brittle manner, a damage zone does develop which is analogous to the plastic zone for ductile materials. Using this concept in conjunction with equation (5) yields:

$$\overline{K} = Y \sigma_N (a_0 + C_0)^m \quad (6)$$

where  $C_0$  is defined as an inherent flaw size. The term inherent flaw size is used since unnotched strength,  $\sigma_0$ , of a composite laminate is given by equation (6) for the case of vanishing  $a_0$ ,

$$\overline{K} = Y_0 \sigma_0 (C_0)^m \quad (7)$$

where  $Y_0$  is the correction factor for infinite plate.

It should be noted that  $C_0$  does not physically refer to an inherent crack, but a characteristic dimension of damage zone at the tip of a notch or crack prior to ultimate failure.

The question we may ask now is whether  $\overline{K}$  and  $C_0$  are material constants. Before we reach a conclusion, certain equations are helpful in answering this question.

Substituting equation (7) into equation (6), and after some manipulations, we obtain the following important equations that will be used to determine parameter  $\bar{K}$ ,  $C_0$  and notched strength of composite laminates

$$C_0 = \frac{a_0}{\left( \frac{\sigma_0}{\bar{Y}_{ON}} \right)^{1/m} - 1} \quad (8)$$

$$\bar{K} = a_0^m Y_0 \sigma_0 \left\{ \left( \frac{\bar{Y}_{ON}}{\sigma_0} \right)^{-1/m} - 1 \right\}^{-m} \quad (9)$$

$$\frac{\sigma_N}{\sigma_0} = \frac{1}{\bar{Y}} \left\{ \frac{C_0}{a_0 + C_0} \right\}^m \quad (10)$$

or

$$\frac{\sigma_N}{\sigma_0} = \frac{1}{\bar{Y}} \frac{1}{\left\{ 1 + \left( \frac{Y_0 \sigma_0}{\bar{K}} \right)^{1/m} a_0 \right\}^m} \quad (11)$$

where

$$\bar{Y} = \frac{Y}{Y_0}$$

In the following sections,  $\bar{K}$  will be called the equivalent stress intensity factor for composite materials.

#### DETERMINATION OF EQUIVALENT STRESS INTENSITY FACTOR, $\bar{K}$ AND INHERENT FLAW SIZE $C_0$

Reference 8 provides extensive fracture test data of boron/aluminum laminates with various proportions of  $0^\circ$  and  $\pm 45^\circ$  plies. Hence, this test data will be used to characterize the fracture behavior of boron/aluminum composite laminates.



### EQUIVALENT STRESS INTENSITY FACTOR, $\bar{K}$

From Reference 18, the order of stress singularity at the boron/aluminum interface,  $m$  equals to .347. Substituting  $m = .347$  in equation (9), the equivalent stress intensity factor for boron/aluminum composite laminate with center crack can be written as follows:

$$\bar{K} = a_0^{.347} \sigma_0 \left\{ \left( \frac{Y_{ON}}{\sigma_0} \right)^{-2.88} - 1 \right\}^{-.347} \quad (12)$$

Equation (12) is used to characterize the critical equivalent stress intensity factor of boron/aluminum laminates with various layups.

By using the fracture test results from Reference 8, equivalent stress intensity factors were calculated from equation (12) and are tabulated on Tables 1 through 4 for boron/aluminum composite with laminate constructions  $[0]_{6T}$ ,  $[0_2/\pm 45]_S$ ,  $[\pm 45/0_2]_S$  and  $[0/\pm 45]_S$  respectively. Note the test results shown in Tables 1 to 4 are average test results of Reference 8. As shown in Tables 1 to 4,  $\bar{K}$  values seem to be a material property and vary with different laminate orientations.  $\bar{K}$  values are also plotted on Figures 3 to 6.  $\bar{K}_{AVG}$  is the average value of  $\bar{K}$  from all the crack sizes. As shown in the figures,  $\bar{K}_{AVG}$  can be approximately treated as a material constant. It has to be pointed out here that  $\bar{K}_{AVG}$  was obtained by averaging three different widths of plate. For  $w = 101.6\text{mm}$   $\bar{K}$  values are almost the same for different  $2a_0/w$  ratios.

The detailed calculations of  $\bar{K}$  are shown in Reference 18.

The above tests are for center crack specimens. For other crack types and locations<sup>5</sup>, the calculated equivalent stress intensity factors are shown on Table 5, and are obtained from Reference 18. It can be seen that  $\bar{K}$  for these unidirectional boron/aluminum composites is constant for different crack conditions. The reason for the slightly different  $\bar{K}$  as compared to Table 1 is due to a different value of ultimate tensile strength.

### INHERENT FLAW SIZE, $C_0$

Two methods were used to calculate the inherent flaw sizes for a composite laminate with center crack.

#### Least Square Fit

Equation (8), in which  $C_0$  is a proportional constant, can be rearranged to yield

$$a_0 = C_0 \left\{ \left( \frac{Y_{GN}}{\sigma_0} \right)^{-2.88} - 1 \right\} \quad (13)$$

By using the fracture test data as shown in Tables 1 to 4, and the least square fit,  $C_0$  for various laminate constructions are determined as shown in Table 6.

#### Average Equivalent Stress Intensity Method

From Equation (7) we have

$$\bar{K}_{AVG} = \sigma_0 (C_0)^m \quad (14)$$

where  $m = .347$  for boron/aluminum.

The inherent flaw size can be derived from equation (14) as follows:

$$C_0 = \left( \frac{\bar{K}_{AVG}}{\sigma_0} \right)^{1/m} \quad (15)$$

In the case of boron/aluminum composite, equation (15) becomes

$$C_0 = \left( \frac{\bar{K}_{AVG}}{\sigma_0} \right)^{2.88} \quad (16)$$

The inherent flaw sizes for various laminate constructions were calculated using this method and were also tabulated on Table 6.

We pointed out earlier that  $C_0$  does not physically refer to an inherent crack, but rather to a characteristic dimension of damage zone at a crack tip, prior to fracture failure. Comparing the dimension of  $C_0$  with respect to the crack size of B/Al specimens as shown in Table 1 to 4, it is clear that  $C_0$  cannot be neglected in the calculations of equivalent stress intensity factor. The significance of  $C_0$  will be further discussed later in this paper.

Equation (7) is used to calculate critical equivalent stress intensity factor based on the  $C_0$  determined from least square fit method. These values are also plotted on Figures 3 to 6 as  $\bar{K}_{LSF}$ . It can be seen from the plots that there is not much difference between  $\bar{K}_{LSF}$  and  $\bar{K}_{AVG}$  except in the plot for the  $[0/+45]_S$  laminates, where though there is a greater difference between  $\bar{K}_{AVG}$  and  $\bar{K}_{LSF}$ ,  $\bar{K}_{AVG}$  provides a better result. For this reason  $\bar{K}_{AVG}$  will be adopted in this paper and will be denoted as  $\bar{K}_Q$ .

#### APPLICATIONS

Once the critical equivalent stress intensity factor  $\bar{K}_Q$  is known, the fracture strength of the composite laminates can be obtained from equations (10) and (11).

From equation (11), we have a fracture strength prediction formula as follows:

$$\frac{\sigma_N}{\sigma_0} = \frac{1}{Y} \left\{ 1 + \left( \frac{\bar{K}_Q}{Y_0 \sigma_0} \right)^{-1/m} a_0 \right\}^{-m} \quad (17)$$

From Equation (17), it can be seen that the larger the term  $\bar{K}_Q/\sigma_0$  the lesser the notch sensitivity and so from equation (10), we can conclude that the larger the inherent flaw size (i.e., the damage zone size),  $C_0$ , the lesser the notch sensitivity.

In the following subsections, the theory developed here is used to predict the fracture strength of various composite laminates.

## BORON/ALUMINUM (B/Al) COMPOSITE

### Notched Strength Prediction

For B/Al composite laminates,  $m = .347$  and equation (17) becomes

$$\frac{\sigma_N}{\sigma_0} = \frac{1}{Y} \left\{ 1 + \left( \frac{\bar{K}_0}{Y_0 \sigma_0} \right)^{-2.88} a_0 \right\}^{-.347}$$

(18)

where for a composite laminate with a center crack,  $Y$  is assumed to be the same as that for an isotropic material<sup>8</sup>.

$$Y = \left\{ \sec \left( \frac{\pi a_0}{w} \right) \right\}^{1/2}$$

For convenience, data from Tables 1 to 4 and 6 are summarized on Table 7 to be used for the following analysis. Substituting  $\sigma_0$  and  $\bar{K}_0$  from Table 7 for different ply conditions into equation (18) values for  $\sigma_N/\sigma_0$  can be obtained for various crack sizes and are tabulated on Column 7 of Tables 1 to 4. The error shown on Column 8 is defined as the difference between calculated results and test results divided by test results. The analytical results are also plotted on Figures 7 to 10.

As can be seen, the prediction represents the experimental results reasonably well.

The  $\bar{K}_0$  values obtained from center cracked specimens are also used to calculate the strength of B/Al specimens with center holes. Comparison of the analytical results and test results<sup>14</sup> are shown in Figures 11 to 13. Figure 11 shows excellent correlation between test and calculated results for  $[0]_{6T}$  laminates with center holes, while in Figure 12 and 13, the maximum percentage error for analytical results is around 13%. The detailed calculations are in reference 18. This confirms the findings of reference 19 and 20 that the length of discontinuity and not the shape appeared to control the fracture strength.

### Notch Sensitivity of Boron/Aluminum (B/Al) Composite Laminate

The  $\sigma_N/\sigma_0$  test data in Tables 1 to 4 are plotted on Figures 14 to 16 for composite laminate of various widths to check the notched sensitivity of B/Al composites. It is obvious that  $[\pm 45/0_2]_S$  is the most notch-sensitive, while  $[0/\pm 45]_S$  is the least sensitive to the notch size. For  $2a_0/W \leq .1$   $[0]_{6T}$  is more sensitive to the notch size than  $[0_2/\pm 45]_S$ . For  $2a_0/W \geq .1$ , the  $\sigma_N/\sigma_0$  vs  $2a_0/W$  curve for  $[0]_{6T}$  and  $[0_2/\pm 45]_S$  laminates are almost identical. The trend mentioned above can be detected by using a parameter<sup>15</sup> defined by the ratio  $\bar{K}_0/\sigma_0$  as shown in Table 7. The ranking of various laminate configurations for the  $\bar{K}_0/\sigma_0$  index is  $[0/\pm 45]_S$ ,  $[0_2/\pm 45]_S$ ,  $[0]_{6T}$  and  $[\pm 45/0_2]_S$  in descending order. The relative values of  $\bar{K}_0/\sigma_0$  show a similar trend to that of damage zone size,  $C_0$ .

It can be concluded that the larger the ratio  $\overline{K_Q}/\sigma_0$  (or the damage zone size  $C_0$ ) the less fracture sensitivity there is to the crack size.

#### GRAPHITE/EPOXY (Gr/Ep) COMPOSITE

Equation (9) is used to characterize the  $\overline{K_Q}$  for Gr/Ep composites<sup>6</sup>. The detailed calculations are shown in reference 18.  $\overline{K_Q}$  for various ply orientations is plotted as shown in Figures 17 to 19. It can be seen that  $\overline{K_Q}$  for Gr/Ep composites can be treated as a material constant. Table 8 summarizes the characterization results of Gr/Ep composite laminates. For Thornel 300 graphite fibers in Narmco 5208 epoxy resin,  $m = .297$ .

#### Notched Strength Prediction and Notch Sensitivity

For Gr/Ep composite with center crack, equation (17) becomes

$$\frac{\sigma_N}{\sigma_0} = \frac{1}{Y} \left\{ 1 + \left( \frac{\overline{K_Q}}{\sigma_0} \right)^{-3.367} a_0 \right\}^{-.297}$$

(19)

Substituting  $\overline{K_Q}$  and  $\sigma_0$  from Table 8, into equation (19), the fracture strengths of graphite/epoxy for various laminate constructions can be obtained and are plotted on Figure 20. The detailed calculations are shown in reference 18. As can be seen from the figure, the correlation between calculated and experimental results is very good.

It can also be seen from Figure 20 that the ratio  $\overline{K_Q}/\sigma_0$  (or the inherent flaw size) in Table 8 can be used as a notch sensitivity indicator. The  $[0/90/\pm 45]_S$  laminate is less notch sensitive than the  $[0/\pm 45]_S$  and  $[0/\pm 45]_{2S}$  laminates and accordingly it has a larger ratio of  $\overline{K_Q}/\sigma_0$  (or  $C_0$ ) than the other two laminates.

#### COMPARISON OF ANALYTICAL RESULTS BETWEEN ANISOTROPIC AND NEW APPROXIMATE MODELS

Composite materials made by combining two materials with different elastic moduli are by nature anisotropic in the gross sense. The anisotropic model for composite materials is to assume that the composite is a homogeneous, anisotropic solid. For an anisotropic fracture  $m = .5$ .<sup>17</sup> Applying the inherent flaw concept<sup>3</sup> for an anisotropic mode with center crack, we have

$$K_Q = Y\sigma_N(a_0 + C_0)^{1/2}$$

(20)

$$K_Q = \sigma_0 (C_0^*)^{1/2} \quad (21)$$

Note that  $K_Q$  has dimensions different from that of  $\overline{K_Q}$  and  $C_0^*$  is the inherent flaw size corresponding to an anisotropic model.

Examining equations (20) and (21), we can derive the following useful equations for an anisotropic model

$$C_0^* = \frac{a_0}{\left(\frac{\sigma_0}{Y\sigma_N}\right)^2 - 1} \quad (22)$$

$$\frac{\sigma_N}{\sigma_0} = \frac{1}{Y} \left( \frac{C_0^*}{a_0 + C_0^*} \right)^{1/2} \quad (23)$$

$$K_Q = \sigma_0 (a_0)^{1/2} \left\{ \left( \frac{Y\sigma_N}{\sigma_0} \right)^{-2.0} - 1 \right\}^{-.5} \quad (24)$$

Equation (22) can be used to obtain  $C_0^*$  while equation (23) can be used to predict the fracture strength of composite laminates.

Figures 21 to 24 show the comparison of calculated results between the new approximate and anisotropic models. It is clear that the new approximate model predicts better results than the anisotropic model.

## CONCLUSIONS AND RECOMMENDATIONS

### CONCLUSIONS

- . The methodology developed here can be used to characterize the fracture toughness of the composite laminates and can be used as a design tool to predict the fracture strength of various composite laminates.
- . The parameter  $\bar{K}_0$  which was called critical equivalent stress intensity factor is defined, and can be treated as a material constant for various composite laminates.
- . The new approximate model provides better results than those of the anisotropic model.
- . The larger the ratio  $\frac{\bar{K}_0}{\sigma_0}$  (or the damage zone size,  $C_0$ ), the higher the damage tolerance.

### RECOMMENDATIONS

- . Further verification of the new approximate theory with test results of various composite materials is needed.
- . Apply the theory developed here to predict the fracture strength of composite laminates with various crack angles.
- . Develop a methodology to predict the inherent flaw size at the crack tip before fracture.



## REFERENCES

1. Adams, D. F. and Mahishi, J.M. "Delamination Micromechanics Analysis", NASA Report, N85-31237, May 1985.
2. Whitney, J. M., "Fracture Analysis of Laminates", Composites Engineered Materials Handbook, ASM International, Volume 1, 1987.
3. Waddoups, M. G., Eisenmann, J. R. and Kaminski, B.E., "Macroscopic Fracture Mechanics of Advanced Composite Materials", Journal of Composite Material, Vol. 5, 1971, p. 446.
4. Bowie, O. L., "Analysis of an Infinite Plate Containing Radial Cracks Originating from the Boundary of an Internal Circular Hole," Journal of Mathematics and Physics, Vol. 35, 1956, p. 60.
5. Adsit, N. R. and Waszczak, J. P. "Fracture Mechanics Correlation of Boron/Aluminum Coupon Containing Stress Risers", ASTM STP 593, 1975.
6. Morris, D. H. and Hahn, H. T., "Fracture Resistance Characterization of Graphite/Epoxy Composites", Composites Materials: Testing and Design, ASTM, STP 617, pp. 5-17, 1976.
7. Awerbuch, J., and Hahn, H. T., "Crack Tip Damage and Fracture Toughness of Boron/Aluminum Composites," Journal of Composite Materials, Vol. 13, April 1979, pp. 82-107.
8. Poc, C. C. Jr., and Sova, J. A. "Fracture Toughness of Boron/Aluminum Laminates with Various Proportions of  $0^{\circ}$  and  $\pm 45^{\circ}$  Plies," NASA TP 17.7, 1980.
9. Mar, J. W. and Lin, K. Y., "Fracture Mechanics Correlation for Tensile Failure of Filamentary Composites with Holes", Journal of Aircraft, Vol. 14, p. 703, 1977.
10. Lin, K. Y. and Mar, J.W., "Finite Element Analysis of Stress Intensity Factors for Cracks at a Bi-Material Interface", International Journal of Fracture, 12, pp. 521-531, 1976.
11. Bogy, D. B., "On the Plane Elastostatic Problem of a Loaded Crack Terminating at a Material Interface" Journal of Applied Mechanics Transaction ASME, 38, Series E., No. 4 pp. 911-918, December 1971.
12. Zak, A. R. and Williams, M. L. "Crack Point Stress Singularities at a Bi-Material Interface". Journal of Applied Mechanics, 30. Transaction of ASME, 85, Series E. pp. 142-143, March 1963.
13. Irwin, G. R. "Analysis of Stresses and Strains Near the End of a Crack Traversing a Plate," Journal of Applied Mechanics, Transactions ASME, Vol. 24, 1957.
14. Johnson, W. S. and Bigelow, C. A., "Experimental and Analytical Investigation of Fracture Process of Boron/Aluminum Laminates Containing Notches", NASA TP 2187, 1983.
15. Mandell, J. F., Wang, Su-Su, McGarry, J. Frederick "The Extension of Crack Tip Damage Zones in Fiber Reinforced Plastic Laminates". Journal of Composite Materials, Vol. 9, July 1975.

16. Nuismer, R. J. and Whitney, J. M. "Uniaxial Failure of Composite Laminates Containing Stress Concentrations," Fracture Mechanics of Composites, ASTM STP 593, American Society for Testing and Materials, Philadelphia, pp. 117-142, 1975.
17. Wu, E.M., "Strength and Fracture of Composites", Fracture and Fatigue, Composite Materials, Vol. 5, 1974.
18. Tsai, H.C. and Arocho, A., "A New Approximate Fracture Mechanics Analysis Methodology for Composites with Cracks or Holes". Report No. NADC-88118-60, 1988.
19. Goree, J. G. and Dharani, R. "Mathematical Modeling of Damage in Unidirectional Composites", NASA Contractor Report 3453, 1981
20. Mar, J. W. and Lin, K.Y., "Fracture of Boron/Aluminum Composites with Discontinuities", Journal of Composite Materials, Vol. 11, Oct. 1977, pp. 405-421.

Table 3. Equivalent Stress Intensity Factor For  $[\pm 45/0]_s$  B/Al Composite.

w (mm)	$a_0$ (mm)	$\xi$	Y	$\left(\frac{\sigma_N}{\sigma_0}\right)_{\text{TEST}}$	R (MPa(mm) <sup>-3/4</sup> )	$\left(\frac{\sigma_N}{\sigma_0}\right)$	Error %
19.1	.25	.025	1.001	—	—	—	—
19.1	.65	.068	1.003	—	—	—	—
50.8	1.25	.05	1.001	.619	674.7	.633	2.3
50.8	2.55	.1	1.006	.531	716.6	.517	-2.6
50.8	7.6	.3	1.06	.361	720.8	.349	-3.5
50.8	12.7	.5	1.189	.245	647.7	.262	7.0
101.6	2.55	.05	1.001	.528	707.6	.520	-1.6
101.6	5.1	.1	1.006	.423	703.8	.417	-1.3
101.6	15.25	.3	1.06	.281	706.2	.276	-1.6
101.6	25.4	.5	1.189	.201	673.0	.207	3.1

$$R^{\text{AVG}} = 693.8 \text{ MPa(mm)}^{-3/4}$$

$$\sigma_0 = 910.5 \text{ MPa}, \quad \xi = 2a_0/W$$

$$Y = \sqrt{\sec\left(\frac{\pi}{2}\xi\right)}$$

Table 4. Equivalent Stress Intensity Factor For  $[0/\pm 45]_s$  B/Al Composite.

w (mm)	$a_0$ (mm)	$\xi$	Y	$\left(\frac{\sigma_N}{\sigma_0}\right)_{\text{TEST}}$	R (MPa(mm) <sup>-3/4</sup> )	$\left(\frac{\sigma_N}{\sigma_0}\right)$	ERROR %
19.1	.25	.025	1.001	—	—	—	—
19.1	.65	.068	1.003	.828	564.6	.865	4.4
50.8	1.25	.05	1.001	.796	645.8	.789	-1.0
50.8	2.55	.1	1.006	.730	710.1	.688	-5.7
50.8	7.6	.3	1.06	.458	597.8	.481	5.2
50.8	12.7	.5	1.189	.329	563.1	.367	11.5
101.6	2.55	.05	1.001	.699	656.5	.692	-1.0
101.6	5.1	.1	1.006	.620	702.0	.569	-8.2
101.6	15.25	.3	1.06	.413	678.0	.388	-6.0
101.6	25.4	.5	1.189	.271	583.9	.293	8.2

$$R^{\text{AVG}} = 633.5 \text{ MPa(mm)}^{-3/4}$$

$$\sigma_0 = 581.4 \text{ MPa}, \quad \xi = 2a_0/W$$

$$Y = \sqrt{\sec\left(\frac{\pi}{2}\xi\right)}$$

Table 1. Equivalent Stress Intensity Factor For [0]<sub>6T</sub> B/Al Composite.

w (mm)	a <sub>0</sub> (mm)	ξ	Y	$\left(\frac{\sigma_N}{\sigma_0}\right)_{\text{TEST}}$	R (MPa(mm) <sup>.347</sup> )	$\left(\frac{\sigma_N}{\sigma_0}\right)$	Error %
19.1	.25	.025	1.001	.818	1125.0	.878	7.4
19.1	.65	.068	1.003	.6845	1136.0	.760	11.0
50.8	1.25	.05	1.001	.592	1166	.663	12.0
50.8	2.55	.1	1.006	.555	1455	.546	-1.6
50.8	7.6	.3	1.06	.4003	1479	.3705	-7.5
50.8	12.7	.5	1.189	.3098	1518	.279	-10.0
101.6	2.55	.05	1.001	.580	1455	.549	-5.3
101.6	5.1	.1	1.006	.468	1435	.443	-5.3
101.6	15.25	.3	1.06	.3024	1399	.295	-2.6
101.6	25.4	.5	1.189	.232	1430	.221	-4.7

$$R^{\text{AVG}} = 1360 \text{ MPa (mm)}^{.347}$$

$$\sigma_0 = 1672 \text{ MPa} , \xi = 2a_0/W$$

$$Y = \sqrt{\sec\left(\frac{\pi}{2}\xi\right)}$$

Table 2. Equivalent Stress Intensity Factor For [0<sub>2</sub>/±45]<sub>s</sub> B/Al Composite.

w (mm)	a <sub>0</sub> (mm)	ξ	Y	$\left(\frac{\sigma_N}{\sigma_0}\right)_{\text{TEST}}$	R (MPa(mm) <sup>.347</sup> )	$\left(\frac{\sigma_N}{\sigma_0}\right)$	Error %
19.1	.25	.025	1.001	.878	652.6	.891	1.5
19.1	.65	.068	1.003	.782	681.9	.782	0.
50.8	1.25	.05	1.001	.721	740.	.686	-4.8
50.8	2.55	.1	1.006	.571	683.1	.570	0.
50.8	7.6	.3	1.06	.395	697.8	.389	-1.5
50.8	12.7	.5	1.189	.274	639.0	.293	7.0
101.6	2.55	.05	1.001	.579	695.1	.572	-1.2
101.6	5.1	.1	1.006	.464	680.6	.464	0.
101.6	15.25	.3	1.06	.321	711.5	.310	-3.5
101.6	25.4	.5	1.189	.229	674.6	.232	1.6

$$R^{\text{AVG}} = 685.6 \text{ MPa (mm)}^{.347}$$

$$\sigma_0 = 800.1 \text{ MPa} , \xi = 2a_0/W$$

$$Y = \sqrt{\sec\left(\frac{\pi}{2}\xi\right)}$$

Table 5. Critical Equivalent Stress Intensity Factor Of Unidirectional B/Al<sup>5</sup> Composite.

SPECIMEN *	$\frac{2a_o}{w}$ or $\frac{2R}{w}$	$\bar{K}_{AVG}$ MPa (mm) <sup>.347</sup>
CH	.25	1196.00
CS	.40	1227.00
DEN	.30	1214.00

\* CH - CENTER HOLE SPECIMEN

CS - CENTER SLIT SPECIMEN

DEN - DOUBLE EDGE NOTCH SPECIMEN

Table 6. Inherent Flaw Size, C<sub>o</sub> (mm).

	Least Square Fit	$\bar{K}_{AVG}$ Method
[0] <sub>6T</sub>	.633	.552
[0 <sub>2</sub> /±45] <sub>s</sub>	.593	.641
[±45/0 <sub>2</sub> ] <sub>s</sub>	.405	.457
[0/±45] <sub>s</sub>	.976	1.28

Table 7. Fracture Parameters For Various Laminate Configurations Of B/Al.

Ply Configuration	$\sigma_o$ (MPa)	$\bar{K}_Q$ MPa (mm) <sup>.347</sup>	$\frac{\bar{K}_Q}{\sigma_o}$ MPa (mm) <sup>.347</sup>	$C_o$ (mm)
[0] <sub>6T</sub>	1672	1360	.81	.552
[0 <sub>2</sub> /±45] <sub>s</sub>	800.1	685.6	.867	.641
[±45/0 <sub>2</sub> ] <sub>s</sub>	910.5	693.8	.762	.457
[0/±45] <sub>s</sub>	581.4	633.5	1.09	1.28

Table 8. Fracture Parameters For Various Laminate Configurations Of Gr/Ep.

Ply Configuration	$\sigma_o$ (MPa)	$\bar{K}_Q$ MPa (mm) <sup>.297</sup>	$\frac{\bar{K}_Q}{\sigma_o}$ (mm) <sup>.297</sup>	$C_o$ (mm)
[0/±45] <sub>2s</sub>	541.0	408.6	.755	.389
[0/±45] <sub>s</sub>	541.0	393.5	.727	.342
[0/90/±45] <sub>s</sub>	454.0	437.7	.964	.884

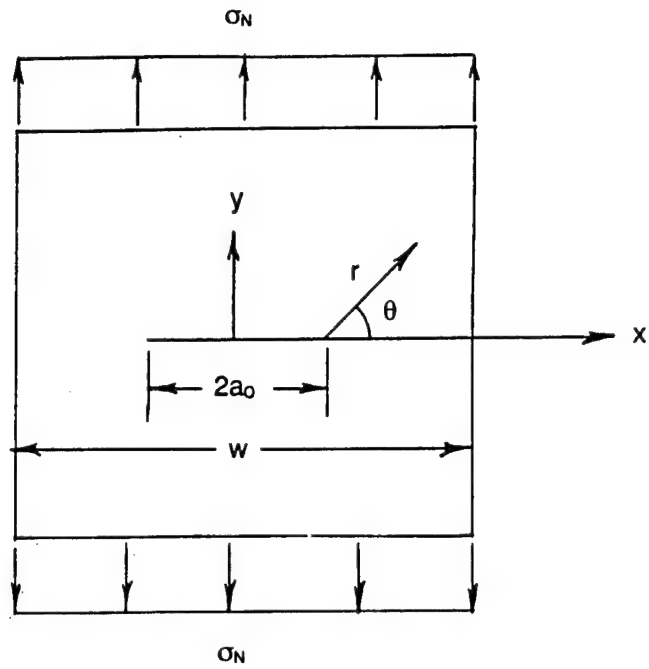


Figure 1. Model For Equations For Stresses At A Point Near A Crack.

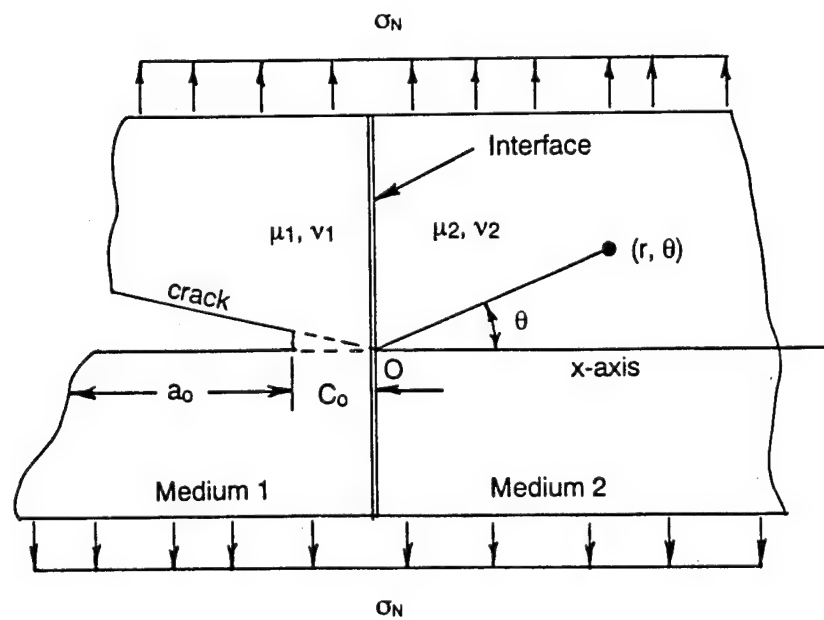


Figure 2. Crack Normal To The Bi-Material Interface With Inherent Flaw,  $C_0$ .



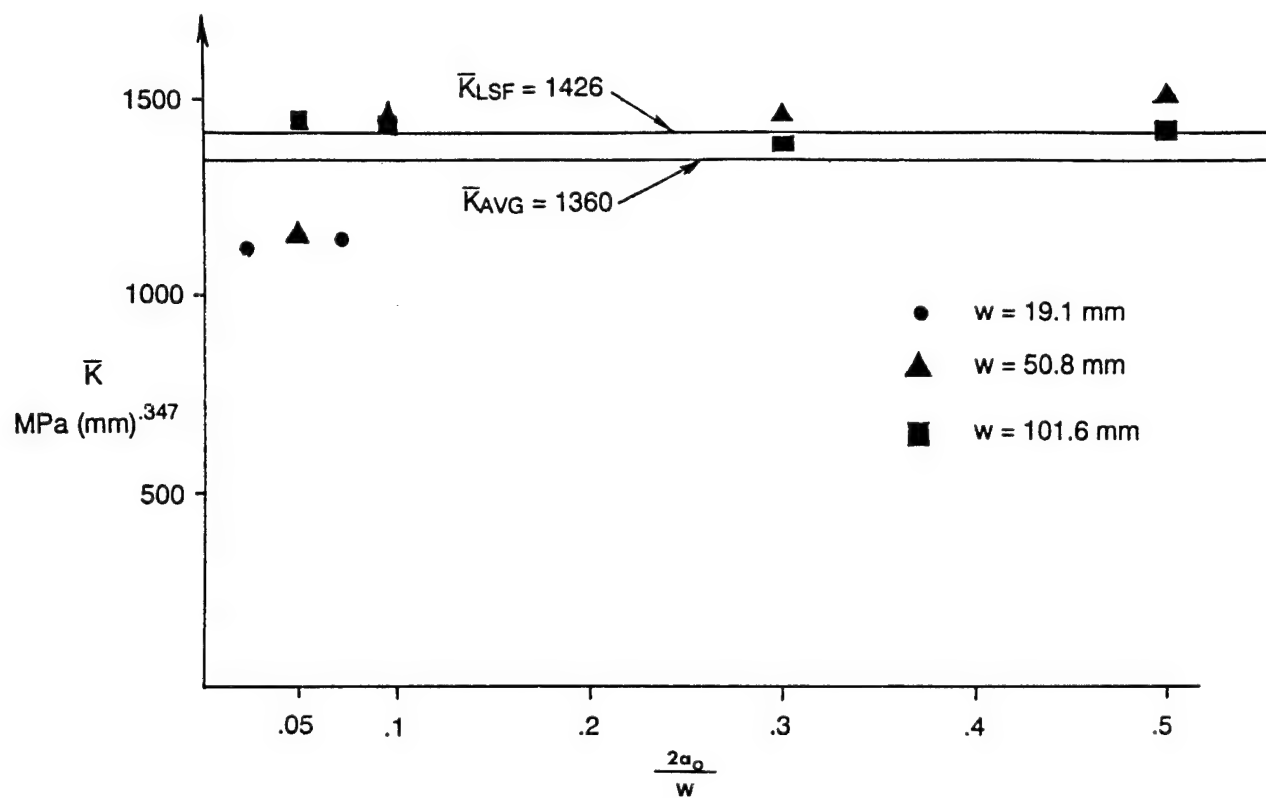


Figure 3. Equivalent Stress Intensity Factor For  $[0]_6T$  B/Al Composite.

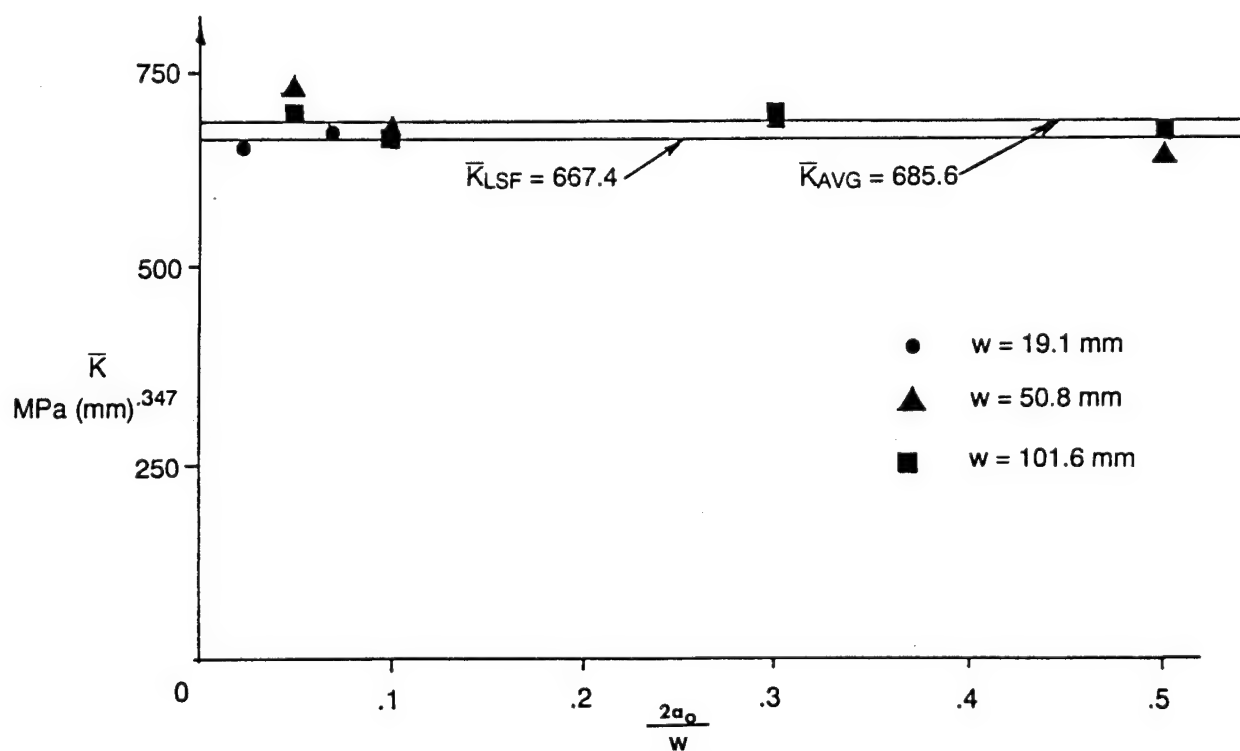


Figure 4. Equivalent Stress Intensity Factor For  $[0_2/\pm 45]_s$  B/Al Composite.

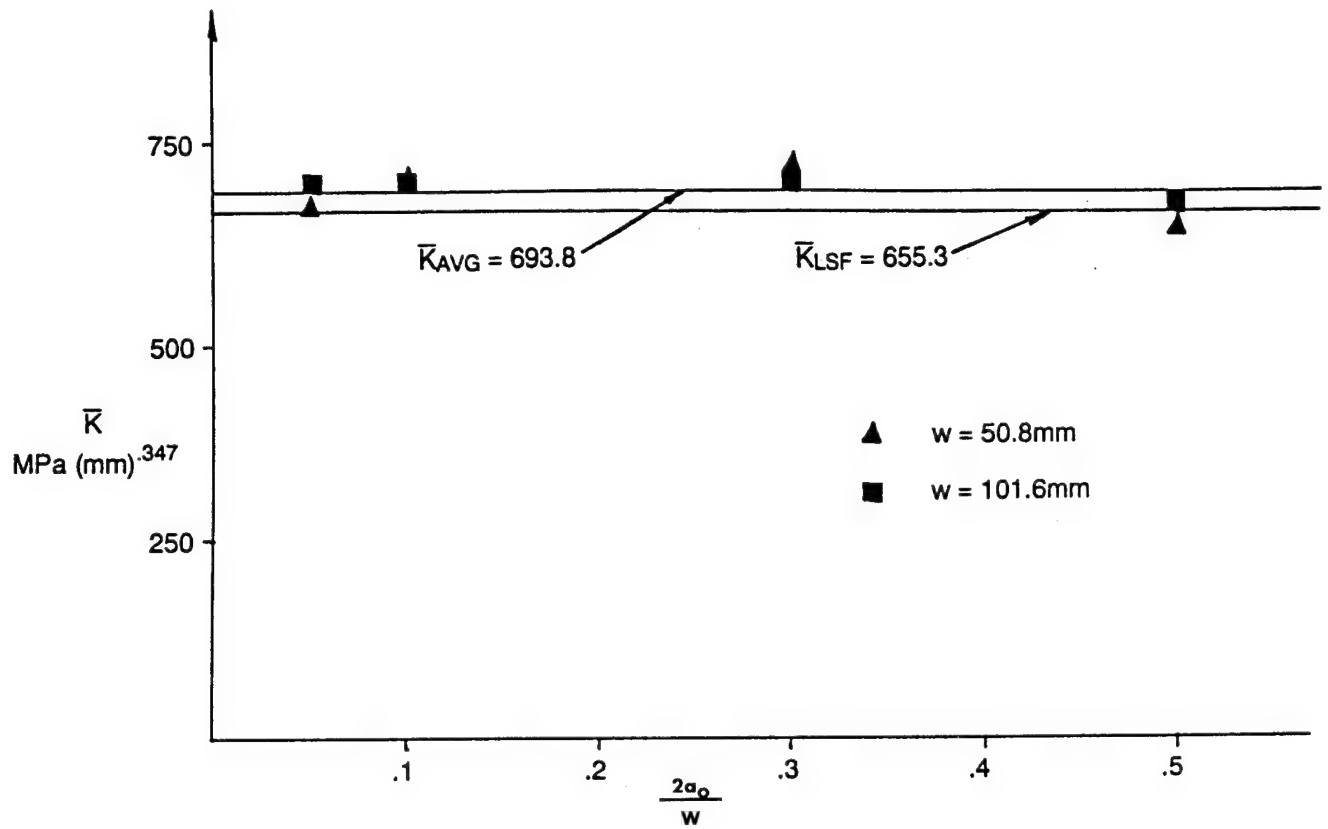


Figure 5. Equivalent Stress Intensity Factor For  $[\pm 45/0_2]_s$  B/Al Composite.

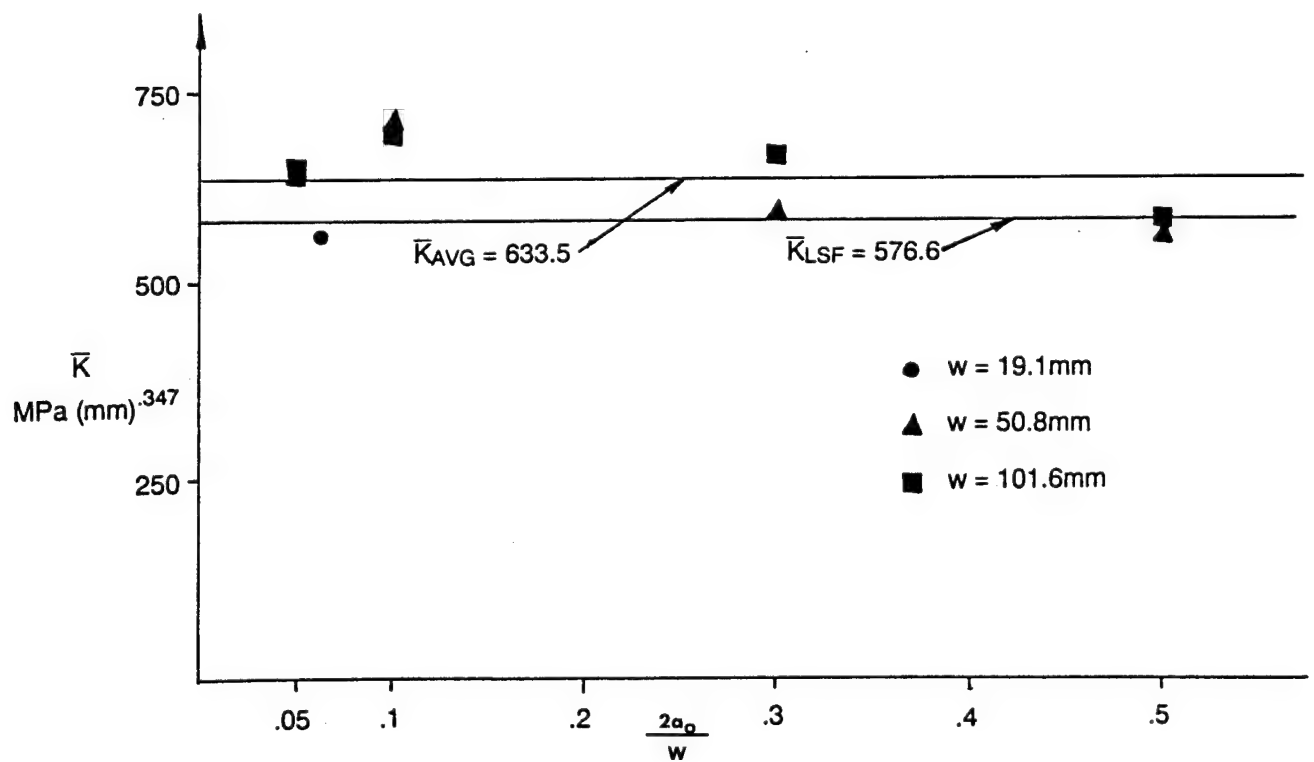


Figure 6. Equivalent Stress Intensity Factor For  $[0/\pm 45]_s$  B/Al Composite.

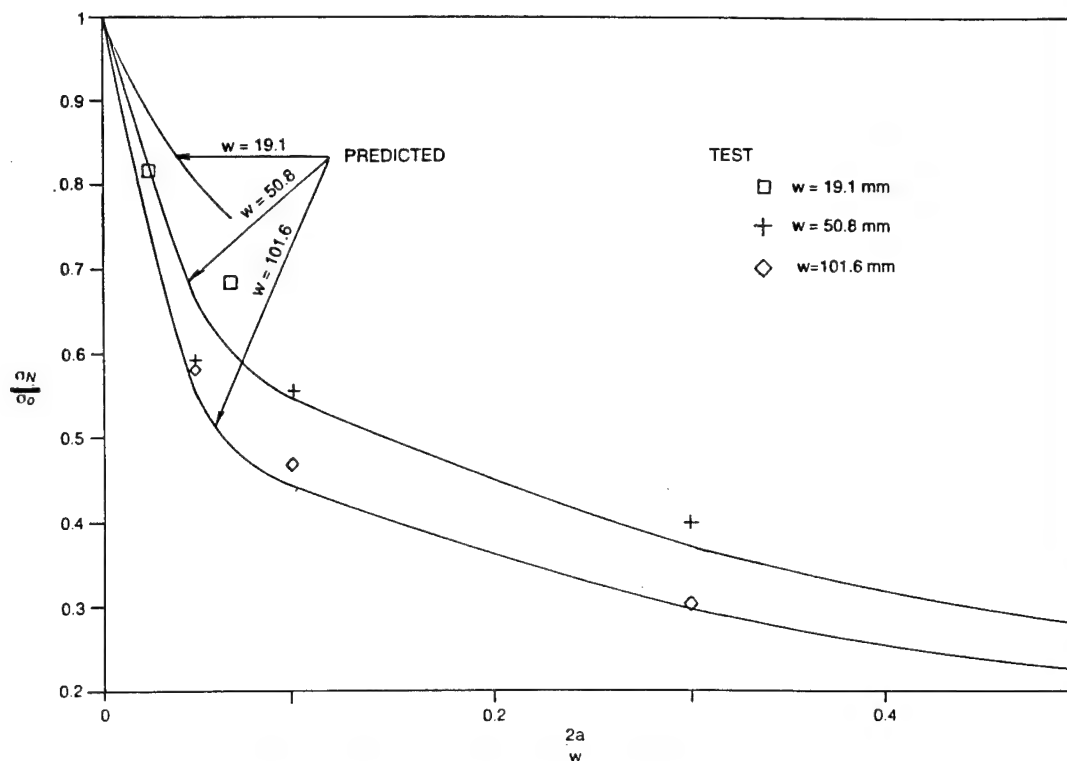


Figure 7. Comparison Of Predicted And Experimental Notched Strength Results For B/AI  $(0^\circ)_6T$  Composites.

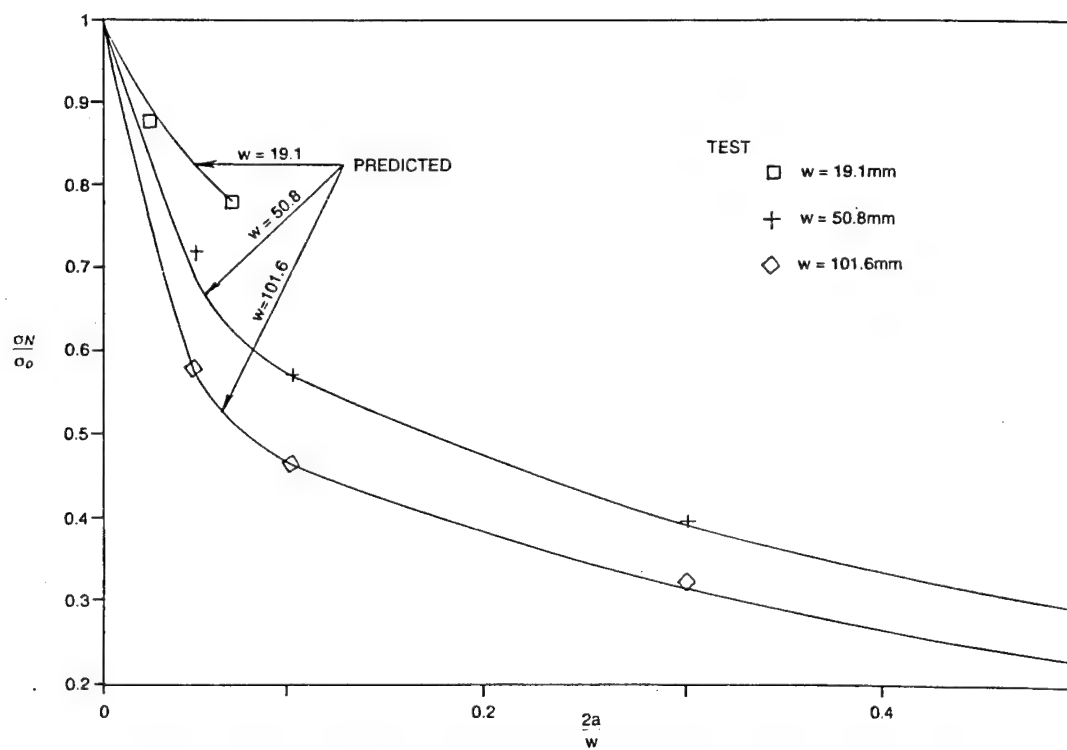


Figure 8. Comparison Of Predicted And Experimental Notched Strength Results For B/AI  $[0_2/\pm 45]_6$  Composites.

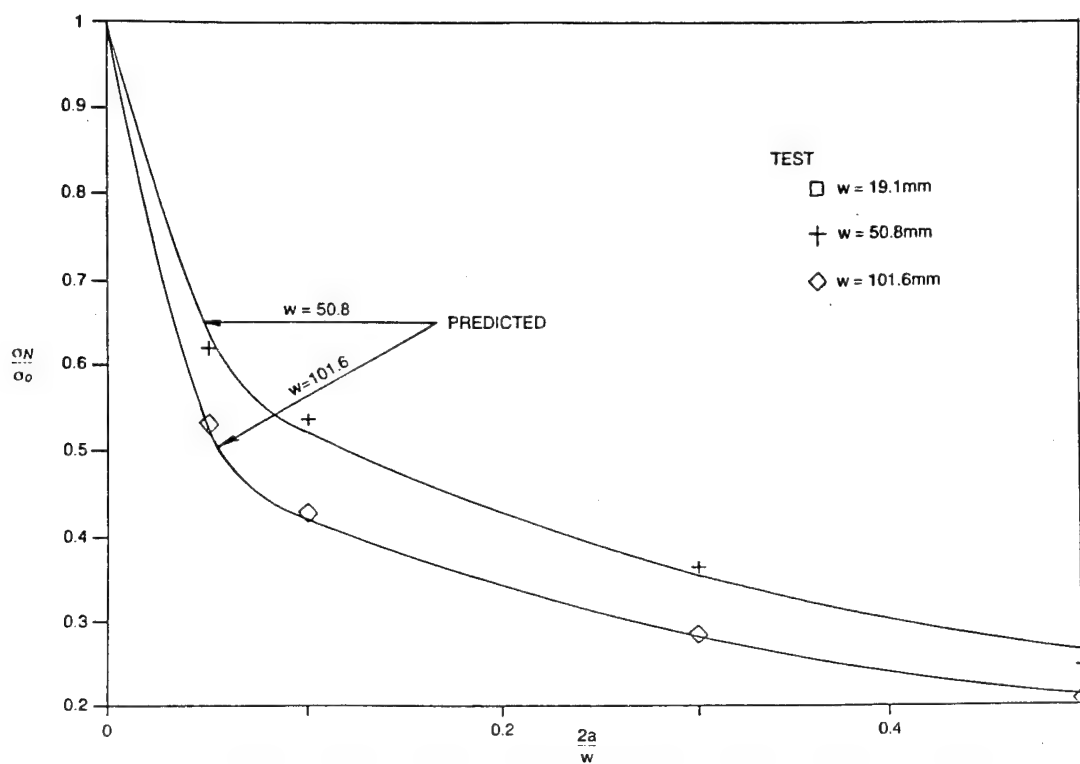


Figure 9. Comparison Of Predicted And Experimental Notched Strength Results For B/AI  $[\pm 45/0]_s$  Composites.

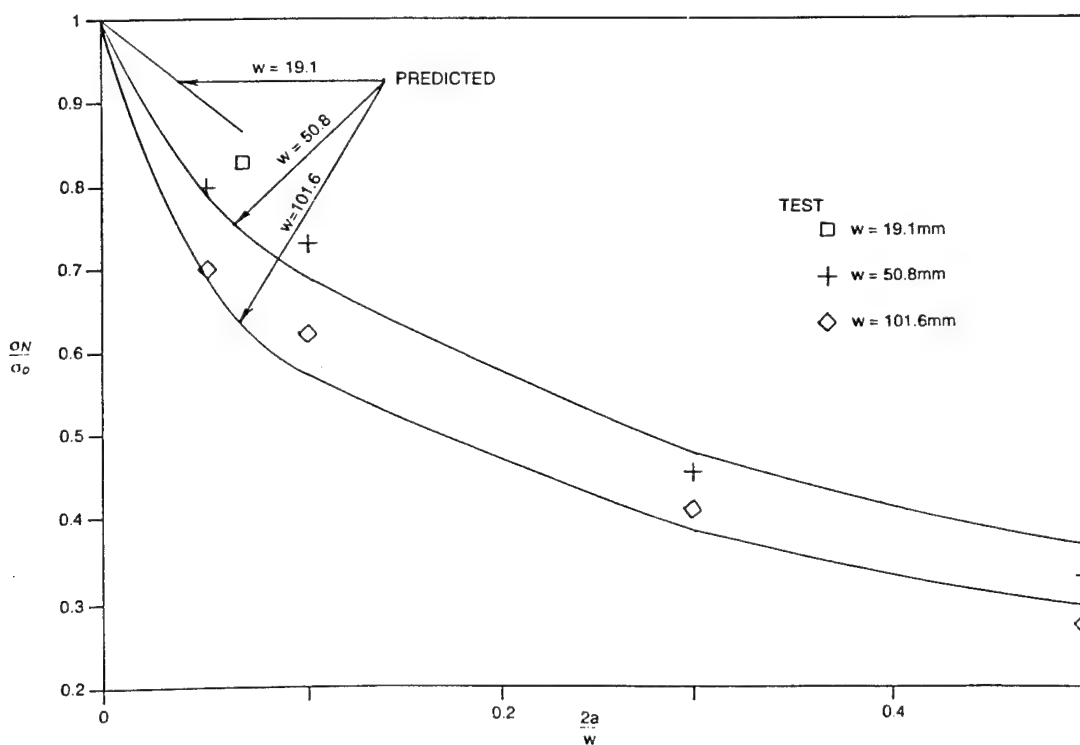


Figure 10. Comparison Of Predicted And Experimental Notched Strength Results For B/AI  $[0/\pm 45]_s$  Composites.

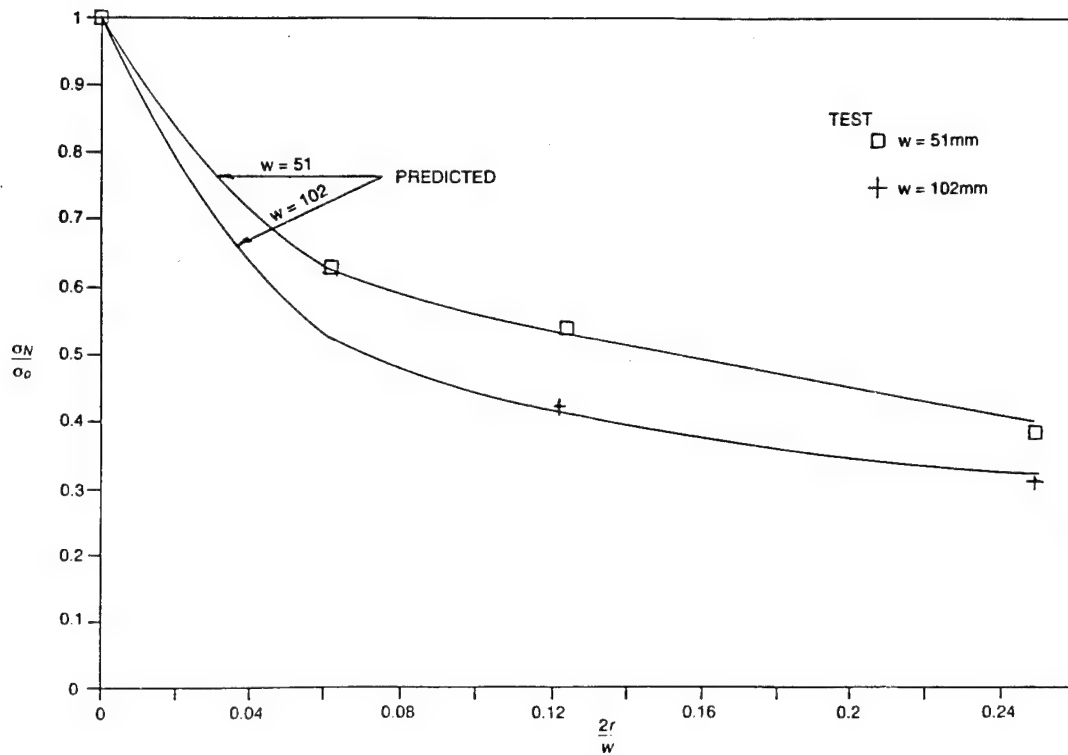


Figure 11. Notched Strength Prediction For B/AI [0]6T Composite With Center Hole.

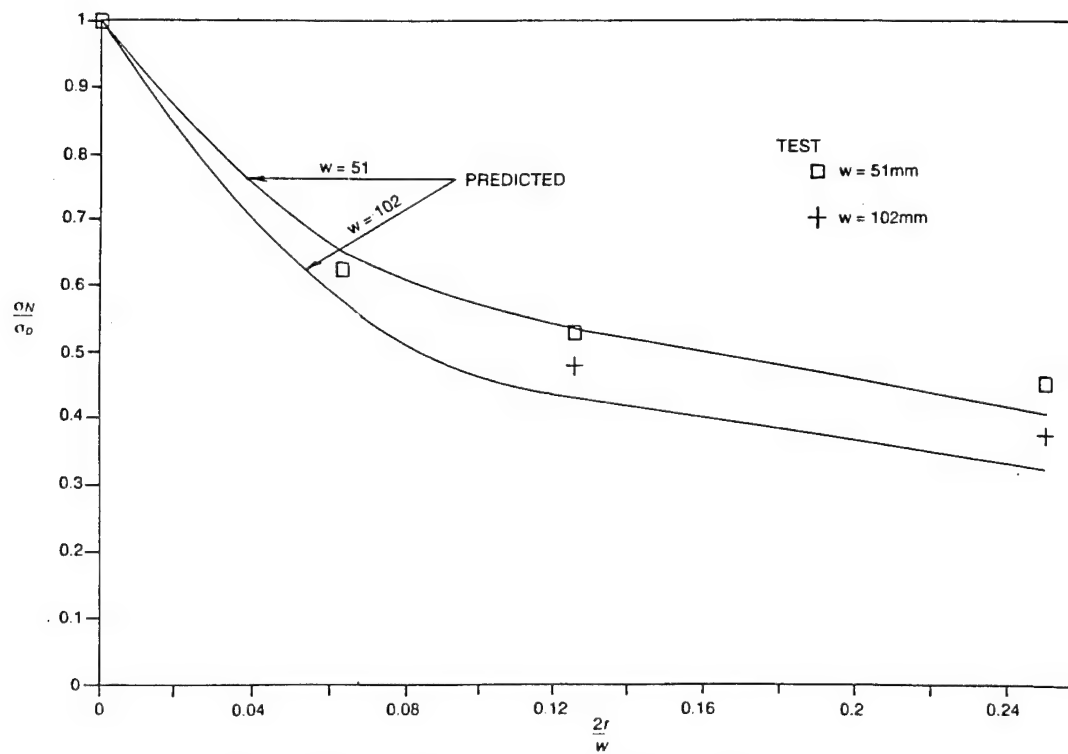


Figure 12. Notched Strength Prediction for B/AI [0<sub>2</sub>/±45]<sub>S</sub> Composites With Center Hole.

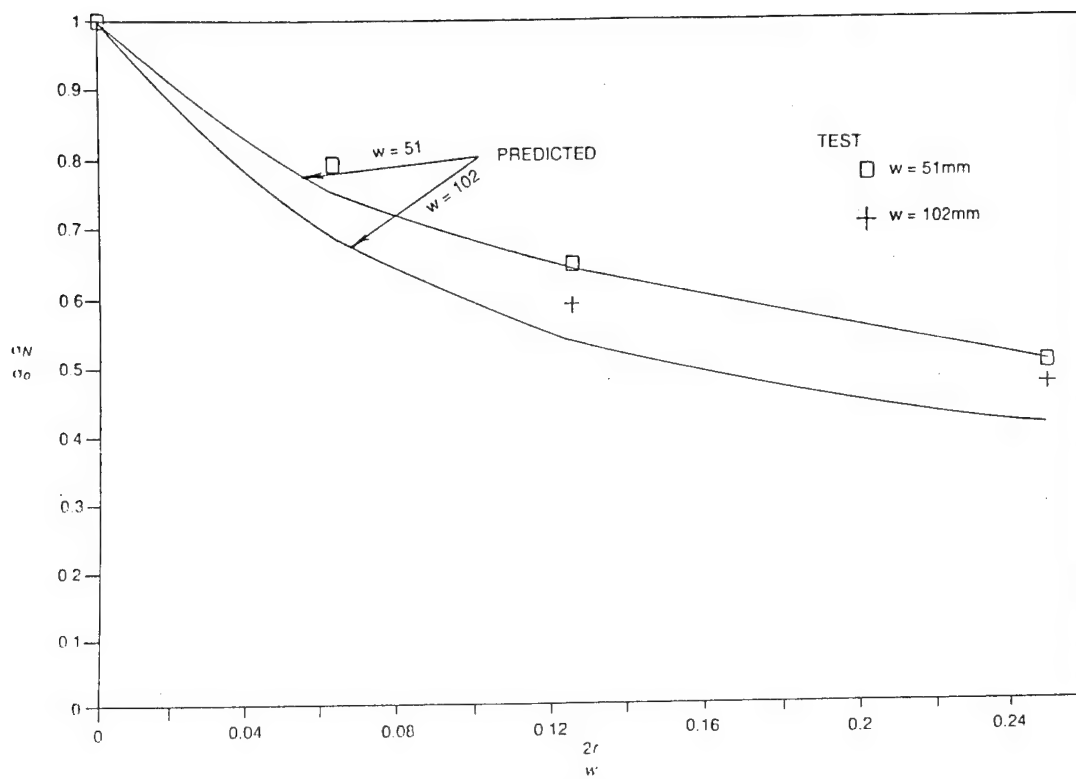


Figure 13. Notched Strength Prediction For B/AI  $[0/\pm 45]_s$  Composite With Center Hole.

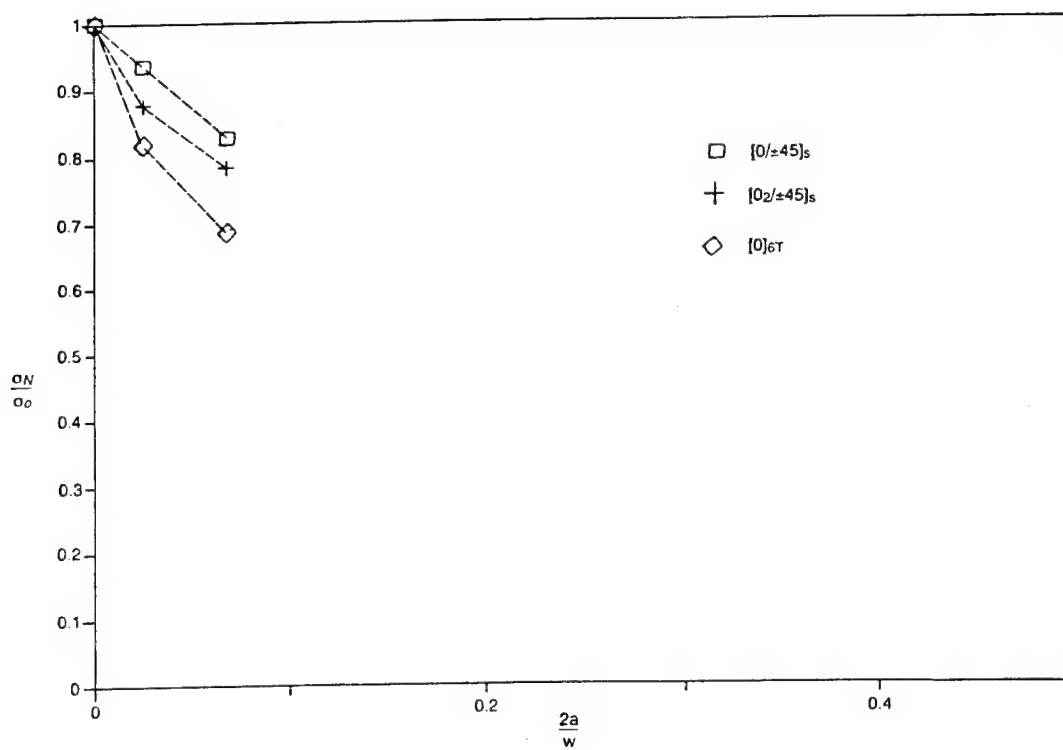


Figure 14. Notch Sensitivities For Various B/AI Laminate Orientations ( $w = 19.1\text{mm}$ ).

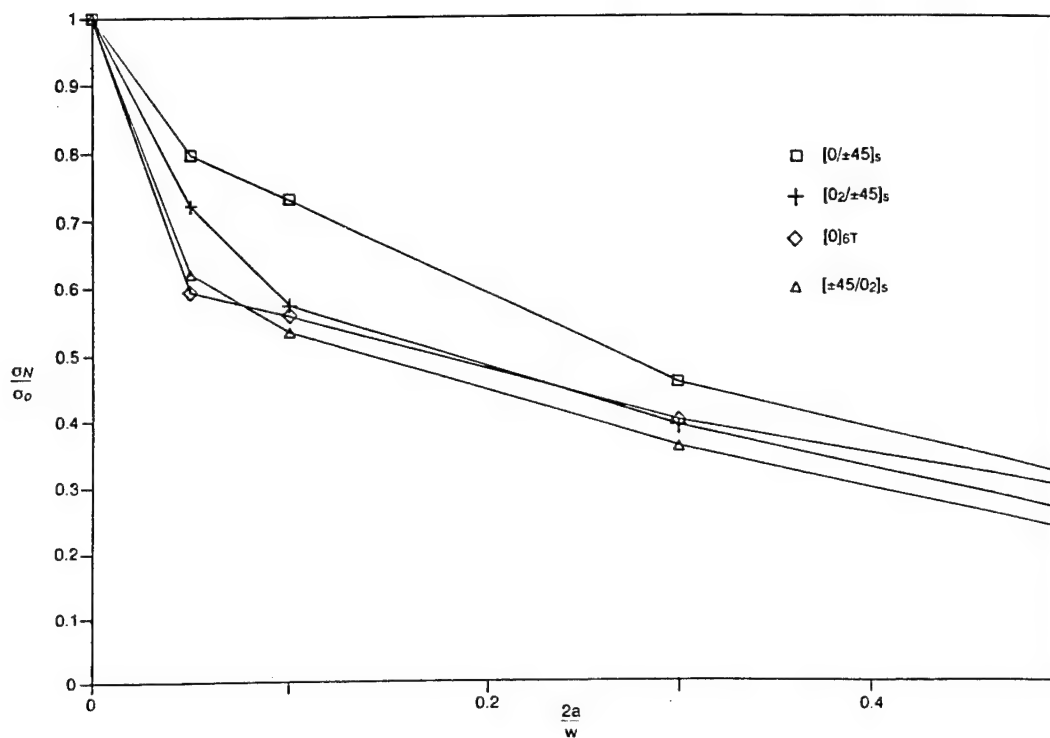


Figure 15. Notch Sensitivities For Various B/AI Laminate Orientations ( $w = 50.8\text{mm}$ ).

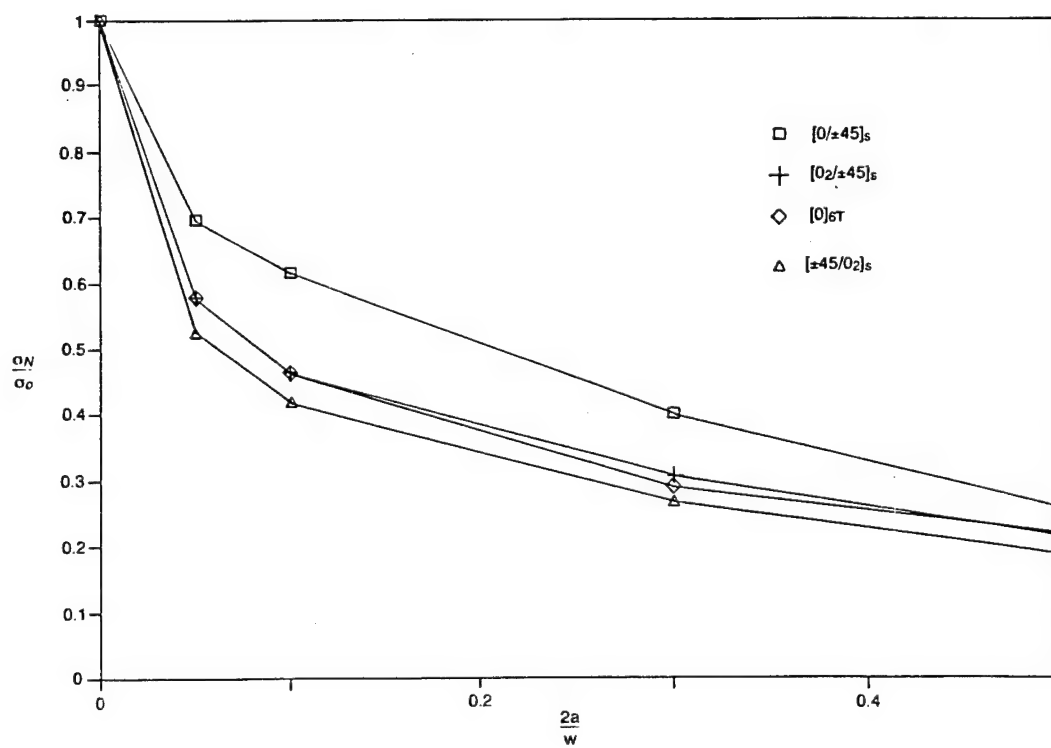


Figure 16. Notch Sensitivities For Various B/AI Laminate Orientations ( $w = 101.6\text{mm}$ ).



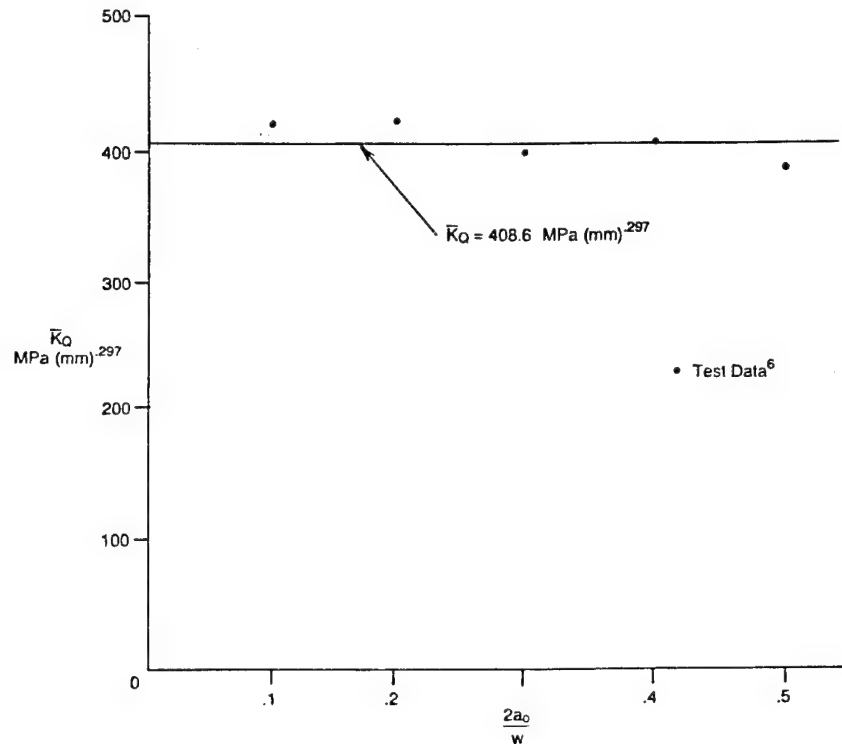


Figure 17.  $\bar{K}_Q$  For Gr/Ep With Ply Orientation  $[0/\pm 45]_{2s}$ .

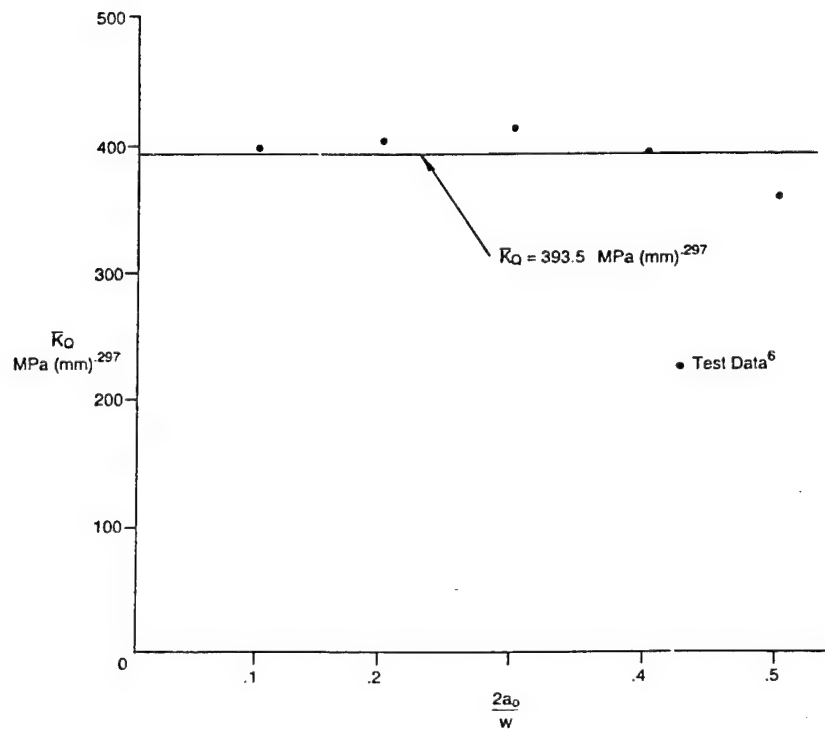


Figure 18.  $\bar{K}_Q$  for Gr/Gp With Ply Orientation  $[0/\pm 45]_s$ .

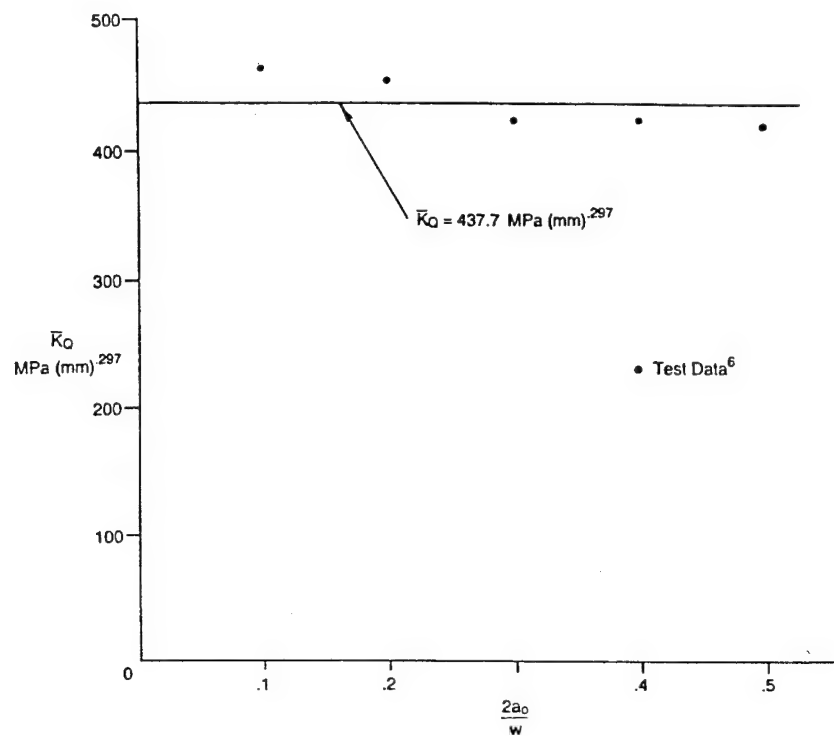


Figure 19.  $K_Q$  For Gr/Ep With Ply Orientation  $[0/90/\pm 45]_s$ .

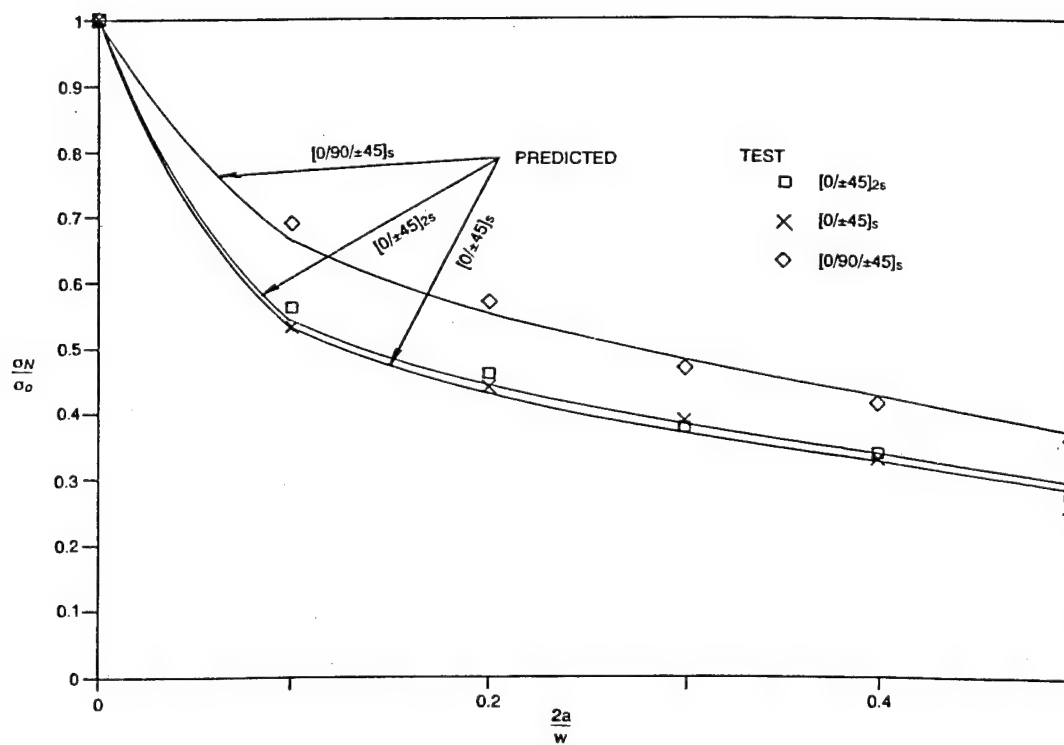


Figure 20. Notch Strength And Notch Sensitivities For Various Gr/Ep Laminate Orientations.

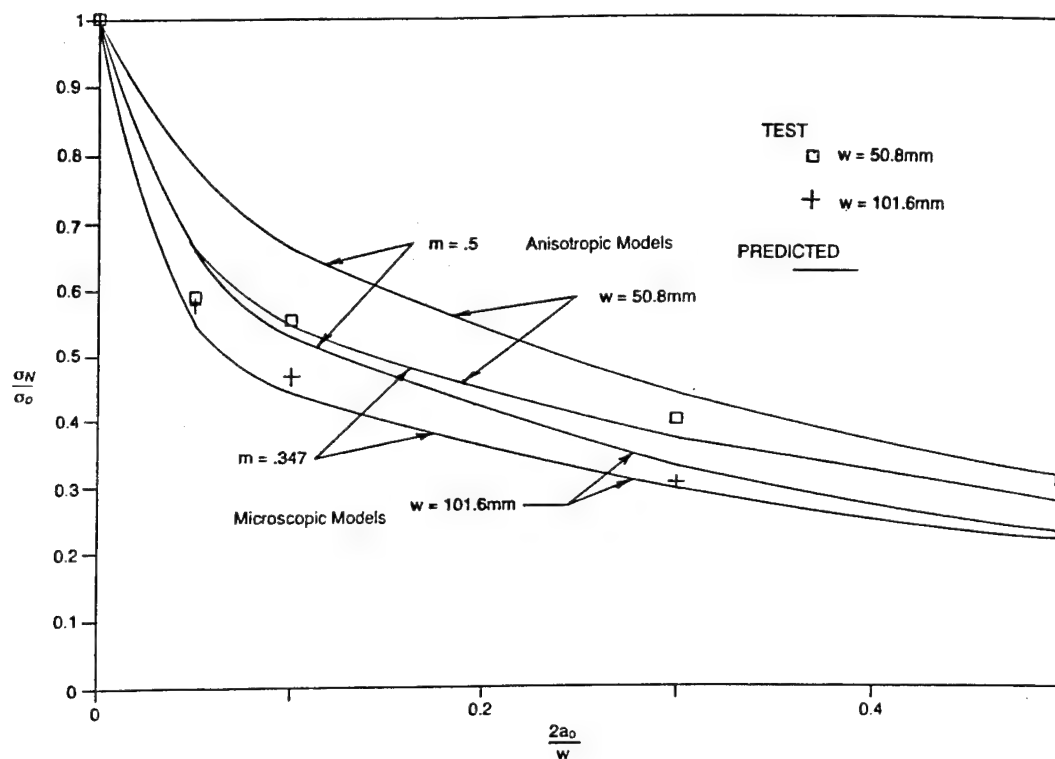


Figure 21. Comparison Of Analytical Results Between Anisotropic And New Approximate Models B/AI (0)6T

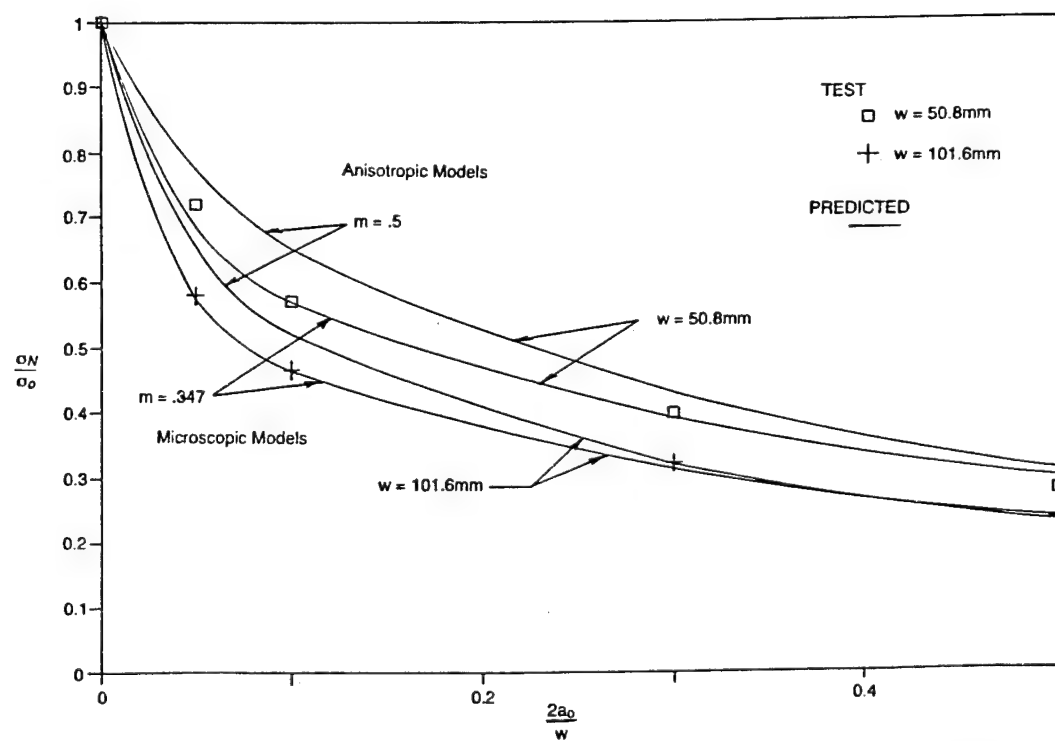


Figure 22. Comparison Of Analytical Results Between Anisotropic And New Approximate Models B/AI (02/±45)5

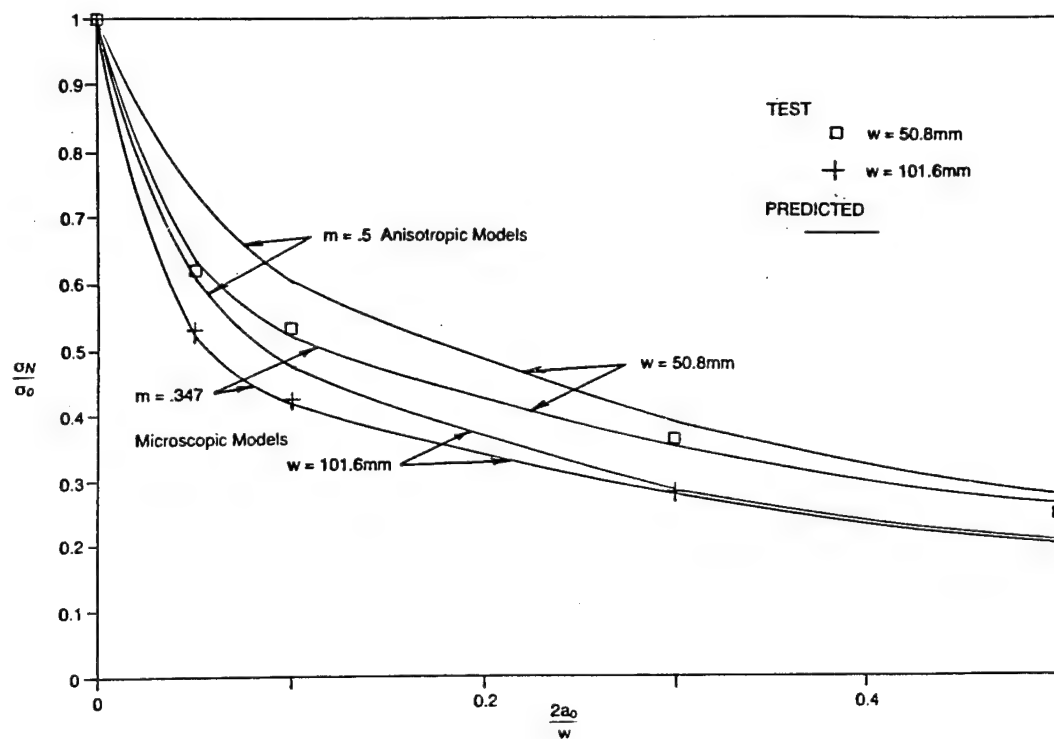


Figure 23. Comparison Of Analytical Results Between Anisotropic And New Approximate Models B/AI  $(\pm 45/0)_2$

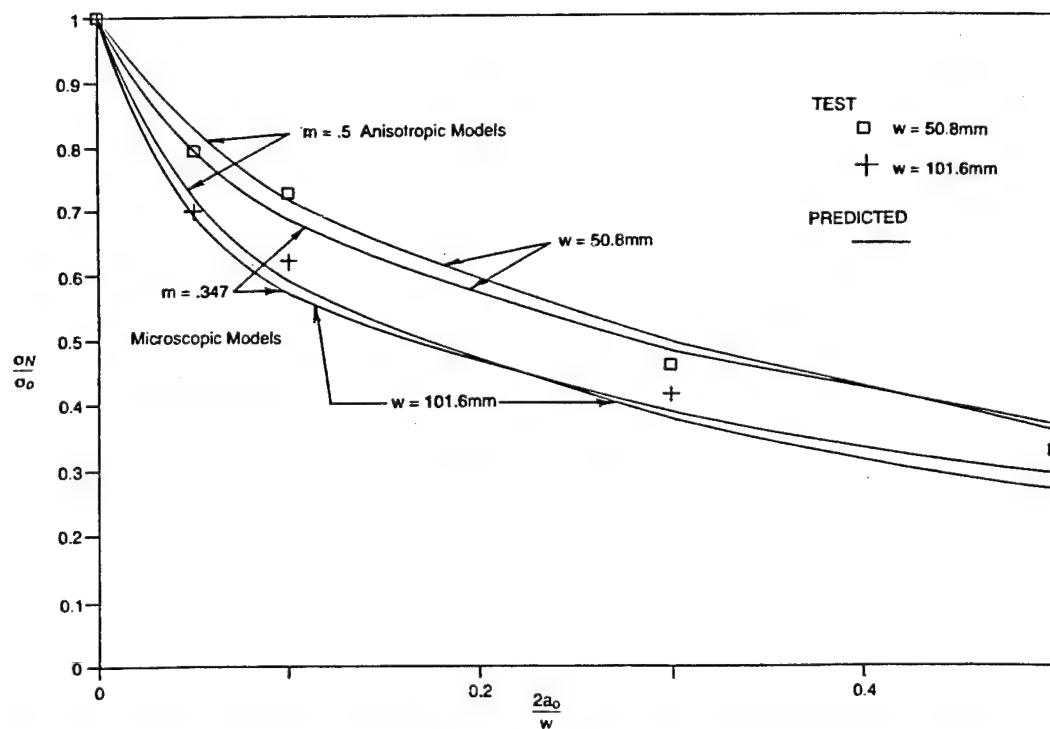


Figure 24. Comparison Of Analytical Results Between Anisotropic And New Approximate Models B/AI  $(0/\pm 45)_2$

# COMPUTATIONAL SIMULATION OF STRUCTURAL FRACTURE IN FIBER COMPOSITES

C. C. Chamis<sup>1</sup> and P. L. N. Murthy<sup>2</sup>

NASA Lewis Research Center

## ABSTRACT

A methodology has been developed for the computational simulation of structural fracture in fiber composites. This methodology consists of step-by-step procedures for mixed mode fracture in generic components and of an integrated computer code CODSTRAN (Composite Durability Structural Analysis). The generic types of composite structural fracture include: (1) single and combined mode fracture in beams, (2) laminate free-edge delamination fracture, and (3) laminate center flaw progressive fracture. Structural fracture is assessed in one or all of the following: (1) the displacements increase very rapidly, (2) the frequencies decrease very rapidly, (3) the buckling loads decrease very rapidly, or (4) the strain energy release rate increases very rapidly. These rapid changes are herein assumed to denote imminent structural fracture. Based on these rapid changes, parameters/guidelines are identified which can be used as criteria for (1) structural fracture, (2) inspection intervals, and (3) retirement for cause.

## INTRODUCTION

It is generally accepted that flawed structures fail when the flaws grow or coalesce to a critical dimension such that (1) the structure cannot safely perform as designed and qualified or ((2) catastrophic fracture is imminent. This is true for structures made from traditional homogeneous materials or fiber composites. The difference between fiber composites and traditional materials is that composites have multiple fracture modes that initiate local flaws compared to only a few for traditional materials. Any predictive approach to simulate structural fracture in fiber composites needs to formally quantify (1) these multiple fracture modes, (2) the types of flaws they initiate, and (3) the coalescing and propagation of these flaws to critical dimensions for imminent structure fracture.

One of the ongoing research activities at NASA Lewis Research Center is directed toward the development of a methodology for the "computational simulation of structural fracture in fiber composites." A part of this methodology consists of step-by-step procedures to simulate individual and mixed mode fracture in a variety of generic composite components. Another part has been incorporated into an integrated computer code identified as CODSTRAN for Composite Durability Structural Analysis. The objective of the proposed paper is to describe the fundamental aspects of this methodology and to illustrate its application to a variety of generic composite structures.

The generic types of composite structural fracture include (1) single and combined mode fracture in beams, (2) laminate free-edge delamination fracture, and (3) laminate center flaw progressive fracture. Structural fracture is assessed in one or all of the following: (1) the displacements increase very rapidly, (2) the frequencies decrease very rapidly, (3) the buckling loads decrease very rapidly, or (4) the strain energy release rate increases very rapidly. These rapid changes are herein assumed to denote imminent structural fracture. Based on these rapid changes, parameters/guidelines are identified which can be used as criteria for (1) structural fracture, (2) inspection intervals, and (3) retirement for cause.

<sup>1</sup>Senior Aerospace Scientist

<sup>2</sup>Aerospace Engineer

Both in the Structures Division

In the present study, computational simulation is defined in a specific way. Also general remarks are included with respect to (1) generalization of the procedure to large structures and/or structural systems, (2) lessons learned about conducting such a long duration research activity, and (3) research needs in order to increase its computational efficiency, gain confidence, and expedite its application.

#### COMPUTATIONAL SIMULATION-DEFINITION

During the course of this research activity computational simulation has evolved to have a specific means which is defined as follows:

"Description and quantification of the physics by progressive/multiple application of elementary math models, which are derivable from fundamental concepts, through the use of computers to obtain the desired structural response with acceptable engineering accuracy."

In the context of the above definition, computational simulation is not

1. Applied Mathematics
2. Approximate Analysis
3. Numerical Analysis
4. Numerical Testbed
5. Solution Algorithm

However, it may include some or all of the above, plus many others.

#### END-NOTCH BEAM FRACTURE

In this section we describe the application of the Structural Fracture concept to beams with end notches. Specifically, we describe Structural Fracture dominated by: (1) Mode I, (2) Mode II, (3) combined Modes I and II, and (4) combined Modes I, II, and III. The general procedure for the computational simulation of structural fracture for beams with these types of fracture modes are summarized in figure 1. This general procedure is complemented with progressive substructuring as was already mentioned and as will be described in some detail later for clarification purposes.

Mode I - A schematic depicting the strain-energy release rate (SERR) in a double cantilever is shown in figure 2. Two curves are shown in this figure: (1) the solid line for global is determined using the displacement under the loads, and (2) the local is determined by a crack closure technique. Structural Fracture is imminent when the crack length progresses to about 1.15 inch. This length is determined by the intercept of the tangent to the rapidly increasing portion of the SERR curve. The important observation is that the general concept is applicable to even this relatively simple structure.

Mode II - A schematic of the end-notches inducing Mode II and combined Modes I and II is shown in figure 3. Schematics of the finite element model and the local progressive substructuring are shown in figures 4 and 5 respectively. The details are described in reference 1. Typical results obtained for Mode II are shown in figure 6 where the measured range is also shown. The crack length for imminent structure fracture is about 1.18 inches based on the global SERR curve.

Three points are worth noting:

1. Mode II fracture exhibited some stable growth
2. The local approach predicts optimistic results relative to "critical" crack length but pessimistic results relative to the critical SERR magnitude.
3. The "critical" parameters (a and G) are within the measured range.

The important observation is that the computational simulation procedure captures the whole history of the process which leads to structural fracture induced by Mode II fracture.

Combined Modes I and II - Typical results for combined modes I and II fracture in end notch beams are shown in figure 7. Structural fracture is imminent when the crack length progresses to about 1.14 inches (global SERR curve). The local curve, again, predicts optimistic magnitudes for critical crack length but pessimistic magnitudes for the critical SERR.

The decomposition to Modes I and II is also shown. These curves were determined using the local closure technique (ref. 1). Interestingly, structural fracture for this condition is driven by Mode I. Also, the curves for Modes I and II resemble their respective independent parts in figures 2 and 6. Furthermore, superposition of Modes I and II appears to apply to the local mixed mode curve but not to the global curve. The important observation is that structural fracture in beams subjected to combined (mixed) modes I and II fracture can be computationally simulated and the respective "critical" parameters quantified.

Mixed Modes I, II, and III - The schematic used to computationally simulate structural fracture in beams subjected to mixed modes I, II, and III fracture is illustrated in figure 8. An enlargement of the regions modeled in the vicinity of the crack tip is shown in figure 9. The details are described in reference 2. Typical results of SERR versus crack length for various unsymmetric laminate angles are shown in figure 10. The important observation to be made is that the Mode III contribution to structural fracture is relatively insignificant compared to the other two. Also, use of the global SERR is inclusive of the individual modes as well as any influences of integrated structural effects. The influences of integrated structural effects are not easily or, even at all, captured by local crack-closure techniques.

Collectively the four different types of structural fracture described demonstrate that

1. Structural fracture can be computationally simulated with respect to
2. Its history from initiation to the onset of rapid (unstable) propagation described.
3. Its critical parameters (for imminent rapid propagation) quantified
4. The predominant fracture modes that drive it identified.

The very important point to be noted is that all of the above were obtained without resorting to any of the experiments that are usually required in traditional fracture mechanics.

#### LAMINATE FREE-EDGE DELAMINATION FRACTURE

In this section we summarize the application of the structural fracture to components subjected to free-edge delaminations. Specifically, we describe the following types of delaminations: center, pocket, and internal. Detailed descriptions on the simulation procedural steps are given in references 3 and 4. Also the effects of delamination on buckling will be briefly described. A schematic illustrating the origin of the interlaminar free edges that induce free-edge delamination is shown in figure 11. A typical simulation result is shown in figure 12 where the global strain energy release rate (SERR) is plotted versus percent area delaminated. Although the SERR initially rises very rapidly, it levels off by the 10 percent delamination and settles into a stable delamination growth up to 70 percent.

Center Delamination - A photograph of a C-scan of a laboratory specimen with edge delamination and a schematic of its corresponding one obtained by computational simulation are shown in figure 13. The corresponding SERR for three different composite systems is shown in figure 14. The behavior of all three curves in figure 14 is similar to that in figure 12 - early rapid rise followed by subsequent stable growth.



The observations to be made are (1) free edge delamination in the presence of in-plane loads is benign; (2) different materials can be readily evaluated with respect to their structural fracture resistance; and (3) substantial area may delaminate simultaneously with no change in the in-plane stress states.

Pocket Delaminations - These delaminations are believed to occur as follows: first, transply splits develop simultaneously at several places along the free edge; second, local delaminations develop in the vicinity of these splits due to high local stresses. These local delaminations are called, herein, pocket delaminations. Upon subsequent loading, these pocket delaminations merge to center delaminations.

Computational simulation results for these types of delaminations are shown in figure 15 for three different composite systems. The merging of pocket delaminations to center delamination is identified by the "jump" in the SERR curve followed by a rapid decrease and subsequent stable growth similar to that for center delamination in the previous section. The important observation is that computational simulation captures the progression of this complex delamination. The "jump" and subsequent "rapid decrease" can be used to guide strategic experiments to verify this sequence of events. They can also be used to interpret "stick-slip" type of progressive fracture prevalent in adhesively bonded joints.

Interior/Center Delamination - These types of delaminations may result from lack of bonding during fabrication; or they may occur as a result of inadvertent damage. Their growth to imminent structural fracture can be computationally simulated as the other types of delaminations. Results from these types of simulations for in-plane tensile stress are shown in figure 16. As can be seen, their influence is negligible until large areas (greater than 50 percent) have delaminated, whereupon the delaminations have reached the free edges. From here on, it behaves like a center-edge delamination.

The very important point to be noted is that internal delaminations are benign in-plane tensile stress fields.

Delamination Effects on Structural Response - The delamination effects on structural response can be computationally simulated as described in reference 4. Typical results for the effects of center-edge delamination on buckling load are shown in figure 17 for three different composite systems. The decrease in buckling load appears to be linear and is relatively small (about 20 percent for 7- percent delaminated area). The observation to be made is that local delaminations have negligible effect on buckling loads. Although results are now shown here, internal/-embedded delaminations have even less effect. The same observations hold for delamination effects on vibration frequencies.

#### CENTER-FLAW PROGRESS FRACTURE

Flaws in plate/shell type structures propagate to critical sizes for imminent structural fracture. Research activities on progressive composite fracture at Lewis during the last ten years have culminated in the development of the CODSTRAN computer code (ref. 1). CODSTRAN (Composite Durability Structural Analysis) has been specifically developed for the computational simulation of progressive fracture in fiber composites (refs. 5, 6, and 7). The modules comprising CODSTRAN are (1) the executive module, containing communication links to all other modules; (2) the I/O module; (3) the Analysis module; (4) The Composite Mechanics module; and (5) the Fracture Mechanics module.

A schematic showing the logic of the code, with an analysis model and typical results is shown in figure 18. The code tracks the damage growth flaw propagation up to structural fracture. Simulation of progressive fracture for different flaw types is shown in figure 18, and for different loading conditions in figure 19. The structural degradation in terms of vibration frequencies and buckling load is shown in figure 20. The collective results from figures 18 to 20 demonstrate that

progressive fracture in composites can be computationally simulated: (1) to any level of detail, (2) for any loading condition, and (3) for any structural response.

#### GENERAL REMARKS

Based on the continuing research effort described, some general remarks are appropriate. These remarks include (1) generalization, (2) lessons learned, and (3) research needs.

Generalization - The procedures described previously can be generalized for structural fracture in composites as follows:

1. Develop global structural/stress analysis model
2. Apply specified loading conditions
3. Identify hot spots for these loading conditions
4. Introduce flaws in the hot spots
5. With specified loads on the global model propagate flaws
6. Monitor structural performance degradation (displacement, buckling loads, frequencies) versus flaw propagation
7. Identify flaw size for unacceptable performance degradation level
8. Set qualification, inspection intervals, and retirement-for-cause criteria based on the simulated history of structural performance degradation versus flaw propagation.

Lessons Learned - The lessons learned during this rather extensive research effort are

1. Continuity in research activity
2. Participants' composite knowledge in
  - (i) Structural mechanics principles
  - (ii) Finite element analysis
  - (iii) Composite mechanics
  - (iv) Fracture mechanics concepts
3. Participants willing to question traditional approaches
4. Participants willing to adopt/invent new approaches
5. Continuing and unwavering management support
6. Availability of computer facilities and supporting personnel

Research Needs - Assuming the state-of-the-art on composite structural fracture is as described herein, the authors consider the following as near-future research needs:

1. Incorporation of uncertainties
2. Development of specialty: (1) finite elements, (2) boundary elements, (3) functions all of which include local details and capable of capturing steep gradients
3. Efficient self-adaptive global/multilocal scale methods
4. Time dependence
5. Formulation/programming for parallel processors
6. Adaptation to smart structures and health monitoring systems

#### CONCLUSIONS

Based on the results of the research on computational simulation for structural fracture in composite the following conclusions are made:

1. Computational simulation of structural fracture in composite structures is ready for extension to wide use applications
2. Reluctance to adopt it is natural because of
  - (i) Unfamiliarity
  - (ii) Attachment to traditional approaches

3. Reluctance can be overcome by
  - (i) Education
  - (ii) Using it first in parallel with traditional approaches
  - (iii) Make it a specification requirement by the procuring agencies

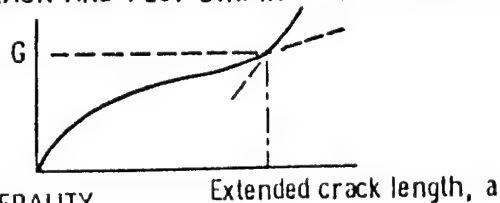
#### REFERENCES

1. Murthy, P. L. N. and Chamis, C. C.: Interlaminar Fracture Toughness: Three Dimensional Finite-Element Modeling of End-Notch and Mixed Mode Fracture. NASA TM 87138, 1985.
2. Murthy, P. L. N. and Chamis, C. C.: Composite Interlaminar Fracture Toughness: 3-D Finite Element Modeling of Mixed Mode I, II, and III Fracture. NASA TM 88872, 1986.
3. Murthy, P. L. N. and Chamis, C. C.: A Study of Interply Layer Effects on the Free Edge Stress Field of Angleplied Laminates. NASA TM 86924, 1984.
4. Wilt, T. E., Murthy, P. L. N., and Chamis, C. C.: Fracture Toughness Computational Simulation of General Delaminations in Fiber Composites. NASA TM 101415, 1988.
5. Chamis, C. C. and Smith, G. T.: CODSTRAN Composite Durability Structural Analysis. NASA TM 79070, 1978.
6. Chamis, C. C.: Computational Simulation of Progressive Fracture in Fiber Composites. NASA TM 87341, 1986.
7. Minnetyan, L., Murthy, P. L. N., and Chamis, C. C.: Structural Behavior of Composites with Progressive Fracture. NASA TM 102370, 1989.

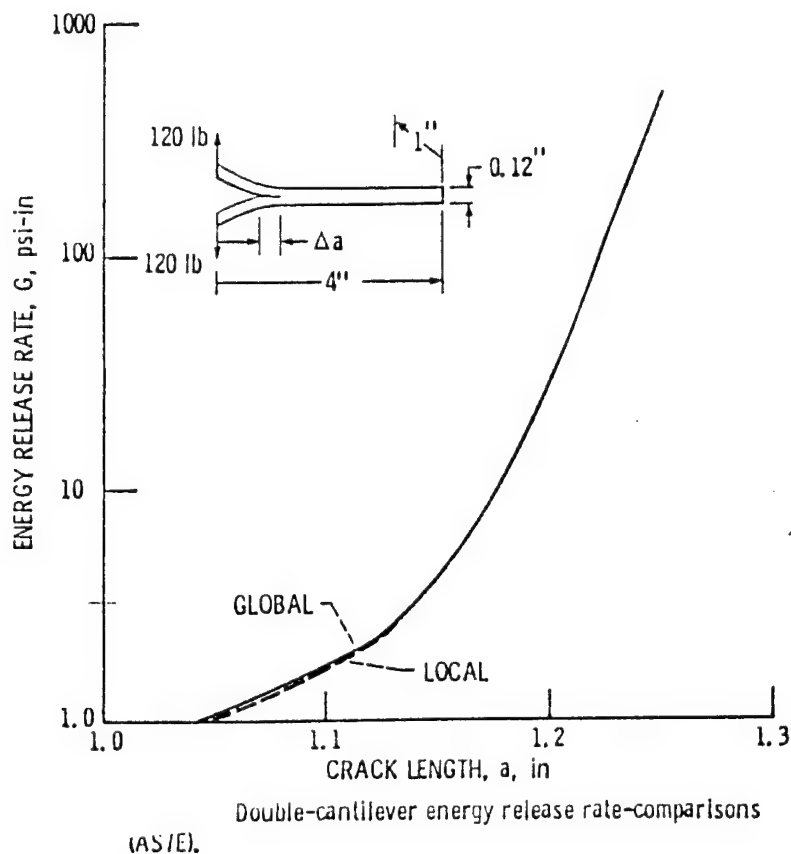
**FIGURE 1**

**GENERAL PROCEDURE FOR PREDICTING COMPOSITE  
FRACTURE TOUGHNESS**

- DETERMINE REQUISITE PROPERTIES AT DESIRED CONDITIONS USING COMPOSITE MICROMECHANICS
- RUN 3-D FINITE ELEMENT ANALYSIS FOR AN ARBITRARY LOAD
- SCALE LOAD TO MATCH INTERLAMINAR SHEAR STRESS AT ELEMENT NEXT TO CRACK-TIP
- WITH SCALED LOAD EXTEND CRACK AND PLOT STRAIN ENERGY RELEASE RATE VS CRACK LENGTH
- SELECT CRITICAL "G" }  
AND CRITICAL "a" } →
- METHOD HAS VERSATILITY/GENERALITY

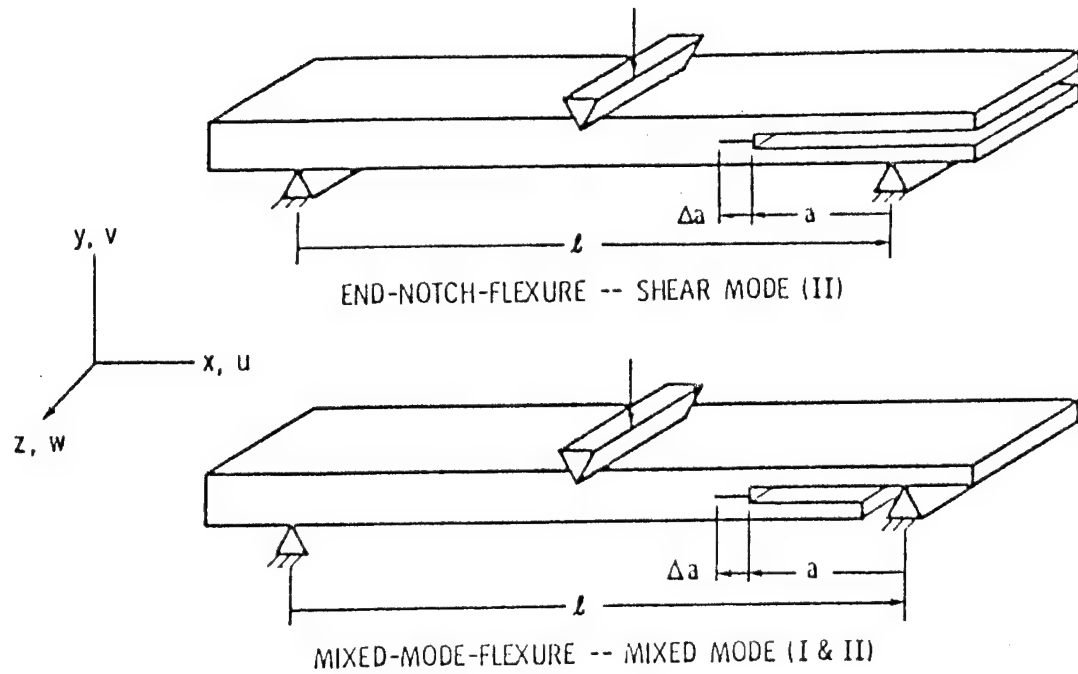


**FIGURE 2**



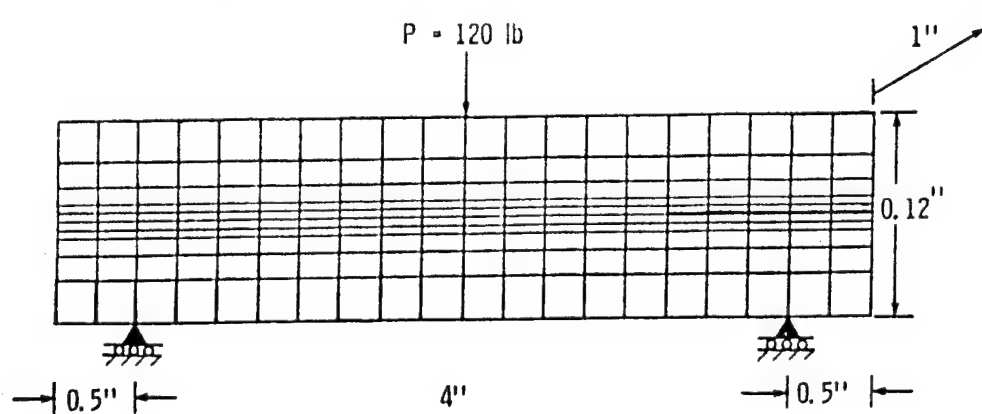
**FIGURE 3**

**SCHEMATIC OF FLEXURAL TEST FOR INTERLAMINAR  
FRACTURE MODE TOUGHNESS**



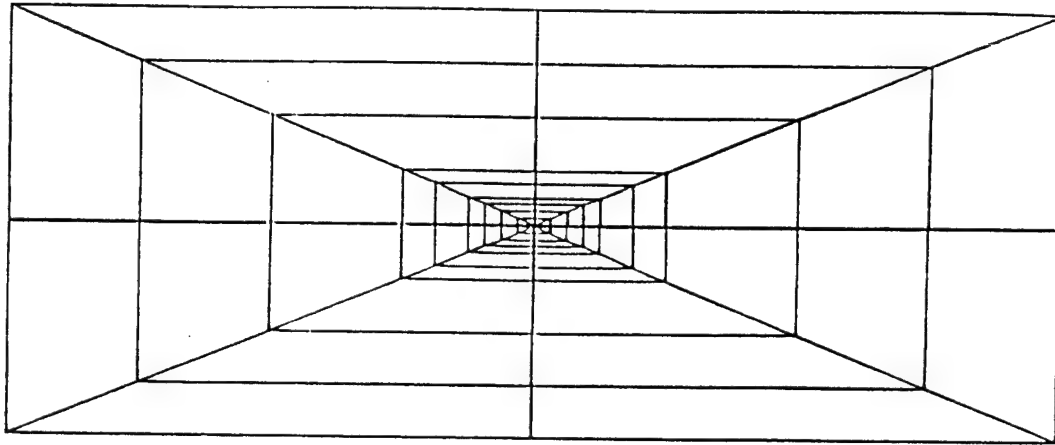
**FIGURE 4**

**MODEL GEOMETRY AND F.E. SCHEMATIC**



**FIGURE 5**

**CRACK REGION SUPER ELEMENT MODEL DETAILS-FRONT VIEW**

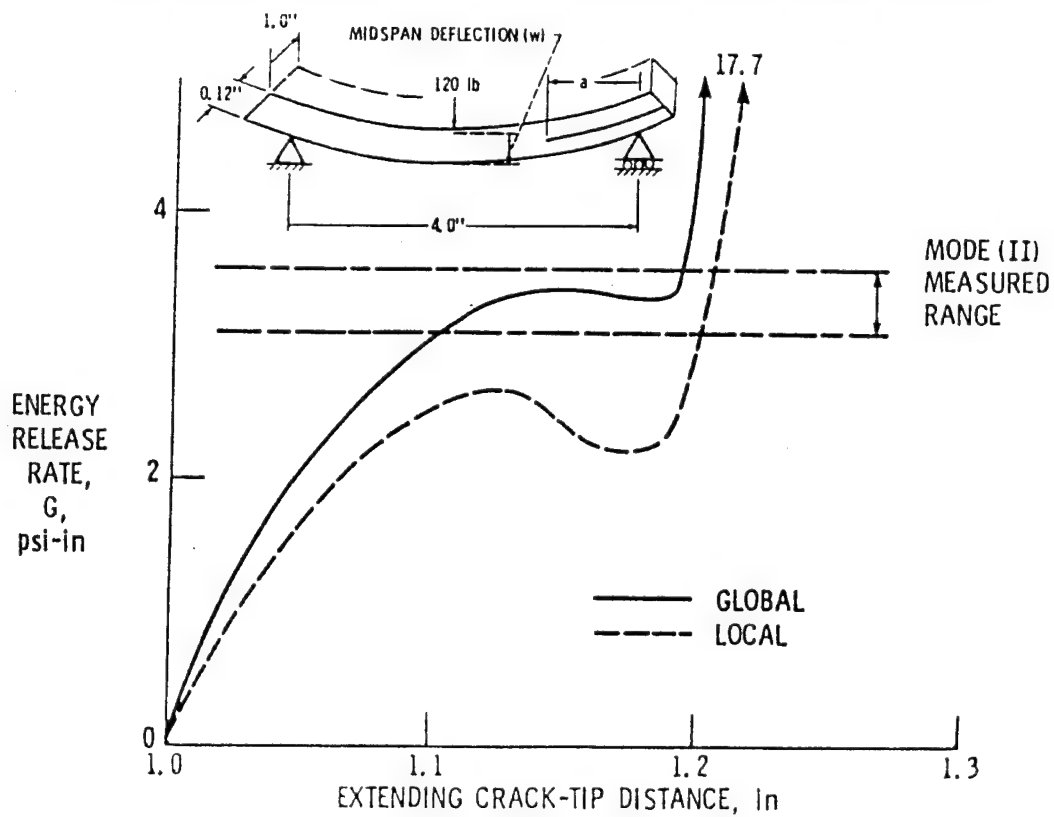


- 360 BRICKS
- 32 6-NODE PENTAHEDRONS
- 328 8-NODE HEXAHEDRONS

CD-86-19252

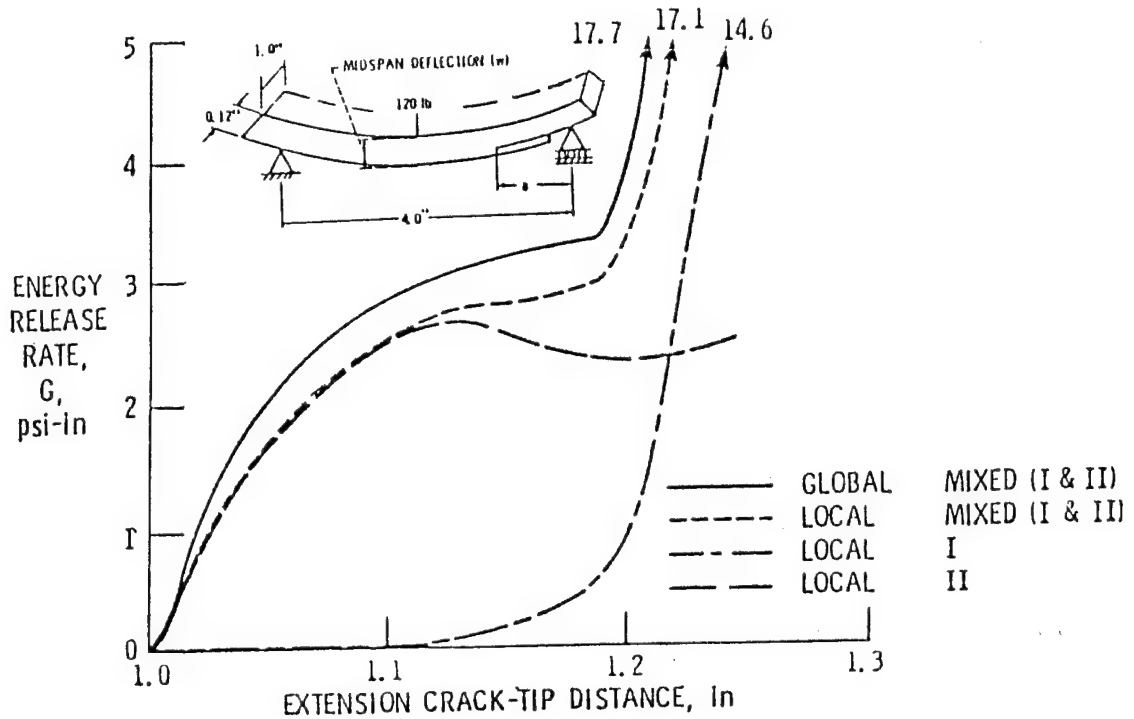
**FIGURE 6**

**END-NOTCH-FLEXURE ENERGY RELEASE RATE-COMPARISONS**



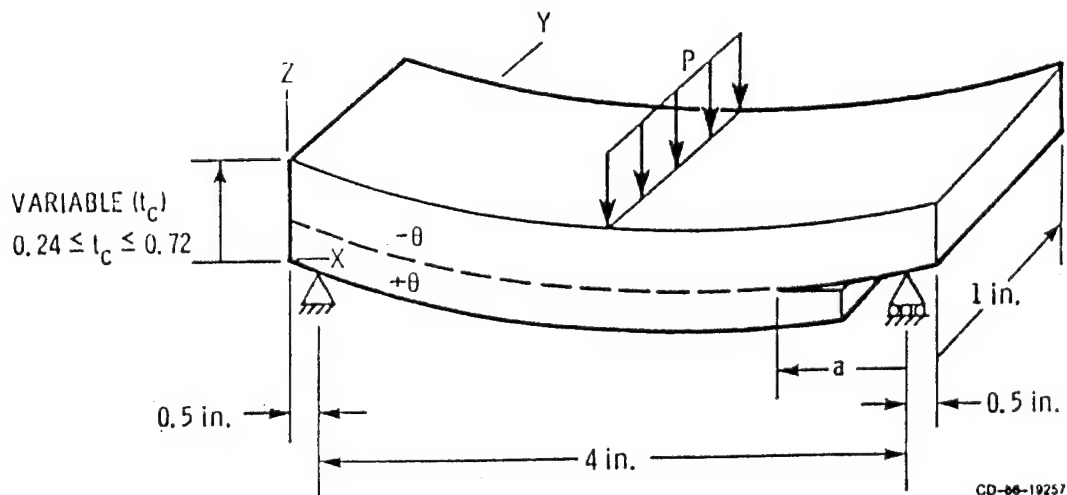
**FIGURE 7**

**MIXED-MODE-FLEXURE ENERGY RELEASE RATE AND COMPONENTS (AS/E)  
SINGLE POINT CONSTRAINED (LEWIS) METHOD**



**FIGURE 8**

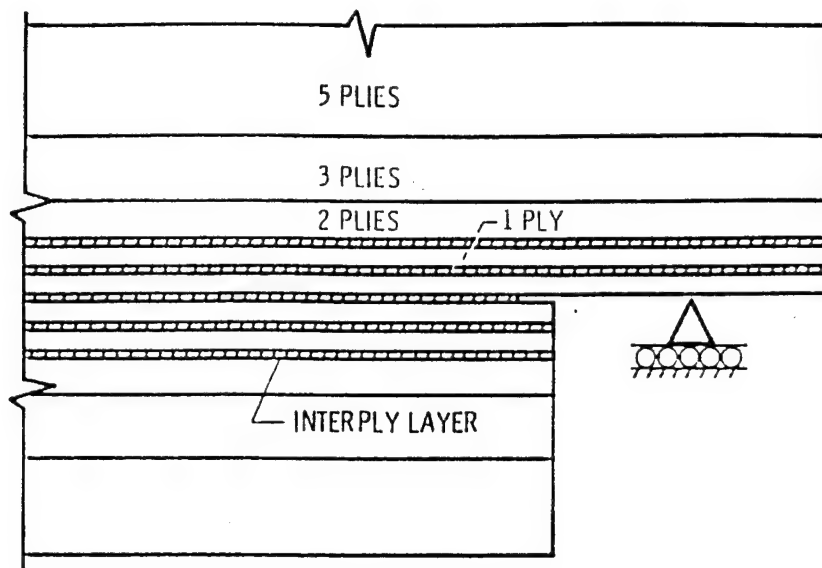
**LAMINATE GEOMETRY AND LOADING**





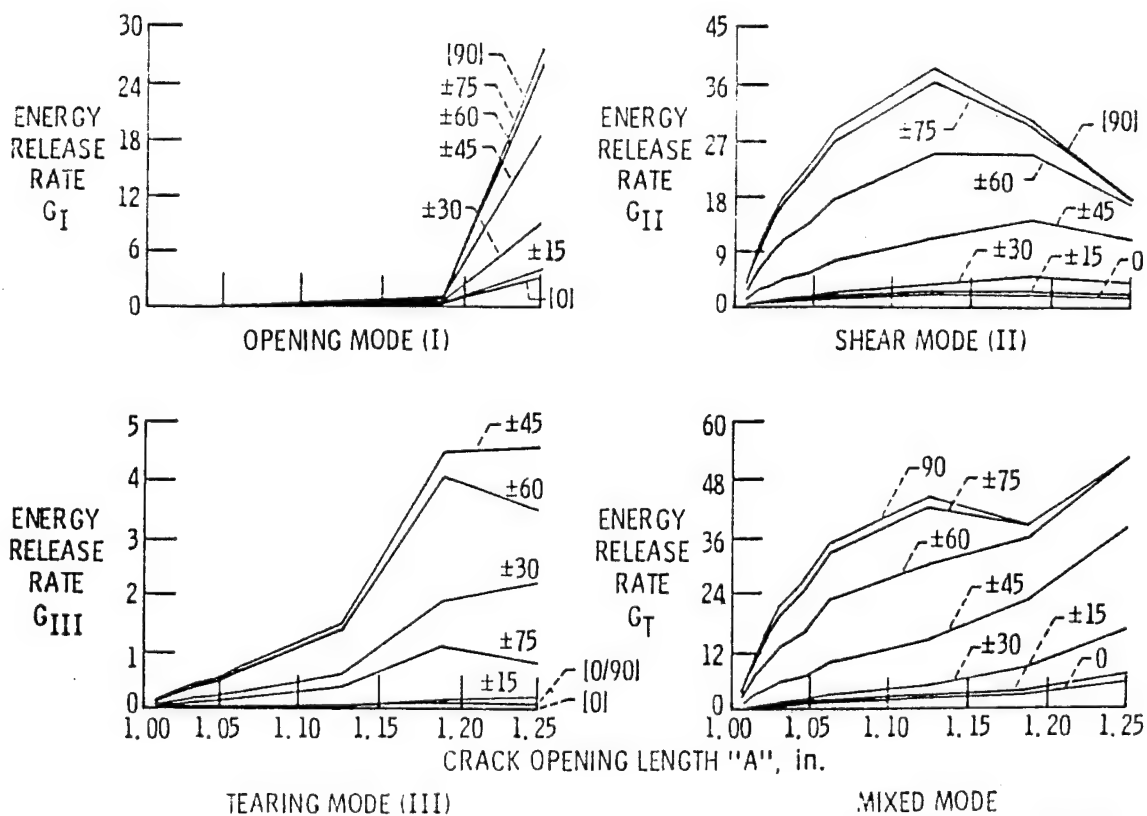
**FIGURE 9**

SCHEMATIC OF F.E. MODEL THROUGH-THE-THICKNESS DETAILS



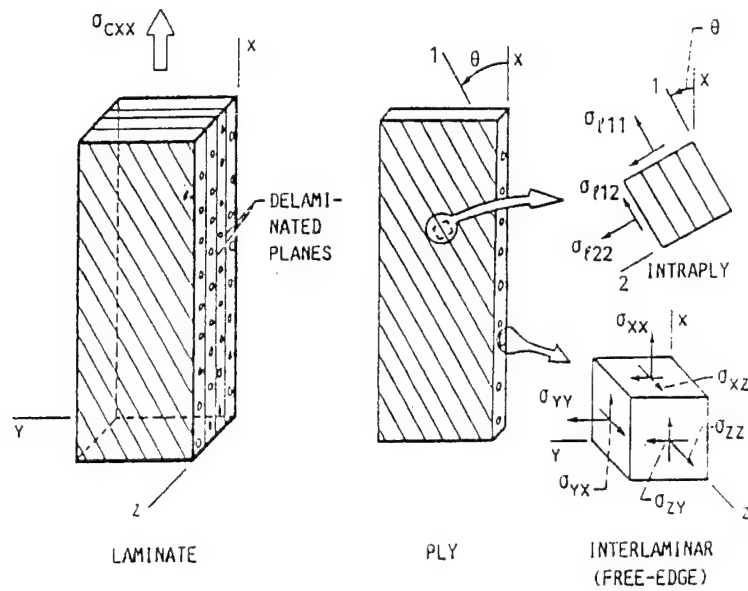
**FIGURE 10**

EFFECTS OF CRACK LENGTH AND PLY ORIENTATION ON STRAIN ENERGY RELEASE RATES (in.-lb/in.<sup>2</sup>) [ $-\theta_{36}/+\theta_{12}$ ]



**FIGURE 11**

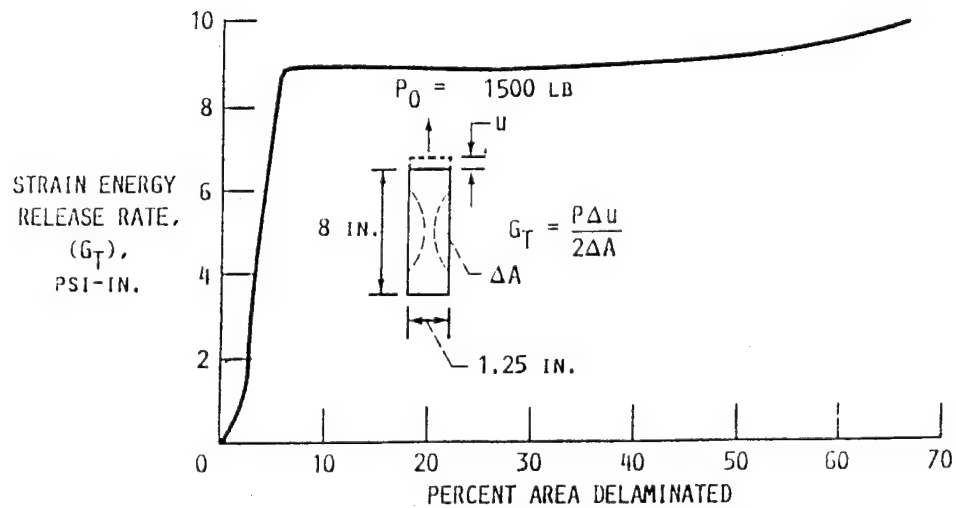
LAMINATION DECOMPOSITION FOR FREE-EDGE INTERLAMINAR STRESSES



**FIGURE 12**

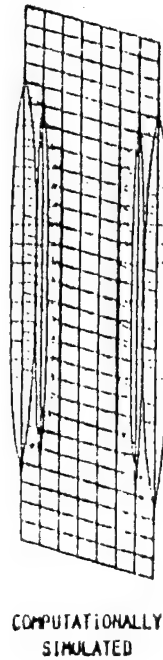
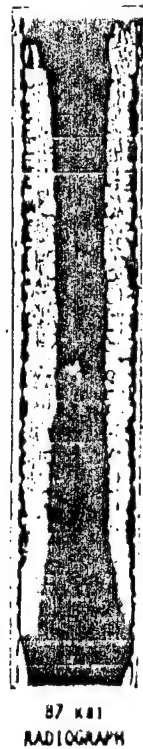
STRAIN ENERGY RELEASE RATE FOR A "TYPICAL" LAB SPECIMEN

(AS/E  $[\pm 30/90]_S$  0.6 FVR COMPOSITE)



**FIGURE 13**

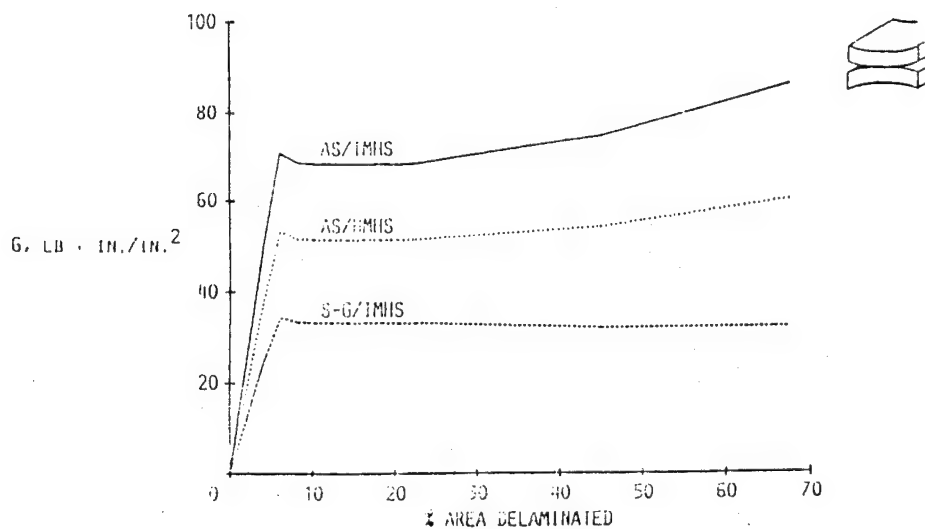
FREE-EDGE PROGRESSIVE DELAMINATION CAN  
BE COMPUTATIONALLY SIMULATED



60-87-20079

**FIGURE 14**

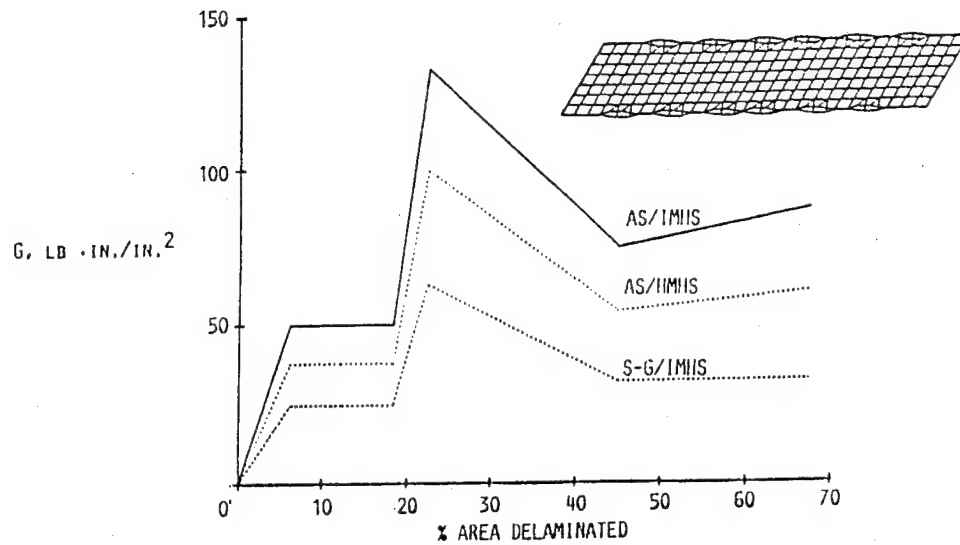
STRAIN ENERGY RELEASE RATE  
5-PLY CENTER DELAMINATION



**FIGURE 15**

**STRAIN ENERGY RELEASE RATE**

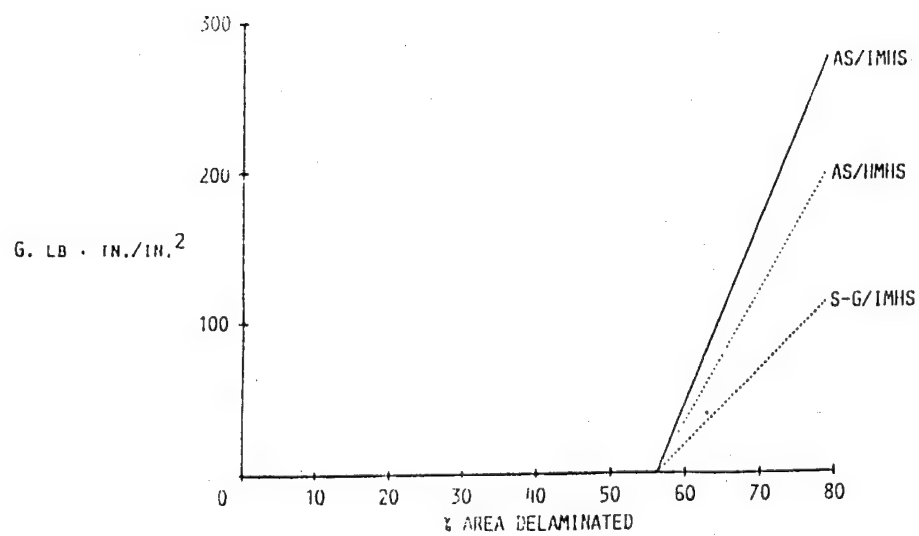
6-PLY CENTER/POCKET DELAMINATION



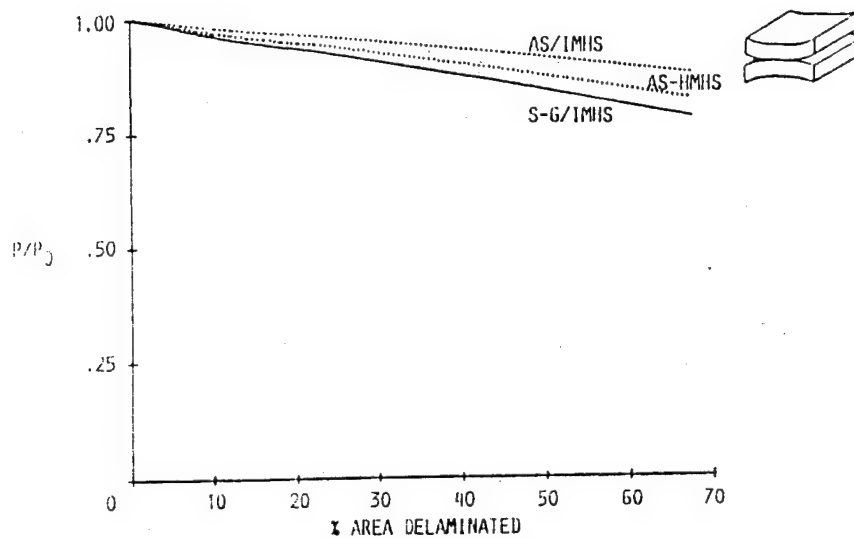
**FIGURE 16**

**STRAIN ENERGY RELEASE RATE**

6-PLY INTERIOR/CENTER DELAMINATION

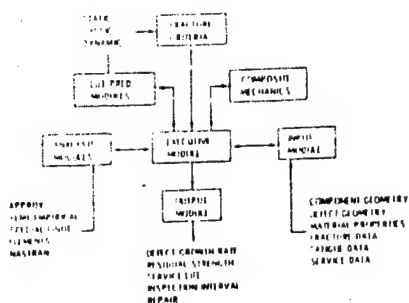


**FIGURE 17**  
**BUCKLING LOAD**  
 6-PLY CENTER DELAMINATION



**FIGURE 18**

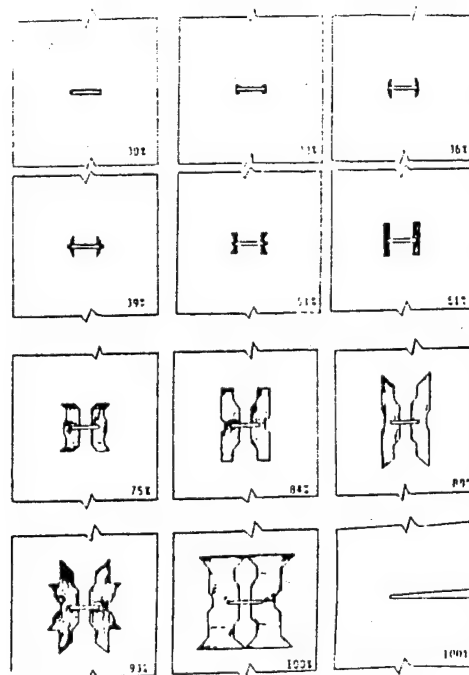
COMPUTATIONAL SIMULATION OF PROGRESSIVE FRACTURE IN FIBER COMPOSITES



CODSTRAN

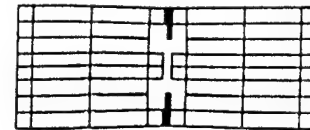
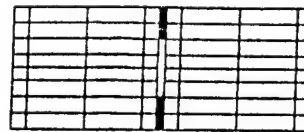
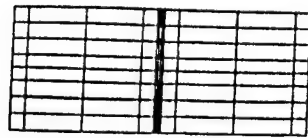


FINITE ELEMENT MODEL OF A



PROGRESSIVE FRACTURE AT VARIOUS PERCENTAGES  
 OF FRACTURE LOAD

**FIGURE 19**  
**PROGRESSIVE FRACTURE FOR INDIVIDUAL**  
**AND COMBINED LOADING**



80% MAX. LOAD

99% MAX. LOAD

**AXIAL TENSION**



67.5% MAX. LOAD

100% MAX. LOAD

**IN-PLANE SHEAR/BENDING**



89% MAX. LOAD

100% MAX. LOAD

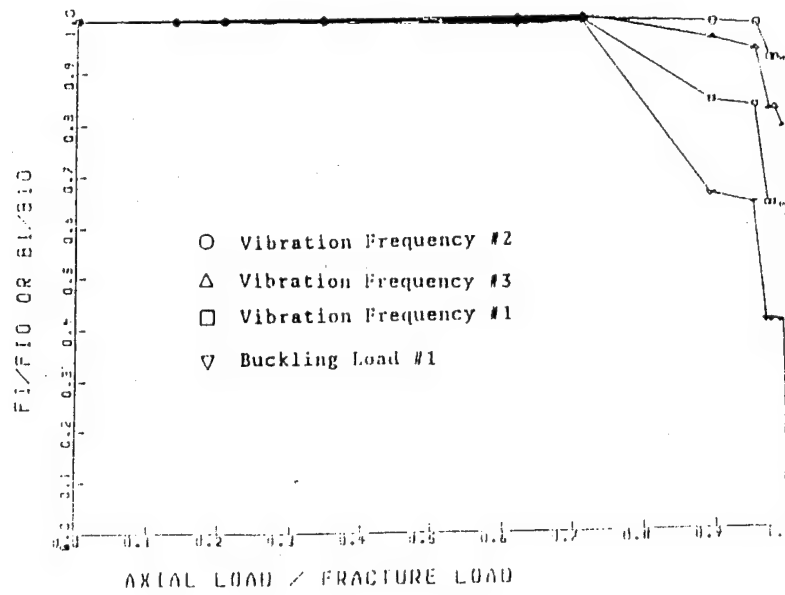
**COMBINED AXIAL TENSION WITH IN-PLANE SHEAR**

**FIGURE 20**

THE EFFECT OF STRUCTURAL DEGRADATION ON  
NATURAL FREQUENCIES AND BUCKLING LOAD

COMPOSITE: T-300/EPOXY

(SUPPORT COND. 1 - EDGES PARALLEL TO LOADING FREE)





# SCALING OF FIBER COMPOSITE STRUCTURES

Todd M. Wieland\* and John Morton\*\*  
Engineering Science and Mechanics Department  
Virginia Polytechnic Institute and State University  
Blacksburg, Virginia

## ABSTRACT

Structural scaling is being investigated using graphite/epoxy Z-section stiffeners loaded in compression. Sections of various web, flange and web-to-flange corner radii dimensions are being considered. Initial local buckling loads and modes have been determined analytically, numerically and by experiment. A normalizing parameter has been developed for initial buckling data. Postbuckling behavior has been evaluated numerically and experimentally. The nature of the load redistribution following buckling is a key factor in relating the response of the various section sizes. Additional experiments and the development of scaling parameters for postbuckling and crippling are underway.

\* Graduate student

\*\* Professor

## 1. INTRODUCTION

Much progress has been made in the fabrication and introduction of advanced composite components in primary aircraft structures. This has involved the production of costly prototypes and large scale experimental verification of certain design concepts. The development of scaling parameters for specific modes of the structural response of composite components would greatly streamline this procedure, and allow significant cost savings by permitting simplified small scale experimental programs to be performed.

General scaling laws for structural composites are not available. Principles of similitude offer general guidelines, and have been applied to composites [1] for impact response. These principles of similitude lead to the conclusion that compromises are required and that progress can be made by developing scaling laws and parameters appropriate to a specific problem.

The present study takes a graphite/epoxy composite Z-section stiffener as a representative structural member and investigates the effects of varying the relative and absolute values of the various geometric parameters upon the initial buckling, postbuckling and crippling behavior.

## 2. THEORETICAL CONSIDERATIONS

One approach to the scaling problem is simply to derive appropriate governing equations in nondimensional form. This provides, directly, nondimensional groups or parameters for design and testing for the presence of size or scaling effects. Individual terms in the nondimensional groups can be varied in any way provided the nondimensional group itself remains unchanged in value, and the same response will be obtained. This, of course, requires the analytical model to be complete.

For a composite Z-section stiffener subjected to axial loading an analysis is available for the case of sharp or zero radius corners. This is based on a classical model of local buckling of plate elements due to Bulson [2]. This was further extended by Lee [3] to include the case of sections comprised of single layer orthotropic plates. The governing equation for such a plate element may be written as

$$D_{11} \frac{\partial^4 w}{\partial x^4} + 2(D_{12} + 2D_{66}) \frac{\partial^4 w}{\partial x^2 \partial y^2} + D_{22} \frac{\partial^4 w}{\partial y^4} + P \frac{\partial^2 w}{\partial x^2} = 0,$$

where  $D_{ij}$  ( $i, j = 1, 2, 6$ ) are the orthotropic plate bending stiffnesses,  $w$  is the out-of-plane deflection,  $x$  and  $y$  are in-plane coordinates, and  $P$  is the axial load per unit of width. The

usual method of determining the buckling load consists of assuming a displacement function representing the buckled form:

$$w = f(y) \sin \frac{m\pi x}{a}, \text{ where } a \text{ is the plate length.}$$

This function is substituted into the governing equation to obtain a fourth order ordinary differential equation for  $w$  in terms of  $y$ . For a section consisting of connected plates the differential equation is solved to form expressions for the end restraining moment in terms of the rotation. Equilibrium and compatibility conditions are applied at plate junctions to obtain for the Z-section, for example,

$$\left[ \frac{F(\text{SS-symmetric})}{F(\text{clamped-symmetric})} \right]_{\text{web}} + \frac{B_w}{B_f} \left[ \frac{F(\text{SS-free})}{F(\text{clamped-free})} \right]_{\text{flange}} = 0, \text{ where}$$

each function  $F$  is the 'characteristic equation' for a plate element under the indicated boundary conditions on the longitudinal edges, SS refers to a simply-supported boundary, symmetric refers to the plate edge being in a plane of symmetry, and  $B_f$  and  $B_w$  refer to the flange and web widths, respectively. Each characteristic equation represents the expanded determinant of the coefficient matrix formed by application of the indicated boundary conditions to the general expression for the out-of-plane deflection.

For the present work, it is necessary to modify the above solution by removing the condition  $D_{12} = \nu_{12}D_{22}$ , which was used by Lee. This equality is not generally valid for the case of multi-layered composites. The result of the current analysis is the local buckling stress resultant  $N_x$  for the composite Z-section, and the nondimensional group

$$\frac{N_x B_w^2}{\sqrt{D_{11} D_{22}}}.$$

This analysis is restricted to the case of zero corner radius, as noted above, and also neglects the effect of  $D_{16}$  and  $D_{26}$ , since these terms represent coefficients of odd derivatives of  $w$  which would preclude use of the assumed separable form of the deflection function. Also this solution is applicable only to initial buckling.

For a more general treatment of the case of practical composite sections a numerical treatment is needed. The ABAQUS finite element code has the general capability of handling buckling and postbuckling of composite structures. This code was used to refine the analysis model to account for the presence of the finite corner radius, which represents

a key variable in this work and to extend the analysis through the postbuckling regime until crippling.

The finite element analysis was based on the following material properties, which are typical of the AS4/3502 graphite/epoxy system:

$$E_{11} = 18.5 \text{ Msi}, E_{22} = 1.64 \text{ Msi}, G_{12} = 0.87 \text{ Msi}, \nu_{12} = 0.30 .$$

Nine-node shell elements with 5 to 6 degrees of freedom per node were used to define the model. A typical mesh which contains 160 elements is shown in Figure [1]. The case of zero corner radius was also modelled to allow comparison with the analytical solution.

The first phase of the finite element calculations provided buckling loads and corresponding modes. For postbuckling studies, the perfectly flat elements of the model were perturbed by the addition of buckling displacements corresponding to the first two modes, normalized such that the maximum buckling displacement was one tenth of the laminate thickness. The postbuckling analyses were carried out until the largest local strain exceeded one percent.

### 3. EXPERIMENTAL PROGRAM

The analytical and numerical studies were used to define an experimental program aimed at determining the relative importance of the flange-to-web and corner radius-to-flange or web width ratios relative to initial buckling, postbuckling and crippling behavior of the composite Z-sections.

Previous studies [4,5] used AS4/3502 graphite/epoxy Z-sections with the stacking sequence  $[+45/-45/0/90]_s$ , a web size of 1.25 in., flanges of 1.25 and 0.75 in. and corner radii of 0.125 and 0.25 in. These studies provided material around which the current program was designed. Table 1 summarizes the geometries chosen for this study. These consist of the core program based on a web of 1.25 in., with flanges varying from 0.50 to 1.25 in. and corner radii of 0.125 and 0.25 in., (see Figure [2] for the convention used to define these dimensions), and various sections based on web sizes of 1.75 and 0.75 in. Currently, experimental results are available only from the core program. Note that the lengths were chosen to ensure that local rather than global buckling would occur.

The ends of the cut sections were potted in filled epoxy within steel rings to prevent end brooming and to promote uniform load introduction. The potted ends were machined flat and parallel in preparation for loading in compression between the platens of a 60,000 lb Tinius-Olsen Testing Machine.

Electric resistance strain gages were placed at the numerically predicted wave crest positions at flange, web and corner locations, front and back. These gages allowed investigation of the load redistribution when one of more of these elements buckled. A

typical strain gage pattern is shown in Figure [3]. Displacement transducers were applied to monitor the end shortening and out-of-plane displacement. Typically seven such transducers were used. Shadow moire was also employed on one flange. Shadow moire is an optical technique which yields contour maps of out-of-plane displacement. These fringe patterns provided a convenient means of detecting the onset of flange buckling and identifying the modes, which were observed to change in some cases during postbuckling. Still photography and video recording were also used during specimen testing. Specimens were loaded at a rate of 1200 lbs per minute under machine control until buckling, and thereafter at a manually controlled rate of approximately 500 lbs per minute until final failure.

#### 4. EXPERIMENTAL RESULTS

The instrumented buckling experiments produced a large amount of data with which to determine the initial buckling loads and to follow the load redistribution through postbuckling until failure. Load-end shortening curves are readily obtained in the experiment. Such curves, normalized with respect to nominal cross-sectional area and equivalent longitudinal elastic modulus, are shown in Figure [4] for a range of flange sizes and a corner radius of 0.125 in. These data fall on a single line at low loads, representing a common prebuckling axial stiffness. Departure from this straight line is indicative of the onset of buckling. It is observed that the larger the flange size, the lower the normalized buckling load and the greater the postbuckling regime. Note that the curves are terminated at the maximum experimental loads.

The strain gages allowed point by point measurements at locations which were predicted to correspond to crests in the waves of the buckled shape based on the numerical calculations. The back-to-back arrangement provided a means for determining membrane and bending components of strain at given points. Generally, the strain gages indicated the presence of bending at loads which were well below the local buckling loads estimated from Figure [4], and from the shadow moire observations. Therefore, instead of being used as a primary means of determining when buckling occurred, the strain gages were more useful for following the load redistribution as the flanges and web buckled, thereby shedding load onto the corner regions. Figures [5a,b] show typical membrane and bending components of strain as a function of flange size across a developed cross-section at loads of 1.2 times buckling, and 0.98 times the ultimate load, respectively. Figure [6] presents a similar membrane and bending strain distribution illustrating the effect of corner radius at a load of 1.2 times the buckling load. Note that the lines connecting the point-wise data are provided only for clarity.

## 5. DISCUSSION

### 5.1 Initial Buckling

A comparison of the local buckling loads is presented in Table 2. This table includes values determined from the analytical model which did not include the finite corner radius, experimental values from load-end shortening data and shadow moire, and linear and nonlinear finite element models. General agreement between all estimates of initial buckling is good. The maximum error of any estimate compared to experimental values from load-end shortening data is 12 percent, with typical values being 5 to 10 percent. Even the analytical solution provides good approximations to the experiments on finite corner radius sections. The analytical solution and the finite element model with a zero corner radius agree to within 4 percent. The results are grouped by corner radius. The numerical models agree more closely with the analytical solution as the corner radius decreases, as is to be expected. The buckling loads estimated by the nonlinear finite element analyses are lower than those from the linear analyses and are generally in better agreement with experimental data. Predictions of buckling from the shadow moire can be made only to within about 50 lbs, but within these limitations, reasonable agreement with observed buckling loads is apparent.

The analytical approach provided a normalizing parameter which can be used to present all the buckling data on a single curve. Experimental results to data are plotted in Figure [7], which can then be used to predict buckling loads for the other section geometries in the program. The experimental data on both radii straddle the analytical curve for zero corner radius. As the relative flange size decreases, the effect of the corner radius becomes more pronounced. Departure from a single curve for a fixed radius suggests the presence of scale effects and/or inadequacies in the modelling of the mechanics.

The buckling modes observed in the experiments (as defined by the number of half-waves) were generally the same as in the numerical models. One exception was observed, whereby one specimen of an identical pair adopted mode 2, while the other adopted mode 1. In general, the buckling loads for modes 1 and 2 estimated by the numerical analyses were very close.

### 5.2 Postbuckling

The load-end shortening curves provide a convenient means for comparing experimental and numerical results. Typical comparisons are presented in Figures [8a,b] for the smallest and largest flange sizes, respectively. Figure [8a] shows that the large flange causes buckling at low loads. A well defined buckling load is followed by

extensive, highly nonlinear postbuckling behavior. The finite element results based on the assumed material property data show a higher initial (prebuckling) stiffness compared to experiment by about 5 percent. Departures in the postbuckling region were more significant and reached about 15 percent at failure, which occurred at about 4 times the buckling load. Figure [8b] shows that the smallest flange produced a high buckling load (about 2.5 times that of the largest flange), but has a relatively short, almost linear postbuckling region. Again the initial stiffness of the finite element model is about 5 percent greater than the experimentally observed values. The finite element model overestimates the load at crippling by about 10 percent, compared to the experiment. Rather than mesh refinement, it is thought that major improvements to the numerical model (e.g. shear deformable elements, and/or permitting different material properties in tension versus compression) might be needed to obtain better agreement in the postbuckling region.

The finite element model also provides strain data which can be compared to those from the experiments. These strain data were used to follow the load redistribution during postbuckling. A typical comparison is shown in Figures [9a,b] for a load just below failure. The figures, which show distributions of membrane and bending components of strain across the section, indicate good agreement between the experiment and the numerical model even for loads within 2 percent of failure.

Figures [5a,b] illustrate the role of flange size in the severity and rate of load redistribution during postbuckling. At a load 20 percent above buckling, Figure [5a] shows that concentration of strain into the corner regions occurs much more rapidly as the flange size is decreased. The load-end shortening data, Figure [4], show that the postbuckled stiffness is decreased as the flange size is reduced. This results from the higher load at buckling for the case of smaller flanges producing a greater bending moment after buckling. The result of this decreased stiffness is a more rapid concentration of strain into the corner regions. Note from Figure [5b] that the section having the larger flange ultimately reaches higher strain levels in the corner, although this concentration occurs more slowly. Figure [6] presents limited data concerning the effect of corner radius on this load redistribution. The data suggest more strain is concentrated into the corner region in the case of the smaller radius. As the loads are not significantly different between the two cases, the dominating effect may be the lesser area in the smaller radius corner which must support the load being shed by the flanges and web.

### 5.3 Crippling

It has been observed that after buckling, load is redistributed between the flanges, web and corners. Strains have been determined at several locations throughout loading



until failure. In considering crippling it is interesting to determine the locations of damage and driving mechanisms responsible. The strain distributions across the sections suggest that the corners themselves or the free ends of the flanges may be the sites of initial failure. The maximum measured local strain values range from 0.7 to 1.3 percent, with typical values being nominally 1 percent. At this stage it is not possible to identify clearly the failure locations or modes. However, the promising agreement between the finite element and experimental strain distributions suggests that some rational failure criteria might be developed to predict failure loads for the range of parameters included in this study.

#### 5.4 Scaling Parameters

A prime aim of this work is to investigate scaling effects in buckling, postbuckling and crippling of composite sections. The objective is to isolate scaling effects where they exist and to formulate scaling parameters. The application of mechanics principles leads directly to nondimensional parameters; for example the buckling analysis for an ideal Z-section (zero corner radius) has produced the parameter

$$\frac{N_x B_w^2}{\sqrt{D_{11} D_{22}}}$$

which when plotted against  $B_f / B_w$  condenses all data onto a single curve. Departures from this behavior represent deviation from the mechanics model or some scaling effect. In the present study the finite corner radius presents a departure from the ideal case, and of course, a new nondimensional parameter is needed to describe the model; for example a parameter such as  $r / B_w$ . If this were introduced into Figure [7], a family of curves would result. The numerical model suggests that for large  $B_f / B_w$  the corner radius is not significant relative to determining the initial buckling load, so that the parameter for the ideal model would be sufficient.

Postbuckling involves a complex redistribution of load between the various elements of the section so that the detailed geometric parameters are important. A simple means of presenting data in a nondimensional form is shown in Figures [10a,b] in which the experimental compressive loads are normalized with respect to the initial buckling load (determined from experimental load-end shortening data). Figures are presented for two values of corner radii. Note that the scales differ between the figures due to the differences in range of flange sizes considered, and that Figure [10b] contains a duplicate specimen. This normalization has the effect of producing a single curve for prebuckling behavior with regular departures in the postbuckling regime as the flange size increases. The various

postbuckling curves can themselves be normalized with appropriate stiffness parameters and an origin at initial buckling. Calculations using the Rayleigh-Ritz technique are currently underway to provide these stiffness parameters.

This method of presentation clearly shows a systematic variation in the crippling load ratio with normalized end shortening. Large flange sizes produce greater normalized load ratios and end shortening at crippling. A failure criterion is needed to investigate scaling effects in the crippling loads.

## 6. CONCLUSIONS AND FURTHER WORK

Preliminary results show that initial buckling of the graphite/epoxy Z-sections can be predicted confidently to within about 10 percent. Experimental initial buckling loads could be determined equally by shadow moire or from load-end shortening data. Generally, the nonlinear finite element analyses gave the best prediction. The analytical model, which did not account for the finite corner radius, gave satisfactory results, particularly for the cases of larger flange sizes.

Postbuckling behavior was predicted less well by the numerical model. However, generally good agreement between strain gage results and numerical analyses was obtained for the load redistribution in the postbuckling regime, even to within 2 percent of the crippling load.

Preliminary presentation of the experimental results in nondimensional form confirms the usefulness of the parameter developed for initial buckling. Further work is underway to identify postbuckling and crippling parameters.

The experimental program also contains a planned investigation of smaller and larger web sizes in order to examine the generality of the scaling parameters developed.

## Acknowledgment

This work was sponsored by the NASA Langley Research Center under Grant NAG1-343 (NASA-Virginia Tech Composites Program).

## REFERENCES

1. Morton, J., "Scaling of Impact Loaded Fiber Composites," AIAA Journal, Vol. 26, No. 8, August 1988, pp. 989-994.
2. Allen, H. G. and Bulson, P. S., Background to Buckling, McGraw-Hill Book Company (UK) Ltd., Maidenhead-Berkshire, 1980.
3. Lee, D. J., The Local Buckling Coefficient for Orthotropic Structural Sections, Aeronautical Journal, July 1978, pp. 313-320.
4. Tyahla, S. T., "Failure and Crippling of Graphite-Epoxy Stiffeners Loaded in Compression," Master of Science Thesis, Virginia Polytechnic Institute and State University, Blacksburg, Virginia, May 1984.
5. Bonnani, D. L. and Johnson, E. R., "Local Crippling of Thin-Walled Graphite-Epoxy Stiffeners," AIAA paper number 88-2251, in Proceedings of the AIAA/ASME/ASCE/AHS 29th Structures, Structural Dynamics and Materials Conference, Williamsburg, Virginia, April 18-20 1988, pp. 313-323.

Table 1. Z-section geometries included in program

flange width (in.)	web width (in.)			length (in.)
1.25	1.75*	1.25**	----	10.0
1.00	1.75*	1.25**	----	10.0
0.75	1.75*	1.25**	0.75*	6.0
0.50	1.75*	1.25**	0.75*	6.0

\* corner radius = 0.125 in.

\*\* corner radii = 0.125 and 0.25 in.  
 laminate is [+45/-45/0/90]<sub>s</sub>  
 nominal thickness is 0.04 in.

Table 2. Observed and predicted buckling loads

flange width (in.)	corner radius (in.)	Experimental (lb)		Analytical / Numerical (lb)			
		load - disp.	Moire	Analytical	FEM r=0	FEM linear	FEM nonlinear
1.25	0.125	958	1050	1056	1056	1064	1000
1.00	0.125	1349	1200	1377	1364	1378	1264
0.75	0.125	1771	2000	1950	1947	1976	1782
0.50	0.125	2462	2450	2744	2646	2692	2350
1.00	0.250	1434	1500	1377	1364	1511	1434
0.75	0.250	2173	2100	1950	1947	2262	1968
0.75	0.250	2077	2100	1950	1947	2262	1968
0.50	0.250	2951	2900	2744	2646	3171	2759

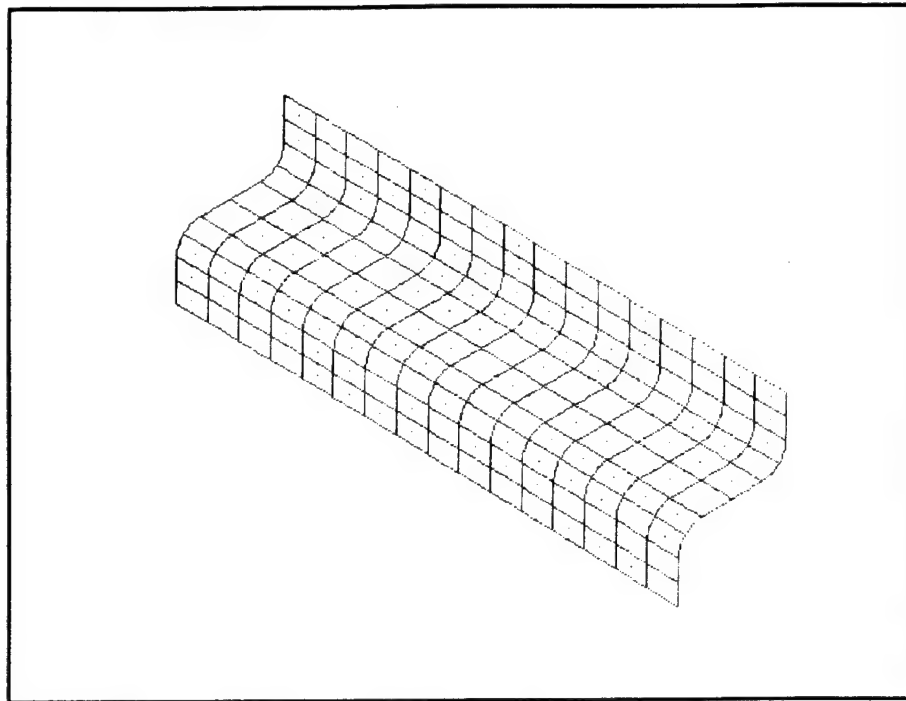


Figure 1. Typical ABAQUS finite element mesh containing 160 nine-node shell elements.

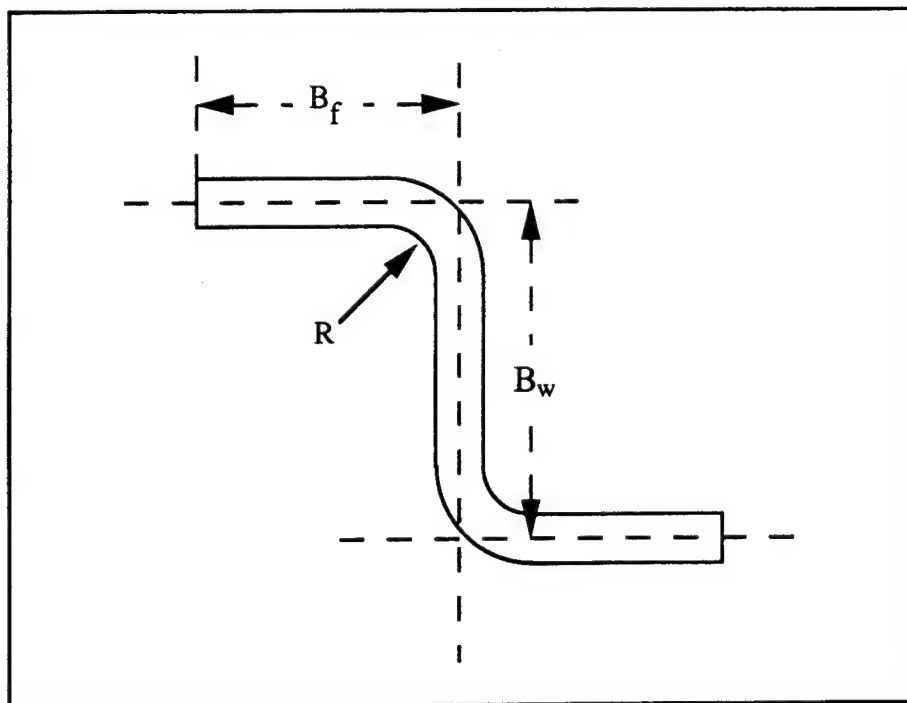


Figure 2. Convention for Z-section geometrical variables in this program

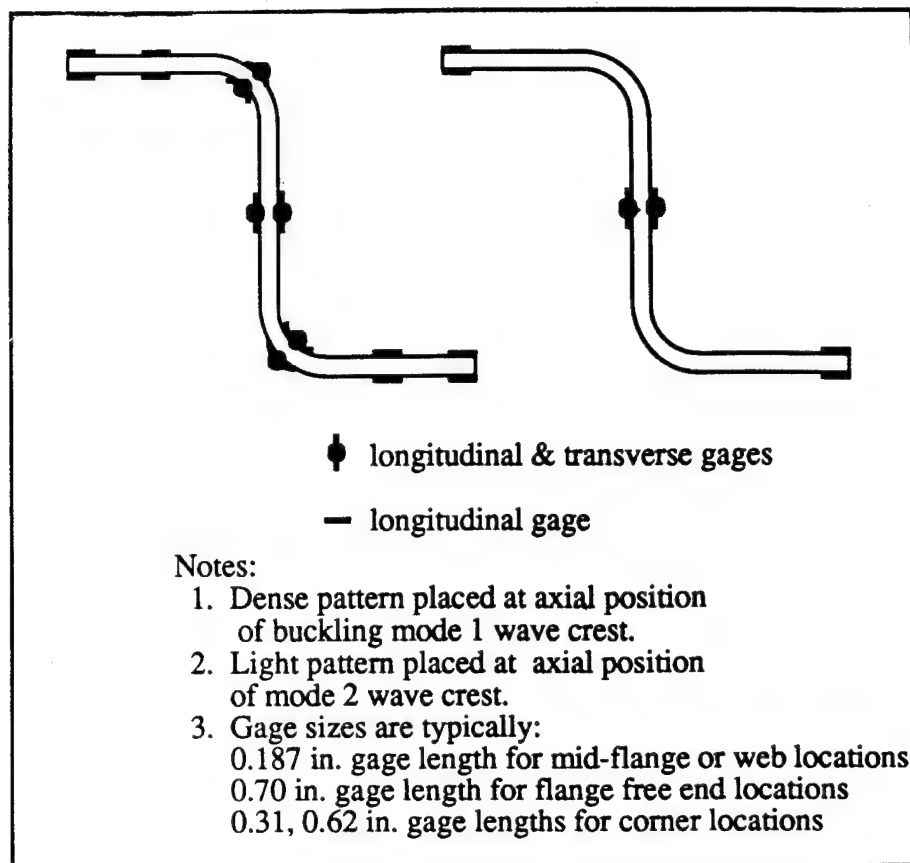


Figure 3. Electrical resistance strain gage pattern across the Z-section

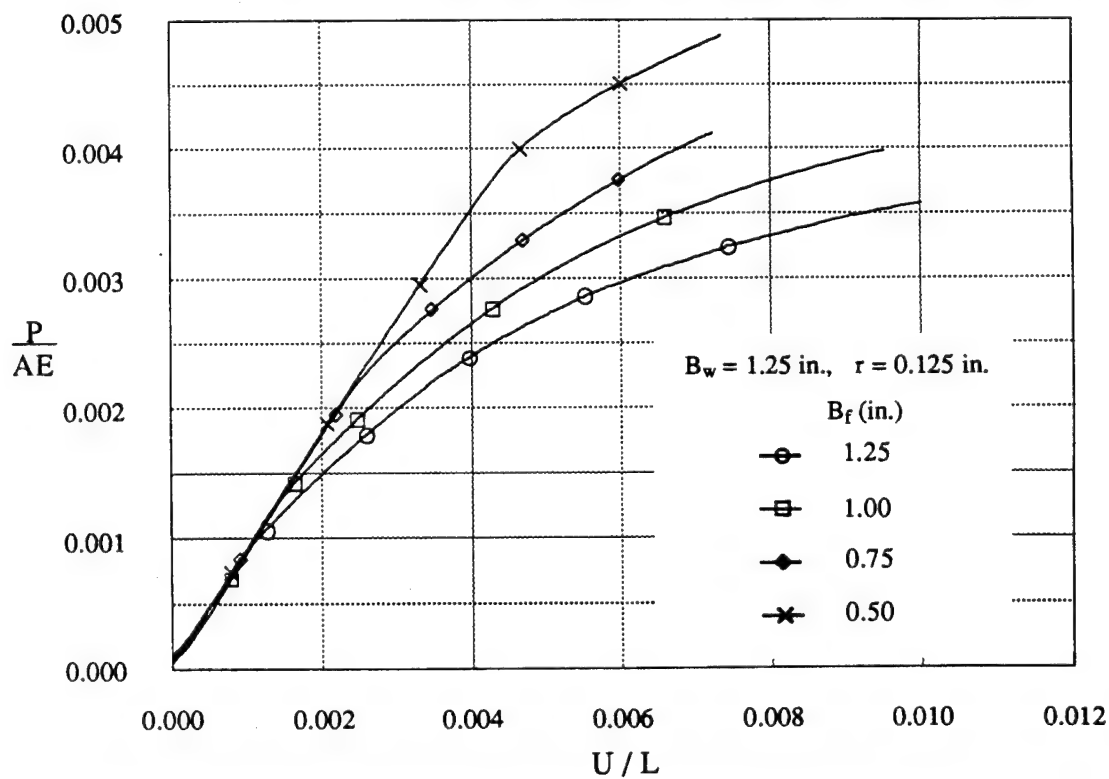


Figure 4. Normalized load versus end shortening. Load is normalized with respect to nominal cross-sectional area and equivalent longitudinal elastic modulus. End shortening is normalized with respect to original axial length.

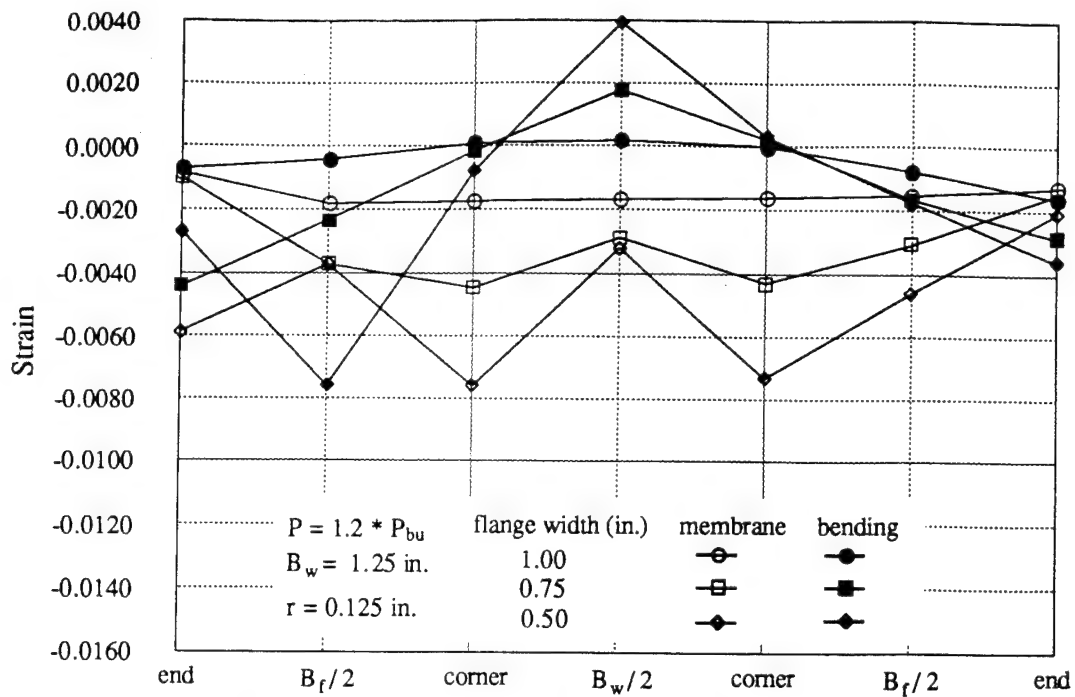


Figure 5a. Postbuckling membrane and bending strain distributions across developed cross-section as a function of the flange width. Load is 1.2 times the buckling load.

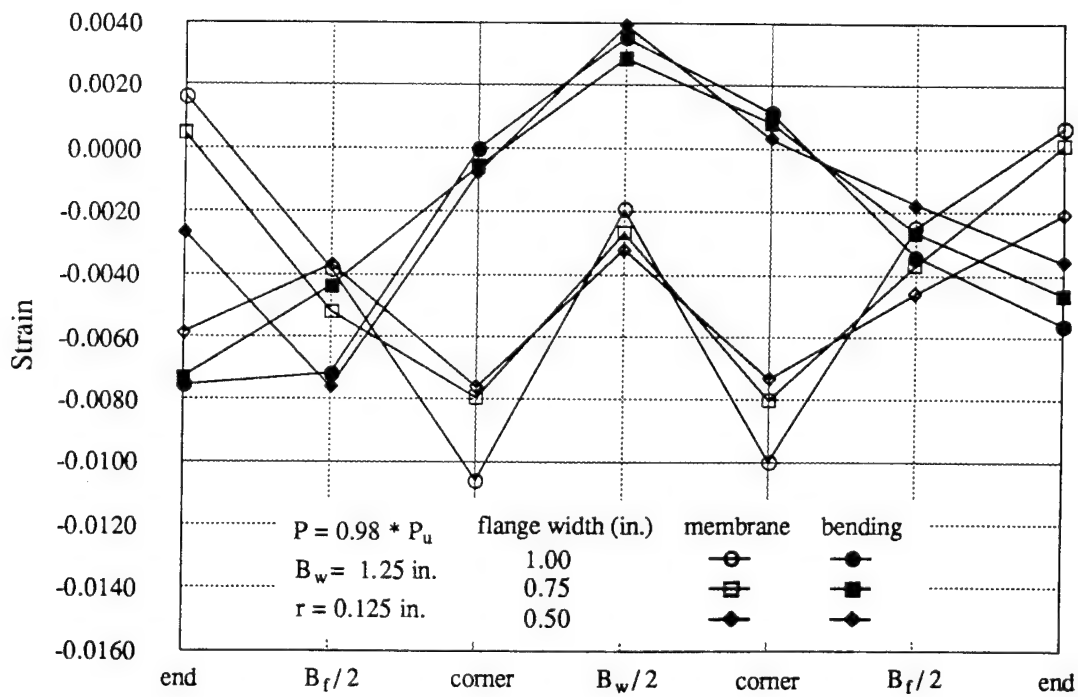


Figure 5b. Postbuckling membrane and bending strain distributions across developed cross-section as a function of the flange width. Load is 0.98 times the final failure load.

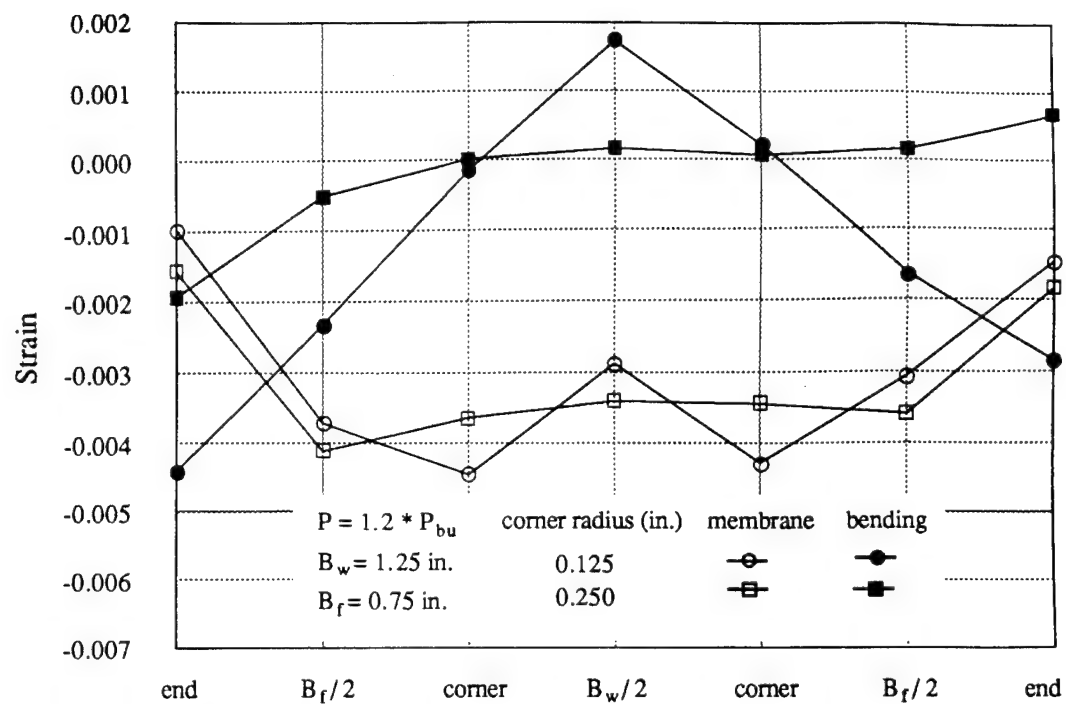


Figure 6. Effect of corner radius on the postbuckling membrane and bending strain distributions measured experimentally.

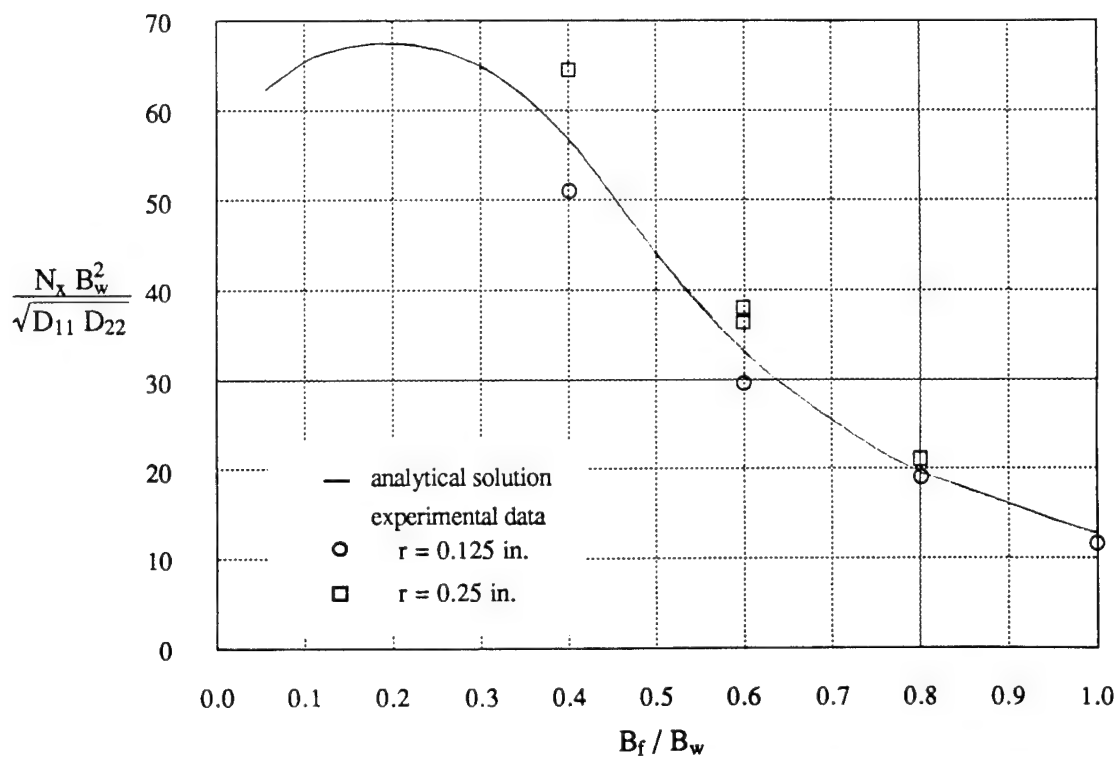


Figure 7. Normalized initial buckling load as a function of flange-to-web width ratio. The normalizing parameter was developed from the classical analysis procedure.



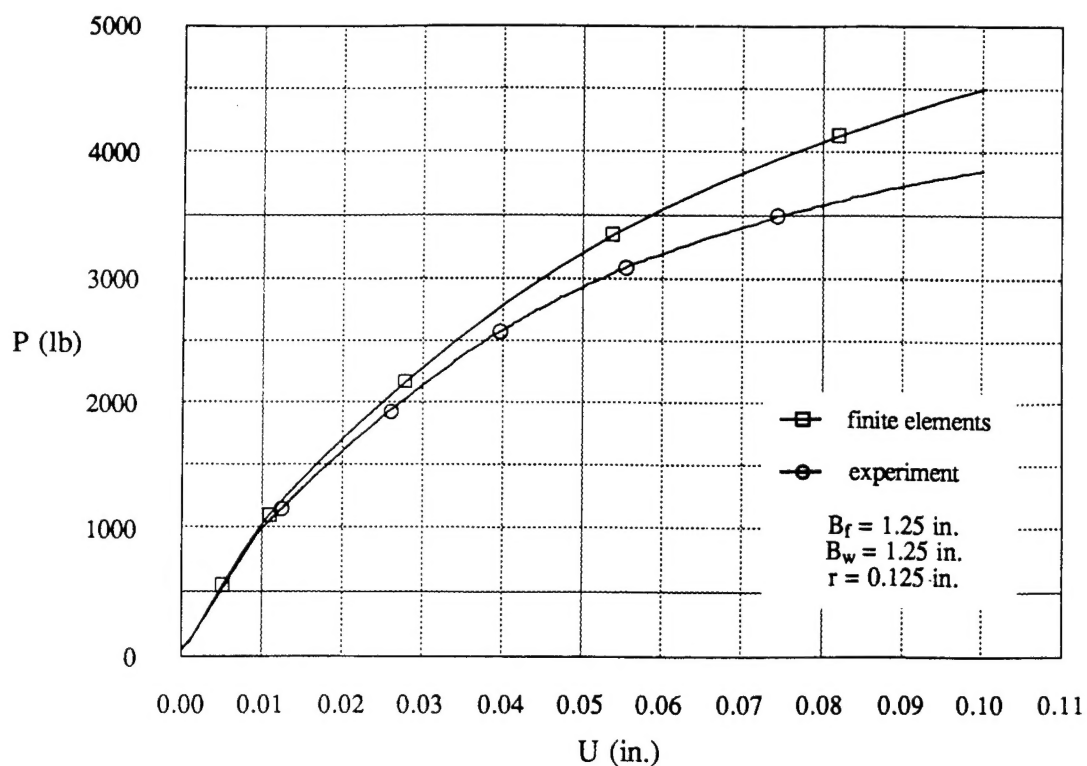


Figure 8a. Axial load versus end shortening comparison between experiment and finite element analysis for a large flange size.

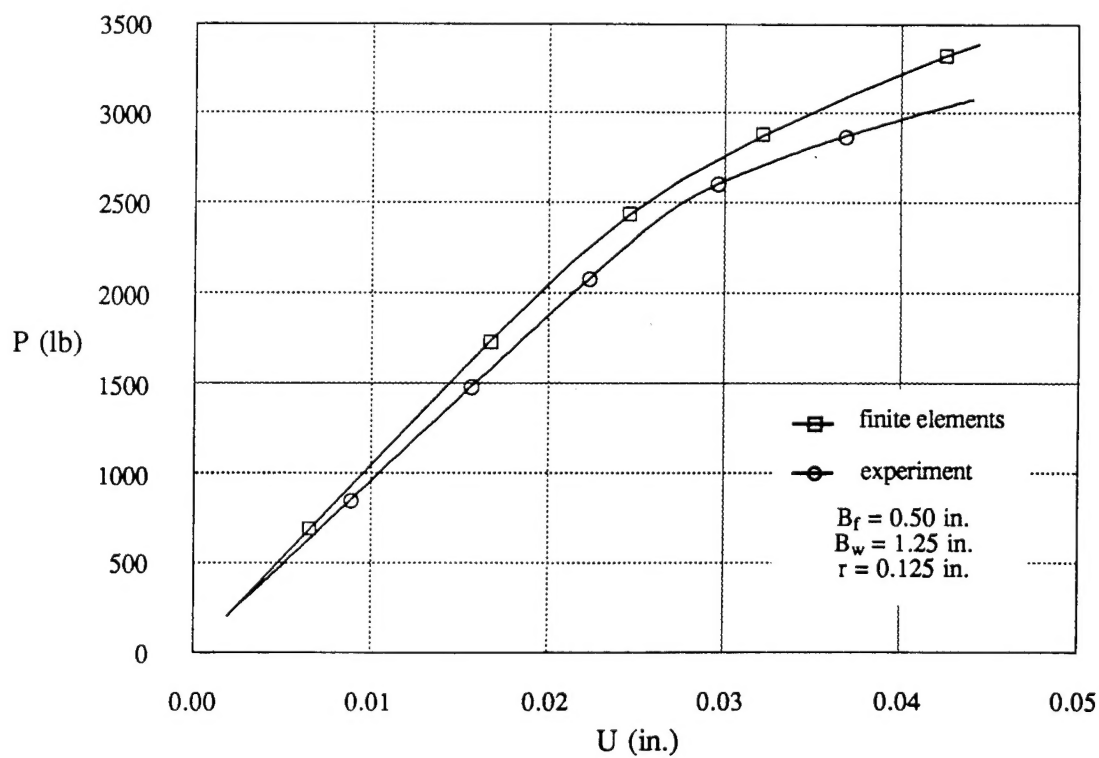


Figure 8b. Axial load versus end shortening comparison between experiment and finite element analysis for a small flange size.

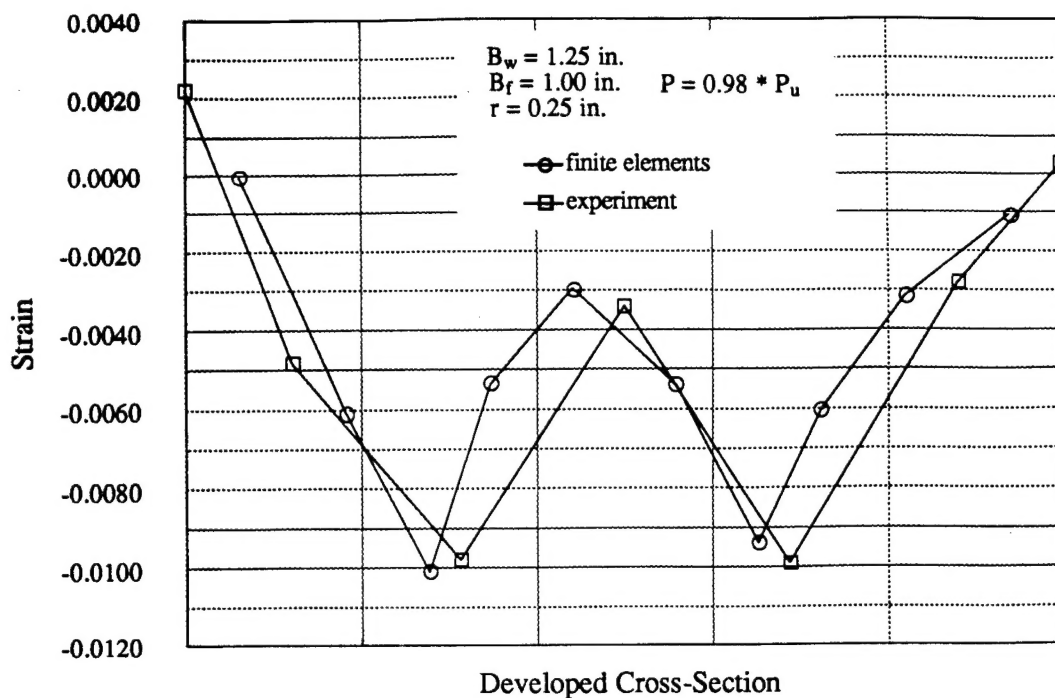


Figure 9a. Comparison of membrane strain distributions across a developed cross-section from strain gage measurements and finite element predictions. Web, flange and corner radii dimensions are 1.25, 1.00 and 0.25 in., respectively.

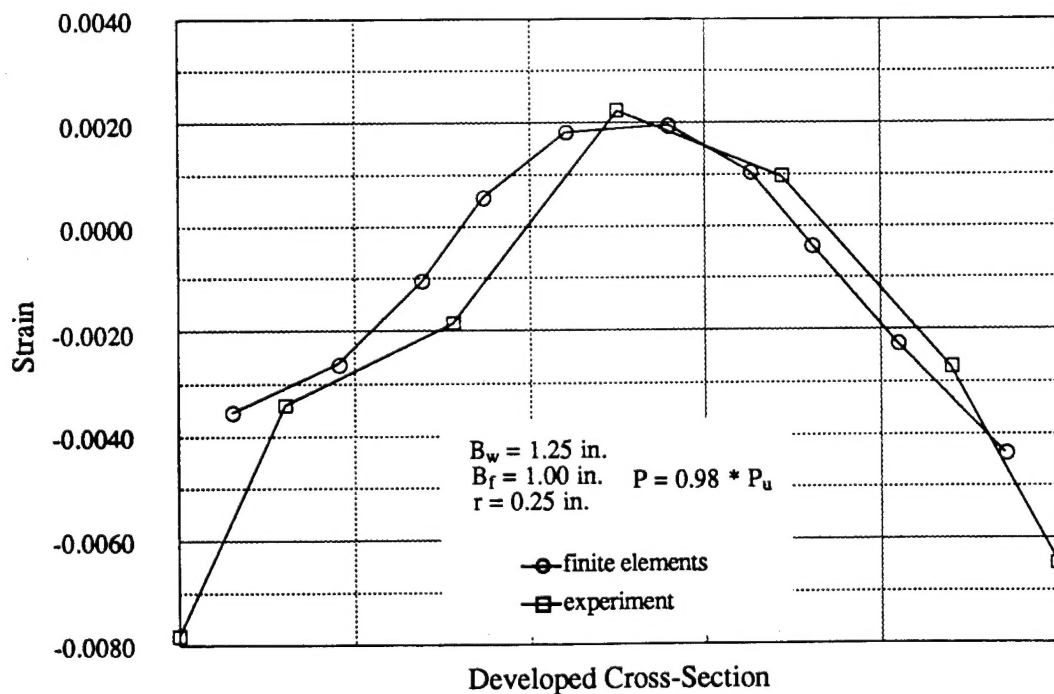


Figure 9b. Comparison of bending strain distributions across a developed cross-section from strain gage measurements and finite element predictions. Web, flange and corner radii dimensions are 1.25, 1.00 and 0.25 in., respectively.

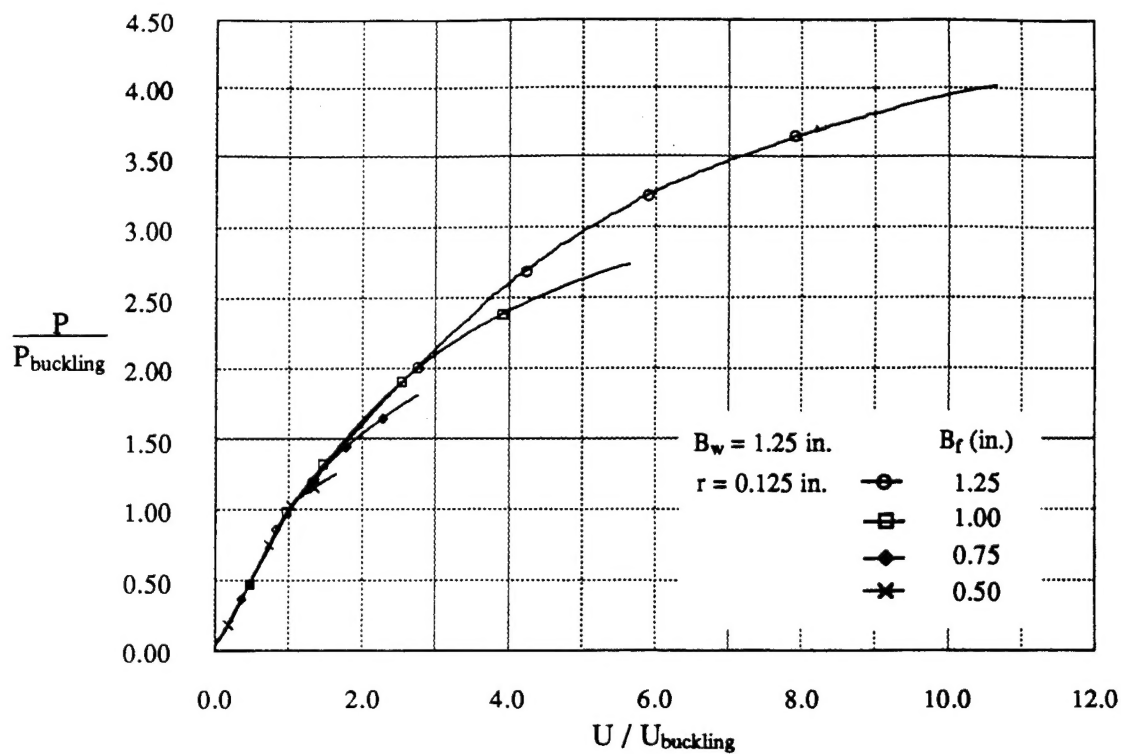


Figure 10a. Normalized axial load-end shortening response for available experimental data. Load is normalized with respect to the initial buckling load. End shortening is normalized with respect to the value at buckling. Corner radius is 0.125 in.

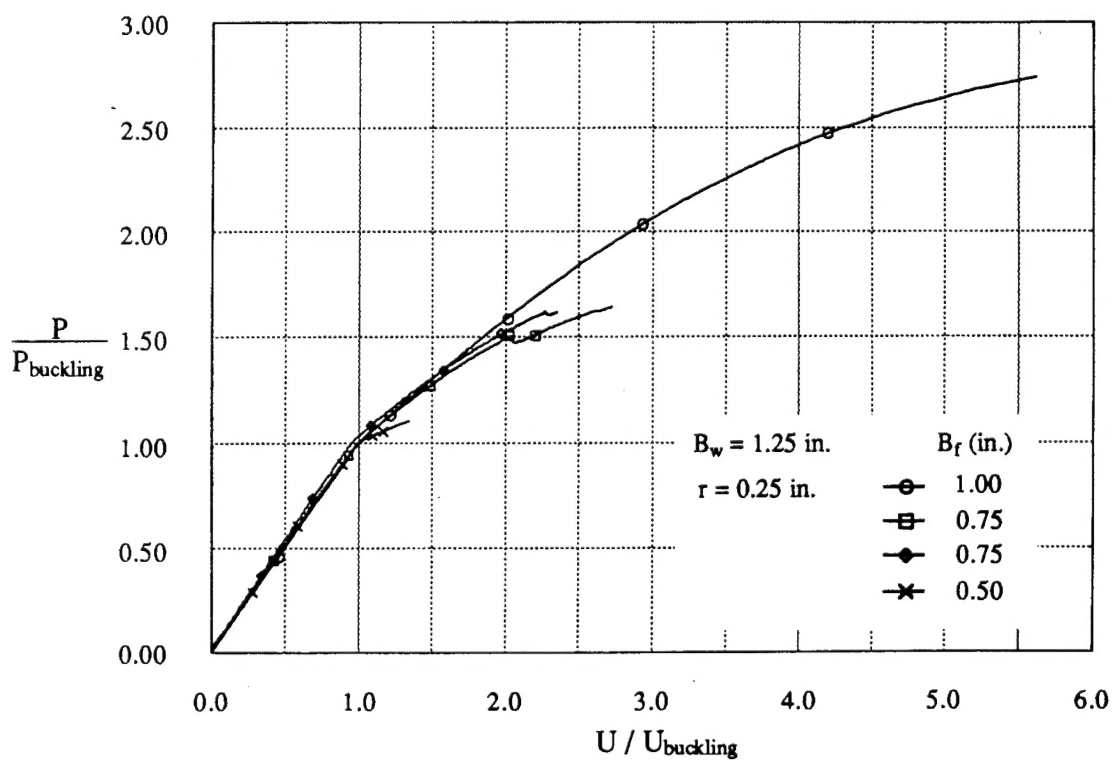


Figure 10b. Normalized axial load-end shortening response for available experimental data. Load is normalized with respect to the initial buckling load. End shortening is normalized with respect to the value at buckling. Corner radius is 0.25 in.



## Report Documentation Page

1. Report No. NASA CP-3087, Part 1	2. Government Accession No.	3. Recipient's Catalog No.	
4. Title and Subtitle Eighth DoD/NASA/FAA Conference on Fibrous Composites in Structural Design		5. Report Date September 1990	
		6. Performing Organization Code	
7. Author(s) James H. Starnes, Jr., Herman L. Bohon, and Sherry B. Garzon, Compilers		8. Performing Organization Report No. L-16832	
9. Performing Organization Name and Address NASA Langley Research Center Hampton, VA 23665		10. Work Unit No. 505-63-01-09	
		11. Contract or Grant No.	
12. Sponsoring Agency Name and Address National Aeronautics and Space Administration Washington, DC 20546, Department of Defense, Washington, DC 20301, and Federal Aviation Administration, Washington, DC 20553		13. Type of Report and Period Covered Conference Publication	
		14. Sponsoring Agency Code	
15. Supplementary Notes James H. Starnes, Jr.: Langley Research Center, Hampton, Virginia. Herman L. Bohon: Lockheed Engineering & Sciences Company, Hampton, Virginia. Sherry B. Garzon: Langley Research Center, Hampton, Virginia.			
16. Abstract This conference publication contains the proceedings of the Eighth DoD/NASA/FAA Conference on Fibrous Composites in Structural Design held in Norfolk, Virginia during November 28-30, 1989. Presentations were made in the following areas of composite structural design: perspectives in composites; applications in design; concepts in design; methodology in design, and reliability in design.			
17. Key Words (Suggested by Authors(s)) Composite structural design Composite airframe applications Composite armament applications Composite analysis methods Composite reliability		18. Distribution Statement FEDD  REVIEW for general release September 30, 1992  Subject Category 24	
19. Security Classif. (of this report) Unclassified	20. Security Classif. (of this page) Unclassified	21. No. of Pages 713	22. Price